NASA Workshop on Distributed Parameter Modeling and Control of Flexible Aerospace Systems

Compiled by
Virginia B. Marks and Claude R. Keckler

June 1994

NASA Workshop on Distributed Parameter Modeling and Control of Flexible Aerospace Systems

Compiled by
Virginia B. Marks and Claude R. Keckler
Langley Research Center • Hampton, Virginia

June 1994

Preface

A three-day workshop on distributed parameter modeling and control of flexible aerospace systems was held in Williamsburg, Virginia, on June 8–10, 1992. The purpose of the workshop was to assess the state of the art in continuum modeling and to evaluate its current state of application in the control of flexible systems. This compendium of presentations reflects the diversity in the use of continuum modeling as well as the extent of its application to various control problems.

The conference was divided into a number of sessions dealing with such topics as Structural Dynamics Modeling, Aeroelasticity Applications, Parameter Estimation, Integrated Controls-Structures Design, Control of Flexible Systems, Simulation and Modeling Software. These sessions were carried out in serial fashion to permit participants to attend all presentations.

Use of trade names or names of manufacturers in this report does not constitute an official endorsement of such products or manufacturers, either expressed or implied, by the National Aeronautics and Space Administration.

Foreword

Although significant advances have been made in modeling and controlling flexible systems, there remains a need for improvements in model accuracy and in control performance. The finite element models of flexible systems are unduly complex and are almost intractable to optimum parameter estimation for refinement using experimental data.

Distributed parameter or continuum modeling offers some advantages and some challenges in both modeling and control. Continuum models often result in a significantly reduced number of model parameters, thereby enabling optimum parameter estimation. The dynamic equations of motion of continuum models provide the advantage of allowing the embedding of the control system dynamics, thus forming a complete set of system dynamics. There is also increased insight provided by the continuum model approach.

The challenges of distributed parameter modeling include 1) overcoming the burden of the complexity of partial derivative equations, 2) developing software for model making and analysis, and 3) overcoming complacency. Workshops on continuum modeling and control serve to educate and to encourage development of needed techniques. It is hoped that these proceedings will be useful to practitioners of modeling and controlling flexible systems.

Lawrence W. Taylor, Jr.
NASA Langley Research Center
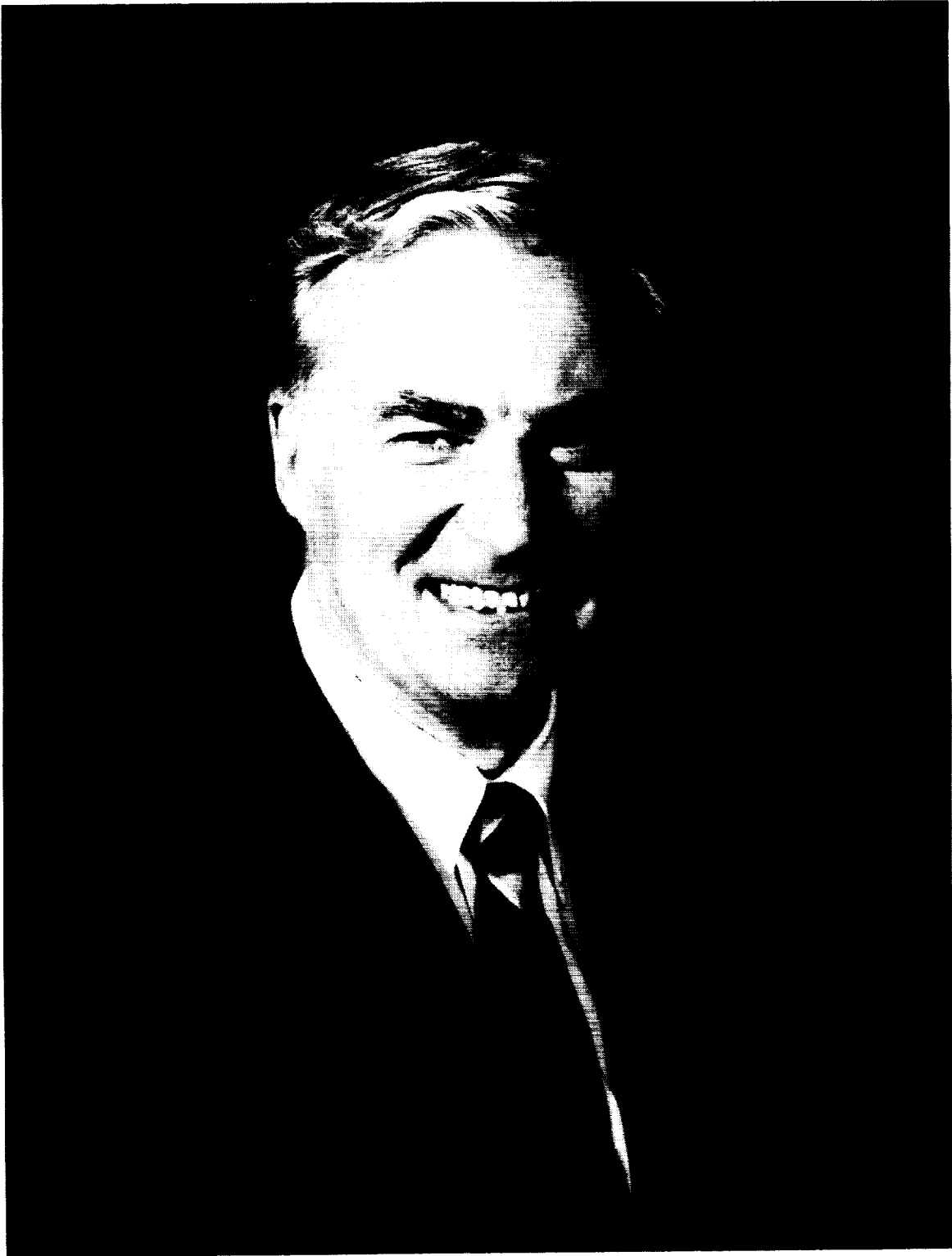
Lawrence W. Taylor, Jr.

DEDICATED
to the Memory of
LAWRENCE W. TAYLOR, JR.

These proceedings are a compilation of papers presented at the conference organized by **Lawrence W. Taylor, Jr.,** on *Distributed Parameter Modeling and Control of Flexible Aerospace Systems.* This publication is dedicated to the memory of Larry, who passed away on January 15, 1993, at the age of 59.

Larry was the Chief Scientist of Langley's Guidance and Control Division and an Associate Fellow of the AIAA. He received his bachelor's degree from the University of Kansas and his master's degree from the University of Southern California. After graduation he served two years in the U.S. Air Force as an aerospace engineer before joining NASA in 1957 at the Dryden Flight Research Center (DFRC) in California. He made major contributions at DFRC in the theoretical formulation and development of modified Newton-Raphson techniques for applying maximum likelihood estimation to system identification. These algorithms continue to be used throughout the world and were the basis for three awards from NASA and AIAA. In 1970 Larry came to Langley and later became manager of the Active Controls Project Office in 1974, with responsibility for developing and coordinating the expanding NASA program in active control.

In 1975 he was assigned to NASA Headquarters, serving three years as Deputy Director for Guidance, Control, and Information Systems in the Office of Aeronautics and Space Technology's Electronics Division. In that position he was responsible for managing NASA's research program in aircraft avionics and control. He returned to Langley to continue his research, was selected head of the Flight Dynamics Branch in 1980 and later head of the Spacecraft Controls Branch. As branch head, he led research to develop advanced system identification methodology for large space systems and was also responsible for the development of new analytical techniques for the modeling and analysis of post-stall and spin aircraft dynamics. Larry was appointed Chief Scientist of the Guidance and Control Division in 1986. He then continued his personal research in controls and distributed parameter modeling.

As an internationally recognized expert in aircraft controls, Larry was asked to serve on a wide range of technical planning committees. In addition to being author of over 60 technical papers, he was a member of the AIAA, Tau Beta Pi, and Sigma Gamma Tau. Larry also received numerous NASA and AIAA awards.

CONTENTS

STRUCTURAL DYNAMICS MODELING

AEROELASTICITY APPLICATIONS

PARAMETER ESTIMATION

INTEGRATED CONTROLS-STRUCTURES DESIGN

CONTROL OF FLEXIBLE SYSTEMS

SIMULATION AND MODELING SOFTWARE

STRUCTURAL DYNAMICS MODELING

Distributed Parameter Modelling
of Flexible Spacecraft: Where's
the Beef?

D. C. Hyland

Harris Corporation

Melbourne, Florida

Abstract

This presentation discusses various misgivings concerning the directions and productivity of Distributed Parameter System (DPS) theory as applied to spacecraft vibration control. We try to show the need for greater cross-fertilization between DPS theorists and spacecraft control designers. We recommend a shift in research directions toward exploration of asymptotic frequency response characteristics of critical importance to control designers.

Distributed Parameter System Theory:

A knife without a blade for which the handle is missing?

or

We used to worry about DPS theory's relevance to Space Structure Control but we're ok now!

D. C. Hyland
Harris Corporation

4

Some time ago, Larry Taylor asked me to give the initial presentation for this workshop. Larry encouraged me to share some of my misgivings on Distributed Parameter System (DPS) theory as an area of ongoing research activity in hopes of arousing controversy and stimulating discussions during the meeting.

Having agreed to help with the workshop, I found it quite a struggle to arrive at an appropriate title. First, a broken arm and leg suffered early last year put me into a rather futile mood, and gave rise to the melancholic thought expressed by the first title. But then, after my broken limbs began to mend, I devised the second title, reflecting a mood of recovery and optimism. Finally, backing away from undue optimism (we're not okay yet!), I settled on the title indicated on the first page. This title strikes a better balance between futility and enthusiasm. "Where's the beef?" means "What is the substantive contribution?" At least implicitly, the question admits the possibility that there is substance. Indeed, I approach this field as a worried friend, concerned to find precisely those areas in which DPS theory can truly contribute.

- A Few Preliminary Observations -

* Distributed Parameter System theory is a necessary part of our engineering culture - should be widely taught and learned.

* There are so many ways in which the usual lumped parameter models differ from the actual system. A knowledge of DPS theory heightens our awareness of these crucial differences.

* Provides unifying framework for understanding -e.g. connections between modal dynamics and wave propagation.

* Crucial for settling matters of general principle - e.g., existence questions, controllability, stability guarantees, etc.

In any case the criticisms voiced here have nothing to do with the intrinsic merit of the DPS field as a valuable body of mathematical knowledge, but are concerned with where it has been and is going as an unfolding research enterprise. We should take particular care to establish how DPS theory fits in (or whether or not it fits in) to design practice. Unfortunately, many people who build working systems consider DPS research as a form of "middle-class welfare." To counter this perception we need to honestly identify the aspects of DPS theory that are truly essential to control engineering.

First, it is reasonable to observe the intrinsic merits of DPS as a body of knowledge, apart from its *direct* relevance to applications. These merits are listed in the panel. The reader will note many papers in the Workshop that develop these crucial areas of value.

Having said all this, the problem with the DPS research enterprise can be stated in terms of pins and angels. Recall the medieval theological controversy: "How many angels can fit on the end of a pin?" If you are a theologian, then it's quite appropriate to argue this question. On the other hand, if you are a pin manufacturer, the question is irrelevant and it is your duty to worry about other aspects of pins. The trouble comes when theology is mixed in with manufacturing!

First, one is witnessing theology (not engineering) when one hears claims of *universal, infallible* truth. An example is the common argument for adopting a DPS theoretical setting, namely that DPS models are the only models that truly capture the underlying physical reality of aerospace structures. In the panel we list two of the many ways in which this claim is refuted. Indeed, as are all other models, DPS models are also inherently approximate.

In fact, the claim considered here is essentially a claim to guru-hood -i.e., the unique possession of arcane, transcendent knowledge.

Distributed Parameter System Models are Superior Because They Capture the Underlying Physical Reality of Aerospace Structures

---

* Quantum Mechanics (not continuum mechanics) prevails at small scales; at sufficiently high frequency there are no modes.

* Real Sensors (for feedback control) have limited resolution
  ☞ observable closed-loop system is necessarily finite (albeit large) dimensional.

The trouble is, the claim of transcendent wisdom is a very heavy burden. The more extreme the pretension, the more severe the embarrassment. One of the most obvious pretensions is that DPS theory can model infinitely many modes.

The panel sketches the behavior of the "mode count," $N(\omega)$ (number of modes below a given frequency) as a function of frequency for a "simple," simply-supported beam. The mode count function gives at least a rough idea of the frequency spacing of adjacent modes - a significant characteristic for control design considerations. It is obvious from the $N(\omega)$ chart that the vast majority of DPS work that postulates classical Bernoulli-Euler models for beams, succeeds in modelling infinitely many modes completely erroneously!

Distributed Parameter System Theory can Model
Infinitely Many Modes ...

... with infinitely many errors:
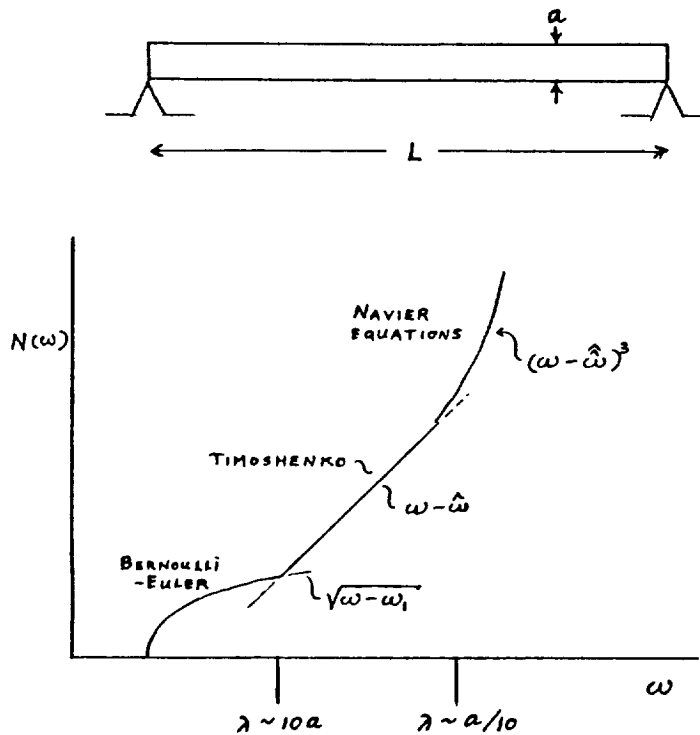
For example, even the gross number of modes per octave band may be completely wrong.

Of course, the essence of guru-hood is the claim to secret, esoteric knowledge, without which the engineering problems can not be solved. An often implied, subliminally repeated message is that DPS theory is an absolute prerequisite to successful vibration control design. On the contrary, numerous successful control designs *have* been arrived at without the use of DPS theory (but using control theory) and have been verified experimentally. Indeed, we have yet to see an experimental result that has used DPS theory in a truly substantive way for control *design*.

Of course there are interesting DPS theoretical results that pose qualitative warnings to the designer -e.g., the nonconvergence of LQG design if system dissipation is neglected, the inherent instability of infinite-dimensional systems under certain types of feedback when transport delay is introduced, etc. However, most of these qualitative warnings that are relevant to design could have been formulated without DPS theory. In place of the DPS postulate one could use the hypothesis that the plant is a finite, but arbitrary large dimensional system.

At this point, enough said about theology. Let us consider DPS from the point of view of pin manufacturers (make 'em good and cheap). Let us honestly discuss the aspects of DPS modelling that *are* pertinent to vibration control design. To begin such a discussion, I think we need to return to some elementary *control design* concepts, e.g., the concepts of phase stabilization, gain stabilization and robust performance. These items are now discussed in turn.

DPS Theory is an Absolute Prerequisite
to Successful Vibration Control Design!

---

* Numerous successful vibration control designs have been arrived at without use of DPS theory (but using *control theory*) & verified experimentally - see e.g., NASA CSI Guest Investigator Program, Phase I.

* Try to identify experimental results that have used DPS theory in a substantive way for control *design!*

* What aspects of DPS modelling *are* pertinent to vibration control design?

   To answer this, we need to get back to some elementary *control design* concepts, e.g.:
      • Phase Stabilization
      • Gain Stabilization
      • Robust Performance

First recall the Nyquist diagram - that simple but comprehensive way of visualizing the structure/control interaction and the basic design problem. As sketched here, the Nyquist diagram (assuming rate sensing) is a sequence of loops. Where the loops are large, one tries to shape the phase so that they fall into the 1st or 4th quadrant (phase stabilization). Where phase is bad, one tries to shape gain so that the magnitude is small, thereby avoiding -1 (gain stabilization). These considerations provide a guide to modelling fidelity and simplification. For example, it is clear that structural modes that have insignificant performance impact in the open-loop *and* are phase stabilized can safely be deleted from both open and closed-loop models. The same can be said for gain stabilized modes outside the controller bandwidth. There may be (and perhaps are) infinitely many such ignorable modes. For practical fidelity, design models should include the modes contributing most to open-loop performance degradation and the modes near the unity gain cross over points or in the band over which cross overs occur frequently. The size of such practical models is usually quite modest. Thus, ignoring elementary control design insights can grossly exaggerate the dimensionality problem.

Remember Mr. Nyquist?

Gain stabilized modes
may be deleted from
O.L. and C.L. models

Phase stabilized and O.L.
performance insignificant
modes can be deleted from
O.L. and C.L. models

There may be infinitely many
such "ignorable" modes
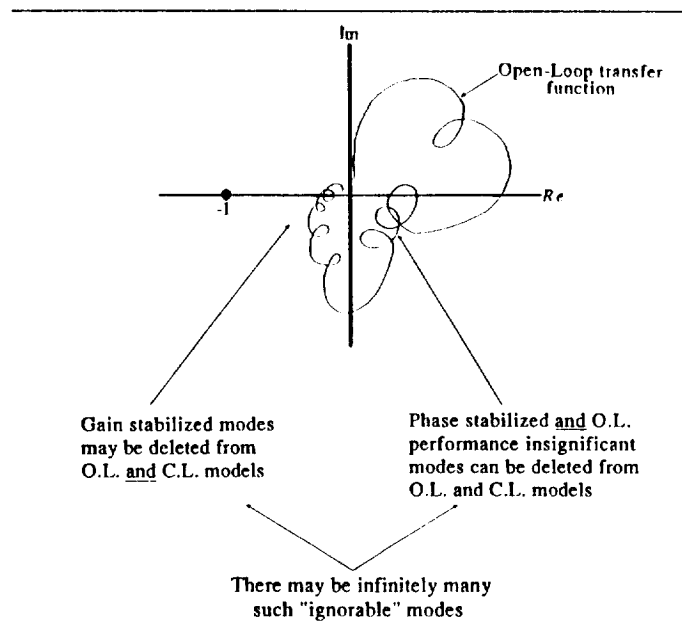
In practice control design models must include:

1. O.L., performance-significant modes
2. modes near (unity gain) cross over

* Size of such models is usually modest.
* Ignoring *control design* insights can grossly exaggerate the dimensionality problem.

To illustrate the occurrence of numerous ignorable modes consider frequency response test data and modelling for the NASA/MSFC ACES test bed*. This test bed structure actually has over 40 modes below 10 Hz, as determined via modal survey. But, as shown in this frequency response function (FRF) and corresponding Eigensystem Realization Algorithm (ERA) model, relatively few of the modes show up in the actuators-to-sensors transfer functions that contain the information pertinent to control design. This occurs because most modes are insignificant to performance and control. In fact, by appropriate control design, we manage to phase stabilize these modes so that they are ignorable in the closed-loop.
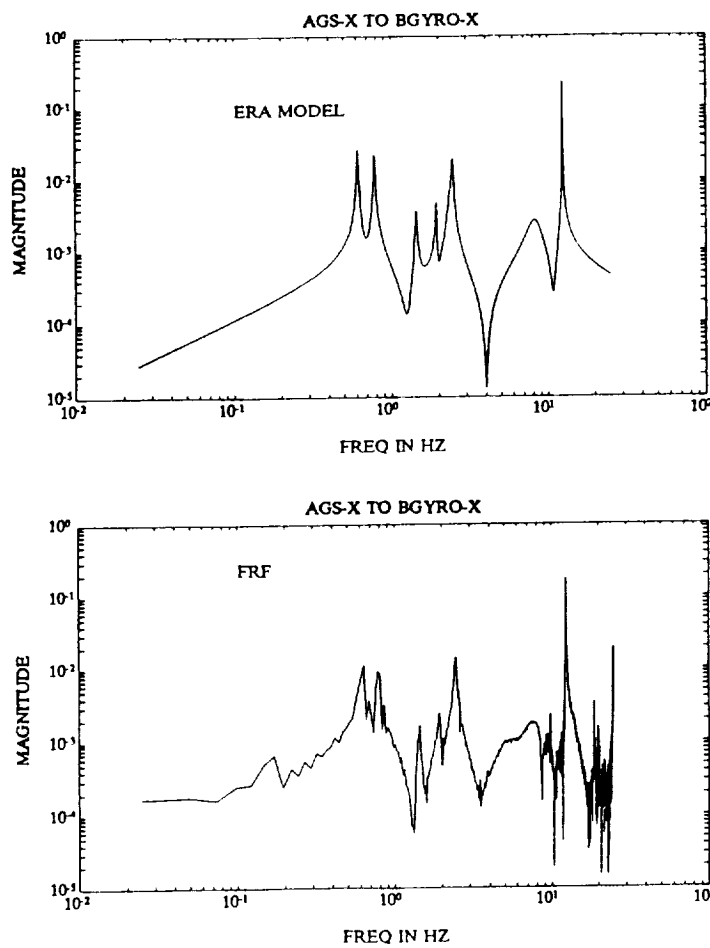
The ERA model for the AGS-X to BGYRO-X loop closely resembles the FRF generated fro test data.

*   E. G. Collins, Jr., D. J. Phillips, and D. C. Hyland, "Design and Implementation of Robust Decentralized Control Laws for the ACES Structure at Marshall Space Flight Center," NASA Contractor Report 4310, Langley Research Center, July 1990.

12

For the reasons discussed above, real life design models are of modest dimensions. This is illustrated here by tabulation of the dimensions of models used in our NASA CSI Guest Investigator Program*. As can be seen for ACES, one can often break the problem into decentralized pieces; the size of the models for each piece may be very low indeed.

To repeat: The dimensionality required of models is best judged using *control design* insights.

A Compendium of Dimensions for Harris NASA
CSI GIP Phase I Models & Controllers

Test Article	Controller	Model Order	Controller Order
ACES (Has > 40 Modes under 10 Hz)	AGS-X to BGYRO-X	17	4
	AGS-Y to BGYRO-Y	19	6
	IMC-X to DET-Y	4	3
	IMC-Y to DET-X	4	3
	Total, Decentralized	44	16
Mini-MAST	Decentralized	40	24
	Centralized	54	33

* See:

E. G. Collins, Jr., J. A. King, D. J. Phillips and D. C. Hyland, "High Performance Accelerometer-Based Control of the Mini-Mast Structure," *AIAA J. Guid. Contr. Dyn.*, Vol. 15, pp. 885-892, July 1992.

E. G. Collins, Jr., D. J. Phillips, and D. C. Hyland, "Robust Decentralized Control Laws for the ACES Structure," *Contr. Sys. Mag.*, Vol. 11, pp. 62-70, April 1991.

Next, let us discuss stability robustness and performance robustness. The motivation for a concern with robustness is illustrated here. Real structures differ from their idealizations in numerous ways, including nonuniformities in stiffness and inertia, nonideal boundary conditions, etc. Even when such errors appear to be insignificantly small, there may be a very significant impact on sufficiently high frequency dynamics. Thus we need control system robustness to deal with the sensitivity of structural model characteristics to modelling errors. But robustness with respect to what?

SENSITIVITY TO MODELLING DATA
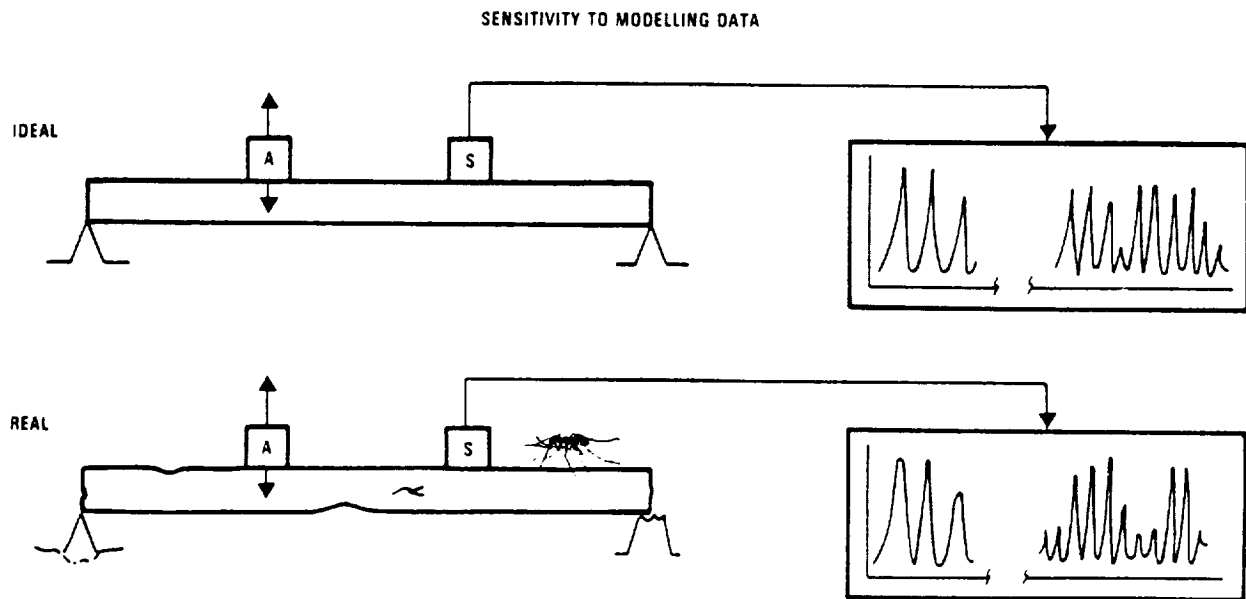
- SLIGHT ERRORS IN PHYSICAL MODELLING — LARGE ERRORS IN HIGH ORDER MODES

- DPS MODELS CAN ENCOMPASS ONLY LIMITED INFORMATION

- ARE SUCH MODELS MEANINGFUL WITHOUT CHARACTERIZATIONS OF UNCERTAINTY?

- WHAT INFORMATION MUST DPS MODELS REFLECT?

- SURELY THOSE FEATURES THAT REMAIN "SHARP" DESPITE ERRORS IN DETAIL

The usual concern is robustness with respect to stability. But even when one presumes collocated actuators and sensors and, as in the reference cited in the panel, one adopts an LQG design that is positive real (hence inherently stable), one does not resolve all robustness questions. This is because robust stability does not imply robust performance, and it is reliable performance that we must ultimately secure.

To illustrate the above point, the positive real LQG design recommended in the cited reference was applied to a single mode (with a nominal value of 10 Hz for the resonant frequency). The chart at the bottom of the panel shows, for various cases, the magnitude of the transfer function from the disturbance to the structural velocity. When the model frequency assumes the 10 Hz value used in the design model, it is seen that the controller greatly attenuates the open loop response. However, a second pair of curves show the open and closed-loop frequency response magnitudes for an off-nominal value (11.5 Hz) of the frequency. In this case, the closed-loop performance is little better than the open-loop behavior. Thus, although the system remains stable, the system performance is very sensitive to modelling error. To achieve practical results that produce substantial and reliable performance benefits from active structural control, we need to secure robustness with respect to performance. This need has been appreciated for some time and some responsiveness on the part of DPS theorists is overdue.

Robust Performance ≠ Robust Stability
Example: Positive Real LQG Control

Explicit LQG Solution (One Mode) From:

A.V. Balakrishman, *Proc. 5th NASA/DoD CSI Technology Conference*, Lake Tahoe, Nevada, March 1992.

Transfer function from
disturbance to structure
velocity
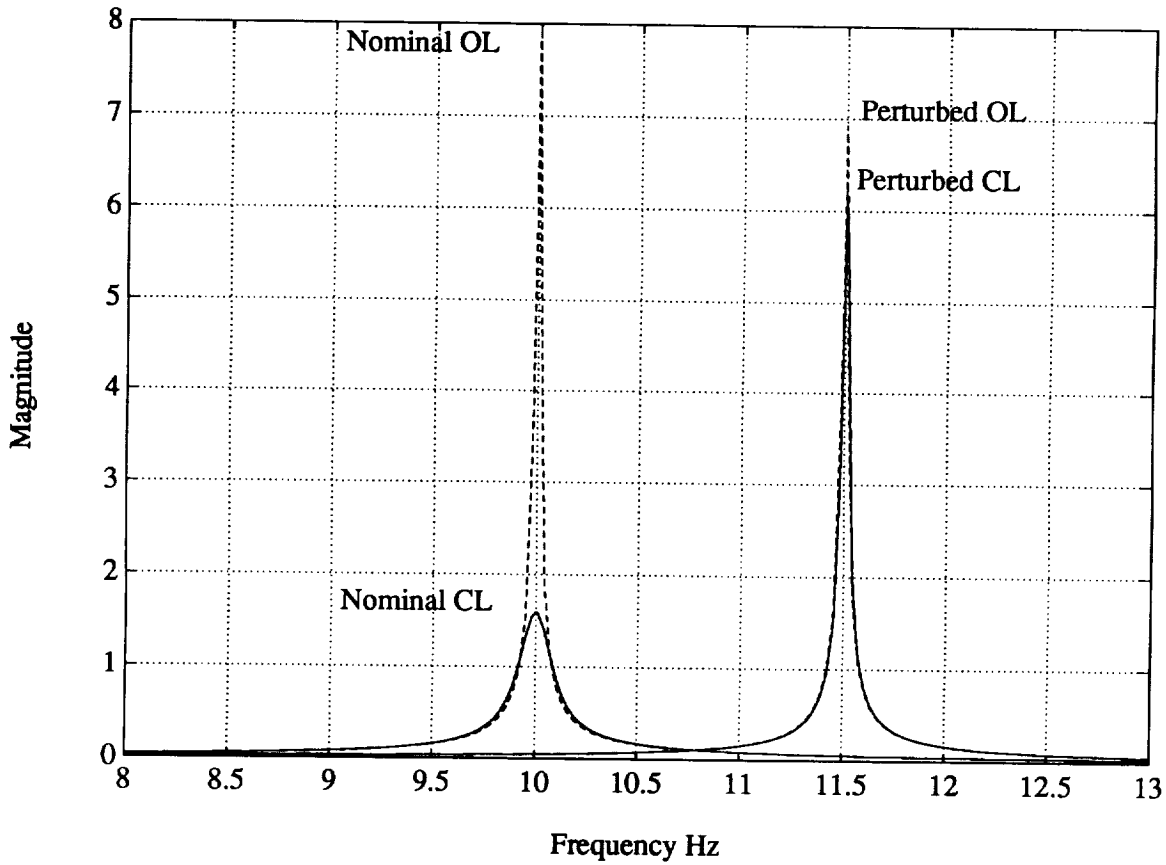
Note that LQR or LQG designs have been (and remain) the controls paradigms for DPS developments. Unfortunately, it has been known for quite a long time that LQG design is *not* robust[*] and that the complexity (dimension) of LQG controllers is often prohibitive for implementation. For these and many other reasons, control theory has moved far beyond LQG (μ-synthesis, Ω-bounds, multivariable Popov synthesis, etc). We recommend that DPS control developments need to more fully acknowledge the evolution of *control theory* over the past decade.

Model of "DPS Control Theory Results" Generation

Finite-Dimensional
Setting

Semi-Group Theory,
∞-dimensional Hilbert
Space

LQR or LQG design —— Translate ——> DPS control
result #1 —— assumptions ——> result #1
& notation

LQR or LQG design ——————————> DPS Control
result #2 ——————————> result #2

.   .
.   .
.   .

---
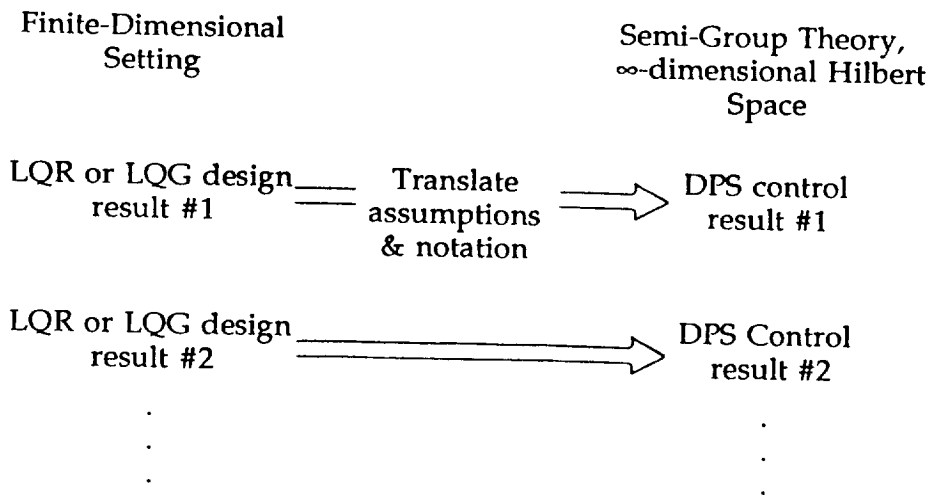
* LQG design is *not* robust

* Complexity of LQG controllers often prohibitive

* For these and many other reasons, *control theory* has moved far beyond LQG

[*] For the famous counterexample, see:

J. C. Doyle, "Guaranteed Margins for LQG Regulations," *IEEE Trans. Autom. Contr.*, Vol. AC-23, August 1978, pp. 756-757.

For nonrobust LQG performance in connection with realistically complex systems, see:

D. S. Bernstein and S. W. Greeley, "Robust Controller Synthesis Using the Maximum Entropy Design Equations," *IEEE Trans. Autom. Contr.*, Vol. AC-31, pp. 362-364, 1986.

Lest it be thought, at this point, that I would bury DPS theory, let me point out that it's a friend's part to rebuke a friend's errors. We firmly believe that there are aspects of DPS modelling that *are* pertinent to vibration control design. When all is said and done, there are people facing *real* problems in controlling real distributed parameter systems.

To link up more fully with the real world, we need to acknowledge that in actual practice, a control design model is tantamount to a complete set of transfer functions. This is rigorous if all performance variables are also sensed variables and is approximately true otherwise. Control designers want DPS theory to provide them the tools for modelling the external (frequency domain) representation of DPS. In particular, we need the capability to estimate or over-bound certain key aspects of the high frequency phenomena. The information needed is not the details of all modes but just a few critical parameters. As is clear from the following discussion, these critical high frequency parameters pertain to phenomena entirely beyond the reach of lumped-parameter models and can only be addressed via DPS theory.

Control-Design Model is Equivalent to the set of transfer functions from all actuator commands to all sensor outputs - e.g.,

MHPE L1 Velocity Estimate; Open Loop vs. New Analog Closed Loop

MHPE L1 Velocity Estimate; Open Loop vs. New Analog Closed Loop

Frequency
limit of modelling
or test-data
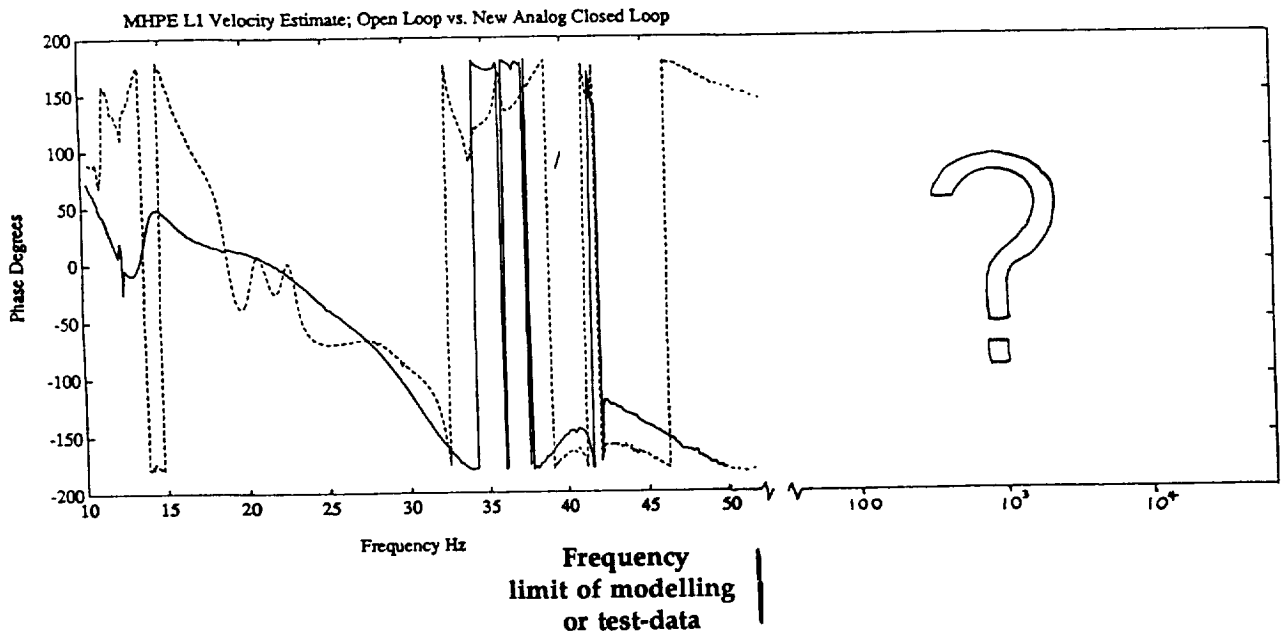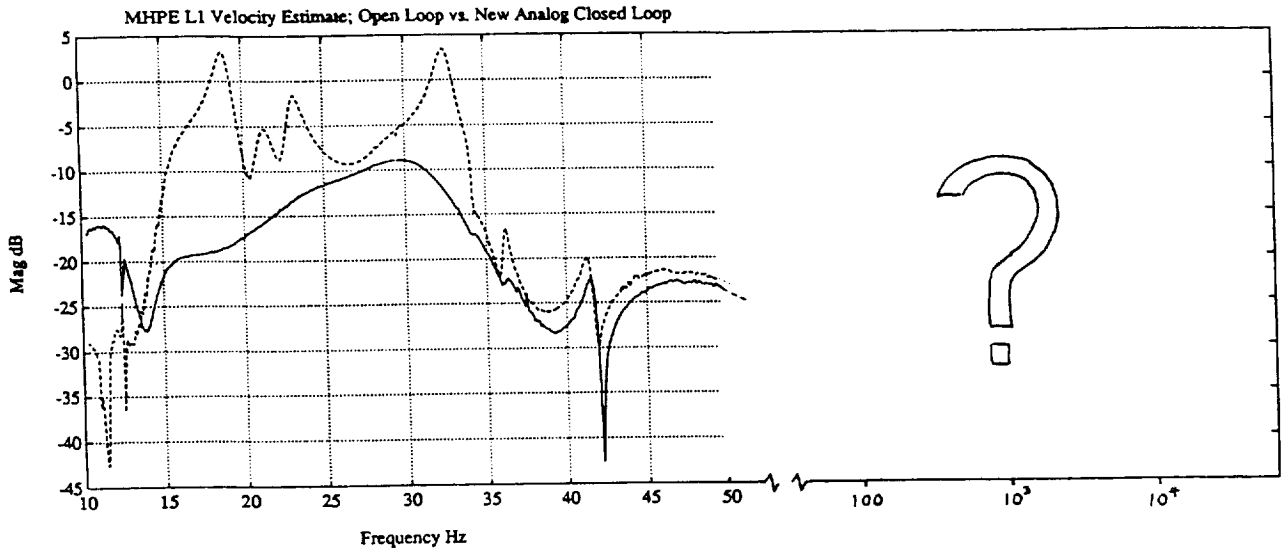
We need the ability to estimate certain key aspects of the high frequency phenomena (not details of all modes but just a few critical parameters).

19

The most critical design information sought is: Where and how to roll-off? In this panel, we highlight specific requirements. G denotes the compensator gain matrix and b_κ and c_κ are the actuation and sensing "signature vectors" for the κth mode. In other words the vector b_κ contains the actuator modal influence coefficients for the κth mode.

The graphs show, in histogram form, various components of closed-loop modal dampings. The closed-loop modal dissipation has an inherent component, d_κ, and a control component given as $Re(b_\kappa^T G c_\kappa)$ from a small gain asymptotic approximation. At high frequency, phase goes bad (due to instrumentation, communication delay, etc.) and one needs to roll off $\|G\|$. As illustrated in the charts sketched here, the design challenge is to get from the large gain, phase-stabilizing G at in-band modes to low gain, gain-stabilizing F on out-of-band modes. The lower chart in the panel shows when this is properly done. "Rolling-off" the controller to guarantee the stability of high frequency dynamics requires key information on all modes above cross-over that can only be provided by distributed parameter models. In particular, the minimum frequency separation is needed to determine "how fast" to roll-off, while the minimum open-loop dissipation and maximum modal signature gains are essential to knowing how small $\|G\|$ must be to gain-stabilize.

If DPS theory can respond to the challenge of illuminating key high frequency characteristics of the types described above, then a truly substantive and practically useful contribution will have been made.

Most critical design information:

Where and how to roll-off

$G \triangleq$ compensator gain matrix (including actuator & sensor dynamics)

$b_\kappa, c_\kappa \triangleq$ κ^{th} mode actuation and sensing signature vectors

Closed-loop modal dissipation

$Re\ (b_\kappa^T G c_\kappa)$

$d_\kappa = \ |\ 2\ \min\ \eta_\kappa \Omega_\kappa$

$d_{\kappa+1}$

$d_{\kappa+2}$

$\omega \rightarrow$

Ω_κ

$\Omega_{\kappa+1}$

In-Band Modes

Phase goes bad due to hardware limitiations. If |G| is not rolled off, unstability results

$Re\ (b_\kappa^T G C_\kappa)$

$\leq$ |b| |c| |G|

d_κ

$d_{\kappa+1}$

$\omega \rightarrow$

Ω_κ

$\Omega_{\kappa+1}$

Ω_κ

|G| properly rolled off, out-of-band modes gain stabilized
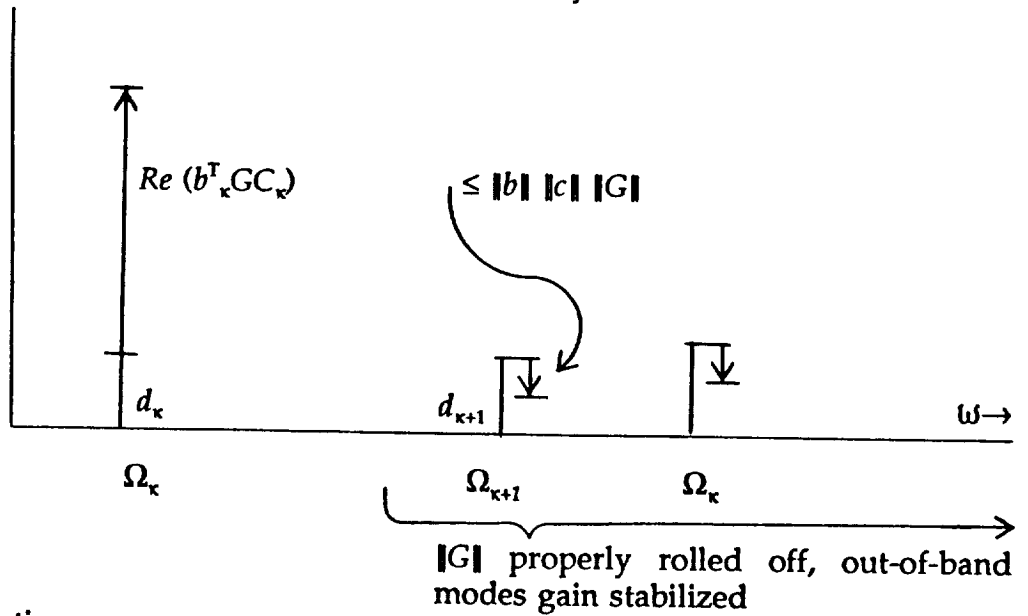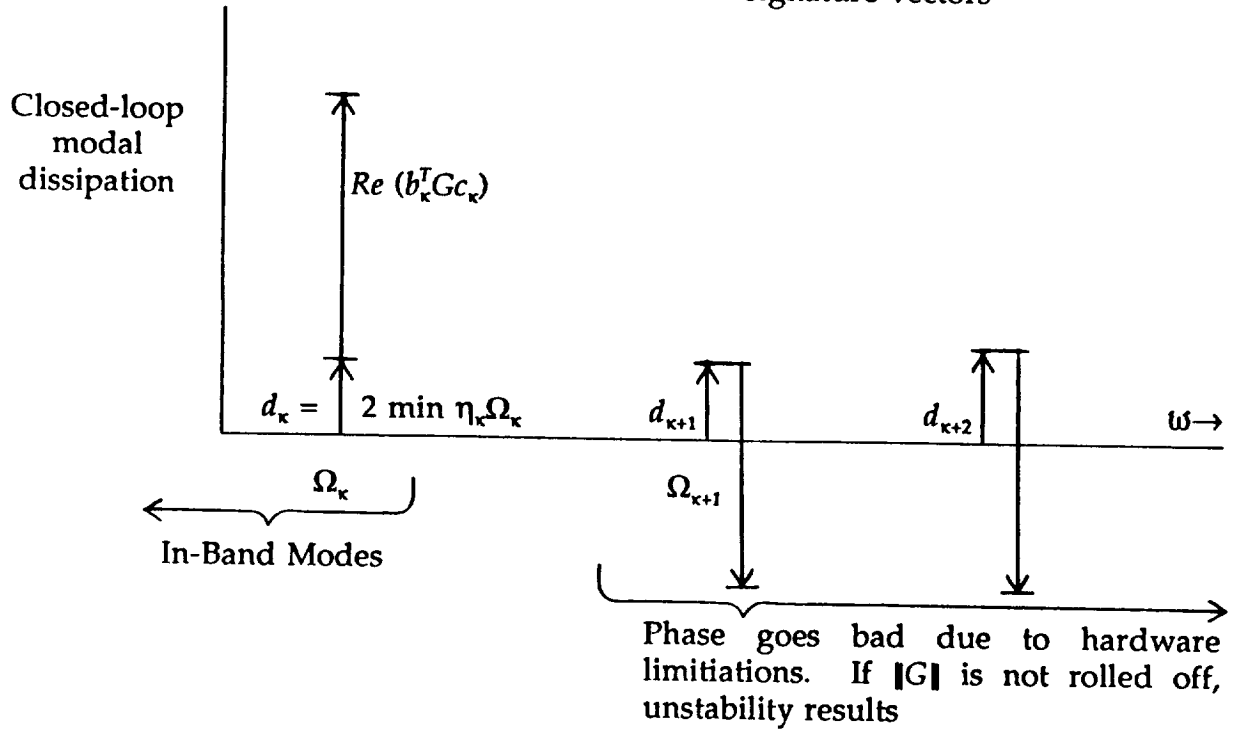
Key DPS Information:

Minimum O.L. dissipation	:	Min $\eta_\kappa \Omega_\kappa$
Minimum frequency separation	:	Min $|\Omega_{\kappa+1} - \Omega_\kappa|$
Maximum modal signature gains	:	Max $|b_\kappa|$, Max $|c_\kappa|$

21

In closing, I fling down the gauntlet! Here's the Multi-Hex Prototype Experiment (MHPE). This is one of the most "traceable" vibration control test beds. The MHPE has been operational for the past four years at Harris and is open to guest researchers. If you disagree with my criticisms, show how MHPE may be *better* modelled and/or controlled *specifically* by virtue of application of DPS theory!
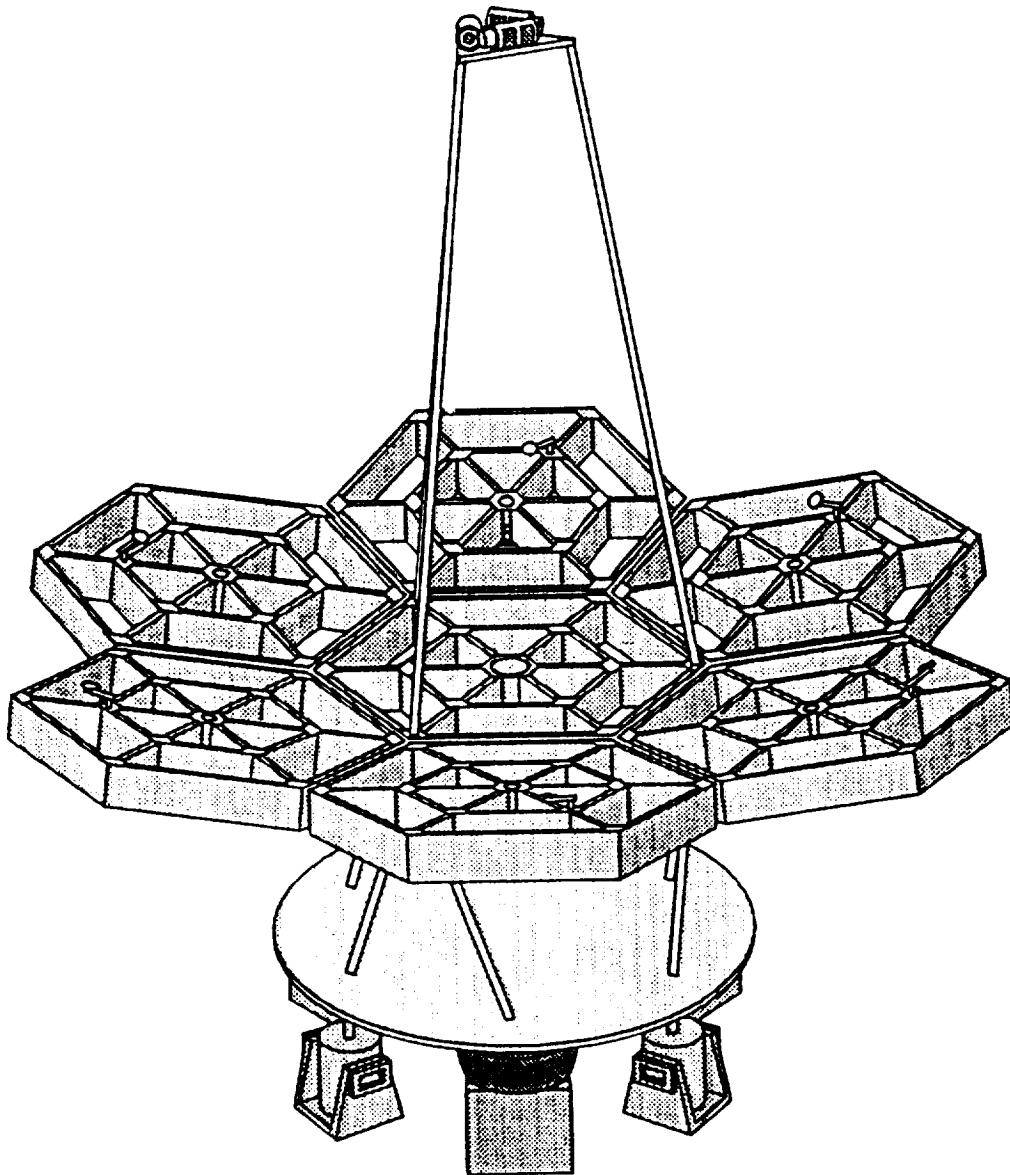
THE MULTI-HEX PROTOTYPE

MANEUVERING AND CONTROL OF FLEXIBLE SPACE ROBOTS†

Leonard Meirovitch* and Seungchul Lim**
Department of Engineering Science and Mechanics
Virginia Polytechnic Institute and State University
Blacksburg, VA 24061

SUMMARY

This paper is concerned with a flexible space robot capable of maneuvering payloads. The robot is assumed to consist of two hinge-connected flexible arms and a rigid end-effector holding a payload; the robot is mounted on a rigid platform floating in space. The equations of motion are nonlinear and of high order. Based on the assumption that the maneuvering motions are one order of magnitude larger than the elastic vibrations, a perturbation approach permits design of controls for the two types of motion separately. The rigid-body maneuvering is carried out open loop, but the elastic motions are controlled closed loop, by means of discrete-time linear quadratic regulator theory with prescribed degree of stability. A numerical example demonstrates the approach. In the example, the controls derived by the perturbation approach are applied to the original nonlinear system and errors are found to be relatively small.

1. INTRODUCTION

A variety of space missions can be carried out effectively by space robots. These missions include the collection of space debris, recovery of spacecraft stranded in a useless orbit, repair of malfunctioning spacecraft, construction of a space station in orbit and servicing the space station while in operation. To maximize the usefulness of the space robot, the manipulator arms should be reasonably long. On the other hand, because of weight limitations, they must be relatively light. To satisfy both requirements, the manipulator arms must be highly flexible. Hence, space robots share some of the dynamics and control technology with articulated space structures.

Robotics has been an active research area for the past few decades, but applications have been concerned primarily with industrial robots, which are ground based and tend to be very stiff and bulky. In contrast, space robots are based on a floating platform and tend to be highly flexible. Hence, whereas industrial and space robots have a number of things in common, the differences are significant. More recent investigations have been concerned with flexible industrial robots (Refs. 1-4). On the other hand, some investigations are concerned with space robots consisting of rigid links (Refs. 5-7). Research on flexible space robots has come to light only recently (Refs. 8,9).

  * University Distinguished Professor
  ** Graduate Research Assistant

This paper is concerned with a flexible space robot capable of maneuvering payloads. The robot is assumed to consist of two hinge-connected flexible arms and a rigid end-effector holding a payload; the robot is mounted on a rigid platform floating in space (Fig. 1). The platform is capable of translations and rotations, the flexible arms are capable of rotations and elastic deformations and the end-effector/payload can undergo rotations relative to the connecting flexible arm. Based on a consistent kinematical synthesis, the motions of one body in the chain take into consideration the motions of the preceding body in the chain. This permits the derivation of the equations of motion without the imposition of constraints. The equations of motion are derived by the Lagrangian approach. The equations are nonlinear and of relatively high order.

Ideally, the maneuvering of payloads should be carried without exciting elastic vibration, which is not possible in general. However, the elastic motions tend to be small compared to the rigid-body maneuvering motions. Under such circumstances, a perturbation approach permits separation of the problem into a zero-order problem (in a perturbation theory sense) for the rigid-body maneuvering of the space robot and a first-order problem for the control of the elastic motions and the perturbations from the rigid-body motions. The maneuvering can be carried out open loop, but the elastic and rigid-body perturbations are controlled closed loop.

The robot mission consists of carrying a payload over a prescribed trajectory and placing it in a certain orientation relative to the inertial space. For planar motion, the end-effector/payload configuration is defined by three variables, two translations and one rotation. At the end of the mission, the vibration should be damped out, so that the robot can be regarded as rigid at that time. Still, the rigid robot possesses six degrees of freedom, two translations of the platform and one rotation of each of the four bodies, including the platform. This implies that a kinematic redundancy exists. This redundancy is removed in the trajectory planning so as to conserve fuel. For a given end-effector/payload trajectory, the rigid-body maneuvering configuration of the robot can be obtained by means of inverse kinematics. Then, the forces and torques required for the robot trajectory realization are obtained from the zero-order equations by means of inverse dynamics.

The first-order equations for the elastic motions and the perturbations in the rigid-body maneuvering motions are linear, but of high order, time-varying and they are subjected to persistent disturbances. The persistent disturbances are treated by means of feedforward control. All other disturbances are controlled closed loop, with the feedback controls being designed by means of discrete-time linear quadratic regulator (LQR) theory with prescribed degree of stability. A numerical example demonstrates the approach. In the example, the controls derived by the perturbation approach are applied to the original nonlinear system and the errors in the end-effector/payload configuration were found to be relatively small during the maneuver and to vanish soon after the termination of the maneuver.

2. A CONSISTENT KINEMATICAL SYNTHESIS

To describe the motion of the space robot, it is convenient to adopt a consistent kinematical synthesis whereby the system is regarded as a chain of bodies and the motion of one body is

24

defined with due consideration to the motion of the preceeding body in the chain. Figure 1 shows the mathematical model of the space robot, consisting of a rigid platform (Body 1), two hinge-connected flexible arms (Bodies 2 and 3) and a rigid end-effector holding the payload (Body 4). The various motions are referred to a set of inertial axes and sets of body axes to be defined shortly.

The object is to derive the system equations of motion, which can be done by means of Lagrange's equations in terms of quasi-coordinates (Ref. 10). Because in the case at hand the motion is planar, it is more expedient to use the standard Lagrange's equations. This requires the kinetic energy, potential energy and virtual work. The kinetic energy, in turn, requires the velocity of a typical point in each of the bodies.

The position of a nominal point on the platform is given by

$$\mathbf{R}_1 = \mathbf{R}_0 + \mathbf{r}_1 \tag{1}$$

where $\mathbf{R}_0 = [X \ Y]^T$ is the position vector of the origin O_1 of the body axes x_1, y_1 (Fig. 1) relative to the inertial axes X, Y and in terms of X, Y components and $\mathbf{r}_1 = [x_1 \ y_1]^T$ is the position vector of the nominal point on the platform relative to the body axes x_1, y_1 and in terms of x_1, y_1 components. The velocity vector of a point on the platform can be expressed in terms of x_1, y_1 components as follows:

$$\mathbf{V}_1 = C_1 \dot{\mathbf{R}}_0 + \tilde{\omega}_1 \mathbf{r}_1 \tag{2}$$

where

$$C_1 = \begin{bmatrix} c\theta_1 & s\theta_1 \\ -s\theta_1 & c\theta_1 \end{bmatrix} \tag{3}$$

is a matrix of direction cosines between axes x_1, y_1, and X, Y, in which $s\theta_1 = \sin\theta_1$, $c\theta_1 = \cos\theta_1$,

$$\dot{\mathbf{R}}_0 = [\dot{X} \ \dot{Y}]^T \tag{4}$$

is the velocity vector of O_1 in terms of X, Y components and

$$\tilde{\omega}_1 = \begin{bmatrix} 0 & -\dot{\theta}_1 \\ \dot{\theta}_1 & 0 \end{bmatrix} \tag{5}$$

The second body is flexible, so that we must resolve the question of body axes. We define the body axes x_2, y_2 as a set of axes with the origin at the hinge O_2 and embedded in the undeformed body such that x_2 is tangent to the body at O_2 (Fig. 2). Then, we define the motion of axes x_2, y_2 as rigid-body motion and measure the elastic motion relative to x_2, y_2. Hence, the velocity of a point in the second body (first flexible arm) in terms of x_2, y_2 components is

$$\begin{aligned} \mathbf{V}_2 &= C_{2-1}\mathbf{V}_1(O_2) + \tilde{\omega}_2(\mathbf{r}_2 + \mathbf{u}_2) + \dot{\mathbf{u}}_{2rel} \\ &= C_2\dot{\mathbf{R}}_0 + C_{2-1}\tilde{\omega}_1\mathbf{r}_1(O_2) + \tilde{\omega}_2(\mathbf{r}_2 + \mathbf{u}_2) + \dot{\mathbf{u}}_{2rel} \end{aligned} \tag{6}$$

where C_{2-1} and C_2 are matrices similar to C_1, Eq. (3), except that θ_1 is replaced by $\theta_2 - \theta_1$ and θ_2, respectively, $\tilde{\omega}_2$ has the same structure as $\tilde{\omega}_1$ but with $\dot{\theta}_2$ replacing $\dot{\theta}_1$, $\mathbf{r}_1(O_2) = [d_1 \ h_1]^T$, $\mathbf{r}_2 =$

$[r_2 \ 0]^T$, $\mathbf{u}_2 = [0 \ u_2]^T$ and $\dot{\mathbf{u}}_{2\text{rel}} = [0 \ \dot{u}_2]$, in which $u_2 = u_2(x_2, t)$ and $\dot{u}_2 = \dot{u}_2(x_2, t)$ are the elastic displacement and velocity, respectively.

Using the analogy with the second body, the velocity of a point in the third body (second flexible arm) in terms of x_3, y_3 components can be shown to be

$$
\begin{aligned}
\mathbf{V}_3 &= C_{3-2}\mathbf{V}_2(L_2) + \tilde{\omega}_3(\mathbf{r}_3 + \mathbf{u}_3) + \dot{\mathbf{u}}_{3\text{rel}} \\
&= C_3\dot{\mathbf{R}}_0 + C_{3-1}\tilde{\omega}_1\mathbf{r}_1(O_2) + C_{3-2}\{\tilde{\omega}_2[\mathbf{r}_2(L_2) + \mathbf{u}_2(L_2, t)] + \dot{\mathbf{u}}_{2\text{rel}}(L_2, t)\} \\
&\quad + \tilde{\omega}_3(\mathbf{r}_3 + \mathbf{u}_3) + \dot{\mathbf{u}}_{3\text{rel}}
\end{aligned}
\tag{7}
$$

The fourth body consists of the end-effector and payload combined, and is treated as rigid. Following the established pattern, the velocity of a point in the fourth body in terms of x_4, y_4 components is

$$
\begin{aligned}
\mathbf{V}_4 &= C_{4-3}\mathbf{V}_3(L_3) + \tilde{\omega}_4\mathbf{r}_4 \\
&= C_4\dot{\mathbf{R}}_0 + C_{4-1}\tilde{\omega}_1\mathbf{r}_1(O_2) + C_{4-2}\{\tilde{\omega}_2[\mathbf{r}_2(L_2) + \mathbf{u}_2(L_2, t)] + \dot{\mathbf{u}}_{2\text{rel}}(L_2, t)\} \\
&\quad + C_{4-3}\{\tilde{\omega}_3[\mathbf{r}_3(L_3) + \mathbf{u}_3(L_3, t)] + \dot{\mathbf{u}}_{3\text{rel}}(L_3, t)\} + \tilde{\omega}_4\mathbf{r}_4
\end{aligned}
\tag{8}
$$

The consistent kinematical synthesis just described permits the formulation of the equations of motion for the whole system without invoking constraint equations. Such constraint equations must be used to eliminate redundant coordinates in a formulation in which equations of motion are derived separately for each body.

3. SPATIAL DISCRETIZATION OF THE FLEXIBLE ARMS

The velocity expressions derived in Sec. 2 involve rigid-body motions depending on time alone and elastic motions depending on the spatial position and time. Equations of motion based on such formulations are hybrid, in the sense that the equations for the rigid-body motions are ordinary differential equations and the ones for the elastic motions are partial differential equations. Designing maneuvers and controls on the basis of hybrid differential equations is likely to cause serious difficulties, so that the only viable alternative is to transform the hybrid system into one consisting of ordinary differential equations alone. This amounts to discretization in space of the elastic displacements, which can be done by means of series expansions. Assuming that the flexible arms act as beams in bending, the elastic displacements can be expanded in the series

$$
u_i(x_i, t) = \sum_{j=1}^{n_i} \phi_{ij}(x_i)\eta_{ij}(t) = \phi_i^T(x_i)\eta_i(t), \quad i = 2, 3
\tag{9}
$$

where $\phi_{ij}(x_i)$ are *admissible functions*, often referred to as *shape functions*, and $\eta_{ij}(t)$ are generalized coordinates; ϕ_j and η_i are corresponding n_i-dimensional vectors ($i = 2, 3; \ j = 1, 2, \ldots, n_i$)

The question arises as to the nature of the admissible functions. Clearly, the object is to approximate the displacements with as few terms in the series as possible. This is not a new

problem in structural dynamics, and the very same subject has been investigated recently in Ref. 11, in which a new class of functions, referred to as *quasi-comparison functions*, has been introduced. Quasi-comparison functions are defined as linear combinations of admissible functions capable of satisfying the boundary conditions of the elastic member. As shown in Fig. 2, the beam is tangent to axis x_i at $O_i (i = 2, 3)$. Hence, the admissible functions must be zero and their slope must be zero at $x_i = 0$. At $x_i = L_i$, the displacement, slope, bending moment and shearing force are generally nonzero. Quasi-comparison functions are linear combinations of functions possessing these characteristics. Admissible functions from a single family of functions do not possess the characteristics, but admissible functions from several suitable families can be combined to obtain them. In the case at hand, quasi-comparison functions can be obtained in the form of suitable linear combinations of clamped-free and clamped-clamped shape functions.

4. LAGRANGE'S EQUATIONS

Before we can derive Lagrange's equations, we must produce expressions for the kinetic energy, potential energy and virtual work. To this end, and following the spatial discretization indicated by Eqs. (9), we introduce the configuration vector

$$q(t) = \left[X(t) \ Y(t) \ \theta_1(t) \ \theta_2(t) \ \theta_3(t) \ \theta_4(t) \ \eta_2^T(t) \ \eta_3^T(t) \right]^T \tag{10}$$

so that the velocity vectors, Eqs. (2), (6)-(8), can be written in the compact form

$$V_i = D_i \dot{q}, \quad i = 1, 2, 3, 4 \tag{11}$$

where

$$D_1 = \begin{bmatrix} c\theta_1 & s\theta_1 & -y_1 & 0 & \ldots & 0^T \\ -s\theta_1 & c\theta_1 & x_1 & 0 & \ldots & 0^T \end{bmatrix}$$

$$D_2 = \begin{bmatrix} c\theta_2 & s\theta_2 & d_1 s(\theta_2 - \theta_1) - h_1 c(\theta_2 - \theta_1) & -\phi_2^T \eta_2 & 0 & 0 & 0^T & 0^T \\ -s\theta_2 & c\theta_2 & d_1 c(\theta_2 - \theta_1) + h_1 s(\theta_2 - \theta_1) & x_2 & 0 & 0 & \phi_2^T & 0^T \end{bmatrix} \tag{12}$$

Then, the kinetic energy is simply

$$T = \frac{1}{2} \sum_{i=1}^{4} \int_{m_i} V_i^T V_i \, dm_i = \frac{1}{2} \dot{q}^T M \dot{q} \tag{13}$$

where

$$M = \sum_{i=1}^{4} \int_{m_i} D_i^T D_i \, dm_i \tag{14}$$

is the mass matrix. Typical entries in the mass matrix are

$$m_{11} = m, \quad m_{12} = 0, \quad m_{13} = -(m_2 + m_3 + m_4)(h_1 c\theta_1 + d_1 s\theta_1)$$

$$m_{14} = -\left[\bar{\phi}_2^T + (m_3 + m_4)\phi_2^T(L_2) \right] \eta_2 c\theta_2 - [S_2 + (m_3 + m_4)L_2] s\theta_2$$

$$m_{18} = - \left[\overline{\phi}_3^T + m_4 \phi_3^T(L_3) \right] s\theta_3$$

$$m_{22} = m, m_{23} = -(m_2 + m_3 + m_4)(h_1 s\theta_1 - d_1 c\theta_1) \qquad (15)$$

$$\cdots\cdots\cdots\cdots\cdots\cdots\cdots\cdots\cdots\cdots\cdots\cdots\cdots\cdots\cdots\cdots$$

$$m_{28} = \left[\overline{\phi}_3^T + m_4 \phi_3^T(L_3) \right] c\theta_3$$

$$\cdots\cdots\cdots\cdots\cdots\cdots\cdots\cdots\cdots\cdots\cdots\cdots\cdots\cdots\cdots\cdots$$

$$m_{88} = \int_{\text{Body } 3} \phi_3 \phi_3^T dm_3 + m_4 \phi_3(L_3) \phi_3^T(L_3)$$

in which

$$m = \sum_{i=1}^4 m_i, \quad \overline{\phi}_i = \int_{m_i} \phi_i dm_i, \quad i = 2,3, \quad S_i = \int_{m_i} x_i dm_i, \quad i = 1,2,3,4 \qquad (16)$$

The potential energy, assumed to be entirely due to bending, has the form

$$V = \frac{1}{2} \int_0^{L_2} EI_2 \left[u_2''(x_2, t) \right]^2 dx_2 + \frac{1}{2} \int_0^{L_3} EI_3 \left[u_3''(x_3, t) \right]^2 dx_3 = \frac{1}{2} \mathbf{q}^T K \mathbf{q} \qquad (17)$$

in which $EI_i (i = 2,3)$ are bending stiffnesses and primes denote spatial derivatives. Moreover,

$$K = \text{block} - \text{diag}[0 \ K_2 \ K_3] \qquad (18)$$

is the stiffness matrix, where

$$K_i = \int_0^{L_i} EI_i \phi_i''(\phi_i'')^T dx_i, \quad i = 2,3 \qquad (19)$$

are stiffness matrices for the flexible arms.

Next, we propose to derive the virtual work expression. To this end, we must specify first the actuators to be used. There are three actuators acting on the platform, two thrusters F_{x1} and F_{y1} acting in directions aligned with the body axes and a torquer M_1 acting at O_1. Three other torquers M_2, M_3 and M_4 are located at the hinges O_2, O_3 and O_4, respectively, the first acting on the platform and first arm, the second acting on the first and second arm and the third acting on the second arm and end-effector. In view of this, the virtual work can be written as follows:

$$\begin{aligned}
\delta W =& F_{x1}\left(\cos\theta_1 \delta X + \sin\theta_1 \delta Y\right) + F_{y1}\left(-\sin\theta_1 \delta X + \cos\theta_1 \delta Y\right) + M_1 \delta\theta_1 \\
&+ M_2 \delta\left(\theta_2 - \theta_1\right) + M_3 \delta\psi_3 + M_4 \delta\psi_4 + M_5 \delta\left[\theta_2 + \phi_2'^T(L_2/3)\eta_2\right] \\
&+ M_6 \delta\left[\theta_2 + \phi_2'^T(2L_2/3)\eta_2\right] + M_7 \delta\left[\theta_3 + \phi_3'^T(L_3/3)\eta_3\right] + M_8\left[\theta_3 + \phi_3'^T(2L_3/3)\eta_3\right] \quad (20)
\end{aligned}$$

where $\delta X, \delta Y, \ldots$ are virtual displacements. Moreover, denoting the angles between the two arms and between the second arm and the end-effector by

$$\psi_3 = \theta_3 - \theta_2 - \left.\frac{\partial u_2}{\partial x_2}\right|_{x_2=L_2} = \theta_3 - \theta_2 - \phi_2'^T(L_2)\eta_2$$

$$\psi_4 = \theta_4 - \theta_3 - \left.\frac{\partial u_3}{\partial x_3}\right|_{x_3=L_3} = \theta_4 - \theta_3 - \phi_3'^T(L_3)\eta_3 \qquad (21)$$

we can write

$$\delta\psi_3 = \delta\theta_3 - \delta\theta_2 - \phi_2'^T(L_2)\,\delta\eta_2, \quad \delta\psi_4 = \delta\theta_4 - \delta\theta_3 - \phi_3'^T(L_3)\,\delta\eta_3 \tag{22}$$

Inserting Eqs. (22) into Eq. (20), we can express the virtual work in terms of generalized forces and generalized virtual displacements in the form

$$\delta W = \mathbf{Q}^T \delta\mathbf{q} \tag{23}$$

where $\mathbf{Q} = [F_X \ F_Y \ \Theta_1 \ \Theta_2 \ \Theta_3 \ \Theta_4 \ \mathbf{N}_2^T \ \mathbf{N}_3^T]^T$ is the generalized force vector, in which

$$
\begin{aligned}
F_X &= F_{x1}\cos\theta_1 - F_{y1}\sin\theta_1, \quad F_Y = F_{x1}\sin\theta_1 + F_{y1}\cos\theta_1 \\
\Theta_1 &= M_1 - M_2, \quad \Theta_2 = M_2 - M_3 + M_5 + M_6 \\
\Theta_3 &= M_3 - M_4 + M_7 + M_8, \quad \Theta_4 = M_4 \\
\mathbf{N}_2 &= M_5\phi_2'(L_2/3) + M_6\phi_2'(2L_2/3) - M_3\phi_2'(L_2) \\
\mathbf{N}_3 &= M_7\phi_3'(L_3/3) + M_8\phi_3'(2L_3/3) - M_4\phi_3'(L_3)
\end{aligned}
\tag{24}
$$

and $\delta\mathbf{q} = [\delta X \ \delta Y \ \delta\theta_1 \ \delta\theta_2 \ \delta\theta_3 \ \delta\theta_4 \ \delta\eta_2^T \ \delta\eta_3^T]^T$ is the generalized virtual displacement vector. Equations (24) express the generalized forces and torques in terms of the actual actuator forces and torques and can be expressed in the compact form

$$\mathbf{Q} = E\mathbf{F} \tag{25}$$

where $\mathbf{F} = [F_{x1} \ F_{y1} \ M_1 \ M_2 \ \dots \ M_8]^T$ is the actual control vector and

$$E = E(\theta_1) =$$

$$
\begin{bmatrix}
\cos\theta_1 & -\sin\theta_1 & 0 & 0 & 0 & 0 & 0 & 0 & 0 & 0 \\
\sin\theta_1 & \cos\theta_1 & 0 & 0 & 0 & 0 & 0 & 0 & 0 & 0 \\
0 & 0 & 1 & -1 & 0 & 0 & 0 & 0 & 0 & 0 \\
0 & 0 & 0 & 1 & -1 & 0 & 1 & 1 & 0 & 0 \\
0 & 0 & 0 & 0 & 1 & -1 & 0 & 0 & 1 & 1 \\
0 & 0 & 0 & 0 & 0 & 1 & 0 & 0 & 0 & 0 \\
0 & 0 & 0 & 0 & -\phi_2'(L_2) & 0 & \phi_2'(\tfrac{L_2}{3}) & \phi_2'(\tfrac{2L_2}{3}) & 0 & 0 \\
0 & 0 & 0 & 0 & 0 & -\phi_3'(L_3) & 0 & 0 & \phi_3'(\tfrac{L_3}{3}) & \phi_3'(\tfrac{2L_3}{3})
\end{bmatrix}
\tag{26}
$$

is a time-varying coefficient matrix, because θ_1 varies with time.

Lagrange's equation can be expressed in the general symbolic vector form

$$\frac{d}{dt}\left(\frac{\partial T}{\partial \dot{\mathbf{q}}}\right) - \frac{\partial T}{\partial \mathbf{q}} + \frac{\partial V}{\partial \mathbf{q}} = \mathbf{Q} \tag{27}$$

Observing that $M = M(\mathbf{q})$, we can write

$$\frac{\partial T}{\partial \dot{\mathbf{q}}} = M\dot{\mathbf{q}}, \quad \frac{d}{dt}\left(\frac{\partial T}{\partial \dot{\mathbf{q}}}\right) = M\ddot{\mathbf{q}} + \dot{M}\dot{\mathbf{q}}$$

$$\frac{\partial T}{\partial \mathbf{q}} = \frac{1}{2}\dot{\mathbf{q}}^T \frac{\partial M}{\partial \mathbf{q}}\dot{\mathbf{q}}, \quad \frac{\partial V}{\partial \mathbf{q}} = K\mathbf{q} \tag{28}$$

Inserting Eqs. (28) into Eq. (27), we obtain Lagrange's equations in the more explicit form

$$M\ddot{\mathbf{q}} + \left(\dot{M} - \frac{1}{2}\dot{\mathbf{q}}^T \frac{\partial M}{\partial \mathbf{q}}\right)\dot{\mathbf{q}} + K\mathbf{q} = \mathbf{Q} \tag{29}$$

in which

$$\dot{M} = \sum_{j=1}^{6+2n} \frac{\partial M}{\partial q_j}\dot{q}_j, \quad \dot{\mathbf{q}}^T \frac{\partial M}{\partial \mathbf{q}} = \begin{bmatrix} \dot{\mathbf{q}}^T \partial M / \partial q_1 \\ \dot{\mathbf{q}}^T \partial M / \partial q_2 \\ \vdots \\ \dot{\mathbf{q}}^T \partial M / \partial q_{6+2n} \end{bmatrix} \tag{30}$$

5. A PERTURBATION APPROACH TO THE CONTROL DESIGN

Equation (29) represents a high-order system of nonlinear differential equations, and is not very suitable for control design. Hence, an approach capable of coping with the problems of high-dimensionality and nonlinearity is highly desirable. Such an approach must be based on the physics of the problem. The ideal maneuver is that in which the robot acts as if its arms were rigid. In reality, the arms are flexible, so that some elastic vibrations are likely to take place. It is reasonable to assume, however, that the elastic motions are one order of magnitude smaller than the maneuvering motions. This permits treatment of the elastic motions as perturbations on the maneuvering motions. In turn, the elastic perturbations give rise to perturbations in the "rigid-body" maneuvering motions. This suggests a perturbation approach, whereby the problem is separated into a zero-order problem for the "rigid-body" maneuvering of the payload and a first-order problem for the control of the elastic motions and the perturbations in the rigid-body maneuvering motions. The zero-order problem is nonlinear, albeit of relatively low dimension. It can be solved independently and the control can be open loop. On the other hand, the first-order problem is linear, but of relatively high dimension. It is affected by the solution to the zero-order problem, where the effect is in the form of time-varying coefficients and persistent disturbances. The control for the first-order problem is to be closed loop.

We consider a first-order perturbation solution characterized by

$$\mathbf{q} = \mathbf{q}_0 + \mathbf{q}_1, \quad \mathbf{Q} = \mathbf{Q}_0 + \mathbf{Q}_1 \tag{31}$$

where the subscripts 0 and 1 denote zero-order and first-order quantities, with the zero-order quantities being one order of magnitude larger than the first-order ones. Inserting Eqs. (31) into Eq. (29) and separating quantities of different orders of magnitude, we obtain the equation for the zero-order problem

$$M_0\ddot{\mathbf{q}}_0 + \left(M_v - \frac{1}{2}M_v^T\right)\dot{\mathbf{q}}_0 = \mathbf{Q}_0 = E_0\mathbf{F}_0 \tag{32}$$

30

where $q_0 = [X_0 \ Y_0 \ \theta_{10} \ \theta_{20} \ \theta_{30} \ \theta_{40} \ 0^T \ 0^T]^T$, $Q_0 = [F_{X0} \ F_{X0} \ \Theta_{10} \ \Theta_{20} \ \Theta_{30} \ \Theta_{40} \ 0^T \ 0^T]^T$ are zero-order displacement and generalized control vectors, $E_0 = E(\theta_{10})$ is the matrix E, Eq. (26), evaluated at $\theta_1 = \theta_{10}$, $F_0 = [F_{x0} \ F_{y0} \ M_{10} \ M_{20} \ \dots \ M_{80}]^T$ and

$$M_0 = M(q_0), \quad M_v = \left[\frac{\partial M}{\partial q_1} \dot{q}_0 \quad \frac{\partial M}{\partial q_2} \dot{q}_0 \quad \dots \quad \frac{\partial M}{\partial q_{6+2n}} \dot{q}_0 \right]\Bigg|_{q=q_0} \qquad (33a,b)$$

Moreover, we obtain the equation for the first-order problem

$$M_0 \ddot{q}_1 + \left(M_v + M' - M_v^T \right) \dot{q}_1 + \left(M_a + M_{vv} - \frac{1}{2} M'_{vv} + K \right) q_1 = Q_1 + Q_d \qquad (34)$$

where $q_1 = [X_1 \ Y_1 \ \theta_{11} \ \theta_{21} \ \theta_{31} \ \theta_{41} \ \eta_2^T \ \eta_3^T]^T$, $Q_1 = [F_{X1} \ F_{Y1} \ \Theta_{11} \ \Theta_{21} \ \Theta_{31} \ \Theta_{41} \ N_2^T \ N_3^T]^T$ are first-order displacement and generalized control vectors, $Q_d = [0 \ 0 \ 0 \ 0 \ 0 \ 0 \ F_{d2}^T \ F_{d3}^T]^T$ is a persistent disturbance vector and

$$M_a = \left[\frac{\partial M}{\partial q_1} \ddot{q}_0 \quad \frac{\partial M}{\partial q_2} \ddot{q}_0 \quad \dots \quad \frac{\partial M}{\partial q_{6+2n}} \ddot{q}_0 \right]\Bigg|_{q=q_0} \qquad (35a)$$

$$M' = \sum_{j=1}^{6+2n} \frac{\partial M}{\partial q_j}\Bigg|_{q=q_0} \dot{q}_{0j} \qquad (35b)$$

$$M_{vv} q_1 = \sum_{j=1}^{6+2n} \sum_{k=1}^{6+2n} \frac{\partial^2 M}{\partial q_j \partial q_k}\Bigg|_{q=q_0} q_{1k} \dot{q}_{0j} \dot{q}_0 \qquad (35c)$$

$$M'_{vv} q_1 = \dot{q}_0^T \sum_{k=1}^{6+2n} \frac{\partial^2 M}{\partial q \partial q_k}\Bigg|_{q=q_0} q_{1k} \dot{q}_0 \qquad (35d)$$

From Eqs. (25) and (26), however, we can write

$$Q_1 = E_0 F_1 + E_1 F_0 = E_0 F_1 + F_0^* q_1 \qquad (36)$$

where $E_1 = [\partial E / \partial \theta_1 | \theta_1 = \theta_{10}] \theta_{11}$. Moreover, the matrix F_0^* has the entries

$$
\begin{aligned}
F_{011}^* &= - (F_{x10} \sin \theta_{10} + F_{y10} \cos \theta_{10}) \\
F_{021}^* &= F_{x10} \cos \theta_{10} - F_{y10} \sin \theta_{10} \\
F_{0ij}^* &= 0, \quad i = 3, 4, \dots, 6 + n_2 + n_3; \quad j = 2, 3, \dots, 6 + n_2 + n_3
\end{aligned} \qquad (37)
$$

In view of this, the equation for the first-order problem can be rewritten as

$$M_0 \ddot{q}_1 + (M_v + M' - M_v^T)\dot{q}_1 + (M_a + M_{vv} - \frac{1}{2} M'_{vv} + K - F_0^*) q_1 = E_0 F_1 + Q_d \qquad (38)$$

6. TRAJECTORY PLANNING

The mission consists of delivering the payload to a certain point in space and placing it in a certain orientation. For planar motion, the final payload configuration is defined by three variables, two translations and one rotation. The trajectory planning, designed to realize this

final configuration, will be carried out as if the robot system were rigid, with the expectation that all elastic motions and perturbations in the rigid-body maneuvering motions will be annihilated by the end of the maneuver. The rigid-body motion of the robot is described by the zero-order problem and it consists of six components, two translations of the platform and one rotation of each of the four bodies. This implies that a kinematical redundancy exists, as there is an infinity of ways a six-dimensional configuration can generate a three-dimensional trajectory. This redundancy can be removed by controlling three of the configuration variables, such as the translations and rotation of the platform, so as to conserve fuel. Under these circumstances, the rigid space robot can be treated as a nonredundant manipulator.

Next, we denote the end-effector configuration by $\mathbf{X}_E$, so that from kinematics we can write

$$\mathbf{X}_E = \mathbf{f}(\mathbf{q}_0) \tag{39}$$

where $\mathbf{f}$ is a three-dimensional vector function. From differential kinematics, we have

$$\dot{\mathbf{X}}_E = J(\mathbf{q}_0)\dot{\mathbf{q}}_0 \tag{40}$$

where

$$J(\mathbf{q}_0) = [\partial \mathbf{f}/\partial \mathbf{q}_0] \tag{41}$$

is the 3×6 Jacobian matrix. Introducing the notation

$$\mathbf{q}_0 = \left[\mathbf{q}_S^T \mid \mathbf{q}_M^T\right]^T \tag{42}$$

where

$$\mathbf{q}_S = [X_0 \ Y_0 \ \theta_{10}]^T, \quad \mathbf{q}_M = [\theta_{20} \ \theta_{30} \ \theta_{40}]^T \tag{43a,b}$$

are the controlled platform configuration vector and the open-loop controlled manipulator configuration vector, and partitioning the Jacobian matrix accordingly, or

$$J = \left[J_S \mid J_M\right] \tag{44}$$

Eq. (40) can be rewritten as

$$\dot{\mathbf{X}}_E = J_S\dot{\mathbf{q}}_S + J_M\dot{\mathbf{q}}_M \tag{45}$$

Then, on the assumption that $\dot{\mathbf{q}}_S$ is determined so as to minimize the fuel consumption, and for a given end-effector trajectory $\mathbf{X}_E$, we can determine the manipulator velocity vector from

$$\dot{\mathbf{q}}_M = J_M^{-1}\left(\dot{\mathbf{X}}_E - J_S\dot{\mathbf{q}}_S\right) \tag{46}$$

The end-effector trajectory was taken in the form of a sinusoidal function so as to prevent excessive vibration. Finally, with $\mathbf{q}_0$ given, we can obtain the required open-loop control $\mathbf{F}_0$ by inverse dynamics, which amounts to using Eq. (32).

32

7. FEEDBACK CONTROL OF THE ELASTIC MOTIONS AND RIGID-BODY PERTURBATIONS

The elastic motions and the perturbations in the rigid-body maneuvering motions are governed by the equation defining the first-order problem, Eq. (38). The persistent disturbances are controlled open loop and all other disturbances are controlled closed loop. To this end, we express the control vector in the form

$$\mathbf{F}_1 = \mathbf{F}_{1o} + \mathbf{F}_{1c} \tag{47}$$

where the subscripts o and c indicate open loop and closed loop, respectively. Recognizing that E_0 is a rectangular matrix, the open-loop control can be written as

$$\mathbf{F}_{1o} = -E_0^\dagger \mathbf{Q}_d \tag{48}$$

in which

$$E_0^\dagger = \left(E_0^T E_0\right)^{-1} E_0^T \tag{49}$$

is the psuedo-inverse of E_0.

For the closed-loop control, we consider a linear quadratic regulator (LQR), which requires recasting the equations of motion in state form. Adjoining the identity $\dot{q}_1 = \dot{q}_1$, the state equations can be expressed as

$$\dot{\mathbf{x}}(t) = A(t)\mathbf{x}(t) + B(t)E_0\mathbf{u}_c(t) + B(t)D\mathbf{d}(t) \tag{50}$$

where $\mathbf{x} = [q_1^T \ \dot{q}_1^T]^T$ is the state vector, $\mathbf{u}_c = \mathbf{F}_{1c}$ is the control vector, $\mathbf{d} = \mathbf{Q}_d$ is the disturbance vector and

$$A = \begin{bmatrix} 0 & I \\ -M_0^{-1}(M_a + M_{vv} - \frac{1}{2}M'_{vv} + K - F_0^*) & -M_0^{-1}(M_v + M' - M_v^T) \end{bmatrix} \tag{51a}$$

$$B = \begin{bmatrix} 0 \\ M_0^{-1} \end{bmatrix}, \quad D = \left(I - E_0 E_0^\dagger\right) \tag{51b,c}$$

are coefficient matrices. It should be noted here that, if the matrix E_0 is not square, the matrix D is not zero, so that the open-loop control does not annihilate the persistent disturbances completely. As the number of actuator approaches the number of degrees of freedom of the system, the matrix E_0 tends to become square. When the number of actuators coincides with the number of degrees of freedom the matrix E_0 is square, in which case the pseudo-inverse becomes an exact inverse and the matrix D reduces to zero.

The state equations, Eq. (50), possess time-varying coefficients and are subject to residual persistent disturbances. Due to difficulties in treating such systems in continuous time, we propose to discretize the state equations in time. Following the usual steps (Ref. 12), the state equations in discrete time can be shown to be

$$\mathbf{x}_{k+1} = \Phi_k \mathbf{x}_k + \Gamma_k E_{0k} \mathbf{u}_{ck} + \Gamma_k D_k \mathbf{d}_k, \quad k = 0, 1, \dots \tag{52}$$

where

$$\mathbf{x}_k = \mathbf{x}(kT), \quad \mathbf{u}_{ck} = \mathbf{u}_c(kT), \quad \mathbf{d}_k = \mathbf{d}(kT), \quad k = 0, 1, \dots$$
$$\Phi_k = \exp A_u T, \quad \Gamma_k = (\exp A_k T - I)A_k^{-1}B_k, \quad k = 0, 1, \dots \tag{53}$$
$$E_{0k} = E_0(kT), \quad D_k = D(kT), \quad k = 0, 1, \dots$$

in which T is the sampling period. In view of the above discussion, we assume that the effect of the persistent disturbances has been reduced drastically by the feedforward control, and design the feedback control in its absence. This design is according to a discrete-time LQR with prescribed degree of stability. To this end, we consider the performance measure

$$J = x_N^T P_N x_N + \sum_{k=0}^{N-1} e^{2\alpha k} \left(x_k^T Q_k x_k + u_{ck}^T R_k u_{ck} \right) \tag{54}$$

where P_N and Q_k are symmetric positive semidefinite matrices, R_k is a symmetric positive definite matrix, α is a nonnegative constant defining the degree of stability and NT is the final sampling time.

The optimization process using the performance measure given by Eq. (54) can be reduced to a standard discrete-time LQR form by means of the transformation

$$\hat{x}_k = e^{\alpha k} x_k, \quad \hat{u}_{ck} = e^{\alpha k} u_{ck}, \quad \hat{P}_N = e^{-2\alpha N} P_N \tag{55a, b, c}$$

Multiplying Eqs. (52) through by $e^{\alpha(k+1)}$ using Eqs. (55a,b) and ignoring the small perturbing term, we obtain the new state equations

$$\hat{x}_{k+1} = e^{\alpha} \left(\Phi_k \hat{x}_k + \Gamma_k E_{0k} \hat{u}_{ck} \right), \quad k = 0, 1, \ldots, N-1 \tag{56}$$

Similarly, inserting Eqs. (55) into Eq. (54), we obtain the new performance measure

$$J = \hat{x}_N^T \hat{P}_N \hat{x}_N + \sum_{k=0}^{N-1} \left(\hat{x}_k^T Q_k \hat{x}_k + \hat{u}_{ck}^T R_k \hat{u}_{ck} \right) \tag{57}$$

It can be shown (Ref. 12) that the optimal control law has the form

$$\hat{u}_{ck} = G_k \hat{x}_k, \quad k = 0, 1, \ldots, N-1 \tag{58}$$

where G_k are gain matrices obtained from the discrete-time Riccati equations

$$G_{N-i} = - \left(e^{2\alpha} E_{0,N-i}^T \Gamma_{N-i}^T \hat{P}_{N+1-i} \Gamma_{N-i} E_{0,N-i} + R_{N-i} \right)^{-1} e^{2\alpha} E_{0,N-i}^T \Gamma_{N-i}^T \hat{P}_{N+1-i} \Phi_{N-i},$$
$$i = 1, 2, \ldots, N; \hat{P} = e^{-2\alpha N} P_N \tag{59a}$$

$$\hat{P}_{N-i} = e^{2\alpha} \left(\Phi_{N-i} + \Gamma_{N-i} E_{0,N-i} G_{N-i} \right)^T \hat{P}_{N+1-i} \left(\Phi_{N-i} + \Gamma_{N-1} E_{0,N-i} G_{N-i} \right),$$
$$+ G_{N-i}^T R_{N-i} G_{N-i} + Q_{N-i}, \quad i = 1, 2, \ldots, N; \hat{P}_N = e^{-2\alpha N} P_N \tag{59b}$$

Equations (59a) and (59b) are evaluated alternately for $G_{N-1}, \hat{P}_{N-1}, G_{N-2}, \hat{P}_{N-2}, \ldots, G_0$, given the final value of $\hat{P}_N$.

Inserting the control law, Eqs. (58), into Eqs. (56), we obtain the closed-loop transformed state equations

$$\hat{x}_{k+1} = e^{\alpha} \left(\Phi_k + \Gamma_k E_{0k} G_k \right) \hat{x}_k, \quad k = 0, 1, \ldots \tag{60}$$

34

Then, recalling Eq. (55a) and restoring the persistent disturbance term, the closed-loop state equations for the original system can be written in the form

$$x_{k+1} = (\Phi_k + \Gamma_k E_{0k} G_k) x_k + \Gamma_k D_k d_k, \quad k = 0, 1, \ldots \tag{61}$$

8. NUMERICAL EXAMPLE

The example involves the flexible space robot shown in Fig. 1. Numerical values for the system parameters are as follows:

$$L_1 = 1 \text{ m}, \ d_1 = 0.5 \text{ m}, \ L_2 = L_3 = 5m, \ L_4 = 1.66m$$
$$m_1 = 10 \text{ kg}, \ m_2 = m_3 = 1\text{kg}, \ m_4 = 0.1 \text{ kg}$$
$$J_1 = 20 \text{ kgm}^2, \ J_2 = 3 \text{ kgm}^2, \ EI_2 = EI_3 = 122.28 \text{ Nm}^2$$

The quasi-comparison functions for the flexible arm were chosen as a linear combination of clamped-free and clamped-clamped shape functions. Both families of shape functions have the functional form

$$\phi_i = \frac{1}{\sqrt{L}} \left[\cosh \lambda_i x / L - \cos \lambda_i x / L - \sigma_i \left(\sinh \lambda_i x / L - \sin \lambda_i x / L \right) \right], i = 1, 2, \ldots, n$$

The values of λ_i and σ_i are given in Table 1. They correspond to two clamped-free and three clamped-clamped shape functions, for a total of $n = 5$ for each flexible arm.

The initial and final end-effector positions are defined by

$$X_i = 9.757 \text{ m}, \ Y_i = 1.914 \text{ m}, \ \theta_{4f} = 0 \text{ rad}$$
$$X_f = 5.000 \text{ m}, \ Y_f = 1.914 \text{ m}, \ \theta_{4f} = \pi/2 \text{ rad}$$

and we note that the path from the initial to the final position represents a straight-line translation, while the orientation undergoes a 90° change. In terms of time, the translational and rotational accelerations represent one-cycle sinusoidal curves.

The maneuver time is $t_f = 2.5$ s. The zero-order actuator forces and torques to carry out the maneuver are shown in Fig. 3.

The control of the elastic motions and the perturbations in the rigid-body motions was extended to $t = 4$ s. Not that for 2.5 s $< t < 4$ s the system is time-invariant, during which time the control gains can be regarded as constant. The weighting matrices in the performance measure are

$$Q_k = 10I, \ R_k = I, \ P_N = 10I$$

The degree of stability constant is $\alpha = 0.1$. Moreover, the samping period is $T = 0.01$ s and the number of time increments is $N = 350$.

Time-lapse plots of the uncontrolled and controlled robot configuration are shown in Figs. 4a and 4b, respectively, at the instants 0, 1, 1.5 and 2.5 s. Figures 5 and 6 show time histories of the

errors in the end-effector position. The discrete-time open-loop and closed-loop poles are given in Tables 2 and 3. For comparison, Fig. 7 shows the time history of the errors and Table 4 gives the closed-loop poles for $\alpha = 1$.

It should be pointed out that the actuator dynamics is also included in the formulation and the numerical results, but the effect turned out to be small.

9. CONCLUSIONS

An orderly kinematic synthesis in conjunction with the Lagrangian approach permits the derivation of the equations of motion for an articulated multibody system, such as those describing the dynamical behavior of a flexible space robot, without the imposition of constraints. The equations are nonlinear and of relatively high order. A perturbation approach permits the separation of the problem into a zero-order problem (in a perturbation sense) for the rigid-body maneuvering of the space robot and a first-order problem for the control of the elastic motions and the perturbations from the rigid-body motions. The robot mission consists of carrying a payload over a prescribed trajectory and placing it in a cerrtain orientation relative to the inertial space. This represents the zero-order problem and the control can be carried out open loop. The first-order equations defining the first-order problem (in a perturbation sense) are linear, time-varying, of high-order and subject to persistent disturbances. The persistent disturbances are treated by means of feedforward control. All other disturbances are controlled closed loop, with the feedback control being designed by means of discrete-time LQR theory with prescribed degree of stability. In a numerical example, the controls derived by the perturbation approach are found to work satisfactorily when applied to the original nonlinear system.

10. REFERENCES

1. Book, W.J., Maizza-Neto, A., and Whitney, D.E.: Feedback Control of Two Beam, Two Joint Systems with Distributed Flexibility. *ASME Journal of Dynamic Systems, Measurement, and Control*, vol. 97, Dec. 1975, pp.424-431.

2. Kozel, D. and Koivo, A.J.: A General Force/Torque Relationship and Kinematic Representation for Flexible Link Manipulators. *Journal of Robotic Systems*, vol. 8, no. 4, 1991, pp. 531-556.

3. Wang, D. and Vidyasagar, M.: Control of a Class of Manipulators with a Single Flexible Link-Part I: Feedback Linearization. *ASME Journal of Dynamic Systems, Measurement, and Control*, vol. 113, Dec. 1991, pp. 655-661.

4. Nathan, P.J., and Singh, S.N.: Sliding Mode Control and Elastic Mode Stabilization of a Robotic Arm with Flexible Links. *ASME Journal of Dynamic Systems, Measurement, and Control*, vol. 113, Dec. 1991.

5. Umetani, Y. and Yoshida, K.: Continuous Path Control of Space Manipulators Mounted on OMV. *Acta Astronautica*, vol. 15, no. 12, 1987, pp. 981-986.

6. Nenchev, D., Umetani, Y., and Yoshida, K.: Analysis of a Redundant Free-Flying Spacecraft/Manipulator System., *IEEE Transactions on Robotics and Automation*, vol. 8, no. 1, 1992, pp. 1-6.

7. Nakamura, Y. and Mukherjee, R.: Nonholonomic Path Planning of Space Robots via a Bidirectional Approach. *IEEE Transactions on Robotics, and Automation*, vol. 7, no. 4, 1991, pp. 500-514.

8. Usoro, P.B., Nadira, R., Mahil, S.S.: Control of Lightweight Flexible Manipulators: A Feasibility Study. *Proceedings of the American Control Conference*, vol. 3, San Diego, CA, June 1984, pp. 1209-1216.

9. Meirovitch, L., Stemple, T., and Kwak, M.K.: Dynamics and Control of Flexible Space Robots. *Proceedings of the CSME Mechanical Engineering Forum*, Toronto, Ontario, 1990.

10. Meirovitch, L.: Hybrid State Equations of Motion for Flexible Bodies in Terms of Quasi-Coordinates. *Journal of Guidance, Control, and Dynamics*, vol. 14, no. 5, 1991, pp. 1008-1013.

11. Meirovitch, L. and Kwak, M.K.: Convergence of the Classical Rayleigh-Ritz Method and the Finite Element Method. *AIAA Journal*, vol. 28, no. 8, 1990, pp. 1509-1516.

12. Kuo, B.C.: *Digital Control Systems*, SRL Publishing Co., Champaign, IL, 1977.

Table 1. Shape Function Coefficients

i	λ_i	σ_i
1	1.87510407	0.734095514
2	4.69409113	1.018467319
3	7.85475744	0.999224497
4	10.99554073	1.000033553
5	14.13716839	0.999998550

Table 2. Discrete-Time Open-Loop Poles

No.	Pole Location	Mag.	No.	Pole Location	Mag.
1,2	-0.840±0.543i	1.000	17,18	0.991±0.135i	1.000
3,4	-0.778±0.629i	1.000	19,20	0.994±0.107i	1.000
5,6	-0.700±0.714i	1.000	21,22	1.000	1.000
7,8	-0.690±0.724i	1.000	23,24	1.000	1.000
9,10	0.586±0.810i	1.000	25,26	1.000	1.000
11,12	0.629±0.778i	1.000	27,28	1.000	1.000
13,14	0.902±0.431i	1.000	29,30	1.000	1.000
15,16	0.921±0.390i	1.000	31,32	1.000	1.000

Table 3. Discrete-Time Closed-Loop Poles

No.	Pole Location	Mag.	No.	Pole Location	Mag.
1,2	$-0.169 \pm 0.546i$	0.572	18,19	$0.803 \pm 0.976 \times 10^{-1}i$	0.809
3	0.493×10^{-2}	0.005	20	0.805	0.805
4	0.120×10^{-1}	0.012	21	0.807	0.807
5	0.125	0.125	22,23	$0.814 \pm 0.362 \times 10^{-2}i$	0.814
6	0.204	0.204	24,25	0.817	0.817
7,8	$0.302 \pm 0.148i$	0.336	26	0.817	0.817
9,10	$0.454 \pm 0.493i$	0.670	27	0.819	0.819
11,12	$0.468 \pm 0.323i$	0.569	28,29	$0.821 \pm 0.366 \times 10^{-2}i$	0.821
13,14	$0.536 \pm 0.500i$	0.733	30	0.822	0.822
15,16	$0.749 \pm 0.860 \times 10^{-2}i$	0.754	31	0.822	0.822
17	0.792	0.792	32	0.827	0.827

Table 4. Discrete-Time Closed-Loop Poles for $\alpha = 1$

| No.	Pole Location	Mag.	No.	Pole Location	Mag.
1	-0.566	0.566	17,18	$0.139 \pm 0.844 \times 10^{-2}i$	0.139
2,3	$-0.160 \pm 0.186i$	0.246	19,20	$0.150 \pm 0.022i$	0.152
4,5	$-0.109 \pm 0.275i$	0.296	21,22	$0.187 \pm 0.145i$	0.236
6,7	$0.062 \pm 0.088i$	0.108	23,24	$0.198 \pm 0.288 \times 10^{-1}i$	0.200
8	-0.177×10^{-1}	0.018	25	0.251	0.251
9,10	$0.779 \times 10^{-2} \pm 0.209i$	0.209	26,27	$0.252 \pm 0.180i$	0.310
11,12	$0.072 \pm 0.088i$	0.114	28,29	$0.279 \pm 0.490i$	0.564
13,14	$0.118 \pm 0.016i$	0.119	30,31	$0.328 \pm 0.148i$	0.360
15,16	$0.132 \pm 0.920 \times 10^{-2}i$	0.132	32	0.430	0.430
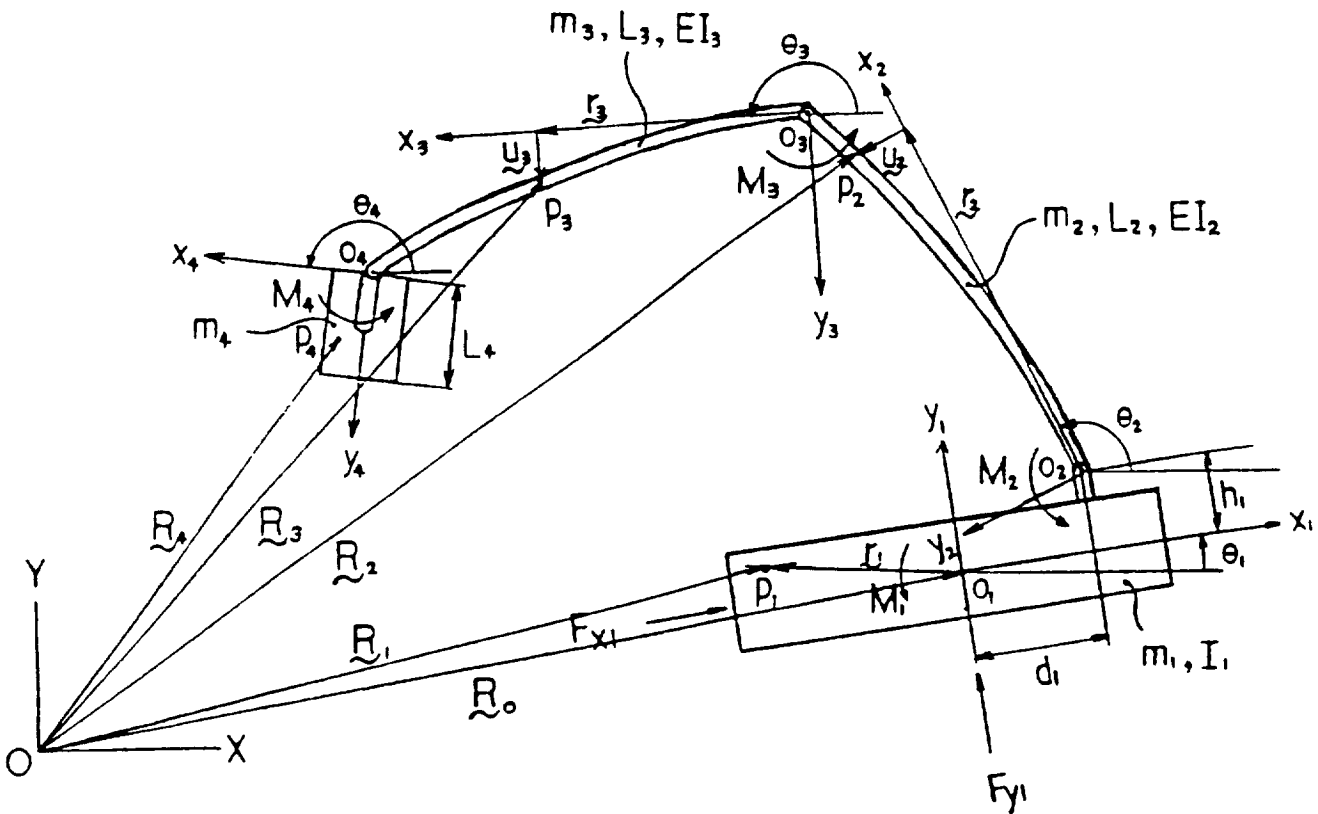
Figure 1. Flexible Space Robot
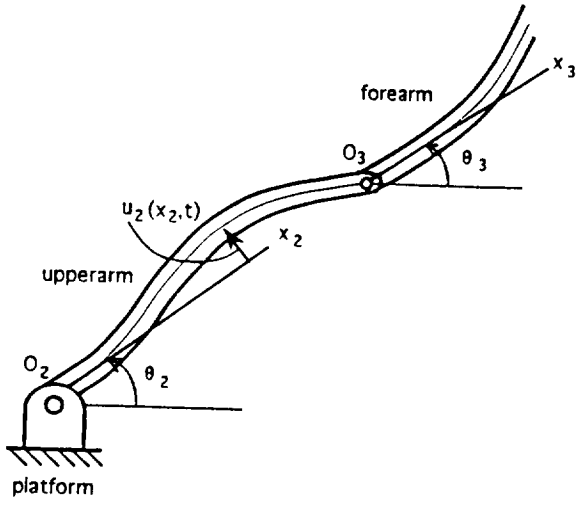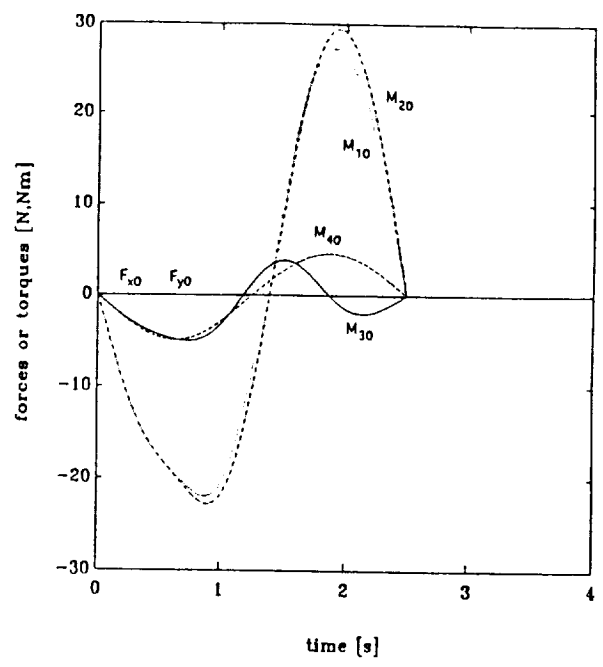
Figure 2. Definition of Body Axes

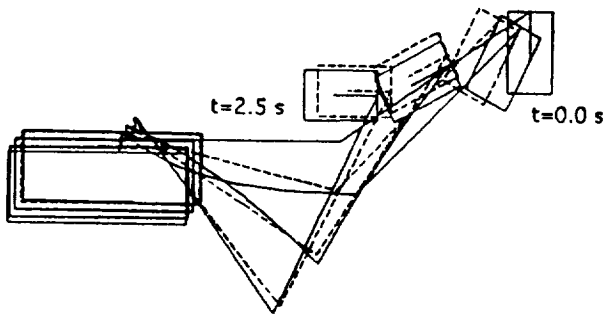Figure 3. Zero-Order Forces and Torques

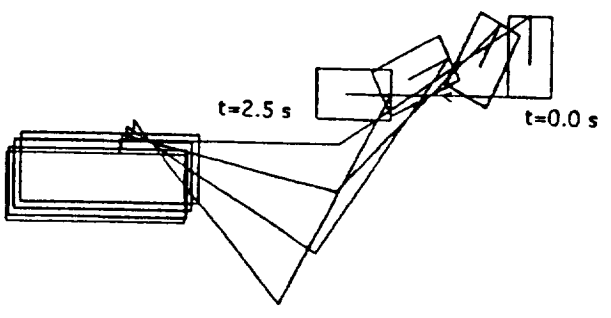Figure 4a. Uncontrolled Maneuver

Figure 4b. LQR-Controlled Maneuver
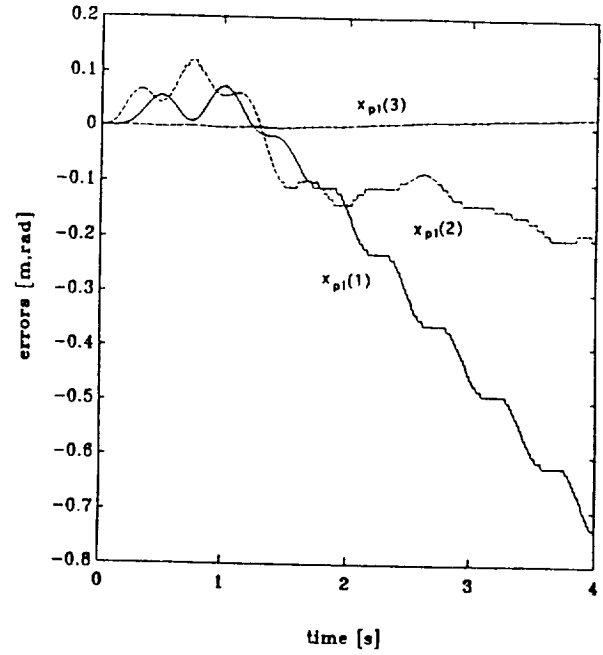
Figure 5. Uncontrolled End-Effector
Position Errors
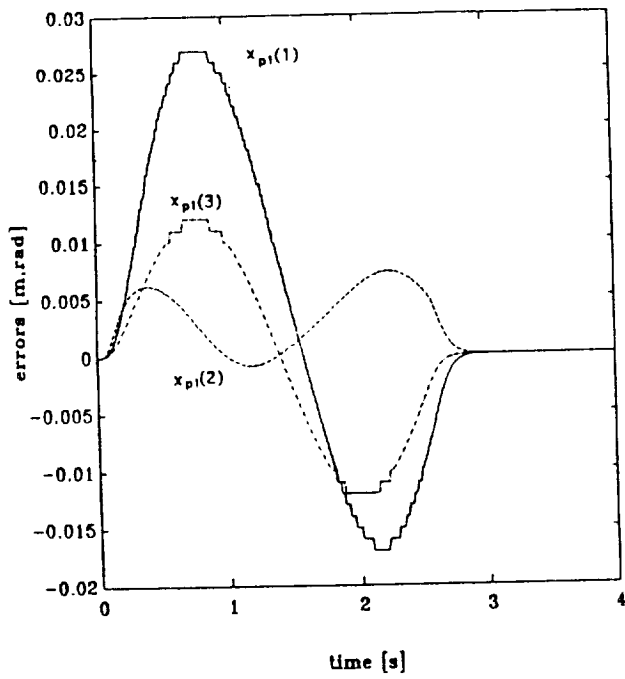
Figure 6. LQR-Controlled End-Effector
Position Errors for $\alpha = 0.1$
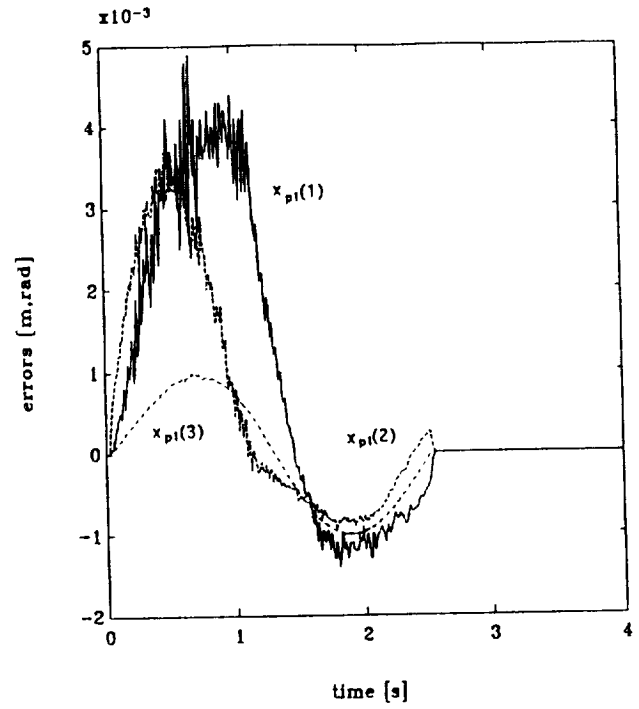
Figure 7. LQR-Controlled End-Effector
Position Errors for $\alpha = 1$

40

DISTRIBUTED PARAMETER MODELING OF REPEATED TRUSS STRUCTURES

Hanching Wang*
Department of Electrical Engineering
University of California , Los Angeles

Abstract

A new approach to find homogeneous models for beam-like repeated flexible structures is proposed which conceptually involves two steps.

Step one: Approximation of 3-D non-homogeneous model by a 1-D periodic beam model. The structure is modeled as a 3-D non-homogeneous continuum. The displacement field is approximated by Taylor series expansion. Then, the cross sectional mass and stiffness matrices are obtained by energy equivalence using their additive properties. Due to the repeated nature of the flexible bodies, the mass and stiffness matrices are also periodic. This procedure is systematic and requires less dynamics detail.

Step two: Homogenization from 1-D periodic beam model to 1-D homogeneous beam model. The periodic beam model is homogenized into an equivalent homogeneous beam model using the additive property of compliance along the generic axis. The major departure from previous approaches in literature is using compliance instead of stiffness in homogenization. An obvious justification is that the stiffness is additive at each cross section but not along the generic axis. The homogenized model preserves many properties of the original periodic model.

1 Introduction

As the number of repeated cells in a truss structure increases, the 3-D model can be approximated better and better by an equivalent 1-D model. The repeated structure then can be modeled as a homogeneous anisotropic continuum beam. The parameters of the continuum beam are functions of the element properties of the truss structure.

Finding the 1-D homogeneous anisotropic beam model from the reference model, the 3-D non-homogeneous anisotropic model, of the truss structure may be referred to as a homogenization process, of which there are many examples.

The approach presented here follows that of Noor's [1, 2] and Lions's [3]. See [3] for mathematical details of the homogenization process, where some results are taken by our paper for granted. The Noor's method is a direct averaging method. which justifies equivalence in the sense of equal kinetic energy and potential energy under the condition of equal nodal displacements and velocities. It imposes a kinematic assumption on the displacement field, then averages the stiffness and mass matrices (by FEM) over a repeated cell. Although the stiffness matrix is additive at each cross-section, it is not along the generic axis. Thus, this method always gives higher stiffness than it should be. This shortcoming will be overcome by our approach.

Our approach consists of two steps, as illustrated in Figure (2). The first step deals with the approximation of 3-D non-homogeneous model of a repeated structure by the 1-D periodic beam model. The second step then homogenized it to a 1-D homogeneous beam model. The 3-D non-homogeneous model is a collection of the Eulerian Equation of Motion of each element of the structure, and is referred to as a reference model for the successive approximation. By applying the Taylor series expansion and energy equivalence. a 1-D periodic beam model is found systematically. Solid beam is used to clarify the basic idea, then an extension from solid beam to non-solid structure(eg. lattice structure) is presented in section (5).
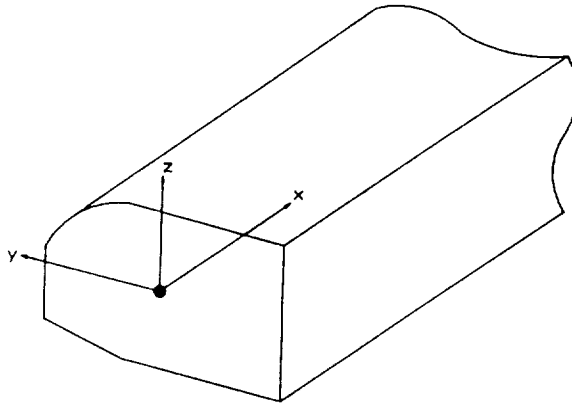

Figure 1: Anisotropic Beam

Consider a structure constructed by linear elastic anisotropic materials as shown in figure (1). The material coordinates attached have x-axis as the generic axis along the centroids, and y-z as the principal axes of the area inertia of cross sections. This choice of reference will be adopted throughout the paper.

Let the bounded open set $\Omega \subset R^3$ denote the space occupied by the structure and Γ the boundary of Ω. Let U, V, and W be the displacements in x, y and z direction, respectively, measured w.r.t. the natural state (undeformed position), observed from inertial coordinates, and represented in the material coordinates. The equation of motion [4, 5] is

$$
\begin{aligned}
\rho \ddot{U} &= \sigma_{xx,x} + \sigma_{yx,y} + \sigma_{zx,z} + f_x \\
\rho \ddot{V} &= \sigma_{xy,x} + \sigma_{yy,y} + \sigma_{zy,z} + f_y \qquad \text{in } \Omega \\
\rho \ddot{W} &= \sigma_{xz,x} + \sigma_{yz,y} + \sigma_{zz,z} + f_z
\end{aligned}
\tag{1}
$$

with well-posed initial and boundary conditions to render existence of unique solution, where

$$
\rho = \rho(x, y, z) \in L^\infty(\Omega)
$$

and f(x,y,z) is the external body force. The constitutive law is

$$
\sigma = C^0 e
\tag{2}
$$

and

$$
\sigma = \begin{bmatrix} \sigma_{xx} \\ \sigma_{yy} \\ \sigma_{zz} \\ \sigma_{yz} \\ \sigma_{xz} \\ \sigma_{xy} \end{bmatrix}, \quad
e = \begin{bmatrix} \epsilon_{xx} \\ \epsilon_{yy} \\ \epsilon_{zz} \\ \gamma_{yz} \\ \gamma_{xz} \\ \gamma_{xy} \end{bmatrix} =
\begin{bmatrix} U_{,x} \\ V_{,y} \\ W_{,z} \\ V_{,z} + W_{,y} \\ U_{,z} + W_{,x} \\ U_{,y} + V_{,x} \end{bmatrix}
\tag{3}
$$

where σ denotes stresses ,e strains and C^0 a real symmetric positive-definite matrix with

$$
c_{ij}^0 = c_{ij}^0(x, y, z) \in L^\infty(\Omega)
$$

Here equation (1) is taken as the reference model of the beam. Our task is to approximate the 3-spatial-dimensional (3-D) equation (1) by a 1-spatial-dimensional (1-D) beam eq. to arbitrary accuracy of the displacement field. Instead of going through the term by term scrutinizing as in solid continuum mechanics, we provide a unified and systematic approach. This will insight the general pattern and properties of the 1-D beam eq.

The final goal is the capability of modeling repeated truss structure as a 1-D beam. The properties of repeated truss structure, though non-homogeneous (i.e. $\rho = \rho(x,y,z)$), are periodic along the generic axis x. A homogenization process then is needed as will be described in section 8.

2 Justification of Taylor's Expansion

Before applying the Taylor approximation in the next section, let's justify its applicability to our problem first. Let $\mathcal{H} = L^2(\Omega)$ be real valued Hilbert space and

$$\vec{U}(t,x,y,z) = \begin{bmatrix} u_1 \\ u_2 \\ u_3 \end{bmatrix} = \begin{bmatrix} U \\ V \\ W \end{bmatrix}$$

Let the equation of motion be written as, by equation (1),

$$\rho\ddot{\vec{U}} + \mathcal{L}\vec{U} = f \qquad in \ \Omega \tag{4}$$

with well-posed homogeneous boundary conditions specified by forces or displacements in Γ, and

$$u_i(0,x,y,z) \in \mathcal{V}, \quad \dot{u}_i(0,x,y,z) \in \mathcal{H} \quad where \mathcal{V} = \mathcal{H}^1(\Omega)$$

If all coefficients are in $L^\infty(\Omega)$ and the strain energy associated with $\mathcal{L}$ is positive definite, then there exists a unique solution

$$u_i \in L^2((0,T);\mathcal{V}) \quad with \quad u_i' \ and \ \dot{u}_i \ in \ L^2((0,T);\mathcal{H})$$

Proposition 1

$$\exists \ H_n X_n \to \vec{U} \qquad strongly \ in \ [L^2((0,T);\mathcal{V})]^3$$

with X_n the solution of $M_n \ddot{X}_n + A_n X_n = f_n$, where
$H_n = H_n(y,z) \quad X_n = X_n(t,x) \in [L^2((0,T);\tilde{V})]^n$

$$(H_n X_n)' \to \vec{U}' \qquad in \quad [L^2((0,T);\mathcal{H})]^3 = \mathcal{W}_1$$

$$H_n \dot{X}_n \to \dot{\vec{U}} \qquad in \quad \mathcal{W}_1$$

X_n' and $\dot{X}_n \in [L^2((0,T);\tilde{H})]^3 = \mathcal{W}_2$, with
$\tilde{H} = L^2(0,L) \quad \tilde{V} = \tilde{H}^1 \quad and$

$$M_n(x) = \int\int_A H_n^*(y,z)\rho(x,y,z)H_n(y,z)dy\,dz$$

$$C_n(x) = \int\int_A T_n^*(y,z)C_o(x,y,z)T_n(y,z)dy\,dz$$

$$f_n(t,x) = \int\int_A H_n^*(y,z)f(t,x,y,z)dy\,dz$$

$$[C_n c_X^n, c_\Psi^n]_{\mathcal{W}_2} = [A_n X_n, \Psi_n]_{\mathcal{W}_2}$$

Proof:

For each $u_i(t, x, y, z)$

$$\exists \quad u_{im} \quad \rightarrow \quad u_i \quad \text{strongly in} \quad L^2((0, T); \mathcal{V})$$
$$u'_{im} \quad \rightarrow \quad u'_i \quad \text{strongly in} \quad L^2((0, T); \mathcal{H})$$
$$\dot{u}_{im} \quad \rightarrow \quad \dot{u}_i \quad \text{strongly in} \quad L^2((0, T); \mathcal{H})$$

where u_{im} defined in $(0, T)$ is analytic function in y and z. The strong convergence is guaranteed since analytic functions are dense in $L^2((0, T); \mathcal{V})$

Let

$$u^{(1)}(a, b) = \sum_{i=y,z} D_i u(a) b_i$$
$$u^{(2)}(a, b) = \sum_{i=y,z} \sum_{j=y,z} D_{i,j} u(a) b_i b_j \qquad (5)$$
$$u^{(3)}(a, b) = \sum_{i=y,z} \sum_{j=y,z} \sum_{k=y,z} D_{i,j,k} u(a) b_i b_j b_k$$
$$\vdots$$

By Taylor's theorem

$$u_{im} = \sum_{k=0}^{n} \frac{1}{k!} u_{im}^{(k)}((t, x, 0, 0), (t, x, y, z)) + H.O.T. \qquad (6)$$
$$= H_n(y, z) X_{imn}(t, x) + H.O.T.$$

By strong convergence of the Taylor series

$$H_n X_{imn} \quad \rightarrow \quad u_{im} \quad \text{strongly in} \quad L^2((0, T); \mathcal{V})$$
$$(H_n X_{imn})' \quad \rightarrow \quad u'_{im} \quad \text{strongly in} \quad L^2((0, T); \mathcal{H})$$
$$H_n \dot{X}_{imn} \quad \rightarrow \quad \dot{u}_{im} \quad \text{strongly in} \quad L^2((0, T); \mathcal{H})$$

Therefore, in general, we have

$$H_n X_n \rightarrow \vec{U} \qquad \text{strongly in} \quad [L^2((0, T); \mathcal{V})]^3 \qquad (7)$$

where

$H_n = H_n(y, z)$ $X_n = X_n(t, x)$ and $X_n \in [L^2((0, T); \tilde{V})]^n$

$$(H_n X_n)' \rightarrow \vec{U}' \qquad \text{in} \quad \mathcal{W}_1$$
$$H_n \dot{X}_n \rightarrow \dot{\vec{U}} \qquad \text{in} \quad \mathcal{W}_1$$

Also,

$$T_n \epsilon_n \to \epsilon \quad \text{by} \quad (H_n X_n)' \to \vec{U}'$$

Therefore,

$$[\rho \ddot{\vec{U}} + \mathcal{L}\vec{U}, \Phi]_{W_1} = [f, \Phi]_{W_1} \qquad \forall \quad \Phi \in [L^2((0,T); \mathcal{V})]^3$$

$$\Rightarrow -[\rho \ddot{\vec{U}}, \dot{\Phi}]_{W_1} + [C^0 e_U, e_\Phi]_{W_1} = [f, \Phi]_{W_1}$$

or,

$$\lim_n \{-[\rho H_n \dot{X}_n, H_n \dot{\Psi}_n]_{W_1} + [C_o T_n \epsilon_X^n, T_n \epsilon_\Psi^n]_{W_1}\} = [f, H_n \Psi_n]_{W_1}$$

$$\lim_n \{-[H_n^* \rho H_n \dot{X}_n, \dot{\Psi}_n]_{W_2} + [T_n^* C_o T_n \epsilon_X^n, \epsilon_\Psi^n]_{W_2}\} = [H_n^* f, \Psi_n]_{W_2}$$

Using $M_n(x), C_n(x)$ and $f_n(t,x)$ defined before, we have

$$\lim_n \{-[M_n \dot{X}_n, \dot{\Psi}_n]_{W_2} + [C_n \epsilon_X^n, \epsilon_\Psi^n]_{W_2}\} = [f_n, \Psi_n]_{W_2}$$

$$\lim_n [M_n \ddot{X}_n + A_n X_n, \Psi_n]_{W_2} = [f_n, \Psi_n]_{W_2} \qquad (8)$$

Equations (5) and (6) imply

$$H_n X_n \to \vec{U} \quad \text{with} \quad X_n \text{ the solution of } M_n \ddot{X}_n + A_n X_n = f_n$$

This completes the proof and justifies the applicability of Taylor's expansion.

3 Taylor Series Approximation

Let cross sections with concentrated forces be taken as boundary sections (boundary points in beam equations) and local effects of applied forces be neglected. Assume the physical displacements U, V and W are analytic in y and z so that the Taylor series expansion is applicable. We apply the Taylor series expansion, using equations (5) and (6), at each cross section x and any time t to have

$$U(t,x,y,z) = U + \frac{\partial U}{\partial y}y + \frac{\partial U}{\partial z}z + \frac{\partial^2 U}{\partial y^2}\frac{y^2}{2} + \frac{\partial^2 U}{\partial z^2}\frac{z^2}{2} + \frac{\partial^2 U}{\partial y \partial z}yz + H.O.T. \qquad (9)$$

where all terms on the RHS are evaluated at (t,x,0,0). Similar equations can be written down for V(t,x,y,z) and W(t,x,y,z).

The displacement field can well be approximated by a few dominant terms for most physical beams. The generalized displacements of the beam eq. can be chosen by order of magnitude analysis. For example, for an 8-generalized-displacement (8-d) beam eq., we choose

$$
X = \begin{bmatrix} u \\ v \\ w \\ \phi_1 \\ \phi_2 \\ \phi_3 \\ \bar{u} \\ \epsilon_{23} \end{bmatrix} = \begin{bmatrix} U \\ V \\ W \\ \frac{1}{2}(\frac{\partial W}{\partial y} - \frac{\partial V}{\partial z}) \\ \frac{\partial U}{\partial z} \\ -\frac{\partial U}{\partial y} \\ \frac{\partial^2 U}{\partial y \partial z} \\ \frac{1}{2}(\frac{\partial W}{\partial y} + \frac{\partial V}{\partial z}) \end{bmatrix}_{(t,x,0,0)} \tag{10}
$$

We will call X the generalized displacements .

The approximation of the displacement field up to the specified accuracy then is, by equations (9) and (10),

$$
\begin{aligned}
U(t,x,y,z) &\doteq u - \phi_3 y + \phi_2 z + \bar{u} y z \\
V(t,x,y,z) &\doteq v + (\epsilon_{23} - \phi_1)z \\
W(t,x,y,z) &\doteq w + (\epsilon_{23} + \phi_1)y
\end{aligned} \tag{11}
$$

or

$$
\begin{bmatrix} U \\ V \\ W \end{bmatrix} \doteq H X \tag{12}
$$

with cross sectional shape function H=H(y,z) found from equation (11). The equation (11) is known as kinematic assumption in Structural Dynamics, viewed as a polynomial approximation to the displacement field.

Since dynamic eq. of the beam is completely characterized by mass and constitutive properties, the approximation of 3-D eq. by the 1-D beam is equivalent to transforming the point properties to sectional properties, ie, from mass density ρ and constitutive matrix C^0 to mass matrix M and stiffness matrix C , respectively. The mass inertia (M) and stiffness (C) have additive property at any given cross-section; therefore we can find M and C by approximating the cross-sectional kinetic and potential energy, respectively. This additive property justifies the validity of domain extension from material-domain to structure-domain.

4 Energy Equivalence Method

We can find the sectional mass matrix by approximating the kinetic energy using equations (10) and (12). The kinetic energy of a piece of the beam (between any two cross sections) is

$$
KE = \frac{1}{2} \int \int \int \rho(\dot{U}^2 + \dot{V}^2 + \dot{W}^2) dA \, dx
$$

$$\doteq \frac{1}{2} \int \int \int \rho \dot{X}^T H^T H \dot{X} \, dA \, dx$$

$$= \frac{1}{2} \int \dot{X}^T M \dot{X} \, dx$$

It can be shown that, for anti-symmetric mass distribution,

$$M = \int \int \rho H^T H \, dA = \{m_{ij}(x)\}$$

$$= \begin{bmatrix} m_{11} & \cdot & \cdot & \cdot & \cdot & \cdot & -m_{56} & \cdot \\ & m_{11} & \cdot & \cdot & \cdot & \cdot & \cdot & \cdot \\ & & m_{11} & \cdot & \cdot & \cdot & \cdot & \cdot \\ & & & m_{55}+m_{66} & \cdot & \cdot & \cdot & m_{66}-m_{55} \\ & & & & m_{55} & m_{56} & m_{57} & \cdot \\ & & & & & m_{66} & m_{67} & \cdot \\ s & y & m & & & & m_{77} & \cdot \\ & & & & & & & m_{55}+m_{66} \end{bmatrix} (13)$$

The M in eq. (13) is the most general pattern of mass matrix for anti-symmetric anisotropic 8-d beams. The first (6×6) part of M is the general pattern of mass matrix for Timoshenko beams.

We can also find the sectional stiffness matrix C by approximating the potential energy of the beam. From equations (2) and (11), we have

$$e = \begin{bmatrix} \epsilon_{xx} \\ \epsilon_{yy} \\ \epsilon_{zz} \\ \gamma_{yz} \\ \gamma_{xz} \\ \gamma_{xy} \end{bmatrix} \doteq \begin{bmatrix} u' - \phi_3' y + \phi_2' z + \bar{u}' yz \\ 0 \\ 0 \\ 2\epsilon_{23} \\ \phi_2 + w' + (\bar{u} + \epsilon_{23}' + \phi_1')y \\ -\phi_3 + v' + (\bar{u} + \epsilon_{23}' - \phi_1')z \end{bmatrix} = T\epsilon \qquad (14)$$

where T=T(y,z) is a (6×9) matrix ;

$$\epsilon = \begin{bmatrix} u' \\ v' - \phi_3 = \gamma_{12} \\ w' + \phi_2 = \gamma_{13} \\ \phi_1' \\ \phi_2' \\ \phi_3' \\ \bar{u}' \\ \bar{u} + \epsilon_{23}' \\ 2\epsilon_{23} = \gamma_{23} \end{bmatrix} = \begin{bmatrix} X' \\ \cdots \\ 0 \end{bmatrix} + \begin{bmatrix} 0 \\ -\phi_3 \\ \phi_2 \\ 0 \\ 0 \\ 0 \\ 0 \\ \bar{u} \\ 2\epsilon_{23} \end{bmatrix}$$

$$= KX' + GX \qquad (15)$$

$$G = \begin{bmatrix} 0_{3\times3} & L_1 & 0_{3\times2} \\ 0_{3\times3} & 0_{3\times3} & 0_{3\times2} \\ & & 0 \quad 0 \\ 0_{3\times3} & 0_{3\times3} & 1 \quad 0 \\ & & 0 \quad 2 \end{bmatrix}_{9\times8}$$

$$L_1 = \begin{bmatrix} 0 & 0 & 0 \\ 0 & 0 & -1 \\ 0 & 1 & 0 \end{bmatrix} \quad \text{and} \quad K = \begin{bmatrix} I_{8\times8} \\ 0_{1\times8} \end{bmatrix}_{9\times8}$$

The potential energy of a piece of the beam is

$$PE = \frac{1}{2}\int\int\int e^T C^0 e \, dA \, dx$$

$$= \frac{1}{2}\int\int\int \epsilon^T T^T C^0 T \epsilon \, dA \, dx$$

$$= \frac{1}{2}\int \epsilon^T C \epsilon \, dx$$

The stiffness matrix for anti-symmetric of c_{ij}^0 is

$$C = \int\int T^T C^0 T \, dA = \{c_{ij}(x)\}$$

$$= \begin{bmatrix} c_{11} & c_{12} & c_{13} & \cdot & \cdot & \cdot & c_{17} & \cdot & c_{19} \\ & c_{22} & c_{23} & \cdot & \cdot & \cdot & c_{27} & \cdot & c_{29} \\ & & c_{33} & \cdot & \cdot & \cdot & c_{37} & \cdot & c_{39} \\ & & & c_{44} & c_{45} & c_{46} & c_{47} & c_{48} & \cdot \\ & & & & c_{55} & c_{56} & c_{57} & c_{58} & \cdot \\ & & & & & c_{66} & c_{67} & c_{68} & \cdot \\ & s & y & m & & & c_{77} & c_{78} & c_{79} \\ & & & & & & & c_{88} & \cdot \\ & & & & & & & & c_{99} \end{bmatrix} \quad (16)$$

The stiffness matrix C in eq. (16) is the most general pattern for anti-symmetric anisotropic 8-d beams. The first (6×6) part is that of Timoshenko beams. Knowing the general patterns of M and C is very useful, especially in assuming the model structure in system identification. Since most of the truss structures ever built are at least cross-sectional anti-symmetric, we consider this case only hereafter.

5 Extension to Lattice Structures

For non-solid beams, we need to apply the concept of domain extension, from material-domain to structure-domain, so that the results in the above sections can

be applied. Let's take a rectangular lattice structure as an example. The space physically occupied by the structure material is called the material-domain. The smallest simple-connected rectangular space enclosing the structure is called the structure-domain(Ω), which includes the space not occupied by the structure material(Ω_e).

A displacement field is assumed for the space not occupied by the structure material so that the displacement field on structure-domain is in $\mathcal{H}^1(\Omega)$. Therefore, the Taylor series expansion and energy equivalence method for calculating sectional properties can be applied directly. The sectional properties shall not be affected by the introducing of the displacement field in Ω_e, since both the kinetic energy and potential energy are zero in Ω_e. We can then pretend we are dealing with a solid flexible structure in regular shape.

6 Generalized Beam Equations

The governing eq. can be found from integrating by parts of potential energy.

$$
\begin{aligned}
2PE &= \int \epsilon^T C(x) \epsilon \, dx = \int \epsilon^T F \, dx \\
&= \int (KX' + GX)^T F \, dx \\
&= \int \{[-KX]^T F' + (GX)^T F\} \, dx + (KX)^T F \big|_0^\ell \\
&= \int X^T [-K^T F' + G^T F] \, dx + X^T (K^T F) \big|_0^\ell
\end{aligned}
$$

The dynamic eq. in force-acceleration form is

$$
M(x)\ddot{X} - K^T F' + G^T F = 0 \tag{17}
$$

or

$$
M(x)\ddot{X} = K^T F' - G^T F = \begin{bmatrix} N' \\ Q'_{12} \\ Q'_{13} \\ M'_t \\ M'_2 - Q_{13} \\ M'_3 + Q_{12} \\ M'_{23} - M_4 \\ M'_4 - 2Q_{23} \end{bmatrix} \tag{18}
$$

The above two equations are valid for beams which are nonhomogeneous along the generic axis.

From equation (15),

$$
F = C\epsilon = C(KX' + GX)
$$

we have, for a special case of homogeneous beams.

$$-K^T F' + G^T F = -K^T C K X'' - (K^T C G - G^T C K) X' + G^T C G X.$$

The dynamic eq. in mass-stiffness form is

$$M \ddot{X} - K^T C K X'' - (K^T C G - G^T C K) X' + G^T C G X = 0 \qquad (19)$$

where

$$M = \begin{bmatrix} m_{11} & \cdot & \cdot & \cdot & \cdot & \cdot & m_{17} & \cdot \\ & m_{22} & \cdot & \cdot & \cdot & \cdot & \cdot & \cdot \\ & & m_{33} & \cdot & \cdot & \cdot & \cdot & \cdot \\ & & & m_{44} & \cdot & \cdot & \cdot & m_{48} \\ & & & & m_{55} & m_{56} & m_{57} & \cdot \\ s & y & m & & m_{66} & m_{67} & \cdot \\ & & & & & m_{77} & \cdot \\ & & & & & & & m_{88} \end{bmatrix} \qquad (20)$$

$$K^T C K = \begin{bmatrix} c_{11} & c_{12} & c_{13} & \cdot & \cdot & \cdot & c_{17} & \cdot \\ & c_{22} & c_{23} & \cdot & \cdot & \cdot & c_{27} & \cdot \\ & & c_{33} & \cdot & \cdot & \cdot & c_{37} & \cdot \\ & & & c_{44} & c_{45} & c_{46} & c_{47} & c_{48} \\ & & & & c_{55} & c_{56} & c_{57} & c_{58} \\ & & & & & c_{66} & c_{67} & c_{68} \\ s & y & m & & & & c_{77} & c_{78} \\ & & & & & & & c_{88} \end{bmatrix} \qquad (21)$$

$$K^T C G - G^T C K = \begin{bmatrix} \cdot & \cdot & \cdot & c_{13} & -c_{12} & \cdot & 2c_{19} \\ \cdot & \cdot & \cdot & c_{23} & -c_{22} & \cdot & 2c_{29} \\ \cdot & \cdot & \cdot & c_{33} & -c_{23} & \cdot & 2c_{39} \\ & & & \cdot & \cdot & c_{48} & \cdot \\ & & & \cdot & \cdot & c_{58} - c_{37} & \cdot \\ & & & \cdot & c_{68} + c_{27} & \cdot \\ s & k & e & w & & \cdot & 2c_{79} - c_{88} \\ s & y & m & & & \cdot \end{bmatrix} \qquad (22)$$

$$G^T C G = \begin{bmatrix} \cdot & \cdot & \cdot & \cdot & \cdot & \cdot & \cdot \\ & \cdot & \cdot & \cdot & \cdot & \cdot & \cdot \\ & & \cdot & \cdot & \cdot & \cdot & \cdot \\ & & & \cdot & \cdot & \cdot' & \cdot \\ & & & c_{33} & -c_{23} & \cdot & 2c_{39} \\ & & & & c_{22} & \cdot & -2c_{29} \\ s & y & m & & & c_{88} & \cdot \\ & & & & & & c_{99} \end{bmatrix} \qquad (23)$$

with m_{ij} from equation (13) and c_{ij} from equation (16) .

The end boundary conditions are either $X_i = 0$ or $F_i = 0$. There are 2^8 possible combinations, theoretically. For example:$X_b = 0$ for clamped end, $K^T F_b = (K^T CK)X_b' + K^T CGX_b = 0$ for free end.

If there are lumped masses, then the conditions become :

(a) for interior points

$$M_b \ddot{X}_b - (K^T CK) \, \Delta X_b' = 0$$

where

$$\Delta X_b = X(b^+) - X(b^-)$$

(b) for exterior points

$$M_b \ddot{X}_b + sig[(K^T CK)X_b' + (K^T CG)X_b] = 0$$

where

$$sig = \begin{cases} 1, & \text{for positive ends (ends with positive outward normal);} \\ -1, & \text{for negative ends.} \end{cases}$$

and

$$K^T CG = \begin{bmatrix} \cdot & \cdot & \cdot & \cdot & c_{13} & -c_{12} & \cdot & 2c_{19} \\ \cdot & \cdot & \cdot & \cdot & c_{23} & -c_{22} & \cdot & 2c_{29} \\ \cdot & \cdot & \cdot & \cdot & c_{33} & -c_{23} & \cdot & 2c_{39} \\ \cdot & \cdot & \cdot & \cdot & \cdot & \cdot & c_{48} & \cdot \\ \cdot & \cdot & \cdot & \cdot & \cdot & \cdot & c_{58} & \cdot \\ \cdot & \cdot & \cdot & \cdot & \cdot & \cdot & c_{68} & \cdot \\ \cdot & \cdot & \cdot & \cdot & c_{37} & -c_{27} & c_{78} & 2c_{79} \\ \cdot & \cdot & \cdot & \cdot & \cdot & \cdot & c_{88} & \cdot \end{bmatrix} \tag{24}$$

7 Timoshenko Beams

The Timoshenko beam eq. is obtained by deleting the last two generalized displacements (ie., $\bar{u}$ and ϵ_{23} in X) in equation (19), to have

$$M_t \ddot{X}_t - C_t X_t'' - A_1 X_t' + A_0 X_t = 0 \tag{25}$$

where

$$M_t = \begin{bmatrix} m_{11} & \cdot & \cdot & \cdot & \cdot & \cdot \\ & m_{22} & \cdot & \cdot & \cdot & \cdot \\ & & m_{33} & \cdot & \cdot & \cdot \\ & & & m_{44} & \cdot & \cdot \\ s & y & m & & m_{55} & m_{56} \\ & & & & m_{56} & m_{66} \end{bmatrix}$$

$$C_t = \begin{bmatrix} c_{11} & c_{12} & c_{13} & \cdot & \cdot & \cdot \\ & c_{22} & c_{23} & \cdot & \cdot & \cdot \\ & & c_{33} & \cdot & \cdot & \cdot \\ & & & c_{44} & c_{45} & c_{46} \\ s & y & m & & c_{55} & c_{56} \\ & & & & & c_{66} \end{bmatrix} = \begin{bmatrix} c_1 & 0_{3\times3} \\ 0_{3\times3} & c_2 \end{bmatrix}$$

$$L = \begin{bmatrix} \cdot & \cdot & \cdot & \cdot & c_{13} & -c_{12} \\ \cdot & \cdot & \cdot & \cdot & c_{23} & -c_{22} \\ \cdot & \cdot & \cdot & \cdot & c_{33} & -c_{23} \\ \cdot & \cdot & \cdot & \cdot & \cdot & \cdot \\ \cdot & \cdot & \cdot & \cdot & \cdot & \cdot \\ \cdot & \cdot & \cdot & \cdot & \cdot & \cdot \end{bmatrix} = \begin{bmatrix} 0_{3\times3} & c_1 L_1 \\ 0_{3\times3} & 0_{3\times3} \end{bmatrix}$$

$$A_1 = L - L^T$$

$$A_0 = \begin{bmatrix} 0_{3\times3} & \cdot & \cdot & \cdot \\ & & \cdot & \cdot \\ & & c_{33} & -c_{23} \\ sym & & & c_{22} \end{bmatrix} = \begin{bmatrix} 0_{3\times3} & 0_{3\times3} \\ 0_{3\times3} & L_1^T C_1 L_1 \end{bmatrix}$$

The force boundary conditions are

$$M_b \ddot{X}_b - C_t \, \Delta X_b' - L \, \Delta X_b = F_b \tag{26}$$

and the geometric boundary conditions are X_b = specified value.

8 Multi-scale Averaging Method

For Periodic Beam-like structure, M and C are periodic in x with period ℓ.

$$M = M(x), \quad C = C(x), \quad \text{K and G are constant matrices}$$

The equation of motion of Timoshenko beam from equation (17) in section 6 can be rewritten as

$$M\ddot{X} - (K^T C K X' + K^T C G X)' + G^T C K X' + G^T C G X = f \tag{27}$$

Let

$$B_1 = K^T C K \quad B_2 = K^T C G \quad B_3 = G^T C G$$

We have

$$M\ddot{X} - (B_1 X')' - (B_2 X)' + B_2^T X' + B_3 X = f \tag{28}$$

Let

$$AX = -(B_1 X')' - (B_2 X)' + B_2^T X' + B_3 X \tag{29}$$

We will consider the following structure

$$M\ddot{X} + AX = f \tag{30}$$

$$X(0) = 0 \quad, \quad K^T C K X' + K^T C G X = B_1 X' + B_2 X = 0 \quad,\text{at} \quad x = L$$

$$A = A^*, \quad A > 0$$

Let $s = \frac{x}{\ell} \in R$, $\quad C^\ell(x) = C(\frac{x}{\ell}) = C(s)$, $\quad B_1^\ell(x) = B_1(s)$,
$B_2^\ell(x) = B_2(s)$, $\quad B_3^\ell(x) = B_3(s)$
For $\quad X_i^\ell(t,x) = X_i(t,x,\frac{x}{\ell}) = X_i(t,x,s)$

$$X_i' = \frac{\partial X_i}{\partial x} + \ell^{-1}\frac{\partial X_i}{\partial s} \tag{31}$$

We have

$$\begin{aligned}
AX_i &= -(B_1 X_i')' - (B_2 X_i)' + B_2^T X_i' + B_3 X_i \\
&= \ell^{-2} A_0 X_i + \ell^{-1} A_1 X_i + \ell^0 A_2 X_i
\end{aligned} \tag{32}$$

where

$$A_0 X_i = -\frac{\partial}{\partial s}(B_1 \frac{\partial X_i}{\partial s}) \tag{33}$$

$$A_1 X_i = -\frac{dB_1}{ds}\frac{\partial X_i}{\partial x} - 2B_1\frac{\partial^2 X_i}{\partial x \partial s} - (B_2 - B_2^T)\frac{\partial X_i}{\partial s} - \frac{dB_2}{ds} X_i \tag{34}$$

$$A_2 X_i = -B_1\frac{\partial^2 X_i}{\partial x^2} - (B_2 - B_2^T)\frac{\partial X_i}{\partial x} + B_3 X_i \tag{35}$$

Let [3, 6]

$$\begin{aligned}
X^\ell(t,x) &= X_0 + \ell X_1 + \ell^2 X_2 + \ell^3 X_3 + \cdots \\
X_i &= X_i(t,x,s) \quad i = 0,1,2,\cdots \quad \text{periodic in } s
\end{aligned}$$

$$\begin{aligned}
f &= AX + M\ddot{X} \\
&= \ell^{-2}(A_0 X_0 + \ell A_0 X_1 + \ell^2 A_0 X_2 + \ell^3 A_0 X_3 + \cdots) \\
&+ \ell^{-1}(A_1 X_0 + \ell A_1 X_1 + \ell^2 A_1 X_2 + \ell^3 A_1 X_3 + \cdots) \\
&+ (A_2 X_0 + \ell A_2 X_1 + \ell^2 A_2 X_2 + \ell^3 A_2 X_3 + \cdots) \\
&+ M(\ddot{X}_0 + \ell \ddot{X}_1 + \ell^2 \ddot{X}_2 + \ell^3 \ddot{X}_3) \\
&= \ell^{-2}(A_0 X_0) + \ell^{-1}(A_1 X_0 + A_0 X_1) \\
&+ (A_2 X_0 + A_1 X_1 + A_0 X_2 + M\ddot{X}_0) \\
&+ \ell(A_2 X_1 + A_1 X_2 + A_0 X_3 + M\ddot{X}_1) \\
&+ \ell^2(\cdots)
\end{aligned}$$

The above is valid for all ℓ. Thus, we need

$$A_0 X_0 = 0 \tag{36}$$

$$A_1 X_0 + A_0 X_1 = 0 \tag{37}$$

$$M \ddot{X}_0 + A_2 X_0 + A_1 X_1 + A_0 X_2 = f \tag{38}$$

$$M \ddot{X}_1 + A_2 X_1 + A_1 X_2 + A_0 X_3 = 0 \tag{39}$$

$$\vdots$$

Proposition 2

$$X_0 = X_0(t, x) \quad (not \quad depend \quad on \quad s) \tag{39}$$

Proposition 3

$$X_1(t, x, s) = -Y_1 \frac{\partial X_0}{\partial x} - Y_2 X_0 + \tilde{X}_1(t, x) \tag{40}$$

with

$$A_0 Y_1 = -\frac{dB_1}{ds} \tag{41}$$

$$A_0 Y_2 = -\frac{dB_2}{ds} \tag{42}$$

Y_1 and Y_2 are periodic in s since X_1 is. Moreover, Y_1 and Y_2 can be independent of t and x and unique up to a constant additive. Note that solution of Y_1 and Y_2 are guaranteed since

$$\int_{|S|} \frac{dB_1}{ds} ds = 0$$

$$\int_{|S|} \frac{dB_2}{ds} ds = 0$$

Proposition 4

$$
\begin{aligned}
f(x) &= -\frac{1}{|S|} \int_{|S|} (B_1 - B_1 \frac{dY_1}{ds}) ds \; \frac{\partial^2 X_0}{\partial x^2} \\
&\quad - \frac{1}{|S|} \int_{|S|} (B_2 - B_2^T - B_1 \frac{dY_2}{ds} + B_2^T \frac{dY_1}{ds}) ds \; \frac{\partial X_0}{\partial x} \\
&\quad + \frac{1}{|S|} \int_{|S|} (B_3 - B_2^T \frac{dY_2}{ds}) ds X_0 + \frac{1}{|S|} \int_{|S|} M(s) ds \; \ddot{X}_0 \\
&= A_h X_0 + M_h \ddot{X}_0 \tag{43}
\end{aligned}
$$

The above is the homogenized eq. found by the multi-scale perturbation method.

55

Proof:

From eq.(38), to render the sol. of X_2, we need

$$\int_{|S|} (A_2 X_0 + A_1 X_1 + M \ddot{X}_0) ds = \int_{|S|} f(x) ds = |S| f(x) \tag{44}$$

$$A_2 X_0 = -B_1 \frac{\partial^2 X_0}{\partial x^2} - (B_2 - B_2^T) \frac{\partial X_0}{\partial x} + B_3 X_0$$

$$A_1 X_1 = -\frac{dB_1}{ds} \frac{\partial X_1}{\partial x} - 2B_1 \frac{\partial^2 X_1}{\partial x \partial s} - (B_2 - B_2^T) \frac{\partial X_1}{\partial s} - \frac{dB_2}{ds} X_1$$

$$= -\frac{dB_1}{ds} (-Y_1 \frac{\partial^2 X_0}{\partial x^2} - Y_2 \frac{\partial X_0}{\partial x} + \frac{\partial \tilde{X}_1}{\partial x})$$

$$- 2B_1 (-\frac{dY_1}{ds} \frac{\partial^2 X_0}{\partial x^2} - \frac{dY_2}{ds} \frac{\partial X_0}{\partial x})$$

$$- (B_2 - B_2^T)(-\frac{dY_1}{ds} \frac{\partial X_0}{\partial x} - \frac{dY_2}{ds} X_0)$$

$$- \frac{dB_2}{ds} (-Y_1 \frac{\partial X_0}{\partial x} - Y_2 X_0 + \tilde{X}_1(x))$$

(Note that terms associated with $\frac{\partial \tilde{X}_1}{\partial x}$ and $\tilde{X}_1(x)$ are 0 after integration.)

$$= (2B_1 \frac{dY_1}{ds} + \frac{dB_1}{ds} Y_1) \frac{\partial^2 X_0}{\partial x^2}$$

$$+ \left(\frac{dB_1}{ds} Y_2 + 2B_1 \frac{dY_2}{ds} + (B_2 - B_2^T) \frac{dY_1}{ds} + \frac{dB_2}{ds} Y_1 \right) \frac{\partial X_0}{\partial x}$$

$$+ \left((B_2 - B_2^T) \frac{dY_2}{ds} + \frac{dB_2}{ds} Y_2 \right) X_0$$

$$= (B_1 \frac{dY_1}{ds}) \frac{\partial^2 X_0}{\partial x^2} + (B_1 \frac{dY_2}{ds} - B_2^T \frac{dY_1}{ds}) \frac{\partial X_0}{\partial x} + (-B_2^T \frac{dY_2}{ds}) X_0$$

Collecting terms together, we have eq.(43) immediately.

9 Properties of Homogenized Operator

$$M_h = \frac{1}{|S|} \int_{|S|} M(s) ds \tag{45}$$

$$M(s) > 0, \quad M^*(s) = M(s) \quad \forall\, s$$

$$[M_h X, X] = \frac{1}{|S|} \int_{|S|} [M(s)X, X] ds > 0 \quad \forall X \neq 0$$

$$\Rightarrow \quad M_h > 0$$

$$M_h^* = \frac{1}{|S|} \int_{|S|} M^*(s)ds = \frac{1}{|S|} \int_{|S|} M(s)ds = M_h$$

$$\Rightarrow \quad M_h \quad \text{self} - \text{adjoint}$$

Consider the special case where $X(t,x) = X_h(t)$

$$\begin{aligned}
KE_c &= \int_{|S|} [M_h \dot{X}_h, \dot{X}_h]ds = |S|[M_h \dot{X}_h, \dot{X}_h] \\
&\doteq KE_d = [M_d \dot{X}_d, \dot{X}_d]
\end{aligned}$$

Let

$$\dot{X}_d \doteq T_m \dot{X}_h$$

Then

$$M_h = \frac{1}{|S|}(T_m^T M_d T_m) \tag{46}$$

Therefore, equivalent mass matrix found by Noor's method agrees with that by homogenization theory, though not the case in the stiffness matrix.

$$\begin{aligned}
\bar{B}_1 &= \frac{1}{|S|} \int_{|S|} (B_1 - B_1 \frac{dY_1}{ds})ds \\
&= \frac{1}{|S|} \int_{|S|} [B_1 \frac{d}{ds}(Is - Y_1), \frac{d}{ds}(Is)]ds
\end{aligned} \tag{47}$$

By eq.(41)

$$A_0 Y_1 = -\frac{dB_1}{ds}$$

or

$$\int_{|S|} [-\frac{d}{ds}(B_1 \frac{dY_1}{ds}) + \frac{dB_1}{ds}, \Psi]ds = 0 \quad \forall \Psi \in \{H^1 : \text{ periodic}\}$$

$$\Rightarrow \int_{|S|} [B_1 \frac{dY_1}{ds} - B_1, \frac{d\Psi}{ds}]ds = 0$$

$$\Rightarrow \int_{|S|} [B_1 \frac{d}{ds}(Y_1 - Is), \frac{\partial \Psi}{\partial s}]ds = 0 \tag{48}$$

Take $\Psi = Y_1$
from eq.(47) and (48)

$$\bar{B}_1 = \frac{1}{|S|} \int_{|S|} [B_1 \frac{d}{ds}(Is - Y_1), \frac{d}{ds}(Is - Y_1)]ds \tag{49}$$

which is positive-definite and self-adjoint.

$$\begin{aligned}
\bar{B}_2 &= \frac{1}{|S|} \int_{|S|} [(B_2 - B_1 \frac{dY_2}{ds}) - B_2^T(I - \frac{dY_1}{ds})]ds \\
&= \frac{1}{|S|} \int_{|S|} \left([B_1^{-1}(B_2 - B_1 \frac{dY_2}{ds}), B_1(I - \frac{dY_1}{ds})] - B_1^{-1}[B_1(I - \frac{dY_1}{ds}), (B_2 - B_1 \frac{dY_2}{ds})] \right) ds
\end{aligned} \tag{50}$$

$$\bar{B}_3 = \frac{1}{|S|} \int_{|S|} (B_3 - B_2^T \frac{dY_2}{ds})ds$$

by

$$\int_{|S|} [B_1 \frac{dY_2}{ds} - B_2), \frac{d\Psi}{ds}]ds = 0 \quad \forall \Psi \in \{H^1 : \text{ periodic}\}$$

Take $\Psi = Y_2$, we have

$$\int_{|S|} [(B_1 \frac{dY_2}{ds} - B_2), \frac{dY_2}{ds}] = 0$$

or

$$\int_{|S|} B_1^{-1}[(B_1 \frac{dY_2}{ds} - B_2), B_1 \frac{dY_2}{ds}] = 0$$

$$\int_{|S|} B_1^{-1}[(B_1 \frac{dY_2}{ds} - B_2), (B_1 \frac{dY_2}{ds} - B_2)] = \int_{|S|} [-B_2^T \frac{dY_2}{ds} + B_2^T B_1^{-1} B_2]ds$$

Therefore,

$$\bar{B}_3 = \frac{1}{|S|} \int_{|S|} \left((B_3 - B_2^T B_1^{-1} B_2) + B_1^{-1}[(B_1 \frac{dY_2}{ds} - B_2), (B_1 \frac{dY_2}{ds} - B_2)] \right) ds \quad (51)$$

Let $L_2 = L_2(0, \text{L})$

$$[A_h X_0, X_0]_{L_2} = \frac{1}{|S|} \int_{|S|} \left[B_1^{-1} V, V \right]_{L_2} ds$$

$$+ \frac{1}{|S|} \int_{|S|} [(B_3 - B_2^T B_1^{-1} B_2) X_0, X_0]ds \quad (52)$$

where

$$V = B_1 \frac{d}{ds}(Is - Y_1)\frac{\partial X_0}{\partial x} + (B_1 \frac{dY_2}{ds} - B_2)X_0$$

$$A_h = A_h^* \qquad A_h > 0$$

Proposition 5

$$f(x) = -\bar{B}_1 \frac{\partial^2 X_0}{\partial x^2} - \bar{B}_2 \frac{\partial X_0}{\partial x}$$

$$+ \bar{B}_3 X_0 + M_h \ddot{X}_0$$

$$= A_h X_0 + M_h \ddot{X}_0 \quad (53)$$

where $\bar{B}_1$ $\bar{B}_2$ $\bar{B}_3$ M_h are constant matrices given in eq.(49) (50) (51) (45), respectively. Also, A_h and M_h are self-adjoint and positive-definite.

All the above procedures are formal. In general, B's are not differentiable and the differential eq. should be interpreted in the weak sense. Note that it can be shown that the homogenized operators do not depend on B.C.

58

10 Calculation of Operator's Parameter

By eq.(41)

$$A_0 Y_1 = -\frac{dB_1}{ds}$$

$$\Rightarrow -\frac{d}{ds}(B_1 \frac{dY_1}{ds}) = -\frac{dB_1}{ds} \quad (Y_1 \text{ function of s only})$$

$$\Rightarrow B_1 \frac{dY_1}{ds} = B_1 - C_1 \quad (B_1 > 0 \quad C_1 \text{ a constant matrix})$$

$$\Rightarrow \frac{dY_1}{ds} = I - B_1^{-1} C_1$$

$$(Y_1 \text{ periodic}) \Rightarrow \int_{|S|} \frac{dY_1}{ds} ds = 0$$

Therefore,

$$Y_1 \text{ periodic} \Rightarrow \int_{|S|} (I - B_1^{-1} C_1) ds = 0$$

$$C_1 = (\frac{1}{|S|} \int_{|S|} B_1^{-1} ds)^{-1} \tag{54}$$

By eq.(43), therefore,

$$\begin{aligned}
\bar{B}_1 &= \frac{1}{|S|} \int_{|S|} (B_1 - B_1 \frac{dY_1}{ds}) ds \\
&= \frac{1}{|S|} \int_{|S|} C_1 ds \\
&= C_1 \\
&= (\frac{1}{|S|} \int_{|S|} B_1^{-1} ds)^{-1} \tag{55}
\end{aligned}$$

$$\bar{B}_1 = \bar{B}_1^*, \qquad \bar{B}_1 > 0, \qquad \bar{B}_1 \leq \frac{1}{|S|} \int_{|S|} B_1 ds$$

From eq.(42)

$$\frac{dY_2}{ds} = B_1^{-1} B_2 - B_1^{-1} C_2$$

$$\int_{|S|} (B_1^{-1} B_2 - B_1^{-1} C_2) ds = 0$$

$$\begin{aligned}
C_2 &= (\int_{|2|} B_1^{-1} ds)^{-1} \int_{|S|} B_1^{-1} B_2 ds \\
&= C_1 \frac{1}{|S|} \int_{|S|} B_1^{-1} B_2 ds
\end{aligned}$$

Using the above results and eq.(43)

$$\bar{B}_2 = \frac{1}{|S|} \int_{|S|} (B_2 - B_2^T - B_1 \frac{dY_2}{ds} + B_2^T \frac{dY_1}{ds}) ds$$

$$= \frac{1}{|S|} \int_{|S|} [B_2 - B_2^T - B_1(B_1^{-1}B_2 - B_1^{-1}C_2)$$

$$\qquad + B_2^T(I - B_1^{-1}C_1)] ds$$

$$= \frac{1}{|S|} \int_{|S|} (C_2 - B_2^T B_1^{-1} C_1) ds$$

$$= C_2 - \frac{1}{|S|} \int_{|S|} B_2^T B_1^{-1} ds C_1$$

$$= C_1 \frac{1}{|S|} \int_{|S|} B_1^{-1} B_2 ds - \frac{1}{|S|} \int_{|S|} B_2^T B_1^{-1} ds C_1 \qquad (56)$$

$$\bar{B}_2^* = -\bar{B}_2$$

By (43)

$$\bar{B}_3 = \frac{1}{|S|} \int_{|S|} (B_3 - B_2^T \frac{dY_2}{ds}) ds$$

$$= \frac{1}{|S|} \int_{|S|} [B_3 - B_2^T(B_1^{-1}B_2 - B_1^{-1}C_2)] ds$$

$$= \frac{1}{|S|} \int_{|S|} (B_3 - B_2^T B_1^{-1} B_2) ds$$

$$\quad + \frac{1}{|S|} \int_{|S|} [B_2^T B_1^{-1} C_1 \frac{1}{|S|} \int_{|S|} B_1^{-1} B_2 ds] ds$$

$$= \frac{1}{|S|} \int_{|S|} (B_3 - B_2^T B_1^{-1} B_2) ds$$

$$\quad + (\frac{1}{|S|} \int_{|S|} B_2^T B_1^{-1} ds) C_1 (\frac{1}{|S|} \int_{|S|} B_1^{-1} B_2 ds) \qquad (57)$$

Proposition 6

$$\bar{B}_3^* = \bar{B}_3 \quad \text{and} \quad \bar{B}_3 \geq 0$$

Proof:

$$C > 0 \quad \Rightarrow \quad [C(KZ_1 + GZ_2), (KZ_1 + GZ_2] \geq 0 \quad \forall \quad Z_1, Z_2$$

$$\Rightarrow \left[\begin{pmatrix} K^T C K & K^T C G \\ G^T C K & G^T C G \end{pmatrix} \begin{pmatrix} Z_1 \\ Z_2 \end{pmatrix}, \begin{pmatrix} Z_1 \\ Z_2 \end{pmatrix} \right] \geq 0 \quad \forall \quad Z_1, Z_2$$

$$\Rightarrow \begin{pmatrix} B_1 & B_2 \\ B_2^T & B_3 \end{pmatrix} \geq 0, \quad \forall s, \quad \forall \quad Z_1, Z_2$$

Take $Z_1 = -B_1^{-1} B_2 Z_2$

$$\left[\begin{pmatrix} B_1 & B_2 \\ B_2^T & B_3 \end{pmatrix} \begin{pmatrix} Z_1 \\ Z_2 \end{pmatrix}, \begin{pmatrix} Z_1 \\ Z_2 \end{pmatrix} \right] = [(B_3 - B_2^T B_1^{-1} B_2) Z_2, Z_2]$$

$$\Rightarrow B_3 - B_2^T B_1^{-1} B_2 \geq 0 \quad \forall \quad s \quad QED.$$

Proposition 7 *The homogenized eq. is*

$$
\begin{aligned}
f(x) &= -\bar{B}_1 \frac{\partial^2 X_0}{\partial x^2} - \bar{B}_2 \frac{\partial X_0}{\partial x} \\
&\quad + \bar{B}_3 X_0 + M_h \ddot{X}_0 \\
&= A_h X_0 + M_h \ddot{X}_0
\end{aligned}
\tag{58}
$$

where $\bar{B}_1$ $\bar{B}_2$ $\bar{B}_3$ can be calculated directly from the original B's parameters as in eq.(55), (56) and (57), respectively. Also, A_h is self-adjoint and semi-positive definite.

Proof:
This is a similar result to the Proposition (5). Here we use the numerically calculable equations to prove it. The equations for $\bar{B}$'s have been shown already and the self-adjoint and positiveness are as follows:

$$
\begin{aligned}
[A_h X_0, X_0] &= [-C_1 \frac{\partial^2 X_0}{\partial x^2}, X_0] \\
&\quad + \left[[-C_1 \frac{1}{|S|} \int_{|S|} B_1^{-1} B_2 ds + \frac{1}{|S|} \int_{|S|} B_2^T B_1^{-1} ds C_1] \frac{\partial X_0}{\partial x}, X_0 \right] \\
&\quad + \left[[\frac{1}{|S|} \int_{|S|} (B_3 - B_2^T B_1^{-1} B_2) ds + \frac{1}{|S|} \int_{|S|} B_2^T B_1^{-1} ds C_1 \frac{1}{|S|} \int_{|S|} B_1^{-1} B_2 ds] X_0, X_0 \right] \\
&= \left[C_1 \left(\frac{\partial X_0}{\partial x} + \frac{1}{|S|} \int_{|S|} B_1^{-1} B_2 ds X_0 \right), \left(\frac{\partial X_0}{\partial x} + \frac{1}{|S|} \int_{|S|} B_1^{-1} B_2 ds X_0 \right) \right] \\
&\quad + [\frac{1}{|S|} \int_{|S|} (B_3 - B_2^T B_1^{-1} B_2 ds X_0, X_0] \geq 0, \quad \forall \quad X_0
\end{aligned}
\tag{59}
$$

and

$$
\begin{aligned}
[A_h X_0, Y_0] &= [-\bar{B}_1 \frac{\partial^2 X_0}{\partial x^2} - \bar{B}_2 \frac{\partial X_0}{\partial x} + \bar{B}_3 X_0, Y_0] \\
&= [X_0, -\bar{B}_1^* \frac{\partial^2 Y_0}{\partial x^2} + \bar{B}_2^* \frac{\partial Y_0}{\partial x} + \bar{B}_3^* Y_0] \\
&= [X_0, -\bar{B}_1 \frac{\partial^2 Y_0}{\partial x^2} - \bar{B}_2 \frac{\partial Y_0}{\partial x} + \bar{B}_3 Y_0] \\
&= [X_0, A_h^* Y_0] \quad \text{self} - \text{adjoint}
\end{aligned}
\tag{60}
$$

11   Conclusion

The differences between our approach and the direct averaging method [1, 2] are two fold.

- We know that the stiffness is additive at each cross section and the compliance is additive along the generic axis. The energy equivalence method averages the stiffness over one repeated cell and thus violates the additivity principle. Our approach intrinsically follows the additivity principle.

- Our approach finds the periodic governing equation first then homogenizes it. Namely, we replace the real structure by a 1-D periodic one, then average the four matrices to replace it again by a homogeneous beam. The direct averaging method averages the properties then finds the governing equation. Namely, the method averages two matrices for replacing the real structure by a homogeneous beam, then finds its governing equation.

These are the major reasons why our approach is more accurate than any previous.

References

[1] A. K. Noor et al. Continuum models for beam-and platelike lattice structures. *AIAA Journal*, Vol 16(No. 12):pp. 1219–1228, Dec. 1978.

[2] A.K. Noor and W.C. Russell. Anisotropic continuum models for beam-like lattice trusses. *Computer Methods in Applied Mechanics and Engineering*, Vol. 57:pp.257–277, Sept. 1986.

[3] J. L. Lions. *Some Methods in The Mathematical Analysis of Systems and Their Control*. Science Press, Beijing, China, 1981.

[4] J. E. Marsden and T. J. Hughes. *Mathematical Foundations of Elasticity*. Prentice-Hall, N.J., 1983.

[5] Y. C. Fung. *Foundations of Solid Mechanics*. Prentice-Hall, N.J., 1965.

[6] J. L. Lions, A. Bensoussan and G. Papanicolaou. *Asymptotic Analysis for Periodic Structures*. North-Holland Publishing Co., Amsterdam, 1978.
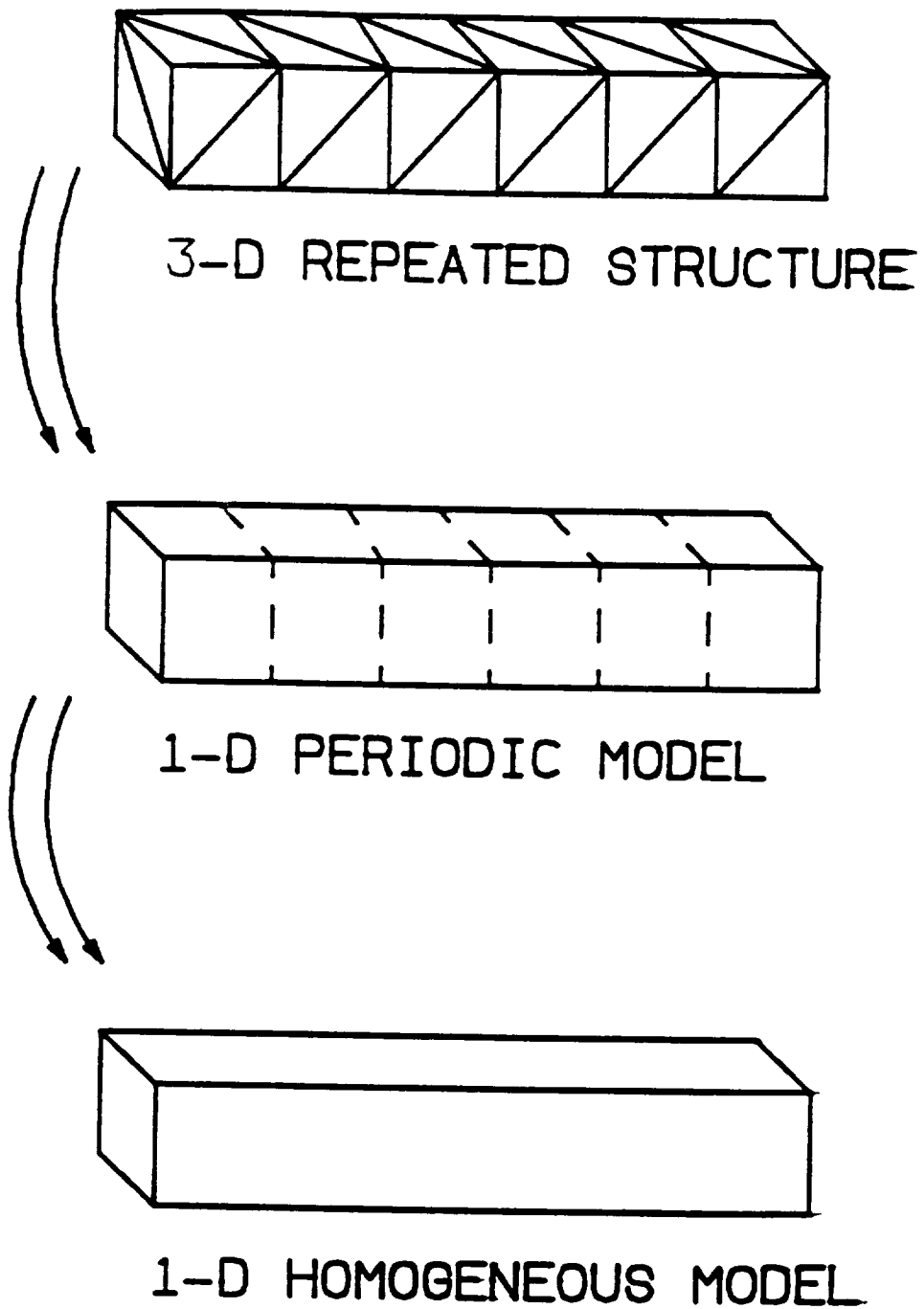
3-D REPEATED STRUCTURE

1-D PERIODIC MODEL

1-D HOMOGENEOUS MODEL

Figure 2: Schematics of Approximation

Integrated Design of Structures, Controls, and Materials

G.L. Blankenship[1]
Techno-Sciences, Inc.
7833 Walker Drive, Suite 620
Greenbelt, Maryland 20770

06/01/92

Abstract: In this talk we shall discuss algorithms and CAD tools for the design and analysis of structures for high performance applications using advanced composite materials. An extensive mathematical theory for optimal structural (e.g., shape) design has been developed over the past thirty years. Aspects of this theory have been used in the design of components for hypersonic vehicles and thermal diffusion systems based on homogeneous materials. Enhancement of the design methods to include optimization of the microstructure of the component is a significant innovation which can lead to major enhancements in component performance. Our work is focused on the adaptation of existing theories of optimal structural design, e.g., optimal shape design, to treat the design of structures using advanced composite materials, e.g., fiber reinforced, resin matrix materials. In this talk we shall discuss models and algorithms for the design of simple structures from composite materials, focussing on a problem in thermal management. We shall also discuss methods for the integration of active structural controls into the design process.

---

[1] Also with the Electrical Engineering Dept, University of Maryland, College Park, MD.

Problem: Integrated design of structures, their materials, and embedded active controls

Issues:

1. Shape optimization

2. Material analysis and design

3. Actuator design and placement

Shape Design: Find shape of an object to optimize a design criterion and satisfy design constraints.

Abstract Formulation:

- $\Omega \subset \mathbf{R}^n$ the object shape

- $A(u, \Omega) = 0$ defines $u(x) \in \mathbf{R}^m$, $x \in \Omega$

- Given $f(u, \Omega)$ a real–valued function

  Optimal Shape Design Problem:

  $$\min_{\Omega \in \mathcal{O}} \{ f(u, \Omega), \ A(u, \Omega) = 0 \}$$

Two essential problems:

1. Select the topology for the structure (cylindrical, rectangular, etc.); and

2. Within the designated topology find the best shape.

Remarks:

- The first problem is very difficult; e.g., introduction of internal holes in a structure to reduce the weight without violating design constraints

- The second problem (initial and final topologies are the same) can usually be treated by gradient methods.

Example: Optimal Compliance Design of an Elastic Structure

Problem: Design an elastic structure containing a large number of "cells" in a continuous array; e.g., fiber reinforced structure.

Remark: If the array is locally periodic, the macroscopic moduli may be computed using homogenization theory.

Design Parameters: dimensions (a, b) and orientation θ of the microscopic elements.

67
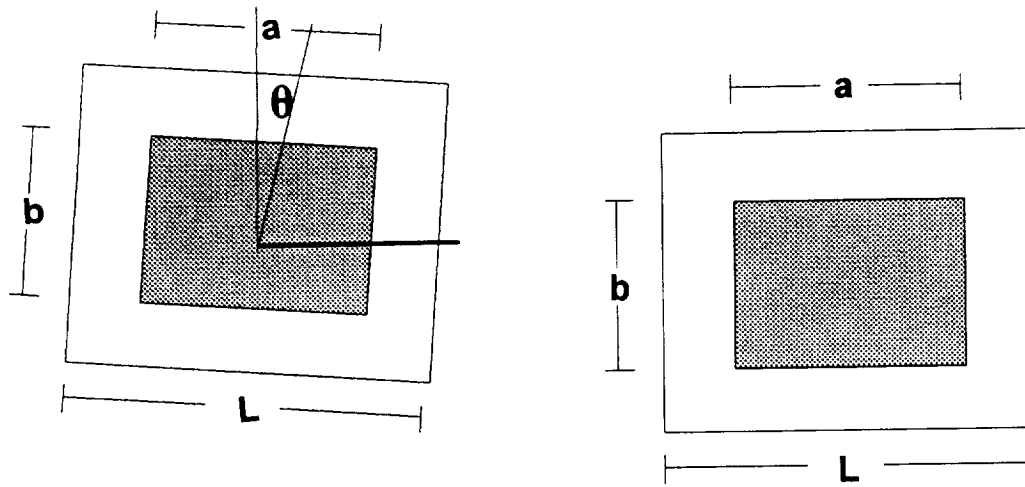
Design Parameters

Design Algorithm:

1. Use homogenization to compute the local effective elasticity tensor $E^H(x, (a, b, c, \theta))$.

2. Compute gradient of performance function

3. Steepest descent on design parameters

Matrix

Fiber
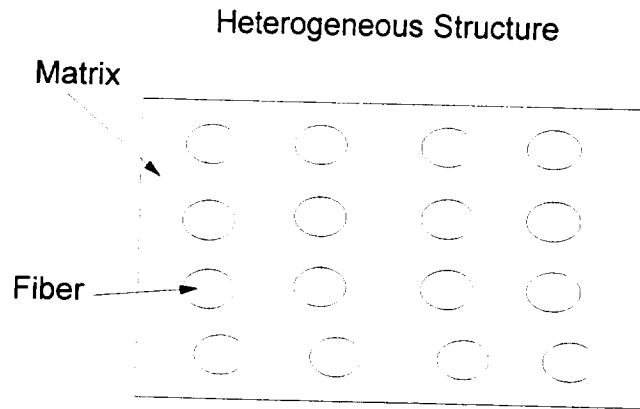
Effective Parameter Model:

"Effective" elasticity tensor $E^H(x)$ may be computed using homogenization theory.

1. Solve cell problem

$$\sum_{i,j,m,n=1}^{2} \int_Y E_{ijmn} \frac{\partial \chi_m^{(k\ell)}}{\partial y_n} \frac{\partial v_i}{\partial y_j} dY =$$

$$\sum_{i,j,m,n=1}^{2} \int_Y E_{ijmn} \frac{\partial v_i}{\partial y_j} d\dot{Y}$$

for the *characteristic deformation* $\chi_m^{(k\ell)}$

2. Compute the *homogenized elasticity tensor*

$$E_{ijk\ell}^H = \sum_{m,n=1}^{2} \int_Y \left(E_{ijk\ell} - E_{ijmn} \frac{\partial \chi_m^{(k\ell)}}{\partial y_n} \right) dY$$

Displacement Model: Assume smooth variation across structure.

$$E_{ijk\ell}^{H,(a,b,\theta)}(x) = \sum_{IJKL=1}^{2} E_{IJKL}^{H} R_{iI}[\theta(x)] \cdot$$

$$R_{jJ}[\theta(x)] R_{kK}[\theta(x)] R_{\ell L}[\theta(x)]$$

$$R[\theta(x)] = \begin{bmatrix} \cos\theta & -\sin\theta \\ \sin\theta & \cos\theta \end{bmatrix}$$

is the (local) rotation matrix.

Macroscopic Behavior: (For each $\Theta = (a, b, \theta)$)

$$\sum_{ijk\ell=1}^{2} \int_{\Omega} E_{ijk\ell}^{H,\Theta}(x) \frac{\partial u_k}{\partial x_\ell} \frac{\partial \nu_i}{\partial x_j} d\Omega$$

$$= \sum_{i=1}^{2} \int_{\Omega} f_i \nu_i d\Omega + \sum_{i=1}^{2} \int_{\Gamma_\tau} \tau_i \nu_i d\Gamma$$

$f_i, i = 1, 2$ are the applied body forces in Ω, $\tau_j, j = 1, 2$ are the tractions applied on the boundary $\Gamma_\tau \subset \Gamma = \partial\Omega$.

$$\min_{\{\Theta=(a,b,\theta)\}} \sum_{ijk\ell=1}^{2} \int_{\Omega} E_{ijk\ell}^{H,\Theta}(x) \frac{\partial u_k}{\partial x_\ell} \frac{\partial v_i}{\partial x_j} d\Omega$$

subject to the constraint (*) and

$$\int_{\Omega} (1 - a(x)b(x))d\Omega \leq |\Omega_F|$$

Ω_F = the maximum volume fraction allocated to the reinforcing material.

Using a penalty method, the optimization problem is approximated by

$$\max_{\Theta} \min_{\nu \in V} \Pi^\epsilon(\nu)$$

where $\Pi^\epsilon(\nu)$ is the total potential energy

$$\Pi^\epsilon(\nu) = \frac{1}{2} \sum_{ijk\ell=1}^{2} \int_{\Omega} E_{ijk\ell}^{H,\Theta}(x) \frac{\partial \nu_k}{\partial x_\ell} \frac{\partial \nu_i}{\partial x_j} d\Omega$$

$$+ \frac{1}{2} \sum_{i=1}^{2} \int_{\Gamma_D} \frac{1}{\epsilon}(\nu_i - g_i)^2 d\Gamma \quad \cdot$$

$$- \sum_{i=1}^{2} \int_{\Omega} f_i \nu_i d\Omega - \sum_{i=1}^{2} \int_{\Gamma_\tau} \tau_i \nu_i d\Gamma$$

Introduce the Lagrangian

$$\mathcal{L} = \Pi^\epsilon - \lambda \left(\int_\Omega (1 - ab) d\Omega - \Omega_F \right)$$

where $\lambda \leq 0$ is a Lagrange multiplier.

Taking the variation of $\mathcal{L}$ with respect to u and the design variables $\Theta = (a, b, \theta)$ gives the optimality conditions:

$$\int_\Omega \sum_{ijk\ell=1}^{2} \frac{1}{2} \left[\frac{\partial E_{ijk\ell}^{H,\Theta}}{\partial a} \frac{\partial u_k}{\partial x_\ell} \frac{\partial u_i}{\partial x_j} + \lambda b \right] \delta a \, d\Omega \geq 0$$

$$\forall \delta a = a^* - a, \quad 0 \leq a^* \leq 1 \in \Omega$$

* * *

Optimality conditions:

$$a = \min \left\{ \max \left[0, a - \rho_a \left(\frac{1}{2} \frac{\partial E_{ijk\ell}^{H,\Theta}}{\partial a} \frac{\partial u_k}{\partial x_\ell} \frac{\partial u_i}{\partial x_j} + \lambda b \right) \right], 1 \right\}$$

$$b = \min \left\{ \max \left[0, b - \rho_b \left(\frac{1}{2} \frac{\partial E_{ijk\ell}^{H,\Theta}}{\partial b} \frac{\partial u_k}{\partial x_\ell} \frac{\partial u_i}{\partial x_j} + \lambda a \right) \right], 1 \right\}$$

$$\lambda = \min \left\{ 0, \lambda - \rho_\lambda \left(\int_\Omega (1 - ab) d\Omega - \Omega_F \right) \right\}$$

$$\frac{1}{2} \frac{\partial E_{ijk\ell}^{H,\Theta}}{\partial \theta} \frac{\partial u_k}{\partial x_\ell} \frac{\partial u_i}{\partial x_j} = 0$$

for arbitrary positive numbers $\rho_a, \rho_b, \rho_\lambda$

Example: Optimal design of a thermal diffuser using composites

Problem: Select the shape Ω of the diffuser and the parameterization Θ of Ω_f (volume fraction, orientation, packing, etc.) of the material infrastructure to minimize the weight of the diffuser and meet operational objectives.

(i) the maximum temperature at the payload — diffuser interface must not exceed T_m;

(ii) no part of the diffuser can be thinner than some constant d; and

(iii) for convective cooling, the flux on the transmission interface of the diffuser must be below q_m.

Composite Material Thermal Diffuser

73
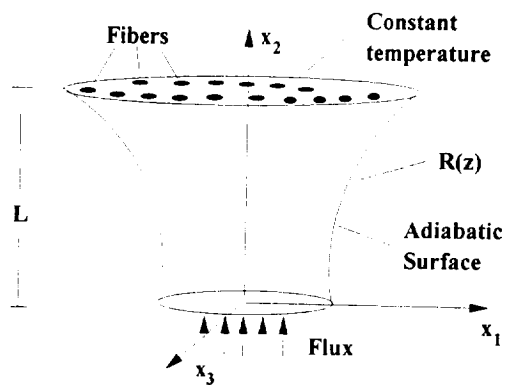
Model:

Assume: Conductivity of the fiber material is k, conductivity of the matrix material is K (could be anisotropic)

Conductivity tensor: $\{a_{ij}^{\Theta}(x,y,z), i,j = 1,2,3\}$

$$\frac{\partial}{\partial x_i}\left(a_{ij}^{\Theta}(x)\frac{\partial T^{\Theta}}{\partial x_j}\right) = 0$$

with the boundary conditions

$$\frac{\partial T^{\Theta}}{\partial \eta_{a\Theta}} = q_{in} \text{ on } \Sigma_1; \quad \frac{\partial T^{\Theta}}{\partial \eta_{a\Theta}} = 0 \text{ on } \Sigma_2$$

$$\frac{\partial T^{\Theta}}{\partial \eta_{a\Theta}} + \kappa(T^{\Theta})^p = q_s \text{ on } \Sigma_3$$

$\partial/\partial \eta_{a\Theta}$ is the conormal derivative at the surface.

Design Parameters: Θ, the fiber orientation and packing, and $R(z), 0 \leq z \leq L$ the curve defining the shape of the boundary, and L.

Performance Index: Mass of diffuser

$$\Pi(\Theta, R(\cdot), L) = \pi \int_0^L \int\int_{C(z)} \rho^{\Theta}(x,y,z)R(z)^2 dx\,dy\,dz$$

$\rho^{\Theta}(x,y,z)$ is the mass density in a cross section $C(z)$.

The *optimal design problem* is

$$\min_{\Theta, R(\cdot), L} \Pi(\Theta, R(\cdot), L)$$

74

Homogenization: (local)

Effective Conductivity:

$$\alpha_{ij} = \mathcal{M}(a_{ij}) - \mathcal{M}\left(a_{ik}\frac{\partial \chi^j}{\partial y_k}\right)$$

Macroscopic Behavior:

$$\stackrel{\triangle}{=} \mathcal{A}u = -\alpha_{ij}\frac{\partial^2 u^0}{\partial x_i \partial x_j} = f$$

"Corrector:"

$$-\frac{\partial}{\partial y_i}\left(a_{ij}(y)\frac{\partial}{\partial y_j}\chi^j\right) = -\frac{\partial a_{ij}(y)}{\partial y_i}$$

Optimal Design:

Adjoin constraints to performance function:

$$\sqcap_\mu(\Theta, R(\cdot), L)(\nu) = \sqcap(\Theta, R(\cdot), L)$$

$$+\frac{1}{2}\sum_{ij=1}^{2} \alpha_{ij}^{\Theta}(x)\frac{\partial \nu}{\partial x_i}\frac{\partial \nu}{\partial x_j} + \int_\Omega f\nu d\Omega$$

$$+\frac{1}{2}\sum_{ij=1}^{2}\frac{1}{\mu}\int_{\Gamma_2}(\nu - g)^2 d\Gamma$$

$\mu > 0$ is a small parameter.

Define the Lagrangian:

$$\mathcal{L}(\nu, \Theta, R(\cdot), L, \Lambda) = \Pi_\mu(\nu)$$

$$-\Lambda[\int_{\Omega_F} \rho_F dx dy dz - M_F]$$

Lagrange multiplier $\Lambda \leq 0$.

Optimality Criteria:

Obtained from variation of $\mathcal{L}$ with respect to state u and design variables $(\Theta, R(\cdot), L)$.

Applying Transfer Matrix Method
to the Estimation of the Modal Characteristics
of the NASA Mini-Mast Truss

Ji Yao Shen
Dept. of Mechanical Engineering
North Carolina A&T State University
Greensboro, NC 27411

Lawrence W. Taylor, Jr.
Guidance & Control Division
NASA Langley Research Center
Hampton, VA 23665

Abstract

It is beneficial to use a distributed parameter model for large space structures, because the approach minimizes the number of model parameters. Holzer's transfer matrix method provides a useful means to simplify and standardize the procedure for solving the system of partial differential equations. Any large space structures can be broken down into sub-structures with simple elastic and dynamical properties. For each single element, such as beam, tether, or rigid body, we can derive the corresponding transfer matrix. Combining these elements' matrices enables the solution of the global system equations. The characteristic equation can then be formed by satisfying the appropriate boundary conditions. Then natural frequencies and mode shapes can be determined by searching the roots of the characteristic equation at frequencies within the range of interest. This paper applies this methodology, and the maximum likelihood estimation method, to refine the modal characteristics of the NASA Mini-Mast Truss by successively matching the theoretical response to the test data of the truss. The method is being applied to more complex configurations.

1. Introduction

Control of flexible spacecraft is best analyzed by representing, in a single set of equations, all of the structural modes and the control system dynamics. Distributed parameter models enable this approach based upon the classical partial differential equation theories. In the early 1960's, the distributed parameter approach was developed simultaneously with the lumped parameter approach [1-3]. With the event of high-speed and large-memory computers the finite element method has been developed much more extensively than the distributed parameter approach. However, the advantages of the distributed parameter approach to control synthesis, parameter estimation and integrated design have been largely neglected by

the technical community. It is the purpose of this paper to show the advantage of employing the distributed parameter approach to large space structures.

Holzer's transfer matrix method provides a useful means to simplify and standardize the procedure for solving the system of partial differential equations. Also, the transfer matrix method enables the construction of a relatively simple mathematical model for complicated structures. It is of great practical value to take advantage of catalogs of the most important transfer matrices readily available. A complex structure, then, only requires combining individual matrices to represent the structure which consists of connected elements. The similarity of this concept to that of the transfer function is particularly useful to control analysis.

The transfer matrix method itself has been a matured method [4], and its power has been shown in several technical areas [5,6]. But, little use of the transfer matrix method has been made for the distributed modeling, parameter estimation and control of large flexible space structures.

In this paper we applied the transfer matrix method, accompanied by the maximum likelihood estimation technique, to estimate the lateral bending characteristics of the NASA Mini-Mast truss (Fig.1.1)[7] by matching the theoretical transient response to test data. The Mini-Mast truss is a ground testbed for the Control-Structure Interaction (CSI) program. The total height of the truss is 20.16 meters, containing 18 deployable bays. Two instrumentation platforms have been installed at Bay10 and Bay18. Mini-Mast has 162 major structural elements. Finite element models of the truss involve thousands of elements. The distributed parameter model of the Mini-Mast truss used in this paper consists of two flexible beam elements and two rigid bodies.

The shear deformation of the truss requires a Timoshenko beam model in order to match the frequencies at higher mode numbers. It is also necessary to extend the simple model by adding the so-called "appendage model" to account for the effects of dynamics of diagonal struts and associated hinge bodies. The method of this paper is shown to be applicable to more complex configurations.

2. Derivation of Transfer Matrix

Holzer's transfer matrix method [4] provides a useful means to simplify and standardize the procedure for solving the partial differential equations. Any large space structures can be broken down into sub-structures with simple elastic and dynamical properties. For each single element, such as beam in bending, rigid body, we can derive the corresponding field matrix and point matrix. Combining these elements' matrices in a required manner, one can calculate the responses, i.e. the solution to the global system equation, by proceeding from one point of the system to the other.

This paper concentrates on the estimation of the lateral bending frequency of the NASA Mini-Mast Truss. The truss is modeled as two successive beam elements with two rigid bodies at the Bay10, and Bay18 (tip of the truss), respectively. To derive the transfer matrix we consider a
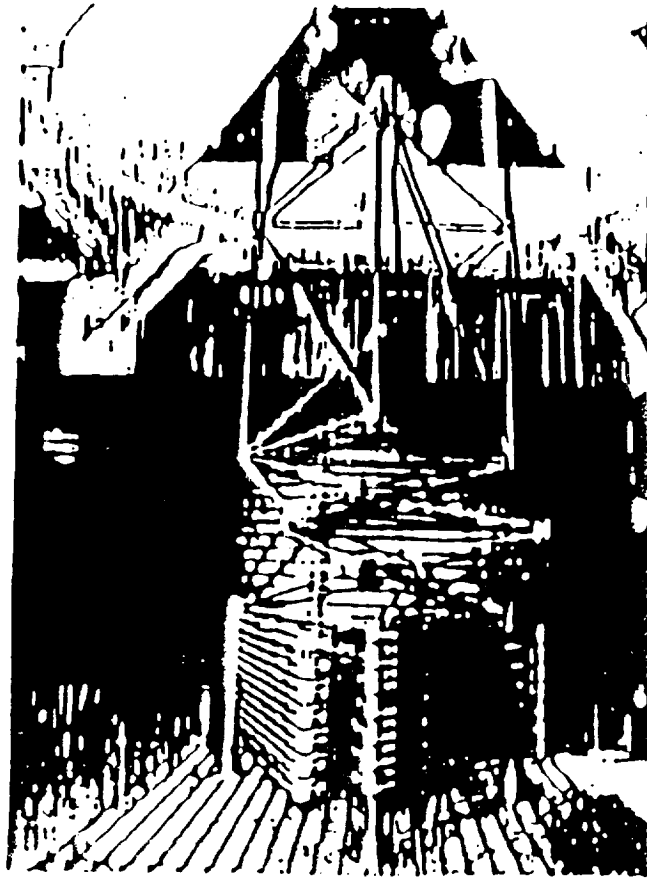
Fig. 1.1 NASA Mini-Mast Truss

"original photo not available"

cascaded beam-body system (Fig.2.1). The jth section consists of a flexible beam whose elastic and dynamical properties will be described by a field matrix, and a rigid body whose dynamical property is presented by a point matrix. When necessary, we will designate any corresponding quantities to the left and right of a rigid body by superscripts L and R.
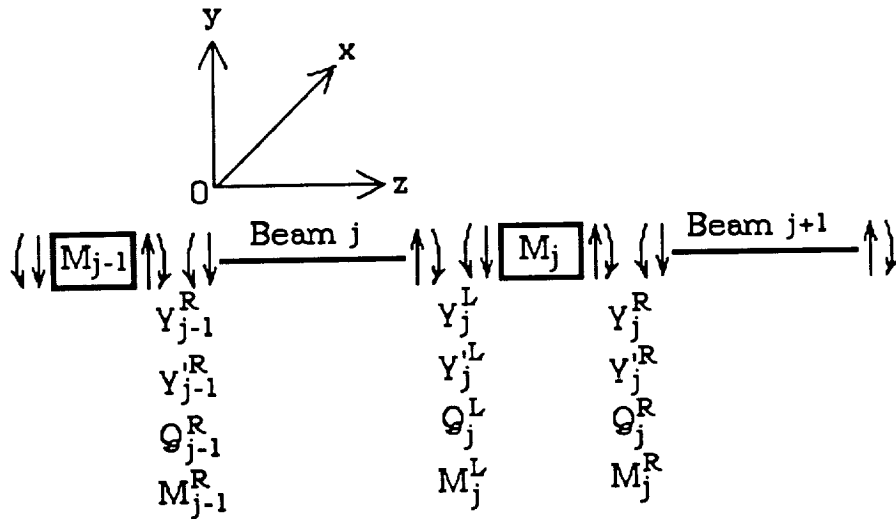

Fig. 2.1 A Cascaded Beam-Body System

The lateral bending of the beam is represented by the Bernoulli-Euler beam equation,

$$\frac{\partial^4 y}{\partial z^4} + \frac{1}{a^2}\frac{\partial^2 y}{\partial t^2} = 0 \qquad (2.1)$$

where, $y(z,t)$ is the lateral displacement, and $a^2 = k/m$ where $k = EI$ bending stiffness and $m = \rho A$ mass per length of the beam. By separation of variables $y(z,t) = Y(z)T(t)$, we have two ordinary differential equations in $Y(z)$ and $T(t)$,

$$Y''''(z) - \beta^4\, Y(z) = 0 \qquad (2.2)$$

and

$$\ddot{T}(t) + \omega^2\, T(t) = 0 \qquad (2.3)$$

where, $\beta^4 = \omega^2/a^2$. The solution to the Eq.(2.2) has the form,

$$Y(z) = A\sin\beta z + B\cos\beta z + C\sinh\beta z + D\cosh\beta z \qquad (2.4)$$

At the left end of the beam (z=0), the displacement Y(0), slope Y'(0), shear Q(0), and bending moment M(0) will be

80

$$Y^R_{j-1} = B_j + D_j$$

$$Y'^R_{j-1} = A_j\beta_j + C_j\beta_j$$

$$Q^R_{j-1} = -k_j Y_j'''(0) = A_j k_j \beta_j^3 - C_j k_j \beta_j^3$$

$$M^R_{j-1} = -k_j Y_j''(0) = B_j k_j \beta_j^2 - D_j k_j \beta_j^2$$

or written in matrix form as,

Thus,

$$\begin{Bmatrix} Y \\ Y' \\ Q \\ M \end{Bmatrix}^R_{j-1} = \begin{bmatrix} 0 & 1 & 0 & 1 \\ \beta & 0 & \beta & 0 \\ k\beta^3 & 0 & -k\beta^3 & 0 \\ 0 & k\beta^2 & 0 & -k\beta^2 \end{bmatrix}_j \begin{Bmatrix} A \\ B \\ C \\ D \end{Bmatrix}_j$$

$$\begin{Bmatrix} A \\ B \\ C \\ D \end{Bmatrix}_j = \begin{bmatrix} 0 & 1 & 0 & 1 \\ \beta & 0 & \beta & 0 \\ k\beta^3 & 0 & -k\beta^3 & 0 \\ 0 & k\beta^2 & 0 & -k\beta^2 \end{bmatrix}_j^{-1} \begin{Bmatrix} Y \\ Y' \\ Q \\ M \end{Bmatrix}^R_{j-1} = \begin{bmatrix} 0 & \dfrac{1}{2\beta} & \dfrac{1}{2k\beta^3} & 0 \\ \dfrac{1}{2} & 0 & 0 & \dfrac{1}{2k\beta^2} \\ 0 & \dfrac{1}{2\beta} & -\dfrac{1}{2k\beta^3} & 0 \\ \dfrac{1}{2} & 0 & 0 & -\dfrac{1}{2k\beta^2} \end{bmatrix}_j \begin{Bmatrix} Y \\ Y' \\ Q \\ M \end{Bmatrix}^R_{j-1} \quad (2.5)$$

Similarly, at the right end of the beam (z=L$_j$), the corresponding quantities are,

$$Y^L_j = A_j\sin\beta_j L_j + B_j\cos\beta_j L_j + C_j\sinh\beta_j L_j + D_j\cosh\beta_j L_j$$

$$Y'^L_j = A_j\beta_j\cos\beta_j L_j - B_j\beta_j\sin\beta_j L_j + C_j\beta_j\cosh\beta_j L_j + D_j\beta_j\sinh\beta_j L_j$$

$$Q^L_j = kY_j'''(L) = -A_j k_j\beta_j^3\cos\beta_j L_j + B_j k_j\beta_j^3\sin\beta_j L_j + C_j k_j\beta_j^3\cosh\beta_j L_j + D_j k_j\beta_j^3\sinh\beta_j L_j$$

$$M^L_j = kY_j''(L) = -A_j k_j\beta_j^2\sin\beta_j L_j - B_j k_j\beta_j^2\cos\beta_j L_j + C_j k_j\beta_j^2\sinh\beta_j L_j + D_j k_j\beta_j^2\cosh\beta_j L_j$$

or written in matrix form as,

$$\begin{Bmatrix} Y \\ Y' \\ Q \\ M \end{Bmatrix}^L_j = \begin{bmatrix} \sin\beta L & \cos\beta L & \sinh\beta L & \cosh\beta L \\ \beta\cos\beta L & -\beta\sin\beta L & \beta\cosh\beta L & \beta\sinh\beta L \\ -k\beta^3\cos\beta L & k\beta^3\sin\beta L & k\beta^3\cosh\beta L & k\beta^3\sinh\beta L \\ -k\beta^2\sin\beta L & -k\beta^2\cos\beta L & k\beta^2\sinh\beta L & k\beta^2\cosh\beta L \end{bmatrix}_j \begin{Bmatrix} A \\ B \\ C \\ D \end{Bmatrix}_j \quad (2.6)$$

Substituting Eq.(2.5) into Eq.(2.6) we obtain

$$\begin{Bmatrix} Y \\ Y' \\ Q \\ M \end{Bmatrix}_j^L = [FM]_j \begin{Bmatrix} Y \\ Y' \\ Q \\ M \end{Bmatrix}_{j-1}^R \qquad\qquad (2.7)$$

where, the field matrix of the jth beam element,

$$[FM]_j = \begin{bmatrix} \frac{1}{2}(\cos\beta L+\cosh\beta L) & \frac{1}{2\beta}(\sin\beta L+\sinh\beta L) & \frac{1}{2k\beta^3}(\sin\beta L-\sinh\beta L) & \frac{1}{2k\beta^2}(\cos\beta L-\cosh\beta L) \\[2mm] -\frac{\beta}{2}(\sin\beta L-\sinh\beta L) & \frac{1}{2}(\cos\beta L+\cosh\beta L) & \frac{1}{2k\beta^2}(\cos\beta L-\cosh\beta L) & -\frac{1}{2k\beta}(\sin\beta L+\sinh\beta L) \\[2mm] \frac{1}{2}k\beta^3(\sin\beta L+\sinh\beta L) & -\frac{1}{2}k\beta^2(\cos\beta L-\cosh\beta L) & -\frac{1}{2}(\cos\beta L+\cosh\beta L) & \frac{\beta}{2}(\sin\beta L-\sinh\beta L) \\[2mm] -\frac{1}{2}k\beta^2(\cos\beta L-\cosh\beta L) & -\frac{1}{2}k\beta(\sin\beta L-\sinh\beta L) & -\frac{1}{2\beta}(\sin\beta L+\sinh\beta L) & -\frac{1}{2}(\cos\beta L+\cosh\beta L) \end{bmatrix}_j$$
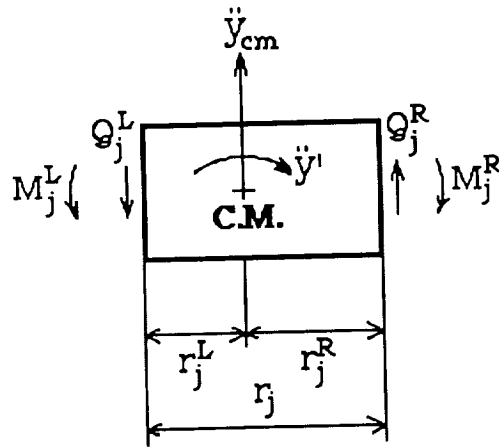
Fig. 2.2 Free Diagram of a Rigid Body

Next, let us consider the jth body (Fig.2.2). The translational and rotational motions of the body can be described by the following equations,

$$m_j \ddot{y}_{cm} = Q_j^R - Q_j^L \qquad\qquad (2.8)$$

$$I_j \ddot{y}'^L = M_j^R - M_j^L - Q_j^R r_j^R - Q_j^L r_j^L \qquad\qquad (2.9)$$

For homogeneous motions, Eqs.(2.8) and (2.9) can be written as,

$$Q_j^R = Q_j^L - m_j\omega^2 Y_{cm} \qquad\qquad (2.10)$$

$$M_j^R = M_j^L + Q_j^R r_j^R + Q_j^L r_j^L - I_j\omega^2 Y'^L_j \qquad\qquad (2.11)$$

But, the displacement of the center of mass, Y_{cm}, is related to Y_j^R and Y_j^L by,

$$Y_j^R = Y_{cm} - r_j^R \, Y_j'^R \qquad (2.12)$$

$$Y_j^L = Y_{cm} + r_j^L \, Y_j'^L \qquad (2.13)$$

From Eq.(2.13), we see that

$$Y_{cm} = Y_j^L - r_j^L \, Y_j'^L \qquad (2.14)$$

To keep the compatibility of the deflection, it must be that

$$Y_j'^R = Y_j'^L \qquad (2.15)$$

Substitution of Eqs.(2.14) and (2.15) into Eq.(2.12) gives

$$Y_j^R = Y_j^L - r_j \, Y_j'^L \qquad (2.16)$$

where, $r_j = r_j^L + r_j^R$.

Substituting Eq.(2.14) into Eq.(2.10) we obtain

$$Q_j^R = Q_j^L - m_j\omega^2 \, (Y_j^L - r_j^L \, Y_j'^L) \qquad (2.17)$$

Substituting Eq.(2.17) into Eq.(2.11) we can derive

$$M_j^R = M_j^L + r_j \, Q_j^L - m_j\omega^2 r_j^R Y_j^L - (I_j - m_j r_j^L r_j^R)\omega^2 Y_j'^L \qquad (2.18)$$

Collecting Eqs.(2.16), (2.15), (2.17) and (2.18), and writing in the matrix form we obtain

$$\begin{Bmatrix} Y \\ Y' \\ Q \\ M \end{Bmatrix}_j^R = [PM]_j \begin{Bmatrix} Y \\ Y' \\ Q \\ M \end{Bmatrix}_j^L \qquad (2.19)$$

where, the point matrix of the rigid body element,

$$[PM]_j = \begin{bmatrix} 1 & -r_j & 0 & 0 \\ 0 & 1 & 0 & 0 \\ -m_j\omega^2 & m_j\omega^2 r_j^L & 1 & 0 \\ -m_j\omega^2 r_j^R & -(I_j - m_j r_j^R r_j^L)\omega^2 & r_j & 1 \end{bmatrix}$$

Substituting Eq.(2.7) into Eq.(2.19) we obtain

$$\begin{Bmatrix} Y \\ Y' \\ Q \\ M \end{Bmatrix}_j^R = [\Phi]_{j,\,j-1} \begin{Bmatrix} Y \\ Y' \\ Q \\ M \end{Bmatrix}_{j-1}^R \qquad (2.20)$$

where, the transfer matrix of the jth section,

$$[\Phi]_{j,\,j-1} = [PM]_j [FM]_j = \begin{bmatrix} \Phi_{11} & \Phi_{12} & \Phi_{13} & \Phi_{14} \\ \Phi_{21} & \Phi_{22} & \Phi_{23} & \Phi_{24} \\ \Phi_{31} & \Phi_{32} & \Phi_{33} & \Phi_{34} \\ \Phi_{41} & \Phi_{42} & \Phi_{43} & \Phi_{44} \end{bmatrix}_{j,\,j-1}$$

The elements of the transfer matrix are listed below:

$$\Phi_{11} = \tfrac{1}{2}(\cos\beta L + \cosh\beta L) + \tfrac{1}{2}\beta r(\sin\beta L - \sinh\beta L)$$

$$\Phi_{12} = \frac{1}{2\beta}(\sin\beta L + \sinh\beta L) - \frac{r}{2}(\cos\beta L + \cosh\beta L)$$

$$\Phi_{13} = \frac{1}{2k\beta^3}(\sin\beta L - \sinh\beta L) - \frac{r}{2k\beta^2}(\cos\beta L - \cosh\beta L)$$

$$\Phi_{14} = \frac{1}{2k\beta^2}(\cos\beta L - \cosh\beta L) + \frac{r}{2k\beta}(\sin\beta L + \sinh\beta L)$$

$$\Phi_{21} = -\frac{\beta}{2}(\sin\beta L - \sinh\beta L)$$

$$\Phi_{22} = \tfrac{1}{2}(\cos\beta L + \cosh\beta L)$$

$$\Phi_{23} = \frac{1}{2k\beta^2}(\cos\beta L - \cosh\beta L)$$

$$\Phi_{24} = -\frac{1}{2k\beta}(\sin\beta L + \sinh\beta L)$$

$$\Phi_{31} = -\tfrac{1}{2}m\omega^2(\cos\beta L + \cosh\beta L) - \tfrac{1}{2}\beta m\omega^2 r^L(\sin\beta L - \sinh\beta L) + \tfrac{1}{2}k\beta^3(\sin\beta L + \sinh\beta L)$$

$$\Phi_{32} = -\frac{1}{2\beta}m\omega^2(\sin\beta L + \sinh\beta L) + \tfrac{1}{2}m\omega^2 r^L(\cos\beta L + \cosh\beta L) - \tfrac{1}{2}k\beta^2(\cos\beta L - \cosh\beta L)$$

$$\Phi_{33} = -\frac{m\omega^2}{2k\beta^3}(\sin\beta L - \sinh\beta L) + \frac{m\omega^2 r^L}{2k\beta^2}(\cos\beta L - \cosh\beta L) - \tfrac{1}{2}(\cos\beta L + \cosh\beta L)$$

$$\Phi_{34} = -\frac{m\omega^2}{2k\beta^2}(\cos\beta L - \cosh\beta L) - \frac{m\omega^2 r^L}{2k\beta}(\sin\beta L + \sinh\beta L) + \frac{\beta}{2}(\sin\beta L - \sinh\beta L)$$

$$\Phi_{41} = -\tfrac{1}{2}m\omega^2 r^R(\cos\beta L + \cosh\beta L) + \frac{\beta}{2}(I - mr^R r^L)\omega^2(\sin\beta L - \sinh\beta L)$$
$$+ \tfrac{1}{2}k\beta^3 r(\sin\beta L + \sinh\beta L) - \tfrac{1}{2}k\beta^2(\cos\beta L - \cosh\beta L)$$

$$\Phi_{42} = -\frac{1}{2\beta}m\omega^2 r^R(\sin\beta L + \sinh\beta L) - \frac{1}{2}(I\text{-}mr^R r^L)\omega^2(\cos\beta L + \cosh\beta L)$$

$$-\frac{1}{2}k\beta^2 r(\cos\beta L - \cosh\beta L) - \frac{1}{2}k\beta(\sin\beta L - \sinh\beta L)$$

$$\Phi_{43} = -\frac{1}{2k\beta^3}m\omega^2 r^R(\sin\beta L - \sinh\beta L) - \frac{1}{2k\beta^2}(I\text{-}mr^R r^L)\omega^2(\cos\beta L - \cosh\beta L)$$

$$-\frac{r}{2}(\cos\beta L + \cosh\beta L) - \frac{1}{2\beta}(\sin\beta L + \sinh\beta L)$$

$$\Phi_{44} = -\frac{1}{2k\beta^2}m\omega^2 r^R(\cos\beta L - \cosh\beta L) + \frac{1}{2k\beta}(I\text{-}mr^R r^L)\omega^2(\sin\beta L + \sinh\beta L)$$

$$+\frac{1}{2}\beta r(\sin\beta L - \sinh\beta L) - \frac{1}{2}(\cos\beta L + \cosh\beta L)$$

3. Characteristic Equation: Eigenvalue and Eigenfunction

After establishing the equation of motion of a global system by combining the transfer functions of all necessary elements, the natural frequency and mode shape function can be solved by satisfying the appropriate boundary conditions.
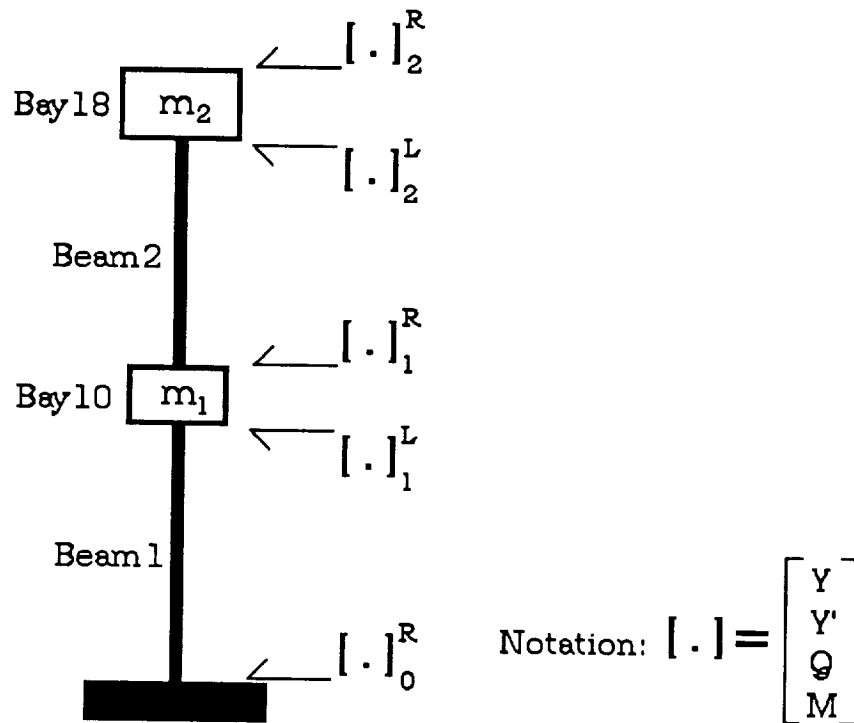

Fig. 3.1 The Mathematical Model for NASA Mini-Mast

As a mathematical model of the NASA Mini-Mast truss, it consists of two successive beam elements with two rigid bodies at the Bay10 and Bay18 (Fig.3.1). Using the transfer function in Eq.(2.20) we can see

$$\begin{Bmatrix} Y \\ Y' \\ Q \\ M \end{Bmatrix}_2^R = [\Phi]_{2,1}[\Phi]_{1,0} \begin{Bmatrix} Y \\ Y' \\ Q \\ M \end{Bmatrix}_0^R = [\Phi]_{2,0} \begin{Bmatrix} Y \\ Y' \\ Q \\ M \end{Bmatrix}_0^R \qquad (3.1)$$

Now let us consider the boundary conditions. At the fixed end we have

$$Y_0 = Y'_0 = 0 \qquad (3.2)$$

at the free end,

$$Q_2 = M_2 = 0 \qquad (3.3)$$

Applying the BC.'s to the Eq.(3.1) we get

$$\begin{Bmatrix} Y \\ Y' \\ 0 \\ 0 \end{Bmatrix}_2^R = [\Phi]_{2,0} \begin{Bmatrix} 0 \\ 0 \\ Q \\ M \end{Bmatrix}_0^R \qquad (3.4)$$

Rearranging the state vector we will have

$$[A] \begin{Bmatrix} Y_2 \\ Y'_2 \\ Q_0 \\ M_0 \end{Bmatrix}^R = [0] \qquad (3.5)$$

The condition for Eq.(3.5) having non-trivial solution is that the determinant of the coefficient matrix equals to zero, that is,

$$\text{Det}[A] = \text{Det} \begin{bmatrix} -1 & 0 & \Phi_{13} & \Phi_{14} \\ 0 & -1 & \Phi_{23} & \Phi_{24} \\ 0 & 0 & \Phi_{33} & \Phi_{34} \\ 0 & 0 & \Phi_{43} & \Phi_{44} \end{bmatrix} = 0 \qquad (3.6)$$

where, $\Phi_{i,j}$'s (i=1 to 4, j=3,4) are the elements of the transfer matrix $[\Phi]_{2,0}$. Eq.(3.6) is the so-called characteristic equation. Expanding the determinant in Eq.(3.6) we can rewrite the characteristic equation as

$$\Phi_{33} \Phi_{44} - \Phi_{34} \Phi_{43} = 0 \qquad (3.7)$$

Solving for the roots of the characteristic equation, Eq.(3.7), we can get the eigenvalue's β's. To verify the theoretical derivation we have deduced the characteristic equations for two simple examples from the foregoing characteristic equation (Eq.3.7) as follows:
For a cantilevered beam:

$$\cos\beta L \cdot \cosh\beta L = -1$$

For a cantilevered beam with a tip body:

$$1 + \cos\beta L \cdot \cosh\beta L = -\frac{W}{W_b}\beta L\,(\cos\beta L\sinh\beta L - \sin\beta L\cosh\beta L)$$

where W_b is the weight of the beam; W is the weight of the body. These results are identical with those given in commonly used textbooks [8].

To establish the mode shape functions we must solve the Eqs.(3.5) and (2.19) simultaneously, that is,

$$\begin{bmatrix} -1 & 0 & \Phi_{13} & \Phi_{14} \\ 0 & -1 & \Phi_{23} & \Phi_{24} \\ 0 & 0 & \Phi_{33} & \Phi_{34} \\ 0 & 0 & \Phi_{43} & \Phi_{44} \end{bmatrix} \begin{Bmatrix} Y_2 \\ Y'_2 \\ Q_0 \\ M_0 \end{Bmatrix}^R = 0 \qquad (3.8)$$

and

$$\begin{Bmatrix} Y \\ Y' \\ Q \\ M \end{Bmatrix}^R_1 = [PM]_1 \begin{Bmatrix} Y \\ Y' \\ Q \\ M \end{Bmatrix}^L_1 \qquad (3.9)$$

The later equation represents the compatible conditions of the deflections, forces, and moments between the two sides of the Body1. Because of the translational and rotary inertias of the Body1, the shear and bending moment have jumps at the connection point of the two beam elements, while the deflection functions are still continuous.

According to the solution function, Eq.(2.4), we can express the state vectors in Eqs.(3.8) and (3.9) in terms of the coefficients A_j, B_j, C_j and D_j $(j=1,2)$ by using the following relations:

$$Q_0^R = A_1 k_1 \beta_1^3 - C_1 k_1 \beta_1^3$$
$$M_0^R = B_1 k_1 \beta_1^2 - D_1 k_1 \beta_1^2$$

$$Y_1^L = A_1\sin\beta_1 L_1 + B_1\cos\beta_1 L_1 + C_1\sinh\beta_1 L_1 + D_1\cosh\beta_1 L_1$$
$$Y'^L_1 = A_1\beta_1\cos\beta_1 L_1 - B_1\beta_1\sin\beta_1 L_1 + C_1\beta_1\cosh\beta_1 L_1 + D_1\beta_1\sinh\beta_1 L_1$$
$$Q_1^L = - A_1 k_1 \beta_1^3\cos\beta_1 L_1 + B_1 k_1 \beta_1^3\sin\beta_1 L_1 + C_1 k_1 \beta_1^3\cosh\beta_1 L_1 + D_1 k_1 \beta_1^3\sinh\beta_1 L_1$$
$$M_1^L = - A_1 k_1 \beta_1^2\sin\beta_1 L_1 - B_1 k_1 \beta_1^2\cos\beta_1 L_1 + C_1 k_1 \beta_1^2\sinh\beta_1 L_1 + D_1 k_1 \beta_1^2\cosh\beta_1 L_1$$

$$Y_1^R = B_2 + D_2$$
$$Y'^R_1 = A_2\beta_2 + C_2\beta_2$$

(3.10)

$$Q_1^R = A_2 k_2 \beta_2^3 - C_2 k_2 \beta_2^3$$
$$M_1^R = B_2 k_2 \beta_2^2 - D_2 k_2 \beta_2^2$$

$$Y_2^R \cong Y_2^L = A_2 \sin\beta_2 L_2 + B_2 \cos\beta_2 L_2 + C_2 \sinh\beta_2 L_2 + D_2 \cosh\beta_2 L_2$$
$$Y'^R_2 = Y'^L_2 = A_2\beta_2\cos\beta_2 L_2 - B_2\beta_2\sin\beta_2 L_2 + C_2\beta_2\cosh\beta_2 L_2 + D_2\beta_2\sinh\beta_2 L_2$$

Substituting the quantities in Eq.(3.10) into Eqs.(3.8) and (3.9) we obtain a matrix equation in the coefficients A_j, B_j, C_j and D_j (j=1,2),

$$
\begin{bmatrix}
k_1\beta_1^3\Phi_{13} & k_1\beta_1^2\Phi_{14} & -k_1\beta_1^3\Phi_{13} & -k_1\beta_1^2\Phi_{14} & \alpha_{15} & \alpha_{16} & \alpha_{17} & \alpha_{18} \\
k_1\beta_1^3\Phi_{23} & k_1\beta_1^2\Phi_{24} & -k_1\beta_1^3\Phi_{23} & -k_1\beta_1^2\Phi_{24} & \alpha_{25} & \alpha_{26} & \alpha_{27} & \alpha_{28} \\
k_1\beta_1^3\Phi_{33} & k_1\beta_1^2\Phi_{34} & -k_1\beta_1^3\Phi_{33} & -k_1\beta_1^2\Phi_{34} & 0 & 0 & 0 & 0 \\
k_1\beta_1^3\Phi_{43} & k_1\beta_1^2\Phi_{44} & -k_1\beta_1^3\Phi_{43} & -k_1\beta_1^2\Phi_{44} & 0 & 0 & 0 & 0 \\
\alpha_{51} & \alpha_{52} & \alpha_{53} & \alpha_{54} & 0 & -1 & 0 & -1 \\
\alpha_{61} & \alpha_{62} & \alpha_{63} & \alpha_{64} & -\beta_2 & 0 & -\beta_2 & 0 \\
\alpha_{71} & \alpha_{72} & \alpha_{73} & \alpha_{74} & -k_2\beta_2^3 & 0 & k_2\beta_2^3 & 0 \\
\alpha_{81} & \alpha_{82} & \alpha_{83} & \alpha_{84} & 0 & -k_2\beta_2^2 & 0 & k_2\beta_2^2
\end{bmatrix}
\begin{Bmatrix}
A_1 \\ B_1 \\ C_1 \\ D_1 \\ A_2 \\ B_2 \\ C_2 \\ D_2
\end{Bmatrix} = [0] \quad (3.11)
$$

The elements expressed in α_{ij}'s in coefficient matrix are listed below:

$\alpha_{15} = - \sin\beta_2 L_2$

$\alpha_{16} = - \cos\beta_2 L_2$

$\alpha_{17} = - \sinh\beta_2 L_2$

$\alpha_{18} = - \cosh\beta_2 L_2$

$\alpha_{25} = - \beta_2\cos\beta_2 L_2$

$\alpha_{26} = \beta_2\sin\beta_2 L_2$

$\alpha_{27} = - \beta_2\cosh\beta_2 L_2$

$\alpha_{28} = - \beta_2\sinh\beta_2 L_2$

$\alpha_{51} = \sin\beta_1 L_1 - r_1\beta_1\cos\beta_1 L_1$

$\alpha_{52} = \cos\beta_1 L_1 + r_1\beta_1\sin\beta_1 L_1$

$\alpha_{53} = \sinh\beta_1 L_1 - r_1\beta_1\cosh\beta_1 L_1$

$\alpha_{54} = \cosh\beta_1 L_1 - r_1\beta_1\sinh\beta_1 L_1$

$\alpha_{61} = \beta_1\cos\beta_1 L_1$

$\alpha_{62} = - \beta_1\sin\beta_1 L_1$

$\alpha_{63} = \beta_1\cosh\beta_1 L_1$

$\alpha_{64} = \beta_1\sinh\beta_1 L_1$

$$\alpha_{71} = - m_1\omega_1^2\sin\beta_1L_1 + m_1\omega^2r_1^L\beta_1\cos\beta_1L_1 - k_1\beta_1^3\cos\beta_1L_1$$

$$\alpha_{72} = - m_1\omega^2\cos\beta_1L_1 - m_1\omega^2r_1^L\beta_1\sin\beta_1L_1 + k_1\beta_1^3\sin\beta_1L_1$$

$$\alpha_{73} = - m_1\omega^2\sinh\beta_1L_1 + m_1\omega^2r_1^L\beta_1\cosh\beta_1L_1 + k_1\beta_1^3\cosh\beta_1L_1$$

$$\alpha_{74} = - m_1\omega^2\cosh\beta_1L_1 + m_1\omega^2r_1^L\beta_1\sinh\beta_1L_1 + k_1\beta_1^3\sinh\beta_1L_1$$

$$\alpha_{81} = - m_1\omega^2r_1^R\sin\beta_1L_1 - (I_1-m_1r_1^Rr_1^L)\omega^2\beta_1\cos\beta_1L_1 - r_1k_1\beta_1^3\cos\beta_1L_1 - k_1\beta_1^2\sin\beta_1L_1$$

$$\alpha_{82} = - m_1\omega^2r_1^R\cos\beta_1L_1 + (I_1-m_1r_1^Rr_1^L)\omega^2\beta_1\sin\beta_1L_1 + r_1k_1\beta_1^3\sin\beta_1L_1 - k_1\beta_1^2\cos\beta_1L_1$$

$$\alpha_{83} = - m_1\omega^2r_1^R\sinh\beta_1L_1 - (I_1-m_1r_1^Rr_1^L)\omega^2\beta_1\cosh\beta_1L_1 + r_1k_1\beta_1^3\cosh\beta_1L_1 + k_1\beta_1^2\sinh\beta_1L_1$$

$$\alpha_{84} = - m_1\omega^2r_1^R\cosh\beta_1L_1 - (I_1-m_1r_1^Rr_1^L)\omega^2\beta_1\sinh\beta_1L_1 + r_1k_1\beta_1^3\sinh\beta_1L_1 + k_1\beta_1^2\cosh\beta_1L_1$$

The solution to the Eq.(3.11) will give infinite sets of coefficients corresponding to each order of eigenvalue, which are usually called the modal participant coefficients. Assume that the solution is normalized with respect to D_2, that is, $D_2=1$. Then we will have a specific set of coefficients corresponding to an eigenvalue β_{ji}, which is now assumed in the form of

$$
\begin{array}{llll}
A_1 = c_{1_i}, & B_1 = c_{2_i}, & C_1 = c_{3_i}, & D_1 = c_{4_i} \quad \text{For Beam1} \\
A_2 = c_{5_i}, & B_2 = c_{6_i}, & C_2 = c_{7_i}, & D_2 = 1 \quad \text{For Beam2}
\end{array}
\tag{3.12}
$$

Substituting the coefficients in Eq.(3.12) into the solution equation Eq.(2.4), we obtain the eigenfunctions, or the mode shape functions,

$$
Y_i(z) = \begin{cases}
c_1\sin\beta_{1i}z + c_2\cos\beta_{1i}z + c_3\sinh\beta_{1i}z + c_4\cosh\beta_{1i}z & \text{For Beam1} \\
c_5\sin\beta_{2i}z + c_6\cos\beta_{2i}z + c_7\sinh\beta_{2i}z + \cosh\beta_{2i}z & \text{For Beam2}
\end{cases}
\tag{3.13}
$$

4. Theoretical Response

When the proportional damping is taken into account the Bernoulli-Euler beam equation will be

$$m\frac{\partial^2 y}{\partial t^2} + c\frac{\partial y}{\partial t} + k\frac{\partial^4 y}{\partial z^4} = 0 \tag{4.1}$$

where, c is a damping constant of proportionality which is assumed as $c=2bm$. After separation of variables and introducing the generalized coordinates $T_i(t)$, we obtain

$$\sum_i \ddot{T}_i(t)\int_0^L [mY_iY_j]\,dz + \sum_i \dot{T}_i\int_0^L [cY_iY_j]\,dz + \sum_i T_i\int_0^L [kY_iY_j]\,dz = 0$$

which yields all zeros except for the one term in each when i=j according to the orthogonal property of the eigenfunctions, that is,

$$m_i \ddot{T}_i(t) + c_i \dot{T}_i(t) + k_i T_i(t) = 0 \qquad (4.2)$$

where,

$$m_i = \int_0^L m \, Y_i^2 \, dz \qquad \text{generalized mass}$$

$$k_i = \int_0^L k \, Y_i^2 \, dz \qquad \text{generalized stiffness}$$

$$c_i = \int_0^L c \, Y_i^2 \, dz = 2bm_i \qquad \text{generalized damping}$$

Expressing Eq.(4.2) in modal form we obtain

$$\ddot{T}_i + 2\xi_i\omega_i \dot{T}_i + \omega_i^2 T_i = 0 \qquad (4.3)$$

where, $2\xi_i \omega_i = c_i/m_i$ and $\omega_i^2 = k_i/m_i$. The solution to Eq.(4.3) is now

$$T_i(t) = e^{-\xi\omega t} (A_i \cos \omega_d t + B_i \sin \omega_d t) \qquad (4.4)$$

where, A_i and B_i are the coefficients dependent on the initial conditions. By superposition, the solution to the Eq.(4.1) can be written as

$$y(z, t) = \sum_i Y_i(z) e^{-\xi\omega t} (A_i \cos \omega_d t + B_i \sin \omega_d t) \qquad (4.5)$$

where, the eigenfunction $Y_i(z)$ has been derived in Eq.(3.13). Recall that we have defined that

$$a^2 = k/m, \qquad 2b = c/m, \qquad \text{and} \qquad \beta^4 = \omega^2/a^2 \qquad (4.6)$$

Then the damping ratio ξ_i and the damped natural frequency ω_{di} can be expressed in terms of the parameters a and b,

$$\xi_i = \frac{c_i}{2m_i\omega_i} = \frac{b}{a\beta_i^2}, \quad \text{and} \quad \omega_{d_i} = \omega_i \sqrt{1 - \xi_i^2} = \sqrt{(a\beta_i^2)^2 - b^2} \qquad (4.7)$$

By superposition, finally, the solution to the Eq.(4.1) can also be written in terms of the parameters a and b,

$$y(z, t) = \sum_i Y_i(z) \, e^{-bt} \left(A_i \cos t \sqrt{(a\beta_i^2)^2 - b^2} + B_i \sin t \sqrt{(a\beta_i^2)^2 - b^2} \right) \qquad (4.8)$$

5. Estimation of Modal Characteristics of NASA Mini-Mast

The maximum likelihood estimation method (MLE) is used to estimate the modal characteristics of the NASA Mini-Mast truss. The iterative formula for the MLE estimator has been derived in Ref.[9],

$$\hat{\theta} = \theta_0 + \left[\sum_{j=1}^{m} (\nabla_\theta y_j)^T R^{-1} (\nabla_\theta y_j) \right]^{-1} \left[\sum_{j=1}^{m} (\nabla_\theta y_j)^T R^{-1} (y_j - \bar{y}_{j_0}) \right] \qquad (5.1)$$

where,

$\bar{y}_0$ nominal response calculated by using θ_0

θ_0 nominal θ vector

$\nabla_\theta y_j$ gradient of y with respect to θ

R covariance of the measurement noise

The unknown parameter vector θ will be defined as

$$\theta = [a, \, b, \, A_1, A_2, \ldots, A_n, B_1, B_2, \ldots, B_n]^T \qquad (5.2)$$

Because we have got the closed-form solution y(z,t) (Eq.4.8), the gradient $\nabla_\theta y_j$ can be easily obtained by directly taking the derivatives of y with respect to the unknowns. The closed-form expressions of the gradients have been derived,

$$\frac{\partial y}{\partial a}(z,t) = \sum_i Y_i(z) \, e^{-bt} \frac{\beta_i^2 \, a \, t}{\sqrt{(a\beta_i^2)^2 - b^2}} \left[- A_i \sin t \sqrt{(a\beta_i^2)^2 - b^2} + B_i \cos t \sqrt{(a\beta_i^2)^2 - b^2} \right]$$

$$\frac{\partial y}{\partial b}(z,t) = \sum_i Y_i(z) \, t \, e^{-bt} \left\{ - A_i \cos t \sqrt{(a\beta_i^2)^2 - b^2} - B_i \sin t \sqrt{(a\beta_i^2)^2 - b^2} \right.$$

$$\left. + \frac{b}{\sqrt{(a\beta_i^2)^2 - b^2}} \left[A_i \sin t \sqrt{(a\beta_i^2)^2 - b^2} - B_i \cos t \sqrt{(a\beta_i^2)^2 - b^2} \right] \right\}$$

$$\frac{\partial y}{\partial A_i}(z,t) = Y_i(z) \, e^{-bt} \cos t \sqrt{(a\beta_i^2)^2 - b^2}$$

$$\frac{\partial y}{\partial B_i}(z,t) = Y_i(z) \, e^{-bt} \sin t \sqrt{(a\beta_i^2)^2 - b^2}$$

$$(5.3)$$

Now we use Eq.(5.1) iteratively, considering y_j as the measurements on a certain location of the beam at each time instant, and $\overline{y}_{j_0}$ as the iterative response values calculated by using the updated θ_0, at the same location and instant. When the innovation of the unknown parameter vector reaches the required criterion we may obtain the estimate $\hat{\theta}$ of θ. All the modal properties are related to the parameters a and b (Eq.4.7), thus we can obtain the modal properties as long as these unknown parameters are determined.

The test data is contained in Ref.[10], which was measured by one displacement sensor installed at Bay18, mounted parallel to the flat face on the corner joints of the structure and positioned to measure deflections normal to the face.

Table 5.1 shows the estimated frequencies which are compared with those obtained from Finite Element Analysis (FEA) and an Eigensystem Realization Algorithm (ERA) [11]. Fig.5.1 shows that the reconstructed response obtained from the estimated parameters and the measured response have a reasonably good fit.

6. Concluding Remarks

This paper has demonstrated the principles for applying a transfer matrix method to the parameter estimation of large space structures. The transfer matrix for the system with flexible beam elements and rigid bodies has been derived. The procedure for establishing natural frequency and mode shape has been described in detail. Maximum likelihood estimation method has served to conduct the parameter estimation. Comparing with the finite element model, the decrease in the number of unknown parameters by the present method is significant. The calculation, therefore, becomes highly efficient. The estimated results are compatible with those obtained by other traditional methods.

Further research is needed to formulate a more general method for more complicated structures. Some problems require coordinate transformation for non-perpendicular attachment elements. Transfer matrix for a branched structure must be considered. It is also desirable to develop a more efficient computer software based on the transfer matrix method, such as the new version of PDEMOD [12].

7. References

1.   Butkovskii, A.G. and Lerner, A.Y., "The Optimal Control of Systems with Distributed Parameters," Autom. Remote Control, Vol.21, pp472-477, 1960
2.   Wang, P.K.C., "Control of Distributed Parameter Systems," Advances in Control Systems, Vol.1, 1964
3.   Brogan, W.L., "Theory and Application of Optimal Control for Distributed Parameter," Automatic, Vol.4, pp.107-120, 1967
4.   Pestel E.C. and Leckie, F.A., "Matrix Methods in Elastomechanics," McGraw-Hill Book Company, Inc., New York, 1963

5.   Horner, G.C., "The Riccati Transfer Matrix Method," Ph.D. Dissertation, University of Virginia, Charlottesville, VA. May, 1975

6.   Uhrig, R., "The Transfer Matrix Method Seen as One Method of Structural Analysis Among Others," Journal of Sound and Vibration, Vol.4, No.2, Sept. 1966, pp136-148

7.   Adams, L.R., "Design, Development and Fabrication of a Deployable/ Retractable Truss Beam Model for Large Space Structures Application," NASA CR 178287, Astro Aerospace Corporation, 1987

8.   Thomson, W.T., "Theory of Vibration with Application," Prentice-Hall,Inc., Englewood Cliffs, New Jersey, 1972

9.   Shen, J.Y., "Maximum Likelihood Estimation for Distributed Parameter Models of Large Beam-like Structures," Ph.D. Dissertation, Dept. of Mechanical Engineering & Mechanics, Old Dominion University, Norfolk, VA. May 1991

10.   Liu, K. and Skelton, R., "The Q-Markov Cover and Its Application to Flexible Structure Identification," School of Aeronautics and Astronautics, Purdue University, 1990

11.   Pappa, R.S., Schenk, A. and Noll, C., "ERA Modal Identification Experiences with Mini-Mast," 2nd USAF/NASA Workshop on System Identification and Health Monitoring of Precision Space Structures, Pasadena, CA. March 1990

12.   Taylor, L.W. Jr., "PDEMOD: Computer Software for Distributed Parameter Estimation for Flexible Spacecraft Applied to NASA Mini-Mast Truss Experiment," 2nd USAF/NASA Workshop on System Identification and Health Monitoring of Precision Space Structures, Pasadena, CA. March 1990

Table 5.1 Comparison of Estimated Bending Frequencies (Hz.)

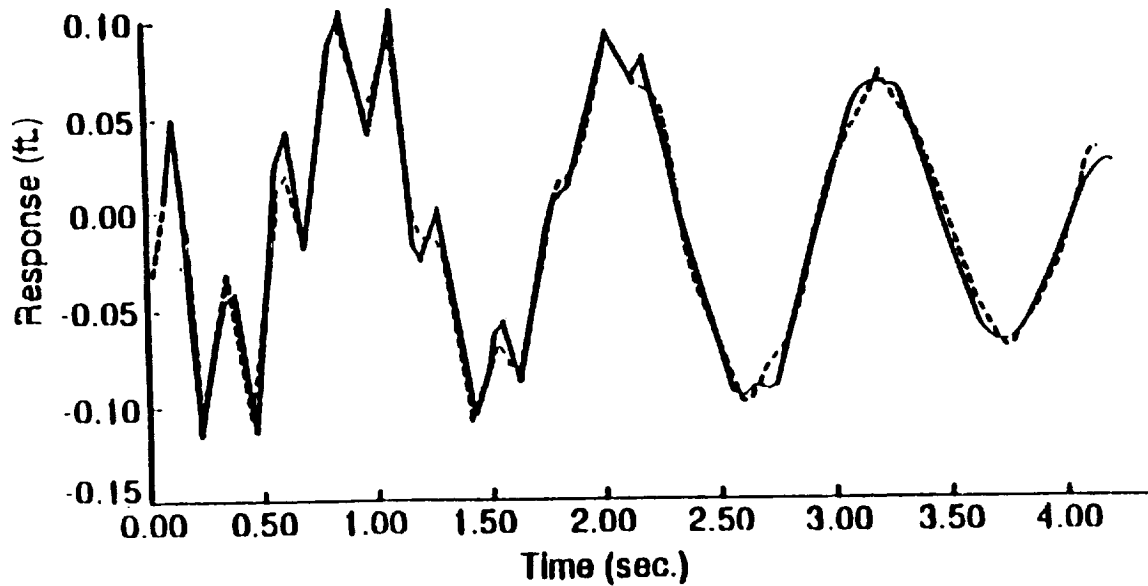| No.	F.E.A.	E.R.A.	D.P.A.
1	0.80	0.86	0.77
2	6.16	6.18	6.64
3	32.06	32.39	29.77
4	44.86	43.23	50.92

Fig. 5.1 Comparison of Reconstructed and Measured Responses

CONTROL OF FLEXIBLE STRUCTURES WITH DISTRIBUTED SENSING AND PROCESSING

Dave Ghosh
Lockheed Engineering and Sciences Company
Hampton, Virginia

Raymond C. Montgomery
NASA Langley Research Center
Hampton, Virginia

ABSTRACT

Technology is being developed to process signals from distributed sensors using distributed computations. These distributed sensors provide a new feedback capability for vibration control that has not been exploited. Additionally, the sensors proposed are of an optical and distributed nature and could be employed with known techniques of distributed optical computation (Fourier optics, etc.) to accomplish the control system functions of filtering and regulation in a distributed computer. This paper extends the traditional digital, optimal estimation and control theory to include distributed sensing and processing for this application. The design model assumes a finite number of modes which make it amenable to empirical determination of the design model via familiar modal-test techniques. The sensors are assumed to be distributed, but a finite number of point actuators are used. The design process is illustrated by application to a Euler beam. A simulation of the beam is used to design an optimal vibration control system that uses a distributed deflection sensor and nine linear force actuators. Simulations are also used to study the influence of design and processing errors on the performance.

PRESENTATION OUTLINE

- MOTIVATION

- OPTICAL SENSING AND PROCESSING

- DESIGN PHILOSOPHY

- OVERVIEW OF THEORY

- EXAMPLE AND SENSITIVITY STUDIES

- CONCLUSIONS AND FUTURE PLANS

Technology is being developed for optical sensing and processing of images that can represent distributed deflections of space structures. The motivation for this is summarized below.

MOTIVATION

- ADVANTAGES OF OPTICAL DISTRIBUTED SENSING AND PROCESSING

    - Non-contacting, high precision distributed position and velocity measurements

    - Parallel computations

    - Immunity to Electromagnetic Interference

- COMBINE TRADITIONAL, EMPIRICAL, MODEL-BASED CONTROLLER DESIGN WITH OPTICAL DISTRIBUTED SENSING AND PROCESSING

A portion of the BEAM is illuminated by a coherent laser source which is gathered by LENS optics and optically input to a DISTRIBUTED OPTICAL SENSOR which produces as its SENSOR OUTPUT a coherent light wherein position or velocity information over the illuminated portion of the simply-supported beam is represented by spatial intensity variations.

OPTICAL SENSOR
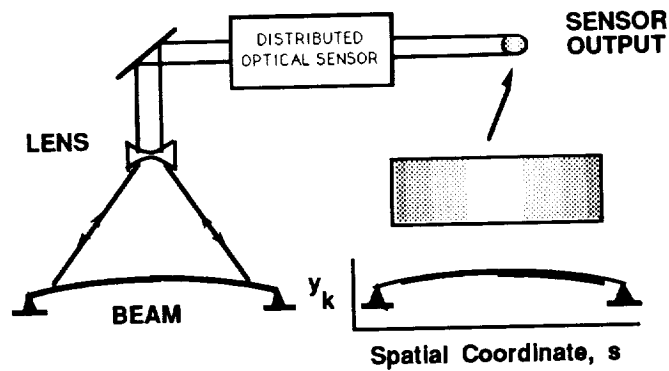
Images from the sensor output are then processed by a distributed optical processor the features of which are listed below.

OPTICAL PROCESSING

- SAMPLED-DATA IMAGE PROCESSING

- SIGNALS REPRESENTED BY IMAGES WITH
  SPATIAL INTENSITY VARIATIONS

- ADDITION AND SUBTRACTION USING
  COHERENT BEAMS

- INTEGRAL AND DIFFERENTIAL
  OPERATORS VIA FOURIER OPTICS

Distributed sensing is combined with traditional Kalman filtering and optimal control techniques for control system design. The technique is model-based and uses a finite number of modes. Also, the number of actuators considered is finite. Implementation is performed by distributed processing.

DESIGN PHILOSOPHY

- DESIGN MODEL -- EMPIRICALLY DERIVED

    - FINITE NUMBER OF MODES
    - DISTRIBUTED SENSOR
    - FINITE NUMBER OF ACTUATORS

- CONTROL LAW DESIGN -- DISCRETE KALMAN FILTER AND REGULATOR THEORY

$$X = \begin{bmatrix} \text{Modal Amplitude} \\ \text{Modal Velocity} \end{bmatrix}$$

- IMPLEMENTATION VIA DISTRIBUTED PROCESSING

100

The form of measurement is shown below. It is similar to the form used for point sensors except that the finite dimensional vector representing locations of point sensors in traditional formulation is replaced by a spatial coordinate, s, which is defined over the segment that lies in the sensors "field of view". The sensor noise characteristics at any point are assumed to be independent of any other point as shown by the last equation on this page.

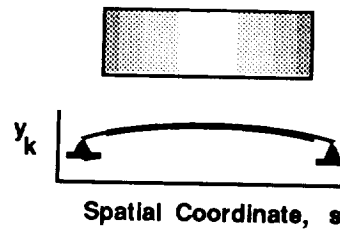# MEASUREMENT MODEL -- FINITE MODES with DISTRIBUTED SENSING

FORM OF MEASUREMENT

$$y_k = y(s, t_k) = H'(s)x_k + n_k(s)$$

$$s \in \Omega_M$$

SENSOR NOISE

Spatial Coordinate, s

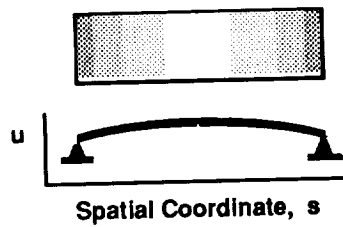$$E\{n_k(s) \, n_k'(s_1)\} = R(s) \, \delta(s\text{-}s_1)$$

The state is assumed to be distributed and defined over the entire structure and can be expressed in terms of mode-shapes and corresponding modal amplitudes. The modal amplitude can be recovered from the modal state by integrating over the domain of the structure as shown by the last equation on this page.

DISTRIBUTED PROCESSING
SIGNAL REPRESENTATION

$$u = u(s,t_k) = \phi'(s) [I \mid 0] x(t_k)$$

$$v = \frac{\partial u}{\partial t}(s,t_k) = \phi'(s) [0 \mid I] x(t_k)$$

$$s \in \Omega$$

Spatial Coordinate, s

$$[I \mid 0] x(t_k) = \int_{\Omega} \phi(\sigma) u(\sigma, t_k) d\sigma$$

102

With the assumption of finite modes, an appropriate model for the evolution of the modal state as a sampled data system is shown below. The noise term is added to account for process noise.

DYNAMICS MODEL -- FINITE MODES
with DISTRIBUTED SENSING

MODAL STATE $\qquad x_k = x(t_k) = \begin{bmatrix} \text{Amplitude} \\ \text{Velocity} \end{bmatrix}$

DYNAMICS $\qquad x_{k+1} = \Phi x_k + \Gamma f_k + w_k$

PROCESS NOISE $\qquad E(w_j w'_k) = Q \delta_{jk}$

Noise is introduced during distributed processing. The noise terms W, N and M appearing in the prediction, update and regulator equations, respectively, are modeled as white Gaussian noise.

OPTICAL PROCESSING
WITH NOISE

PREDICTOR $\quad u_{k+1}^{(-)}(s) = \mathbb{F}\, u_k^{(+)}(s) \;+\; \phi'(s)\,\Gamma f_k \;+\; W$

$\qquad\qquad$ **where** $\mathbb{F} = \{\, \phi'(s)\,\Phi \displaystyle\int_\Omega \phi(\sigma)\,(\,\bullet\,)\,d\sigma \}$

UPDATE $\quad u_k^{(+)}(s) = u_k^{(-)}(s)$

$\qquad + \displaystyle\int_{\Omega_M} \phi'(s)\,K(\sigma)\,[y_k(\sigma) - H'(\sigma)\int_\Omega \phi(\eta)\,u_k^{(-)}(\eta)\,d\eta]\,d\sigma \;+\; N$

REGULATOR $\quad f_k = \displaystyle\int_\Omega G\,\phi(\eta)\,u_k^{(+)}(\eta)\,d\eta \;+\; M$

The method was applied to a simply supported beam with nine linear force actuators and a distributed deflection sensor. Distributed processing was simulated on a digital computer.

SIMULATION STUDIED

|←—.36 L —→|
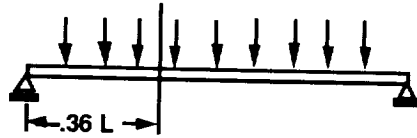
- SIMPLY SUPPORTED BEAM

- 9 LINEAR FORCE ACTUATORS

- DISTRIBUTED DEFLECTION SENSOR

- DIGITAL SIMULATION OF DISTRIBUTED
  PROCESSING

For simulation only the first three modes were used. The characteristics of the first three modes of the beam are summarized below.

MODAL CHARACTERISTICS OF THE BEAM

MODE	FREQ. (HZ)	DAMPING	MODE-SHAPE
1	0.600	0.0100	
2	2.400	0.0050	
3	5.400	0.0045	

106

In empirically derived models, errors can be introduced from different sources in the identification process. The model errors can be found in frequency, damping and mode-shape.

MODEL-ERRORS AND NOISE

- **MODEL- ERRORS**

    Frequency
    Damping
    Mode-shape

- **NOISE**

    Sensor noise : included in K-Filter Design

   **Process noise : included in K-Filter Design**

    Distributed processing noise: W, M, N -cannot be included Kalman Filter Design

The beam was allowed to vibrate freely from an initial displacement (0.1^n, n=1,2,3). After ten seconds of free vibration an LQG based controller designed for the first mode was activated. The response below shows the measurements obtained at one point (.36L from the left end) and the corresponding estimations. It takes about five seconds for the estimations to converge to the measurements. The closed-loop segment of the response shows that the vibrations are effectively damped out.
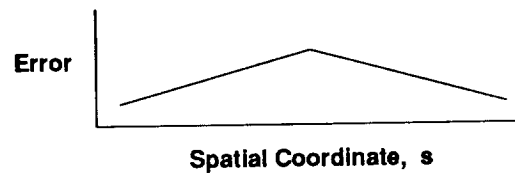
CONTROLLER PERFORMANCE
NOMINAL DESIGN
DISPLACEMENT AT .36L FROM LEFT END

TIME, SEC.
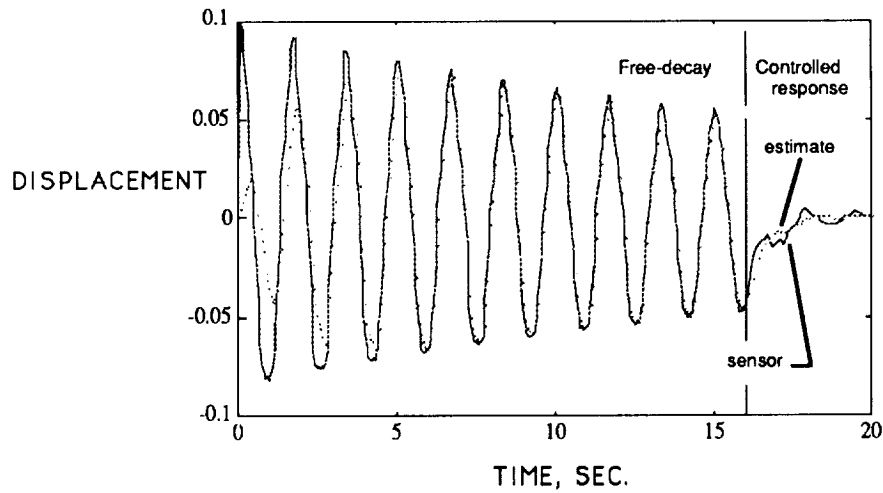
Parameters of the model were varied to study its effect on the performance of the estimator and controller. The verified ranges in which the variation of frequency, damping-ratio and mode-shape of the first mode did not produce instability during closed-loop simulations is listed below. The first mode shape was varied by superposing a triangle shaped error on the mode shape with the height of the error triangle represented as a percentage of the amplitude of the nominal mode shape.

VERIFIED STABILITY RANGE
Mode 1

FREQUENCY   -50 % to 100 %

DAMPING RATIO   -80 % to 100 %

MODE SHAPE   -5 %* to 100 %

Error

Spatial Coordinate, s

* Unstable < -5 %

The reponse below shows the controller perfromance with 100% mode-1 frequency error.
In the open-loop segment the estimations are erroneous as expected but after the controller is
activated, the frequency errors observed in the open-loop estimations are eliminated and the
vibrations are controlled effectively.

CONTROLLER PERFORMANCE
100% MODE 1 FREQUENCY ERROR
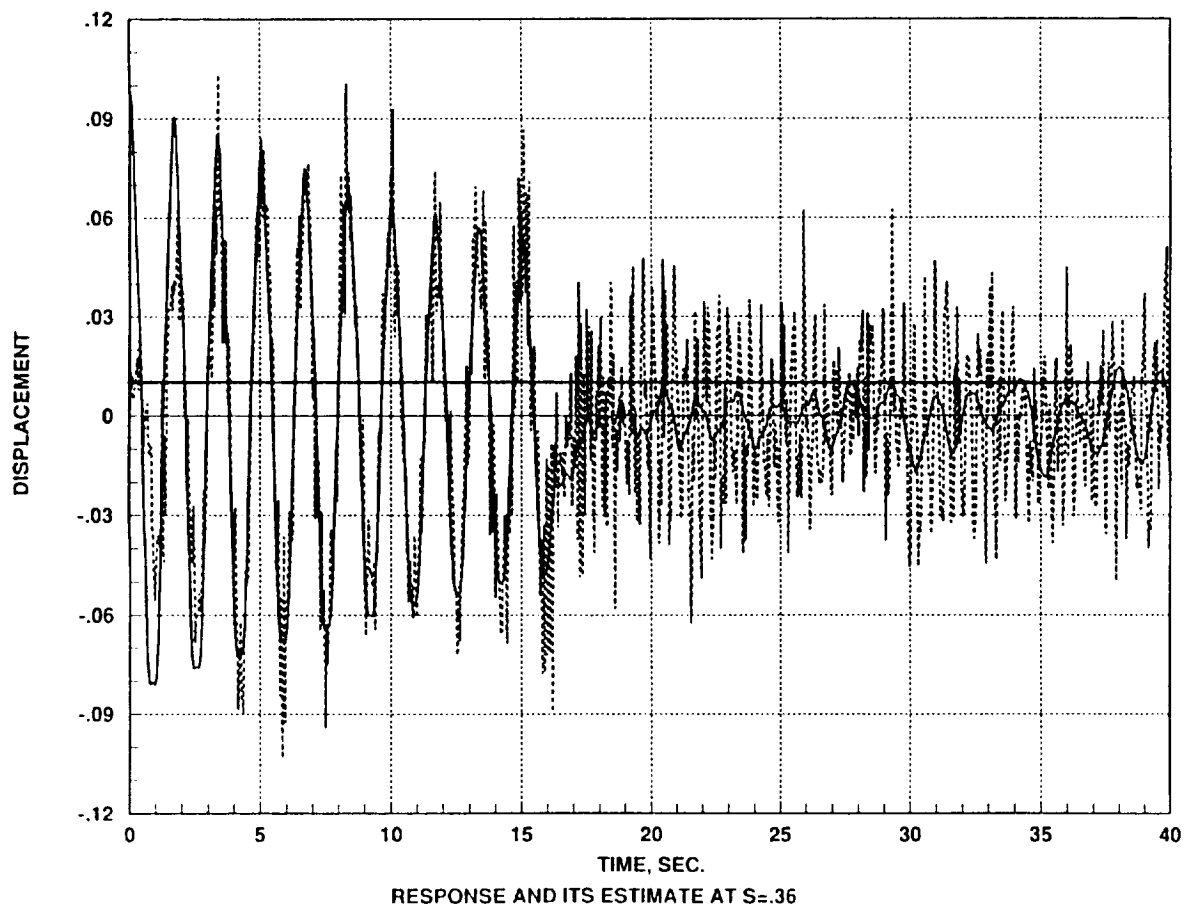## DISPLACEMENT AT .36L FROM LEFT END
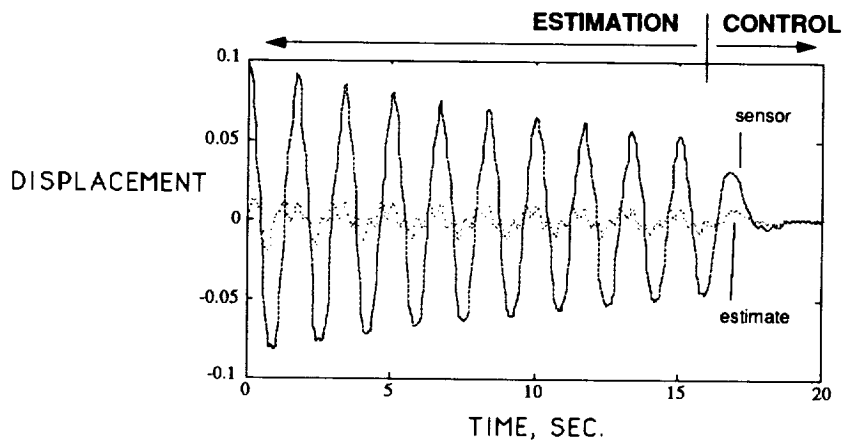
The response below shows the effect of optical prediction noise with RMS noise intensity of 0.01 which is 10 percent of the initial displacement of .1 units. The noise intensity level is indicated as a thick horizontal line. The solid line represents the measurement and the broken line, its estimation. Both the open-loop and the closed -loop estimations are noisy because the filter does not take into account the optical processing noise. In the closed-loop segment the response does not show any unbounded growth, thus demonstrating the robustness of the system to optical processing noise.

RESPONSE WITH PREDICTION NOISE

DISPLACEMENT AT .36L FROM LEFT END

RMS Noise Intensity : 0.01

TIME, SEC.

RESPONSE AND ITS ESTIMATE AT S=.36

111

A simulation study was also made with RMS noise intensity of 0.08, an eight-fold increase over the previous study. As before, the noise intensity level is indicated as a thick horizontal line. The solid line represents the measurement and the broken line, its estimation. The estimations are noisy and do not bear any similarity with the measurements. In the closed-loop segment the plant responds to the actuator noise only and does not show any unbounded growth, thereby demonstrating again the robustness of the system to optical prediction noise.

RESPONSE WITH PREDICTION NOISE

DISPLACEMENT AT .36L FROM LEFT END

RMS Noise Intensity : 0.08

RESPONSE AND ITS ESTIMATE AT S=.36

112
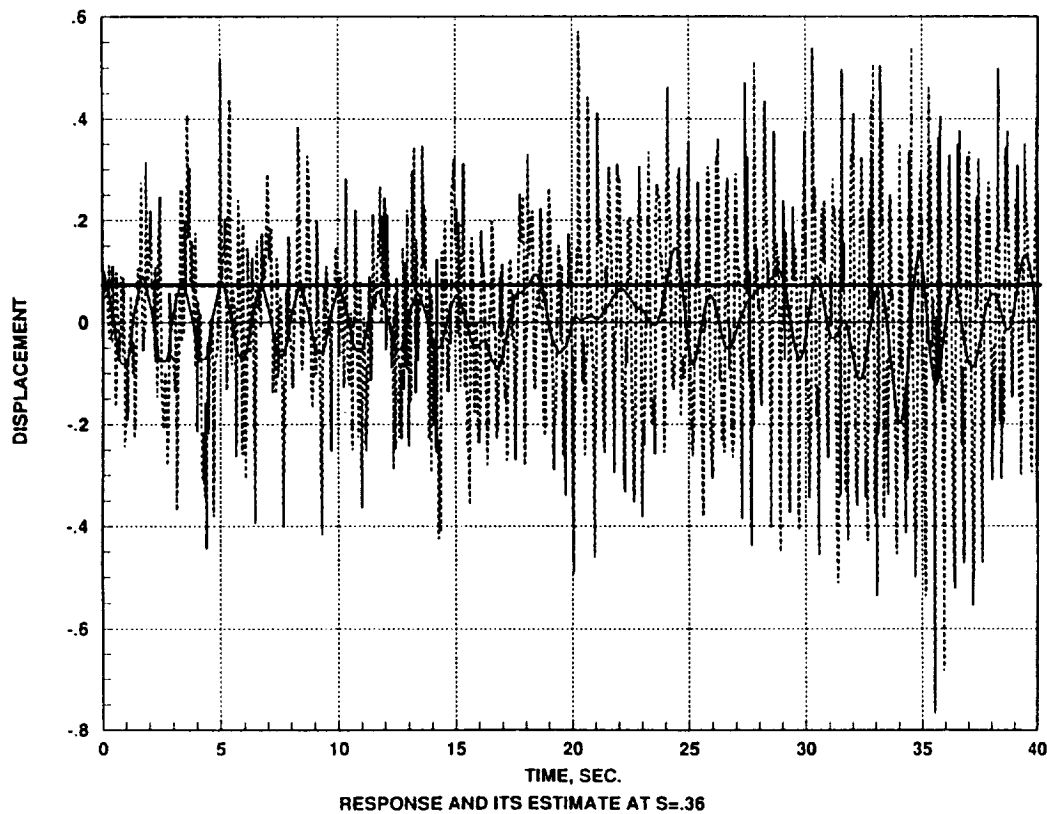
The response below shows the effect of actuator command generation noise with RMS noise intensity of 0.1. After the controller is activated the response amplitudes are reduced, albeit noisy because of the command generation noise. The closed -loop estimations are also noisy because the filter does not take into account the actuator command generation noise.

RESPONSE WITH ACTUATOR COMMAND GENERATION NOISE

DISPLACEMENT AT .36L FROM LEFT END

RMS Noise Intensity : 0.10

RESPONSE AND ITS ESTIMATE AT S=.36

113
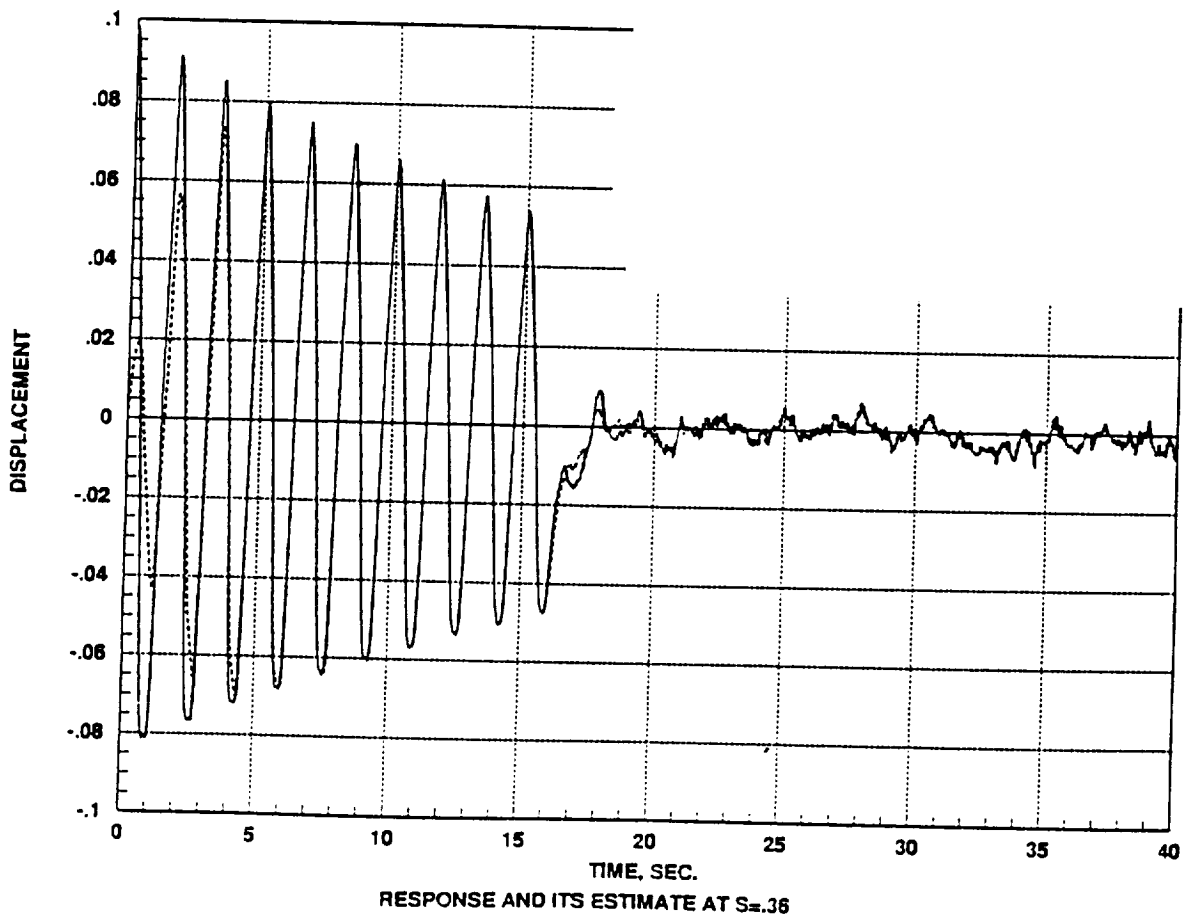
In this presentation a design process for distributed sensing and processing was developed and demonstrated using a distributed processing simulator. It was shown that the process is robust to modelling errors and distributed processing noise. Future plans include experimental verification of the concepts outlined.

CONCLUSIONS AND FUTURE PLANS

- DEVELOPED DESIGN PROCESS FOR DISTRIBUTED SENSING AND PROCESSING

- TESTED USING A DISTRIBUTED PROCESSING SIMULATOR

- PROCESS IS ROBUST TO MODELLIING ERRORS IN FREQUENCY, DAMPING, AND MODE-SHAPE AND DISTRIBUTED PROCESSING NOISE

- EXPERIMENTAL VERIFICATION OF THE CONCEPTS

Variations in the Modal Characteristics of

A Telescopically Deploying Beam

Anthony K. Amos[†]

Penn State University

University Park, PA 16802

P- 17

SUMMARY

The equations of motion for a two-segment deploying telescopic beam are derived through application of Lagrange's equation. The outer tube of the beam is fixed at one end and the inner tube slides freely relative to the fixed segment. The resulting nonlinear, non-autonomous set of equations is linearized and simplified to the standard Euler-Bernoulli partial differential equations for an elastic beam by freezing the deployment process at various stages of deployment, and examining the small amplitude and natural modes of vibration of the resulting configuration. Application of the natural boundary conditions and compatibility of motion relations for the two segments in their common region of overlap leads to a transcendental characteristic equation in the frequency parameter βL, where

$$(\beta L)^4 = \frac{\omega^2 m L^4}{EI}; \quad L = \text{length of beam}$$

m = mass / unit length of fixed beam segment

EI = flexural rigidity of the beam

ω = frequency

Numerical solution of the equation for the characteristic roots determines the modal frequencies, and the corresponding mode shapes are obtained from the general solution of the Euler-Bernoulli equation tailored to the natural boundary conditions.

Sample results of modal frequencies and shapes are presented for various stages of deployment and discussed. It is shown that for all intermediate stages of deployment (between 0% and 100%) the spectral distribution is drastically altered by the appearance of regions of very closely spaced modal frequencies. The sources of this modal agglomeration are explored.

---

† *Professor of Aerospace Engineering*

INTRODUCTION

The dynamics of spacecraft in earth orbit or interplanetary travel is uniquely different from earth-bound system dynamics in as much as equilibrium and stability result from the strong interactions among the laws of rigid body dynamics and those of flexible vibrational motions. If in addition, the spacecraft undergoes spatial and temporal redistribution of inertial and stiffness properties as during deployment and assembly operations, the dynamics of this configuration evolution must also be accommodated in this self-contained dynamic system, without uncontrollable deviations from desired flight paths and attitude configurations.

The material presented in this paper is part of an ongoing basic research effort to develop greater understanding of and appreciation for these interactions, and in the process to develop analytical procedures for high fidelity simulations of on-orbit operations needed for the validation of designs of future systems prior to their construction on-orbit. Both of these research objectives have high relevance to future civilian and military space systems which are expected to be constructed on orbit. For many of the members used in the construction, critical design loads can be expected to occur from handling loads during construction.

One major thrust of the ongoing research is the modeling of selected deployment mechanisms isolated from their orbiting parent spacecraft, and the systematic investigation of their dynamic characteristics as influenced by design, configurational and deployment parameters. A two-segment telescoping beam is one such mechanism, and the subject of this paper.

Problem Definition

Determination of the natural modes of vibration of a deploying two-segment telescopic beam at various stages of deployment is the specific problem addressed in this paper. The conceptual physical model is that of a non-uniform beam comprised of an inner tube sliding freely inside an outer tube which is cantilevered from one end. Figure 1 illustrates the physical model, with the beam in a partially deployed configuration. Both tubes are considered to be thin-walled, and their diameters are sufficiently large compared to the wall thickness so that the two tubes can be considered to have the same flexural rigidity (I), area (A), and mass per unit length(m). The natural vibration frequencies and mode shapes of this model are to be determined for several stages of deployment between 0% and 100%.
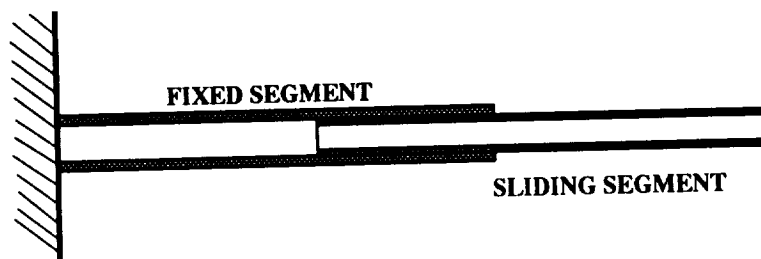

Figure 1: Telescopic Beam

MATHEMATICAL MODELING

Equations of Motion

The idealized model comprises two beams sliding freely relative to each other, as shown in Figure 2 below. The overlapping segments of the two are constrained to move together as a unit. The equations of motion are developed from application of Lagrange's equation which can be stated as:

$$\frac{d}{dt}\left(\frac{\partial T}{\partial \dot{q}_j}\right) - \frac{\partial T}{\partial q_j} + \frac{\partial V}{\partial q_j} = 0$$

where
(1)

$T = $ Kinetic energy of the system

$V = $ Potential energy of the system

$= U - W_e$

$U = $ Strain Energy of the system

$W_e = $ Virtual Work of external forces
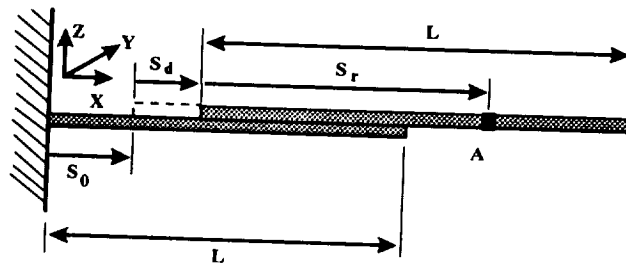
$q_j = $ Generalized coordinate

Figure 2: Idealized Telescopic Beam

Equations for the sliding segment:

With reference to the above figure, let

S_0 be the position of the overlap end of the sliding segment at some reference time t_0

S_d is the displacement of the end due to deployment motion

S_r is the deformed position of the reference point A

X_r is the Eulerian coordinate of A

v is the displacement of A in the y-direction

w is the displacement of A in the z-direction

117

Then

$$S_d = \int_{t_0}^{t} U_D \, dt \tag{2}$$

$$S_r = X_r + u_e - \frac{1}{2}\int_{0}^{X_r}\left[\left(\frac{\partial v}{\partial x}\right)^2 + \left(\frac{\partial w}{\partial x}\right)^2\right]dx \tag{3}$$

where

U_D = Deployment velocity

u_e = Displacement of A due to elasticity

The velocity vector of A is then given by:

$$\dot{\underline{r}}_A \cong \left[U_D + \dot{u}_e - \frac{1}{2}\left(\dot{v}\frac{\partial v}{\partial x} + v\frac{\partial \dot{v}}{\partial x} + \dot{w}\frac{\partial w}{\partial x} + w\frac{\partial \dot{w}}{\partial x}\right)\right]\hat{\underline{i}} + \dot{v}\hat{\underline{j}} + \dot{w}\hat{\underline{k}} \tag{4}$$

Now define a displacement u such that

$$\dot{u} = U_D + \dot{u}_e - \frac{1}{2}\left(\dot{v}\frac{\partial v}{\partial x} + v\frac{\partial \dot{v}}{\partial x} + \dot{w}\frac{\partial w}{\partial x} + w\frac{\partial \dot{w}}{\partial x}\right) \tag{5}$$

Then

$$\dot{\underline{r}}_A = \dot{u}\hat{\underline{i}} + \dot{v}\hat{\underline{j}} + \dot{w}\hat{\underline{k}} \tag{6}$$

The kinetic energy of the system can now be determined as

$$T = \frac{1}{2}m\int_{0}^{L}\dot{\underline{r}}_A \bullet \dot{\underline{r}}_A \, dx$$

$$= \frac{1}{2}m\int_{0}^{L}\left(\dot{u}^2 + \dot{v}^2 + \dot{w}^2\right)dx \tag{7}$$

The strain energy and virtual work quantities can be expressed as

$$U = \frac{1}{2}\int_{0}^{L}\left[EI_y\left(\frac{\partial^2 v}{\partial x^2}\right)^2 + EI_z\left(\frac{\partial^2 w}{\partial x^2}\right)^2 + EA\left(\frac{\partial u_e}{\partial x}\right)^2\right]dx \tag{8}$$

$$W_e = \int_{0}^{L}\left(p_y v + p_z w\right)dx: \quad \text{where } p_y \text{ and } p_z \text{ are external distributed loads.} \tag{9}$$

118

It should be noted that in the above equations, the variable u introduced by definition is not a state variable like v and w, but is rather a function of the last two and the elastic displacement u_e. Hence the generalized coordinates are u_e, v, and w.

Performing the variations indicated in the Lagrange's equations, and noting that, as in Hamilton's Principle, admissible variations all vanish at the boundaries of the integration domain, the following nonlinear and non-autonomous equations result.

$$m\ddot{u} - EA\frac{\partial^2 u_e}{\partial x^2} = 0$$

(10)

$$m\left[\ddot{v} - \frac{1}{2}\left(\ddot{u}\frac{\partial v}{\partial x} + \dot{u}\frac{\partial \dot{v}}{\partial x} + \dot{v}\frac{\partial \dot{u}}{\partial x}\right)\right] + EI_y\frac{\partial^4 v}{\partial x^4} = p_y$$

(11)

$$m\left[\ddot{w} - \frac{1}{2}\left(\ddot{u}\frac{\partial w}{\partial x} + \dot{u}\frac{\partial \dot{w}}{\partial x} + \dot{w}\frac{\partial \dot{u}}{\partial x}\right)\right] + EI_z\frac{\partial^4 w}{\partial x^4} = p_z$$

(12)

Equations for the Fixed Segment:

The above equations are directly applicable to the fixed segments with the modification that the quantity u is defined without the deployment velocity U_D, i.e.

$$\dot{u} = \dot{u}_e - \frac{1}{2}\left(\dot{v}\frac{\partial v}{\partial x} + v\frac{\partial \dot{v}}{\partial x} + \dot{w}\frac{\partial w}{\partial x} + w\frac{\partial \dot{w}}{\partial x}\right)$$

(13)

Characteristic Equations

For the purpose of determining the modal characteristics, the above equations of motion are reduced to a quasi-static form by dropping the deployment velocity related terms and all nonlinear terms to yield

$$m\ddot{u} - EA\frac{\partial^2 u_e}{\partial x^2} = 0$$

(14A)

$$m\ddot{v} + EI\frac{\partial^4 v}{\partial x^4} = 0$$

(14B)

$$m\ddot{w} + EI\frac{\partial^4 w}{\partial x^4} = 0$$

(14C)

The equations are completely uncoupled and can be studied independently of one another. The following treatment is therefore confined to vibrations in the x-z plane, governed by the last of the three equations above. This is a standard beam equation of the Euler-Bernoulli type. The homogeneous part defines the modal characteristics of the beam system.

The general solution of the homogeneous equation is given by:

$$w(x,t) = \left(A_1 \cosh \beta x + A_2 \sinh \beta x + A_3 \cos \beta x + A_4 \sin \beta x\right)\sin(\omega t - \varphi)$$

$$= \phi(x)\sin(\omega t - \varphi) \tag{15}$$

where

$$\beta^4 = \omega^2 \frac{m}{EI} \tag{16}$$

At any stage of deployment, the telescopic beam can be idealized as a three segment beam as shown in Figure 3.
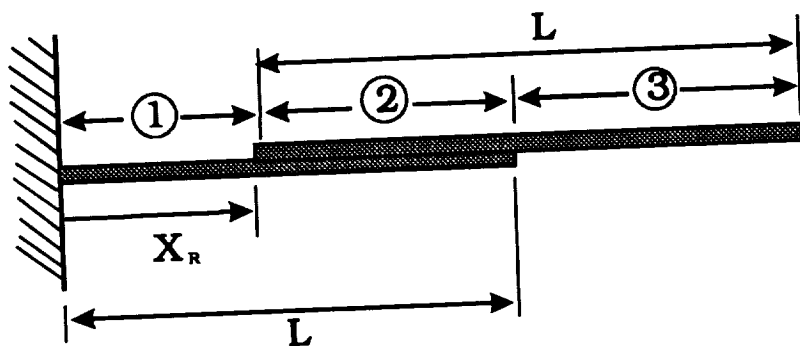

Figure 3: Uniform segments of the idealized telescopic beam.

The general solution above is applicable to each of the segments to yield

$$\phi(x) = \begin{cases} A_1 \cosh \beta_1 x + A_2 \sinh \beta_1 x + A_3 \cos \beta_1 x + A_4 \sin \beta_1 x; & 0 \le x \le X_R \\ B_1 \cosh \beta_2 x + B_2 \sinh \beta_2 x + B_3 \cos \beta_2 x + B_4 \sin \beta_2 x; & X_R \le x \le L \\ C_1 \cosh \beta_3 x + C_2 \sinh \beta_3 x + C_3 \cos \beta_3 x + C_4 \sin \beta_3 x; & L \le x \le L + X_R \end{cases} \tag{17}$$

where

$$\beta_1^4 = \omega^2 \frac{m_1}{EI_1}; \qquad \beta_2^4 = \omega^2 \frac{m_2}{EI_2}; \qquad \beta_3^4 = \omega^2 \frac{m_3}{EI_3} \tag{18}$$

m_1, m_2, m_3 are the mass per unit length of the respective segments;

EI_1, EI_2, and EI_3 are bending rigidities of the respective segments.

The constants in these displacement expressions are to be evaluated from a set of boundary conditions and compatibility relations at the two interfaces of the segments.

120

The boundary conditions are given by:

$$\phi_1(0) = 0$$

$$\frac{d\phi_1(0)}{dx} = 0$$

$$\frac{d^2\phi_3(L+X_R)}{dx^2} = 0$$

$$\frac{d^3\phi_3(L+X_R)}{dx^3} = 0$$

(19)

and the compatibility conditions are given by

$$\phi_1(X_R) = \phi_2(X_R)$$

$$\frac{d\phi_1(X_R)}{dx} = \frac{d\phi_2(X_R)}{dx}$$

$$EI_1 \frac{d^2\phi_1(X_R)}{dx^2} = EI_2 \frac{d^2\phi_2(X_R)}{dx^2}$$

$$EI_1 \frac{d^3\phi_1(X_R)}{dx^3} = EI_2 \frac{d^3\phi_2(X_R)}{dx^3}$$

$$\phi_2(L) = \phi_3(L)$$

$$\frac{d\phi_2(L)}{dx} = \frac{d\phi_3(L)}{dx}$$

$$EI_2 \frac{d^2\phi_2(L)}{dx^2} = EI_3 \frac{d^2\phi_3(L)}{dx^2}$$

$$EI_2 \frac{d^3\phi_2(L)}{dx^3} = EI_3 \frac{d^3\phi_3(L)}{dx^3}$$

(20)

Introducing the appropriate functions into these conditions results in twelve homogeneous equations. The determinant of the coefficient matrix must vanish for non-trivial solution of the constants. Hence

$$\begin{vmatrix} [A]_{2X4} & & \\ [B]_{4X4} & [C]_{4X4} & \\ & [D]_{4X4} & [E]_{4X4} \\ & & [F]_{2X4} \end{vmatrix} = 0$$

(21)

where

$$[A]=\begin{bmatrix} 1 & 0 & 1 & 0 \\ 0 & 1 & 0 & 1 \end{bmatrix} \tag{22}$$

$$[B]=\begin{bmatrix} \cosh\alpha_1 & \sinh\alpha_1 & \cos\alpha_1 & \sin\alpha_1 \\ \beta_1\sinh\alpha_1 & \beta_1\cosh\alpha_1 & -\beta_1\sin\alpha_1 & \beta_1\cos\alpha_1 \\ EI_1\cosh\alpha_1 & EI_1\sinh\alpha_1 & -EI_1\cos\alpha_1 & -EI_1\sin\alpha_1 \\ EI_1\sinh\alpha_1 & EI_1\cosh\alpha_1 & EI_1\sin\alpha_1 & -EI_1\cos\alpha_1 \end{bmatrix} \tag{23}$$

$$[C]=\begin{bmatrix} -\cosh\alpha_2 & -\sinh\alpha_2 & -\cos\alpha_2 & -\sin\alpha_2 \\ -\beta_2\sinh\alpha_2 & -\lambda_1\cosh\alpha_2 & \lambda_1\sin\alpha_2 & -\lambda_1\cos\alpha_2 \\ -\lambda_1{}^2EI_2\cosh\alpha_2 & -\lambda_1{}^2EI_2\sinh\alpha_2 & \lambda_1{}^2EI_2\cos\alpha_2 & \lambda_1{}^2EI_2\sin\alpha_2 \\ -\lambda_1{}^3EI_2\sinh\alpha_2 & -\lambda_1{}^3EI_2\cosh\alpha_2 & -\lambda_1{}^3EI_2\sin\alpha_2 & \lambda_1{}^3EI_2\cos\alpha_2 \end{bmatrix} \tag{24}$$

$$[D]=\begin{bmatrix} \cosh\alpha_3 & \sinh\alpha_3 & \cos\alpha_3 & \sin\alpha_3 \\ \sinh\alpha_3 & \cosh\alpha_3 & -\sin\alpha_3 & \cos\alpha_3 \\ \cosh\alpha_3 & \sinh\alpha_3 & -\cos\alpha_3 & -\sin\alpha_3 \\ \sinh\alpha_3 & \cosh\alpha_3 & \sin\alpha_3 & -\cos\alpha_3 \end{bmatrix} \tag{25}$$

$$[E]=\begin{bmatrix} -\cosh\alpha_4 & -\sinh\alpha_4 & -\cos\alpha_4 & -\sin\alpha_4 \\ -\lambda_2\sinh\alpha_4 & -\lambda_2\cosh\alpha_4 & \lambda_2\sin\alpha_4 & -\lambda_2\cos\alpha_4 \\ -\lambda_2{}^2\cosh\alpha_4 & -\lambda_2{}^2\sinh\alpha_4 & \lambda_2{}^2\cos\alpha_4 & \lambda_2{}^2\sin\alpha_4 \\ -\lambda_2{}^3\sinh\alpha_4 & -\lambda_2{}^3\cosh\alpha_4 & -\lambda_2{}^3\sin\alpha_4 & \lambda_2{}^3\cos\alpha_4 \end{bmatrix} \tag{26}$$

$$[F]=\begin{bmatrix} \cosh\alpha_5 & \sinh\alpha_5 & -\cos\alpha_5 & -\sin\alpha_5 \\ \sinh\alpha_5 & \cosh\alpha_5 & \sin\alpha_5 & -\cos\alpha_5 \end{bmatrix} \tag{27}$$

and

$$\alpha_1=\beta_1 X_R; \qquad \alpha_2=\beta_2 X_R; \qquad \lambda_1=\frac{\beta_2}{\beta_1}$$

$$\alpha_3=\beta_2 L; \qquad \alpha_4=\beta_3 L; \qquad \lambda_2=\frac{\beta_3}{\beta_2}$$

$$\alpha_5=\beta_3(L+X_R) \tag{28}$$

The determinant equation is nondimensionalized by introducing

$$k=\beta_1 L; \qquad \xi_R=\frac{X_R}{L} \tag{29}$$

122

Then

$$\alpha_1 = k\,\xi_R; \qquad \alpha_2 = \lambda_1 k\,\xi_R$$
$$\alpha_3 = \lambda_1 k; \qquad \alpha_4 = \lambda_1\,\lambda_2 k; \qquad \alpha_5 = \lambda_1\,\lambda_2 k(1+\xi_R) \qquad (30)$$

SAMPLE RESULTS AND DISCUSSION

A numerical algorithm has been developed for solving the determinant equation for a specified number of the first consecutive eigenvalues (k_n) of the system and the corresponding eigenvectors representing the unknown coefficients of the displacement functions. The mode shapes are also calculated from the eigenvectors.

Table 1 lists the first 10 eigenvalues for a number of deployment stages. The first and last columns represent data for straight beams at the fully collapsed and at the fully deployed lengths. Figure 4 is a graphical display of the same data.

Mode #	βL for Different Deployment Stages(%)								
	0	5	10	25	50	75	90	95	100
1	1.8751	1.7739	1.6959	1.5325	1.3527	1.2115	1.1360	1.1120	0.9375
2	4.6941	4.4846	4.3572	4.0142	3.2388	2.6482	2.4442	2.3985	2.3470
3	7.8548	7.5461	7.3600	6.4243	5.0683	4.4664	4.1495	4.0468	3.9274
4	10.996	10.400	9.2000	8.5100	7.2910	6.2220	5.7000	5.5600	5.4980
5	14.137	10.503	9.2001	8.8400	7.3110	7.0904	6.7390	7.0318	7.0685
6	17.279	10.712	9.7300	9.0030	7.4015	7.1000	6.8010	7.1000	8.6395
7	20.420	10.812	9.8100	9.1010	7.5011	7.9100	7.3003	7.3103	10.210
8	23.562	10.910	9.9112	9.2004	7.6000	8.0100	7.6293	7.8314	11.781
9	26.704	11.000	10.010	9.6100	8.1545	8.1120	7.7002	8.0000	13.352
10	29.845	11.100	10.600	9.7200	8.2100	8.2004	7.9401	8.1506	14.922

Table 1: Frequency Parameter Variations with Deployment

Two trends are immediately evident from the data:
1. A compaction of the frequencies towards the lower end as deployment proceeds, thus increasing the modal density in regions of normal dynamic interest, and
2. The appearance of very close, nearly repeated roots from about the third mode upwards, for all the partially deployed configurations

The mode shapes provide clues as to the basis for these trends. Figures 5 through 10 show the first six mode shapes for the 0% and 5% deployment configurations. The first four mode shapes are very similar for the two configurations. The fifth and sixth differ markedly between the two configurations. The partially deployed configuration shows large motions in that portion of the deploying segment that protrudes from the fixed segment in comparison with the motions of the fixed segment. These modes can properly be described as " tip whip " modes, in analogy with the classical " antenna whip " motions of automobile radio antennas. The fixed segment is seen to be

vibrating essentially in its third mode under both the fifth and sixth coupled modes. It is clear that these two modes are the result of a coupling between the cantilevered modes of the fixed segment, and those of the protruding portion of the deploying segment. This coupling is believed to be the primary mechanism for the *agglomeration* of the modes.

As the protruding portion of the deploying segment increases in length with deployment, its natural frequencies decrease and the coupling with fixed segment modes occurs at lower frequencies. Figures 11 through 13 illustrate the first five mode shapes at 25%, 50% and 90% deployment stages.

Figure 4: Variation of Modal Parameter with % Deployment

The observed changes in modal characteristics with deployment can be expected to have serious impacts. Control design for such a system would be made more difficult by virtue of the increased modal density and near coalescence of certain of the modes. Transient dynamic analyses cannot be readily performed by modal synthesis due to the continuous variations in the basis functions (mode shapes). Stability implications of the modal agglomeration can also be serious and will be explored in future studies.

CONCLUSION

The modal characteristics of the two-segment telescopic beam at all stages of partial deployment have been shown to vary drastically from those of either the completely collapsed or fully extended configurations. This variation manifests itself in an agglomeration of the modal frequencies near the lower end of the spectrum, and is attributable to the sharp discontinuities in mass and stiffness distributions between the region of overlap between the inner and outer segments and the non-overlap regions near the root and the free end respectively.

BIBLIOGRAPHY

1. Banerjee, A.K., and Kane, T.R., "Extrusion of a Beam from a Rotating Base," AIAA J. Guidance, vol 12, No 2, March-April 1989.
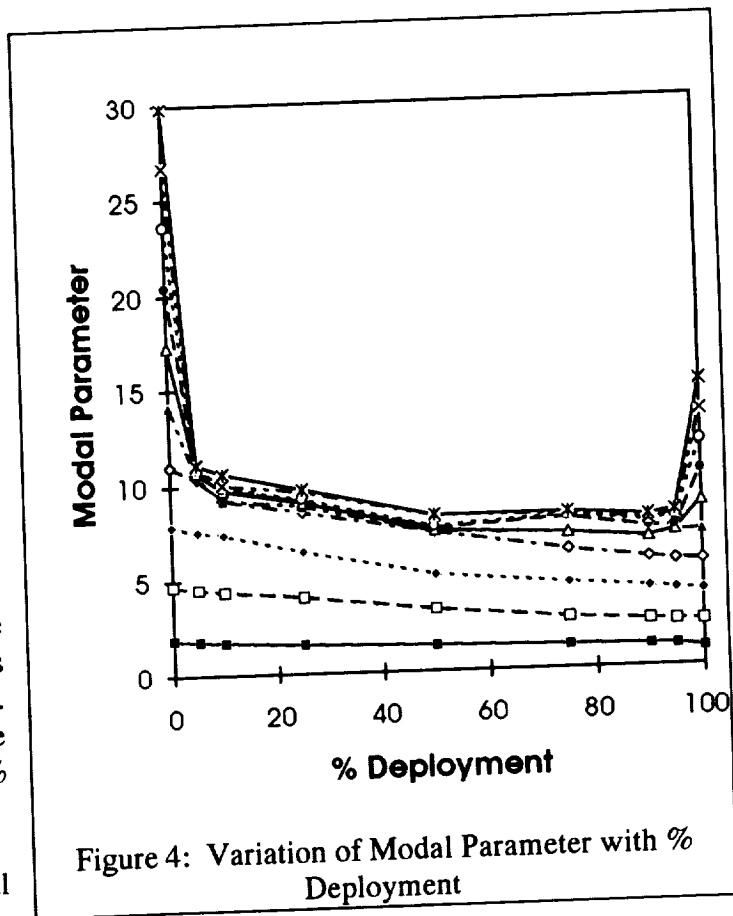
2. Kalaycioglu, S. and Misra, A.K., "Analytical Expressions for Vibratory Displacements of Deploying Appendages," AIAA paper 88-4250-CP, 1988.

3. Modi, V.J., and Ibrahim, A.M., "A General Formulation for Librational Dynamics of Spacecraft with Deploying Appendages," AIAA J. Guidance, vol 7, No 5, Sept-Oct 1984.

4. Tsuchiya, K., "Dynamics of a Spacecraft During Extension of Flexible Appendages," AIAA J. Guidance, vol 6, No 2, 1983.

5. Ibrahim, A.E., and Misra, A.K., "Attitude Dynamics of a Satellite During Deployment of Large Plate-Type Structures," AIAA J. Guidance, vol 5, No 5, Sep-Oct 1982.

6. Lips, K.W., and Modi, V.J., "Three-Dimensional Response Characteristics for Spacecraft with Deploying Flexible Appendages," AIAA J. Guidance and Control, vol 4, No 6, Nov-Dec 1981.

7. Tabarrok, B., Leech, C.M., and Kim, Y.I., " On the Dynamics of an Axially Moving Beam," J. Franklin Institute, vol 297, pp 201-220, 1974.

8. Atluri, S.N. and Amos, A.K.,(ed) Large Space Structures: Dynamics and Control, Springer-Verlag, 1988.
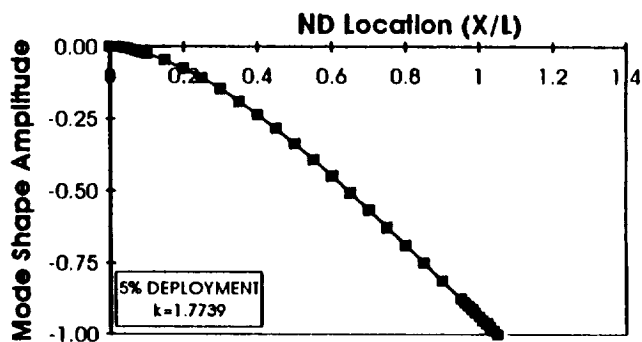
ACKNOWLEDGEMENT

Figure 5: Mode 1 Shapes for 0% & 5% Deployment

Figure 6: Mode 2 Shapes for 0% & 5% Deployment
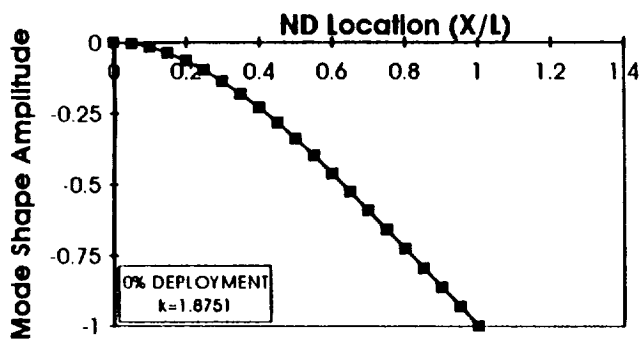
Figure 7: Mode 3 Shapes for 0% & 5% Deployment

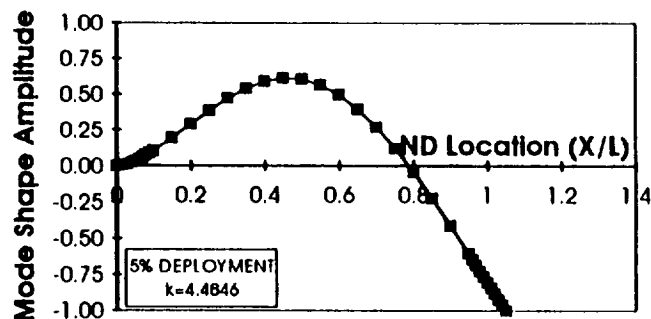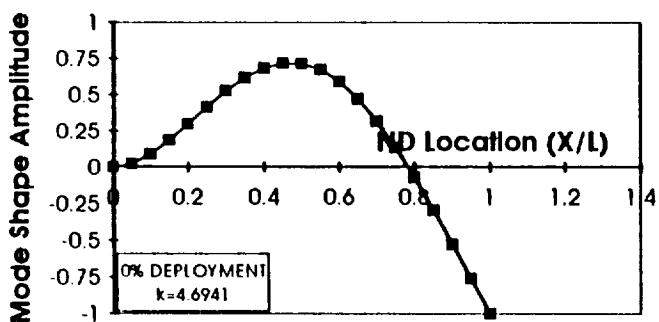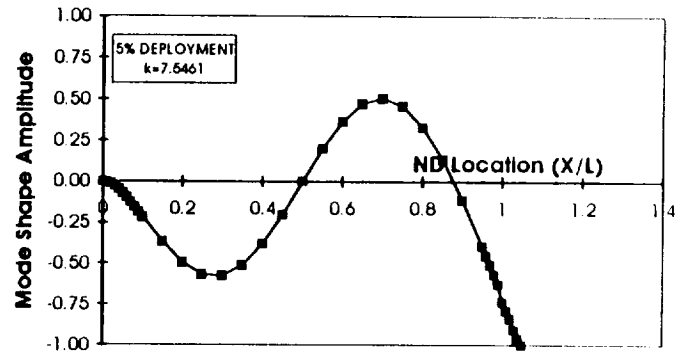
Figure 8: Mode 4 Shapes for 0% & 5% Deployment

127

Figure 9: Mode 5 shapes for 0% & 5% Deployment

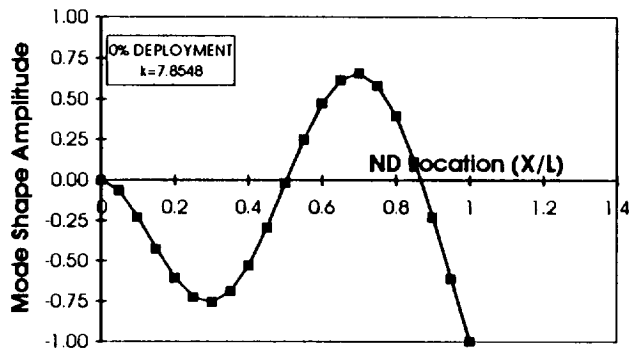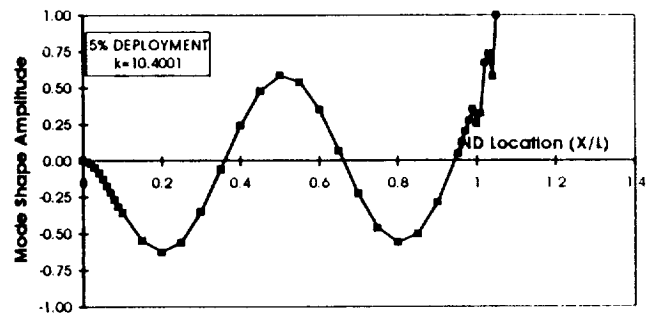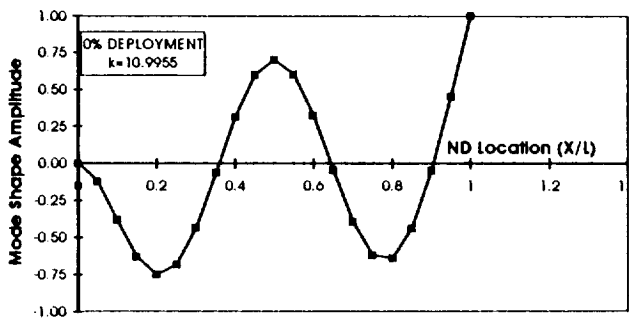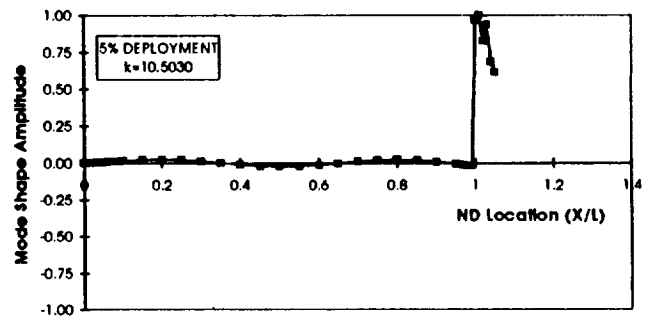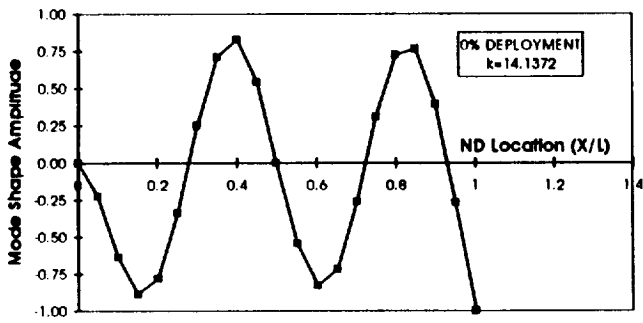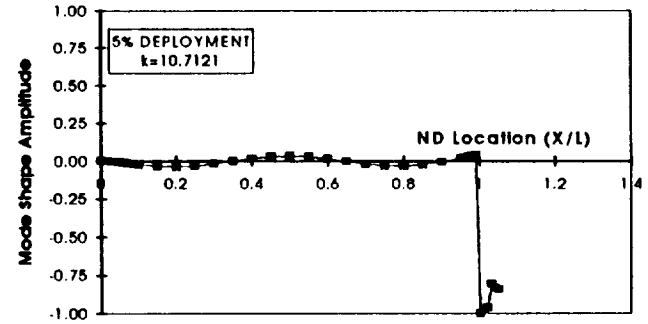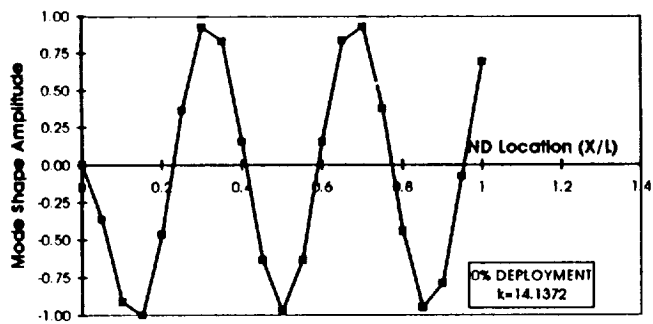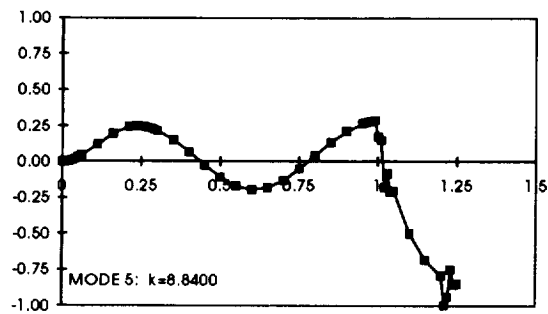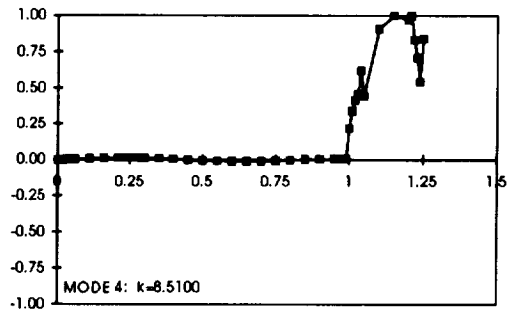Figure 10: Mode 6 shapes for 0% & 5% Deployment
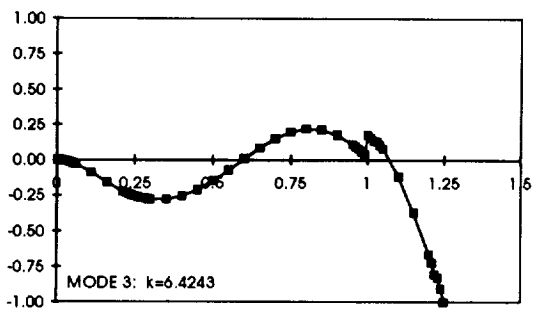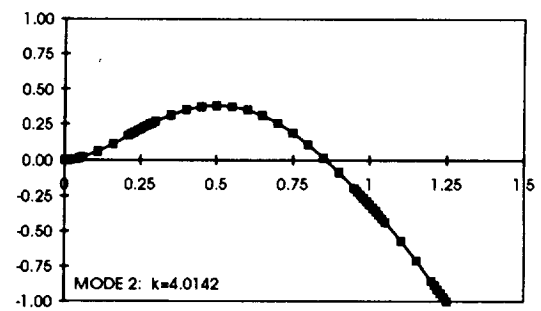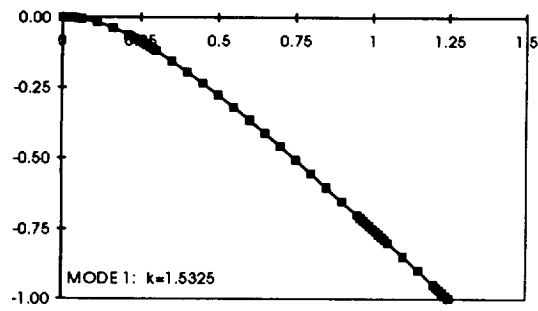
Figure 11: Mode Shapes at 25% Deployment

MODE 1: k=1.3527

MODE 2: k=3.2388

MODE 3: k=5.0683

MODE 4: k=7.2910

MODE 5: k=7.311
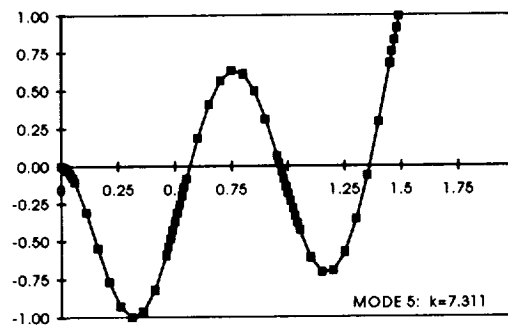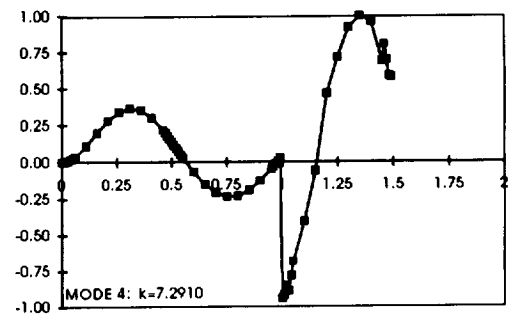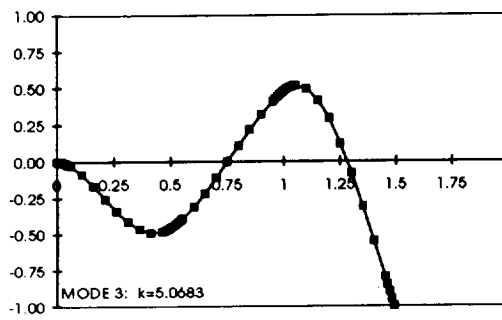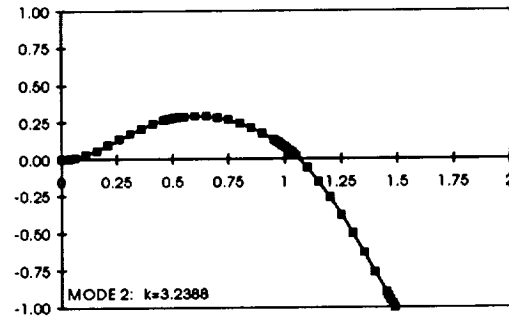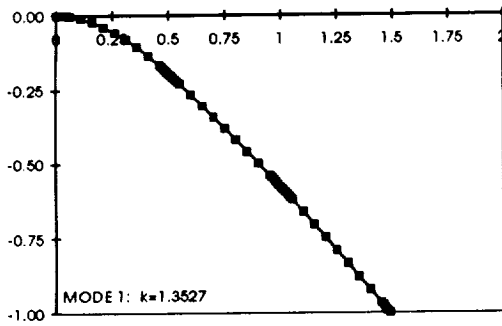
Figure 12: Mode Shapes at 50% Deployment
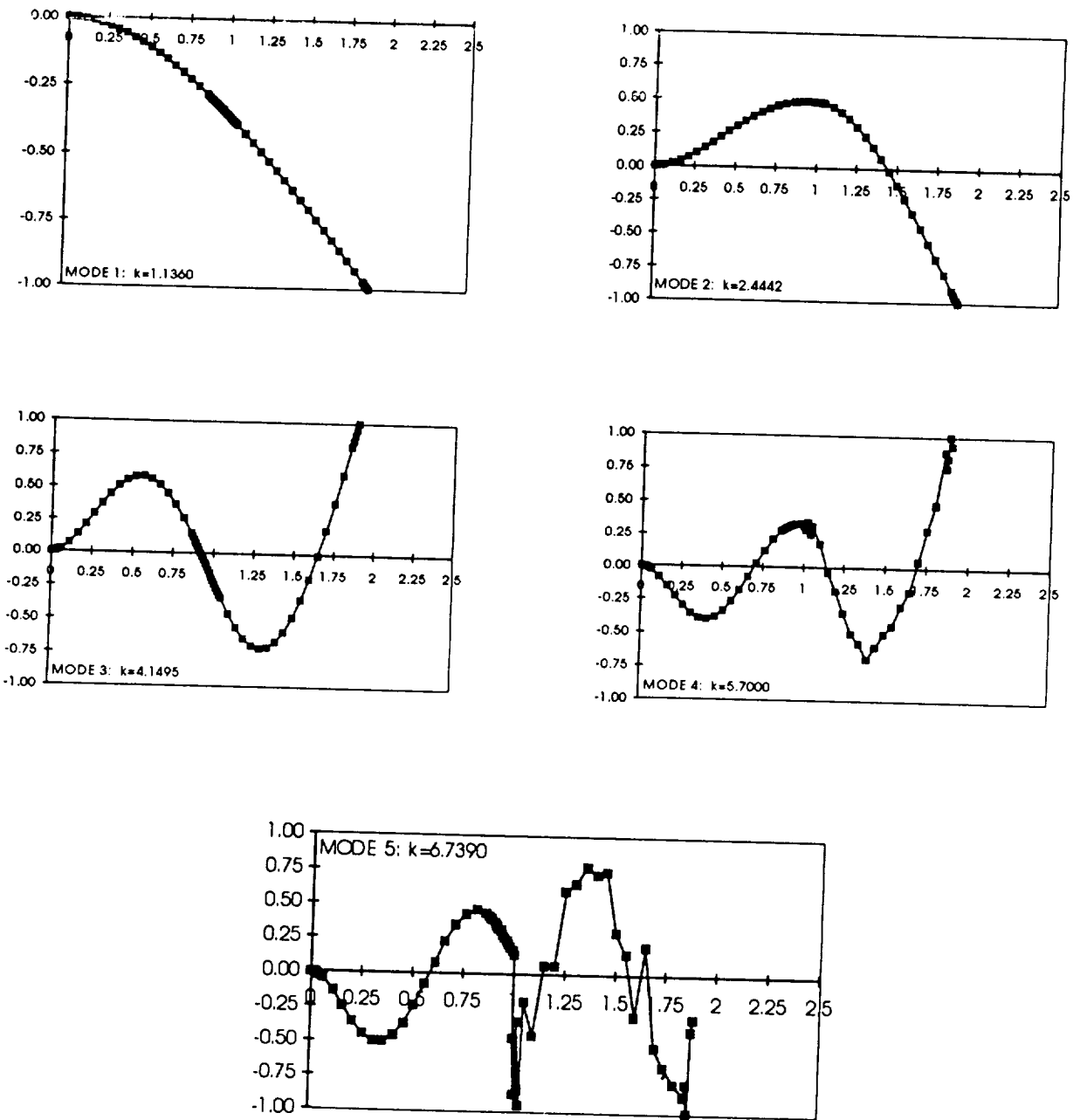
Figure 13: Mode Shapes at 90% Deployment

AEROELASTICITY APPLICATIONS

FLUTTER SUPPRESSION DIGITAL CONTROL LAW DESIGN AND TESTING FOR THE AFW WIND-TUNNEL MODEL

Vivek Mukhopadhyay
NASA Langley Research Center,
Hampton, Virginia

SUMMARY

Design of a control law for simultaneously suppressing the symmetric and antisymmetric flutter modes of a sting mounted fixed-in-roll aeroelastic wind-tunnel model is described. The flutter suppression control law was designed using linear quadratic Gaussian theory, and involved control law order reduction, a gain root-locus study and use of previous experimental results. A 23% increase in the open-loop flutter dynamic pressure was demonstrated during the wind-tunnel test. Rapid roll maneuvers at 11% above the symmetric flutter boundary were also performed when the model was in a free-to-roll configuration.

INTRODUCTION

A summary of the Active Flexible Wing (AFW) Program is presented in Ref. 1. Within the operating range of the Langley Research Center Transonic Dynamics Tunnel, the sting mounted AFW aeroelastic model had both symmetric and antisymmetric flutter modes, in a fixed-in-roll configuration, and a symmetric flutter mode only, when the model was in a free-to-roll configuration. The active flutter suppression system (FSS) test goals were to demonstrate: a) simultaneous symmetric and antisymmetric flutter suppression for the fixed-in-roll configuration, and b) symmetric flutter suppression in the free-to-roll configuration. An additional goal was to test a rolling maneuver load alleviation system along with the FSS above the open-loop flutter boundary. Since the free-to-roll symmetric flutter and the fixed-in-roll symmetric and antisymmetric flutter modes had very similar characteristics, a single FSS control law was designed and demonstrated for both the flutter test configurations, a) and b) as stated above. This paper addresses the mathematical modeling, control law design and wind-tunnel test results.

NOMENCLATURE

A, B	control law state-space matrices
C, D	control law output matrices
B_o	Kalman state estimator gain matrix
C_o	optimal regulator gain matrix
E	expectation operator
F, G	plant state-space matrices
G_w	gust input matrix
g	gravitational acceleration constant
H	sensor output matrix

I	identity matrix
M	Mach number
P	estimator Riccati equation solution
q	dynamic pressure, psf
q_f	flutter dynamic pressure, psf
Q_1	plant output weighting matrix
Q_2	control input weighting matrix
R_v	measurement noise intensity matrix
R_w	gust input noise intensity
S	regulator Riccati equation solution
s	Laplace variable
T	sample period, seconds
t	time, seconds
u	control input vector
v	measurement noise vector
w	gust input noise
ω	frequency, radians/second
x	plant state vector
x_c	control law state vector
y	measurement vector
$\ddot{z}$	accelerometer output, g's
δ	control surface angular position, degrees

Subscripts:

LEI	wing leading edge inboard
LEO	wing leading edge outboard
TEI	wing trailing edge inboard
TEO	wing trailing edge outboard
tip	wing tip

Abbreviations:

AFW	active flexible wing
CL	closed loop
CPE	controller performance evaluation
FSS	flutter suppression system
LQG	linear quadratic Gaussian
OL	open loop
psf	pounds per square foot
RMLA	rolling maneuver load alleviation
rms	root mean square
SISO	single-input single-output

AFW EQUATIONS OF MOTION

The description of the AFW aeroelastic wind-tunnel model and the wing-tip ballast stores, including details of the accelerometer sensor positions and multiple control surface actuation capabilities, are provided in Ref. 2. The accelerometer sensors and the control surface locations on the wing-plan form are shown in figure 1. The development of the aeroelastic equations of motion is described in Ref. 3. The equations for the symmetric and antisymmetric motion were developed separately, using ten flexible modes for each

configuration. The flexible mode shapes and natural frequencies were derived from a finite-element modal analysis and were corrected using ground vibration test data.

State-space Equations

A set of state-space mathematical models were developed[3] for control law design. For the aeroelastic equations, the doublet-lattice oscillatory aerodynamics approximation used four aerodynamic lag terms for each flexible mode. In addition, the state-space models included corrections for control surface effectiveness based on results from the 1989 wind-tunnel test[2], and the third-order transfer functions of the actuator dynamics derived from ground test of the unloaded control surfaces. A Dryden gust spectrum transfer function, driven by a white noise process, was used to simulate the random vertical gust of the wind-tunnel. The complete linear equations of motion at a specified dynamic pressure were expressed by the state-space equations,

$$dx/dt = Fx + Gu + G_w w \qquad (1)$$
and
$$y = Hx + v \qquad (2)$$

where x is the state vector, u is the control input vector, w is the gust input noise, y is the accelerometer sensor output vector, and v is the measurement noise vector. Equations (1) and (2) were scaled such that the units of the control inputs were in degrees, the units of the sensor outputs were in g's, and the gust input unit was in feet/second.

Open-loop Dynamic Pressure Root-locus

Using these state-space mathematical models at six dynamic pressures, q = 100, 150, 200, 250, 300 and 350 psf, the flexible-mode root-loci with dynamic pressure were studied. The open-loop, dynamic pressure root-locus of the first four flexible symmetric and antisymmetric modes, for the fixed-in-roll configuration, are shown in figures 2 and 3, respectively. The figures 2 and 3 indicate that the second and third flexible mode frequencies coalesced to produce the flutter instability. The unstable mode was primarily wing-tip torsion, for both the symmetric and the antisymmetric motions. The sixth and seventh symmetric flexible mode frequencies also tended to coalesce (not shown in figure 2). At Mach 0.5, the analytical open-loop symmetric flutter dynamic pressure was estimated to be 248 psf at 11.2 Hz. The analytical open-loop antisymmetric flutter dynamic pressure was estimated to be 233 psf at 10.9 Hz. The closed-loop dynamic-pressure root-locus is also shown in figures 2 and 3 and will be discussed later.

CONTROL LAW DESIGN

The flutter suppression design objective was to develop low-order robust digital control laws which would simultaneously suppress the symmetric and antisymmetric flutter modes of the model in the fixed-in-roll configuration with allowable control surface activity. The maximum permissible control surface rms deflection and rates were 1.0 degree (at 11.2 Hz flutter frequency) and 75 degrees/second, respectively. From the 1989 test [2], the antisymmetric flutter frequency was known to be 1.8 Hz below the analytical value. The control law was also required to be sufficiently robust to compensate for this difference.

The FSS control laws were designed using linear quadratic Gaussian (LQG) theory and involved control law order reduction, a gain root-locus study, and use of previous experimental results[2]. Since the symmetric and antisymmetric flutter modes had very similar characteristics for the fixed-in-roll configuration (see figures 2 and 3), a single FSS control law was designed to suppress both the flutter modes. This control law used the $\ddot{z}$tip pair of accelerometers and the TEO pair of control surfaces on the right and left wings. The block diagram for digital implementation[2] of the symmetric and antisymmetric FSS control laws is shown in Figure 4. The accelerometer outputs from the left and right wing were passed through 25 Hz first-order antialiasing filters, modeled by the transfer function $157/(s+157)$ and converted into digital data at a sampling rate of 200 Hz. The digital controller separated the data into symmetric and antisymmetric components, computed the digital control law outputs and then distributed the processed feedback signals to the right and left actuators after 0.005 seconds computational delay.

Design Plant Model

The 68th order antisymmetric state-space equation at q = 350 psf for the fixed-in-roll configuration was used as the design plant model, since from the analysis and the 1989 test, the antisymmetric flutter mode was found to be most critical and was encountered at a lower dynamic pressure than the symmetric flutter mode. The accelerometer sensors and control surfaces were selected based on the frequency response analysis of the open-loop system. The $\ddot{z}$TEO and $\ddot{z}$tip accelerometer responses were predominant at the wing-tip torsion frequencies due to the excitation from TEI and TEO control surfaces. In addition, the $\ddot{z}$tip sensor exhibited relatively low response at frequencies above 25 Hz. Therefore, the $\ddot{z}$TEO and $\ddot{z}$tip accelerometer sensors and TEI and TEO control surfaces were initially studied as candidates for measurement inputs and control outputs, respectively.

Full-order LQG Design

A full order LQG control law was designed using the design plant model state-space equations (1) and (2). The full-order LQG control law which is given by equations (3) and (4), minimizes a weighted quadratic cost function defined by $E[y^TQ_1y + u^TQ_2u]$, where Q_1 and Q_2 are the plant output and control input weighting matrices [4,5].

$$dx_C/dt = A_ox_C + B_oy, \qquad (3)$$
$$u = C_ox_C, \qquad (4)$$

where

$$A_o = [F - B_oH + GC_o]$$
$$B_o = PH^TR_v^{-1}$$
$$C_o = -Q_2^{-1}G^TS.$$

The matrices B_o and C_o are the Kalman state estimator gains and the full-state optimal regulator gains, respectively. The matrices P and S are the positive definite solution of the steady state dual matrix Riccati equations, given by

$$FP + PF^T + G_wR_wG_w^T - PH^TR_v^{-1}HP = 0$$
$$SF + F^TS + H^TQ_1H - SGQ_2^{-1}G^TS = 0,$$

where R_w and R_v denote the intensity matrices of the gust input and measurement Gaussian white noise processes, w and v, respectively. To obtain the LQG control law, full-state optimal regulator gain matrix C_0 was first determined using a unit output weighting matrix, $Q_1 = I$, and a control weighting matrix $Q_2 = 0.001\ I$, where I is a 2x2 identity matrix. Then the Kalman state estimator gain matrix B_0 was determined using $R_w = 0$ and $R_v = I$. The final selection of these weighting and noise intensity matrices for the full order control law, and the subsequent order reduction process were determined after several design iterations, until a stabilizing low order controller was found for the nominal design plant model. The control law order reduction process is described next.

Order Reduction

The full 68th order LQG control law given by equations (3) and (4) was first block-diagonalized, and then reduced to 11th order by residualization of all the damped modes above 19 Hz. Equations (3) and (4), in block-diagonalized form, are shown in equations (5) and (6), where the vector x_{c1} represents the retained states and the vector x_{c2} represents the remaining states associated with the damped higher frequency dynamics.

$$\frac{d}{dt}\begin{Bmatrix} x_{c1} \\ x_{c2} \end{Bmatrix} = \begin{bmatrix} A_{o1} & 0 \\ 0 & A_{o2} \end{bmatrix}\begin{Bmatrix} x_{c1} \\ x_{c2} \end{Bmatrix} + \begin{bmatrix} B_{o1} \\ B_{o2} \end{bmatrix} y \qquad (5)$$

$$u = \begin{bmatrix} C_{o1} & C_{o2} \end{bmatrix}\begin{Bmatrix} x_{c1} \\ x_{c2} \end{Bmatrix} \qquad (6)$$

In the residualization procedure, only the steady state part of the stable higher frequency dynamics in equation (5) were retained. This was accomplished by setting the state derivative dx_{c2}/dt to zero and solving for x_{c2}, provided the matrix A_{o2} is nonsingular[4]. The reduced state space model of the control law is given by equations (7) and (8).

$$dx_c/dt = A\, x_c + B\, y \qquad (7)$$
$$u = C\, x_c + D\, y \qquad (8)$$

where

$$x_c = x_{c1}, B = B_{o1}, C = C_{o1}$$
$$\text{and } D = -\, C_{o2}\, A_{o2}^{-1}\, B_{o2}.$$

This procedure introduced a direct feedthrough matrix D in equation (8). The residualized 11th-order control law was subsequently reduced to a second-order control law by balanced realization and truncation of the balanced system. The balanced realization procedure finds a linear transformation in which the control law states have equal controllability and observability properties[4]. The weakly controllable and observable states are then truncated. Even with the elimination of these states, the resulting set of equations retained the most important input-output characteristics of the original system. This second-order, two-input two-output control law, is given by equations (9) and (10).

$$\frac{dx_c}{dt} = \begin{bmatrix} -5.2 & 64.6 \\ -64.6 & -5.2 \end{bmatrix} x_c + \begin{bmatrix} 1.25 & 1.95 \\ -0.45 & -0.73 \end{bmatrix}\begin{Bmatrix} \ddot{z}_{TEO} \\ \ddot{z}_{tip} \end{Bmatrix} \qquad (9)$$

$$\begin{Bmatrix} \delta_{TEI} \\ \delta_{TEO} \end{Bmatrix} = \begin{bmatrix} -0.4 & 2.1 \\ 3.6 & -9.4 \end{bmatrix} x_c + \begin{bmatrix} -0.06 & -0.09 \\ 0.13 & 0.21 \end{bmatrix}\begin{Bmatrix} \ddot{z}_{TEO} \\ \ddot{z}_{tip} \end{Bmatrix} \qquad (10)$$

The corresponding Bode diagrams of the four components of this 2x2 control law are shown in Figure 5. This figure indicates that the maximum gain of this control law was 2.5 deg/g (8 dB) with a peak gain at 10.3 Hz. The primary stabilizing gain of this control law was from the sensor $\ddot{z}_{tip}$ to the control surface δ_{TEO}. Although this control law stabilized the symmetric and antisymmetric plant models at 350 psf, the step responses contained high frequency components. With the addition of 25 Hz antialiasing filters to each accelerometer channel, the high frequency components of the step responses were eliminated. However, with the addition of T=0.005 second computational delay (modeled by the first-order Pade approximation (2/T-s)/(2/T+s)), the system was marginally stable. It was also noted that, when this control law was reduced to a single-input single-output (SISO) control law by retaining only the control law input $\ddot{z}_{tip}$ and the output δ_{TEO}, the nominal design plant was also stable. This simplified SISO control law was therefore, studied further in order to compensate for the computational delay effects, and possible uncertainty in the actual flutter frequencies, as mentioned earlier.

SISO Control Law

This simplified SISO control law (plot labeled by $\delta_{TEO}/\ddot{z}_{tip}$, in figure 5) was improved further via gain augmentation. The required gain level was determined using a gain root-locus analysis. The output gain feedback root-locus of the design plant model at 350 psf, with δ_{TEO} as plant input, and $\ddot{z}_{tip}$ as plant output, is shown in figure 6. This root-locus indicated that the open-loop unstable pole (mode 3) near 11 Hz migrated into the stable left half plane, with a negative feedback gain of 1.3 deg/g from $\ddot{z}_{tip}$ to δ_{TEO}. However, the actuator poles near 50 Hz become unstable at a gain of 0.75 deg/g. Therefore, a gain level of at least 1.3 deg/g in the 8 to 12 Hz frequency range, with subsequent gain attenuation at higher frequencies, was necessary to stabilize the system, and accommodate the possible difference between the analytical and experimental flutter frequencies. In addition, compensation for the phase lag effects of the antialiasing filter and one cycle computational delay was also required. The total phase lag introduced by these two effects was about 40 degrees at the frequency 10 Hz.

The gain and phase compensations were achieved by varying the three elements of C and D in the SISO control law, and studying the gain and phase diagrams and the closed loop stability responses. An increase in C_1 and decrease in $|C_2|$ resulted in a desirable phase increase at low frequencies. An increase in D reduced the phase (towards zero) at high frequencies, which was also beneficial. These three parameters were varied, until a gain-level near 1.3 deg/g (2.3 dB) was maintained over the frequency range 8 to 12 Hz, and sufficient phase lead was obtained. The real part of the control law complex pole was also moved from - 5.2 to - 6.0 to achieve a wider gain range. The high frequency gain was kept below 0.75 deg/g. This modified SISO control law is given by equations (11) and (12), assuming negative feedback.

$$\frac{dx_c}{dt} = \begin{bmatrix} -6.0 & 64.6 \\ -64.6 & -6.0 \end{bmatrix} x_c + \begin{bmatrix} 1.95 \\ -0.73 \end{bmatrix} \ddot{z}_{tip} \qquad (11)$$

$$\delta_{TEO} = \begin{bmatrix} 14.4 & -3.1 \end{bmatrix} x_c + 0.63 \ \ddot{z}_{tip} \qquad (12)$$

The corresponding gain and phase plots are shown in figure 5 and are labeled δ_{TEO}/z_{tip} (SISO). The complex poles and zeros of this control law were $-6\pm j64.6$ and $-30\pm j56$, respectively. A second-order notch filter, given by the transfer function $(s^2+42s+44100)/(s^2+84+44100)$, was added to increase the symmetric model gain margin to 6 dB, near 33 Hz. This filter attenuated a 33 Hz lightly damped oscillation due to the interaction of the sixth and seventh symmetric flexible modes. A first-order washout filter, given by the transfer function $s/(s+6)$, was also added to remove any steady state input bias to the sensor signal.

Discretization. The resulting 5th order SISO control law in Laplace domain was discretized using the Tustin transformation $z = (1+sT/2)/(1-sT/2)$, where T is the sampling interval. For the 200 Hz sampling rate used by the digital controller, $T = 0.005$ seconds. With the Tustin transformation at this sampling rate, the Bode diagrams in the Laplace domain and the discrete domain were almost identical below 15 Hz. Hence no frequency warping corrections were applied.

Dynamic-pressure root-locus: The open- and closed-loop dynamic pressure root-locus plots are compared in figures 2 and 3. These comparisons indicated that both the symmetric and antisymmetric models were stable, up to dynamic pressure q = 350 psf. The closed-loop frequency decoupling was due to lowering of the frequency of mode 2 to about 6.8 Hz. The frequency of mode 3 was increased to 11.6 Hz, but the damping ratio was only of the order 0.010 at 300 psf.

Sensitivity studies. The closed-loop system sensitivity was studied by perturbing the second and third modal frequencies in the state-space block-diagonalized plant model by $\pm10\%$ and the nominal gains by ±4 dB at q = 250 psf and examining the closed-loop system step responses, for all possible combinations. These studies indicated that the design could accommodate simultaneous gain and frequency changes for all cases except when the second and third mode frequencies were perturbed to approach each other. Sensitivity studies were also done using the state-space model with and without the 25 Hz antialiasing filters, with and without one cycle delay, with additional delays, and with ± 6 dB gain perturbations at 250 psf. These studies indicated that the symmetric configuration could tolerate one additional delay (or phase lag of 1.8 degrees/Hz) at half the nominal gain, but the antisymmetric configuration would become unstable with an 11 Hz oscillation. The phase and gain margin comparisons with the experimental results, described in the next section, indicated that this particular situation may have been encountered during the experiment. The gain loss was apparent from the experimental Bode diagram.

SUMMARY OF TEST RESULTS

Open-loop Flutter. Based on examination of the peak-hold data obtained during the wind tunnel test with the tip ballast store coupled, the open-loop (*OL*) flutter dynamic pressures were as follows: The free-to-roll *OL* symmetric flutter was at a dynamic pressure of 235 psf, at a frequency of 9.6 Hz. The fixed-in-roll *OL* antisymmetric flutter was at a dynamic pressure of 219 psf, at a frequency of 9.1 Hz. These experimental symmetric and antisymmetric *OL* flutter dynamic pressures were, respectively, 13 and 14 psf below the predicted values, and the flutter frequencies were, respectively, 1.6 Hz and 1.8 Hz below the predicted values.

Open-loop frequency responses. Figures 7 and 8 show the *OL* frequency responses of z_{tip} due to δ_{TEO} from analysis and experiment at 250 psf, for the symmetric and antisymmetric (fixed-in-roll) cases, respectively. At this dynamic pressure, the *OL* plant is unstable. So, the *OL* frequency responses were computed from closed-loop (*CL*) experimental data, using the Controller Performance Evaluation (CPE[6,7]) procedure. Figure 7 indicates good agreement below 9 Hz and qualitative agreement above 12 Hz. Above 12 Hz, the magnitudes differ by about 5 dB while the phase angles are nearly equal. Figure 8 indicates fair agreement, below 7 Hz, and qualitative agreement above 12 Hz. Above 12 Hz, the magnitudes differ by 6 to 8 dB and the phase angles differ by 10 to 20 degrees. Note, that for each phase diagram, the 180 degree crossing occurs near the respective *OL* flutter frequencies, and the difference between their predicted and experimental values is quite apparent.

Closed-loop Tests

The active flutter suppression test results are summarized in figures 9 through 13. Figures 9 and 10 show the wind-tunnel test dynamic pressures versus the free stream Mach number. During the wind-tunnel test, in the fixed-in-roll configuration, with both the symmetric and antisymmetric FSS control laws operating, the *CL* system was stable up to q = 270 psf, at Mach 0.46. This augmented q represents a 23% increase over the *OL* antisymmetric qf.

During the wind-tunnel test, in the free-to-roll configuration, with the symmetric FSS control law operating, the *CL* system was stable up to q = 290 psf, at Mach 0.48. This augmented q represents a 23% increase over the *OL* symmetric qf as shown in figure 10. This FSS control law also suppressed the flutter when a Rolling Maneuver Load Alleviation (RMLA[8]) system was tested with rapid roll maneuvers at q = 260 psf, 11% above the *OL* symmetric flutter boundary. This RMLA control law used LEO and TEI control surfaces, so the interaction with the FSS control law was minimal.

The rms deflection and deflection rate of the right and left side TEO control surface were computed from the data sampled at 200 Hz at each fixed-in-roll FSS test condition. If the value of the right and left differed, the maximum is plotted in figure 11. The maximum rms deflection and rates were less than 0.4 degrees and 25 degrees/second, respectively. These maximum rms deflection and rate demands of the actuators were well below the maximum allowable values of 1 deg and 75 deg/sec as stated earlier in the paper.

The Nyquist-diagram-based gain- and phase-margins were estimated using the CPE technique, during the experiment. These estimates were compared with corresponding analytical quantities in figures 12 and 13, for the symmetric free-to-roll and the antisymmetric fixed-in-roll configurations, respectively. For the symmetric, free-to-roll configuration (figure 12), the analytical and experimental gain margins were above ± 6 dB up to 270 psf. The analytical positive phase margins (at or below 7 Hz) were about 20 degrees, but the negative phase margins (at or above 12 Hz) were well above 45 degrees. The analytical phase margins were close to experimental results up to about 270 psf.

For the antisymmetric, fixed-in-roll configuration (figure 13), the analytical negative gain margins were only -3 dB. The analytical positive phase margins (at or below 7 Hz) were about 20 degrees, but the negative phase margins (at or above 12 Hz) were 45 degrees. The analytical phase margins were close to the experimental data at 250 psf, because the design model was fairly accurate at frequencies below 7 Hz (see figure 8). The negative gain and phase margins at the high frequency end were primarily responsible for

preserving the system stability. The source of additional phase lag with increasing dynamic pressure was possibly due to highly loaded actuators. The gain loss was apparent from the experimental Bode diagram shown in figure 8 in the 8 to 12 Hz frequency range.

CONCLUDING REMARKS

A single-input single-output control law was designed for flutter suppression using linear quadratic Gaussian theory and involved control law order reduction, a gain root-locus study and use of previous experimental results. The control law was digitally implemented and tested. Simultaneous suppression of symmetric and antisymmetric flutter modes in close proximity was demonstrated to 23% above the open-loop antisymmetric flutter boundary when the model was in a fixed-in-roll configuration. Symmetric flutter suppression system operating simultaneously with a rolling maneuver load alleviation system was tested to 23% above the open-loop symmetric flutter boundary, when the model was in a free-to-roll configuration. With this combined system, rapid roll maneuvers were also performed at 11% above the symmetric flutter boundary.

REFERENCES

1 Perry, B. III, Cole, S. R and Miller, G. D., "A Summary of the Active Flexible Wing Program," AIAA Paper 92-2080, April 16-17, 1992.

2 Perry, B. III, Mukhopadhyay, V., Hoadley, S. T., Cole, S. R., Buttrill, C. S. and Houck, J. A., "Digital Implementation, Simulation and Testing of Flutter-Suppression Systems for the Active Flexible Wing Wind-Tunnel Model," AIAA Paper 90-1074, April 1990.

3 Buttrill, C. S., Bacon, B. J., Heeg, J. and Houck, J. A., "Simulation and Model Reduction for the AFW Program," AIAA Paper 92-2081, April , 1992.

4 Maciejowski, J. M., *Multivariable Feedback Design*, Addison Wesley Publishing Co., Great Britain, 1989.

5 Bryson, A. E., Jr, and Ho, Y. C., *Applied Optimal Control*, Hemisphere Publishing Corporation, Washington, 1975.

6 Pototzky, A. S., Wieseman, C. D., Hoadley, S. T. and Mukhopadhyay, V., "Development and Testing of Methodology for Evaluating the Performance of Multi-input/multi-output Digital Control Systems," AIAA Paper 90-3501, August 1990.

7 Pototzky, A. S., Wieseman, C. D., Hoadley, S. T. and Mukhopadhyay, V., "On-line Performance of Multi-loop Digital Control Systems", *Journal of Guidance, Control, and Dynamics*, Vol. 15, No. 3, May-June, 1992 (TBP).

8 Woods-Vedeler, J. A. and Pototzky, A. S., "Rolling Maneuver Load Alleviation Using Active Controls," AIAA Paper 92-2099,April 16-17, 1992.
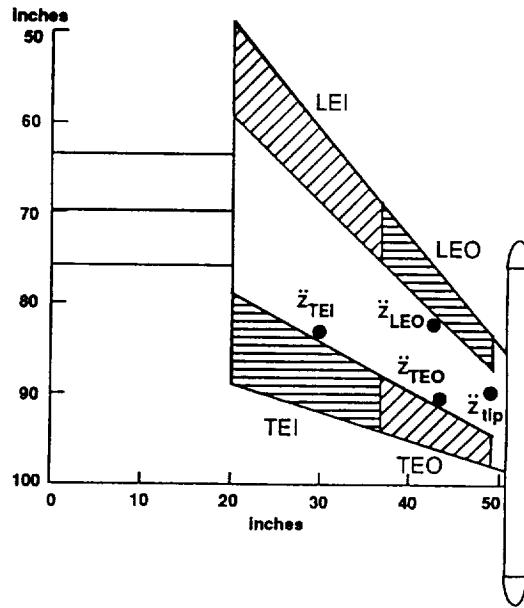
Figure 1. Accelerometer and control surface locations on AFW
wing plan form.
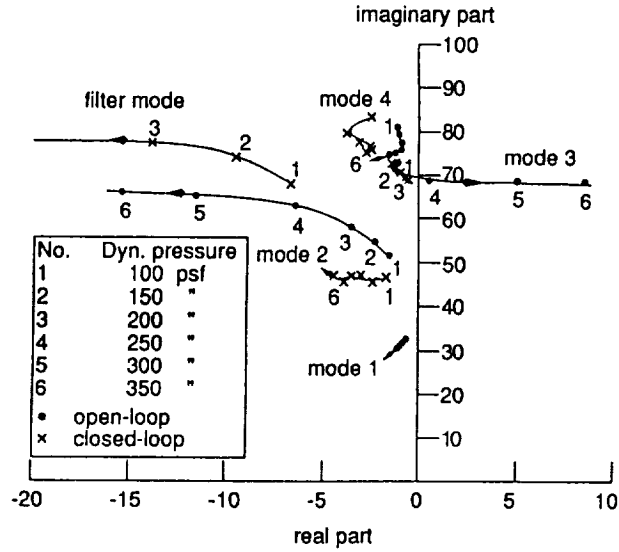
Figure 2. Symmetric open- and closed-loop dynamic pressure
root-locus at M=0.5 (arrows indicate increasing
dynamic pressure).
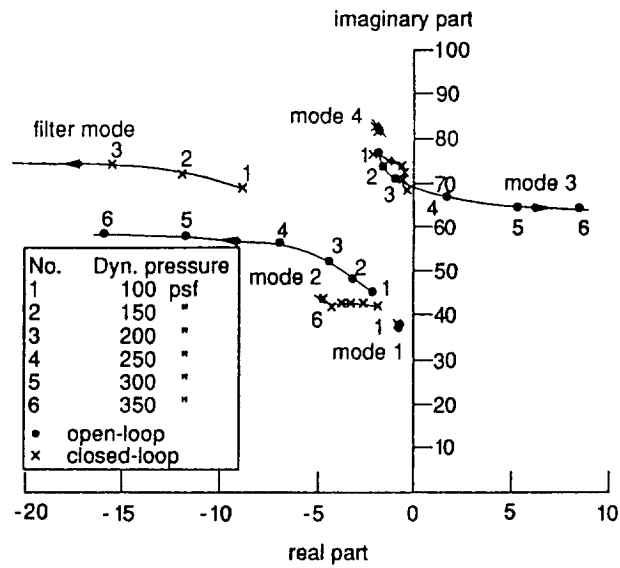
Figure 3. Antisymmetric fixed-in-roll open- and closed-loop
dynamic pressure root-locus at M=0.5 (arrows
indicate increasing dynamic pressure).
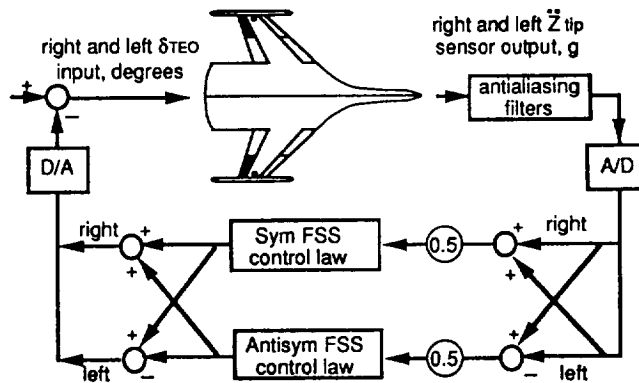
Figure 4. Digital FSS control law implementation block
diagram.
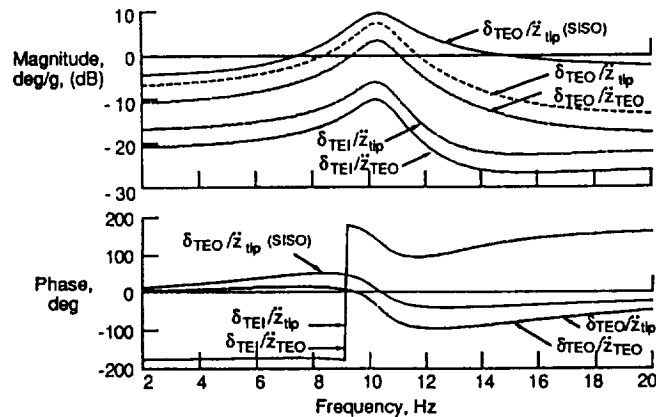
Figure 5. Bode diagram of reduced, second-order control laws .
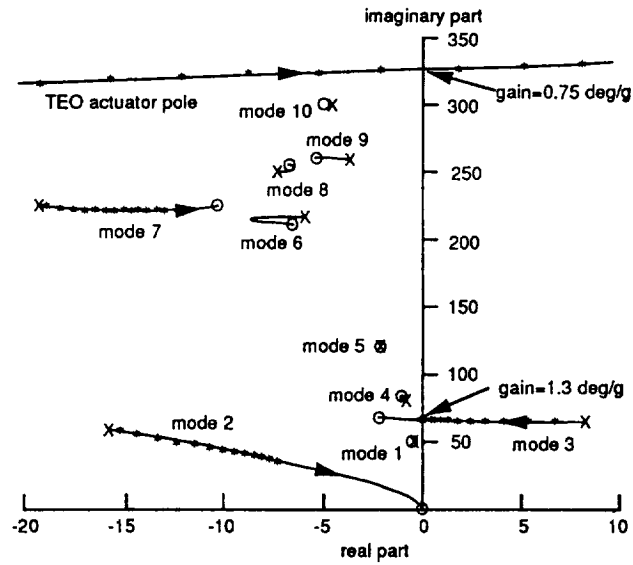
Figure 6. Gain root-locus plot for negative feedback from $\ddot{z}_{tip}$ to δ_{TEO} at 350 psf, antisymmetric fixed-in-roll configuration (x = poles, o = zeros, * indicates gain increment by 0.1).
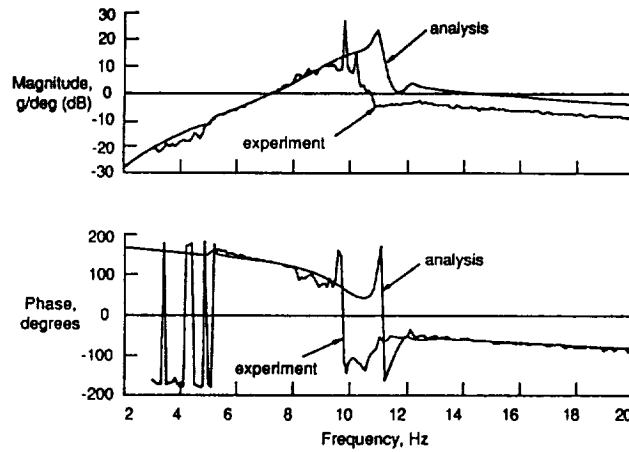
Figure 7. Comparison of $\ddot{z}_{tip}$ / δ_{TEO} Bode diagrams at 250 psf, symmetric configuration.
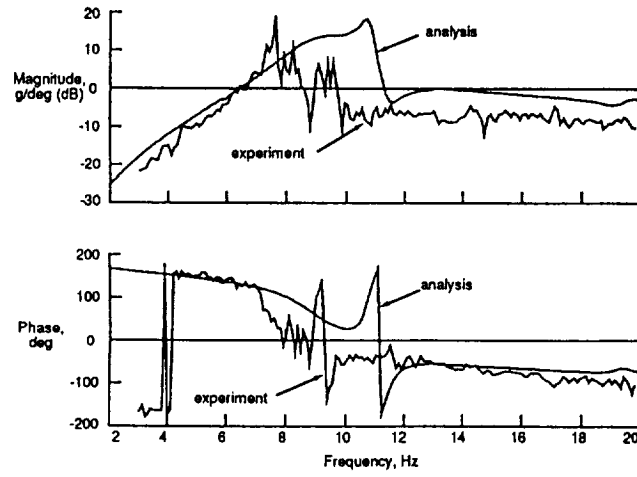
Figure 8. Comparison of $\ddot{z}_{tip} / \delta_{TEO}$ Bode diagram at 250 psf, antisymmetric fixed-in-roll configuration.
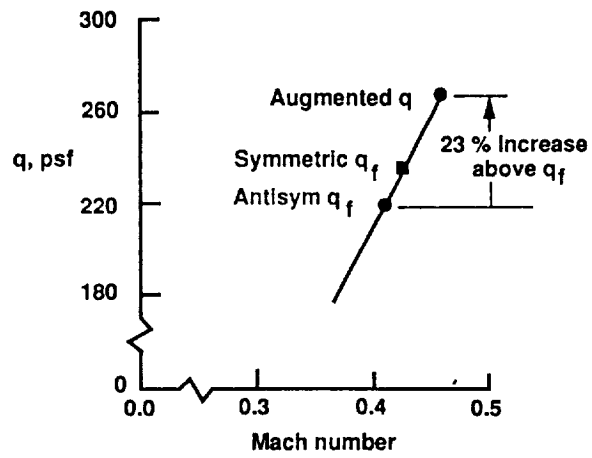
Figure 9. Summary of results for fixed-in-roll FSS wind-tunnel test.
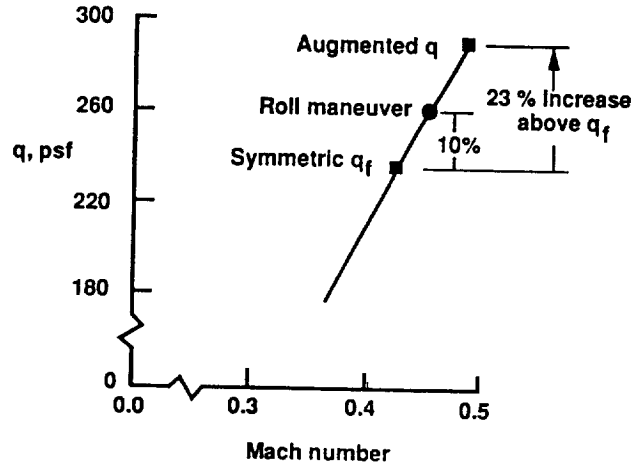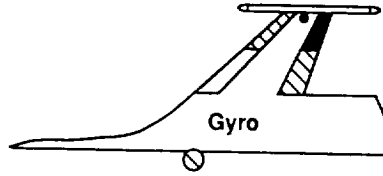
Figure 10. Summary of results for free-to-roll RMLA/FSS
wind-tunnel test.
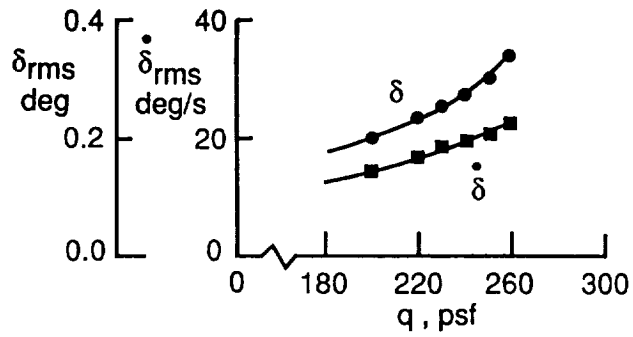
Figure 11. Maximum δ_{TEO} control surface deflection and rates
demands for simultaneous symmetric and
antisymmetric flutter suppression tests.

148
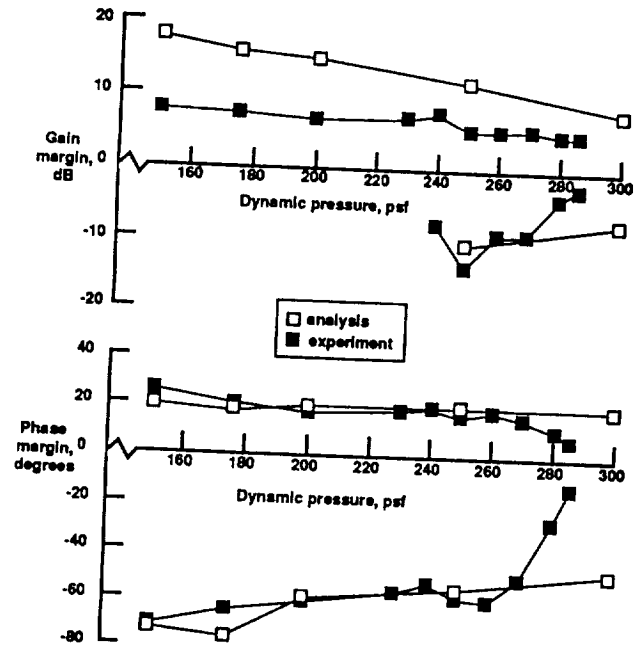
Figure 12. Gain and phase margin comparison (symmetric).
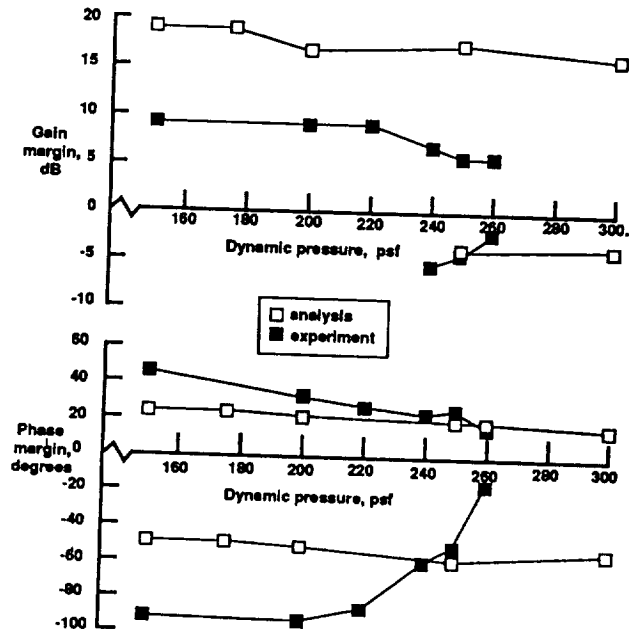
Figure 13. Gain and phase margin comparison (antisymmetric, fixed-in-roll).

SELECTED TOPICS ON THE ACTIVE CONTROL OF HELICOPTER AEROMECHANICAL AND VIBRATION PROBLEMS

Peretz P. Friedmann

Mechanical, Aerospace and Nuclear Engineering Department

University of California

Los Angeles, CA 90024

ABSTRACT

This paper describes in a concise manner three selected topics on the active control of helicopter aeromechanical and vibration problems. The three topics are: (1) The active control of helicopter air-resonance using an LQG/LTR approach; (2) Simulation of higher harmonic control (HHC) applied to a four bladed hingeless helicopter rotor in forward flight; and (3) Vibration suppression in forward flight on a hingeless helicopter rotor using an actively controlled partial span trailing edge flap, mounted on the blade. Only a few selected illustrative results are presented. The results obtained clearly indicate that the partial span actively controlled flap has considerable potential for vibration reduction in helicopter rotors.

NOMENCLATURE

$[A(\psi)]$	system dynamic matrix
$[B(\bar{\psi})]$	control distribution matrix
$[C]$	output matrix
C_W	helicopter weight coefficient, $C_W = W/(\pi R^4 \rho_a \Omega^2)$
J	quadratic cost function
$[K(s)]$	compensator matrix
$[K_c]$	feedback gains
$[K_f]$	filter gains from solution of Riccati equations

M_F	fuselage mass, nondimensional
M_{HS}	control surface hinge moment
N_b	number of blades
P_{IBC}	power required to implement conventional IBC
P_{cs}	power required to implement control based on actively controlled flap
R	rotor radius
$[T]$	HHC transfer matrix
$\{u\}$	control input vector
$[W_\delta]$	diagonal weighting matrix on actively controlled flap deflection angles
W	helicopter weight
$[W_{\Delta\delta}]$	diagonal weighting matrix on change in actively controlled flap deflection angles
$[W_Z]$	diagonal weighting matrix on vibrations
$[W_\theta]$	diagonal weighting matrix on control amplitudes
$\{x\}$	state variable vector
$\{Z(i)\}$	vector of vibration amplitudes
$\{Z_0\}$	vector of baseline vibrations

Greek Symbols

γ	Lock number
$\delta(\psi)$	control surface deflection angle
δ_{NC}, δ_{NS}	N/rev cosine and sine amplitudes of control input
θ_{IBC}	additional pitch inputs for conventional IBC
$\{\theta^*(i)\}$	optimal HHC input vector
$\{\theta(i)\}$	HHC input vector
$\{\Delta\theta(i)\}$	change in HHC input vector
θ_{pk}	pitch input to the kth blade for air resonance suppression
θ_0	collective pitch angle
θ_{1s}, θ_{1c}	cyclic pitch components required for trim

$\Delta\theta_{1s}, \Delta\theta_{1c}$	sine and cosine control components introduced through a non-rotating swashplate
θ_{HH}	higher harmonic control angle in rotating frame
$\theta_{0s}, \theta_{cs}, \theta_{ss}$	amplitudes of HHC sine input in collective, longitudinal, and lateral control degrees of freedom
$\theta_{0c}, \theta_{cc}, \theta_{cs}$	amplitudes of HHC cosine input in collective, longitudinal and lateral degrees of freedom
μ	advance ratio
σ	blade solidity
ρ_a	air density
ψ	blade azimuth
ψ_k	k^{th} blade azimuth
$\omega_{F1}, \omega_{L1}, \omega_{T1}$	rotating first flap, lag and torsional blade frequencies nondimensionalized with respect to Ω
ω_{HH}	HHC frequency
Ω	rotor angular speed
$(\cdot)$	derivative with respect to ψ

INTRODUCTION

The use of active controls whereby the pitch of a helicopter rotor blade is modified by a control system so as to alleviate dynamic effects represents a typical aeroservoelastic problem. The level and scope of the research activity in this area have been increasing steadily during the last twenty years, and the body of related literature is quite substantial. A recent comprehensive survey article has described these topics with considerable detail (ref. 1).

The purpose of this paper is to present in a concise manner three selected topics on the active control of helicopter aeromechanical and vibration problems. The three topics described here are:

(1) The active control of helicopter air resonance using an LQG/LTR approach (refs. 2-5).

(2) Simulation of higher harmonic control (HHC) applied to a four bladed hingeless rotor in forward flight (refs. 6-8).

(3) Vibration suppression in forward flight on a hingeless helicopter rotor using an actively controlled, partial span flap, mounted on the blade (refs. 9 and 25).

It should be emphasized that only concise descriptions and selected results are presented here; the interested reader can find considerable additional material in refs. 1-9, and 25.

ACTIVE CONTROL OF HELICOPTER AIR RESONANCE

Air resonance is an aeromechanical instability experienced by a helicopter in hover or forward flight. It is caused by coupling between the blade lead-lag degree of freedom with fuselage pitch or roll. Air resonance is a fairly mild type of instability when compared to ground resonance (refs. 10-12).

Improved understanding of aeromechanical phenomena such as air resonance in hover and forward flight combined with advances in modern control technology offer the potential for practical active control of air resonance in hover and in forward flight. Previous studies (refs. 13-14) neglected the important effects of blade torsional flexibility, forward flight, and unsteady aerodynamics. Furthermore, for practical applications one has to demonstrate the ability of the control system to operate throughout a wide range of operating conditions encountered, while using a small number of measurements and control inputs. These problems were addressed in detail in a fundamental and innovative series of studies (refs. 2-5). These comprehensive studies demonstrated the feasibility of designing a simple active controller capable of suppressing air resonance throughout the complete range of operating conditions which may be encountered by a hingeless rotor helicopter.

The coupled rotor/fuselage model used in this study is shown in Fig. 1. The fuselage is assumed to be a rigid body with three translational degrees of freedom and two rotational degrees of freedom, namely pitch and roll. Yaw is ignored since its effect on the air resonance problem is known to be small. An offset hinged spring restrained blade model, shown in Fig. 2, is used to represent the hingeless blade. In this model, the blade elasticity is concentrated at a single point called the hinge offset point, and torsional springs are used to represent this flexibility. This assumption simplifies the equations of

motion, while retaining the essential features of the air resonance problem. The dynamic behavior of the rotor blade is represented by three degrees of freedom, which are flap, lag, and torsional motions. The aerodynamic loads of the rotor blades are calculated using a quasi-steady two dimensional potential flow strip theory. Compressibility and dynamic stall effects are neglected, although they could be important at high advance ratios. Unsteady aerodynamic effects, which are created by the time dependent wake shed by the airfoil as it undergoes arbitrary time dependent motion, are accounted for by using a dynamic inflow model. This model is described by a 3-state linear model forced by perturbations in the aerodynamic thrust, roll moment, and pitch moment at the rotor hub. The three states in these equations describe the behavior of the perturbations in the induced inflow through the rotor plane.

The equations of motion of the coupled rotor/fuselage system are complex and contain geometrically nonlinear terms due to moderate blade deflections in the aerodynamic, inertial, and structural forces. For this reason, the equations were derived and analytically linearized about the helicopter trim using a symbolic manipulation program (ref. 5). An ordering scheme was applied to the problem to further simplify the derivation. Despite the simplifications used, the mathematical model is quite substantial. The fuselage has 5 degrees of freedom; each blade has 3 degrees of freedom, thus the four bladed hingeless rotor is represented by 12 degrees of freedom; and there are three aerodynamic states associated with the dynamic inflow model. Thus the equations of motion are represented by 37 states.

The active control inputs to suppress the air resonance instability are introduced through a conventional swashplate; the pitch of the kth rotor blade is given by the expression

$$\theta_{pk} = (\theta_0 + \Delta\theta_0) + (\theta_{1c} + \Delta\theta_{1c})\cos\psi_k + (\theta_{1s} + \Delta\theta_{1s})\sin\psi_k \qquad (1)$$

The terms with Δ are small and these represent the active control inputs, while those without Δ are the inputs necessary to trim the vehicle.

The stability of the system is determined through the linearization of the equations of motion about a blade equilibrium solution and the helicopter trim solution. The helicopter trim and equilibrium are extracted simultaneously using harmonic balance for a

straight and level flight condition. After linearization, a multiblade coordinate transformation is applied, which transforms the set of rotating blade degrees of freedom to a set of hub fixed non-rotating coordinates. The transformation is introduced in order to take advantage of the favorable properties of the non-rotating coordinate representation. The original system, before the transformation, has periodic coefficients with a fundamental frequency of 1/rev; however, the transformed system has coefficients with higher fundamental frequency. These higher frequency periodic terms have a reduced influence on the behavior of the system and can be ignored in some analyses at low advance ratios. In hover, the original system has periodic coefficients with a frequency of 1/rev, but the transformed system has constant coefficients. Two other properties of the model in hover are that the collective modes decouple from the sine and cosine modes of the system, and differential modes become uncontrollable. Thus, in hover, depending on what outputs and inputs are selected, the model may have uncontrollable and unobservable modes.

Once the multiblade coordinate transformation is carried out, the system is rewritten in first order form

$$\{\dot{x}\} = [A(\psi)]\{x\} + [B(\psi)]\{u\} \tag{2}$$

The system is constant coefficient in hover and becomes periodic as the forward flight speed is increased. Stability can be determined by using an eigenvalue analysis or by using Floquet theory for the periodic problem in forward flight (ref. 10). An approximate stability analysis in forward flight is also possible by performing an eigenvalue analysis on the constant coefficient portion of the system matrices in Eq. (2).

The study described in refs. 2-5 consisted of two stages. In the first stage (ref. 2) linear quadratic optimal control theory was used to design full state feedback controllers. It was found that the periodic terms in the model play only a small role for advance ratios below $\mu = 0.40$. However, the torsional degree of freedom and unsteady aerodynamics were found to be important. It was also determined that full state feedback was impractical and partial state feedback is unreliable.

Figure 3, taken from ref. 2, illustrates the effect of unsteady aerodynamics and periodic coefficients on the open loop system. The coupled rotor/fuselage configuration selected was a four bladed, soft-in-plane, hingeless rotor helicopter somewhat similar to the

156

MBB B0105 helicopter, in which certain parameters were modified, so as to induce an unstable air resonance mode, which manifests itself in the regressing lead-lag mode. Figure 3 depicts the damping in the lead-lag mode. The two sets of curves represent air resonance damping with quasi-steady aerodynamics and dynamic inflow, at various advance ratios. Dynamic inflow captures primarily the low frequency unsteady aerodynamic effect which is important for air resonance, and therefore this effect should be included in the controller design. It is also evident from the figure that the effect of periodic coefficients is relatively minor, thus controller design can be based on the constant coefficient approximation of the system represented by Eq. (2).

In the second stage of the research (refs. 3-5), a multivariable compensator was designed using two swashplate inputs and a single body roll rate measurement. The controller design is based on the LQG technique and the Loop Transfer Recovery Method (refs. 15-18). The controller is based on the optimal state estimator in conjunction with optimal feedback gains. A constant coefficient model is assumed, since the results shown in Fig. 3 as well as preliminary control studies (ref. 2) indicated that a periodic model was unnecessary. The compensator has the form (refs. 3-5).

$$[K(s)] = [K_c](S[I] - [A] + [B][K_c] + [K_f][C])^{-1}[K_f] \qquad (3)$$

To introduce "robustness" into the controller the multivariable frequency domain design methods of refs. 15 and 16 were used. The representation of the model error is based on unstructured multiplicative uncertainty at the model output. Details on the design process can be found in refs. 3-5.

The controller design approach used was based on the selection of an operating point to design a constant gain controller, and used this controller throughout the operating range of the helicopter. The design point chosen is at hover ($\mu = 0$) with the nominal weight ($M_F = 32$), which is a point near the region of worst instability for the configuration. A single roll rate measurement of the fuselage and the sine and cosine swashplate inputs are chosen to control the instability.

In order to keep the compensator order low, a reduced model is formed and used in the design process. This reduction is accomplished by transforming the full system to block diagonal form and then removing the modes from the full model that are deemed

unnecessary to characterize the system dynamics in the frequency range of interest. An acceptable design model is one consisting of the body roll, body pitch, lead-lag progressing and the lead-lag regressing modes (refs. 3 and 5).

Typical results demonstrating the effectiveness of this controller are shown in Figs. 4 and 5. The open loop lead-lag regressing mode damping of the helicopter configuration throughout its flight regime is presented in Fig. 4. The horizontal axis is the advance ratio, while the vertical axis is the fuselage mass M_F nondimensionalized by the blade mass of 52 Kg. The figure indicates that the system experiences an air resonance instability throughout most of the flight regime. Marginal stability exists at an advance ratio greater than $\mu = 0.35$ and the point of deepest instability is at $M_F = 30$ and in the vicinity of hover. Figure 5 shows the same system after the controller, designed according to methodology discussed above, has been applied on the helicopter. From the figure it is clear that the lead-lag regressing mode is stable over the whole flight regime, and its stability is lowest in the neighborhood of $M_F = 23$ and $\mu = 0.11$. Time simulations were also conducted to check the controller and to verify that the periodic terms in the full model do not significantly alter the stability results. The time simulation also showed that the closed loop system could suppress angular roll rates as large as 6.5 deg/sec with less than two degrees of swashplate input.

However, it should be mentioned that these studies (refs. 2-5) did not consider interactions between the controller for air resonance suppression and the flight mechanics of the complete helicopter. Therefore, possible interactions between active control systems aimed at air or ground resonance and the conventional stability augmentation system (SAS) present on all helicopters have to be carefully studied in the future to avoid potentially negative interactions from a handling qualities point of view.

AEROELASTIC SIMULATION OF HIGHER HARMONIC CONTROL

One of the most important topics, from a practical point of view, is vibration reduction in forward flight using higher harmonic control (HHC), applied through a conventional swashplate. This approach reduces vibration levels in the fuselage, or at the hub, by modifying the vibratory aerodynamic loads on the blades. Thus vibratory forces

and loads are modified, at their source, before they propagate into the airframe. This is in contrast to conventional means of vibration control which deals with the vibratory loads after they have been generated. Furthermore, it should be noted that this approach also has the potential for reducing vibration in the fuselage caused by rotor fuselage unsteady aerodynamic interference (ref. 1).

The majority of these HHC studies, either analytical or experimental (ref. 1), have been based on linear, quasistatic, frequency domain representations of the helicopter response to control. Least squares or Kalman filter type identification of helicopter control parameters has been used together with a minimum variance of quadratic performance function type controllers to determine the optimal control harmonics for vibration alleviation. A detailed description of the control algorithm used in these studies can be found in refs. 6, 8, 19-21. In these studies the general HHC input is expressed as

$$
\begin{aligned}
\theta_{HH} = {} & [\theta_{0S} \sin \bar{\omega}_{HH} \psi + \theta_{0C} \cos \bar{\omega}_{HH} \psi] \\
& + [\theta_{CS} \sin \bar{\omega}_{HH} \psi + \theta_{CC} \cos \bar{\omega}_{HH} \psi] \cos \psi \\
& + [\theta_{SS} \sin \bar{\omega}_{HH} \psi + \theta_{SC} \cos \bar{\omega}_{HH} \psi] \sin \psi
\end{aligned}
\tag{4}
$$

where $\theta_{0C}, \theta_{0S}, \theta_{CS}, \theta_{CC}, \theta_{SS}$, and θ_{SC} are independent of ψ.

Minimum variance controllers are obtained by minimization of the cost functional

$$
J = E(\{Z(i)\}^T [W_Z]\{Z(i)\} + \{\theta(i)\}^T [W_\theta(i)]\{\theta(i)\} + \{\Delta\theta(i)\}^T [W_{\Delta\theta}]\{\Delta\theta(i)\})
\tag{5}
$$

Typically $\{Z\}, \{\theta\}$, and $\{\Delta\theta\}$ consist of the sine and cosine components of N/rev. vibrations and HHC inputs. The weightings of each of the parameters may be changed to make a particular component more or less important than the other components.

The minimum variance controllers are obtained by taking the partial derivative of J with respect to $\{\theta(i)\}$

$$
\frac{\partial J}{\partial \{\theta(i)\}} = 0
\tag{6}
$$

the resulting set of equations may be solved for the optimal HHC input denoted by $\{\theta^*(i)\}$.

The form of the final algorithm will depend on whether the global or local system model is used and whether a deterministic or cautious controller is desired.

The global model of helicopter response to HHC is based on assuming linearity over the entire range of control application:

$$\{Z(i+1)\} = \{Z_0\} + [T]\{\theta(i)\} \tag{7}$$

The vibration vector $\{Z\}$ at step i + 1 is equal to the baseline uncontrolled vibration level $\{Z_0\}$ plus the product of the transfer matrix $[T]$ and the control vector $\{\theta\}$ at step i. This implies that $[T]$, which is the transfer matrix relating HHC inputs to vibration outputs, is independent of $\{\theta(i)\}$.

The local model of helicopter response to HHC is a linearization of the response about the response to the current value of the control vector:

$$\{Z(i+1)\} = \{Z(i)\} + [T](\{\theta(i+1)\} - \{\theta(i)\}) \tag{8}$$

or

$$\{\Delta Z(i+1)\} = [T]\{\Delta\theta(i+1)\} \tag{9}$$

which implies that the transfer matrix $[T]$ varies with the input $\{\theta\}$.

Each of these two algorithms has two versions, deterministic and cautious; this depends on the assumptions made on the noise characteristics for each row of the $\{Z_0\}$ and $[T]$ matrices.

Another ingredient in this algorithm is associated with identification. In applying HHC algorithms to vibration reduction, it is assumed that the HHC inputs $\{\theta(i)\}$ are known without error. Based on the measurements, different parameters may be identified. For the local model only the transfer matrix $[T]$ is identified. For the global model the transfer matrix $[T]$ and the baseline vibration vector $\{Z_0\}$ are identified. The general discrete Kalman filter is frequently used in the identification process (refs. 19-21).

Recently a comprehensive aeroelastic simulation capability has been developed (refs. 6-8) and used to study a number of fundamental issues in higher harmonic control. The analysis is based on a coupled flap-lag-torsional blade model in forward flight, with time domain unsteady aerodynamics and completely coupled aeroelastic response and trim analysis. The response analysis is based on three flap, two lag and the fundamental torsional mode. The four bladed hingeless rotor is assumed to be attached to a fixed, rigid fuselage; thus only hub shears and moments are simulated analytically. The higher harmonic control input is represented by Eq. (4). A deterministic and cautious minimum variance controller was programmed into algorithms, one for local and one for global HHC

models (refs. 6-8, 21).

The typical hingeless rotor blade considered in refs. 6-8 is shown in Fig. 6. Using this model various aspects of the HHC implementation on a soft-in-plane hingeless rotor were carefully studied. A few useful results and conclusions in these studies are briefly summarized below.

An interesting test of the ability of the controllers to adapt to changing flight conditions was performed by introducing a step change in advance ratio from $\mu = 0.30$ and $\mu = 0.35$. Results for a soft-in-plane hingeless rotor are shown in Fig. 7. A comparison of the three hub shear components and their values for the local and global controllers are shown. It is evident that the global controller has been more successful in reducing shears. Comparison of the effectiveness of the HHC to reduce vibration levels in a four bladed hingeless rotor and an equivalent four bladed articulated rotor was also conducted (ref. 8) and it was found that much larger HHC angles were required to reduce shears for the hingeless rotor. Careful comparisons of the power requirements needed for application of HHC to these two rotor configurations were also conducted, and it was found that the hingeless rotor required substantially more power.

Blade root loads and pitch link loads were also increased substantially when HHC was applied to the hingeless rotor. The conclusions imply that vibration reduction in the hingeless rotor using HHC could be more difficult to implement than in articulated rotors.

The effect of HHC on aeroelastic stability margins was also studied in ref. 6 and it was found that overall aeroelastic stability margins were not significantly degraded by application of HHC to either the articulated or the hingeless rotor configurations.

In another study (ref. 22) an important and closely related question was examined; namely, is vibration reduction at the hub equivalent to vibration reduction at various locations on a flexible fuselage when using HHC? Most analytical studies (refs. 6-8, 19-21) were based on the assumption that the fuselage is rigid and vibration reduction at the hub was assumed to be equivalent to vibration reduction at various fuselage locations. The fundamental study described in ref. 22 was based on a somewhat idealized nonlinear coupled rotor/flexible fuselage analysis capable of modeling the system shown in Fig. 8. It was found that conventional HHC inputs through a conventional swashplate, aimed at hub

shear reduction, cause an increase in the fuselage acceleration and vice versa. Furthermore it was found that for simultaneous reduction of both hub shears and fuselage accelerations, a pitch input consisting of a combination of two higher harmonic components having different frequencies was needed. However this input could not be introduced through a conventional swashplate, and it could only be implemented in the rotating reference frame. This study has also produced a new insight on the vibration reduction in coupled rotor/flexible fuselage systems by examining the sensitivity of hub shears to the frequency and amplitude of the open loop blade pitch input signals introduced in the rotating reference frame. The role of fuselage flexibility for this class of problems was also determined in ref. 22.

VIBRATION REDUCTION IN HELICOPTER ROTORS USING AN ACTIVELY CONTROLLED FLAP LOCATED ON THE BLADE

Recently a (ref. 9) detailed feasibility study was conducted to examine the potential for vibration reduction in hingeless (or bearingless) helicopter rotors by using an actively controlled flap located on the blade. Recall that comparative studies of vibration reduction in forward flight using HHC were conducted for similar articulated and hingeless rotors in refs. 6 and 8. For both configurations substantial vibration reduction was achieved with HHC angles under 3 degrees. However, a comparison of power requirements revealed that the power required to implement HHC on hingeless rotor blades is significantly higher than for equivalent articulated rotor blades. These higher power requirements appear to be associated with the need to drive harmonically the fairly large and coupled structural dynamic system represented by the hingeless blade.

This provided the motivation for exploring an alternative concept where the tailoring of the aerodynamic loads on the blade, for vibration reduction in forward flight, is accomplished through the active control of an aerodynamic surface located on the blade, similar to the partial span flap shown in Fig. 9. It was postulated that such a device would produce substantial reduction in power requirements when compared with HHC or conventional individual blade control (IBC) which require the introduction of cyclic pitch changes for the whole blade. Furthermore, such an actively controlled flap can be operated by a control loop which is separate from the primary control system; thus it will have no

influence on vehicle airworthiness, because it is not part of the primary control system of the vehicle and it will enable one to retain the conventional swashplate for flight control purposes. It should also be mentioned that this concept is not new. Almost twenty years ago Lemnios and Smith (ref. 23) used a servo flap in the context of their research on the controllable twist rotor (CTR). Using a combination of collective and cyclically varying twist distribution on the blade they demonstrated a considerable increase in performance and a 30% decrease in blade bending amplitudes.

The use of an actively controlled aerodynamic surface on each blade to reduce vibrations in forward flight falls into the category of IBC since each aerodynamic surface is individually controlled in the rotating reference frame. Such a configuration has the potential for reducing vibrations, requires less power, and retains the versatility of conventional IBC, without requiring the replacement of the conventional swashplate by a more complex mechanical system.

In the first stage of the feasibility study (ref. 9) a simple blade model consisting of an offset-hinged spring restrained blade with coupled flap, lead-lag and torsional dynamics was selected. This model was similar to that shown in Fig. 2, except that a partial span flap, shown in Fig. 9, has been added to the blade model. This partial span is used to introduce the appropriate control inputs for vibration reduction. The control surface deflection for the kth blade is represented by a sum of harmonic input signals, in the rotating reference frame, having frequencies which are integer multiples of the rotor angular frequency, but greater than the 1/rev frequency needed for vehicle trim, i.e.,

$$\delta(\psi_k) = \sum_{N=2}^{N_c \ max} [\delta_{NC} \cos(N\psi_k) + \delta_{NS} \sin(N\psi_k)] \tag{10}$$

where $N_c \ max$ represents the largest integer multiple of the rotor frequency used in the harmonic control input. In this study $N_c \ max$ was set at 5.

The inertial loads obtained in ref. 9 included the inertial effect associated with the flap mounted on the blade. The aerodynamic loads on the blade were obtained from quasi-steady Greenberg theory and the reversed flow region was included; however compressibility and dynamic stall were neglected. The aerodynamic loads associated with the actively controlled flap were based on a quasi-steady version of Theodorsen's theory. The structural, inertial and aerodynamic loads on the isolated blade are obtained in explicit

form using MACSYMA (ref. 24). The blade equations of motion contain geometrically nonlinear terms due to moderate blade deflections. An ordering scheme is used to keep the explicit expressions to a manageable size (ref. 10). The resulting equations are solved for steady trimmed flight, assuming propulsive trim. The coupled trim/aeroelastic response solution for the blade is obtained using the harmonic balance method.

The control law is obtained by minimizing the objective function represented by Eq. (5). Both global and local controllers were studied. The global controller uses the following optimal control law

$$\{\delta^*(i)\} = [D]^{-1}(-[T]^T[W_Z]\{Z(i-1)\} + [W_{\Delta\delta}]\{\delta^*(i-1)\}) \tag{11}$$

where

$$[D] = ([T]^T[W_Z][T] + [W_\delta] + [W_{\Delta\delta}]) \tag{12}$$

The local controller is governed by

$$\{\delta^*(i) = [D]^{-1}(-[T]^T[W_Z]\{Z(i-1)\} + [W_{\Delta\delta}]\{\delta^*(i-1)\} + [T]^T[W_Z][T]\{\delta^*(i-1)\} \tag{13}$$

Additional algebraic details can be found in ref. 9. Equation (13) represents a closed loop controller where the control input of the ith step is obtained by feedback of the measured response during the $(i-1)$ step $\{Z(i-1)\}$. The local controller converges quickly to the true optimal control law, usually in less than three steps.

Operating the control surface actuators needed to implement the control will of course require power from the helicopter powerplant. As a measure of the power required, the instantaneous power required to drive one control surface is averaged over one rotor revolution and multiplied by the number of blades (four in this case). The instantaneous power consists of the product of the instantaneous control surface hinge moment and the instantaneous angular velocity of the control surface. The net hinge moment consists of the sum of the inertial and aerodynamic moments about the hinge. Detailed expressions for the aerodynamic hinge moment are presented in ref. 9.

The average power required to implement the control using an active control surface on each blade is defined as:

$$P_{cs} = \sum_{k=1}^{N_b=4} \frac{1}{2\pi} \int_0^{2\pi} M_{Hcs}(\psi_k)\dot{\delta}(\psi_k)d\psi_k \tag{14}$$

164

Once the trim and response solution has been obtained, the rotor vibratory hub loads can be determined by summing the contribution from each blade of the rotor. The hub forces and hub moments of each blade are obtained in the rotating reference frame by integrating the distributed loads over the span of the blade. Subsequently the hub loads are transformed to the nonrotating hub fixed reference frame and the contribution from each blade in the rotor is summed over the number of blades. For a four bladed rotor the principal contribution to the rotor vibratory hub loads, after various algebraic and trigonometric manipulations are carried out, is the 4/rev vibratory component.

To illustrate the feasibility of this new approach to vibration reduction a number of active control studies were carried out on a soft-in-plane blade configuration at an advance ratio of $\mu = .30$. The pertinent details on this configuration can be found in ref. 9. The basic properties of this four bladed rotor are included here, so as to provide "physical feel" for the configuration considered. The fundamental rotating frequencies, for the baseline configuration, in flap, lag and torsion, respectively, were: $\omega_{F1} = 1.5$; $\omega_{L1} = 0.57$ and $\omega_{T1} = 2.5$. The thrust coefficient was $C_W = 0.005$, and $\sigma = 0.05$; $\gamma = 5.0$. The control surface was modeled as a 20% span, 1/4 chord partial span trailing edge flap centered about the 75% blade span station. The control input for minimizing the vibratory hub shears and moments consisted of a sum 2,3,4, and 5/rev harmonic input signal. The 3,4 and 5/rev input frequencies were selected because a 4/rev pitch input signal introduced in the nonrotating system through a conventional swashplate, which is frequently used in HHC studies on four bladed rotors, generates a signal consisting of 3,4 and 5/rev components in the rotating reference frame. The 2/rev component was added since it was found in ref. 22, that its role in vibration reduction is as significant as that of the other three components mentioned.

For the results presented here, only the vibration levels were penalized, i.e., $W_\delta = W_{\Delta\delta} = 0$. For this case the quadratic cost functional $J(i)$ consists of the weighted sum of the squares of the hub shears and hub moments, as evident from Eq. (5). The non-dimensional values of the baseline hub moments were an order of magnitude smaller than the hub shears. Therefore, the weights on the hub moments were set at 100 times the weights on the hub shears in order to ensure that an equivalent degree of vibration

reduction is achieved in all vibratory components.

Comparison of the vibration reduction obtained with the actively controlled flap, and individual blade control used on the same blade is presented in Figs. 10 and 11. Individual blade control (IBC) applied on the blade in the conventional sense implies that pitch input is provided at the root of the blade and the whole blade is oscillated in pitch, as a rigid body. When IBC is applied through an actively controlled flap, the pitch input is applied only to the small partial span flap. Figure 10 shows comparison of baseline hub shears and hub moments acting on blade, with those which are present when vibration reduction is implemented by the actively controlled flap. Figure 11 presents a similar comparison for the case of conventional IBC. In both figures results are presented for both the global and local controllers. These results indicate that similar degrees of vibration reduction are obtained for both the global and local approaches. It is also evident from Figs. 10 and 11 that the vertical hub shear was reduced to within 10% of its baseline value when using an actively controlled flap, compared to an average reduction to within 5% of its baseline value using conventional IBC. Very similar results were also obtained for the other five components of the vibratory hub loads. Overall, it appears that conventional IBC is slightly more effective in reducing the vibratory hub leads. However, the difference in the degree of vibration reduction achieved by the two control approaches is very small. A comparison of the optimal control input for vibration reduction using the individually controlled flap and conventional IBC for a blade having a fundamental torsional frequency of 2.5 is shown in Fig. 12. Examination of the optimal input signals reveals that somewhat larger control input amplitudes are required for vibration reduction when using the actively controlled flap compared to the angles required by conventional IBC. A maximum control surface deflection angle of 4 degrees is required compared to a maximum control angle of 0.9 degrees for conventional IBC. Numerous additional results, presented in ref. 9, indicate that larger control input amplitudes were required to achieve approximately the same degree of vibration reduction, when the torsional frequency of the blade is increased.

A comparison of the average power required (per revolution) for the implementation of the vibration reduction using the two control approaches is presented in Fig. 13. The power required for conventional IBC is defined as the average power needed to

166

drive the blade root pitch actuators during one revolution:

$$P_{IBC} = \sum_{k=1}^{N_b=4} \frac{1}{2\pi} \int_0^{2\pi} M_{x3}(\psi_k)\dot{\theta}_{IBC}(\psi_k)d\psi_k \tag{15}$$

where $\theta_{IBC}(\psi)$ represents the instantaneous additional IBC pitch input of the kth blade and $M_{x3}(\psi)$ represents the instantaneous blade root feathering moment.

An examination of Fig. 13 reveals that substantially more power is required to implement vibration reduction using the conventional IBC approach than for vibration reduction based on the actively controlled flap. Vibration reduction using conventional IBC required about 800% more power at the lower blade torsional frequencies, and about 400% more power at the higher blade torsional frequencies. These higher power requirements appear to be associated with the need to drive harmonically the fairly large and coupled structural dynamic system represented by the entire blade, as opposed to the need to drive harmonically a relatively small aerodynamic control surface. It is also evident from this figure that as the torsional frequency of the blade increases, the power required to implement the control increases for both control approaches.

The results presented here together with the additional results presented in ref. 9 clearly indicate that the actively controlled flap is a feasible and very attractive concept, because it can produce the same vibration reduction as conventional IBC, with reasonable control angles and requires substantially less power (4 to 8 times less). Furthermore, it has the additional advantage of having no effect on the airworthiness when compared to conventional IBC.

Further studies on the practical implementation of an actively controlled flap to reduce vibrations in forward flight were presented in ref. 25. In this study, which represents a sequel to ref. 9, the offset hinged spring restrained blade model used previously was replaced by a completely flexible blade model. Control studies based upon the flexible blade model and the spring restrained blade model are compared. It was found that despite large increases in vibration levels due to the more realistic flexible blade model, vibration reduction could still be accomplished without excessive power expenditure or control angle inputs. A careful parametric study in which variations of torsional frequency, spanwise location of the control surface, and hinge moment correction factor was conducted. The results further reinforced the feasibility of this new approach to vibration

reduction. Numerous results obtained in this study can be found in ref. 25.

CONCLUDING REMARKS

During the last few years there has been a steady evolution of the application of active control technology to both stabilization of aeromechanical problems such as air and ground resonance as well as vibration reduction in forward flight.

Aeromechanical problems such as air and ground resonance are due to the low damping level associated with the inplane (lead-lag) degree of freedom and its coupling with fuselage roll. Thus this instability can be easily stabilized using active controls. However it is important to emphasize that the expense associated with using active control technology for aeromechanical stability augmentation can not be justified. Only vibration reduction in forward flight is sufficiently important so as to warrant the additional cost associated with active control technology. Once such a vibration reduction system has been installed it can also be used to stabilize aeromechanical problems. However, additional research is needed before the feasibility of stabilizing potential aeroelastic instabilities in rotors is verified.

Since modern rotor systems appear to move in the direction of hingeless and bearingless designs, the capability of conventional HHC or IBC may be limited by the need to oscillate the complete blade in pitch. In this context the actively controlled, partial span, trailing edge flap offers an attractive alternative which requires substantially less power and is fairly simple to implement. Therefore, this concept should be carefully studied using both simulation as well as wind tunnel tests.

ACKNOWLEDGEMENT

REFERENCES

1. Friedmann, Peretz, P.; Rotary-Wing Aeroservoelastic Problem. AIAA Paper No. 92-2107, Proceedings AIAA Dynamics Specialist Conference, April 16-17, 1992, Dallas, TX, pp. 248-272.

2. Takahashi, M.D.; and Friedmann, P.P.; Active Control of Helicopter Air Resonance in Hover and Forward Flight. AIAA Paper 88-2407, Proceedings of 29th AIAA/ASME/ASCE/AHS Structures, Structural Dynamics and Materials Conference, April 18-20, Williamsburg, VA, pp. 1521-1532.

3. Takahashi, Marc, D.; Active Control of Helicopter Aeromechanical and Aeroelastic Instabilities. Ph.D. Dissertation, Mechanical, Aerospace and Nuclear Engineering Department, University of California, Los Angeles, June 1988.

4. Takahashi, M.D.; and Friedmann, P.P.; Design of a Simple Active Controller to Suppress Helicopter Air Resonance. Proceedings of the 44th Annual Forum of the American Helicopter Society, Washington, DC, June 1988, pp. 305-316.

5. Takahashi, M.D.; and Friedmann, P.P.; Helicopter Air Resonance Modeling and Suppression Using Active Control. *AIAA Journal of Guidance, Control and Dynamics*, vol. 14, no. 6, Nov/Dec 1991, pp. 1294-1300.

6. Robinson, Lawson, H.; Aeroelastic Simulation of Higher Harmonic Control. Ph.D. Dissertation, Mechanical, Aerospace and Nuclear Engineering Department, University of California, Los Angeles, June 1989.

7. Robinson, L.H.; and Friedmann, P.P.; Analytical Simulation of Higher Harmonic Control Using a New Aeroelastic Model. AIAA Paper No. 89-1321, Proceedings of 30th AIAA/ASME/ ASCE/AHS/ACS Structures, Structural Dynamics and Materials Conference, Mobile, AL, April 1989, Part III, pp. 1394-1406.

8. Robinson, L.H.; and Friedmann, P.P.; A Study of Fundamental Issues in Higher Harmonic Control Using Aeroelastic Simulation. *Journal of the American Helicopter Society*, vol. 36, no. 2, April 1991, pp. 32-43.

9. Millott, T.; and Friedmann, P.P.; Vibration Reduction in Helicopter Rotors Using an Active Control Surface Located on the Blade. AIAA Paper No. 92-2451, Proceedings of 33rd AIAA/ASME/AHS/ACS Structures, Structural Dynamics and Materials Conference, April 13-15, 1992, Dallas, TX, pp. 1975-1988.

10. Friedmann, Peretz, P.; Formulation of Rotary-Wing Aeroelastic Stability and Response Problems, *Vertica*, vol. 7, no. 2, pp. 101-141, 1983.

11. Friedmann, Peretz, P.; Recent Trends in Rotary-Wing Aeroelasticity. *Vertica*, vol. 11,

no. 1/2, pp. 139-170, 1987.

12. Friedmann, Peretz, P.; Rotary-Wing Aeroelasticity with Application to VTOL Vehicles. AIAA Paper 90-1115, Proceedings of 31st AIAA/ASME/ASCE/AHS Structures, Structural Dynamics and Materials Conference, Long Beach, CA, April 2-4, 1990, pp. 1624-1670.

13. Straub, F.K.; and Warmbrodt, W.; The Use of Active Controls to Augment Rotor/Fuselage Stability. *Journal of the American Helicopter Society*, vol. 30, no. 3, pp. 13-22, 1985.

14. Straub, Friedrich, K.; Optimal Control of Helicopter Aeromechanical Stability. *Vertica*, vol. 11, no. 3, pp. 12-22, 1987.

15. Doyle, J.C.; and Stein, G.; Multivariable Feedback Design; Concepts for Classical/Modern Synthesis. *IEEE Transactions on Automatic Control*, vol. AC-32, no. 2, February 1987, pp. 105-114.

16. Stein, G.; The LQG/LTR Procedure for Multivariable Feedback Control Design. *IEEE Transactions on Automatic Control*, vol. AC-32, no. 2, February 1987, pp. 105-114.

17. Safonov, M.G.; Laub, A.J.; and Hartmann, G.L.; Feedback Properties of Multivariable Systems: The Role and Use of the Return Difference Matrix. *IEEE Transactions on Automatic Control*, vol. AC-26, no. 1, February 1981, pp. 47-65.

18. Madiwale, A.; and Williams, D.E.; Some Extensions of Loop Transfer Recovery. Proceedings of the American Control Conference, vol. 2, 1985, pp. 790-795.

19. Johnson, Wayne; Self-Tuning Regulators of Multicyclic Control of Helicopter Vibrations. NASA TP 1996, 1982.

20. Molusis, J.A.; Hammond, C.E.; and Cline, J.H.; A Unified Approach to the Optimal Design of Adaptive and Gain Scheduled Controllers to Achieve Minimum Helicopter Vibration. *Journal of the American Helicopter Society*, vol. 28, no. 2, pp. 9-18, April 1983.

21. Davis, Mark, W.; Refinement and Evaluation of Helicopter Real-Time Self-Adaptive Active Vibration Control Algorithms. NASA CR-3821, August 1984.

22. Papavassiliou, I.; Friedmann, P.P.; and Venkatesan, C.; Coupled Rotor/Fuselage Vibra-

tion Reduction Using Multiple Frequency Blade Pitch Control. Paper No. 91-76, Proceedings of Seventeenth European Rotorcraft Forum, September 24-26, 1991, Berlin, Germany, pp. 91-76.1 - 91-76.44.

23. Lemnios, A.Z.; Smith, A.F.; An Analytical Evaluation of the Controllable Twist Rotor Performance and Dynamic Behavior, Kaman Report R-794, 1972.

24. ___; MACSYMA: Reference Manual, Symbolics Inc., June 1986.

25. Millott, T.A.; Friedmann, P.P.; The Practical Implementation of an Actively Controlled Flap to Reduce Vibrations in Helicopter Rotors, Proceedings of 49th Annual Forum of the American Helicopter Society, St. Louis, MO, May 19-21, 1993, pp. 1079-1092.
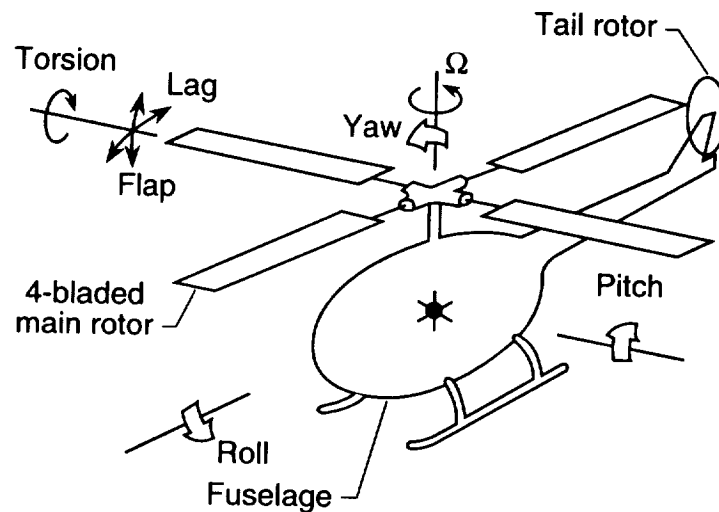
Fig. 1: Coupled rotor fuselage model
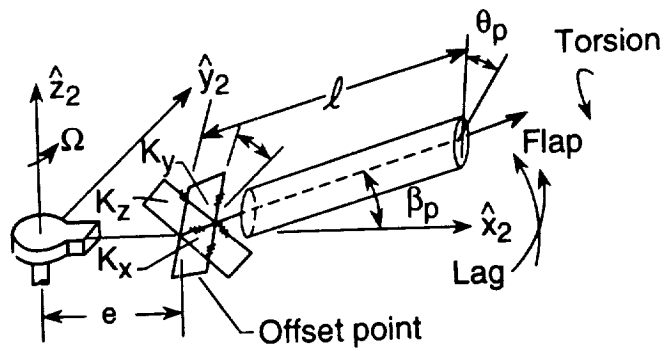
Fig. 2: Offset hinged spring restrained model for hingeless blade.
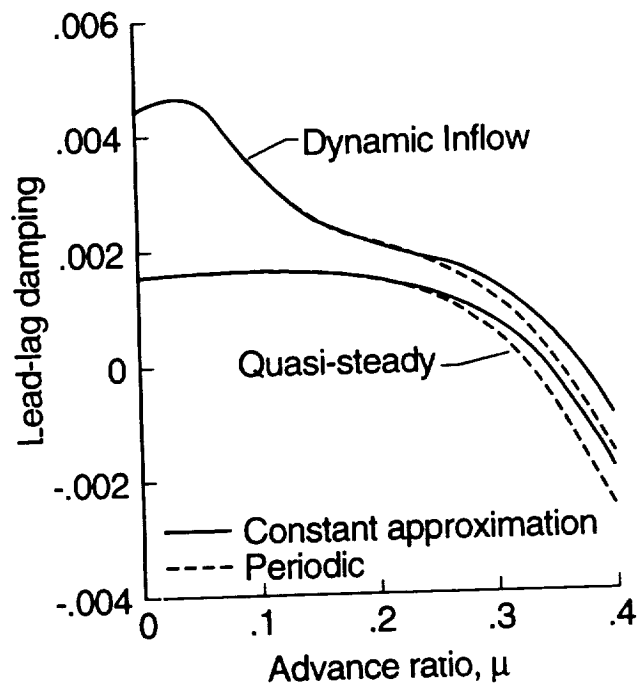
Fig. 3: Open loop lead-lag regressing damping of the nominal configurations with and without dynamic inflow.
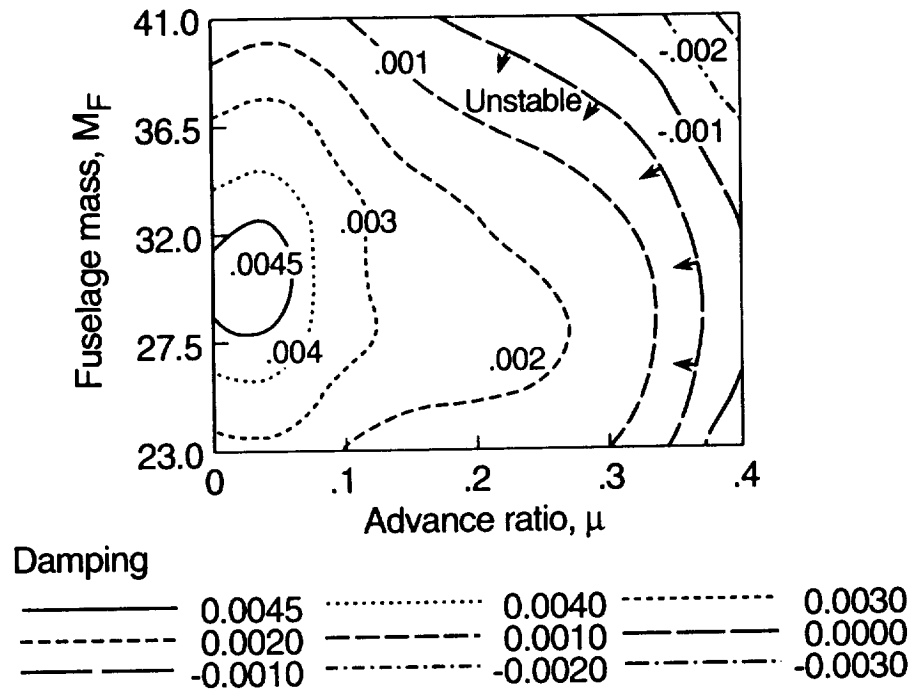
Fig. 4: Open loop lead-lag regressing mode damping at various weights and advance ratios
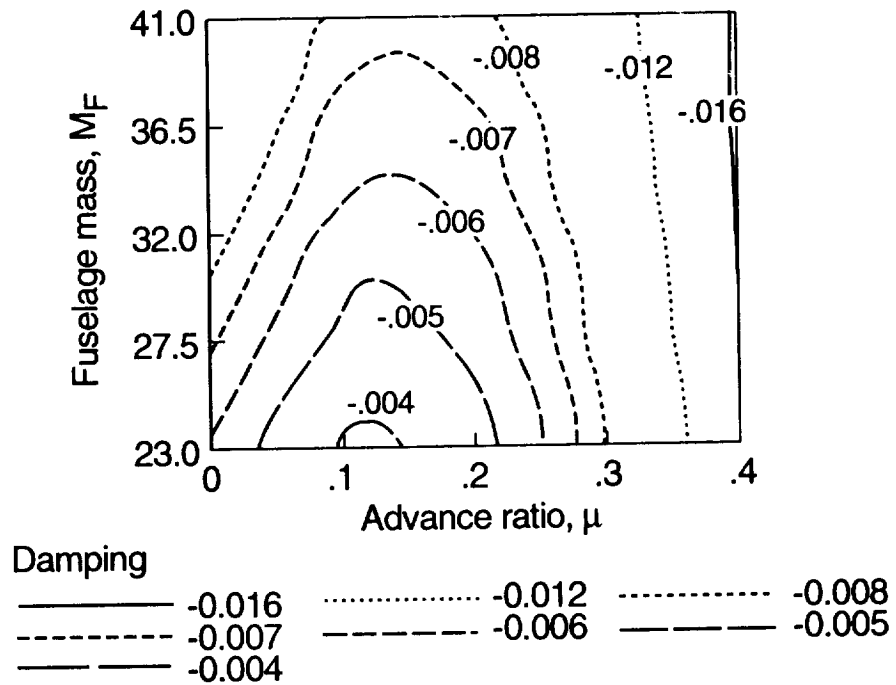
Fig. 5: Closed loop lead-lag regressing mode damping at various fuselage weights and advance ratios, using the active control
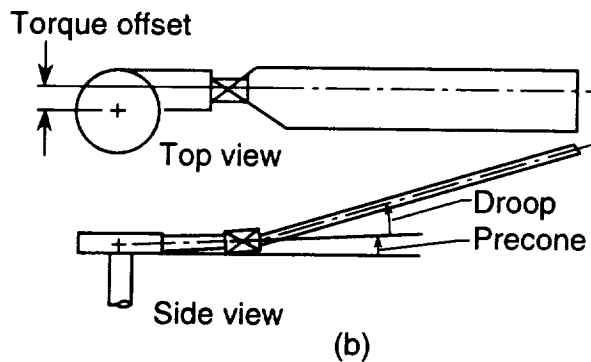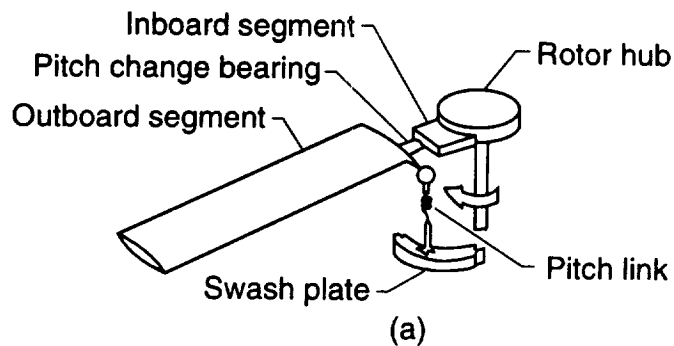
Fig. 6: Typical hingeless rotor blade geometry
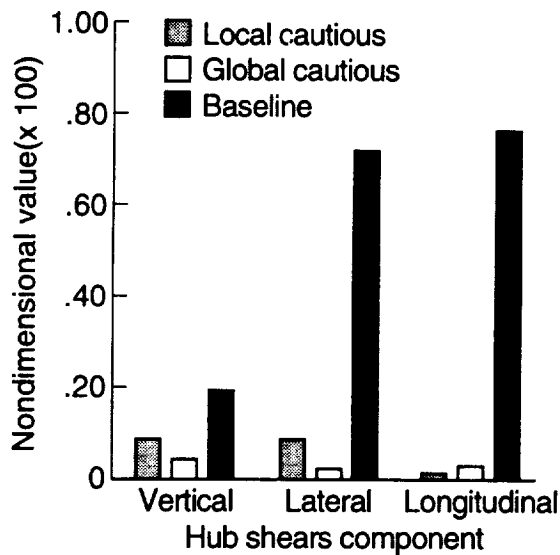
Fig. 7: Baseline shears for $\mu = 0.35$ and shear five iterations after a step change from $\mu = 0.30$ to $\mu = 0.35$, local and global controllers

(a) Offset hinged spring restrained blade model

(b) Elastic blade model

M - Hub Center

Fig. 8: Schematic representation of coupled rotor/flexible fuselage system, including two different types of blade models; (a) offset hinged blade and (b) fully elastic blade

OFFSET POINT

Fig. 9: Offset-hinged spring restrained hingeless rotor blade model with partial span flap

175

Hub Shears

Hub Moments

Fig. 10: Hub shears and moments for IBC using an actively controlled flap at a first rotating torsional frequency of 2.5/rev

Hub Shears

Hub Moments
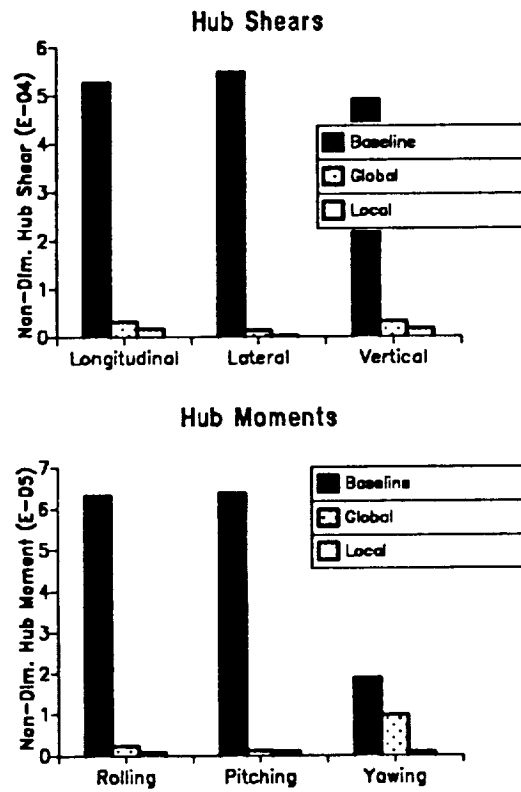
Fig. 11: Hub shears and moments for conventional IBC at a first rotating torsional frequency of 2.5/rev
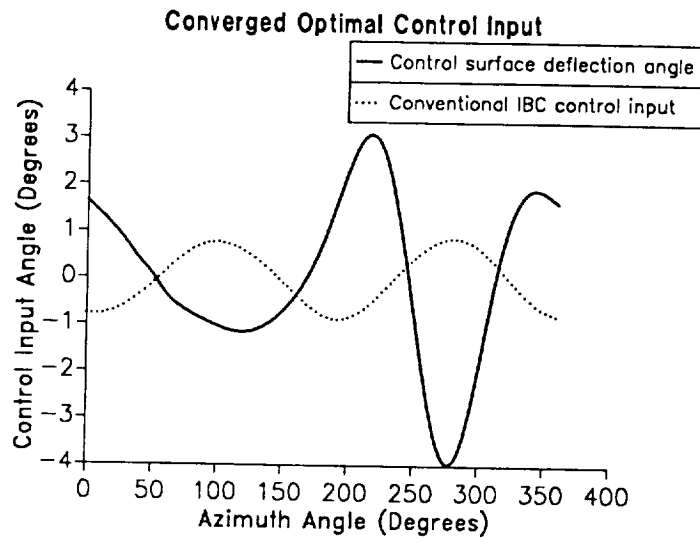
Fig. 12: Optimal control input comparison at a first rotating torsional frequency of 2.5/rev
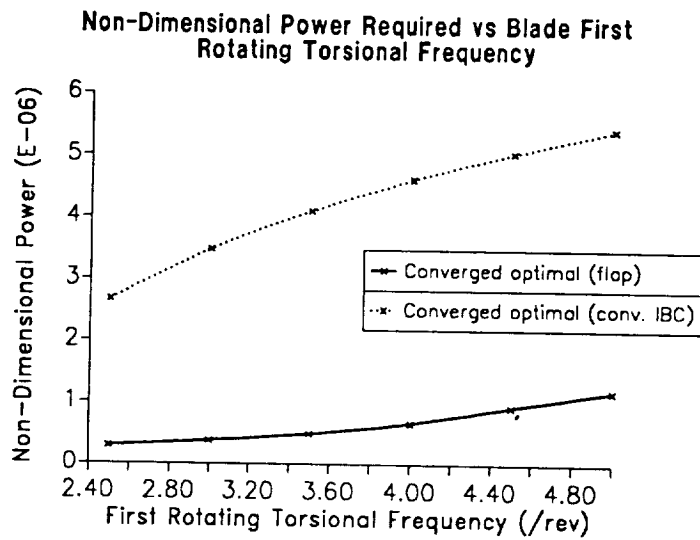
Fig. 13: Power requirements vs. blade first rotating torsional frequency

177

Robust Control Design Techniques for Active Flutter Suppression

Hitay Özbay[1]   and   *Glen R. Bachmann*
Department of Electrical Engineering
The Ohio State University
Columbus, OH 43210

Abstract

In this paper an active flutter suppression problem is studied for a thin airfoil in unsteady aerodynamics. The mathematical model of this system is infinite dimensional, because of Theodorsen's function which is irrational. Several second order approximations of Theodorsen's function are compared. A finite dimensional model is obtained from such an approximation. We use H^∞ control techniques to find a robustly stabilizing controller for active flutter suppression.

1   Introduction

In this paper an active flutter suppression problem is studied for a thin airfoil in unsteady aerodynamics. Because of the interaction between the structure and the flow, flutter (dynamic instability) occurs at a certain flow speed. Therefore, it is important to design active feedback controllers stabilizing the airfoil. A robustly stabilizing feedback compensator is obtained from the H^∞ control theory. This theory gives us the largest amount of uncertainty (due to neglected aerodynamics) which can be tolerated in the problem of active flutter suppression.

In general, mathematical models for airfoils in unsteady aerodynamics are linear time invariant infinite dimensional systems. The basic difficulty in such systems is

---

[1]e-mail: ozbay@ee.eng.ohio-state.edu

to compute the aerodynamic loads due to unsteady flow. The simplest models (in the frequency domain) for the unsteady aerodynamics contain Theodorsen's function as the infinite dimensional part. There are several techniques for designing feedback controllers directly from the infinite dimensional airfoil model see e.g. [1]. In this method the controller itself is infinite dimensional, and hence one has to approximate it in order to obtain an implementable finite dimensional controller. Another method is to approximate the infinite dimensional part of the system and design a finite dimensional controller from the finite dimensional approximate model. In this paper we consider the second method, and design a *robust controller*, which stabilizes not only the finite dimensional model, but also the infinite dimensional model. The main tool used here in the robust controller design is the H^∞ control theory.

In the next section we define a mathematical model for a thin airfoil. Several second order approximations for the Theodorsen's function are compared in Section 3. In Section 4 we present a robust stabilization algorithm for flutter suppression in the presence of unmodeled aerodynamics. Concluding remarks are made in the last section.

2 A mathematical model for the airfoil

We consider the following mathematical model (see e.g. [1], [2]), for a thin airfoil shown in Figure 1,

$$M_s \ddot{z}(t) + B_s \dot{z}(t) + K_s z(t) = \frac{1}{m_s} F(t) + Gu(t), \tag{1}$$

where $z(t) = [h(t), \alpha(t), \beta(t)]^T$, and $u(t)$ represents the control input.
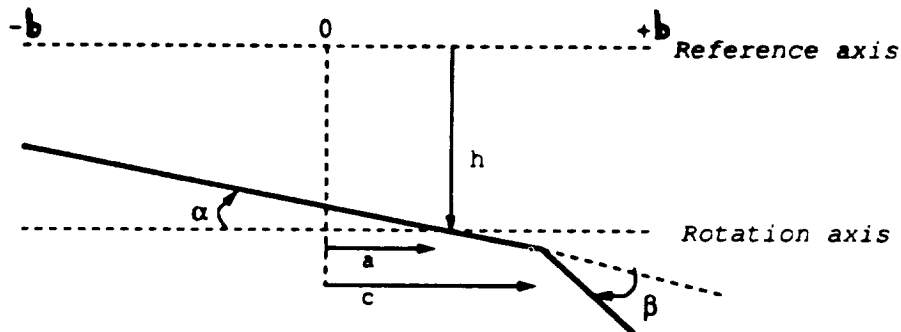
Figure 1: Thin airfoil

180

The matrices M_s, B_s, K_s and G are in the form

$$M_s = \begin{bmatrix} 1 & x_\alpha & x_\beta \\ x_\alpha & r_\alpha^2 & r_\beta^2 + x_\beta(c-a) \\ x_\beta & r_\beta^2 + x_\beta(c-a) & r_\beta^2 \end{bmatrix} , \quad B_s = \begin{bmatrix} 0 & 0 & 0 \\ 0 & 0 & 0 \\ 0 & 0 & 2r_\beta^2\zeta_\beta\omega_\beta \end{bmatrix} ,$$

$$K_s = \begin{bmatrix} \omega_h^2 & 0 & 0 \\ 0 & r_\alpha^2\omega_\alpha^2 & 0 \\ 0 & 0 & r_\beta^2\omega_\beta^2 \end{bmatrix} , \quad G = \begin{bmatrix} 0 \\ 0 \\ r_\beta^2\omega_\beta^2 \end{bmatrix} ,$$

where all the constants are related to the geometry and physical properties of the structure.

In order to apply Laplace transform techniques, we will assume that $z(t) = 0$ for $t \leq 0$. This corresponds to the indicial problem (see e.g. [1], and [3]). Aeroelastic loads are represented by $F(t) = [P(t), M_\alpha(t), M_\beta(t)]^T$. We can represent $F(t)$ as

$$F(t) = M_a \ddot{z}(t) + B_a \dot{z}(t) + K_a z(t) + F_c(t) \tag{2}$$

where $F_c(t)$ is the "circulatory" part of $F(t)$. The matrices M_a, B_a and K_a can be computed in terms of the problem data [9] [8]

$$M_a = -\rho b^2 \begin{bmatrix} \pi & -\pi b a & -T_1 b \\ -a\pi b & \pi b^2(\frac{1}{8} + a^2) & -(T_7 + (c-a)T_1)b^2 \\ -T_1 b & -(T_7 + (c-a)T_1)b^2 & -T_3 b^2/\pi \end{bmatrix}$$

$$B_a = -\rho b^2 V \begin{bmatrix} 0 & \pi & -T_4 \\ 0 & \pi(0.5-a)b & (T_1 - T_8 - (c-a)T_4 + 0.5T_{11})b \\ 0 & (T_4(a-0.5) - T_1 - 2T_9)b & -T_4 T_{11} b/2\pi \end{bmatrix}$$

$$K_a = -\rho b^2 V^2 \begin{bmatrix} 0 & 0 & 0 \\ 0 & 0 & T_4 + T_{10} \\ 0 & 0 & (T_5 - T_4 T_{10})/\pi \end{bmatrix} .$$

where T_i's are Theodorsen's constants, see e.g. [9].

Using Theodorsen's formulation, $F_c(t)$ can be expressed in the frequency domain as (see e.g. [9] pp. 395–396, or [8] pp. 26–28)

$$\widehat{F}_c(s) = C(s)(B_{c1} + sB_{c2})\widehat{z}(s) \tag{3}$$

$C\text{-}3$

where s is the Laplace transform variable, $\,\widehat{}\,$ represents the Laplace transformed version of a time signal, $C(j\omega)$ is the Theodorsen's function, and B_{c1}, B_{c2} are constant matrices given by $B_{c1} = b_1 c_1$ and $B_{c2} = b_1 c_2$ where $b_1 = \rho V b \begin{bmatrix} -2\pi \\ 2\pi b(a + 0.5) \\ T_{12} b \end{bmatrix}$,

$c_1 = V \begin{bmatrix} 0 & 1 & T_{10}/\pi \end{bmatrix}$, and $c_2 = \begin{bmatrix} 1 & b(0.5 - a) & bT_{11}/2\pi \end{bmatrix}$.

Suppose that the measured output for feedback is

$$y(t) := c_1 z(t) + c_2 \dot{z}(t).$$

Then, taking the Laplace transforms of (1) and (2), and then using (3) we obtain a transfer function from u to y, denoted by $P(s)$:

$$\frac{\widehat{y}(s)}{\widehat{u}(s)} = P(s) = \frac{C_o(sI - A)^{-1} B_o}{1 - C_o(sI - A)^{-1} B_1\ C(s)} \tag{4}$$

where $C(s)$ is the Theodorsen's function, and

$$A = \begin{bmatrix} 0_{3\times 3} & I_{3\times 3} \\ (M_s - M_a)^{-1}(K_a - K_s) & (M_s - M_a)^{-1}(B_a - B_s) \end{bmatrix}$$

$$C_o = \begin{bmatrix} c_1 & c_2 \end{bmatrix}, \quad B_1 = \begin{bmatrix} 0_{3\times 1} \\ b_1 \end{bmatrix}, \quad B_o = \begin{bmatrix} 0_{3\times 1} \\ (M_s - M_a)^{-1} G \end{bmatrix}.$$

Note that the plant can be seen as a feedback system whose feedback path consists of the aerodynamics represented by Theodorsen's function, as shown below.
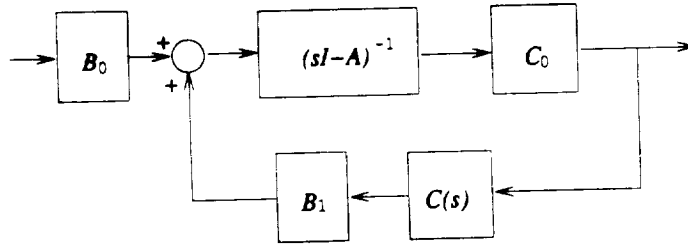
Figure 2: Structure of the plant

The function $C(s)$ is irrational, and in practice it is approximated by a low order rational function, say $C_a(s)$. This leads to an approximate model for the plant to be controlled

$$P_a(s) = \frac{C_o(sI - A)^{-1} B_o}{1 - C_o(sI - A)^{-1} B_1\ C_a(s)}.$$

In Section 4 we will see that a rational feedback controller K_a, which stabilizes P_a, stabilizes the original infinite dimensional model P if and only if the H^∞ norm of the "weighted" closed loop transfer function is less than the inverse of the L^∞ approximation error

$$\|C - C_a\|_\infty := \sup_\omega |C(j\omega) - C_a(j\omega)|.$$

Therefore, we have a better chance of stabilizing P by a rational K_a if we can make the L^∞ error in Theodorsen's function approximation. In the next section we compare the L^∞ errors of several second order approximates of the Theodorsen's function.

3 L^∞ Approximation of the Theodorsen's function

As mentioned above, the Theodorsen's function, $C(s)$ which appears in the feedback path of the plant model, is infinite dimensional. For controller design (synthesis) and simulation (analysis) purposes we would like to use a finite dimensional approximate $C_a(s)$ instead of the exact irrational $C(s)$, which is given by (see e.g. [9])

$$C(j\omega) = \text{Re}[C(j\omega)] + j\text{Im}[C(j\omega)] \tag{5}$$

where

$$\text{Re}[C(j\omega)] = \frac{J_1(\omega)(J_1(\omega) + Y_0(\omega)) + Y_1(\omega)(Y_1(\omega) - J_0(\omega))}{(J_1(\omega) + J_0(\omega))^2 + (Y_1(\omega) - J_0(\omega))^2},$$

$$\text{Im}[C(j\omega)] = \frac{(Y_1(\omega)Y_0(\omega) + J_1(\omega)J_0(\omega))}{(J_1(\omega) + J_0(\omega))^2 + (Y_1(\omega) - J_0(\omega))^2}.$$

(J_0, J_1, Y_0, Y_1 are the Bessel functions). Several second order approximations of (5) can be found in the literature, see for example [8]. These approximations are in the form

$$C_a(s) = \frac{(1 + \tau_1 s)(1 + \tau_2 s)}{(1 + \tau_3 s)(1 + \tau_4 s)} \tag{6}$$

where $\tau_1, \tau_2, \tau_3, \tau_4$ are positive real constants to be chosen. For example, the following sets of numerical values are proposed by R. Jones, W. P. Jones and R. L. Moore respectively

$$\tau_1 = 18.6 \ , \quad \tau_2 = 1.97 \ , \quad \tau_3 = 21.98 \ , \quad \tau_4 = 3.33 \tag{7}$$

$$\tau_1 = 20.62 \ , \quad \tau_2 = 1.85 \ , \quad \tau_3 = 24.39 \ , \quad \tau_4 = 3.125 \tag{8}$$

$$\tau_1 = 10.61 \ , \quad \tau_2 = 1.774 \ , \quad \tau_3 = 13.51 \ , \quad \tau_4 = 2.744 \ . \tag{9}$$

For each of these sets of numbers the error function $|C(j\omega) - C_a(j\omega)|$ is plotted in Figure 3.
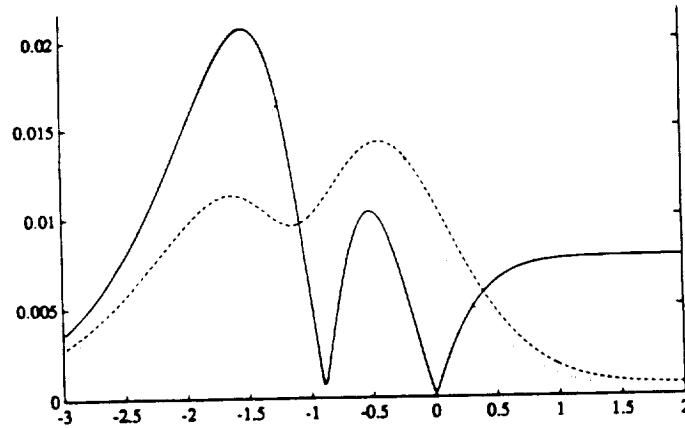
Figure 3: Error function for R. Jones, W. P. Jones and R. L. Moore approximates of the Theodorsen's function .

As we can see from this figure, R. Jones's approximation is the best one (in the L^∞ norm) among the three second order approximates listed above. In different norms, other approximations may be better than the one which is best in L^∞ norm. But since we are going to use H^∞ control techniques (in order to guarantee the robustness of the controllers derived from the approximate plant), we will need an error bound in the L^∞ norm. Below we will show that it is possible to improve the L^∞ error of the R. Jones approximation by fine tuning the values of $\tau_1, \ldots, \tau_4$.

We found that the values of

$$\tau_1 = 18.57 \ , \quad \tau_2 = 2.057 \ , \quad \tau_3 = 21.93 \ , \quad \tau_4 = 3.446 \tag{10}$$

give a function $C_a(j\omega)$ whose magnitude is "close" to being a Chebyshev approximation for the magnitude of $C(j\omega)$, (i.e. the error function $|\ |C_a(j\omega)| - |C(j\omega)|\ |$, shown in Figure 4, "nearly" satisfies the necessary and sufficient conditions for $|C_a(j\omega)|$ to be a Chebyshev approximation of $|C(j\omega)|$).
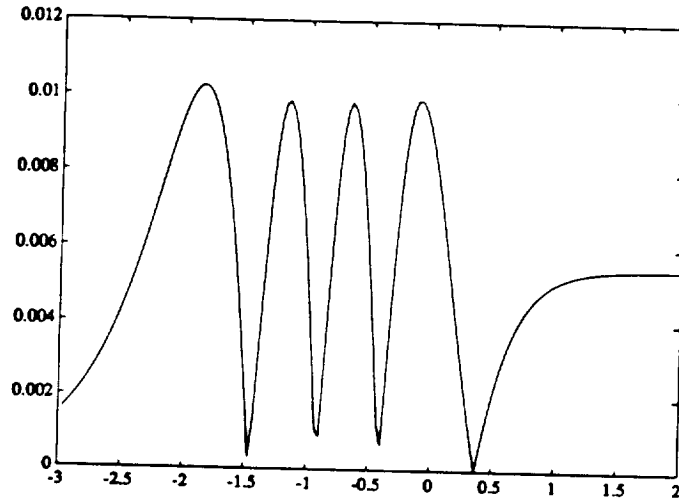
Figure 4: $\left|\ |C_a(j\omega)| - |C(j\omega)|\ \right|$ versus $\log(\omega)$

We have obtained the above values for τ_i's by slightly modifying the approximation scheme proposed in [11]. We would like to determine if this choice for C_a is a "good" L^∞ approximate of C. For this purpose we first point out the following relationship between the L^∞ error and the error in magnitude and phase functions:

Lemma: Let $\phi(\omega)$ and $\phi_a(\omega)$ denote the phase of $C(j\omega)$ and $C_a(j\omega)$ respectively, i.e.

$$C(j\omega) = |C(j\omega)|e^{j\phi(\omega)} \qquad C_a(j\omega) = |C_a(j\omega)|e^{j\phi_a(\omega)}.$$

Then we have

$$|C(j\omega) - C_a(j\omega)| \leq \left|\ |C(j\omega)| - |C_a(j\omega)|\ \right| + |C(j\omega)|\left|\phi(\omega) - \phi_a(\omega)\right|. \tag{11}$$

Proof: By definition following equalities hold

$$|C(j\omega) - C_a(j\omega)| = \left| |C(j\omega)|e^{j\phi(\omega)} - |C_a(j\omega)|e^{j\phi_a(\omega)} \right|$$

$$= \left| |C(j\omega)|e^{j(\phi(\omega)-\phi_a(\omega))} - |C(j\omega)| + |C(j\omega)| - |C_a(j\omega)| \right|$$

$$= \left| |C(j\omega)|(e^{j(\phi(\omega)-\phi_a(\omega))} - 1) + (|C(j\omega)| - |C_a(j\omega)|) \right|.$$

On the other hand, for any $\theta \in [-\pi, \pi]$ we have

$$|e^{j\theta} - 1| \leq |\theta|.$$

Hence we conclude that

$$|C(j\omega) - C_a(j\omega)| \leq \left| |C(j\omega)| - |C_a(j\omega)| \right| + |C(j\omega)| \left| \phi(\omega) - \phi_a(\omega) \right|. \quad \square$$

This lemma says that the Chebyshev approximation error[2] for the magnitude function plus the corresponding "normalized" phase error is an upper bound for the overall L^∞ error. We also deduce from this lemma that in order to get a good L^∞ error bound we may try to develop an approximation scheme such that whenever the magnitude error is large, the normalized phase error is small and vice versa. However, if we obtain C_a from the Chebyshev approximate of $|C(j\omega)|$, this automatically fixes the normalized phase error function, which does not necessarily satisfy the above mentioned nice property. However, we will see from the following numerical example that this property is satisfied for the second order approximation we have proposed by (10). For C_a determined from (10), the two terms in the right hand side of (11), as well as the function in the left hand side of (11), are shown in Figure 5. It is quite surprising that the normalized phase error function alternates with the magnitude error function,

---

[2]What we mean by Chebyshev approximation for the magnitude function is the following: Suppose $|C(j\omega)|$ is known, and we want to approximate the real valued function in the L^∞ norm by a function $|C_a(j\omega)|$; the problem is to find a real rational $C_a(s)$ (whose order is fixed) achieving the smallest Chebyshev error

$$\sup_\omega \left| |C(j\omega)| - |C_a(j\omega)| \right|.$$

In the text we use the term L^∞ approximation for the approximation of the complex valued function $C(j\omega)$, and we use the term Chebyshev approximation for the approximation of the real valued function $|C(j\omega)|$.

i.e. whenever the first term is large the second term is small and vice versa. Also interesting is the fact that for this choice of C_a the function $|C(j\omega) - C_a(j\omega)|$ is an envelope of the two functions appearing in the right hand side of (11).
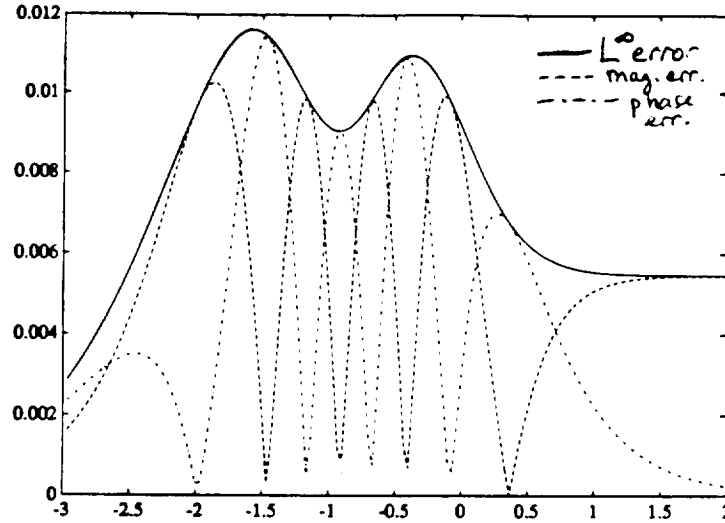
Figure 5: Relations between the L^∞ error function and the magnitude error and normalized phase error functions.

The above observations can be generalized as follows:

Conjecture:

Let $F(s) \in H^\infty$ be a minimum phase and positive real function (possibly irrational), and let $F_a(s) \in H^\infty$ be a fixed order real rational function approximating $F(s)$. If $|F_a(j\omega)|$ is the best Chebyshev approximation of $|F(j\omega)|$, then $F_a(s)$ is the best L^∞ approximate of $F(s)$. □

4 Active flutter suppression

Let us consider the thin airfoil model obtained in Section 2. When flutter occurs the plant $P(s)$ is unstable, and we would like to design a feedback controller stabilizing the closed loop system, shown in Figure 6. In our design we will use C_a given by the numerical values in (10). This gives us an approximate plant model P_a. A robustly

stabilizing finite dimensional controller $K_a(s)$ will be obtained from P_a, and it will be shown that under a certain condition, this controller stabilizes the original infinite dimensional airfoil model, with a certain robustness level.
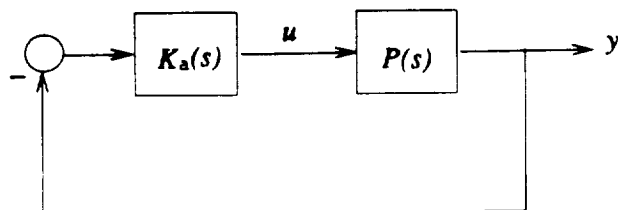
Figure 6: Feedback control system

Consider the approximate plant

$$P_a(s) = \frac{C_o(sI - A)^{-1}B_o}{1 - C_o(sI - A)^{-1}B_1\ C_a(s)}.$$

We can find rational transfer functions $N_1, N_2, M \in H^\infty$ such that

$$C_o(sI - A)^{-1}B_o = \frac{N_o(s)}{M(s)} \quad \text{and} \quad C_o(sI - A)^{-1}B_1 = \frac{N_1(s)}{M(s)}.$$

Therefore we can express P and P_a in the form

$$P_a(s) = \frac{N_o(s)}{M(s) - N_1(s)C_a(s)} \qquad P(s) = \frac{N_o(s)}{M(s) - N_1(s)C(s)}.$$

Thus, P and P_a differ in their denominator, in the sense that

$$P(s) = \frac{N_p(s)}{M_p(s)} \quad \text{and} \quad P_a(s) = \frac{N_p(s)}{M_{pa}(s)}$$

where $N_p(s) = N_o(s)$, $M_p(s) = M(s) - N_1(s)C(s)$, $M_{pa}(s) = M_p(s) + \Delta_M(s)$, and

$$\Delta_M(s) = N_1(s)(C(s) - C_a(s)).$$

188

Let ϵ_a be an upper bound of the L^∞ approximation error for the Theodorsen's function, i.e.

$$\|C - C_a\|_\infty < \epsilon_a,$$

(note that for the choice of C_a given by (10) we can choose $\epsilon_a = 0.012$). Then from [4], [5] and [12] we can deduce that a controller K_a stabilizing P_a and achieving an H^∞ performance

$$\gamma(K_a) = \|N_1 M_{pa}^{-1}(1 + P_a K_a)^{-1}\|_\infty \tag{12}$$

stabilizes the infinite dimensional plant P if[3]

$$\gamma(K_a) \leq \frac{1}{\epsilon_a}. \tag{13}$$

One proves this as follows: A controller K_a stabilizes all plants of the form $P_a = \frac{N_p}{M_{pa} - \Delta_M}$ if the roots of

$$1 + K_a(s)\frac{N_p(s)}{M_{pa}(s) - \Delta_M(s)} = 0$$

are in the left half plane. This condition is satisfied if

$$L_\Delta := 1 - \Delta_M M_{pa}^{-1}(1 + P_a K_a)^{-1}$$

is invertible in H^∞. Since $\|\Delta_M\|_\infty \leq \epsilon_a|N_1(j\omega)|$ and K_a stabilizes P_a (meaning that $(1 + P_a K_a)^{-1} \in H^\infty$), a sufficient condition for L_Δ to be invertible in H^∞ is (13).

In fact, if K_a stabilizes P_a and satisfies (13), then it stabilizes P with a certain robustness level, see e.g. [7]. The controller K_a^{opt}, which minimizes $\gamma(K_a)$ over all controllers stabilizing P_a, has the best chance of satisfying (13). Note also that we increase our chances of satisfying (13) by decreasing ϵ_a.

An interesting question about the stabilization of P by K_a is: How much can we increase ϵ_a so that

$$\gamma_a := \inf_{K_a \text{ stabilizing } P_a} \gamma(K_a) \leq \frac{1}{\epsilon_a} \quad ?$$

---

[3]We would like to point out that the perturbation in the plant is in the denominator only, so the term $\gamma(K_a)$ is slightly different than the one in [5] and [12], where both numerator and denominator perturbations are considered.

The answer to this question gives the largest L^∞ error we can tolerate in approximating $C(j\omega)$ so that we can still find an active feedback controller stabilizing the original plant. The problem of minimizing $\gamma(K_a)$ over all controllers K_a stabilizing P_a is a special case of a one block H^∞ optimal control problem, and can be solved easily by finding the singular values and vectors of a Hankel whose symbol is a rational function, or by using the Nevanlinna Pick interpolation, see e.g. [4] and references therein.

5 Concluding remarks

An active controller design method is illustrated for a thin airfoil. The model P for this system is infinite dimensional. By approximating the infinite dimensional part of the plant we have obtained a finite dimensional approximate model P_a. We have illustrated that using a Chebyshev approximation for the *magnitude* function $|C(j\omega)|$ we obtain a finite dimensional approximate of $C(j\omega)$ which is nearly optimal in the L^∞ norm.

A finite dimensional controller K_a^{opt} can be obtained by solving the one block H^∞ problem posed in Section 4. In the H^∞ problem formulation we used the finite dimensional approximate model P_a. We have shown that if the H^∞ optimal performance γ_a is less than the inverse of the L^∞ approximation error of the Theodorsen's function, ϵ_a, then the controller K_a stabilizes not only the finite dimensional model P_a, but also the original infinite dimensional model P.

References

[1] A. V. Balakrishnan, "Active control of airfoils in unsteady aerodynamics," *Applied Math. and Optimization*, **4** (1978), pp. 171–195.

[2] A. V. Balakrishnan and J. W. Edwards, "Calculation of the transient motion of elastic airfoils forced by control surface motion and gusts," NASA Technical Memorandum 81351, August 1980.

[3] R. L. Bisplinghoff, H. Ashley and R. Halfman, *Aeroelasticity*, Addison-Wesley, Cambridge, 1955.

[4] J. C. Doyle, B. A. Francis and A. R. Tannenbaum, *Feedback Control Theory*, Macmillan New York, 1992.

[5] T. T. Georgiou and M. C. Smith, "Optimal robustness in the gap metric," *IEEE Trans. Automat. Control*, **35** (1990), pp. 673–686.

[6] P. P. Khargonekar and M. A. Rotea, "Mixed H_2/H_∞ control: a convex optimization approach," *IEEE Transactions on Automatic Control*, **36** (1991), pp. 824–837.

[7] D. McFarlane, K. Glover and M. Vidyasagar, "Reduced order controller design using coprime factor model reduction," *IEEE Transactions on Automatic Control* **35** (1990), pp. 369–373.

[8] R. L. Moore, *Aeroservoelastic Stability Analysis of an Airplane with a Control Augmentation System*, PhD dissertation, The Ohio State University, 1978.

[9] R. H. Scanlan and R. Rosenbaum, *Introduction to the Study of Aircraft Vibration and Flutter*, Macmillan, New York, 1951.

[10] M. A. Snyder, *Chebyshev Methods in Numerical Approximation*, Prentice Hall, Englewood Cliffs NJ, 1966.

[11] Vajta, M., "New model reduction technique for a class of parabolic partial differential equations," *Proc. of the IEEE International Conf. on Systems Engineering*, Dayton OH, 1991, pp. 311–315.

[12] M. Vidyasagar and H. Kimura, "Robust controllers for uncertain linear multivariable systems," *Automatica*, **22** (1986), pp. 85–94.

PARAMETER ESTIMATION

ADAPTIVE MODEL REDUCTION FOR CONTINUOUS SYSTEMS
VIA RECURSIVE RATIONAL INTERPOLATION

John H. Lilly

Department of Electrical Engineering

Speed Scientific School

University of Louisville

Louisville, Kentucky 40292 USA

502-588-7518

SUMMARY

A method for adaptive identification of reduced-order models for continuous stable SISO and MIMO plants is presented. The method recursively finds a model whose transfer function (matrix) matches that of the plant on a set of frequencies chosen by the designer. The algorithm utilizes the *Moving Discrete Fourier Transform (MDFT)* to continuously monitor the frequency-domain profile of the system input and output signals. The MDFT is an efficient method of monitoring discrete points in the frequency domain of an evolving function of time. The model parameters are estimated from MDFT data using standard recursive parameter estimation techniques. The algorithm has been shown in simulations to be quite robust to additive noise in the inputs and outputs. A significant advantage of the method is that it enables a type of on-line model validation. This is accomplished by simultaneously identifying a number of models and comparing each with the plant in the frequency domain. Simulations of the method applied to an 8th-order SISO plant and a 10-state 2-input 2-output plant are presented. An example of on-line model validation applied to the SISO plant is also presented.

1. INTRODUCTION

This paper presents a new method of robust adaptive identification for stable continuous SISO and MIMO systems via *recursive rational interpolation*. Interpolation, unlike many identification schemes, is frequency-domain based. It attempts to find a model, frequently a reduced-order model (ROM), whose frequency response (matrix) matches that of the plant at certain frequencies. In this case, the model is said to interpolate the plant data at these frequencies. The goal, of course, is to find a model whose transfer matrix closely matches that of the plant at *all* frequencies.

The interpolation approach has been studied by several researchers (e.g. [1]-[4]). The method presented in this paper is most similar to [4]. In that reference, the problem is cast in the form of a system of simultaneous linear algebraic equations in which the unknowns are the plant parameters. We improve upon the method of [4], however, in that the present method is recursive and therefore much more robust to noise.

The algorithm presented in this paper monitors a number of points in the frequency profiles of the plant inputs and outputs via a recursive version of the Discrete Fourier Transform, which in this paper we call the *Moving Discrete Fourier Transform*, or *MDFT*. This transform has been discussed in [4] in conjunction with SISO model reduction. The transform was also used in another application in [5], where it was called a *frequency sampling filter*. The MDFT has the advantage that it is recursive and therefore gives the evolving DFT at every time step. It has the further advantage that it is not necessary to calculate the DFT at all N frequencies (for an N-point DFT), as is necessary for standard DFTs and FFTs, but only at those frequencies desired, which are usually far fewer than N in number. This makes the algorithm numerically efficient.

The paper is organized as follows. Section 2 briefly discusses the MDFT algorithm. Section 3 describes the SISO identification algorithm and gives a numerical example in which a 2nd-order model is derived for an 8th-order plant. Section 4 describes a method of on-line model validation made possible by the algorithm and gives a numerical example. Section 5 describes the MIMO extension of the algorithm and gives a numerical example in which a 6-state model is derived for a 10-state, 2-input, 2-output plant. This ROM is compared to several others for the same plant. Conclusions are given in Section 6.

196

2. THE MOVING DISCRETE FOURIER TRANSFORM (MDFT)

Let $\{x_i\}$, $i = 0, 1, 2, ..., N-1$ be a set of N consecutive samples of a continuous signal $x(t)$ sampled every Δt seconds. The well-known Discrete Fourier Transform (DFT) of $\{x_i\}$ is the set of complex numbers $\{X_k\}$, $k = 0, 1, 2, ..., N-1$ defined by ([6]):

$$X_k = \sum_{i=0}^{N-1} x_i W^{ki} , \quad k = 0, 1, 2, ..., N-1 \tag{2.1}$$

where $W = \exp(-j2\pi/N)$. Since there are N points in the calculation, this is called an N-point DFT. Under certain circumstances, the complex number X_k can be considered as a frequency component of $x(t)$ at the frequency $f_k = k/N\Delta t$ Hz. We will call the frequencies f_k *DFT frequencies*.

To make the process recursive, assume that a new sample of x becomes available, x_N. Our objective is to calculate a new DFT of x based on the *latest N* samples of x. That is, we will create a "moving" DFT by discarding the oldest sample, in this case x_0, and calculating the DFT of the new sequence $\{x_i\}$, $i = 1, 2, ..., N$. In general, we will be interested in calculating the DFT of the $(n+1)$th sequence of x, i.e. $\{x_{n-N+2}, ..., x_{n+1}\}$, recursively in terms of the DFT of the nth sequence of x, i.e. $\{x_{n-N+1}, ..., x_n\}$. If $X_k^{\{n\}}$ is the kth frequency component of the DFT of the nth sequence of x, then it can be shown (see [4]) that $X_k^{\{n+1\}}$ is expressed recursively in terms of $X_k^{\{n\}}$ as follows:

$$X_k^{\{n+1\}} = [X_k^{\{n\}} - x_{n-N+1} + x_{n+1}]W^{-k} \tag{2.2}$$

Equation (2.2) gives the algorithm for the 1-step-ahead MDFT. Note that the algorithm is very efficient because it involves only the addition of a real number to $X_k^{\{n\}}$ and multiplication by a complex constant W^{-k}. Referring to (2.2), note that $X_k^{\{n+1\}}$ depends only on $X_k^{\{n\}}$ and not on any other frequency component. This means that *it is only necessary to calculate the MDFT at those frequencies which are desired, not all N frequencies*, as is necessary in standard FFTs. This can result in significant savings in calculations since usually derivation of a reduced-order model (see Section 3) requires the DFT at a relatively small number of frequencies, whereas N is usually large.

3. RECURSIVE SISO REDUCED-ORDER MODELING

Assume that a kth-order model for a given stable plant is desired. Then, the model can be described by a kth-order differential equation of the form:

$$\alpha(D)y(t) = \beta(D)u(t) \tag{3.1}$$

where $\alpha(D)$ is a kth-order monic Hurwitz polynomial in the differential operator $D = d/dt$, and $\beta(D)$ is a polynomial of order $k-1$ or less. That is,

$$\alpha(D) = D^k + \sum_{i=0}^{k-1} \alpha_i D^i \tag{3.2}$$

$$\beta(D) = \sum_{i=0}^{k-1} \beta_i D^i \tag{3.3}$$

Equation (3.1) can be rewritten in the form:

$$D^k y = -\alpha_{k-1}D^{k-1}y - \ldots - \alpha_0 y + \beta_{k-1}D^{k-1}u + \ldots + \beta_0 u \tag{3.4}$$

which can be rewritten as

$$Y(t) = \psi^{\mathrm{T}} Z(t) \tag{3.5}$$

where

$$Y(t) = D^k y \tag{3.6}$$

$$\psi^{\mathrm{T}} = \begin{bmatrix} -\alpha_{k-1}, \ldots, -\alpha_0, \beta_{k-1}, \ldots, \beta_0 \end{bmatrix} \tag{3.7}$$

$$Z(t) = \begin{bmatrix} D^{k-1}y, \ldots, y, D^{k-1}u, \ldots, u \end{bmatrix}^{\mathrm{T}} \tag{3.8}$$

We now discuss a way by which the signals u, y, and all necessary derivatives of u and y in (3.5) may be parameterized using MDFT data. It is well-known that the DFT, hence the MDFT, gives an *exact parameterization* of a signal if the signal is sinusoidal and its frequency is exactly equal to one of the DFT frequencies. Specifically, it can be shown that, if n is an integer between 0 and $N/2$,

$$\text{DFT}\left[A\sin\left(\tfrac{2\pi n}{N\Delta t}t + \theta\right)\right] = Me^{j\phi} = \tfrac{AN}{2}\exp\left[j\left(\theta - \tfrac{\pi}{2}\right)\right] \qquad (3.9)$$

at the frequency $\omega_n = 2\pi n/N\Delta t$ radians/sec, and is zero at all other frequencies. In (3.9), A, θ, M, ϕ, N, and Δt are constants, with N and Δt defined as in Section 2. That is, for the sinusoidal signal defined in (3.9), the magnitude of the time-domain signal is given exactly by $2/N$ times the magnitude of the DFT, and the phase angle of the time-domain signal is given exactly by $\pi/2$ plus the angle of the DFT. Therefore, if the plant inputs are bandlimited and contain sinusoidal components at only the DFT frequencies, $u(t)$ and $y(t)$ can be exactly parameterized in terms of MDFT data.

For the ideal case assume $u(t)$ is of the form

$$u(t) = \sum_{n=1}^{N/2} U_n \sin\left(\omega_n t + \alpha_n\right) \qquad (3.10)$$

where $\omega_n = 2\pi n/N\Delta t$ and U_n, α_n are constants. As stated in Section 2, the frequencies ω_n are the DFT frequencies. Note that, if N is large, $u(t)$ can consist of a large number of sinusoidal components. Assuming steady-state has been reached, the plant output corresponding to (3.10) is

$$y(t) = \sum_{n=1}^{N/2} Y_n \sin\left(\omega_n t + \beta_n\right) \qquad (3.11)$$

where Y_n, β_n are constants.

Choose any desired set of k distinct DFT frequencies $\{\omega_{I1}, \omega_{I2}, ..., \omega_{Ik}\}$. We call these the *identification frequencies*. Taking MDFTs of $u(t)$ and $y(t)$ at the identification frequencies and utilizing the appropriate magnitude and phase information can be shown to yield the following parameterizations for u, y, Du, and Dy [4]:

$$u \doteq U_{I1}\sin(\alpha_{I1}) + U_{I2}\sin(\alpha_{I2}) + \ldots + U_{Ik}\sin(\alpha_{Ik}) \qquad (3.12)$$

$$y \doteq Y_{I1}\sin(\beta_{I1}) + Y_{I2}\sin(\beta_{I2}) + \ldots + Y_{Ik}\sin(\beta_{Ik}) \qquad (3.13)$$

$$Du \doteq \omega_{I1}U_{I1}\cos(\alpha_{I1}) + \omega_{I2}U_{I2}\cos(\alpha_{I2}) + \ldots + \omega_{Ik}U_{Ik}\cos(\alpha_{Ik}) \qquad (3.14)$$

$$Dy \doteq \omega_{I1}Y_{I1}\cos(\beta_{I1}) + \omega_{I2}Y_{I2}\cos(\beta_{I2}) + \ldots + \omega_{Ik}Y_{Ik}\cos(\beta_{Ik}) \qquad (3.15)$$

where U_{Ij}, α_{Ij} are the magnitude and phase of the sinusoidal component in $u(t)$ at identification frequency ω_{Ij}, and Y_{Ij}, β_{Ij} are the magnitude and phase of the sinusoidal component in $y(t)$ at identification frequency ω_{Ij}. These magnitudes and phases are derived from the MDFT as explained above. All higher derivatives of $u(t)$ and $y(t)$ may be parameterized in a like manner (see [4]). In this way, all entries in the vectors $Y(t)$ and $Z(t)$ in (3.5) can be parameterized with *constants* at every time step via the MDFT. Therefore, the parameters ψ can be estimated from (3.5) using standard parameter estimation techniques.

Incidentally, note that, although parameterizations for derivatives of u and y are obtained, *no derivatives of the signals are actually taken*. Noise in the signals introduces errors in $Y(t)$ and $Z(t)$, but at worst the errors remain in the same proportion to the signal magnitude with higher derivatives and do not increase in size relative to signal magnitude, as they would if noisy signals were differentiated.

Example

Consider the following 8th-order plant [4]:

$$G_P(s) = -\frac{3}{s+1} + \frac{4}{s+2} - \frac{6}{s+3} + \frac{8}{s+4} + \frac{5}{s+5} - \frac{12}{s+6} + \frac{14}{s+7} + \frac{8}{s+8} \tag{3.16}$$

The plant input $u(t)$ is chosen to be a 0.01 Hz, ± 10 V square wave with an additive noise component which is uniformly distributed between ± 10 V. For the MDFT, we choose $N = 5000$ and $\Delta t = 0.02$. The identification frequencies are then chosen to be 0.01 Hz, 0.03 Hz, and 0.11 Hz, which correspond to DFT frequencies and are present in $u(t)$.

Figure 1 shows parameter estimates for a 2nd-order model found using the recursive rational interpolation method described above and applying the recursive least squares algorithm to find the parameters from (3.5). The model has the form

$$G_R(s) = \frac{c_1 s + c_0}{s^2 + a_1 s + a_0} \tag{3.17}$$

where, from Figure 1, $c_1 = 15.021$, $c_0 = 4.798$, $a_1 = 5.958$, $a_0 = 4.795$.

A comparison of $G_P(s)$ and $G_R(s)$ is shown in Figure 2. There is good agreement at all frequencies. *It should be noted that $u(t)$ is not bandlimited, as specified in (3.10) for ideal inputs, and the noise level in $u(t)$ is comparable to the*

200

magnitude of u(t) itself. This indicates that the algorithm is robust to nonideal conditions.

4. ON-LINE MODEL VALIDATION

It is generally not automatically known whether or not an identified model is good, in the sense that its frequency response closely matches that of the plant over a range of frequencies. This usually necessitates a *model validation* stage following the identification of a candidate model by any method.

It has been found in practice that the identification frequencies for interpolation-based schemes must be chosen with care in order for the algorithm to find a good model. Obviously, choosing correct identification frequencies is difficult if the plant is unknown. This indicates the need for some type of model validation before a model identified by this method can be used with confidence.

The identification algorithm presented in the previous section has the built-in capability for *on-line* model validation due to the fact that frequency-domain plant data are available via the MDFT. Thus, the algorithm may be given a measure of "intelligence" by increasing the number of identification frequencies and *simultaneously* deriving several models using different combinations of identification frequencies. The frequency response of each model can then be compared with the plant at *all* identification frequencies. The model with the least overall fit error can be taken as the best model for the plant of those derived.

Example

Let us consider this strategy applied to the example of Section 3, i.e., we attempt to find a 2nd-order model for the 8th-order plant (3.16). Since we are unsure which identification frequencies to use for the identification, we specify a set of frequencies which span the system passband, e.g., choose $[\omega_{I1}, \omega_{I2}, \omega_{I3}, \omega_{I4}, \omega_{I5}, \omega_{I6}] = 2\pi[0.001, 0.01, 0.1, 1.0, 10.0, 100.0]$. Of course, this necessitates an input which is different from the square wave used in the previous example. It can be, for instance, a sum of six sinusoids for this example. A model is derived using each distinct pair of frequencies, i.e., we derive a model using $(\omega_{I1}, \omega_{I2})$ as the identification frequencies, another model using $(\omega_{I1}, \omega_{I3})$, etc. In all, 15 different models can be derived taking the above identification frequencies two at a time. *It*

is important to remember that the 15 models are derived simultaneously.

If we take as an error measurement the *distance* between the plant and model responses in magnitude and phase summed over all identification frequencies, we get a *figure of merit* for each model. Note that these distances are easily calculated because plant magnitude and phase data at the identification frequencies are available via the MDFT. To illustrate, let us take the following as the fit error:

$$\text{Error} = \sum_{i=1}^{6} \Big\{ \, | \, 20 \log_{10}(\text{mag}(G_P(j\omega_{Ii}))) - 20 \log_{10}(\text{mag}(G_R(j\omega_{Ii}))) \, | $$

$$+ \, | \arg(G_P(j\omega_{Ii})) - \arg(G_R(j\omega_{Ii})) \, | \Big\} \tag{4.1}$$

where $| \cdot |$ stands for absolute value, mag stands for magnitude, and arg stands for argument in degrees. *Of course, this definition of fit error is completely arbitrary.* Whatever the error criterion, however, it must give *a single number* which quantifies the fit error between the plant and model *and be capable of being quickly calculated.*

The model which yields the lowest error can be taken as the best model of those derived. For the present example, we get the following errors corresponding to the above-defined identification frequencies and error criterion:

I.D. Freq.	Error	I.D. Freq.	Error	I.D. Freq.	Error
$(\omega_{I1}, \omega_{I2})$	15.585	$(\omega_{I2}, \omega_{I3})$	14.394	$(\omega_{I3}, \omega_{I5})$	10.164
$(\omega_{I1}, \omega_{I3})$	14.405	$(\omega_{I2}, \omega_{I4})$	3.6617	$(\omega_{I3}, \omega_{I6})$	10.242
$(\omega_{I1}, \omega_{I4})$	3.6938	$(\omega_{I2}, \omega_{I5})$	4.2390	$(\omega_{I4}, \omega_{I5})$	81.438
$(\omega_{I1}, \omega_{I5})$	4.2825	$(\omega_{I2}, \omega_{I6})$	4.2805	$(\omega_{I4}, \omega_{I6})$	81.370
$(\omega_{I1}, \omega_{I6})$	4.3242	$(\omega_{I3}, \omega_{I4})$	7.5107	$(\omega_{I5}, \omega_{I6})$	78.089

Obviously, the model derived using the frequency pair $(\omega_{I2}, \omega_{I4})$, or ROM #7, yields the lowest error and therefore the best fit. This model is given by (3.17) with $c_1 = 17.392$, $c_0 = 5.315$, $a_1 = 7.334$, $a_0 = 5.320$. A comparison of this model with the plant is given in Figure 3. Notice that this model is better than the one derived in Section 3, since we have "optimized" the identification frequencies via on-line model validation.

If no model can be found whose fit error is sufficiently small, the model order can be easily increased. This amounts to changing the number of entries in $Z(t)$ and correspondingly in ψ. *Note that this can be done without changing the inputs or the identification frequencies.* The order of the calculation (3.5) is simply incremented in the algorithm in real time.

Finally, since the input and output MDFTs are monitored in this method, it is possible to make decisions on how fast to update the model parameters or whether to update them at all. If the MDFTs are not changing and a suitable model has been determined, the parameter estimation part of the algorithm can be shut off. In this case, only the MDFTs would proceed as the plant signals evolve. Thus, the monitoring of the plant continues, but the parameter estimation part of the algorithm rests if there is no need for a parameter update.

5. AN EXTENSION TO MIMO SYSTEMS

The above scheme for SISO identification via recursive rational interpolation can be extended to MIMO plants as follows. Assume the plant has input vector $u(t) = [u_1, u_2, ..., u_q]^T$ and output vector $y(t) = [y_1, y_2, ..., y_p]^T$. The MIMO identification process finds constant matrices $P_i \sim (p \times p)$ and $Q_i \sim (p \times q)$, $i = 0, 1, ..., m-1$ such that the model transfer matrix given by

$$T(s) = P^{-1}(s)Q(s) \tag{5.1}$$

where

$$P(D) = D^m I + \sum_{i=0}^{m-1} P_i D^i \tag{5.2}$$

$$Q(D) = \sum_{i=0}^{m-1} Q_i D^i \tag{5.3}$$

matches the plant transfer matrix on a given set of frequencies.

The model can be described by the matrix differential equation

$$P(D)y(t) = Q(D)u(t) \tag{5.4}$$

which can be rewritten in the form:

$$D^m y = -P_{m-1} D^{m-1} y - \ldots - P_0 y + Q_{m-1} D^{m-1} u + \ldots + Q_0 u \qquad (5.5)$$

This can be put in a form analogous to (3.5):

$$Y(t) = \Psi^T Z(t) \qquad (5.6)$$

where now

$$Y(t) = D^m y \qquad (5.7)$$

$$\Psi^T = \begin{bmatrix} -P_{m-1}, & \ldots, & -P_0, & Q_{m-1}, & \ldots, & Q_0 \end{bmatrix} \qquad (5.8)$$

and

$$Z(t) = \begin{bmatrix} D^{m-1} y^T, & \ldots, & y^T, & D^{m-1} u^T, & \ldots, & u^T \end{bmatrix}^T \qquad (5.9)$$

Note that $Y(t) \sim p \times 1$, $\Psi^T \sim p \times m(p+q)$, and $Z(t) \sim m(p+q) \times 1$.

Again, choose any set of k distinct DFT frequencies $\{\omega_{I1}, \omega_{I2}, \ldots, \omega_{Ik}\}$. Denote the set of identification frequencies as $S = \{\omega_{I1}, \omega_{I2}, \ldots, \omega_{Ik}\}$. Choose integers $l_i > 0$, $i = 1, \ldots, q$ such that

$$\sum_{i=1}^{q} l_i = k \qquad (5.10)$$

Let S_i, $i = 1, 2, \ldots, q$ be subsets of S such that S_i contains l_i elements and $S_i \cap S_j = 0$, $i \neq j$. Now the input $u_i(t)$ is specified as containing frequency components at the frequencies contained in S_i. The input u_i may contain any other frequency components also, with the exception that the frequency components of S_i must be unique to u_i.

Again, MDFTs are taken of $u(t)$ and $y(t)$ at the appropriate identification frequencies. Note that, in the MIMO case, MDFTs are taken of the input $u_i(t)$ at only the identification frequencies contained is S_i, but the MDFTs of the output $y_i(t)$ must be taken at *all* identification frequencies.

As in the SISO case, the quantities in $Y(t)$ and $Z(t)$ in (5.6) are parameterized from MDFT data at each time instant. Therefore, standard parameter estimation techniques may be employed to solve for the parameter matrix Ψ in (5.6). The minimum number of identification frequencies necessary for unique identification and

the minimum number of identification frequencies per input are topics of current research.

Example

As a numerical example, the 10-state, 2-input, 2-output plant TGEN given in [7] is considered. This is a linearized model of a large turbo-generator. The original nonlinear model is given in [8]. The A, B, and C matrices for the state-space representation of the linearized model are given in [9]. The corresponding plant transfer matrix is given by

$$G_P(s) = \begin{bmatrix} G_{P11}(s) & G_{P12}(s) \\ G_{P21}(s) & G_{P22}(s) \end{bmatrix} \tag{5.11}$$

$G_P(s)$ is given in the Appendix.

A 6-state model with observability indices equal to 3 is chosen for this system. Thus, for this example, $p=2$, $q=2$, $m=3$, and k is chosen as 6. The identification frequencies are chosen as $[\omega_{I1}, \omega_{I2}, \omega_{I3}, \omega_{I4}, \omega_{I5}, \omega_{I6}]=2\pi[0.01, 0.1, 0.2, 0.5, 1.0, 2.0]$. The plant inputs are specified as:

$$u_1(t) = \sum_{i=1}^{3} \sin\omega_{I_i} t \tag{5.12a}$$

$$u_2(t) = \sum_{i=4}^{6} \sin\omega_{I_i} t \tag{5.12b}$$

The model transfer matrix identified for this system using rational interpolation, $G_R(s)$, is given in the Appendix. Also considered for comparison are a 6-state model for this plant given in [9] (denoted as G_M), and a 6-state model derived from a balanced realization of the plant (denoted as G_B). These models are also given in the Appendix. Figures 4 - 7 show comparisons of the magnitude and phase characteristics of G_P with those of G_R, G_M, and G_B.

To get a numerical measure of the closeness of the models to the plant, the plant magnitude and phase responses are compared with those of the various models at 100 frequencies logarithmically spaced between 10^{-3} and 10^1 cycles/sec. That is, the following fit error is calculated:

$$E_X = \sum_{i=1}^{2} \sum_{j=1}^{2} \sum_{n=1}^{100} \left\{ \, | \, 20 \log_{10}(\text{mag}(G_{P_{ij}}(j\omega_n))) - 20 \log_{10}(\text{mag}(G_{X_{ij}}(j\omega_n))) \, | \right.$$

$$\left. + \, | \arg(G_{P_{ij}}(j\omega_n)) - \arg(G_{X_{ij}}(j\omega_n)) | \, \right\} \tag{5.13}$$

where $X = R$, M, and B, and $\omega_n = 2\pi \times 10^{-3+4(n-1)/99}$. This measure is, of course, completely arbitrary. However, it is one that is easily and accurately calculated and measures ROM fit in the frequency range 10^{-3} - 10^1 cycles/sec, which is the critical range for this plant. Note that this calculation has nothing to do with on-line model validation (Section 4), but is being done simply to compare the goodness of the various ROMs. The resulting fit errors are calculated to be $E_R = 3.0157 \times 10^3$, $E_M = 2.4135 \times 10^4$, and $E_B = 9.4244 \times 10^3$. Although G_R has the lowest error, it should be kept in mind that G_R is designed specifically to match the plant in the frequency range 10^{-3} - 10^1 cycles/sec.

6. CONCLUSIONS

A method of adaptively identifying reduced-order models for SISO and MIMO plants has been presented. The method is based on matching the plant and model transfer matrices at a number of frequencies chosen by the designer. The method recursively monitors frequency components in the plant inputs and outputs via the Moving Discrete Fourier Transform (MDFT). This is a computationally efficient method of recursively calculating the DFT of an evolving function of time. The identification algorithm has the capability for on-line model validation.

There is no necessity in this method for the plant input and output signals to be purely sinusoidal because the MDFT filters out sinusoidal components in these signals. As always, better results are obtained if the system, whatever its order, has a good reduced-order model. Computer simulations indicate that the algorithm is robust to additive input and output noise and non-bandlimited inputs.

Areas of current research include error analysis of the algorithm for nonideal inputs and stochastic disturbances, and determination of meaningful on-line figures of merit for identified models.

REFERENCES

[1] H. Elliott and W. A. Wolovich, "A Frequency Domain Model Reduction Procedure," *Automatica,* Vol. 16, pp. 167-178, March 1980.

[2] B. D. O. Anderson and A. C. Antoulas, "Rational Interpolation and State-Variable Realizations," *Linear Algebra and Its Applications,* Vol. 137/138, pp. 479-509, 1990.

[3] R. Kumaresan, "Identification of Rational Transfer Functions from Frequency Samples," *IEEE Trans. on Aerospace and Electronic Systems,* Vol. 26, No. 6, pp. 925-934, November, 1990.

[4] J. H. Lilly, "Efficient DFT-Based Model Reduction for Continuous Systems," *IEEE Trans. Automatic Control,* Vol. 36, No. 10, pp. 1188-1193, October, 1991.

[5] R. R. Bitmead and B. D. O. Anderson, "Adaptive Frequency Sampling Filters," *IEEE Trans. Circuits and Systems,* Vol. CAS-28, No. 6, pp. 524-534, June 1981.

[6] R. E. Ziemer, W. H. Tranter, and D. R. Fannin, *Signals and Systems Continuous and Discrete,* 2nd Ed., MacMillan, New York, 1989.

[7] Y. S. Hung and A. G. J. MacFarlane, *Multivariable Feedback: A Quasi-Classical Approach,* Springer-Verlag, New York, 1982.

[8] D. J. N. Limebeer, R. G. Harley, and S. M. Schuck, "Subsynchronous Resonance of the Koeberg Turbo-Generators and of a Laboratory System, *Transactions of the South African Institute of Electrical Engineers,* Vol. 70, pp. 278-297, 1979.

[9] J. M. Maciejowski, *Multivariable Feedback Design,* Addison Wesley, New York, 1989.

APPENDIX

The plant transfer matrix is given by (5.11) with

$$G_{P11}(s) = \frac{b_7 s^7 + b_6 s^6 + \ldots + b_0}{\Delta_P}$$

with $b_7 = -4.6075 \times 10^1$, $b_6 = -4.5705 \times 10^3$, $b_5 = -4.7153 \times 10^6$, $b_4 = -1.8619 \times 10^8$, $b_3 = -2.4976 \times 10^9$, $b_2 = -1.2507 \times 10^{10}$, $b_1 = -1.5146 \times 10^{10}$, $b_0 = -3.9506 \times 10^9$,

$$G_{P12}(s) = \frac{b_6 s^6 + b_5 s^5 + \ldots + b_0}{\Delta_P}$$

with $b_6 = -2.0048 \times 10^4$, $b_5 = -1.7916 \times 10^6$, $b_4 = -2.3909 \times 10^9$, $b_3 = -1.1727 \times 10^{11}$, $b_2 = -1.2373 \times 10^{12}$, $b_1 = -2.8374 \times 10^{12}$, $b_0 = -1.8166 \times 10^{12}$,

$$G_{P21}(s) = \frac{b_7 s^7 + b_6 s^6 + \ldots + b_0}{\Delta_P}$$

with $b_7 = -1.1590 \times 10^0$, $b_6 = -6.9327 \times 10^1$, $b_5 = 5.6807 \times 10^5$, $b_4 = 2.3299 \times 10^7$, $b_3 = 2.9400 \times 10^8$, $b_2 = 1.3118 \times 10^9$, $b_1 = 1.4696 \times 10^9$, $b_0 = 1.3869 \times 10^9$, and

$$G_{P22}(s) = \frac{b_8 s^8 + b_7 s^7 + \ldots + b_0}{\Delta_P}$$

with $b_8 = 8.1715 \times 10^2$, $b_7 = 6.5386 \times 10^4$, $b_6 = 7.9770 \times 10^7$, $b_5 = 3.9454 \times 10^9$, $b_4 = 4.6442 \times 10^{10}$, $b_3 = 2.8534 \times 10^{11}$, $b_2 = 1.8656 \times 10^{12}$, $b_1 = 3.7379 \times 10^{12}$, $b_0 = 2.0592 \times 10^{12}$.

In the above, $\Delta_P = s^{10} + a_9 s^9 + \ldots + a_0$ with $a_9 = 1.0098 \times 10^2$, $a_8 = 1.0256 \times 10^5$, $a_7 = 4.2252 \times 10^6$, $a_6 = 6.5835 \times 10^7$, $a_5 = 5.4549 \times 10^8$, $a_4 = 3.2781 \times 10^9$, $a_3 = 1.4535 \times 10^{10}$, $a_2 = 2.7412 \times 10^{10}$, $a_1 = 1.8901 \times 10^{10}$, $a_0 = 3.1027 \times 10^9$.

The ROM transfer matrix $G_R(s)$ is given by

$$G_{R11}(s) = \frac{b_5 s^5 + b_4 s^4 + \ldots + b_0}{\Delta_R}$$

with $b_5 = -7.7158 \times 10^{-3}$, $b_4 = 7.6781 \times 10^{-2}$, $b_3 = -4.6515 \times 10^1$, $b_2 = -4.3011 \times 10^2$, $b_1 = -5.8884 \times 10^2$, $b_0 = -1.5861 \times 10^2$,

$$G_{R12}(s) = \frac{b_5 s^5 + b_4 s^4 + \ldots + b_0}{\Delta_R}$$

with $b_5 = 3.9934 \times 10^0$, $b_4 = -2.6408 \times 10^0$, $b_3 = 1.1580 \times 10^3$, $b_2 = -3.6478 \times 10^4$, $b_1 = -9.6222 \times 10^4$, $b_0 = -6.4423 \times 10^4$,

$$G_{R21}(s) = \frac{b_5 s^5 + b_4 s^4 + \ldots + b_0}{\Delta_R}$$

with $b_5 = -5.9553 \times 10^{-3}$, $b_4 = 3.2304 \times 10^{-2}$, $b_3 = 6.0336 \times 10^0$, $b_2 = 4.6175 \times 10^1$, $b_1 = 5.2247 \times 10^1$, $b_0 = 5.5681 \times 10^1$, and

$$G_{R22}(s) = \frac{b_5 s^5 + b_4 s^4 + \ldots + b_0}{\Delta_R}$$

with $b_5 = -1.6462 \times 10^1$, $b_4 = 1.1952 \times 10^3$, $b_3 = 3.1988 \times 10^3$, $b_2 = 5.7420 \times 10^4$, $b_1 = 1.3469 \times 10^5$, $b_0 = 7.4649 \times 10^4$.

In the above, $\Delta_R = s^6 + a_5 s^5 + \ldots + a_0$ with $a_5 = 1.1105 \times 10^1$, $a_4 = 7.2366 \times 10^1$, $a_3 = 4.5892 \times 10^2$, $a_2 = 1.0098 \times 10^3$, $a_1 = 7.4376 \times 10^2$, $a_0 = 1.2457 \times 10^2$.

The ROM transfer matrix $G_M(s)$ is given by

$$G_{M11}(s) = \frac{b_5 s^5 + b_4 s^4 + \ldots + b_0}{\Delta_M}$$

with $b_5 = 4.8290 \times 10^{-2}$, $b_4 = 1.8757 \times 10^0$, $b_3 = 1.9494 \times 10^0$, $b_2 = -1.2283 \times 10^3$, $b_1 = -5.7616 \times 10^3$, $b_0 = -2.3848 \times 10^3$,

$$G_{M12}(s) = \frac{b_5 s^5 + b_4 s^4 + \ldots + b_0}{\Delta_M}$$

with $b_5 = 2.9153 \times 10^{-2}$, $b_4 = 1.2889 \times 10^0$, $b_3 = -3.0414 \times 10^{-1}$, $b_2 = -2.3880 \times 10^4$, $b_1 = -8.2902 \times 10^5$, $b_0 = -9.5445 \times 10^5$,

$$G_{M21}(s) = \frac{b_5 s^5 + b_4 s^4 + \ldots + b_0}{\Delta_M}$$

with $b_5 = -4.9194 \times 10^{-1}$, $b_4 = 9.4826 \times 10^0$, $b_3 = -4.9046 \times 10^1$, $b_2 = 5.5164 \times 10^2$, $b_1 = -9.3964 \times 10^2$, $b_0 = 9.0758 \times 10^2$, and

$$G_{M22}(s) = \frac{b_5 s^5 + b_4 s^4 + \ldots + b_0}{\Delta_M}$$

with $b_5 = -6.7159 \times 10^{-1}$, $b_4 = 8.0447 \times 10^2$, $b_3 = 2.7814 \times 10^4$, $b_2 = 8.0852 \times 10^4$, $b_1 = 1.2135 \times 10^6$, $b_0 = 1.0820 \times 10^6$.

In the above, $\Delta_M = s^6 + a_5 s^5 + \ldots + a_0$ with $a_5 = 2.8238 \times 10^1$, $a_4 = 2.5831 \times 10^2$, $a_3 = 1.4679 \times 10^3$, $a_2 = 8.2145 \times 10^3$, $a_1 = 8.8012 \times 10^3$, $a_0 = 1.6306 \times 10^3$.

The ROM transfer matrix $G_B(s)$ is given by

$$G_{B11}(s) = \frac{b_6 s^6 + b_5 s^5 + \ldots + b_0}{\Delta_B}$$

with $b_6 = -1.9102 \times 10^{-2}$, $b_5 = -6.0759 \times 10^{-1}$, $b_4 = -1.4699 \times 10^1$, $b_3 = -4.5056 \times 10^1$, $b_2 = -1.4480 \times 10^3$, $b_1 = -3.5314 \times 10^3$, $b_0 = -1.1386 \times 10^3$,

$$G_{B12}(s) = \frac{b_6 s^6 + b_5 s^5 + \ldots + b_0}{\Delta_B}$$

with $b_6 = -1.8202 \times 10^{-2}$, $b_5 = -4.3626 \times 10^{-3}$, $b_4 = -5.6174 \times 10^0$, $b_3 = 3.0908 \times 10^2$, $b_2 = -3.1770 \times 10^4$, $b_1 = -4.7812 \times 10^5$, $b_0 = -5.2357 \times 10^5$,

$$G_{B21}(s) = \frac{b_6 s^6 + b_5 s^5 + \ldots + b_0}{\Delta_B}$$

with $b_6 = 1.5093 \times 10^{-1}$, $b_5 = -2.9259 \times 10^0$, $b_4 = 1.6680 \times 10^1$, $b_3 = -1.1690 \times 10^2$, $b_2 = 6.2777 \times 10^2$, $b_1 = 1.0947 \times 10^2$, $b_0 = 3.9972 \times 10^2$, and

$$G_{B22}(s) = \frac{b_6 s^6 + b_5 s^5 + \ldots + b_0}{\Delta_B}$$

with $b_6 = 1.6164 \times 10^{-1}$, $b_5 = -9.4448 \times 10^0$, $b_4 = 1.0597 \times 10^3$, $b_3 = 1.5933 \times 10^4$, $b_2 = 7.2009 \times 10^4$, $b_1 = 6.9226 \times 10^5$, $b_0 = 5.9350 \times 10^5$.

In the above, $\Delta_B = s^6 + a_5 s^5 + \ldots + a_0$ with $a_5 = 2.0310 \times 10^1$, $a_4 = 1.6829 \times 10^2$, $a_3 = 9.9166 \times 10^2$, $a_2 = 4.7178 \times 10^3$, $a_1 = 4.8675 \times 10^3$, $a_0 = 8.9425 \times 10^2$.
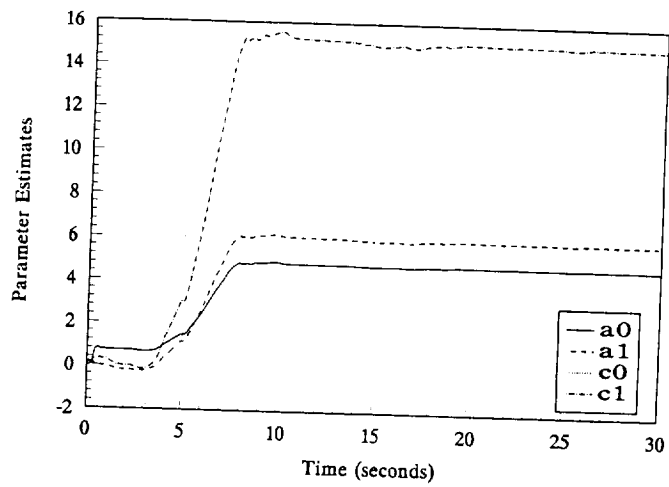
Figure 1 - Parameter estimates via recursive interpolation, ID frequencies = 0.01 Hz, 0.03 Hz, and 0.11 Hz. (a0 and c0 approximately coincide)
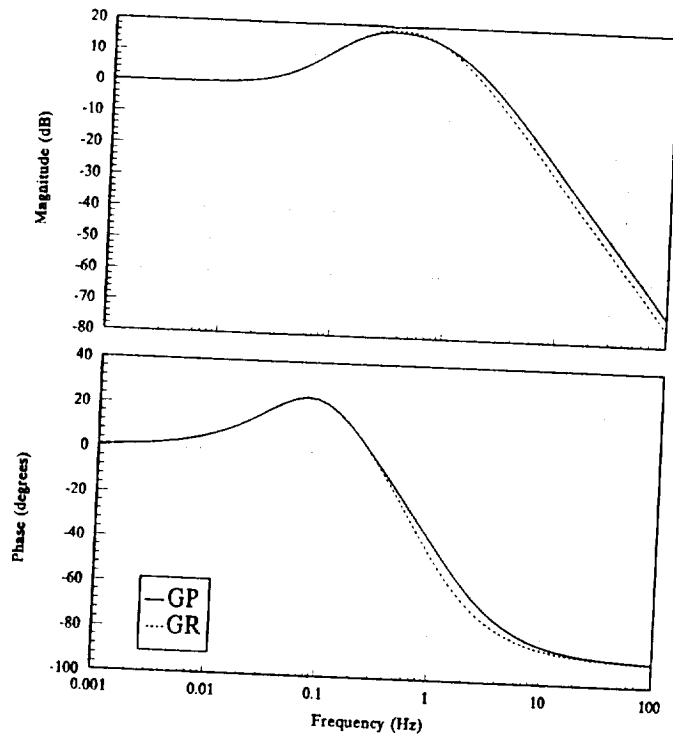

Figure 2 - Comparison of 8th-order plant (GP) with 2nd-order model (GR) derived via recursive interpolation, ID frequencies = 0.01 Hz, 0.03 Hz, and 0.11 Hz

211
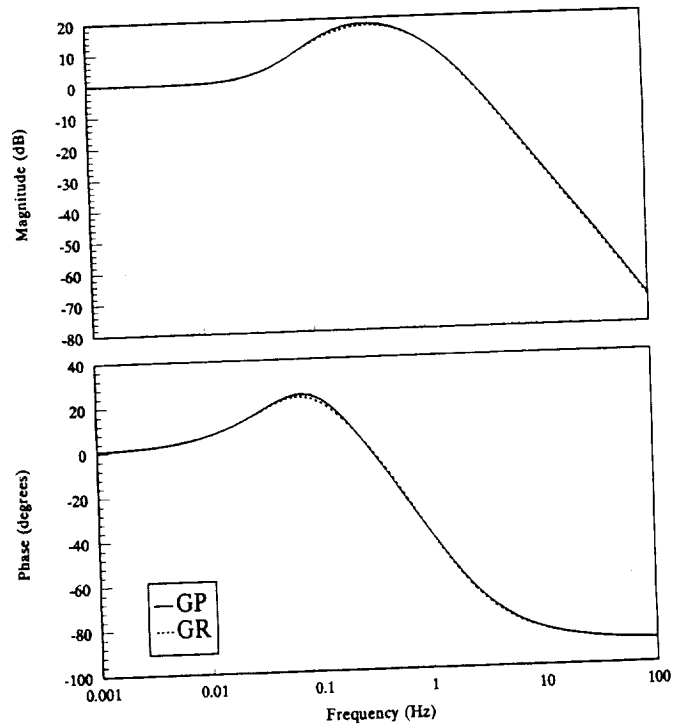
Figure 3 - Comparison of 8th-order plant (GP) with
ROM #7 (GR), derived via recursive interpolation with
on-line model validation

Figure 4 - Comparison of (1,1) elements of plant and
model transfer matrices

Figure 5 - Comparison of (1,2) elements of plant and
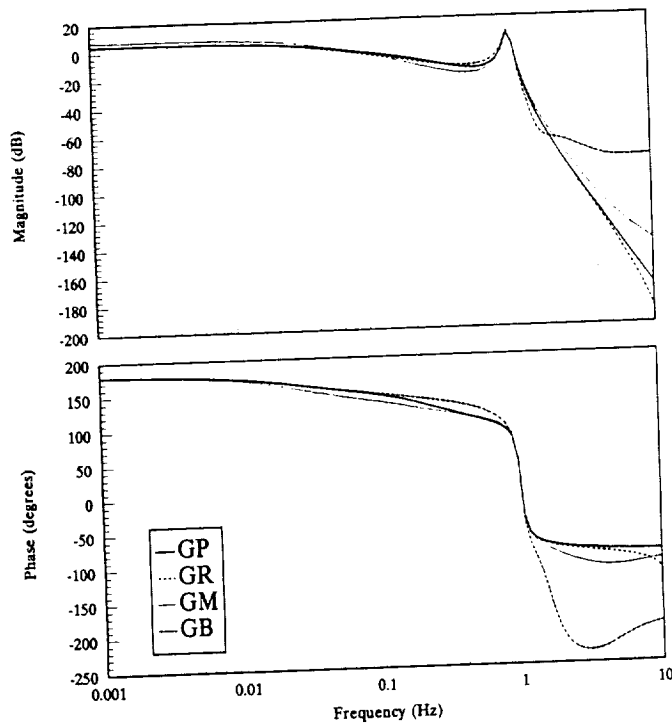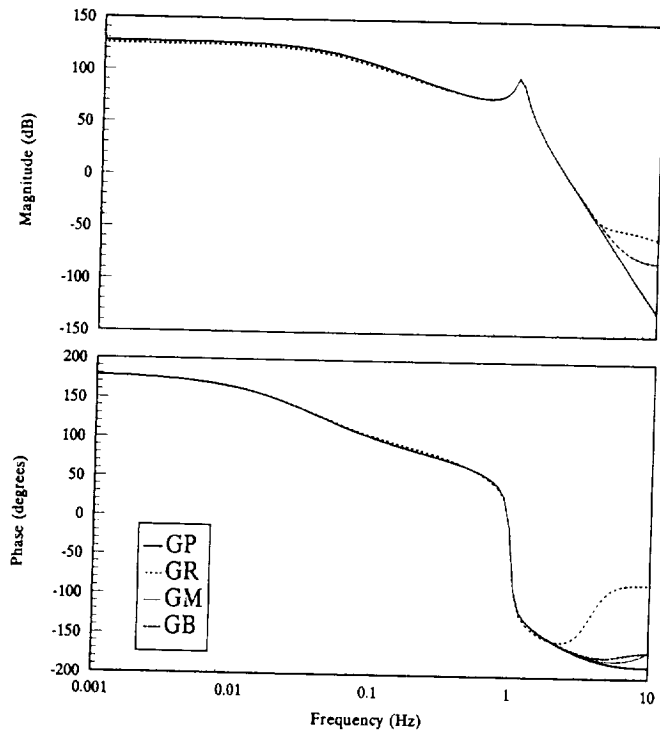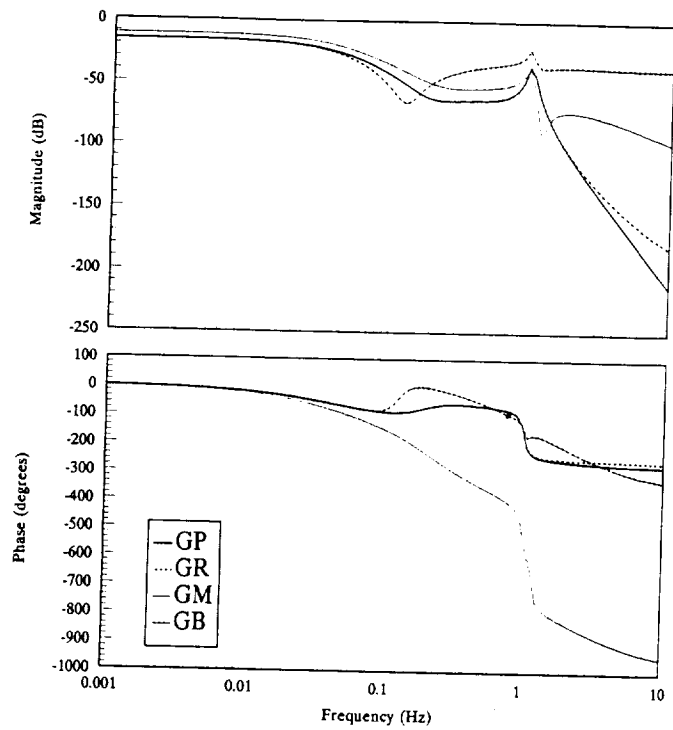model transfer matrices

Figure 6 - Comparison of (2,1) elements of plant and
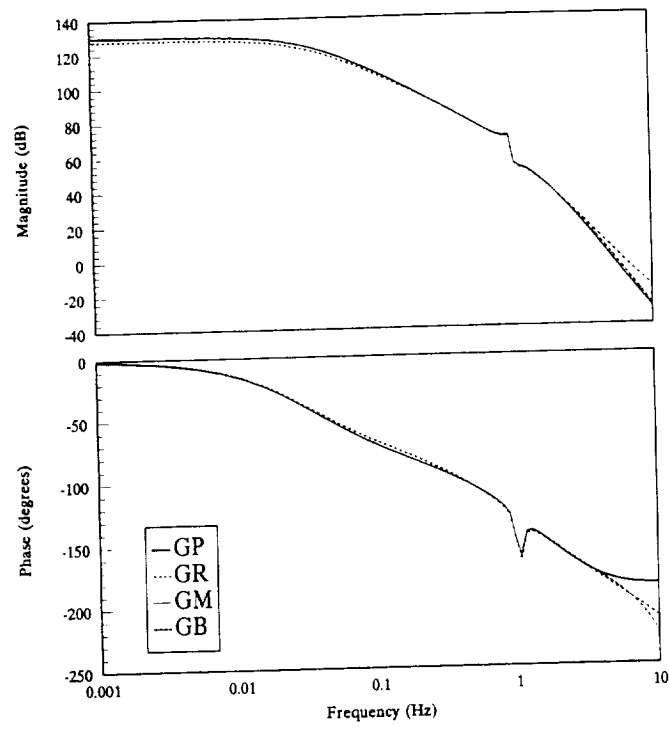model transfer matrices

213

Figure 7 - Comparison of (2,2) elements of plant and
model transfer matrices

Advances in Parameter Estimation Techniques Applied to Flexible Structures

Egbert Maben
David C. Zimmerman
University of Florida
231 Aerospace Building
Gainesville, Florida 32611

OVERVIEW

- **Distributed Parameter Modeling – PDEMOD**
  - **Wittrick–Williams Root Solving**
  - **Time Simulation Capability**

- **Parameter Estimation Formulation**
  - **Modal Parameter**
  - **Time–Domain Data**

- **Parameter Estimation Techniques**
  - **Lee and Hossain Approach**
  - **Modified Steepest Descent**
  - **Genetic Algorithm Approach**

- **Examples – NASA Mini–Mast**

- **Concluding Remarks**

Dynamic Systems and Control Laboratory
University of Florida

In this work, various parameter estimation techniques are investigated in the context of structural system identification utilizing distributed parameter models and "measured" time-domain data. Distributed parameter models are formulated using the PDEMOD software developed by Taylor [1]. Enhancements made to PDEMOD for this work include (i) a Wittrick–Williams based root solving algorithm [2], (ii) a time simulation capability, and (iii) various parameter estimation algorithms. The parameter estimations schemes will be contrasted using the NASA Mini–Mast as the focus structure.

216

PDEMOD - Partial Differential Equation MODeling

- **Generic Configuration**
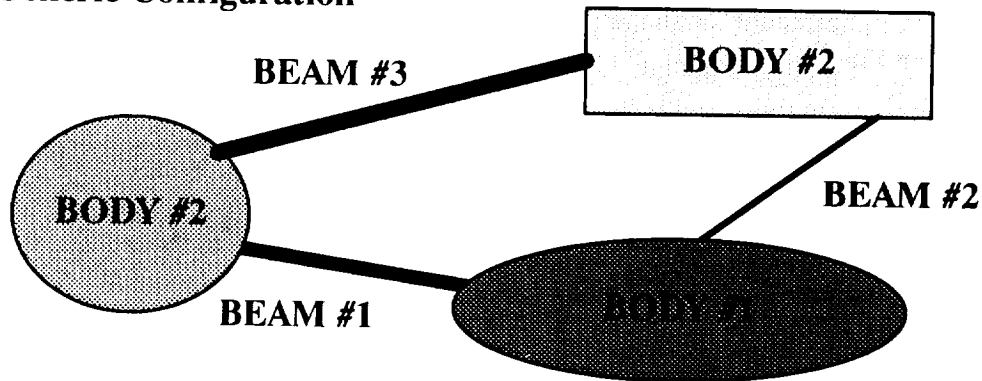
- **3 - Dimensional Spacecraft**
- **Rigid Bodies (Full Inertia Matrices)**
- **Flexible Beams**
  - **Bending - Euler-Bernoulli Equations**
  - **Elongation, Torsion - String Equation**

- **Force, Moment and Constraint Equations Yield Characteristic Equation**

$$\left| A(\omega) \right| = 0$$

- **Dimension of A = 12*Number of Beams**

Dynamic Systems and Control Laboratory
University of Florida

Partial Differential Equation Modelling (**PDEMOD**-Release 1) is capable of modeling complex flexible spacecraft which consist of a three-dimensional network of flexible beams and rigid bodies. Each beam has bending (Euler-Bernoulli) in two directions, torsion, and elongation degrees of freedom. The rigid bodies can be attached to the beam ends at any angle or body location. The eigenvalues are determined by numerically solving for the values of frequencies which cause the determinant of a frequency-dependent matrix to become zero. Eigenfunctions can then be calculated in closed-form at a finite number of specified points.

EXTENSIONS TO PDEMOD

- **Wittrick-Williams Root Solving Capability**

  - **Determines Number of E-values in Given Frequency Range**

  - **Can Indicate Presence of Repeated Roots**

  - **Reduces Computational Burden When Used in Conjunction with Root-Solving Technique**

- **Time-Domain Simulation Capabilities**

  - **Outputs at Discrete Points Calculated From Modal Model**

  - **"Modal Initial Conditions" Determined From Initial Conditions Using Finely Discretized Eigenvectors**

  - **Closed-Form Modal Time Solutions Utilized**

Dynamic Systems and Control Laboratory
University of Florida

In addition to the time-domain based parameter estimation techniques, two enhancements to PDEMOD-1 have been made. The first enhancement is a Wittrick-Williams based root-solving enhancement to the bisection root-solving algorithm. Provided lower and upper frequency limits, the Wittrick-Williams algorithm provides the number of frequencies that exist between the two limits. This information, when used properly, can greatly reduce the computational burden of solving for the eigenvalues of the structure. The second enhancement is the addition of time-simulation capabilities. Sensors can be placed at arbitrary points on the structure. A finite-dimensional (user specified) modal model is then created. Physical initial conditions are transformed to modal initial conditions using the eigenfunctions and mass distribution evaluated at a number of discrete points. It should be noted that for accurate results, the number of discrete points must be chosen relatively "large". The modal time responses are then calculated in closed-form. The resulting physical time response at the sensor locations can then be calculated.

218

PARAMETER ESTIMATION FORMULATION

- **Frequency Domain Formulation**

$$\min J = \sum_{i=0}^{n_{meas}} W_i \underbrace{\left(\omega^i_{exp} - \omega^i_{ana}\right)^2}_{\substack{\text{Frequency} \\ \text{Satisfaction}}} + H_i \underbrace{\| \underline{u}^i_{exp} - \underline{u}^i_{ana} \|_f}_{\substack{\text{Eigenfunction} \\ \text{Satisfaction}}}$$

  wrt physical design parameters

- **Many Sensitivity Formulations Omit Eigenfunction Satisfaction**

- **Weights W and H Allow For Engineering Judgement on Confidence of Measurements**

- **Time–Domain Formulation – This Study**

$$\min J = \sum_{i=0}^{n_{sensor}} W_i \int_{t_0}^{t_f} \left(y^i_{exp}(t) - y^i_{ana}(t)\right)^2 dt$$

  wrt physical design parameters

Many sensitivity–based (and other) parameter estimation techniques are driven by the mis-match in analytical and "measured" modal properties. The parameter estimation problem is then to adjust the physical parameters of the system such that there is an improved match between measured and analytical modal properties, often times subject to various con-straints. An alternate formulation is to work directly with time–history measurements and analytical predictions. This is the approach investigated in this paper.

PARAMETER ESTIMATION TECHNIQUES

- **Lee & Hossain – Time Domain**

$$q^{k+1} = q^k - S^k \frac{\partial J}{\partial q}$$

q^k – Vector of Design Parameters

S^k – Step Size Matrix (???)

$\frac{\partial J}{\partial q}$ – Gradient

- **Experience – Difficulty In Selecting Step Size Matrix**
  (Lee & Hossain Provide No Insight Into Selection)

- **Motivated by CHORDS (SDRC), Vary Only One Variable**
  With Corresponding Highest Gradient Value

  - **Uses 1-D Line Search on Single Physical Variable**
  - **Disadvantage: Loses Significant Gradient Information**

- **Genetic Algorithms**

Three parameter estimation techniques are investigated in this paper. The first is that proposed by Lee & Hossain [3]. In this work, the parameter of physical properties, q, are modified based on gradient information. There was no discussion in Ref. [3] on how to select the step-size matrix, S^k. Improper choice of S^k was found to lead to divergence of the solution (S^k to large), or in minimal improvement (S^k to small). Motivated from an optimization technique utilized in the CHORDS software program, a simplified one-dimension line search was investigated. In this approach, the variable with the highest sensitivity is chosen to be varied, with all others held constant. The optimal step-size of the one-dimensional search was calculated using a quadratic approximation. This approximation required an additional function evaluation. Finally, a Genetic Algorithm [4,5] approach was investigated.

GENETIC ALGORITHMS

- Based on Darwin's "Survival of the Fittest" Theories

- Shows Great Potential for
    - Multi-Modal Objective Functions
    - Discrete and/or Continuous Design Variables
    - Discontinuous Design Space

- Works With a Coding of the Design Variables,
  Not the Design Variables Themselves

- Searches From a Population of Designs,
  Not a Single Design Point

- Uses Payoff (Objective Function) Information,
  Not Gradient Information

- Uses Probabilistic Transition Rules,
  Not Deterministic Rules

Dynamic Systems and Control Laboratory
University of Florida

Genetic algorithms (GA's), as introduced by Holland [4], are one form of directed random search. The form of direction is based on Darwin's "survival of the fittest" theories. GA's are radically different from the more traditional design optimization techniques. GA's work with a coding of the design variables, as opposed to working with the design variables directly. The search is conducted from a population of designs (i.e., from a large number of points in the design space), unlike the traditional algorithms which search from a single design point. The GA requires only objective function information, as opposed to gradient or other auxiliary information. Finally, the GA is based on probabilistic transition rules, as opposed to deterministic rules. These features allow the GA to attack problems with local-global minima, discontinuous design spaces and mixed variable problems, all in a single, consistent framework.

221

GA's - ALGORITHM OVERVIEW

⊛ **Initial Population of Designs Created – Random or Heuristic**

⊛ **Initial Population Allowed to** *"Evolve"* **Over Generations**

⊛ **Conjecture – Evolution is the Best Compromise Between Determinism and Chance**

⊛ **Motivation – GA's are Robust Over a Wide Range of Problems**

Nonlinear Optimization / Genetic Algorithms / Random Walk / Performance / Problem Class
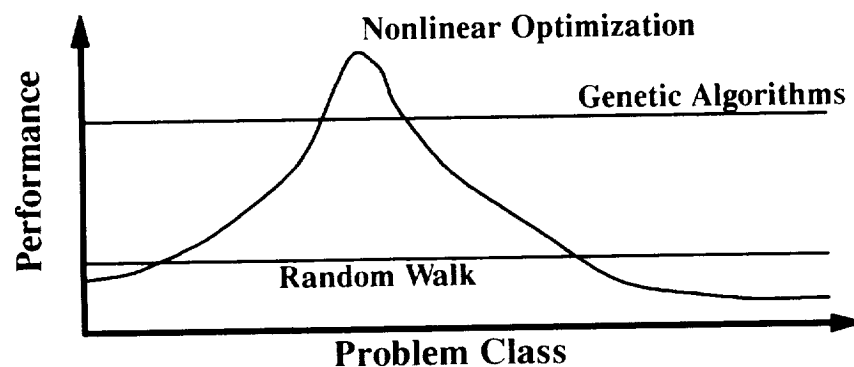
In GA's, a finite number of candidate solutions or designs are randomly or heuristically generated to create an initial population of designs. This initial population is then allowed to evolve over generations to produce new, and hopefully better designs. The basic conjecture behind GA's is that evolution is the best compromise between determinism and chance. The basic motivation behind the development of GA's is that they are robust problem solvers for a wide class of problems. However, it should be noted that they are not as efficient as nonlinear optimization techniques over the class of problems which are ideally suited for nonlinear optimization; namely continuous design variables with a continuous differentiable unimodal design space.

GENETIC ALGORITHM MODULES

- Design Variables *Coded* as a q-Bit Binary Number
  - Continuous Variables Like A/D Converter
  - Discrete Variables Have Unique Binary Strings
  - A Population Member is Just a String of Design Variables

- GA *Evaluation* – Level of *Fitness* Assigned to Each Member
  - Fitness Chosen to be Related to Objective Function
  - GA's Maximize Fitness

- GA *Selection* – Determination of Which Individuals in Current Population Chosen to be Parents
  - Biased Towards More Fit Members
  - Proportional Bias – $p\binom{member}{i} = \dfrac{fitness_i}{\sum\limits_{j=1}^{npop} fitness_j}$
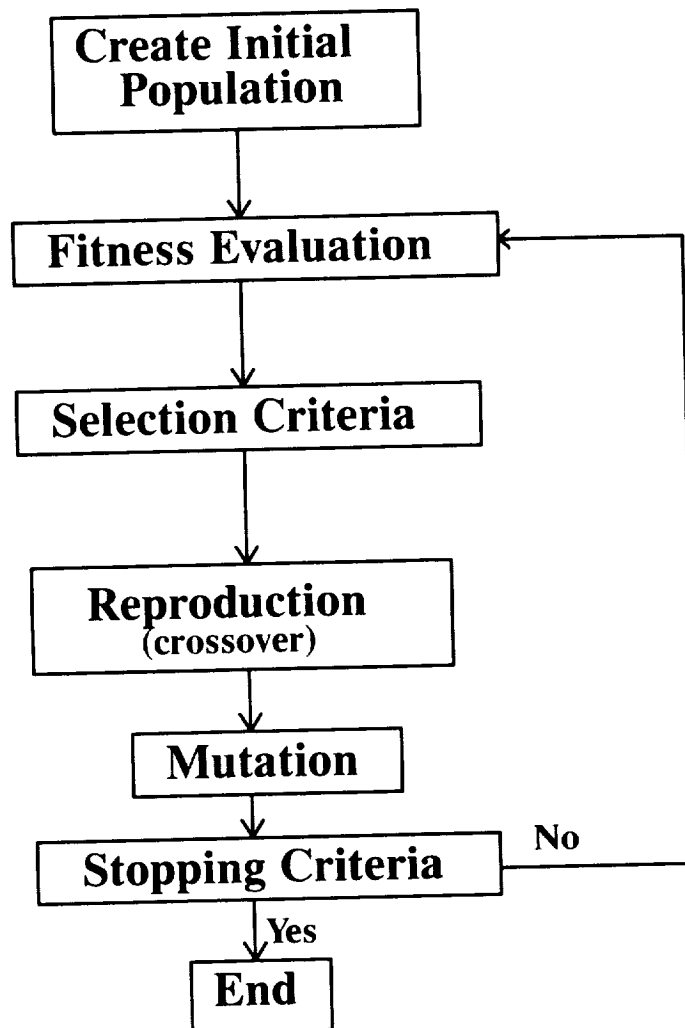
- GA *Crossover* – Transfer of Design Information From Parents to Prodigy

- GA *Mutation* – Low Probability Random Switch of Bits
  - Retains Design Information Over Entire Design Space
  - Aids Search For Global Optimal Solution

Dynamic Systems and Control Laboratory
University of Florida

Each design variable is *coded* as a q-bit binary number. A continuous design variable is approximated by 2^q discrete numbers between lower and upper bounds set for the design variable. Discrete variables would each be assigned a unique binary string. A population member is obtained by concatenating all design variables to obtain a single string of ones and zeros. *Evaluation* is the process of assigning a fitness measure to each member of the current population. Because GA's attempt to maximize the fitness of each member, an objective function which is to be minimized must be converted into an equivalent maximization problem. *Selection* is biased towards the most fit members of the population. Therefore, designs which are better as viewed from the fitness function, and therefore the objective function, are more likely to be chosen as parents. *Crossover* is the process in which design information is transferred to the prodigy from the parents. Many crossover operators (1-point, 2-point, uniform) have been investigated. *Mutation* is a low probability random operation which may perturb the design represented by the prodigy. The operator works on a bit-by-bit basis and is governed by the probability of mutation, p_m. At each bit, a biased coin toss is used to determine whether the bit should be logically "NOTed". The mutation operator is used to retain design information over the entire domain of the design space during the evolutionary process.

223

GENETIC ALGORITHMS - SUMMARY

```
          ┌─────────────────┐
          │  Create Initial │
          │   Population    │
          └─────────────────┘
                   │
                   ▼
          ┌─────────────────┐ ◄─────────┐
          │ Fitness Evaluation │          │
          └─────────────────┘           │
                   │                    │
                   ▼                    │
          ┌─────────────────┐           │
          │ Selection Criteria │          │
          └─────────────────┘           │
                   │                    │
                   ▼                    │
          ┌─────────────────┐           │
          │  Reproduction   │           │
          │   (crossover)   │           │
          └─────────────────┘           │
                   │                    │
                   ▼                    │
          ┌─────────────────┐           │
          │    Mutation     │           │
          └─────────────────┘           │
                   │              No    │
                   ▼                    │
          ┌─────────────────┐───────────┘
          │ Stopping Criteria │
          └─────────────────┘
                   │ Yes
                   ▼
          ┌─────────────────┐
          │      End        │
          └─────────────────┘
```

Dynamic Systems and Control Laboratory
University of Florida

In the implementation of the GA shown above, the prodigies are produced until the number of prodigies created is equal to n_{pop}, the population size. At that point, the current population of parents are discarded and the prodigies are in turn made parents which are capable of producing the next generation of prodigies. Thus, the production of n_{pop} prodigies can be viewed as the completion of one generation cycle in the evolutionary process. During this procedure, it is possible that both the fitness of the most fit member and the average population fitness can be temporarily reduced during the evolutionary process. To overcome this, the concept of a steady-state GA was implemented. In a steady-state GA (SSGA), the fitness of the children after they have been mutated is evaluated. These fitness values are then compared to the fitness of the two least fit parents in the current population. If the mutated child's fitness is higher than the least fit member in the population, the child will replace that member and will instantly become a candidate parent. To keep intact the concept of a generation, a generation is defined to be complete when the number of children produced, but not necessarily accepted into the population, is equal to n_{pop}.

EXAMPLE - NASA MINI-MAST

BAY #

18
16
14
12
10
8
6
4
2
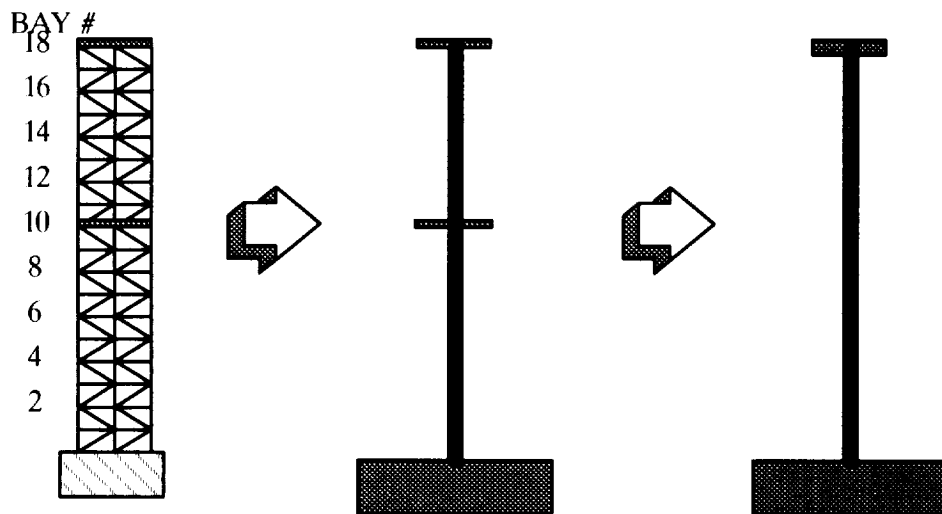
● **Mini-Mast Modeled With One or Two Beam PDEMOD**

● **Single Sensor at Tip (Bay 18)**

● **Initial Conditions:**

$$y(x) = \frac{0.6}{66.24^3}x^3 - \frac{0.4}{66.24}x \quad \text{ft}$$

$$v(x) = 0 \text{ ft/sec}$$

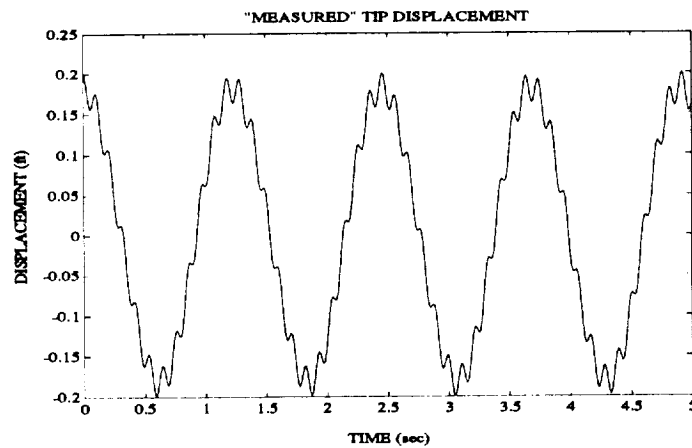Dynamic Systems and Control Laboratory
University of Florida

The NASA Langley Research Center Mini-Mast is an eighteen bay truss structure cantilevered at one end and free at the other. The bays are numbered one to eighteen starting with one at the cantilevered end. Discrete masses are located at bays ten and eighteen. Three different models of the Mini-Mast were created. The first model was a two beam PDEMOD resulting in a frequency matrix of dimension twenty-four. The second model, which was used in the parameter estimation algorithms, was a one beam PDEMOD whose tip mass was adjusted to produce "good" agreement with the two beam model. The reduction in the frequency matrix from twenty-four to twelve greatly reduces the computational burden. In addition, a 30 element FEM was created for comparison purposes. In all models, the single sensor output (position) was located at the tip (bay 18).

NASA MINIMAST - IC AND RESPONSE

● **Initial Condition**

INITIAL DISPLACEMENT PROFILE
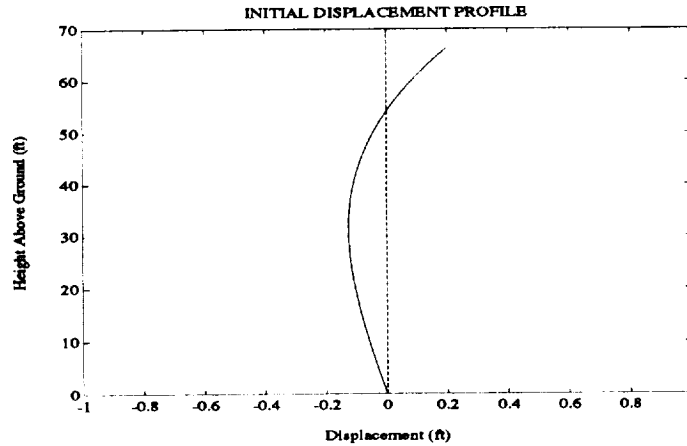
● **Tip Time Response (2 mode summation)**

"MEASURED" TIP DISPLACEMENT

Dynamic Systems and Control Laboratory
University of Florida

The above figures provide the initial displacement and resulting time–history used in the parameter estimation scheme. The initial condition was selected such that multi–modal response was present.
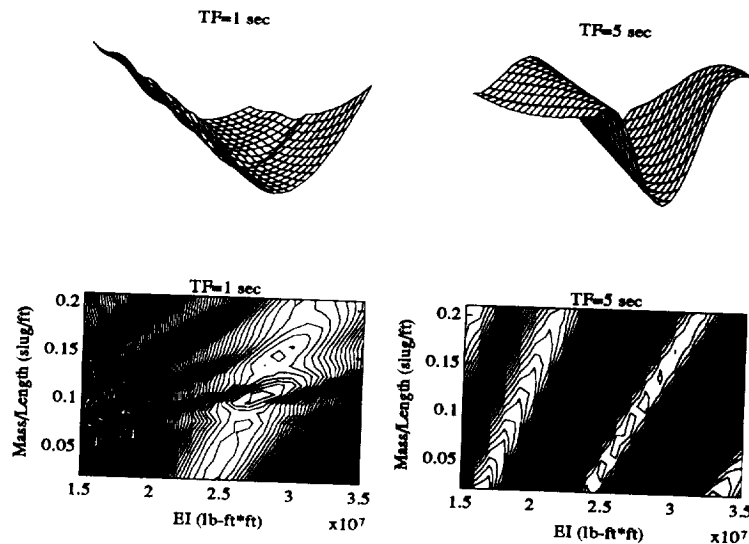
PARAMETER ESTIMATION

- **Determine EI and ϱ Using Measured vs Predicted Time Responses**

$$\min J = \sum_{i=0}^{n_{sensor}} W_i \int_{t_o}^{t_f} \left(y_{exp}^i(t) - y_{ana}^i(t) \right)^2 dt$$

- **Function Space Characteristics (tf = 1sec, tf = 5sec)**

$$1.5e^7 \le EI \le 3.5e^7 \qquad (EI^* = 2.76e^7 \ lb-ft^2)$$
$$0.01 \le \varrho \le 0.21 \qquad (\varrho^* = 0.1075 \ slug/ft)$$

The parameter estimation problem investigated is to minimize J with respect to EI and ρ. In the above Figure, surface profiles of J are presented for the cases of $t_f = 1$ and $t_f = 5$ seconds. The upper figures are mesh plots of J. The lower subfigures are contour plots of J vs the design parameters. From all figures, it is apparent that the function exhibits local minima and maxima. In addition, from the contour plots, it is evident that the "valley" is rippled, in that there are local minima in the valley.

PARAMETER ESTIMATION PROBLEM

- **Contour Plot Expanded (tf = 1sec)**

CONTOURS: INTEGRAL SQUARED ERROR

Mass/Length (slug/ft) vs EI (lb-ft*ft) ×10⁷
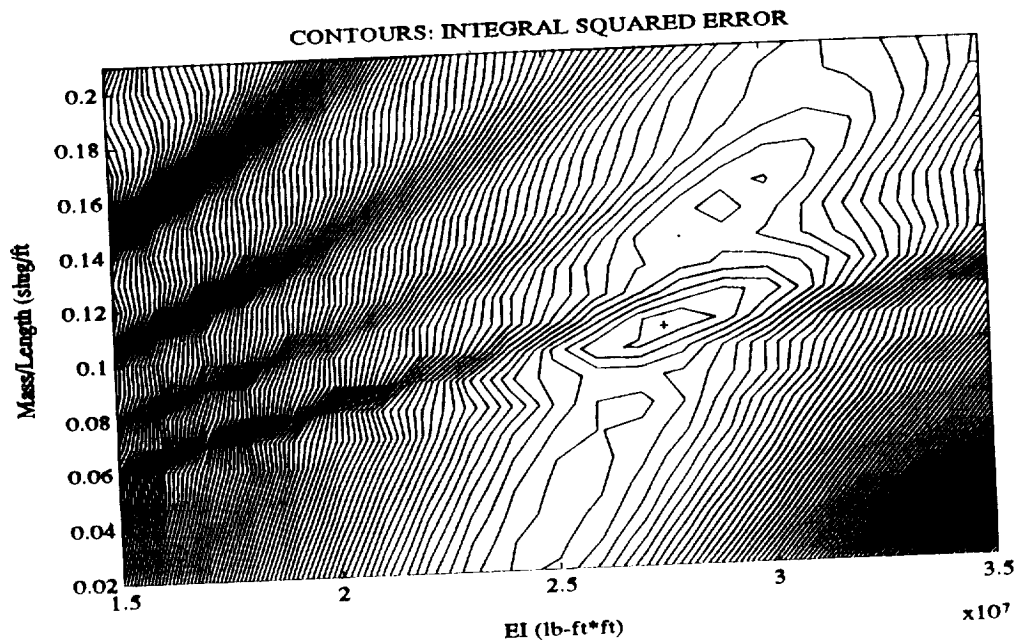
- **Steep/Shallow Walled Problem – similar to classic "Banana Valley Problem**

- **The "Valley" is Rippled**

- **Multi–Modal Function Space**

- **tf = 5sec Case More Difficult Than 1sec Case**

Dynamic Systems and Control Laboratory
University of Florida

The figure above is just an expanded view of the lower left figure of the previous slide. The optimal solution is marked by the " + " symbol. From this, and the previous figure, it is seen that the function has characteristics similar to Rosenbrocks "Banana Valley" problem. The problem at hand has the characteristic steep walled/gentle gradient valley of the "Banana Valley" Problem. The $t_f = 5$sec case represents the more difficult problem in that the walls are steeper.

LEE & HOSSAIN APPROACH

⚫ **Parameter Divergence (S^k = diag(1e5, 175): Large)**
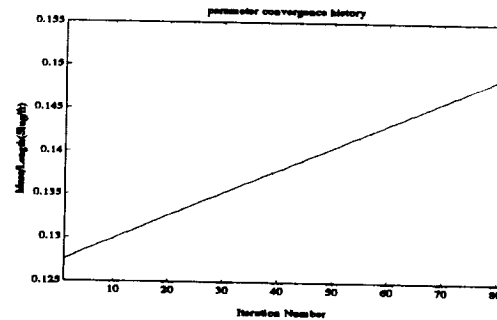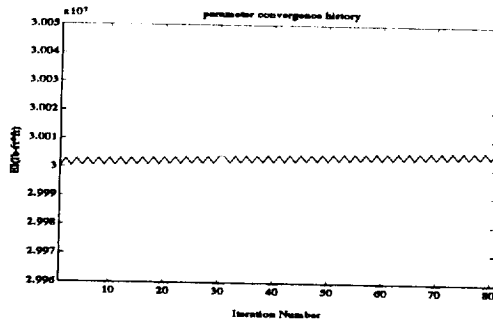
⚫ **Parameter Convergence To Local Minimum (S^k = diag(1e4, 95))**
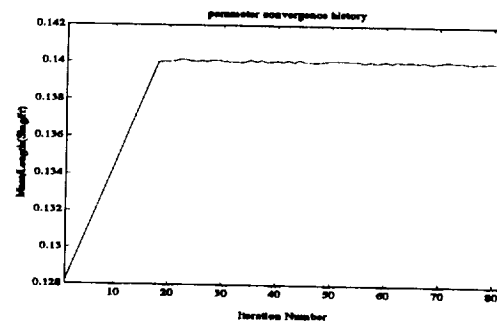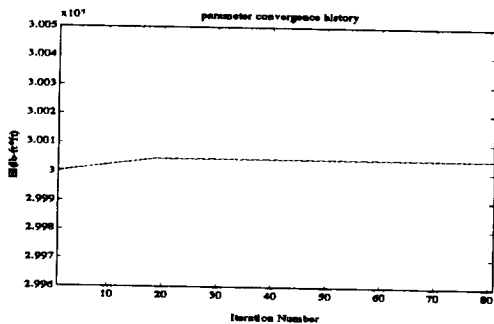
Dynamic Systems and Control Laboratory
University of Florida

The above figures show parameter value vs iteration number for the Lee & Hossain approach. The upper figure corresponds to the case where the step-size matrix, S^k, has been chosen to be to large. It is apparent that the parameter values are diverging and the actual path followed by the design variables is uphill. The lower figure corresponds to the case that there is convergence to a local minima. In comparing the two mass/length plots, it is apparent that the case of choosing S^k to large has caused the algorithm to miss the local minima.

LEE & HOSSAIN APPROACH (cont'd)

● Slower Convergence ($S^k = \text{diag}(1e2, 55)$)
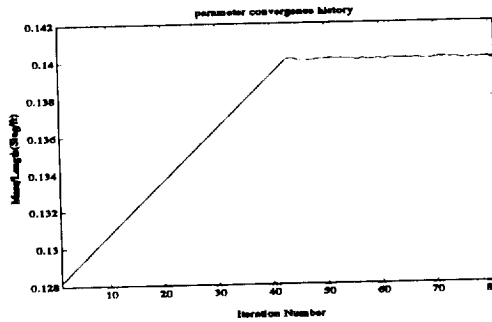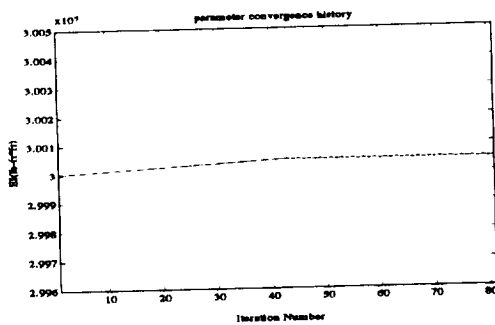
● Algorithm Performance Sensitive To Selection of S^k

● Convergence To Local Minima

In this figure, the value of the step-size matrix was chosen to be lower than the previous case of convergence. The algorithm converges to the same local minima, but requires a greater number of iterations. These slides indicate the sensitivity of the algorithm to step-size selection. Lee & Hossain provide no indication of how to select S^k. Thus, this remains an unresolved research issue for this algorithm.

230

SIMPLIFIED 1-D SEARCH

- Convergence Criteria Set to $\dfrac{\partial J}{\partial q_i} \leq 1e^{-12}$

- Convergence Histories For Four Different Starting Points

Convergence Path:Multiple Starting Points
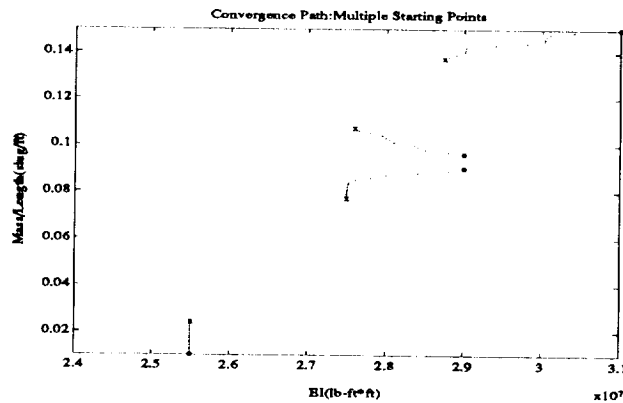
- Starting Points – "o"; Converged Solution – "x"
- One Solution Converges to Global Optimal
- Starting/Converged Points

  (2.55e7, 0.01) ⇨ (2.55e7, 0.024)

  (2.9e7, 0.096) ⇨ (2.76e7, 0.1070) NOTE: OPTIMAL

  (2.9e7, 0.090) ⇨ (2.75e7, 0.077) NOTE:Close to Previous Start

  (3.1e7, 0.150) ⇨ (2.875e7, 0.1370)

Dynamic Systems and Control Laboratory
University of Florida

In the simplified 1–D search strategy, the variable with the corresponding highest gradient is varied. A quadratic approximation technique is used to determine the optimal step–size. The above plot shows the result of the algorithm for four different starting initial conditions. The starting points are indicated by the "o's" and the ending points by "x's". Note that all starting points were in the valley. The stopping criteria used to halt the iterations was when the maximum gradient was lower than approximate machine precision. One of the four starting points ended up near the global minima. However, another nearby starting point actually converged to a farther away local minima.

GENETIC ALGORITHM SOLUTION - Case I

● **Utilized Linear Ranking Scheme to Map Minimization of Integral Into Maximization Problem**

● **Random Initial Population Utilized for Case I**

● **Convergence History**
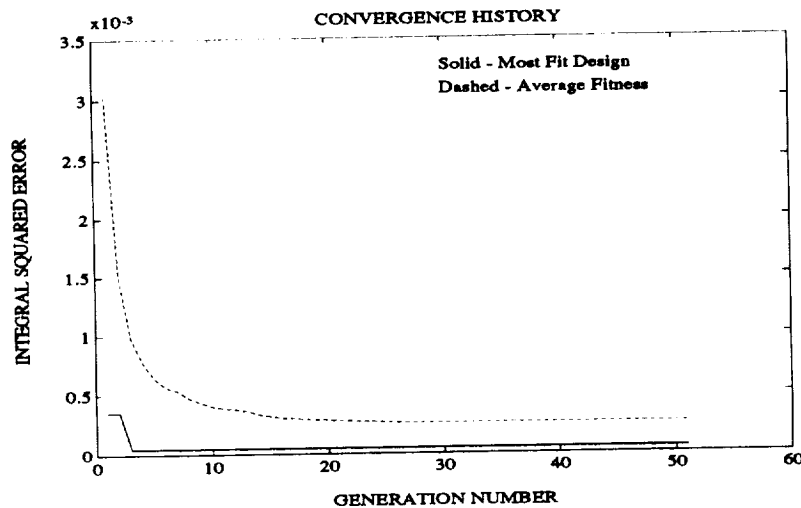
● **Note Rapid Convergence: In reality, could stop at ~ten generations**

The above figure shows the convergence history of the Genetic Algorithm parameter estimation approach. The solid line shows the integral value of the most fit member of the population at any given generation. In a similar manner, the dashed line represents the integral value of the average member of the population at any given generation. A linear ranking scheme was utilized to transform the integral minimization problem into a fitness maximization problem. In this scheme, assuming a population size of 30, the member with the lowest integral value (best member) is assigned a fitness of 30; the member with the highest integral value (worst member) is assigned a fitness of 1. This linear ranking scheme was used to avoid the creation of a "super individual". As is the case with most applications of GA's, there is rapid convergence in early generations; this slows considerably as the generation number increases.

232

GA's POPULATION MIGRATION

⊛ **After Five Generations**

POPULATION MIGRATION: FIVE GENERATIONS

⊛ **After Ten Generations**
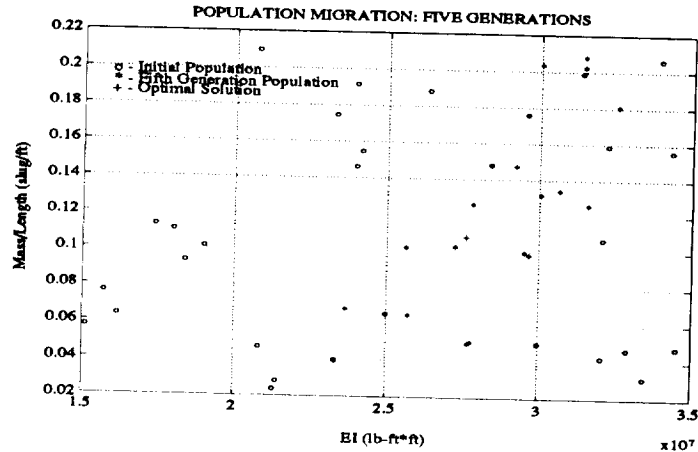
POPULATION MIGRATION: TEN GENERATIONS
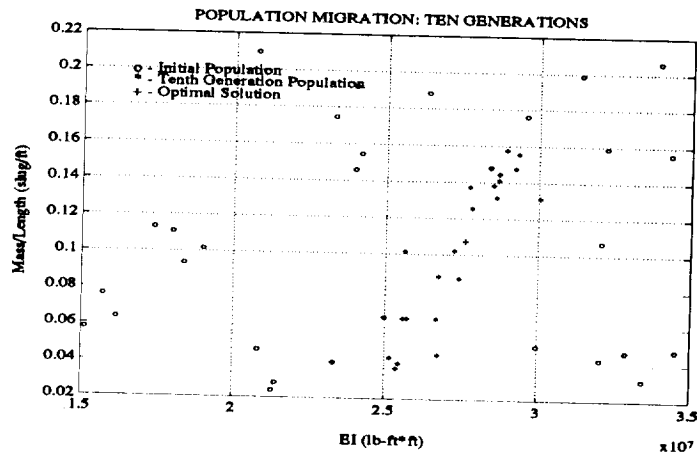
Dynamic Systems and Control Laboratory
University of Florida

This and the next slides show the population migration as a function of generation number. In the figures, the "o's" represent the location of the random, initial population. The "*'s" represent the population members at the stated generation number and the "+" indicates the global minima. After only five generations, most of the members have migrated into the valley. From generations, ten to fifty, it is seen that the migration of members is towards the global minima.

GA's POPULATION MIGRATION

● **After 20 Generations**

POPULATION MIGRATION: TWENTY GENERATIONS

● **After 50 Generations**

POPULATION MIGRATION: FIFTY GENERATIONS
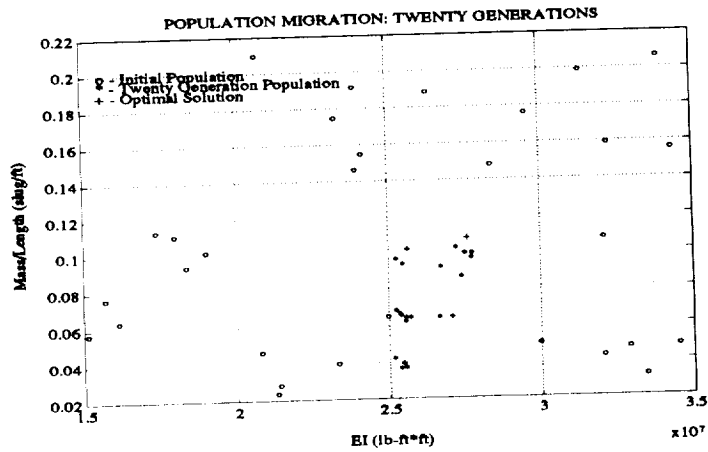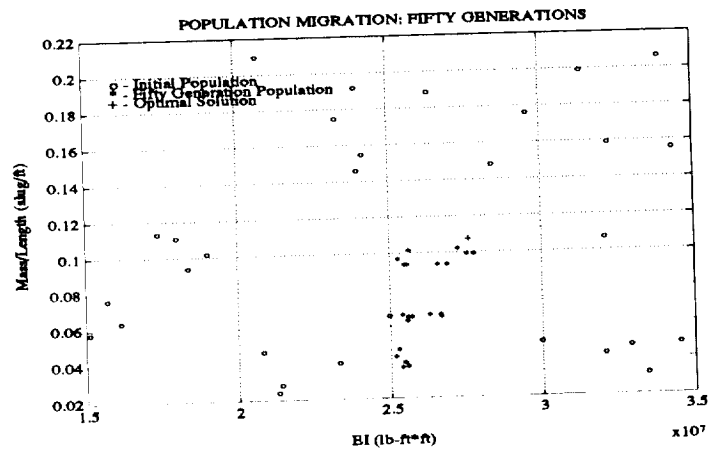
Dynamic Systems and Control Laboratory
University of Florida

GA POPULATION/CONTOURS

⊛ **Population At Generation 20 on Contour Plot**

CONTOURS: INTEGRAL SQUARED ERROR
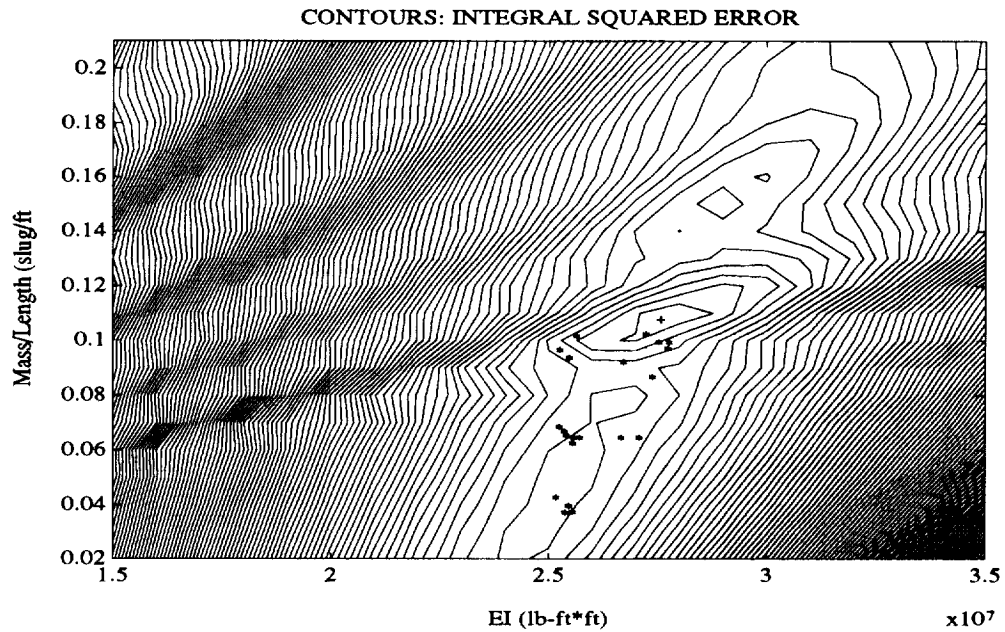
⊛ **All Members in the Valley Searching For Minima**

The above figure superimposes the contour plot with the population location at generation number 20. From this figure, it is clear that the search is now confined to the valley.

GA's - CASE II

- **Initial Population Forced to Low Values of EI and ϱ**
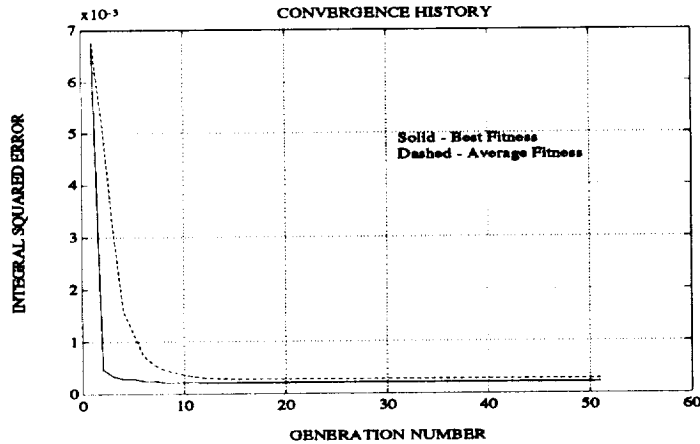
- **Convergence History**

- **Population Migration**
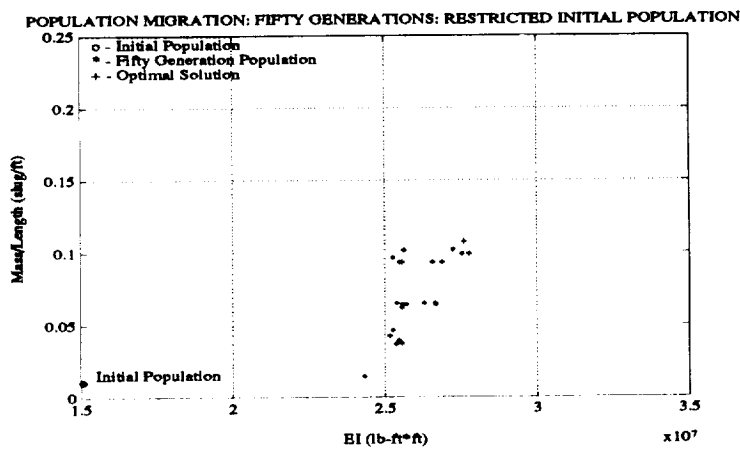
In the previous figures, the initial population was created randomly. Thus, some of the initial members were possibly already in the valley. To truly judge the performance of the GA approach, the initial population in this case was constrained to low values of both design variables. In the lower figure, what appears as a solid dot is really all thirty initial members of the population. After 50 generations, it is obvious that the population has migrated into the valley. The top figure indicates that the majority of the migration was accomplished in the first ten generations.

236

GA's - CASE III (5 sec data)

- **Initial/20 Generation – Random Population**
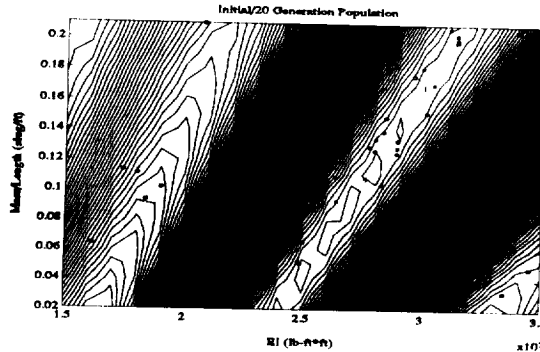
➡ **Population Converging To Valley; Not Yet at Optimal Solution**

- **Initial/50 Generation Scewed Initial**
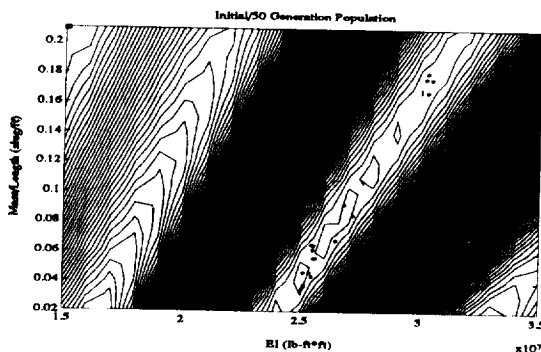
➡ **Population Converging, But Possibly To Local Solution (Would Need Many Generations To Achieve Optimal)**

In Case III, the integral was evaluated over a five second interval. The upper plot shows an overlay of the contours, the initial population (same as in previous random case), and the final population after 20 generations. Again, the population has converged to the valley, but has not yet found the global optimal. In the lower figure, the initial population was constrained to have low values of EI, and high values of ρ. All thirty members are contained in the solid "dot" in the upper left corner of the figure. After 50 generations, all members are in the valley: however, they have not found the global minima. In fact, another 50 generations were run with minimal change in population location. This indicates that although the GA solution appears to perform better than gradient based algorithms for this particular cost function, it still can become trapped in local minima (although theoretically if the number of generations goes to infinity the global minima will be found (by default)).

CONCLUDING REMARKS

- Parameter Estimation Schemes Utilizing Measured Time Domain Data and Distributed Parmeter Modelling Investigated

- "Enhancements" to PDEMOD Include Wittrick-Williams Root Solving and Time-History Simulation

- Demonstrated That "Simple" Time Domain Cost Functions Yield "Difficult" Function Spaces

  ⇨ Need to Search For Improved Time Domain Cost Functions

- Gradient-Based Algorithms Experienced Difficulty With Local Minima and Divergence

- Genetic Algorithms Showed Promise In These Areas, But Used More Function Evaluations

- Note That Mismatch in Function Evaluations Is a Function of Number of Design Variables

  ⇨ Increasing Number of Design Variables Favors Genetic Algorithms

Dynamic Systems and Control Laboratory
University of Florida

In this work, parameter estimation schemes utilizing measured time domain data were investigated. The models used were developed using the PDEMOD approach. Two enhancements to PDEMOD-1 were made in order to develop the parameter estimation algorithms. The first (Wittrick-Williams) reduced the computational burden associated with solving for the structure eigenvalues. The second provided time-simulation capabilities. It was shown by example that a "simple" time-domain cost function actually yielded a difficult function space for the parameter estimation algorithms. The function space was multi-modal and exhibited characteristics similar to the classic "Banana Valley" problem. The gradient-based algorithms experienced severe difficulty. In fact, it was difficult to find starting conditions for which either gradient algorithm converged to the optimal solution. Conversely, the GA approach appeared to perform well. However, the GA used a much greater number of function evaluations. This would not be the case if there were a large number of design variables. For gradient based algorithms, the number of function evaluations per iteration increases approximately linearly with the number of design variables (i.e. each additional design variable requires a gradient calculation). However, because GA's do not require gradient calculations, the number of function evaluations per generation is independent of the number of design variables.

238

REFERENCES

[1] Taylor, L.W., "PDEMOD – Computer Software for Partial Differential Equation Modeling of Flexible Space Structures," Proceedings of the 2nd USAF/NASA Workshop on System Identification and Health Monitoring of Precision Space Structures," Pasadena, California, March, 1990.

[2] Wittrick, W.H. and Williams, F.W., "Natural Frequencies of Elastic Structures," *Journal of Mechanics and Applied Mathematics*, Vol. XXIV, 1971, pp. 265–285.

[3] Lee, K.Y., and Hossain, S.A., "Distributed Systems Approach To Identification of Flexible Structures," *AIAA Journal of Guidance, Control and Dynamics*, Vol. 10, No. 6, 1987, pp. 540–548

[4] Holland, J.H., (1975), *Adaptation in Natural and Artificial Systems*, The University of Michigan Press, Ann Arbor, Michigan.

[5] Zimmerman, D.C. (1991), "A Darwinian Approach to the Actuator Number and Placement Problem with Nonnegligible Actuator Mass," to appear, Journal of Mechanical Systems and Signals.

PARAMETER ESTIMATION OF THE VIBRATIONAL MODEL
FOR THE SCOLE EXPERIMENTAL FACILITY

B.D. Crotts
Y.P. Kakad

Electrical Engineering Department
University of N. Carolina at Charlotte
Charlotte, N.C. 28223

The objective of this study is to experimentally
determine an empirical model of the vibrational dynamics of
the Spacecraft COntrol Laboratory Experiment (SCOLE)
facility. The first two flexible modes of this test article
are identified using a linear least-square identification
procedure and the data utilized for this procedure are
obtained by exciting the structure from a quiescent state
with torque wheels. The time history data of rate gyro
sensors and accelerometers due to excitation and after
excitation in terms of free-decay are used in the parameter
estimation of the vibrational model.

The free-decay portion of the data is analyzed using the
Discrete Fourier transform to determine the optimal model
order to use in modelling the response. Linear least-square
analysis is then used to select the parameters that best fit
the output of an Autoregressive (AR) model to the data. The
control effectiveness of the torque wheels is then
determined using the excitation portion of the test data,
again using linear least squares.

INTRODUCTION

Future NASA space missions may involve very large and highly flexible spacecraft that require active structural dynamics control. Large space structures would require very stringent pointing and vibration suppression requirements. The active controller that can achieve these objectives will have to be designed with very accurate knowledge of the dynamic behavior of the structure to ensure performance robustness to a variety of disturbances and uncertainties. It is recognized by control engineers that there are certain inherent problems in the design of active controllers for this class of large flexible spacecraft. Because of these concerns and of the desire to offer a means of comparing technical approaches directly, a NASA/IEEE Design Challenge [1] was being offered to the technical community. In 1983, the Spacecraft Control Branch at NASA Langley Research Center in Hampton, VA. initiated the Spacecraft Control Laboratory Experiment (SCOLE) program and the NASA/IEEE Design Challenge to promote direct comparison and a realistic test of different approaches to control design against a common open to the public laboratory test article. This facility provides researchers with a highly flexible test article, sensors, actuators, and digital control processing capability. The test article resembles a large space antenna attached to the Space Shuttle Orbiter by a long flexible mast, similar to proposed space flight experiments and various space-based antenna systems. The proposed model is shown in Figure 1. Using SCOLE, control laws for a multi-input output structural dynamics system can be implemented in real time from any remote site that has a computer terminal and modem communications capability. Much interest has been expressed by the research community concerning SCOLE. This is reflected in the technical output of five workshops held since the conception of SCOLE in 1983.

SCOLE APPARATUS

The SCOLE hardware and software support is described in detail in Refs. 2 and 3 and in this paper. For this work, SCOLE contains two major structural elements of interest: a planar, hexagonal tubular structure representing an antenna reflector, and a single tubular flexible mast connecting the antenna to the platform, as shown in Figure 2. The platform is fixed to ground and only the mast and reflector portions are dealt with in this experiment. The system actuators consist of three mast-end mounted reaction wheels that produce torque in three mutually orthogonal directions. The system sensors are comprised of a three-axis reflector-mounted rotational rate sensor and both mast-mounted and reflector-mounted x and y-axis accelerometers. The experiments are run on SCOLE using a digital M68000-based

computer that has a UNIX-like operating system version called UNOS. Programming is accomplished in a combination of C and FORTRAN 77 programs. The computer has analog-to-digital (A/D) converters used for sampling the rate sensor data, digital-to-analog (D/A) converters used to command the reaction torque wheels, and a process timer which achieves precise internal timing of the data sampling process.

SYSTEM MODELS

The model we seek for SCOLE should incorporate the actual natural frequencies, damping ratios, and control effectiveness coefficients of the system. The viscous damping can be modeled in terms of ζ_i, the damping ratio of the ith mode. To this end, each mode of the vibrational dynamics of SCOLE is modeled as a single-input, single-output system [3] described by the state-space equation

$$\dot{x}(t) = Ax(t) + Bu(t), \tag{1}$$

where

$$x = [\eta\,\dot{\eta}]^T \tag{2}$$

$$A = \begin{matrix} 0 & 1 \\ -\omega^2 & -2\zeta\omega \end{matrix} \tag{3}$$

$$B = \begin{matrix} 0 \\ b \end{matrix}. \tag{4}$$

In this equation,

$$\omega^2 = \frac{k}{m}, \tag{5}$$

$$2\zeta\omega = \frac{c}{m}, \tag{6}$$

where

x - modal state vector
u - control input of reflector end reaction torque wheels
b - control effectiveness parameter of actuator location
ω - natural frequency of mode

243

ζ - damping ratio of mode.

The output is of the form

$$y = Hx \tag{7}$$

for a rate sensor,

$$H = [0, c] , \tag{8}$$

where c is the mode slope at the sensor location.

To obtain a difference equation model for digital computer control, the control input is assumed constant over the computer sample time interval of T seconds and the continuous-time model is converted to its discrete-time equivalent by integration over the interval.

Thus, the difference equation describing the motion appears as

$$\underline{x}_{K+1} = \phi \underline{x}_K + \Gamma \underline{u}_K , \tag{9}$$

where

$$\phi = e^{AT} \tag{10}$$

$$\Gamma = \int_0^T e^{At} dt B = (\phi - I) A^{-1} B , \tag{11}$$

since A is nonsingular and I is the 2x2 identity matrix.

The model used in this work is a linear, constant-coefficient, difference equation. To accomplish such a model, an auto-regressive form of the discrete time model is found by taking the z-transform of the last equation and solving for the sampled sensor output, y_k, in terms of the input actuator. The auto-regressive moving average (ARMA) model appears as

$$y_K = a_1 y_{K-1} + a_2 y_{K-2} + (b_1 u_{K-1} + b_2 u_{K-2}) b_{TW} , \tag{12}$$

where

$$a_1 = \phi_{11} + \phi_{22} \tag{13}$$

$$a_2 = \phi_{12} \phi_{21} - \phi_{11} \phi_{22} \tag{14}$$

$$b_1 = \Gamma_{12} \tag{15}$$

$$b_2 = \phi_{12}\Gamma_{22} - \phi_{22}\Gamma_{12} \qquad\qquad (16)$$

$$b_{TW} = c \cdot b. \qquad\qquad (17)$$

Identification of the ARMA model parameters is performed using the linear least-square estimation (LSE) algorithm. This method was selected because of its computation efficiency and implementation simplicity. The error equation used in the estimation is defined to be

$$e_K = y_K - [a_1 y_{K-1} + a_2 y_{K-2} + (b_1 u_{K-1} + b_2 u_{K-2}) b_{TW}]. \qquad (18)$$

The sum of the squared error,

$$J = \frac{1}{2}\sum_{K=0}^{N} e_{K}^2, \qquad\qquad (19)$$

is the performance measure to be minimized with respect to the parameter desired to be found.

PARAMETER IDENTIFICATION TECHNIQUES

Linear least-square estimation (LSE) is used to identify the ARMA model parameters. This method is selected because of its computation efficiency and implementation simplicity. The identification process is carried out for each reaction torque wheel and for each mode. The test data in the identification process of the SCOLE problem is processed in a two-step operation.

For the first step, the AR coefficients a_1 and a_2 of the ARMA are identified using the free-decay portion of the collected data. The spectral content of the free-decay portion of the data is examined using the Discrete Fourier Transform and the Hamming window. The free-decay data are filtered to suppress noise and signals due to any modes not wanted in the model. The filtered data is processed using the standard least-square estimation to identify the AR coefficients, a_1 and a_2, of the modelled mode. The identification of the a_1 and a_2 coefficients for each mode generally depends on the data base used in the estimation. As more significant data are added, the estimates should converge to a value and the variance of the estimates will improve to a limit, which depends on the measurement noise and the model. After convergence occurs, the mean and

variance of the estimates should remain constant. Therefore, the variation of the estimates is examined as data is added to the data base and the mean of the estimates is taken over the last several data base additions. To ascertain confidence in the estimates, the variance of the estimates is also taken into consideration. Also, the damping ratios and frequency of each mode can be computed from the a_1 and a_2 coefficients. In the second step of the parameter identification procedure for the ARMA model, the control effectiveness coefficient b_{TW} of the torque wheel used is determined. Once the values of the a_1 and a_2 coefficients for the mode of interest are determined, a similar linear least-square scheme is employed on the excitation portion of the test data to obtain the control effectiveness of the torque wheel actuator with respect to the mode of interest. Again, the mean and variance of the estimate of b_{TW} is taken into consideration.

EXPERIMENTAL PROCEDURES

Experimental work and testing can be conducted on SCOLE either at the NASA Langley Research Center in Hampton, VA, where SCOLE is located, or at any remote site that has a computer terminal and modem communications capability. The work presented in this paper was conducted both at NASA and from the UNC Charlotte College of Engineering.

A manual structural excitation test is performed wherein data is collected and analyzed to verify physical modal directions and frequencies as predicted by computer simulations of SCOLE. Bias readings of all inertial sensors are always taken before each run to establish a reference frame. For mode 1 testing, the structure is hand held by the reflector and pulled in the center of the +x and +y-axis directions, as shown in Figure 3, approximately six inches or until the displacement angle about the z-axis reaches five degrees. When the reflector is released, free decay data is recorded and collected. The same process occurs for mode 2 testing, with the reflector being released from the center of the -x and +y-axis directions as shown in Figure 4. Data is collected and verified against predicted natural frequencies of modes 1 and 2.

The vibrational dynamic model we seek for SCOLE incorporating the actual natural frequencies, damping ratios, and control effectiveness coefficients are obtained in this work by using the mast-end mounted reaction wheels to excite the structure. Structural excitation tests are individually conducted wherein the structure, initially at rest, is sinusoidally forced by a single reaction wheel for 30 seconds at the predicted mode of interest. The data recording is continued for 60 seconds to obtain free-decay

246

data. Tests are carried out for each of the x,y, and z-axis torque wheels and for both modes 1 and 2 and are summarized in Table 1.

DISCUSSIONS

Experimental data and results of the system identification process are summarized and illustrated in Table 2 and Figures 5 through 10. Tests and analysis using each of the x, y, and z-axis torque wheels at both the first and second modes, .4401 and .4764 Hz respectively, are carried out. The identified parameters a_1, a_2, b_{TW}, and the computed values of ζ and f for all of the tests are tabulated in Table 2.

Figure 5 shows the input excitation signal of the reaction torque wheel. Before each test, the structure was steadied and bias readings of the sensors were taken and accounted for. A sinusoidal forcing signal of amplitude 20 at the desired mode test frequency was applied to the structure for 30 seconds. For mode 1 frequency of .4401 Hz, the x-axis reaction torque wheel excited the structure the most. This was in agreement with the predicted first bending mode shape shown to occur closer to the pitch or y-axis direction. The y-axis torque wheel had the greatest effect on exciting the structure for mode 2 tests, which agreed with the predicted second bending mode shape occurring in the direction of the roll or x-axis. The z-axis torque wheel had the least effect on exciting the structure, as it tended to excite the structure in the yaw or about the z-axis direction. Since the first two vibrational modes occur dominantly in the x-y plane, the z-axis torque wheel had little effect on exciting the structure at the first two modal frequencies.

Figures 6 and 7 illustrate the frequency spectral analysis on the free decay portion of the data using the DFT and Hamming window. The structure would non-periodically vibrate in both translational and rotational directions after about 30 seconds of free decay. Therefore, only the first 30 seconds were considered due to other modes becoming dominant in the decay. The length of the data record used by the DFT was chosen to be equal to an integer number of periods of the sequence. The presence of leakage or significant non-zero frequency components occurred when the data record was improperly truncated. Therefore, an integer number of periods represented by the value of N was chosen. The frequency magnitudes were also proportional to the number of periods included in the record length. The greater the number of periods , the larger the magnitude. To further reduce the effects of the discontinuities introduced by truncating the sequence, Hamming windows were

used. The Hamming windows represent a noticeable improvement in suppressing the magnitude of the side lobes and the unwanted non-zero frequencies while broadening the main lobe frequency. The use of Hamming windows was extremely valuable in detecting and identifying the first and second modal frequencies, which were very close together.

Figures 8 and 9 of each test provide a description of the parameter identification process for the free decay coefficients a_1 and a_2. From these figures, the identified parameters are seen to converge as data is added to the data base for estimation. The identification process was terminated when convergence was achieved based on the deviation of each of the last three iterations from their arithmetic average with a convergence bandwidth of 5 percent. The mean values of a_1 and a_2 for each test are shown in Table 2. The natural frequency and its damping factor were computed based upon the coefficients a_1 and a_2, and are also shown in Table 2. The accuracy of the modal frequency was affected by the characteristics of the LSE identification technique. The frequency calculated from the LSE varied slightly from the frequency given by the DFT as shown on the figures. The characteristics and accuracies of the LSE algorithm and the DFT accounted for a part of the difference.

Figure 10 of each test shows the control effectiveness parameter of the reaction torque wheel, b_{TW}. Control effectiveness parameters were particularly difficult to accurately determine because of weak actuators and were small when compared to their associated frequency and damping parameters. Also, due to the difference between the forced and resonant frequencies of the system, the value of b_{TW} found may be highly inaccurate. The estimate converged as more data was added. It is important to use the mean of b_{TW} taken over a converged portion of the data and not a single point. The mean and variance of b_{TW} are shown on the figures. The presence of a disturbance was induced when the reaction torque wheel was initially started. It is believed that this was the result of start up friction of the reaction torque wheel assembly. Therefore, the first 5 seconds of data were not included in the data base for estimation.

SUMMARY

In this work, an empirical model of the vibrational dynamics of the first two flexible modes of SCOLE was found using the linear least square identification procedure. The experimental apparatus and procedures followed and the system model assumed were also discussed in this study.

248

Testing was done by exciting the structure from a quiescent state with torque wheels and recording the time history data of rate gyro sensors and accelerometers. The torque wheels were then shut down and free-decay data recorded. The DFT and Hamming window were used to analyze the free decay portion of the data. The coefficients of an autoregressive model to the data were determined using linear least square analysis. Next, the control effectiveness of the torque wheels was found using the excitation portion of the test data, again utilizing linear least squares. Experimental data and graphs were also presented to provide a description of the digital signal process algorithms and techniques used in determining the first two flexible modes of SCOLE. The experimental results presented in this paper have the potential to be extremely useful in modelling vibrational dynamics of large flexible spacecraft structures.

REFERENCES

1. Lawrence W. Taylor, Jr. and A.V. Balakrishnan, "A Mathematical Problem and a Spacecraft Control Laboratory Experiment (SCOLE) Used To Evaluate Control Laws For Flexible Spacecraft", SCOLE Workshop - 1984, Proceedings of a Workshop Concerning the NASA - IEEE Design Challenge, pp. 1-27.

2. Jeffrey P. Williams and Rosemary A. Rallo, "Description of the Spacecraft Control Laboratory Experiment (SCOLE) Facility", 3rd Annual NASA SCOLE Workshop, Proceedings of a Workshop Concerning the NASA - IEEE Design Challenge, 1986, pp. 413-457.

3. Danette B. Lenox, "Spacecraft Controls Laboratory Experiment (SCOLE) Software User's Manual", 5th Annual NASA SCOLE Workshop, Proceedings of a Workshop Concerning the NASA - IEEE Design Challenge, 1988, pp. 619-690.

4. Dean W. Sparks, Jr. and Raymond C. Montgomery and Robin C. Elder and Danette B. Lenox, "Parameter Identification For Vibration Control of SCOLE", 5th Annual NASA SCOLE Workshop, Proceedings of a Workshop Concerning the NASA - IEEE Design Challenge, 1988, pp. 547-554.

5. F.E. Thau and T. Eliazov and R.C. Montgomery, "Least Squares Sequential Parameter and State Estimation For Large Space Structures", Proceedings of the 1982 American Control Conference, 1982, pp. 16-21.

6. D. Sparks, Jr., "Initial Test Results on State Estimation On The SCOLE Mast", 4th Annual NASA SCOLE Workshop, Proceedings of a Workshop Concerning the NASA - IEEE Design Challenge, 1987, pp. 181-190.

7. J. Shenhar and D. Sparks, Jr. and J.P. Williams and R.C. Montgomery, "Attitude Control System Testing On SCOLE", Paper presented at the VPI&SU/AIAA Symposium on Dynamics and Control of Large Structures, June 29-July 1, 1987.

8. R.C. Montgomery and Joram Shenhar and J.P. Williams, "On-Line Identification and Attitude Control For SCOLE", Paper presented at the AIAA Guidance, Navigation and Control Conference, August 17-19,1987.

250

9.   Raymond C. Montgomery, "Analytic Redundancy Management For SCOLE", <u>4th Annual NASA SCOLE Workshop</u>, Proceedings of a Workshop Concerning the NASA - IEEE Design Challenge, 1987, pp. 329-346.

10.   Y.P. Kakad, "Slew Maneuver Dyanmics of Spacecraft Control Laboratory Experiment (SCOLE)", <u>5th Annual NASA SCOLE Workshop</u>, Proceedings of a Workshop Concerning the NASA - IEEE Design Challenge, 1988, pp. 247-290.

11.   Lawrence W. Taylor, Jr. and A.V. Balakrishnan, "A Laboratory Experiment Used to Evaluate Control Laws For Flexibe Spacecraft", <u>Dynamics and Control of Large Structures</u>, Proceedings of the 4th VPI&SU/AIAA Symposium, 1983, pp. 311-318.

12.   Jeffrey P. Williams and Raymond C. Montgomery, "Experimental Implementation of Parameter Adaptive Control on a Free-Free Beam", <u>Dynamics and Control of Large Structures</u>, Proceedings of the 4th VPI&SU/AIAA Symposium, 1983, pp. 279-290.

Reflector

Flexible Beam

Shuttle

Z

X
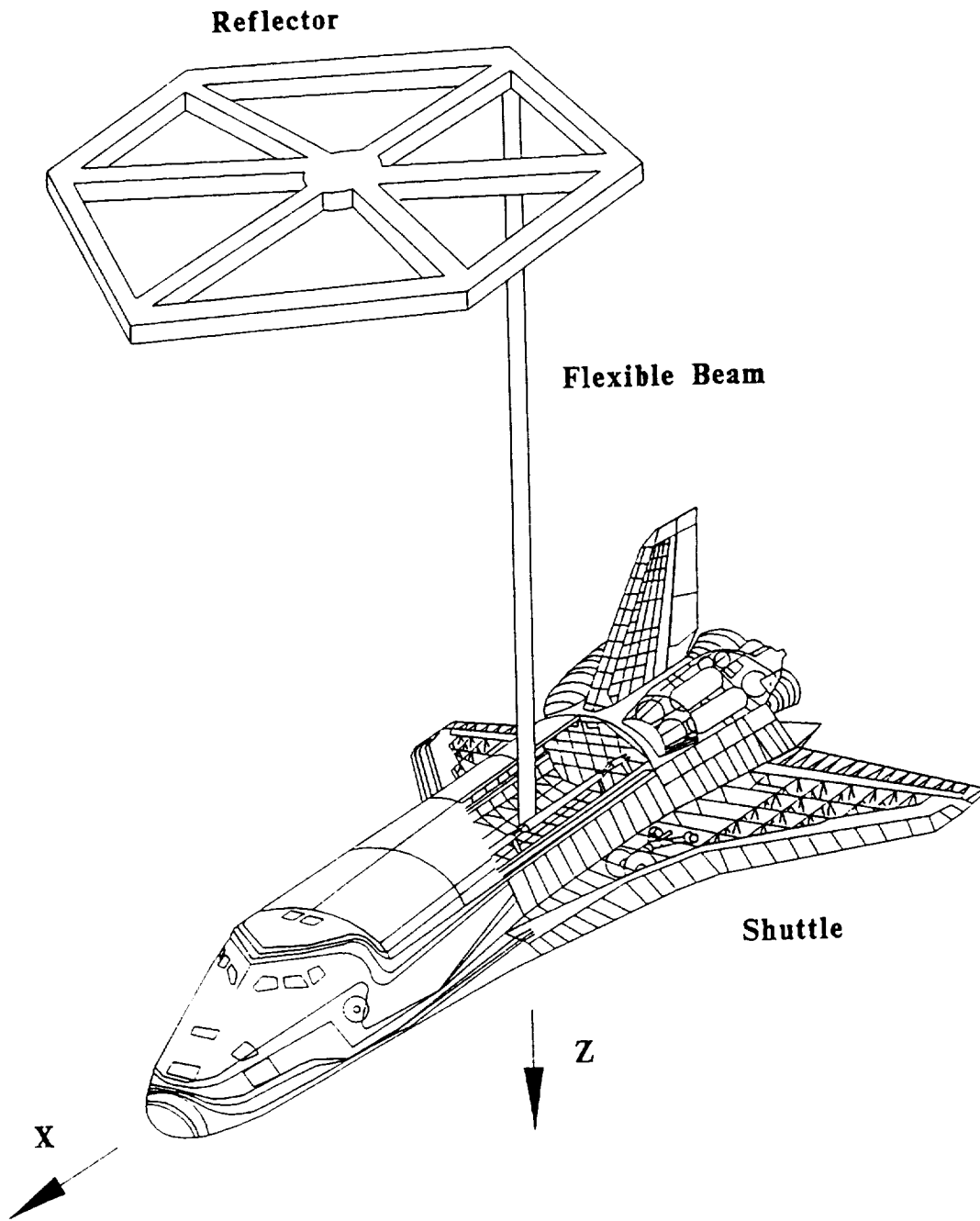
The Space Shuttle Model
Figure 1

The SCOLE Experimental Apparatus

Figure 2

Original photograph unavailable at time of publication
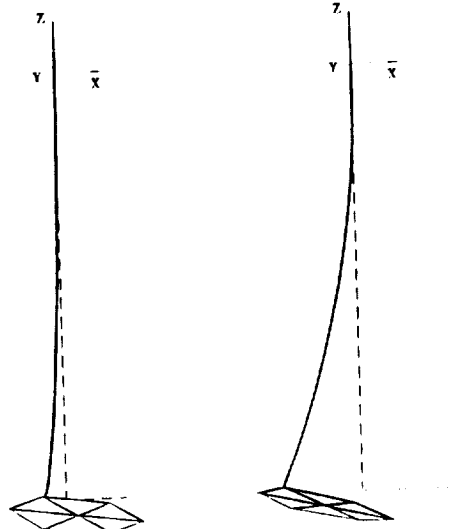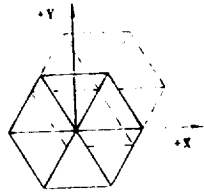
Mode 1 Testing
Figure 3

Mode 2 Testing
Figure 4

U(t) = 20SIN(2.99•t)

TIME (SECS)

Actuator Input

Figure 5

MAGNITUDE

N = 238

FREQUENCY (HZ)

Discrete Fourier Transform

Figure 6

MAGNITUDE

N = 238

FREQUENCY (HZ)

Hamming Window

Figure 7

MEAN A1 = 1.7073690
VARIANCE A1 = .0001020

TIME (SECS)

Arma Coefficient A_1

Figure 8

256

MEAN A2 = -.7947280
VARIANCE A2 = .0000996

Arma Coefficient A_2

Figure 9

MEAN B = 1.5270996
VARIANCE B = .1837367

Control Effectiveness Parameter B
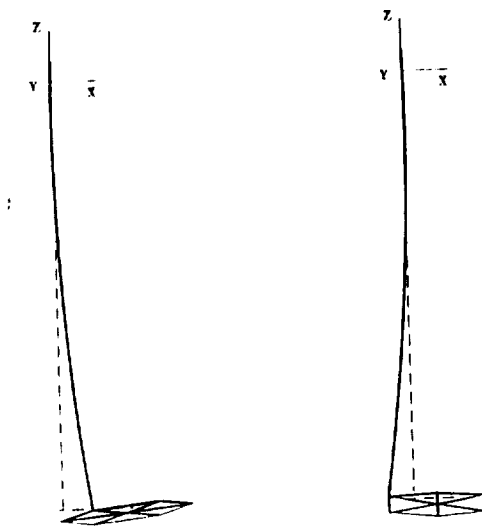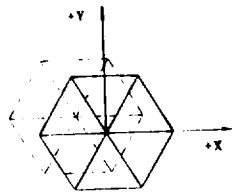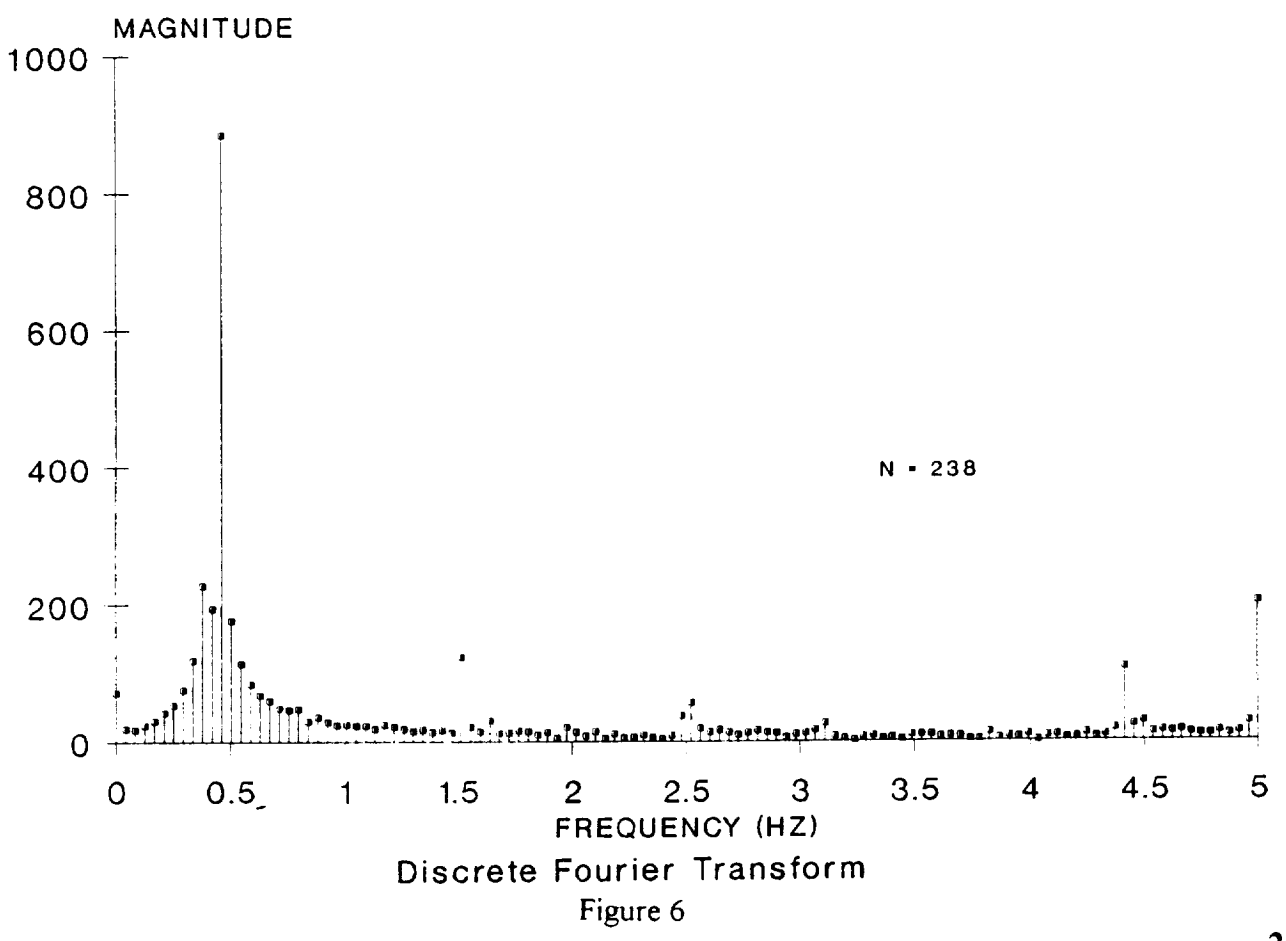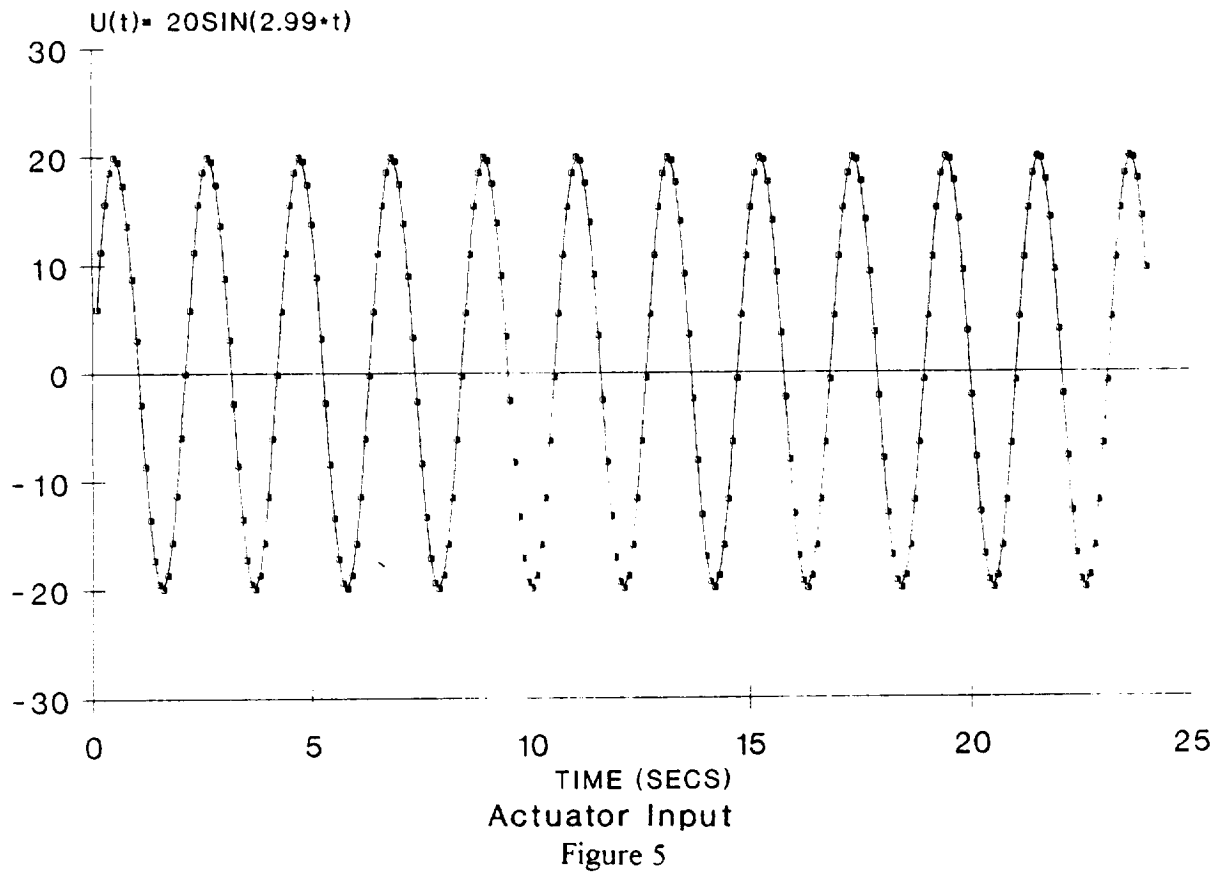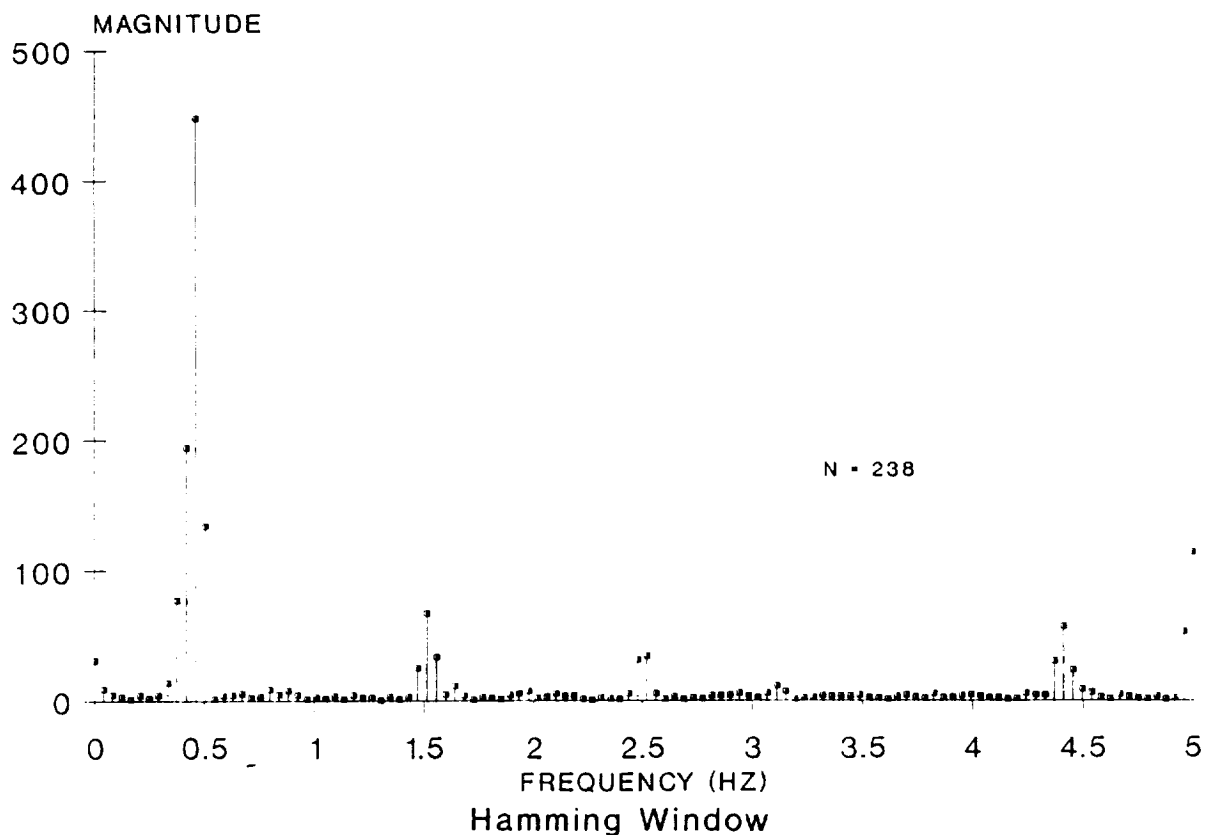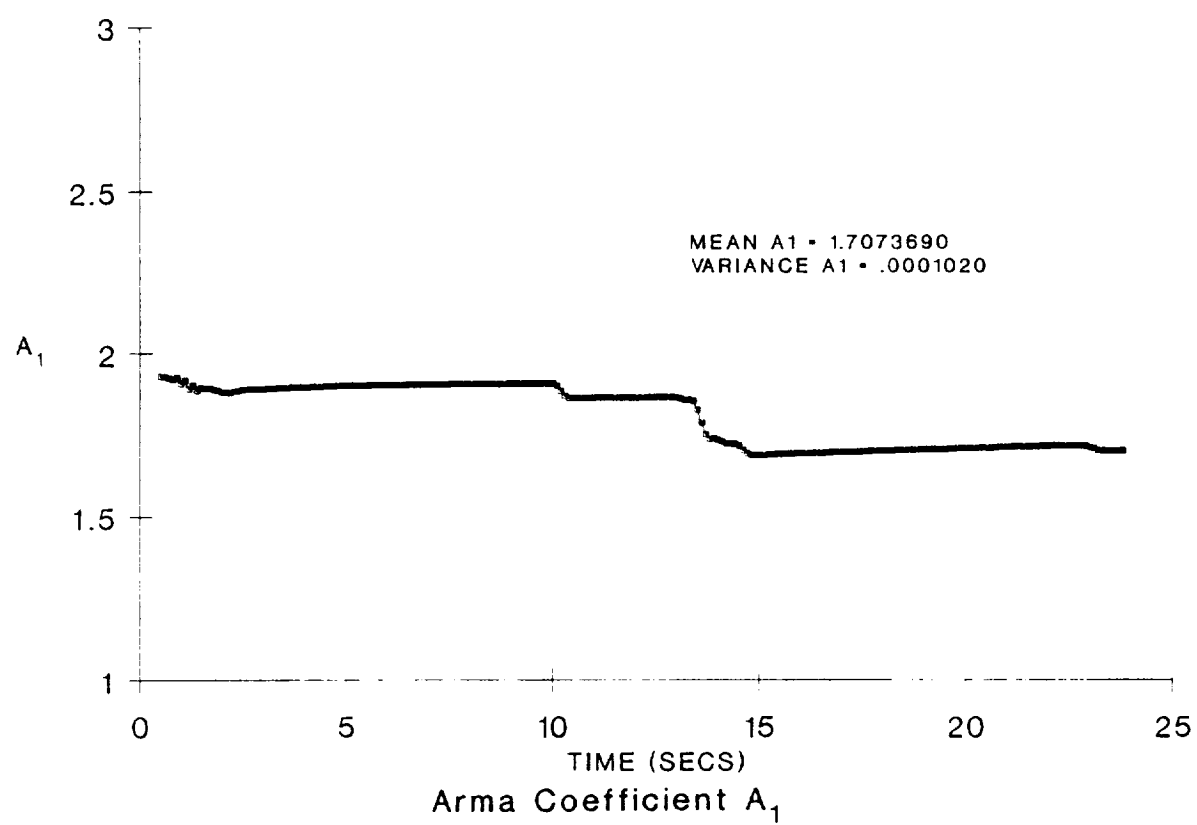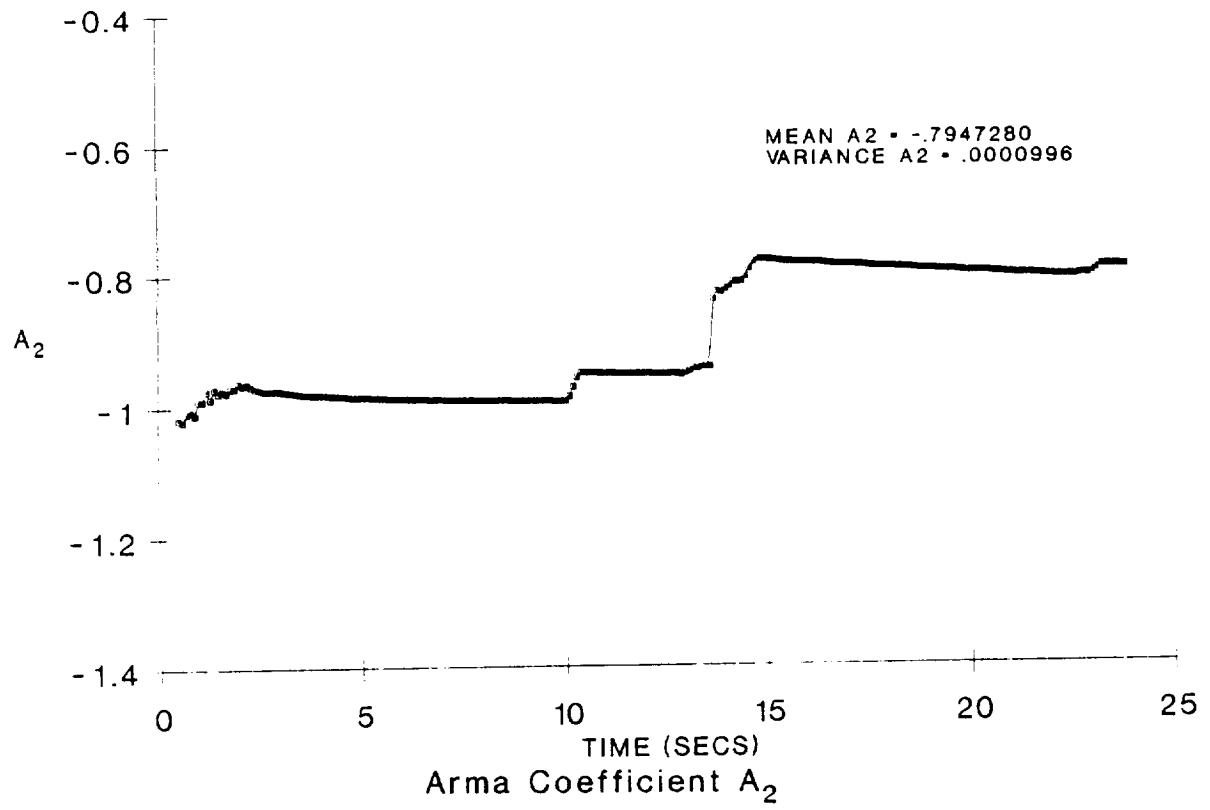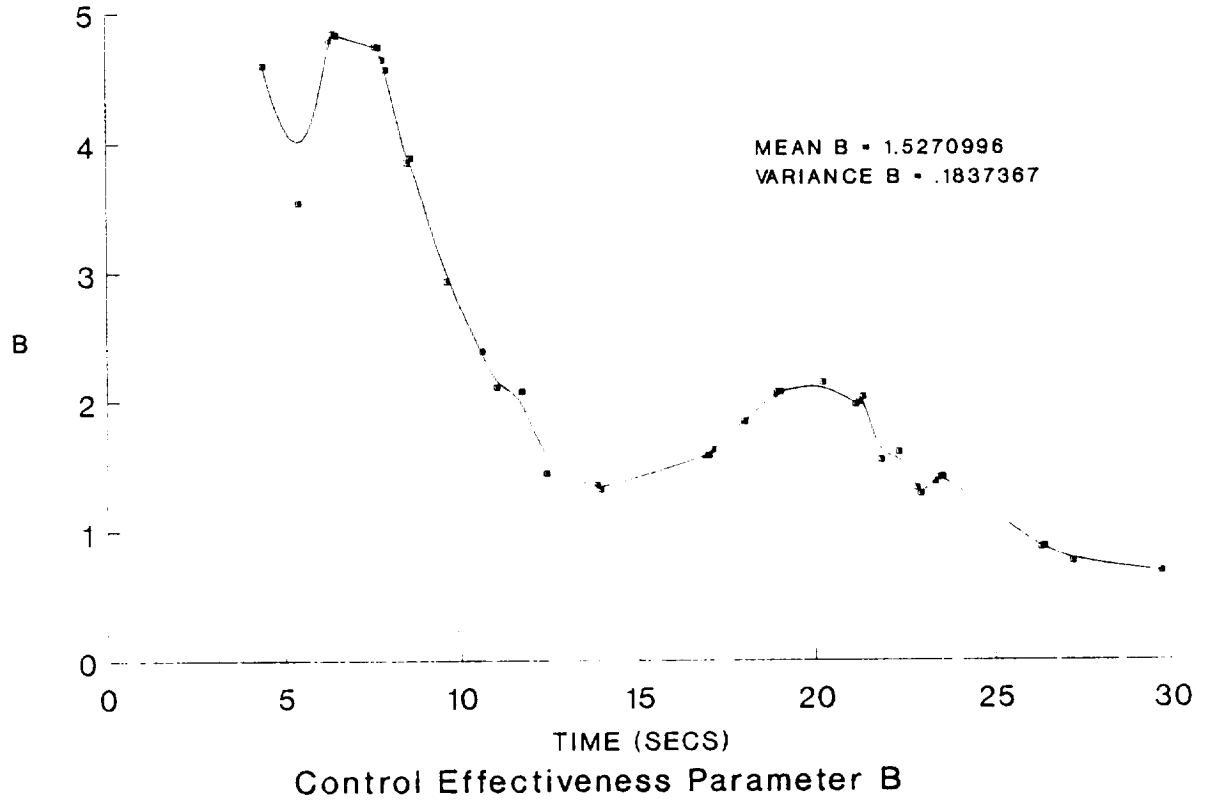
Figure 10

Table 1

Test Parameters

TEST #	REACTION TORQUE WHEEL	MODE	EXCITATION TIME (SECS)	FREQUENCY (Hz)	AMPLITUDE	FREE DECAY TIME (SECS)	SAMPLE INTERVAL (SECS)
1	X-AXIS	1	30	0.4401	20	60	0.1
2	Y-AXIS	1	30	0.4401	20	60	0.1
3	Z-AXIS	1	30	0.4401	20	60	0.1
4	X-AXIS	2	30	0.4764	20	60	0.1
5	Y-AXIS	2	30	0.4764	20	60	0.1
6	Z-AXIS	2	30	0.4764	20	60	0.1

Table 2

Experimental Identification Results

TEST #	REACTION TORQUE WHEEL	MODE	a_1	a_2	GRAPH FREQ (Hz)	LSE FREQ (Hz)	ζ	b_{TW}
1	X-AXIS	1	1.5235475	-0.6120654	0.44715	0.5351800	0.7299576	-5.5898004
2	Y-AXIS	1	1.6931082	-0.7789838	0.44715	0.4978276	0.3992480	0.0080636
3	Z-AXIS	1	1.5868783	-0.6751711	0.44715	0.5223736	0.5983680	-0.8804742
4	X-AXIS	2	1.8732456	-0.6641920	0.46218	0.5164785	0.4766312	0.6327561
5	Y-AXIS	2	1.7073690	-0.7947280	0.46218	0.4997192	0.3658724	1.5270996
6	Z-AXIS	2	1.6953652	-0.7836996	0.46610	0.5042274	0.3846554	-1.4330764

261

A Case Study in Nonlinear Dynamics and Control of Articulated Spacecraft: The Space Station Freedom with a Mobile Remote Manipulator System*

William H. Bennett   Harry G. Kwatny
Chris LaVigna   Gilmer Blankenship

Techno-Sciences, Inc.

Outline

1. Modeling of Articulated Spacecraft as Multi-Flex-Body Systems

2. Nonlinear Attitude Control by Adaptive Partial Feedback Linearizing (PFL) Control

3. Attitude Dynamics & Control for SSF/MRMS

4. Performance Analysis Results for Attitude Control of SSF/MRMS

5. Conclusions

r- 18

Nonlinear Control Design Approach for SSF/MRMS

- Modeling: Attitude Pointing Dynamics of Multi-Flex-Body Systems:
  Hamilton's Principle

- Attitude Control Decoupling/Linearizing Control by Nonlinear Feedback:
  Partial Feedback Linearization

- Adaptive Control: Modified Model Reference Adaptive Control (MRAC):
  Enhance Decoupling and PFL Robustness

- CSI: Keel flexure and MRMS motion results in nonlinear inertial couplings which effect
  attitude control on short time scale

This study addresses attitude control of the SSF with MRMS motion and considers nonlinear dynamic instabilities not previously considered in the work of Mah et al, Automatica 1989 and Wie et al, AIAA GNC 1990. Stability issues considered in these previous works concentrated on the slow time scale disturbance rejection of gravity gradient and cyclic aerodynamic torques on the time scale of the orbital period. This study addresses control of short time scale dynamic instability due to nonlinear inertia coupling which arises due to keel flexure and MRMS motion. The study addressed the following points:

1. Nonlinear inertia coupling due to keel flexure seriously constrains the stabilization of SSF attitude via linear control methods.

2. Feedback Linearization for Attitude Control and MRMS decoupling can achieve precision stabilization subject to limitations of: control authority, actuator bandwidth, and model uncertainty.

3. MRAC based on nonlinear design model with explicit parameter dependence can be effective for stabilization of SSF attitude with uncertain keel stiffness.

Work reported here in modeling and control design builds on previous work reported in:

1. Baillieul & Levi (1987) Physica D

2. Bennett, Kwatny, & Dwyer (1988) AFOSR Technical Report TSI-TR-88-07

262

Lagrangian Dynamics for Mixed LPS/DPS

1. identify configuration space (generalized coordinates)

$$q \in \mathcal{M} \quad \dot{q} \in T_q \mathcal{M}$$

□ choose DPS coordinates to eliminate $\mathcal{G}$ geometric B.C.'s

2. Hamilton's principle: motion is natural if:

$$\int_{t_1}^{t_2} (\delta L + Q^T \delta q) dt = 0$$

System Lagrangian: $L(q, \dot{q}) : \mathcal{M} \times T_q \mathcal{M} \rightarrow \mathcal{R}$ obtains $\mathcal{N} = \{\text{natural B.C.'s}\}$, or

3. solve Euler-Lagrange Eqns.

$$\frac{d}{dt} \frac{\partial L}{\partial \dot{q}_i} - \frac{\partial L}{\partial q_i} = Q_i$$

subject to B.C.'s , $\mathcal{B} = \mathcal{G} \cup \mathcal{N}$.

The approach followed in this study for model construction utilizes quasi-coordinates and generalized Lagrange equations often referred to as Poincare equations. The method includes explicit construction of Finite Element Methods (FEM) for flexure and spatial recursive construction of Multi-Body systems introduced by Rodriguez and Jain (1991) AIAA GNC.

The formalism of Lagrangian dynamics proceeds by identification of configuration space in terms of generalized coordinates and their velocities. Hamilton's principle identifies the natural motion as the solution of a variational problem. If the coordinates are independent then the usual Euler-Lagrange equations result. If the coordinate variations are constrained (e.g. nonholonomic systems) then the d'Alembert-Lagrange equations apply (Neimark & Fufaev 1972).

Lagrangian Dynamics for Mixed LPS/DPS

we say $v \in H^p$ if $\|v\|_p^2 = \int_0^\ell |D^p v|^2 + \cdots + |v|^2 \, dz < \infty$

$v \in H_{\mathcal{G}}^p$ satisfies B.C.'s up to p^{th} order

1. Hamilton's Principle $\Rightarrow$ "weak" (distributional) solutions in $H_{\mathcal{G}}^p$

2. Euler-Lagrange Eqns. $\Rightarrow$ "strong" (pointwise) solutions in $H_{\mathcal{B}}^{2p}$

Finite Dimensional Modeling and FEM Approximations:

- Approximate weak solutions by discretization of Lagrangian and apply Hamilton's Principle

- We use collocation by splines for FEM approximation

The extension of the Lagrangian approach to mixed Lumped Parameter and Distributed Parameter Systems arising in Multi-Flex-Body systems involves reduction based on Finite Element Methods. Our approach utilizes splines for construction of the elements with continuity requirements at knots consistent with the variational problem.

Lagrange's Equations using Quasi-Velocities

Given configuration space $q \in \mathcal{M}$. Consider *quasi-velocities* p such that

$$\dot{q} = V(q)p = [v_1, v_2, \ldots, v_m]p$$
$$p = U(q)\dot{q} = [u_1, u_2, \ldots, u_m]\dot{q}$$

□ generally not related to valid set of coordinates $\dot{\pi} = p$ unless

$$\delta\pi = U(q)dq$$

is an exact differential

□ Hamilton's principle applied to Lagrangian in quasi-velocities $\tilde{L}(q,p) = L(q,\dot{q})$
Poincare equations (Arnold et al 1988)

$$p^t \frac{\partial^2 \tilde{L}}{\partial p^2} = -p^t V^t(q) \frac{\partial^2 \tilde{L}}{\partial q^t \partial p} + \sum_{j=1}^{m} p_j \frac{\partial \tilde{L}}{\partial p} U X_j + \frac{\partial \tilde{L}}{\partial q} V + Q^t V$$

$$X_j = [[v_j, v_1][v_j, v_2] \ldots [v_j, v_m]] \qquad w/\ j = 1, \ldots, m$$

$$\text{commutators:} \quad [v_i, v_j] = \sum_{k=1}^{m} c_{ij}^k(q) v_k$$

□ v_j form right invariant vector field on of Lie group G associated with $\mathcal{M}$
□ If $\mathcal{M}$ is Lie group and v_i are independent, then c_{ij}^k are independent of q

Poincare equations are related to Boltzman-Hamel equations and Caplygin's equations in quasi-coordinates. The use of quasi-velocities extends Lagrangian framework to nonholonomic systems. Poincare equations together with the quasi-velocity definition form a system of first order ODE's describing the equations of motion for the N-body model.

1. Quasi-velocities are not time derivatives of physically significant coordinates.

2. Formulation of Poincare equations considered here is also related to the constructive methods of Kane.

3. The modeling approach has also been applied to much simpler prototype spacecraft attitude slewing of the SCOLE model in Bennett, Kwatny, LaVigna 1991 ASME.

Structure of Poincare's Equations in Quasi-Velocities

Kinetic Energy:

$$\tilde{T}(q,p) = p^t \mathcal{M}(q)p$$

$$\mathcal{M}(q)\dot{p} + C(q,p)p + \mathcal{F}(q) = Q_p$$

where

$$C(q,p) := -\left[\frac{\partial[\mathcal{M}p]}{\partial q}V\right]p + \frac{1}{2}\left[\frac{\partial[\mathcal{M}p]}{\partial q}V\right]^t p + \sum_{j=1}^{m} p_j X_j^t U^t \mathcal{M}$$

$$\mathcal{F}(q) := V^t(q)\frac{\partial V(q)}{\partial q^t}$$

Potential Energy: $V(q)$

Generalized Forces in p-frame:
(often convenient when quasi-velocities are referenced to body frame)

$$Q_p := V^t(q)Q$$

Lagrangian formalism provides an explicit construction of the system dynamic coefficients. The transformation of the generalized forces to the p-frame defined by the quasi-velocities is more convenient for the actuator command frame. The construction facilitates the definition of nonlinear control laws which include explicit model parameter dependence. This is useful for evaluating tradeoffs in gain scheduled vs. adaptive control implementations.

266

Conventional Linearization by Taylor Expansion

- conventional linearization by Taylor expansion is valid in the neighborhood of an equilibrium (when $\dot{q} = 0$ and $\eta = 0$)

- assume $p = 0$, then equilibrium configuration is: $\mathcal{F}(q) = \mathcal{Q}_p$

<u>Linear Perturbation Dynamics:</u>

$$\dot{q} = V(0)p$$

$$\mathcal{M}(0)\dot{p} + \mathcal{C}(0,0)p + \frac{\partial \mathcal{F}}{\partial q}(0) = \triangle \mathcal{Q}_p$$

Conventional Linear Control Design Methods:

- fixed gain control limited to neighborhood of equilibrium

- extension to gain scheduled designs is ad hoc

System equilibria can be identified for the case of constant generalized forces defined in the p-frame. Then conventional methods for identification of linear models proceed by Taylor expansion. Note that dynamical changes in configuration such as deployment of appendages, articulation of robot arms, etc. do not necessarily involve motions relative to a well defined equilibrium.

Partial Feedback Linearization attempts to impose an I/O linear with reference to a nominal system model. Explicit model construction for PFL provides explicit control dependence on parametric model uncertainty.

267

Recursive Formulation for Serial Chain of Bodies

$$V_c := \begin{pmatrix} \omega \\ v_c \end{pmatrix} \quad \begin{array}{l} \text{angular velocity} \\ \text{translation} \end{array}$$

r_{co} — location of C in frame at O

$$V_c = \phi(r_{co})V_o$$

$$\phi(r_{co}) = \begin{bmatrix} I & 0 \\ -\widetilde{r_{co}} & I \end{bmatrix}$$

Serial Chain of Bodies

Serial Chain of Bodies
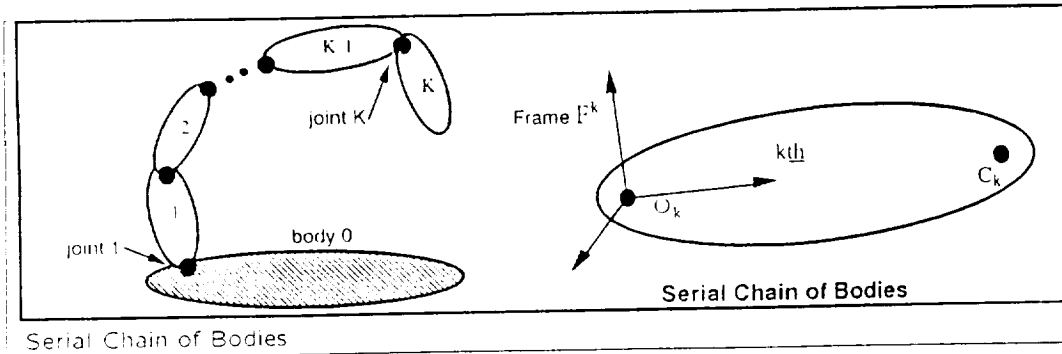
Joint parameters: σ_k of dimension n_k
quasi-velocities: $\beta(k)$

$$\dot{\sigma}_k = \Sigma_k(\sigma_k)\beta(k)$$

$$V_{o_k} - V_{c_{k-1}} = H(k)\beta(k)$$

Recursive Formulation for Serial Chain of Bodies

Notation

$I_{cg}(k)$ -inertia tensor about CG
$m(k)$ -mass
$a(k)$ -location O in k-frame
$M_{cg}(k)$-spatial inertia about CG
$M_o(k)$ -spatial inertia tensor about O

$$M_{cg}(k) = \begin{bmatrix} I_{cg} & 0 \\ 0 & mI \end{bmatrix}$$

$$M_o(k) = \phi^*(a)M_{cg}\phi(a)$$

- Coordinate free recursion (Jain & Rodriguez 1990)

$$V(k) = \phi(r_{co}(k-1))V(k-1) + H(k)\beta(k)$$

Chain model: (constructed from convenient choice of coordinates)
spatial velocity: $V := [V^t(1)\ldots V^t(K)]^t$
joint quasi-velocity: $\beta := [\beta^t(1)\ldots\beta^t(K)]^t$

$$V = \Phi H\beta$$

$$\Phi := \begin{bmatrix} I & & \cdots & 0 \\ \phi(2,1) & I & \cdots & 0 \\ \vdots & & \ddots & 0 \\ \phi(K,1) & \phi(K,2) & \cdots & I \end{bmatrix} \qquad H = \begin{bmatrix} H(1) & & \\ & \ddots & \\ & & H(K) \end{bmatrix}$$

Chain Kinetic Energy: K. E.$_{chain} = \frac{1}{2}\beta^t\mathcal{M}\beta$
in terms of
Chain inertia matrix: $\mathcal{M} = H^*\Phi^*\text{diag}\{M_o(1)\ldots M_o(K)\}\Phi H$

Model Formulation with Sliding 1-DOF Joints with Elastic Bodies

Sliding Joint: 1 DOF relative motion along path $\mathcal{P}$ defined in $k - 1$-frame

- $\mathcal{P}$ defined by map $\gamma : \mathfrak{R} \to \mathfrak{R}^3$ as image of $\epsilon \in [\epsilon_0, \epsilon_1]$

Frame Γ^k

Frame $\mathcal{F}^k$

kth body

C_k

deformed

Frame Γ^k

O_k

undeformed

kth body

C_k

**Sliding Joint configuration
for flexible bodies**

O_k
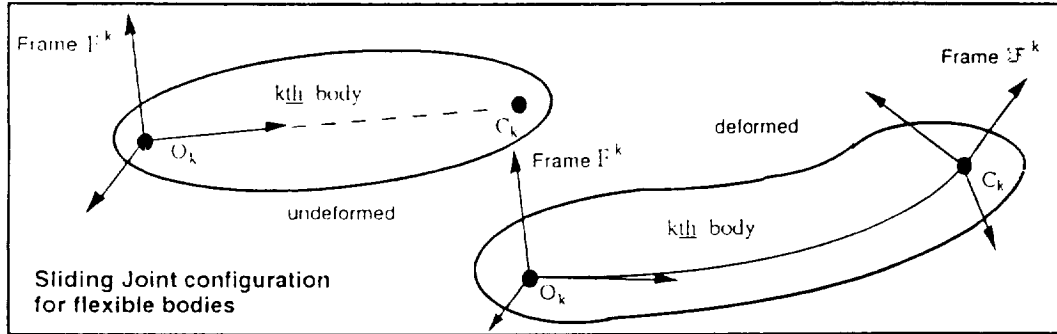
Model Formulation with Sliding 1-DOF Joints

- relative velocity of point P on path $\mathcal{P}$ wrt $(k - 1)$-frame $\mathcal{F}^{k-1}$:

$$v_p^{k-1} = \frac{\partial \gamma}{\partial \epsilon} \dot{\epsilon}$$

inertial velocity of P

$$v_p^{k-1} = v_p^{k-1}(k-1) - \widetilde{[\gamma]} \, \omega^{k-1}(k-1) + \frac{\partial \gamma}{\partial \epsilon} \dot{\epsilon}$$

- $\dot{\epsilon}$ single DOF translational quasi-velocity $\beta(k)$ such that spatial velocity has the form:

$$V^k(k) = \phi(\gamma^{k-1}(\epsilon)) V^{k-1}(k-1) + H^k(k)\beta^k(k)$$

with

$$H^k(k) := \begin{bmatrix} 0_{3\times1} \\ \partial\gamma/\partial\epsilon \end{bmatrix} \qquad \beta^k(k) := \dot{\epsilon}$$

The recursive construction for chains of bodies with revolute joints can be extended to include sliding joints (such as the Mobile Remote Manipulator System) by defining the velocities relative to the joint path constraint defined in a local body fixed frame. The recursive construction for elastic bodies can be established by defining a local body frame fixed at the preceeding joint. Elastic deformations are assumed small in the local body frame but can contribute to large motions in the system inertia frame. Such dynamics can be highly nonlinear.

Dynamic Decoupling & PFL for Multi-Flex-Body Systems

Coordinate partitioning:

$$q = \begin{pmatrix} \xi \\ u \end{pmatrix} \quad \leftarrow \text{body attitude}$$

Quasi-velocities:

$$p = \begin{pmatrix} \omega \\ v \end{pmatrix} \quad \leftarrow \text{body rates}$$

τ — control torques applied to main body

Multi-Flex-Body Model: Poincare equations:

$$\begin{aligned}
\dot{\xi} &= \Gamma(\xi)\omega \\
\dot{u} &= \Sigma(\xi, u)v \\
M_\omega \dot{\omega} + N\dot{v} + F_\omega &= G_\omega \tau \\
N^t \dot{\omega} + M_v \dot{v} + F_v &= G_v \tau
\end{aligned}$$

☐ PFL (decoupling) Control Law: $\tau = \mathcal{A}(\xi, \omega, u, v) + \mathcal{B}(\xi, \omega, u, v)\alpha$
such that in closed loop α is commanded attitude accelerations

$$\ddot{\xi} = \alpha$$

Fact: exact system attitude PFL using torques referenced to the principal body frame; i.e.,
$G_\omega = I, G_v = 0$

$$\begin{aligned}
\mathcal{A} &= F_\omega - N M_v^{-1} F_v + [N M_v^{-1} B^t - M_\omega]\Gamma^{-1}\frac{\partial \Gamma_\omega}{\partial \xi}\Gamma_\omega \\
\mathcal{B} &= [M_\omega - N M_v^{-1} N^t]\Gamma^{-1}
\end{aligned}$$

For multi-DOF revolute joints the angular coordinates can be expressed using Euler angles, quaternions, or Gibbs parameters. Choice is significant for computational complexity and numerical stability of inverse transformation for PFL.

PFL attitude control achieves decoupling of keel flexure, rigid body translational modes, and MRMS motions from attitude dynamics. Moreover this is achieved consistently with nonlinear large angle motions of multi-body articulation.

For application to decoupling of the MRMS motions from the SSF the PFL control is parametrized by the MRMS motions. Thus the attitude regulation includes direct feedforward of the MRMS motion. This is a form of gain scheduling using nonlinear models.

Construction of the inertia matrix using quasi-velocities based on the spatial chain recursion together with the assumption of small deformations in the local body frame simplifies the form inertia matrix to be inverted for PFL. The simplification for on-line PFL is related to the efficiency of the order-n recursions currently in use for efficient simulation of multi-body dynamics. Note the construction works for implementation of nonlinear PFL control laws.

270

Design Considerations for PFL Attitude Control for SSF/MRMS

Performance Objectives:

- Achieve Decoupling of Independent Axis Attitude for Slewing/Pointing Control

- Achieve Decoupling of Flexible Interactions From Primary System Attitude Pointing

- Decouple sensitivity to MRMS motions

- Decouple design of active structural control (smart structures) from principal body attitude control

Practical Limitations

- Requires Additional Control Authority to Achieve Nonlinear Compensation

- Compensation Based on Nominal Design Model

SSF/MRMS System Configuration
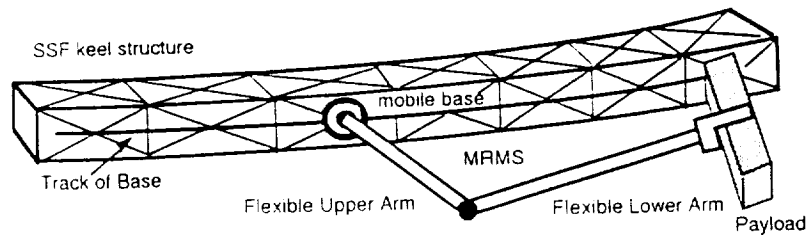
System Physical Data

Body	length (m)	mass (kg)	inertia	cg location (m)	keel beam parameters	
space station	110	211,258	$J_x=2.13\times10^8$ $J_y=2.13\times10^8$ $J_z=880,241.6$	$x=55$ $y=55$ $z=55$	material density	7.860×10^3 [kg/m²]
mobile base	1.5	316.9	$J_x=178.25$ $J_y=178.25$ $J_z=356.5$	$x=0$ $y=0$ $z=0$	elastic modulus	200×10^8 N/m²
upper arm	14.3	3169	$J_x=54,002$ $J_y=54,002$ $J_z=0$	$x=0$ $y=0$ $z=7.15$	shear modulus	79×10^8 N/m²
lower arm	14.3	3169	$J_x=54,002$ $J_y=54,002$ $J_z=0$	$x=0$ $y=0$ $z=7.15$		

The simplified SSF/MRMS model includes four articulated bodies: 1) SSF keel, 2) MRMS base, 3) inner MRMS arm, 4) outer MRMS arm. Each joint is 1 DOF. Bodies 1 and 2 are connected by a sliding joint. The SSF/MRMS is modeled based on physical data taken from Mah, et al. Automatica, 1989. The SSF keel is modeled as a uniform beam with a 5m square cross section. The FEM model for the beam is reduced from Timoshenko assumptions with finite elements constructed from splines. Using 2 elements with 5 DOF. Simulations were conducted on a reduced model with 4 DOF to eliminate fast time scale effects beyond the control bandwidth. The joint velocities and SSF body rates are chosen as quasi-velocities.

Control Laws:

- PFL SSF Attitude Decoupling

- SSF Attitude Decoupling based on linearized equations of motion

- Parameter Adaptive PFL SSF Attitude Decoupling (SSF keel stiffness estimated)

Maneuvers:

- 3 axis simultaneous attitude maneuver of 0.5 rad (Euler angles)

- MRMS 3 simultaneous 1 DOF joint motions
  (translation equivalent to 18m in 60 sec)

Simulated performance evaluation of SSF attitude control with MRMS decoupling was performed for three control law variations including: nonlinear PFL, a linear decoupling control law, and MRAC modified nonlinear PFL control. The maneuvers considered were aggressive enough to differentiate the results.

MRAC PFL Attitude Decoupling Control for SSF/MRMS

ω – body rates
ξ – attitude coordinates
u - MRMS joint & elastic coordinates
ϑ – SSF keel stiffness
τ – SSF attitude control torque
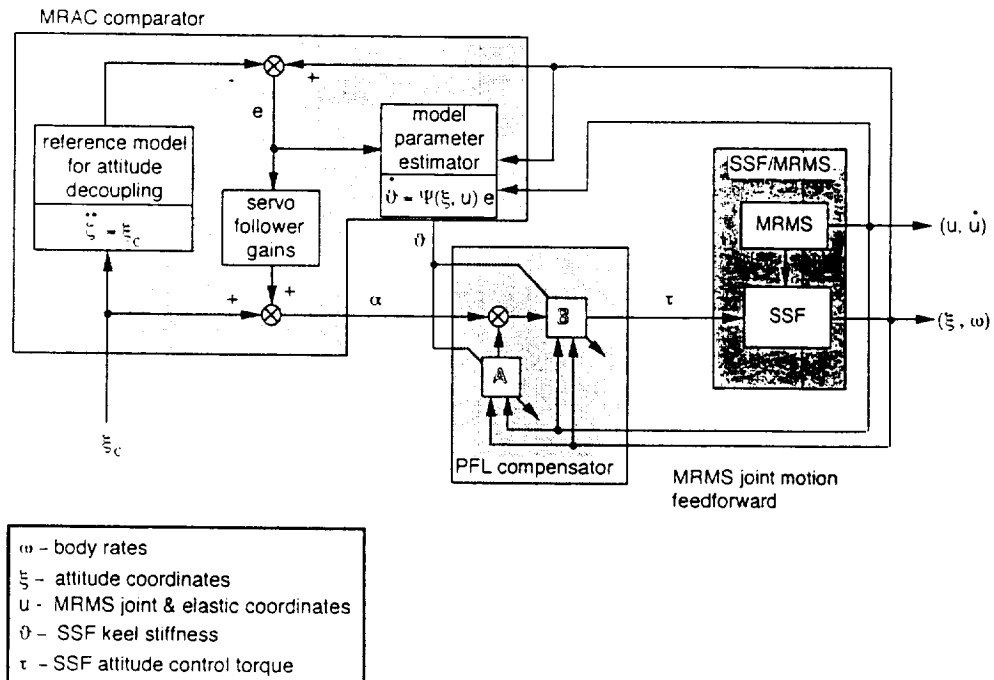
Tradeoff Studies for PFL Attitude Control for SSF/MRMS

1. Nonlinear coupling due to keel flexure in attitude control:
   Nominal (precision model-based) PFL for attitude maneuver compared with Linear, fixed-gain, decoupling control

   - MRMS feedforward accounted in both designs

   - nonlinear inertia variations due to keel flexure limit domain of attraction in linear design

2. PFL robustness to SSF keel stiffness uncertainty

   - marginally stable slew response with 5% uncertainty (reduction) in keel stiffness

   - robustness limited by (active/passive) damping of keel flexure

3. Robustness of PFL attitude control w/ MRAC correction for keel stiffness

   - improved slew response with 10% uncertainty (reduction) in keel stiffness

   - marginal slew response with 20% reduction in keel stiffness

   - guarantee of stability margin in keel flexure response with MRAC is difficult without active structure control

SSF/MRMS Scaling of Control Gains

- Control gains chosen for Decoupled Attitude Linear Dynamics

System Eigenvalues

Open Loop	Closed Loop Nominal (k)	Closed Loop Detuned (k/8)
0	0	0
0	0	0
0	0	0
0	0	0
0	0	0
0	0	0
0^2	-0.1763 ± 3.3205i	-0.1763 ± 3.3205i
0^2	-0.1763 ± 3.3205i	-0.1763 ± 3.3205i
0^2	-0.1364 ± 1.6505i	-0.1364 ± 1.6505i
	-0.1364 ± 1.6505i	-0.1364 ± 1.6505i
-10.4212 ±10.5963i	-0.2000 ± 0.2040i	-0.0250 ± 0.0979i
-10.8762 ±10.5876i	-0.2000 ± 0.2040i	-0.0250 ± 0.0979i
-0.2053 ± 3.3267i	-0.2000 ± 0.2040i	-0.0250 ± 0.0979i
-0.2053 ± 3.3290i		

- Linear controller effective for .01 rad slewing with Detuned Gains

274

SSF/MRMS Attitude Slew with Precision PFL & MRMS Decoupling

PFL with MRMS motion - regulator gains: (-0.8,-0.1632)

SSF/MRMS PFL attitude control nominal response for 3-body maneuver
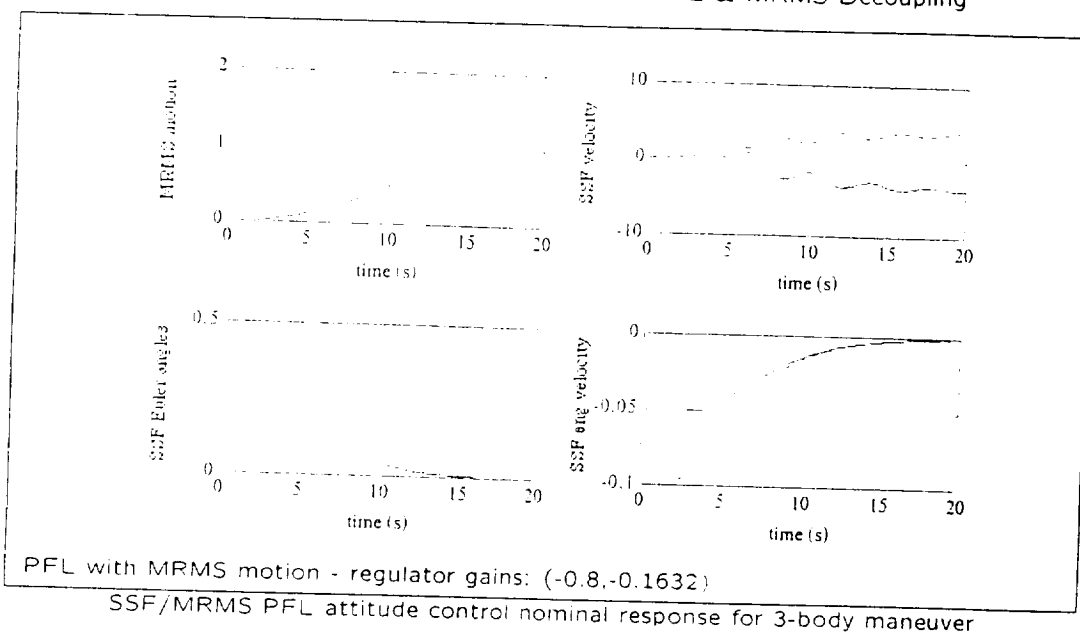
SSF/MRMS Attitude Slew with Precision PFL & MRMS Decoupling
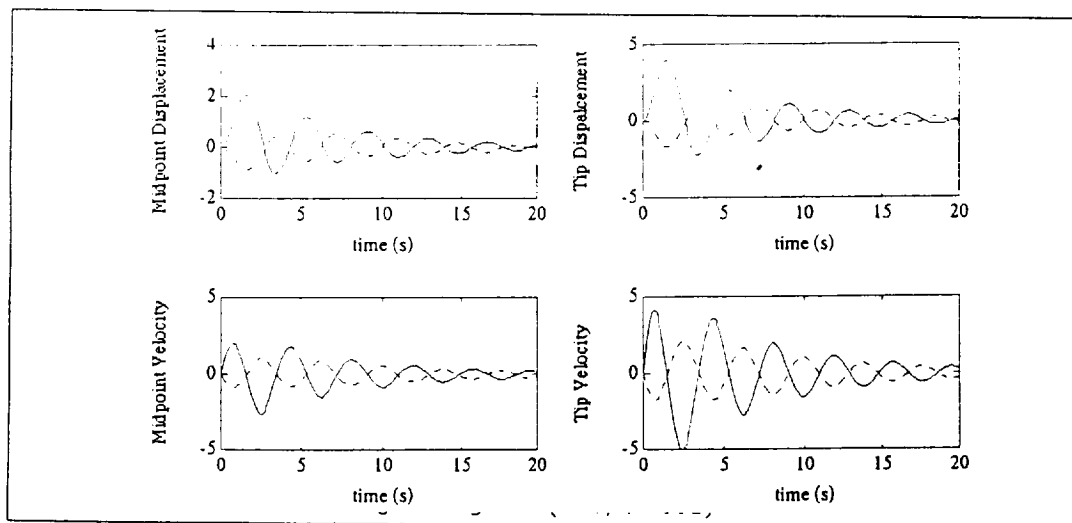
SSF Keel Flexure Response with nominal maneuver

SSF/MRMS PFL Attitude Slew with 5% Keel Stiffness Reduction
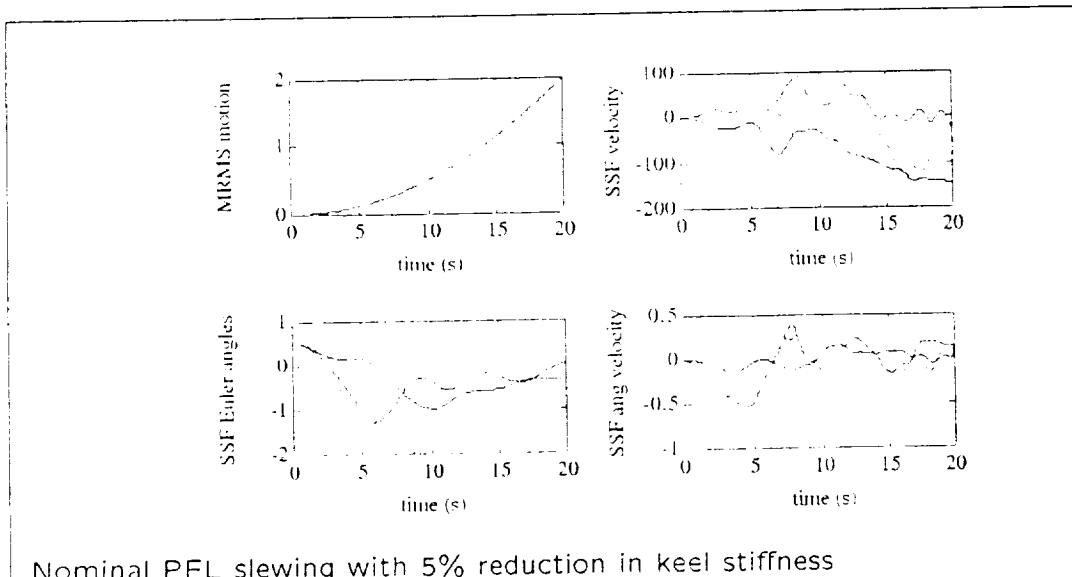
Nominal PFL slewing with 5% reduction in keel stiffness

SSF/MRMS response degradation is evident for nominal PFL attitude control

SSF/MRMS Attitude Slew with MRAC PFL & MRMS Decoupling

MRAC estimation of keel stiffness recovers nominal slew performance
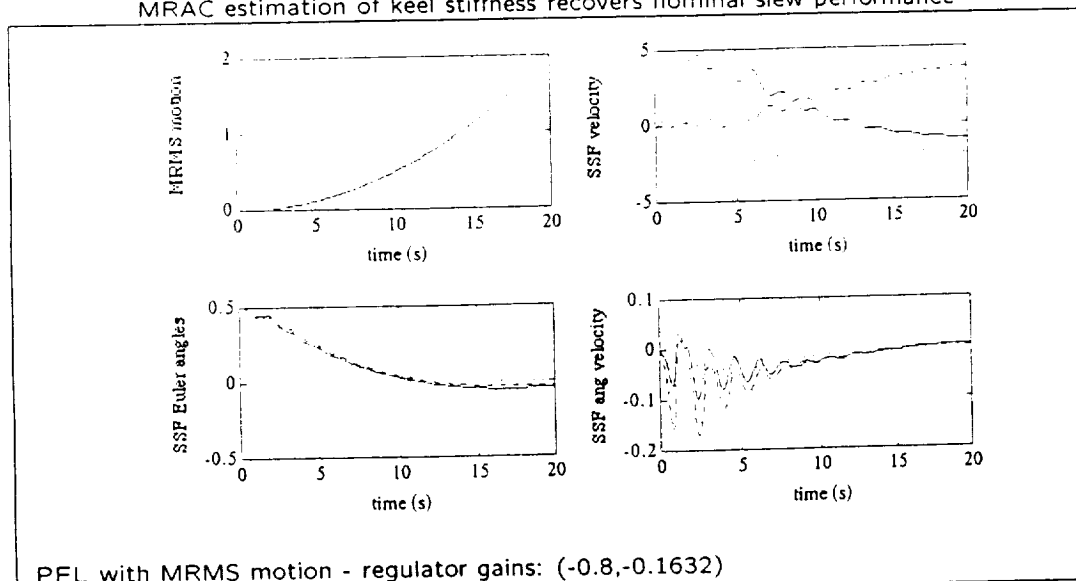
PFL with MRMS motion - regulator gains: (-0.8,-0.1632)

10% reduction in keel stiffness wrt nominal value for PFL t=0

SSF/MRMS Keel Flexure with MRAC PFL & MRMS Decoupling

PFL MRAC obtains stable response in keel flexure
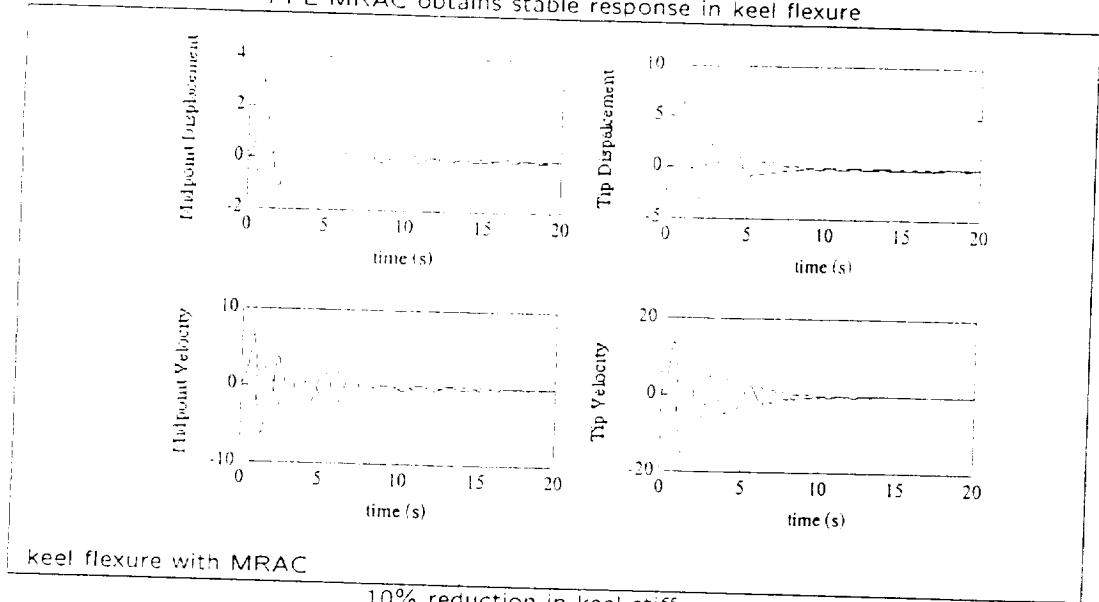
keel flexure with MRAC

10% reduction in keel stiffness

Conclusions from Simulations

Observations from SSF/MRMS Modeling:

- Keel flexibility drastically alters nonlinear inertial coupling in attitude maneuvers

- MRMS motion exacerbates nonlinear inertial coupling

Control Law Comparsions:

- linear, fixed-gain control can achieve stabilization of small amplitude SSF attitude motions on a slow time scale
  - stability robustness limitation is not evident from linear model
  - domain of attraction is limited for fast time scale attitude regulation

- linear, fixed-gain, decoupling control demonstrates extreme sensitivity to MRMS motions & model uncertainty

- PFL stability sensitive to keel stiffness parameters
  5 % reduction in keel stiffness results in oscillations with magnitude on order of length of keel

- Adaptive PFL attitude maneuver control with extreme MRMS multi-DOF motions demonstrated tolerance to initial model uncertainty of up to 10% reduction in keel stiffness

The SSF/MRMS system model predicts a significant elastic deformation response of SSF keel during attitude slewing transients. This leads to large motions in the inertial frame although the beam model assumes small relative displacements in local body frames. The result is significant nonlinear cross axis coupling during attitude maneuvers. For short time scale attitude control of the SSF/MRMS system the significance of the nonlinear inertia coupling due to keel flexure appears more significant than MRMS motion sensitivity—even for drastic, worst-case maneuvers considered in this study.

The robustness and performance limits observed in the linear, decoupling attitude control law appear to arise from a vanishingly small domain of attraction for fast time scale attitude regulation. The tradeoff of attitude control gains vs. domain of attraction cannot be predicted from linear models alone.

PFL decoupling attitude control offers a direct design approach including feedforward of MRMS motions which compensates for predictable inertia changes due to keel deformation. PFL attitude control sensitivity to keel stiffness uncertainty is improved over linear decoupling control. Performance and bandwidth limits in PFL design are traded off against stability of the decoupled dynamics (keel flexure dissipation).

Parameter adaptive methods based on MRAC underlie practical application of nonlinear decoupling control designs where model uncertainty is due to unmeasureable parameter variation.

278

a-4.

AN OVERVIEW OF RECENT ADVANCES IN SYSTEM IDENTIFICATION

Jer-Nan Juang [*]
NASA Langley Research Center
Hampton, Virginia 23681

ABSTRACT

This paper presents an overview of the recent advances in system identification for modal testing and control of large flexible structures. Several techniques are discussed including the Observer/Kalman Filter Identification, the Observer/Controller Identification and the State-Space System Identification in the Frequency Domain. The System/Observer/Controller Toolbox developed at NASA Langley Research Center is used to show the applications of these techniques to real aerospace structures such as the Hubble spacecraft telescope and the active flexible aircraft wing.

INTRODUCTION

Since the mid-sixties the field of system identification has been an important discipline with the automatic control area.[1] One reason is the requirement that mathematical models within a specified accuracy must be used to apply modern control methods. Another reason is the availability of digital computers which can perform complex computations. Since then, there are a multitude of approaches, perspectives and techniques to be used for system identification. Most techniques are found very useful for application to the electrical engineering problems. Nevertheless, most techniques do have difficulties in application to other areas such as the large aerospace structures which can only be accurately described by a large-size model with the dimension in the order of hundreds. In addition, most large aerospace structures possess significant uncertainties and nonlinearities which make system identification even more difficult, if not impossible.

In aerospace structures, there are basically three types of identification work, namely modal parameter identification, structural-model parameter identification and control-model identification. All three types of identification are important technology areas and they have different principal objectives and histories of development. The modal parameter identification and structural-model parameter identification are used in structural engineering whereas the control-model identification is used in control of flexible structures.

In this paper, we will focus on the modal parame-

---

[*]Principal Scientist, Spacecraft Dynamics Branch

ter identification and the control-model identification. Modal parameter identification, which is generally referred to as modal testing in the field of structures, means the process of measuring signals produced by a structure and identifying modal parameters (i.e., damping, frequencies, mode shapes and modal participation factors). System identification in the field of controls means the process of measuring signals produced by a system and building a control-model to represent the system for control design. If the identified model is a linear model in state space representation, the eigensolution of the model provides eigenvalues and eigenvectors which in turn determine modal parameters for structures. Correlation between the fields of modal testing and system identification for controls is evident.

In the past decade, many system identification techniques were developed and/or applied to identify a state space model for modal parameter identification of large flexible structures. The identified state space model is also used in controller design. Many satisfactory results were reported in the literature.[2,3] Most techniques are based on sampled pulse or impulse system response histories which are known as Markov parameters. The usual practice uses the Fast Fourier Transforms (FFT) of the inputs and measured outputs to compute the sampled pulse response histories. The discrete nature of the FFT causes one to obtain pulse response rather than impulse response, and a somewhat rich input is required to prevent numerical ill-conditioning in the computation. Another approach is to solve directly in the time domain for the Markov parameters from the input and output data. The drawbacks of this method include the need to invert an input matrix which necessarily becomes particularly large for lightly damped systems.[4]

Recently, a method has been developed to compute the Markov parameters of a linear system, which are the same as its pulse response history.[5-12] The method, referred to as the Observer/Kalman Filter Identification algorithm (OKID) is formulated entirely in the time domain, and is capable of handling general response data. A fundamental difference in this approach is the introduction of an observer in the identification equations. This makes identification possi-

ble for not only the open-loop system, but also an associated observer which can be later used in controller design. Depending on the noise characteristics, the method identifies a deadbeat observer which is the fastest possible observer in the absence of noises, or a Kalman filter which is an optimal observer in the presence of noises, or any other observer with user specified poles. The method has been successfully applied to identification of real systems, including a linear model of the space shuttle remote manipulator based on a non-linear simulation code,[13] and the Hubble space telescope.[14]

An important extension of the above OKID method is the identification of closed-loop systems. There are several instances when such a need arises. The system may be operating in closed-loop and only closed-loop data is available for identification. An open-loop model of the system may be required to be identified from closed-loop data for the purpose of structural analysis or controller re-design. Certain systems such as an aircraft under the flutter condition are inherently unstable. For such systems, it may not be desirable or even possible to remove the existing feedback control system to perform open-loop identification. For the case where the existing controller dynamics is assumed to be unknown, a method was developed in Ref. 15, referred to as the Observer/Controller Identification algorithm (OCID), to identify an open-loop model, and an effective observer/controller combination. The case where the closed-loop system does not possess a full state feedback structure, but rather a controller with known output feedback dynamics, is treated in a separate paper.[16] The mathematical formulations for the two cases are entirely different since the former case deals with known feedback control signals, whereas the latter case deals with known feedback controller dynamics.

It has been found that the OKID method can effectively identify the state space models using time domain input-output data. However, there are cases in which frequency response data, rather than time histories, are available. This is often the case with the advent of sophisticated spectrum analyzers and associated automatic test equipment. Therefore, the technique of obtaining state space models from frequency response data is of practical interest. Classically, the Inverse Discrete Fourier Transform method (IDFT) is used to transform the frequency response data to time domain data, that is, to transform the frequency response function (FRF) of the system to its pulse response. The pulse response of discrete-time systems is also known as the Markov parameters. The disadvantage of this approach is that the Markov parameter sequence obtained is distorted by time-aliasing effects.[17] Recently, a method called the State Space Frequency Domain (SSFD) identification algorithm[18] has been

developed. This method can estimate Markov parameters from the FRF without windowing distortion and an arbitrary frequency weighting can be introduced to shape the estimation error. The method uses a rational matrix description (the ratio of a matrix polynomial and a monic scalar polynomial denominator) to curve-fit the frequency data and obtains the Markov parameters from this equation. In obtaining the state space models from the Markov parameters, the Eigensystem Realization Algorithm (ERA),[19] or its variant ERA/DC,[20] is used. The disadvantage of this method is that the curve-fitting problem must either be solved by non-linear optimization techniques or by linear approximate algorithms requiring several iterations[18]. Using the same idea as derived for the OKID, a novel method developed in Ref. 21 proposes a simple yet effective way of curve-fitting the FRF data and of constructing the Markov parameters. Instead of using a rational matrix function, this method uses a matrix-fraction for the curve-fitting. Thus the curve-fitting is reformulated as a linear problem which can be solved by the ordinary least-squares method in one step; that is, no iteration is required. The method can match the frequency response data perfectly if the FRF is accurate in ideal cases, and will seek an optimal match if noise and/or distortion are involved in the data. This new approach retains all the advantages associated with the SSFD while avoiding the iterative, approximate curve-fitting procedures.

The objective of this paper is to present an overview of the recent advances in system identification for modal testing and control of large structures. We focus on the Observer/Kalman Filter Identification (OKID)[5-11,12,22,23], the Observer/Controller Identification (OCID)[15,16] and the State Space System Identification in the Frequency Domain.[18,20] Applications to the real aerospace structures will be shown including the Hubble spacecraft telescope[14] and the active flexible aircraft wing[15].

OBSERVER/KALMAN FILTER IDENTIFICATION

There are basically two ways to stochastically characterize system uncertainties including process and measurement noises (see Fig. 1). One way is to describe the input and output uncertainties directly in terms of their covariances. Another way is to specify the Kalman filter equation with its steady state Kalman gain, which is a function of the input and output uncertainty covariances. In the OKID, an observer is identified to characterize the input and output uncertainties. If the data length is sufficiently long, and the number of identified observer Markov parameters (pulse response time histories) is sufficiently large, then the identified observer of the system approaches the Kalman filter.
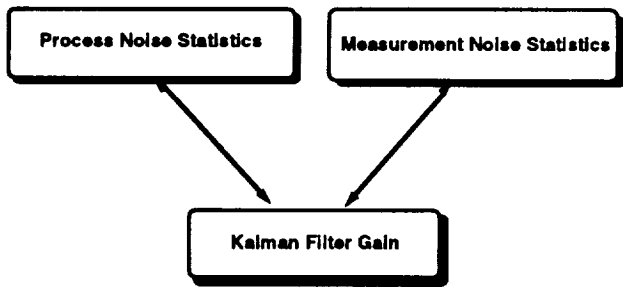
Figure 1: Characterization of system uncertainties

The OKID has two ways of processing the input and output data for system identification. One is the forward-in-time and the other is the backward-in-time as shown in Fig. 2. The forward-in-time means
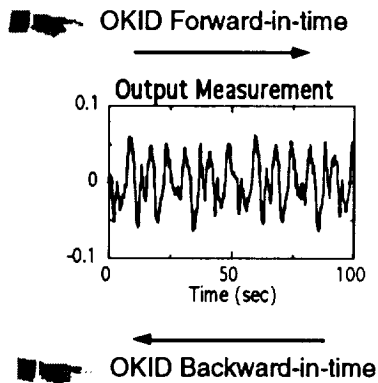

Figure 2: OKID forward and backward

that the current output measurement can be fully estimated by the previous inputs and outputs, and is commonly used for the system identification. If one reverses time in the model to be identified,[24,25] what were damped true system modes become undamped true system modes, growing as the reversed time increases. Physically, it implies that the current output measurement can be fully estimated by the future inputs and outputs. On the other hand, the noise modes in the forward and backward identification still maintain the property that they are stable. This is intuitively reasonable. If the data set is sufficiently long, an unstable noise mode would predict noise contributions to the pulse response data that grow unbounded as the time step in the data set increases. This is inconsistent with the expected contribution of noise in data. Therefore, the backward identification has the advantage of shifting from positive damping to negative damping of the true system modes to distinguish these modes from noise modes. Real experiences have shown that the backward identification may fail to indicate certain system modes in experimental data, perhaps due to the unmatched uncertainty levels in forward and

backward identification.

Given a set of experimental input and output data, the identification algorithm (see Fig. 3) proceeds as follows:
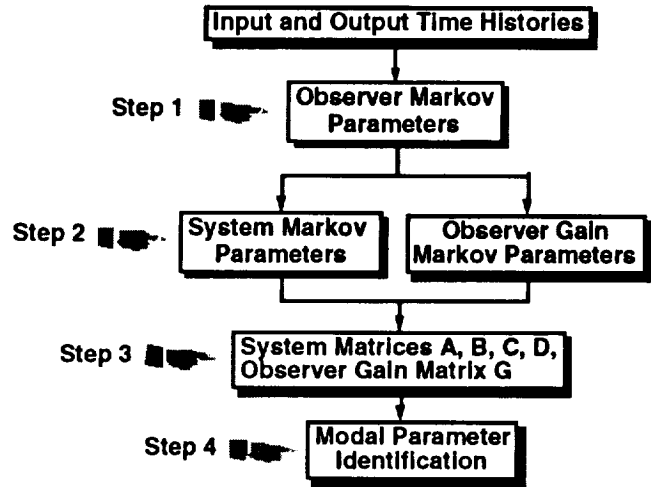
Figure 3: Flow Chart for the OKID

1) Compute observer Markov parameters.

2) Recover the combined system and observer gain pulse response samples from the identified observer Markov parameters.

3) Realize a state space model of the system and the corresponding observer gain from the recovered pulse response samples using ERA or ERA/DC.

4) Find the eigensolution of the realized state matrix and transform the realized model to modal coordinates for modal parameter identification. The modal parameters include frequencies, dampings, and mode shapes at the sensor locations.

To demonstrate the identification procedure using real experimental data, the flight data from the Hubble Space Telescope shown in Fig. 4 is used. There are six gyros located on the Optical Telescope Assembly (OTA) and four torque wheels located on the Spacecraft Subsystem Module (SSM). The OTA is fixed inside the SSM. The gyros are used mainly to measure the motion of the primary mirror. Data from four out of the six gyros are recorded at a time. The measurement resolution is 0.005 arcsec/sec, which implies that the gyro data are not adequate because the requirement is 0.007 arcsec pointing. The angular rates, which are measured along the four gyro directions, are combined and transformed using least-squares to recover the three rates in vehicle coordinates. Least-squares is used to smooth the poor resolution of the data. The input commands are given in terms of angular acceleration in the three rotational vehicle coordinates and then projected on the four torque wheel

281

Figure 4: Hubble Spacecraft Telescope

Figure 5: Computation of observer Markov parameters

shown in Fig. 6. Although the number of identified ob-

axes to excite the telescope mirror and the spacecraft. The data were sampled at 40 Hz. Pulses combined with sine-sweeping in the middle of an ex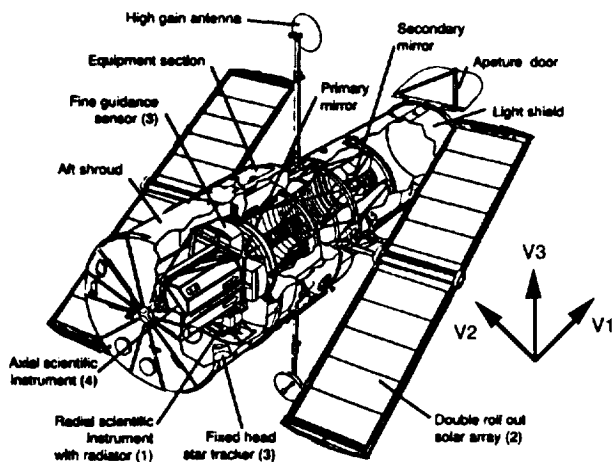citation period (50.975 sec) were used as input commands to the torque wheels. The excitation period was repeated six times for a total of approximately 12,000 samples taken for each experiment. The experiment was repeated three times for the other two vehicle coordinates. As a result, there were three inputs and four outputs for a total of three sets of 12,000 input samples and twelve sets of 12,000 output samples to be used for identification of vibration parameters.

The usual practice of modal parameter identification uses the Fast Fourier Transforms (FFT) of the inputs and measured outputs to compute the pulse response sequence (system Markov parameters). In contrast, the OKID uses an asymptotically stable observer to form a stable state space discrete model for the system to be identified. The primary purpose of introducing an observer is to compress the data and improve system identification results in practice.

The first step is to compute the observer Markov parameters. As shown in Fig. 5, the input and output time histories are several orders longer than the observer pulse response sequence (observer Markov parameters). For illustration, only the input and output time histories from the first vehicle axis are shown. The modal parameters which are excitable by the inputs and measurable by the output sensors are embedded in the identified observer Markov parameters.

The second step is to compute system pulse responses (system Markov parameters) and observer gain pulse responses (observer gain Markov parameters). From the identified observer Markov parameters, the system Markov parameters and the observer gain Markov parameters can be easily computed. The results for the first vehicle axis, V1, are graphically
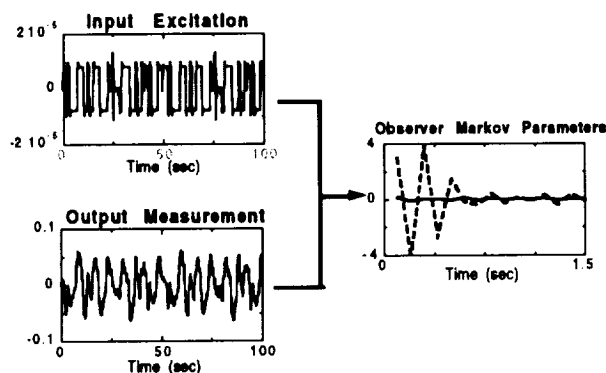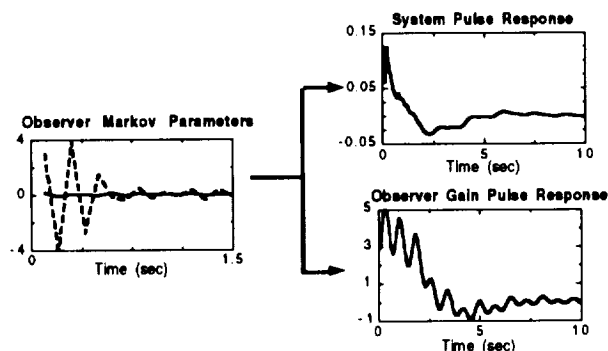
Figure 6: Computation of system and observer gain Markov parameters

server Markov parameters is finite and generally very small, the number of system Markov parameters can be as large as desired. Note that the maximum number of independent system Markov parameters is equal to the number of identified observer Markov parameters. To solve for more system Markov parameters than the number of identified observer Markov parameters, simply set the extra observer Markov parameters to zero.

The third step as shown in Fig. 7 is to compute the system matrices and the observer gain matrix. Knowledge of the actual system Markov parameters and the observer gain Markov parameters allows one to use the ERA or ERA/DC to obtain a state space realization of the system of interest. Modal parameters including natural frequencies, damping ratios, and mode shapes can then be found from the system matrices. The identified observer gain is related to the steady state Kalman filter gain which may be used to characterize the system uncertainties and measurement noises.

The system order identified from ERA/DC, after some singular values truncation, was chosen to be 30 for the realization of system matrices. Seven dominant modes were identified as shown in Table 1. The Mode SV in the table describes the singular value contribu-
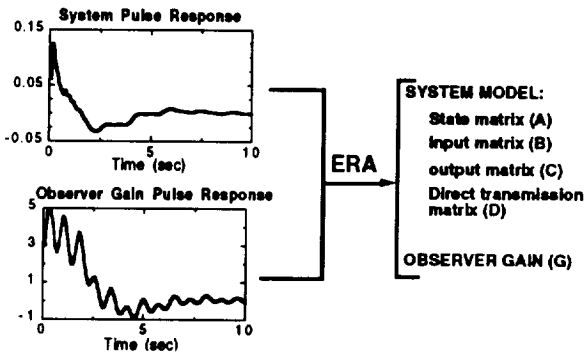
Figure 7: Computation of system and observer gain matrices

Figure 8: Comparison of predicted and estimated output

Table 1: Identified modal parameters for the Hubble Space Telescope

Mode No.	Frequency (Hz)	Damping (%)	Mode SV
1	0.147	55.6	0.76
2	0.155	58.4	0.98
3	0.169	67.4	1.00
4	0.633	57.3	0.68
5	1.273	4.06	0.37
6	2.433	5.23	0.02
7	2.822	6.33	0.01

tion of each individual mode to the system Markov parameters. It has been normalized relative to the maximum singular value. The first three modes are attitude modes. The 0.633 Hz mode is believed to be an in-plane bending mode of the solar array, the 1.273 Hz mode is a coupled solar and membrane mode, and the 2.433 Hz mode is the first mode of the primary deployment mechanism with the solar array housing attached. The identified dampings are higher than expected because there is an attitude control for maneuvering during testing, as well as inherent mechanical friction of the solar array mechanism.

The left figure in Fig. 8 shows the excitation input signal including pulse combined with sine-sweeping components in the middle of an excitation period for the first vehicle axis. The right figures in Fig. 8 show overlapping 50 seconds of the reconstruction from the identified system models, and the test data for the first vehicle axis. The upper right corner in Fig. 8 shows the predicted output in comparison with the real output data. The lower right corner in Fig. 8 shows the estimated output in comparison with the real output data. The predicted output is the output reconstructed from the identified model only whereas the estimated out-

put is the output reconstructed from the identified observer. There are visible differences in the predicted and estimated outputs. Comparison of the observer output with the measured response shows extremely good agreement, indicating that the observer is correcting for the system uncertainties including nonlinearities. The covariance of the estimated output residuals is about three orders less than the predicted output residuals. Similar results of the predicted and estimated outputs were obtained for the second and third vehicle axes, and thus are not shown in this example.

Figure 9 shows the comparison of the forward and backward identification results. The left figure shows
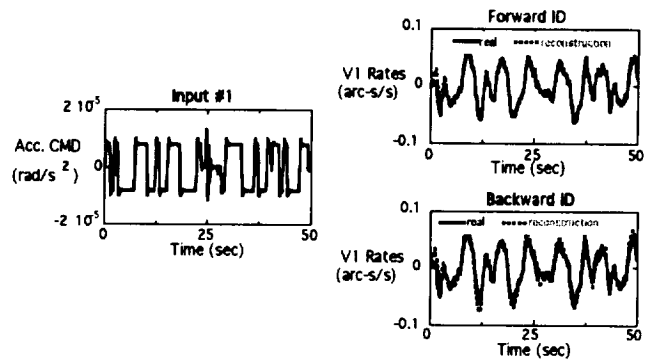
Figure 9: Comparison of OKID-forward and OKID-backward results

the excitation input signal including pulse combined with sine-sweeping components in the middle of an excitation period (50.975 sec). The figures on the right hand side show overlapping 50 seconds of the reconstruction from the identified forward and backward system models, and the test data for the first vehicle axis. There are some visible differences in the backward identification between test and reconstruction but overall the map from the input to the output is reasonably well. The forward identification is somewhat better than the backward identification in damp-

283

ing estimation. The damping ratio estimated from the backward approach appears to be a little low. It is important that the system model be accurate because it is this part that is used as a model for control design.

OBSERVER/CONTROLLER IDENTIFICATION

This section presents a technique that identifies a control system operating under closed-loop conditions with an existing feedback controller, which may or may not include feedback dynamics. The controller and the open-loop system dynamics are assumed to be unknown. The closed-loop system is excited by a known excitation signal, and the closed-loop system output responses and the feedback signal are measured. A schematic diagram of the existing or actual closed-loop system is given in Fig. 10 which shows the measured

Figure 10: Existing (Actual) control system

quantities, and the open-loop system in state-space representation given by the matrices A, B, C, D. An algorithm is developed to identify the open-loop system, an observer gain, and the existing controller gain matrices from closed-loop test data which include the time histories of the excitation signal, the resulting closed-loop response, and the feedback control signal. The technique assumes the identified controller to be of a full state feedback type. A schematic diagram of the identified or effective closed-loop system is shown in Fig. 11, where A, B, C, D again represent the identified

● Find A,B,C,D,G, and F from data at points 1, 2, and 3
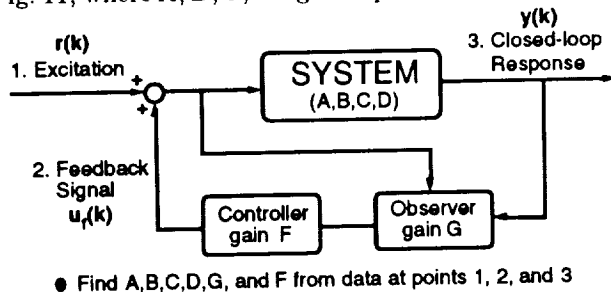
Figure 11: Identified (Effective) control system

open-loop system; G and F represent the identified observer and controller gains, respectively. The method first identifies the Markov parameters of a closed-loop observer, which in turn produce the Markov param-
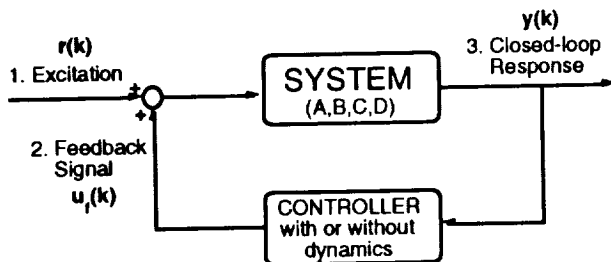
eters for an observer, the open-loop system, and the controller.

The OCID here means the Observer/Controller Identification. Given a set of excitation signal, feedback signal, and closed-loop response data, the identification algorithm (see Fig. 12) proceeds as follows.
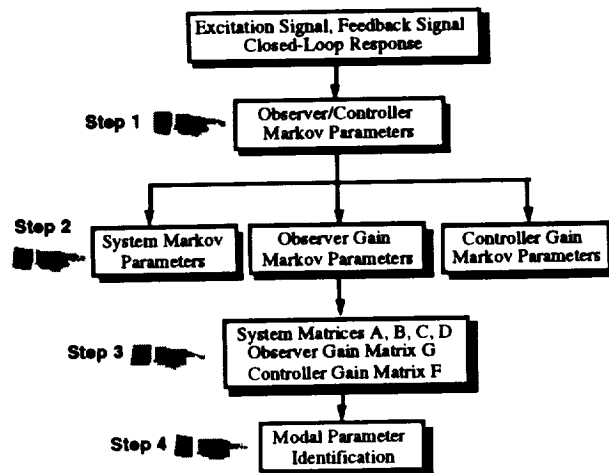
Figure 12: Flow chart for the OCID

1) Compute observer/controller Markov parameters.

2) Recover system, observer gain, and controller Markov parameters.

3) Realize a state space model of the system, the corresponding observer and controller gains from the recovered sequence of the system and observer gain Markov parameters by using ERA or ERA/DC.

4) Find the eigensolution of the realized state matrix and transform the realized model to modal coordinates for modal parameter identification. The modal parameters include frequencies, dampings, and mode shapes at the sensor locations.

The OCID method is illustrated by using actual aircraft flutter test data.[26] Experimental data was obtained from wind tunnel tests of an aeroelastic model with active flutter control operating (see Fig. 13). The model, known as the Active Flexible Wing (AFW), has a digital controller which suppresses flutter by properly phased commands to actuators of eight control surfaces on the wing leading and trailing edge surfaces. During flutter suppression control law testing, acceleration signals from sensors distributed on the model were first filtered for anti-aliasing and then quantized

284
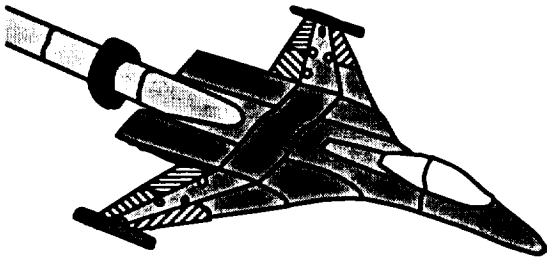
Figure 13: Active flexible wing

Figure 14: Identified Markov parameters

at a 200Hz sample rate. The quantized signals obtained from both sides of the model were then symmetrized in pairs. These symmetrized signals became the inputs to the symmetric and antisymmetric flutter suppression control laws and also the source of the closed-loop response time histories to be used for the identification process. Output signals of the feedback control laws and independent input excitation to the wing provided the remaining time histories necessary for identification of the closed-loop control system. During tests, each of the actuator inputs was excited individually by adding the excitation signal to the feedback control output signal. This procedure allowed the generation of all the responses necessary to identify the multi-input/output control system. The excitation signals themselves were either logarithmic sine sweeps or so-called pseudo-random noise. The excitation signal, the resultant closed-loop response time histories, and the feedback control signal were used with the OCID technique to identify all of the elements of the AFW model including the open-loop system matrices, an observer gain, and the existing controller gains. The flutter mode is then identified by solving the eigenvalues of the open-loop state matrix.

Seven sets of experimental data were used corresponding to different dynamic pressure conditions, 175 pounds per square foot (psf), 200 psf, 230 psf, 240 psf, 250 psf, 260 psf and 280 psf respectively. Results for the 260 psf condition are shown in the following unless otherwise specified. The number of data points used in this case is 600, with a sampling interval of 0.005 sec. apart (200 Hz sampling rate). The actual time histories used in the identification and the identification results are shown in Fig. 14, which are discussed in more details below.

From the data histories shown in Fig. 14 for the first 2 seconds, 30 observer/controller Markov parameters are computed. The identified observer/controller Markov parameters are shown on the middle of Fig. 14 for a duration of 0.15 sec. There are four curves in this plot. Using the identified observer/controller Markov parameters, the system, observer gain, controller gain,
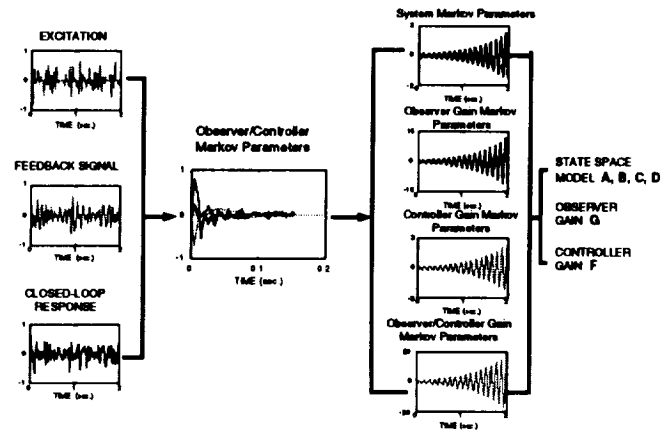
and observer/controller gain Markov parameters are computed, which are shown on the right hand side of Fig. 14. Note that these time histories are not limited to the 0.15 sec. duration. In fact, the system, observer gain, controller gain, and observer/controller gain Markov parameters can be computed for any duration as desired. The pulse responses increase in amplitudes with time, revealing open-loop instability.

Using the computed Markov parameters, a state space model relating the system, the controller gain, and the observer gain are then computed. The system Markov parameters are simply its pulse response samples. The flutter mode is then identified by solving the eigenvalues of the open-loop state matrix.

Figure 15 shows that the identified flutter mode
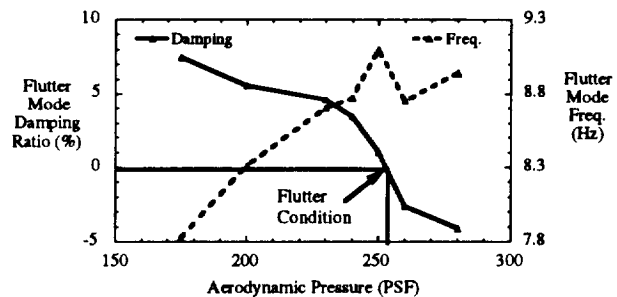
Figure 15: Identified Markov parameters

for the 260 psf condition has an open-loop frequency of 8.78 Hz and 3.34% negative damping, implying open-loop instability. This example illustrates the case where open-loop identification may not be possible or practical for such a system. Similar analysis performed on the six remaing sets of data revealed that the identified flutter mode for the 250 psf condition has an open-loop frequency of 9.06 Hz and 0.26% negative damping, indicating marginal open-loop instabil-

285

ity. The final 280 psf condition was identified to have an open-loop frequency of 8.76 Hz and 5.73% negative damping, indicating even greater open-loop instability. Comparison of the identified with the analytical results showed excellent agreement in frequencies and damping, indicating a coalescing mode switch in frequency.

In general, a specific (or existing) observer is not identifiable because the observer becomes ineffective when the transient responses decay out and the errors between the true states and the estimated states become dominated by the system uncertainties and measurement noises. Therefore, from given excitation signals, feedback signals, and measurement data, one identifies an effective observer determined by the system uncertainties and measurement noises, instead of the specific observer. However, this does not influence the identification of the open-loop system and the feedback controller gain. When the data length is sufficiently long, and the number p is chosen to be sufficiently large, then the identified observer tends to a Kalman filter which may not be the observer given by the controller designer. Also, numerical studies indicate that this technique particularly works well for unstable systems because the signal to noise ratio for an unstable mode is generally higher than that for a stable mode.

FREQUENCY-DOMAIN SYSTEM IDENTIFICATION

The objective of frequency domain state space system identification is to identify state space models from the given frequency response data—the frequency response functions (FRF). The transfer function of a multi-input and multi-output linear system has left and right matrix-fraction descriptions. From the left matrix-fraction description (LMFD), one can derive a simple observable canonical form, whereas from the right matrix-fraction description (RMFD) one can derive a simple controllable canonical form, which is shown as follows. Neither observable nor controllable canonical form is a minimum realization. The minimum realization means a model with the smallest state space dimensions among all realizable systems that have the same input-output relations. Instead of computing canonical-form realizations, one may compute the system Markov parameters and then obtain a minimum state space realization using ERA.

The computational steps for the matrix-fraction description methods are shown in Fig. 16 and summarized as follows:

1. Determine frequency response functions.

2. Curve-fit the frequency response function using the left or right matrix-fraction description method.
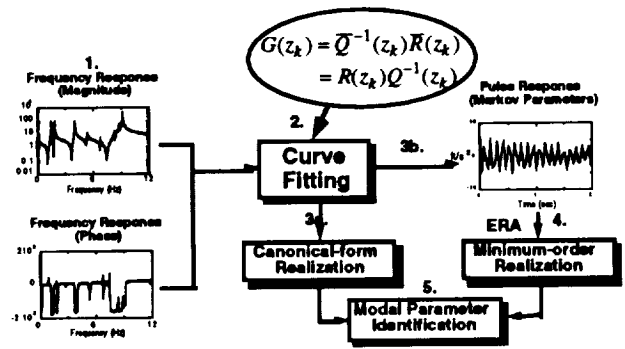
Figure 16: Computational Steps for left of right matrix-fraction description method.

3a. Construct a canonical-form realization. If the left matrix-fraction description method is used, an observable canonical form will be obtained. If the right matrix-fraction description method is used, a controllable canonical form will be obtained.

3b. Compute system Markov parameters as many as desired if a model with minimum order is to be determined.

4. Determine a minimum order realization from the computed system Markov parameters by using a minimum realization technique such as ERA.

5. Find the eigensolution of the realized state matrix and transform the realized model to modal coordinates for modal parameter identification. The modal parameters include frequencies, dampings, and mode shapes at the sensor locations.

The left matrix-fraction description method is illustrated by using the structure shown in Fig. 17 which is a NASA testbed[27] to study the controls and structures interaction problem. The system has eight inputs and
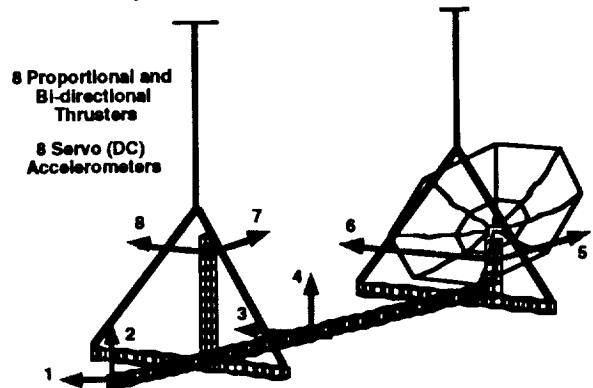
Figure 17: A NASA large space structure testbed.

eight collocated outputs for control. The inputs are

286

air thrusters and the outputs are accelerometers. The locations of the input-output pairs are depicted in Fig. 17. In this example, the structure was excited using random input signals to four thrusters located at positions 1, 2, 6, 7. The input and output signals were filtered using low-pass digital filters with the range set to 78% of the Nyquist frequency (12.8 Hz) to concentrate the energy in the low frequency range below 10 Hz. A total of 2048 data points at a sampling rate of 25.6 Hz from each sensor are used for identification.

Sixteen FRF's from four input and output pairs located at positions 1, 2, 6, 7 are simultaneously used to identify a state space system model to represent the testbed. The order of the matrix polynomial is set to 25, which is sufficient to match as many as 50 modes (a system of dimension 100). A state space model is obtained using ERA/DC with the system order assigned to 100. The reconstructed frequency response data (dash lines) are compared with the experimental data (solid lines) in Figs. 18 and 19.
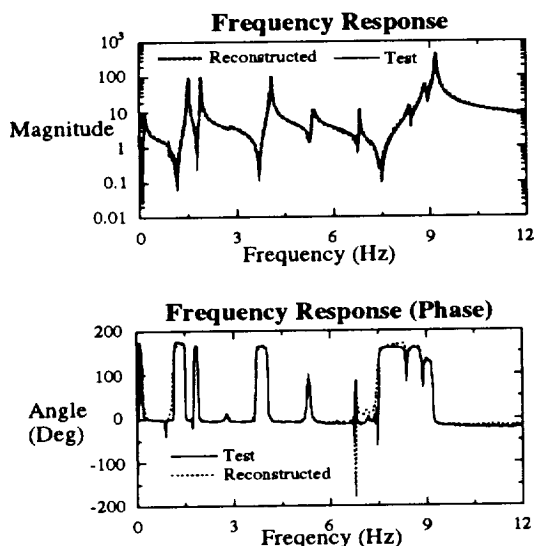
Figure 18: Comparison of the test (solid line) and reconstructed (dash line) input-1/output-1 FRF's. The reconstructed FRF is obtained using the identified system matrices.

Figure 18 is the frequency response of output 1 with respect to input 1, representing a case of a strong signal, while Fig. 19 is the frequency response of output 2 with respect to input 1, representing a case of a weak signal. The signal is weak because sensor 2 is orthogonal to input 1. Similar results are obtained for other input/output pairs which are not shown. The results show that the matching is better for the strong signal cases. This is expected because the strong signal has a larger signal-to-noise ratio than the weaker signal. The results for other input-output pairs are
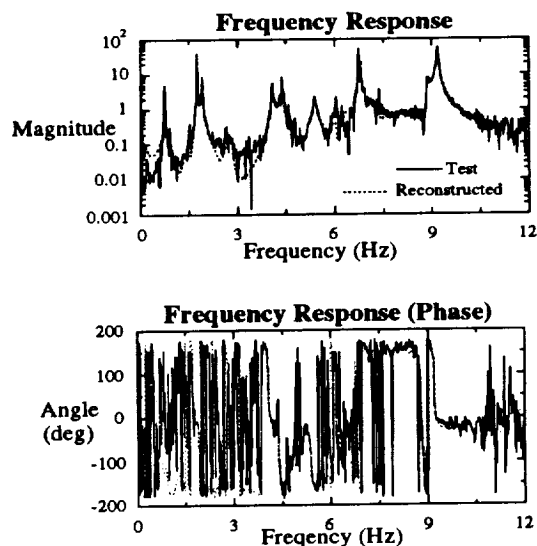

Figure 19: Comparison of the test (solid line) and reconstructed (dash line) input-1/output-2 FRF's. The reconstructed FRF is obtained using the identified system matrices.

similar and hence omitted.

CONCLUDING REMARKS

The field of system identification has expanded continuously and extensively over two decades. This growth is largely associated with corresponding improvements in computer capabilities. These increases in computer capability have permitted more accurate and complete testing and data analysis to occur. Algorithms and approaches thought too extensive in the past are now feasible. In particular, many important numerical tools have been developed including the singular value decomposition which is an essential tool in the derivation of system identification methods. In this paper, an overview of several recently developed techniques are presented including the Observer/Kalman Filter Identification, the Observer/Controller Identification, and the State-Space System Identification in the Frequency Domain. These techniques have been successfully applied to many aerospace structures. However, complex, built-up structures still pose a significant challenge to the best ground-based methodology now available.

REFERENCES

1. Ljung, L., System Identification: Theory for the User, Prentice-Hall, Inc., Englewood Cliffs, New Jersey 07632.

2. Juang, J.-N., and Pappa, R. S., "A Comparative Overview of Modal Testing and System Identifi-

cation for Control of Structures," *Shock and Vibration Digest*, Vol. 20, No. 5, May 1988, pp. 4-15.

3. Pappa, R. S., and Juang, J.-N., "Some Experiences with the Eigensystem Realization Algorithm," *Sound and Vibration*, Vol. 22, No. 1, Jan. 1988, pp. 30-35.

4. Juang, J. N., Horta, G. H., and Longman, R. W., "Input/Output System Identification: Learning From Repeated Experiments," Mechanics and Control of Large Space Structures edited by John L. Junkins, AIAA Monograph on Progress in Astronautics and Aeronautics, Vol 29, 1990, pp. 87-99.

5. Chen, C.-W., Huang, J.-K., Phan, M., and Juang, J.-N., "Integrated System Identification and Modal State Estimation for Control of Large Flexible Space Structures," *Journal of Guidance, Control, and Dynamics*, Vol. 15, No. 1, pp. 88-95, Jan.-Feb. 1992.

6. Phan, M., Juang, J.-N., and Longman, R.W., "Identification of Linear Multivariable Systems from a Single Set of Data by Identification of Observers with Assigned Real Eigenvalues," *Journal of Astronautical Sciences*, Vol. 40, No. 2, April-June 1992, pp. 261-279.

7. Phan, M., Horta, L. G., Juang, J.-N., and Longman, R.W., "Linear System Identification Via an Asymptotically Stable Observer," *NASA Technical Paper 3164*, June 1992.

8. Juang, J.-N., Phan, M., Horta, L. G., and Longman, R.W.., "Identification of Observer/Kalman Filter Markov Parameters: Theory and Experiments," *Proceedings of the AIAA Guidance, Navigation and Control Conference*, New Orleans, Louisiana, Aug. 1991, and also to appear in *Journal of Guidance, Control and Dynamics*.

9. Phan, M., Horta, L. G., Juang, J.-N., and Longman, R. W., "Improvement of Observer/Kalman Filter Identification by Residual Whitening," *Proceedings of Eighth VPI& SU Symposium* edited by L. Meirovitch, Blacksburg, Virginia, May 6-8, 1991, pp. 467-478.

10. Chen, C.-W., Huang, J.-K., and Juang, J.-N.,"Identification of Linear Stochastic System through Projection Filters," *Proceedings of the AIAA 33rd Structures, Structural Dynamics & Materials Conference*, Dallas, TX, April 13-15, 1992, pp. 2320-2340.

11. Chen, C. W., Lee, G., and Juang, J.-N., "Several Recursive Techniques for Observer/Kalman Filter System Identification From Data," Paper No. 92-4386, *AIAA Guidance, Navigation and Con-*

trol Conference, Hilton Head, South Carolina, Aug. 10-12, 1992.

12. Juang, J.-N. and Phan, M.,"Linear System Identification via Backward Observer Models," *NASA Technical Memorandum TM-107632*, May 1992.

13. Scott, M., Gilbert, M., and Demeo, M., "Active Vibration Damping of the Space Shuttle Remote Manipulator System," *Proceedings of the AIAA Guidance, Navigation and Control Conference*, New Orleans, Louisiana, Aug. 1991.

14. Juang, J.-N., Horta, L. G., Belvin, W. K., Sharkey, J., and Bauer, F. H., "An Application of the Observer/Kalman Filter Identification (OKID) Technique to Hubble Flight Data," *NASA/DoD Controls-Structures Interaction (CSI) Technology Conference*, March 3-5, 1992, Harvey's Resort Hotel, Lake Tahoe, Nevada.

15. Juang, J.-N., and Phan, M., "Identification of system, "Observer, and Controller from Closed-Loop Experimental Data," Paper No. 92-4620, *AIAA Guidance, Navigation and Control Conference*, Hilton Head, South Carolina, Aug. 10-12, 1992.

16. Phan, M., Juang, J.-N., Horta, L. G., Longman, R. W., "System Identification from Closed-Loop Data with Known Output Feedback Dynamics," NASA Technical Memorandum 107604, March 1992.

17. Oppenheim, A. V. and Schafer, R. W., *Digital Signal Processing*, Prentice-Hall Inc. Englewood Cliffs, New Jersey., 1975.

18. Bayard, D. S., "An Algorithm for State Space Frequency Domain Identification without Windowing Distortions," *Proceedings of the Control and Decision Conference*, December 1992.

19. Juang, J.-N., and Pappa, R.S., "An Eigensystem Realization Algorithm for Modal Parameter Identification and Model Reduction," *Journal of Guidance, Control, and Dynamics*, Vol. 8, No. 5, Sept.-Oct. 1985, pp. 620-627.

20. Juang, J.-N., Cooper, J.E., and Wright, J.R., "An Eigensystem Realization Algorithm Using Data Correlations (ERA/DC) for Modal Parameter Identification," *Control-Theory and Advanced Technology*, Vol. 4, No. 1, 1988, pp. 5-14.

21. Chen, C. W., Juang, J.-N., and Lee, G., "Frequency Domain State-Space System Identification," *NASA Technical Memorandum 107659*, June 1992.

22. Phan, M., Horta, L.G., Juang, J.-N., and Longman, R.W., "Improvement of Observer/Kalman

Filter Identification by Residual Whitening," *AIAA Guidance, Navigation and Control Conference,* Hilton Head, South Carolina, Aug. 1992.

23. Juang, J.-N., Horta, L.G., and Phan, M., "User's Guide for System/Observer/ Controller Identification Toolbox," *NASA Technical Memorandum 107566,* 1992.

24. Hollkamp, J.J. and Batill, S.M., "Automated Parameter Identification and Order Reduction for Discrete Series Models," *AIAA Journal,* Vol. 29, No. 1, 1991.

25. Hollkamp, J.J. and Batill, S.M., "Structural Identification Using Order Overspecified Time-Series Models," to appear in *Journal of Dynamics Systems, Measurement, and Control,* 1992.

26. Perry III, B., Cole, S. R., and Miller, G. D., "A Summary of the Active Flexible Wing Program," AIAA Paper No. 92-2080, *AIAA Dynamics Specialists Conference,* Dallas, Texas, April 1992.

27. Belvin, W. K., Elliott, K. B., Horta, L. G., Bailey, J. P., Bruner, A. M., Sulla, J. L., Won, J., Ugoletti, R. M. "Langley's CSI Evolutionary Model: Phase 0," *NASA Technical Memorandum 104165,* November 1991.

INTEGRATED CONTROLS-STRUCTURES DESIGN

A Combined Algorithm for
Minimum Time Slewing of Flexible Spacecraft[*]

P. M. Bainum, F. Li, and J. Xu
Department of Mechanical Engineering
Howard University, Washington D.C., 20059, (202)806-6612

ABSTRACT

The use of Pontryagin's Maximum Principle for the large-angle slewing of large flexible structures usually results in the so-called two-point boundary-value problem (TPBVP), in which many requirements (e.g., minimum time, small flexible amplitude, and limited control powers, etc.) must be satisfied simultaneously. The successful solution of this problem depends largely on the use of an efficient numerical computational algorithm. There are many candidate algorithms available for this problem (e.g., quasilinearization, gradient, and shooting, etc.) In this paper, a proposed algorithm, which combines the quasilinearization method with a time shortening technique and a shooting method, is applied to the minimum-time, three-dimensional, and large-angle maneuver of flexible spacecraft, particularly the orbiting Spacecraft Control Laboratory Experiment (SCOLE) configuration.

Theoretically, the nonlinear TPBVP can be solved only through the shooting method to find the "exact" switching times for the bang-bang controls. However, computationally, a suitable guess for the missing initial costates is crucial because the convergence range of the unknown initial costates is usually narrow, especially for systems with high dimensions and when a multi-bang-bang control strategy is needed. On the other hand, the problems of near minimum time attitude maneuver of general rigid spacecraft and fast slewing of flexible spacecraft have been examined by the authors through a numerical approach based on the quasilinearization algorithm with a time shortening technique. Computational results have demonstrated its broad convergence range and insensitivity to initial costate choices.

Consequently, a combined approach is naturally suggested here to solve the minimum time slewing problem. That is, in the computational process, the quasilinearization method is used first to obtain a near minimum time solution. Then, the acquired converged initial costates from the quasilinearization approach are transformed (tailored) to and used as the initial costate guess for starting the shooting method. Finally, the shooting method takes over the remaining calculations until the minimum-time solution converges. The nonlinear equations of motion of the SCOLE are formulated by using Lagrange's equations, with the mast modeled as a continuous beam subject to three-dimensional deformations. The numerical results will be presented and some related computational issues will also be discussed.

INTRODUCTION

*   Future space missions (target acquisition, target tracking, and surveying multiple targets, etc.) require:

    *   large-angle rotational (attitude) maneuver (slew);
    *   3-dimensional (3-D, 3-axis) maneuver;
    *   large flexible spacecraft maneuver;
    *   *minimum time maneuver.*

*   Application of Pontryagin's Maximum Principle to the nonlinear slewing problem:

    I. Non-Minimum-Time Slews:

    1. 3-D Rigid Spacecraft
        Junkins, Turner, Vadali, Wie, Bainum and Li, etc.

    2. 2-D (Single-Axis Rotation) Flexible Spacecraft
        Turner, Junkins, Vadali, Chun, Thompson, Bainum and Li, etc.

    3. 3-D Flexible Spacecraft (SCOLE)
        Bainum, Li and Tan.

    II. Minimum-Time (Near-Minimum-Time) Slews:

    1. 3-D Rigid Spacecraft
        Bainum and Li, Vadali, Wie, etc.

    2. 2-D Flexible Spacecraft
        Singh, Junkins, Vadali, Byers, Bainum and Li.

    3. 3-D Minimum-Time Flexible Spacecraft; Using *Quasilinearization Method and Shooting Method*: present paper.

OUTLINE

1. 3-D Dynamics of Flexible Spacecraft

    - State Equations

2. Time Optimal Control Problem Formulation

    - Two-Point Boundary-Value Problem (TPBVP)

3. Quasilinearization Method for Near Minimum Time Slew

4. Shooting Method

5. Initial Costate Transformation

    - Scale Factors

    - Combined Algorithm

6. Numerical Examples

7. Conclusions
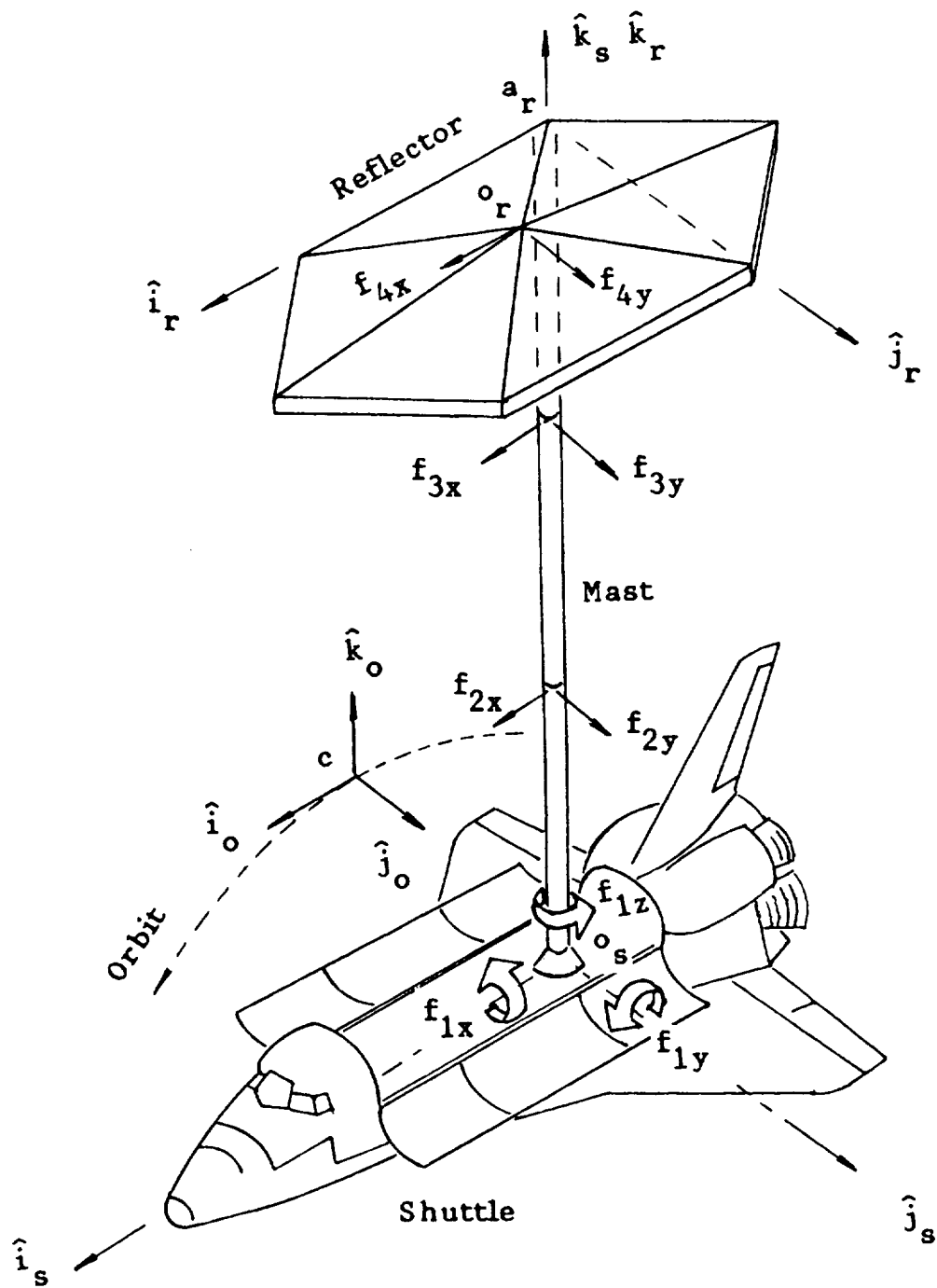
Figure 1. Drawing of the orbiting SCOLE configuration.

3-D DYNAMICS OF FLEXIBLE SPACECRAFT

I. 3-D Deformations of the SCOLE Mast (modal superposition):

$$U = \sum_i \xi_i(z)\alpha_i(t), \quad V = \sum_i \eta_i(z)\alpha_i(t), \quad \phi = \sum_i \zeta_i(z)\alpha_i(t) \tag{1}$$

where

U, V - bending in x and y directions;

ϕ - torsion in z direction;

ξ_i, η_i, and ζ_i - modal shape function vector components;

α_i - a scaled modal amplitude associated with the ith mode;

z - coordinate.

II. State Equations:

$$\dot{q} = \frac{1}{2}\tilde{\omega}q, \quad \text{where} \quad \tilde{\omega} = \begin{bmatrix} 0 & -\omega_1 & -\omega_2 & -\omega_3 \\ \omega_1 & 0 & \omega_3 & -\omega_2 \\ \omega_2 & -\omega_3 & 0 & \omega_1 \\ \omega_3 & \omega_2 & -\omega_1 & 0 \end{bmatrix} \tag{2}$$

$$\dot{\alpha} = \beta \tag{3}$$

$$\dot{y} = \begin{bmatrix} \dot{\omega} \\ \dot{\beta} \end{bmatrix} = (A + B_\alpha)\ddot{\omega} + (C_\beta)\omega + D\alpha + (E + F_\alpha)u \tag{4}$$

where

q is the 4 × 1 quaternion vector,

$B_\alpha = [B_1\alpha \mid B_2\alpha \mid \ldots \mid B_6\alpha]$,

$C_\beta = [C_1\beta \mid C_2\beta \mid C_3\beta]$, $\quad F_\alpha = [F_1\alpha \mid F_2\alpha \mid \ldots \mid F_9\alpha]$,

A, B_i, C_i, D, E, F_i - constant matrices;

$u = [f_{1x} \quad f_{1y} \quad f_{1z} \mid f_{2x} \quad f_{2y} \mid f_{3x} \quad f_{3y} \mid f_{4x} \quad f_{4y}]^T$.

TIME OPTIMAL CONTROL PROBLEM FORMULATION

Two-Point Boundary-Value Problem (TPBVP)

<u>Initial States and Final Required States</u>:

$$q(0), \quad \alpha(0), \quad \omega(0), \quad \beta(0) \tag{5}$$

$$q(t_f), \quad \alpha(t_f), \quad \omega(t_f), \quad \beta(t_f) \tag{6}$$

<u>Cost Function</u>:

$$t_f = \int_0^{t_f} (1) \, dt \tag{7}$$

<u>Saturation-Bounded Controls</u>:

$$|u_i| \le u_{ib}, \quad i = 1, 2, \cdots, 9. \tag{8}$$

<u>Hamiltonian</u>:

$$H = 1 + \gamma^T \beta + \lambda^T [(A + B_\alpha) \dot{\omega} + C_\beta \omega + D\alpha + (E + F_\alpha) u] \tag{9}$$

$p, \gamma, \lambda = [\lambda_1 \; \lambda_2]^T$ - costate vectors associated with q, α, ω, β.

<u>Costate Equations</u> (by Pontryagin's Maximum Principle):

$$\dot{p} = -\frac{\partial H}{\partial q} = \frac{1}{2} \tilde{\omega} p \tag{10}$$

$$\dot{\gamma} = -\frac{\partial H}{\partial \alpha} = -D^T \lambda - (B_\alpha^T \lambda) \dot{\omega} - (F_\alpha^T \lambda) u \tag{11}$$

$$\dot{\lambda}_1 = -\frac{\partial H}{\partial \omega} = -\frac{1}{2} [q] p - [\lambda^T (A + B_\alpha)] \omega - (C_\beta)^T \lambda \tag{12}$$

$$\dot{\lambda}_2 = -\frac{\partial H}{\partial \beta} = -\gamma - (C_\beta^T \lambda) \omega \tag{13}$$

<u>Constraint Condition</u> (a terminal condition to determine t_f):

$$H \equiv 0, \quad o \le t \le t_f \tag{14}$$

<u>Optimal control</u>:

$$u_i = -u_{ib} sign[(E + F_\alpha)^T \lambda]_i, \quad i = 1, \cdots, 9. \tag{15}$$

298

QUASILINEARIZATION AND TIME SHORTENING METHOD (QTS)

The near minimum time slewing problem can be solved by using an iteration approach based on the quasilinearization method.

Different Cost Function (Quadratic Cost Functional):

$$J = \frac{1}{2}\int_0^{t_f}(u^T R u)\,dt \tag{16}$$

where R are weighting matrices, t_f is the slewing time.

Same Costate Equations Eqs. (10)-(13).

Different Control Expression:

Unconstrained Optimal Control:

$$\frac{\partial H}{\partial u} = 0, \quad \rightarrow \quad u = -R^{-1}(E + F_\alpha)^T\lambda \tag{17}$$

Constrained Optimal Control:

$$u_i = \begin{cases} u_{ic}, & if \ |u_{ic}| < u_{ib} \\ u_{ib}\,\mathrm{sgn}(u_{ic}), & if \ |u_{ic}| \geq u_{ib} \end{cases} \tag{18}$$

$$u_{ic} = -[R^{-1}(E + F_\alpha)^T\lambda]_i, \quad i = 1, 2, ..., 9. \tag{19}$$

t_f can be obtained by sequentially shortening the slewing time.

Motivation:

Is this bang-bang control the same as that obtained by using the shooting method? (Do these controls have the same time histories?) If the answer is yes, the results from the QTS approach may be used as the starting solution for the shooting method. (Here, we use the numerical results to prove the equivalence.)

SHOOTING METHOD

Formulation of the TPBVP:

$$\dot{X}(t) = F[X(t), u(t)], \quad 0 \le t \le t_f \tag{20}$$

$$X(0) = K[D] \tag{21}$$

$$L[X(t_f), D, t_f] = 0 \tag{22}$$

$$u_i = -\text{sign}\{g_i[X(t)]\}, \quad i = 1, \ldots, m. \tag{23}$$

D – the $n \times 1$ unknown initial costate vector;

$L[X(t_f), D, t_f]$ – $(n+1) \times 1$ terminal constraint vector;

g_i ($i=1, \ldots, m$) – the switching functions.

Initial Boundary Conditions Correction Process:

To satisfy: $L[X(t_f), D, t_f] = 0$, D and t_f need to be corrected at each iteration:

$$\begin{bmatrix} D^{(k+1)} \\ t_f^{(k+1)} \end{bmatrix} = \begin{bmatrix} D^{(k)} \\ t_f^{(k)} \end{bmatrix} + \begin{bmatrix} \Delta D^{(k)} \\ \Delta t_f^{(k)} \end{bmatrix} \tag{24}$$

where

$$\begin{bmatrix} \Delta D^{(k)} \\ \Delta t_f^{(k)} \end{bmatrix} = -\alpha_k \begin{bmatrix} \delta D^{(k)} \\ \delta t_f^{(k)} \end{bmatrix} \tag{25}$$

$$\begin{bmatrix} \delta D^{(k)} \\ \delta t_f^{(k)} \end{bmatrix} = \begin{bmatrix} \dfrac{\partial L}{\partial D} & \dfrac{\partial L}{\partial t_f} \end{bmatrix}^{-1} L[X^{(k)}(t_f), D^{(k)}, t_f^{(k)}] \tag{26}$$

$D^{(k)}$ and $t_f^{(k)}$ – the values of D and t_f at iteration k;

scalar α_k ($0 \le \alpha_k \le 1$) is chosen as:

$$\alpha_k = \min\left\{1, \frac{\rho\|[D^{(k)}, t_f^{(k)}]\|}{\|[\delta D^{(k)}, \delta t_f^{(k)}]\|}\right\}, \quad 0 < \rho < 1 \tag{27}$$

300

A general algorithm suggested by Lastman has been used in our calculations and can be recast into the following block diagram:

INITIALIZE: Unknown Costates, $D^{(0)}$
Slewing Time, $t_f^{(0)}$

INTEGRATE: $\dot{X} = F(X, u)$, $0 \leq t \leq t_f^{(k)}$
$u_i = -\text{sign}[g_i(X)]$
SOLVE: $g_i(X)=0$, by Newton's Method, Find Switching Times, $t_j^{(k)}$

CHECK: Terminal Constraints
$| L_i[X^{(k)}(t_f), t_f] | \leq \epsilon$?

YES
STOP

NO

CORRECT: $D^{(k+1)} = D^{(k)} + \Delta D^{(k)}$
$t_f^{(k+1)} = t_f^{(k)} + \Delta t_f^{(k)}$
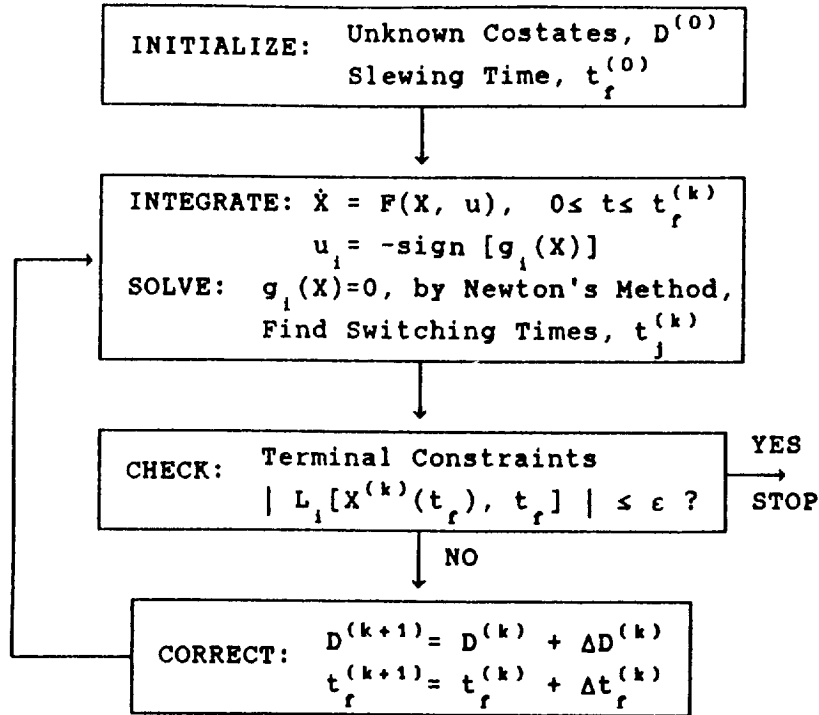
Summary:

I. Difficulty in initialization for the present nonlinear, multi-input system control problem. Improper choice of D and t_f will result in singular correction matrix, and program diverges.

II. Advantages and disadvantages of the two methods:

- Quasilinearization method and time shortening technique has good convergence properties;

- Shooting method generates more accurate final results, but is sensitive to starting solution;

- A combined technique is needed.

INITIAL COSTATE TRANSFORMATION

Different Costate Solutions:

Although the costate equations are the same, the initial costates from these two different formulations of the same problem are different:

1.   Initial costates, $\bar{p}(0)$, $\bar{\gamma}(0)$, and $\bar{\lambda}(0)$ from the QTS method are large;

2. $p(0)$, $\gamma(0)$, and $\lambda(0)$ from the shooting method are finite.

Assumed Relation Between Them:

$$p(0) \approx k_1 \bar{p}(0), \quad \lambda_1(0) \approx k_1 \bar{\lambda}_1(0),$$

$$\gamma(0) \approx k_2 \bar{\gamma}(0), \quad \lambda_2(0) \approx k_2 \bar{\lambda}_2(0). \tag{28}$$

where $k_1 < 1$, and $k_2 < 1$ are scale factors to be determined.

Scale Factors

Assumed Eigen-Axis Rotation for Rigid Spacecraft:

$$\omega = e\dot{\theta}, \quad \dot{\omega} = e\ddot{\theta} \tag{29}$$

$e = [e_1 \ e_2 \ e_3]^{\mathsf{T}}$ - a unit vector representing the eigen-axis,

θ - the rotation angle about this axis.

Resulting Four Related Equations (from rigid dynamic equations) :

$$e\ddot{\theta} = f\dot{\theta}^2 + I^{-1}Bu \tag{30}$$

f - 3 × 1 constant vector; and

$$\ddot{\theta} = e^{\mathsf{T}}f\dot{\theta}^2 + e^{\mathsf{T}}I^{-1}Bu \tag{31}$$

- Let "p" = the "principal" axis among the axes 1, 2, and 3, about which the rotation requires the largest t_f;

- Let "4" = Eq. (31).

302

Further Simplification of Equations:

$$\dot{\theta} = b_i v_i, \quad b_i > 0, \quad |v_i| \le 1, \quad i = 1, 2, 3, 4.$$

"Average" Values of the Initial Costates:

$$p_a = 2/(b_a \theta_f)^{1/2}, \quad \lambda_a = 1/b_a, \quad t_{fa} = 2(\theta_f/b_a)^{1/2}$$

$$b_a = k_p b_p + k_4 b_4, \quad k_p + k_4 = 1$$

θ_f - the required rotation angle about the eigen-axis.

k_1 and k_2:

$$k_1 = p_a/|\overline{p}_p(0)|, \quad k_2 = \lambda_a/|\overline{\lambda}_p(0)|$$

The Initial Costates for Starting the Shooting Method:

$$p(0) = k_1 \overline{p}(0), \quad \lambda_1(0) = k_1 \overline{\lambda}_1(0),$$

$$\gamma(0) = k_2 \overline{\gamma}(0), \quad \lambda_2(0) = k_2 \overline{\lambda}_2(0).$$

NUMERICAL EXAMPLES

Given Slewing Conditions (for all cases considered here):

1. Rest-to-rest slews, i.e.,

$$\omega(0) = 0, \quad \omega(t_f) = 0,$$

$$\alpha(0) = 0, \quad \beta(0) = 0, \quad \alpha(t_f) = 0, \quad \beta(t_f) = 0.$$

2. Three (3) control variables are used.

Example 1 (a scaled rigid spacecraft, $\lambda = \lambda_1$):

$$q(t_f) = [.877582561, \ .434965534, \ .142572492, \ .142572492]^T,$$

$$q(0) = [1.0, \ 0.0, \ 0.0, \ 0.0]^T, \quad \theta_f = 1 \text{ rad}, \quad I = \text{Diag}(1.0, \ 0.9, \ 0.6),$$

$$R = \text{Diag}(1.0, \ 0.7, \ 0.4), \quad p = 1, \quad k_1 = k_p = k_4 = 0.5.$$

QTS Method Results:

$t_f = 1.8$ sec. By transformation, the initial costates for starting the shooting method are obtained:

$$p(0) = \begin{bmatrix} -1.67968 \\ -.248420 \\ .415782 \end{bmatrix}, \quad \lambda(0) = \begin{bmatrix} -.705333 \\ -.0955727 \\ .0481507 \end{bmatrix}, \quad \begin{matrix} t_f = 1.71209 \\ (s) \end{matrix}$$

Shooting Method Results:

$\rho = 0.1$, solutions are obtained in 6 iterations (to 5 digits):

$$p^*(0) = \begin{bmatrix} -1.74008 \\ -.267243 \\ .462349 \end{bmatrix}, \quad \lambda^*(0) = \begin{bmatrix} -.770403 \\ -.115614 \\ .0606796 \end{bmatrix}, \quad \begin{matrix} t_f^* = 1.76403 \\ (s) \end{matrix}$$

The converged values of the switching times are:

u_i	u_3	u_2	u_1	u_3	u_2
$t_i(s)$	0.314356	0.701830	0.874531	1.18114	1.53158

<u>Example 2</u>:

Maneuver of the rigidized SCOLE model. The scaled inertial matrix (set $I_{33} = 1.0$):

$$I = \begin{bmatrix} .16902 & -.001061798 & .01619427 \\ -.001061798 & .9948471 & -.007354633 \\ .01619427 & -.007354633 & 1.0 \end{bmatrix}$$

- Simultaneous 75°, 30°, 45° slew about roll, pitch, yaw axes;
- u = three torquers on the Shuttle, u_{ib} = 10,000 ft-lb;
- R = Diag(1, 1, 1);
- $k_p = k_3 = 0.75$, $k_4 = 0.25$.

<u>Average Values</u>:

$$P_a = 1.01466, \qquad \lambda_a = .461915$$

<u>Initial Costates for Starting Shooting Method</u>:

$$p(0) = \begin{bmatrix} .00238330 \\ 1.24510 \\ -1.01466 \end{bmatrix}, \quad \lambda(0) = \begin{bmatrix} -.00709927 \\ .456237 \\ -.461519 \end{bmatrix}$$

The t_f = 1.6407 sec from the QTS method is used as $t_f^{(0)}$ in the shooting method, ρ = 0.0035. The final converged initial costates:

$$p^*(0) = \begin{bmatrix} .00237568 \\ 1.32922 \\ -1.08389 \end{bmatrix}, \quad \lambda^*(0) = \begin{bmatrix} -.00773848 \\ .496600 \\ -.502920 \end{bmatrix}, \quad t_f^* = 1.64066 \\ (s)$$

305
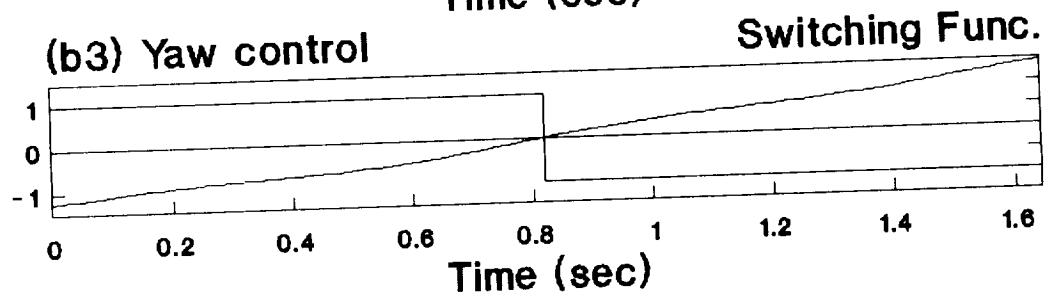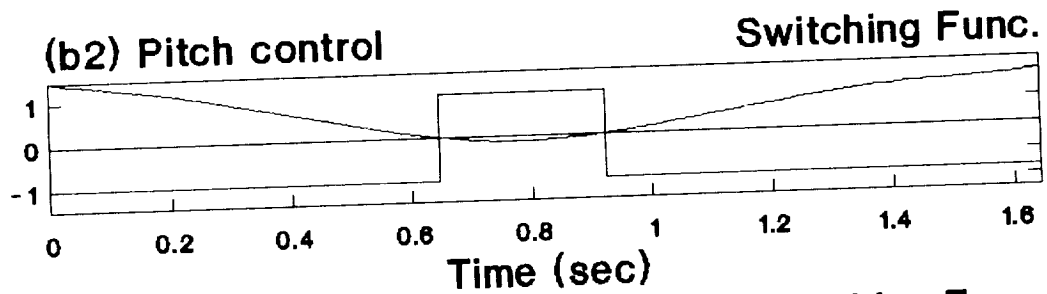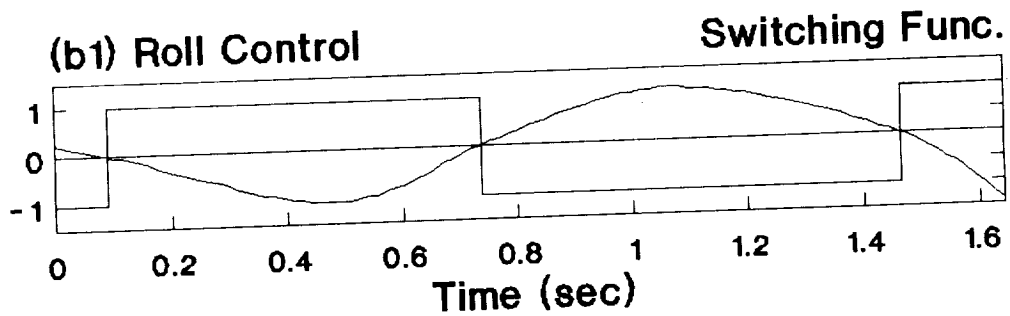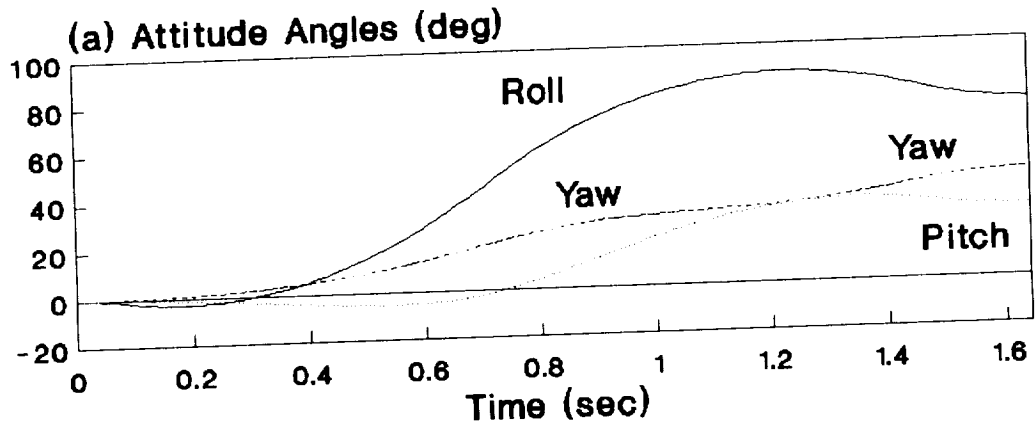
Fig. 2. Rigid SCOLE Maneuver (Scaled Model) 75-30-45 (deg) (Shooting Method)

Example 3:

The maneuver of the both rigidized and flexible orbiting SCOLE model is considered (using the original SCOLE challenge parameters).

- 90° slew about roll axis. Although the expected motion is "single-axis" rotation, the minimum-time dynamic maneuver process is not necessarily a single-axis rotation because of the offset inertia distribution of the SCOLE model. (The three axes for the three control torquers are not principal axes). Therefore, the present slew is a 3-D slew.

- u = three torquers on the Shuttle, u_{ib} = 10,000 ft-lb;

- R = Diag(1.E-4, 1.E-4, 1.E-4);

- $k_p = k_1 = 1.$

- Two flexible modes (the first and the second) are included.

Average Values of Initial Costates:

$$p_a = 24.7475, \qquad \lambda_a = 120.242$$

Initial Costates for Starting Shooting Method:

p(0) (Rigid)	(Flexible)	γ(0)	λ₁(0) (Rigid)	(Flexible)	λ₂(0)
.00000E0	.00000E0	-.90512E-3	.12024E3	.12024E3	.10717E-1
.24747E2	.24747E2	.46390E-2	.67830E1	.51236E1	-.35993E-1
-.19219E0	-.11478E0		.11671E2	.10969E2	
.25248E1	.23758E1				

The t_f = 27.3992 seconds from the QTS method is used as $t_f^{(0)}$ in the shooting method. The final converged initial costates:

p(0) (Rigid)	(Flexible)	γ(0)	λ₁(0) (Rigid)	(Flexible)	λ₂(0)
.00000E0	.00000E0	-.87221E-3	.11894E3	.11587E3	.10331E-1
.24422E2	.23767E2	.44563E-2	.67130E1	.49375E1	-.34685E-1
-.18880E0	-.11001E0		.11544E2	.10570E2	
.24825E1	.22818E1				

The Hamiltonian, H, is observed as a constant during each iteration and is iteratively reduced to the final value:

$$H= 1.2000E-9$$

The time histories of the slews are plotted in Fig. 3 to Fig. 6. In these figures, the results for the attitude angles, the mode amplitudes, the control torques, and the switching functions are presented, whenever applicable.

Fig. 3 shows the rigid SCOLE maneuver by using the QTS method and Fig. 4 shows the rigid SCOLE maneuver by using the shooting method. The results show that the solutions by using the two methods are very close. It is also noted that, during the slew, the yawing control, u_3, switches twice consecutively before other controls (rolling control u_1 or pitching control u_2) switch.

Figs. 5 and 6 show the flexible SCOLE maneuver by using the QTS and the shooting methods, respectively. Again, the results from both methods are close. Due to the inclusion of the flexible modes, the switching number for every control is tripled or even more (23 for u_3) compared with the results for the rigid SCOLE maneuver. The modal amplitudes are very small and the associated vibration of the reflector of the SCOLE and the "Line of Sight" are also very small.

(a) Attitude Angles (deg)

Roll

Pitch   Yaw

Time (sec)

(b) Controls (1E4 ft-lb)

Roll

Pitch

Yaw

Time (sec)

Fig. 3 Rigid SCOLE Maneuver,

Roll Angle = 90° (QTS Method)

(a) Attitude Angles (deg)

(c1) Roll Controls (1E4 ft-lb)   Switching Func.

(c2) Pitch Controls (1E4 ft-lb)   Switching Func.

(c3) Yaw Controls (1E4 ft-lb)   S. Func. (1E-4)

Fig. 4 Rigid SCOLE Maneuver,
Roll Angle = 90° (Shooting Method)

(a) Attitude Angles (deg)

(b) Flexible Modes

(c) Controls (1E4 ft-lb)
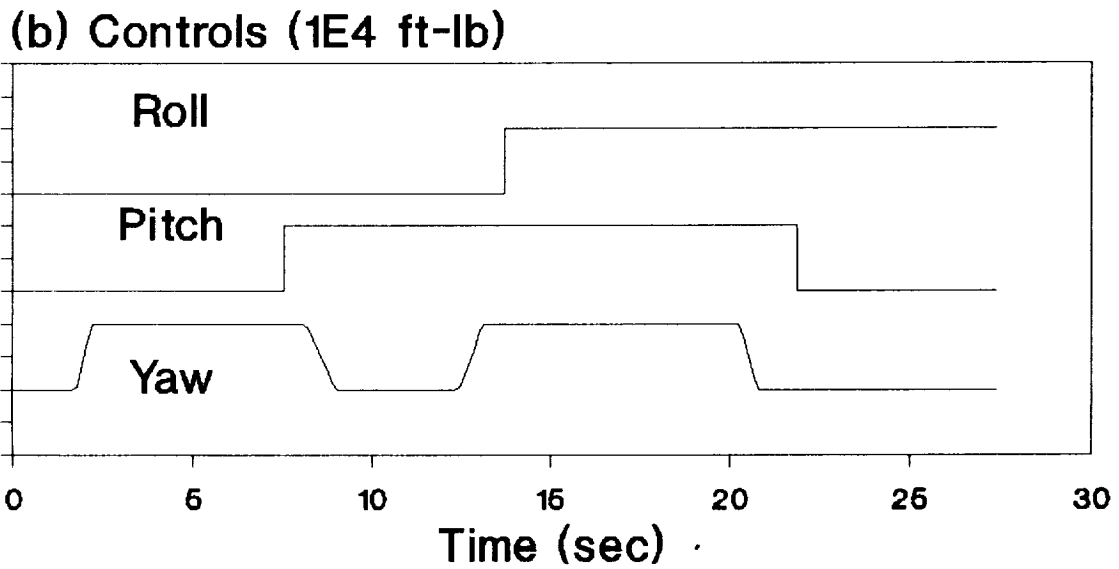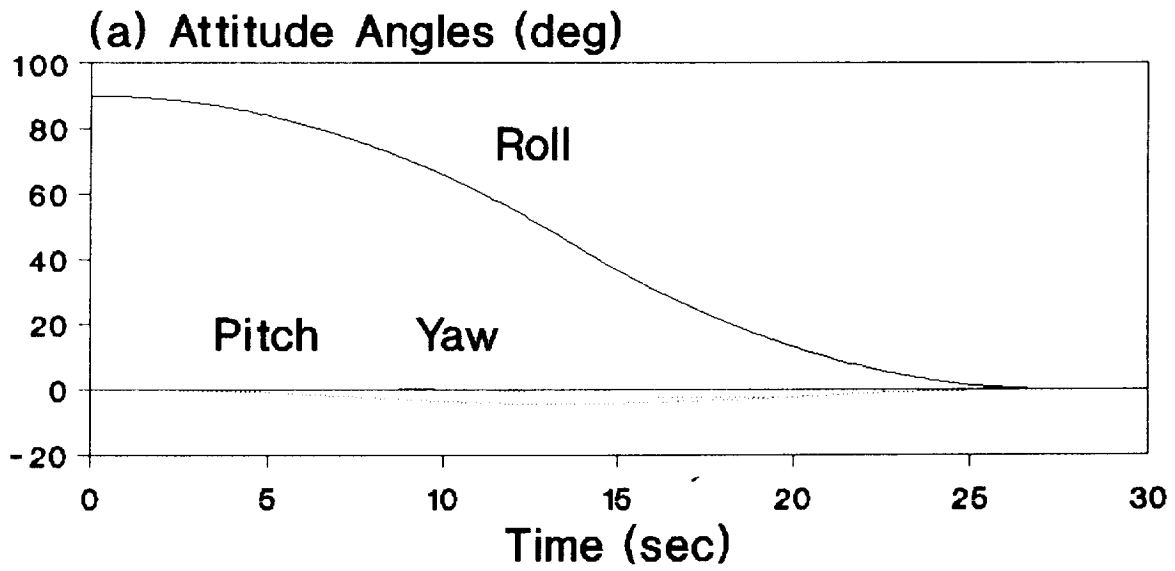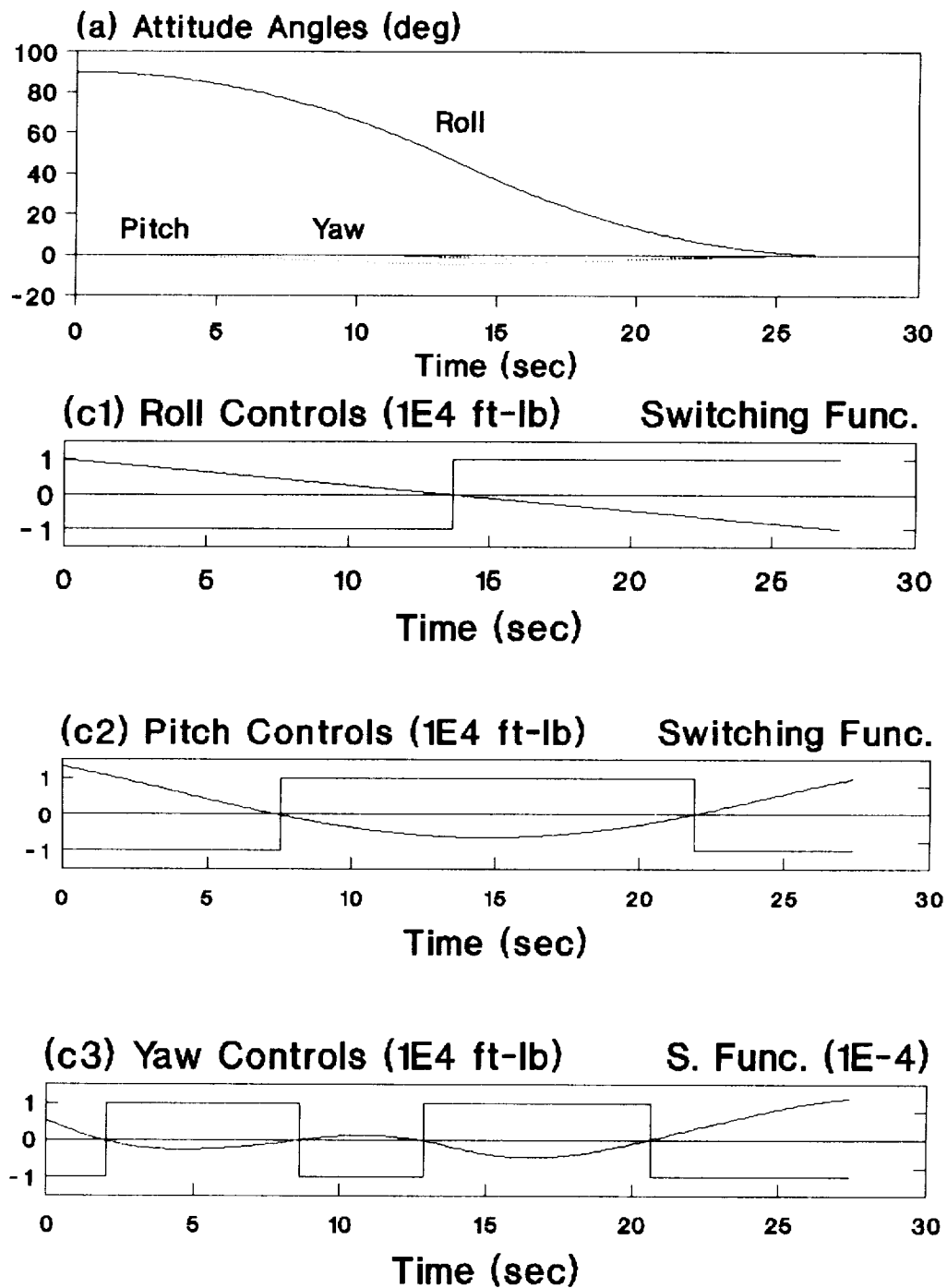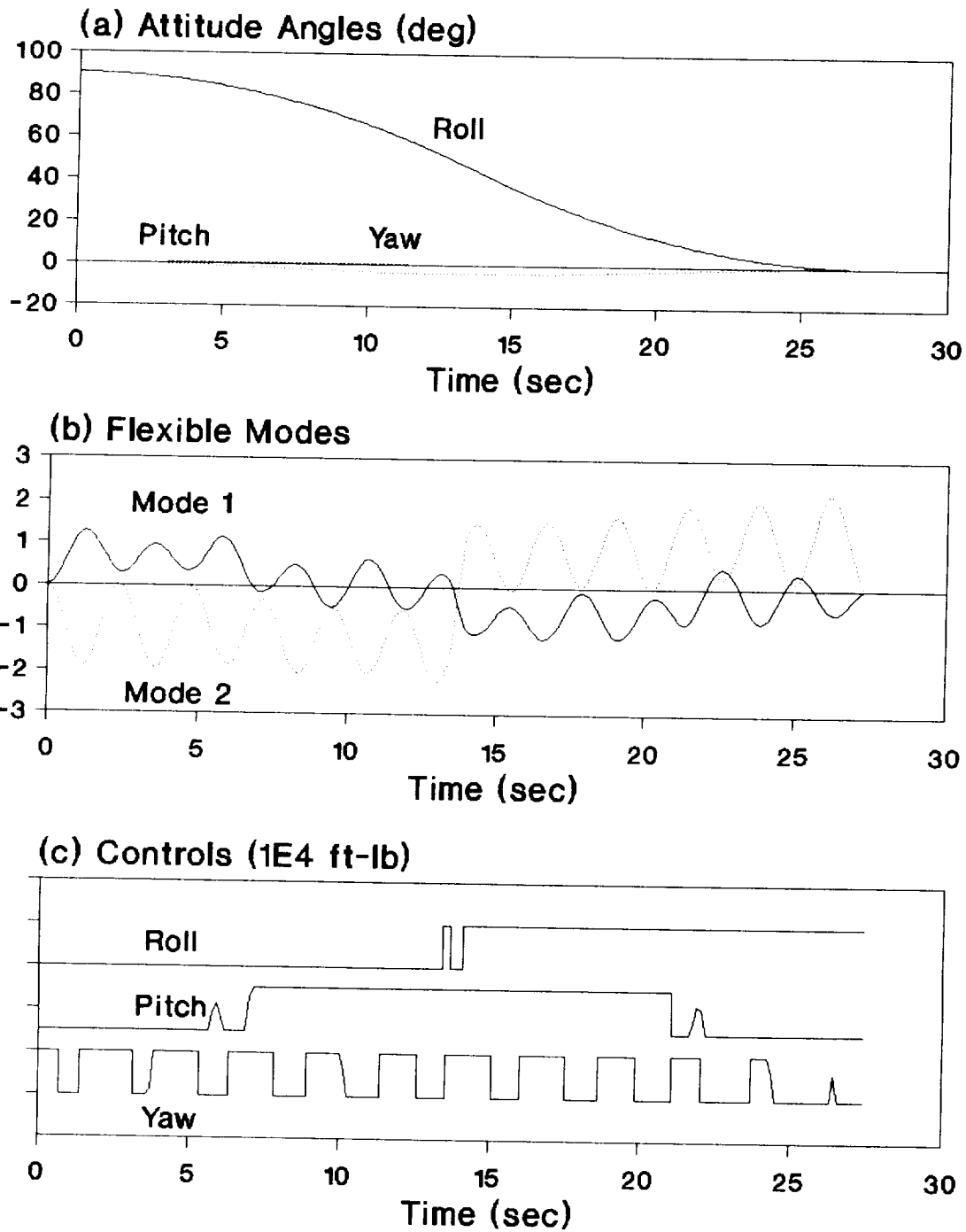
Fig. 5 Flexible SCOLE Maneuver,
Roll Angle = 90° (QTS Method)

Fig. 6 Flexible SCOLE Maneuver,

Roll Angle = 90° (Shooting Method)

(c1) Roll Control (1E4 ft-lb)   Switching Func.

(c2) Pitch Control (1E4 ft-lb)   Switching Func.

(c3) Yaw Control (1E4 ft-lb)   Switching Func.
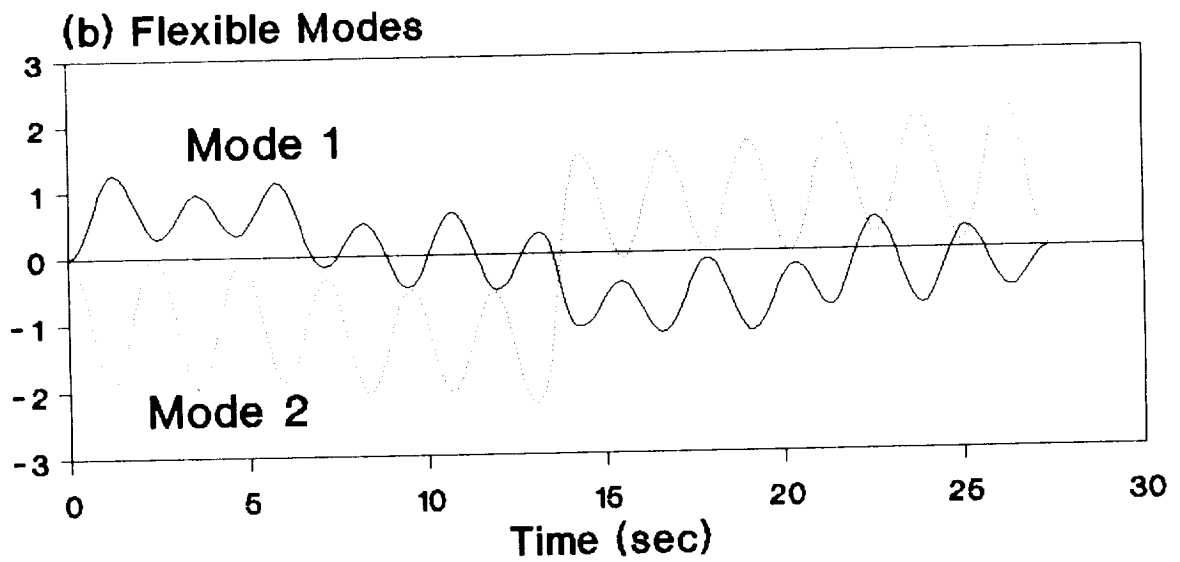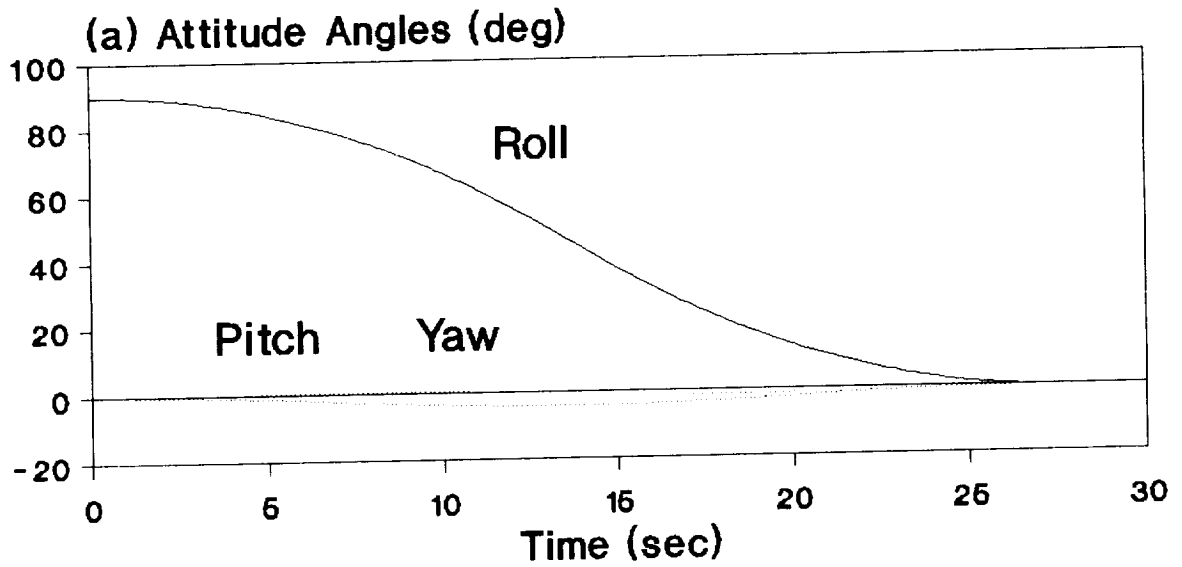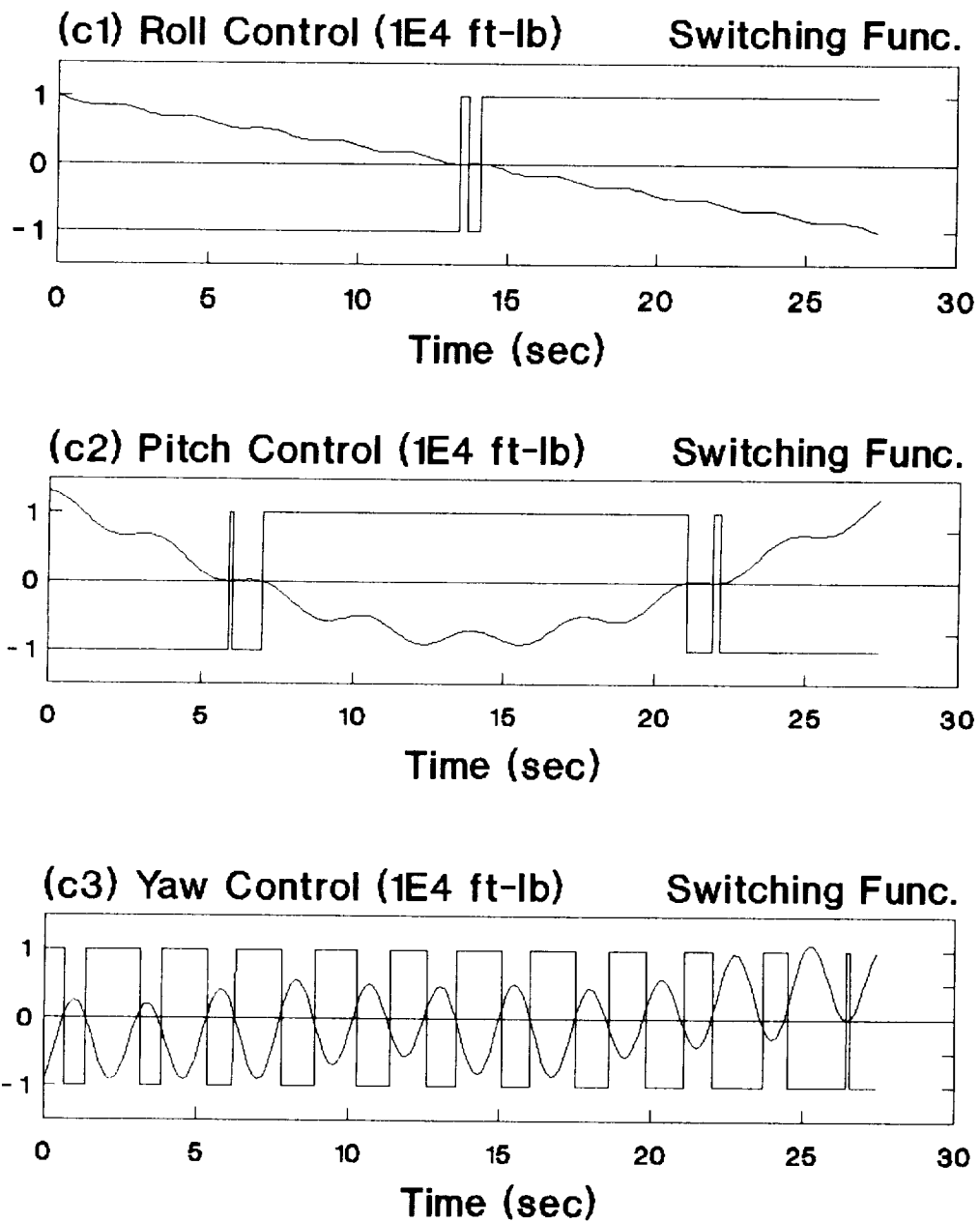
Fig. 6 (Cont'd) Flexible SCOLE Maneuver,
Roll Angle = 90° (Shooting Method)

CONCLUSIONS

1. The QTS method is stable for relatively coarse choices of the unknown initial costates, and the shooting method is not.

2. The QTS method usually results in very large values of the costates which may lead to the numerical overflow in the calculation process, if the "exact" (numerically) switching times are to be found, while the shooting method does not have this problem and exact switching times can be obtained iteratively.

3. A technique to combine these two methods is proposed.

4. The estimated initial values of the costates, $p(0)$, $\gamma(0)$, and $\lambda(0)$, based on the solution from the QTS method, are very close to the converged values of these parameters in the shooting method and hence the convergence of the shooting method has been improved.

5. The costates from both methods are proportional.

6. The control histories from both methods are the same and may imply the uniqueness of the control for the slewing problem.

7. The application of this method to the minimum time maneuver of other flexible spacecraft is suggested.

314

REFERENCES

1. Taylor, L.W. and Balakrishnan, A.V., "A Mathematical Problem and a Spacecraft Control Laboratory Experiment (SCOLE) used to Evaluate Control Laws for Flexible Spacecraft ... NASA/IEEE Design Challenge," *Proceedings of the 4th VPI&SU Symposium on Dynamics and Control of Large Structures*, Blacksburg, VA, June 1983. Revised January 1984.

2. Junkins, J.L. and Turner, J.D., *Optimal Spacecraft Rotational Maneuvers*, Elsevier, Amsterdam, 1986.

3. Vadali, S.R. and Junkins, J.L., "Spacecraft Large Angle Rotational Maneuvers with Optimal Momentum Transfer," *The Journal of the Astronautical Sciences*, Vol. 31, No. 2, 1983, pp. 217-235.

4. Wie, B. and Barba, P.M., "Quaternion Feedback for Spacecraft Large Angle Maneuvers," *Journal of Guidance, Control, and Dynamics*, Vol. 8, No. 3, 1985, pp. 360-365.

5. Li, F. and Bainum, P.M., "Numerical Approach for Solving Rigid Spacecraft Minimum Time Attitude Maneuvers," *Journal of Guidance, Control, and Dynamics*, Vol. 13, No. 1, 1990, pp. 38-45.

6. Li, F. and Bainum, P.M., "An Improved Shooting Method for Solving Minimum-Time Maneuver Problem," *The ASME Winter Annual Meeting*, Dallas, Texas, Nov. 25-30, 1990, DSC-Vol. 20 pp. 13-18.

7. Turner, J.D. and Junkins, J.L., "Optimal Large-Angle Single-Axis Rotational Maneuvers of Flexible Spacecraft," *Journal of Guidance and Control*, Vol. 3, No. 6, 1980, pp. 578-585.

8. Turner, J.D. and Chun, H.M., "Optimal Distributed Control of a Flexible Spacecraft During a Large-Angle Maneuver," *Journal of Guidance, Control, and Dynamics*, Vol. 7, No. 3, 1984, pp. 257-264.

9. Thompson, R.C., Junkins, J.L., and Vadali, S.R., "Near-Minimum Time Open-Loop Slewing of Flexible Vehicles," *Journal of Guidance, Control, and Dynamics*, Vol. 12, No. 1, 1989, pp. 82-88.

10. Singh, G., Kabamba, P.T., and McClamroch, N.H., "Planar, Time-Optimal, Rest-to-Rest Slewing Maneuvers of Flexible Spacecraft," *Journal of Guidance, Control, and Dynamics*, Vol. 12 No. 1, 1989, pp. 71-81.

11. Chun, H.M., Turner, J.D., and Juang, J.-N., "Frequency-Shaped Large-Angle Maneuvers," *The Journal of the Astronautical Sciences*, Vol. 36, No. 3, 1988. pp. 219-234.

12. Byers, R.M., Vadali, S.R., and Junkins, J.L., "Near-Minimum Time, Closed-Loop Slewing of Flexible Spacecraft," *Journal of Guidance, Control, and Dynamics*, Vol. 13, No. 1, 1990, pp. 57-65.

13. Junkins, J.L., Rahman, Z.H., and Bang, H., "Near-Minimum-Time Maneuvers of Flexible Vehicles: a Lyapunov Control Law Design Method," *28th Aerospace Sciences Meeting*, January 8-11, 1990, Reno, Nevada, AIAA Paper 90-0663.

14. Meirovitch, L. and Quinn, R.D., "Maneuvering and Vibration Control of Flexible Spacecraft," *The Journal of the Astronautical Sciences*, Vol. 35, No. 3, 1987, pp. 301-328.

15. Quinn, R.D. and Meirovitch L., "Maneuver and Vibration Control of SCOLE," *Journal of Guidance, Control, and Dynamics*, Vol. 11, No. 6, Nov.-Dec. 1988, pp. 542-553.

16. Kakad, Y.P., "Nonlinear Maneuver Dynamics of Large Flexible Spacecraft," *The ASME Winter Annual Meeting*, Dallas, Texas, Nov. 25-30, 1990, DSC-Vol. 20, pp. 19-27.

17. Bainum, P.M. and Li, F., Rapid In-Plane Maneuvering of the Flexible Orbiting SCOLE," *AAS/AIAA Astrodynamics Specialist Conference*, Stowe, Vermont, August 7-10, 1989, AAS Paper 89-422. To appear: *The Journal of the Astronautical Sciences*, Vol. 39, No. 2, 1991, pp. 233-248.

18. Bainum, P.M. and Li, F., "Optimal Large Angle Maneuvers of a Flexible Spacecraft," *Proceedings of the International Conference: Dynamics of Flexible Structures in Space*, Cranfield, Bedford, UK, May 15-18, 1990, pp. 65-71; *Acta Astronautica* Vol. 25, No. 3, 1991, pp. 141-148.

19. Tan, Z., Bainum, P.M., and Li., F., "Minimum-Time Large Angle Slew of an Orbiting Flexible Shallow Spherical Shell System," *AAS/AIAA Spaceflight Mechanics Meeting*, Houston, Texas, February 11-13, 1991, AAS Paper 91-144.

20. Lastman, G.J., "A Shooting Method for Solving Two-Point Boundary-Value Problems Arising from Non-Singular Bang-Bang Optimal Control Problems," *International Journal of Control*, Vol. 27, No. 4, 1978, pp. 513-524.

21. Miele, A. and Iyer, R.R., "General Technique for Solving Nonlinear Two-Point Boundary-Value Problems Via the Method of Particular Solutions," *Journal of Optimization Theory and Applications*, Vol. 5, No. 5, 1970, pp. 382-399.

22. Robertson, D.K., "Three-Dimensional Vibration Analysis of a Uniform Beam with Offset Inertial Masses at the Ends," NASA TM-86393, September 1985.

OPTIMAL DISTURBANCE REJECTING CONTROL
OF HYPERBOLIC SYSTEMS

Saroj K. Biswas
Department of Electrical Engineering
Temple University
Philadelphia, PA

N. U. Ahmed
Department of Electrical Engineering
University of Ottawa
Ottawa, Ontario, Canada

ABSTRACT

Optimal regulation of hyperbolic systems in the presence of unknown disturbances is considered. Necessary conditions for determining the optimal control that tracks a desired trajectory in the presence of the worst possible perturbations are developed. The results also characterize the worst possible disturbance that the system will be able to tolerate before any degradation of the system performance. Numerical results on the control of a vibrating beam are presented.

I. INTRODUCTION

The H_∞ control problem for regulation of dynamical systems in the presence of perturbations has been a subject of considerable research in recent years [4,5,6,7,10,16]. Although the original formulation of the H_∞ method was in terms of frequency domain terms, extensions in state space terms leading to feedback control using Riccati type equations have been developed [4,7,10,16]. For the infinite dimensional systems, the H_∞ control has started to gain momentum. For a summary of recent results, see the survey paper [3]. Like its finite dimensional counterpart, the frequency domain approach [9,15] as well as the state space analysis [11,12,] in the presence of both bounded and unbounded perturbations has been considered in the literature. The problems pertinent to the H_∞ control design are: a) input-output stability, b) disturbance decoupling, and c) disturbance attenuation.

This paper is concerned with disturbance attenuation of hyperbolic systems in the presence of worst possible disturbances. We utilize the concepts of optimal control theory [1,8] for infinite dimensional systems for deriving the control law for optimum regulation of the system in the presence of worst possible disturbances. The method presented in this paper is a generalization of an H_∞-type method developed in [13,14] for finite dimensional systems. The ratio of disturbance energy to the energy of the controlled system is used as a measure of performance for disturbance attenuation. We present conditions for estimation of the largest perturbation that can be attenuated and the corresponding controller to attenuate this perturbation.

The paper is organized as follows: Section II introduces the H_∞ control problem. Necessary conditions for optimum disturbance attenuation are presented in section III followed by numerical results on control of a vibrating beam in section IV. Some concluding remarks are given in section V.

II. NOTATIONS AND PROBLEM STATEMENT

We shall use the following notations for abstract function spaces throughout the paper. Let H be a Hilbert space, and V a linear subspace of H carrying the structure of a reflexive Banach space with the injection $V \subset H$ continuous. We identify H with its dual so that $V \subset H \subset V'$, where V' is the topological dual of V.

Suppose A be a bounded linear self adjoint operator $A \in \mathcal{L}(V, V')$ satisfying the conditions

$$|\langle A\varphi, \psi \rangle| \leq c \|\varphi\|_V \|\psi\|_V, \quad c \geq 0, \ \varphi, \psi \in V$$

$$\langle A\varphi, \varphi \rangle_{V', V} + \beta |\varphi|_H^2 \geq \alpha \|\varphi\|_V^2, \quad \alpha > 0, \ \beta \in R, \ \varphi \in V \tag{1}$$

Consider the hyperbolic system

$$\frac{\partial^2 y}{\partial t^2} + Ay = Bu + Cv, \quad t \in I \equiv (0, T),$$

$$y(0) = y_0, \qquad \frac{\partial y}{\partial t}(0) = y_0' \tag{2}$$

where the operator A is as defined above. The control applied to the system is denoted $u \in \mathcal{U} \equiv L_2(I, H)$, and B is a bounded linear operator $B \in \mathcal{L}(H)$. Suppose the system is perturbed by a disturbance $v \in L_2(I, H)$ through the operator $C \in \mathcal{L}(H)$. The initial conditions $y_0 \in V$ and $y_0' \in H$ are also considered to be initial disturbances to the system.

With this introduction we now pose the control problem:

Given the perturbed system (2), find the control $u \in L_2(I, H)$ that keeps the state trajectory as close as possible to a desired trajectory in the presence of maximum possible additive disturbance $v \in L_2(I, H)$ and maximum possible initial disturbances $y_0 \in V$ and $y_0' \in H$.

For a mathematical formulation of this control problem, we introduce a cost function:

$$J(u, v, y_0, y_0') = \frac{\frac{1}{2} s_1 \int_\Omega |y_0|^2 \, dx + \frac{1}{2} s_2 \int_\Omega |y_0'|^2 \, dx + \frac{1}{2} \int_{I \times \Omega} r_2 |v|^2 \, dx \, dt}{\frac{1}{2} q_1 \int_{I \times \Omega} |y - y^d|^2 \, dx \, dt + \frac{1}{2} q_2 \int_{I \times \Omega} |y_t - y_t^d|^2 \, dx \, dt + \frac{1}{2} \int_{I \times \Omega} r_1 |u|^2 \, dx \, dt} \tag{3}$$

where s_1, s_2, q_1, q_2, r_1 and r_2 are scalar weighting factors, and y^d and y_t^d are desired trajectories respectively. Then the disturbance rejecting control problem is equivalent to the minimax problem of finding a control u and a scalar λ^* so that

$$\lambda^* = \inf_{\substack{v \neq 0 \\ y_0 \neq 0 \\ y_0' \neq 0}} \sup_{u \in \mathcal{U}} J(u, v, y_0, y_0') \tag{4}$$

subject to the dynamics (2). The quantity λ^* can be interpreted as the disturbance rejection capacity of the system. A larger λ^* implies a better controller in the sense that the system will be able to tolerate larger amount perturbations before degradation of the system performance. A small λ^* means that the system is too sensitive to disturbances; despite the effects of the control the state trajectory is not close to the desired trajectory even in the presence of a small amount of perturbations.

We shall assume that a solution of this minimax problem exists. In what follows, we shall derive a set of necessary conditions that must be satisfied by the optimal controller.

III. MAIN RESULTS

We first give a brief outline of derivation of the main results. The minimax problem introduced above is solved in two steps, with the first step being finding the supremum of J over u assuming that the perturbations v and y_0, y_0' are known, and the second finding the infimum of J over nonzero perturbations. The first step determines the optimal control that regulates the system, and the second step characterizes the worst possible perturbation that the controller will be able to attenuate before a serious degradation of the system performance.

318

Clearly, the problem of finding the supremum of J over u is equivalent to minimizing the denominator of J given in (3) for fixed v, y_0, and y_0' subject to the dynamics (2). This is a well known problem in infinite dimensional control theory for hyperbolic systems (see [1,2,8] for details). Theorems 1 and 2 presented below pertain to this problem. We omit the proofs for brevity.

THEOREM 1. *For a given* $v \in L_2(I,H)$, $y_0 \in V$, *and* $y_0' \in H$, *the system* (1) *has a unique solution* $y \in L_2(I,V) \cap C(\bar{I},V)$, $y_t \in L_2(I,H) \cap C(\bar{I},H)$. *Furthermore, the mapping* $(y_0, y_0', u) \longrightarrow (y, y_t)$ *is continuous from* $V \times H \times L_2(I,H) \longrightarrow L_2(I,V) \times L_2(I,H)$. ∎

For convenience of presentation, we introduce two new variables $\varphi_1 \equiv y$ and $\varphi_2 \equiv y_t$, and rewrite the system (2) as a first order equation:

$$\frac{\partial \varphi}{\partial t} + \mathcal{A}\varphi = \mathcal{B}u + \mathcal{C}v \tag{5}$$

$$\varphi(0) = (y_0, y_0') \equiv \rho$$

where

$$\mathcal{A} = \begin{bmatrix} 0 & -I \\ A & 0 \end{bmatrix}, \quad \mathcal{B} = \begin{bmatrix} 0 \\ B \end{bmatrix} \quad \text{and} \quad \mathcal{C} = \begin{bmatrix} 0 \\ C \end{bmatrix}.$$

Using the above notations, we also rewrite the denominator of the cost function (3) as

$$J_1(u) = \frac{1}{2} \int_0^T \langle \varphi - \varphi^d, Q(\varphi - \varphi^d) \rangle_{H \times H} \, dt + \frac{1}{2} \int_0^T \langle u, R_1 u \rangle_H \, dt \tag{6}$$

where $Q = \text{diag}(q_1, q_2)$ and $R_1 = r_1$. Let q_1 and q_2 be nonnegative, and r_1 strictly positive.

The necessary and sufficient condition that $u_0 \in L_2(I,H)$ be optimal in the sense of minimization of the cost (6) is that

$$J_1'(u_0; u - u_0) \geq 0 \quad \text{for all } u \in \mathcal{U} \tag{7}$$

where $J_1'(u_0; u - u_0)$ is the Gateaux derivative of J_1 at $u_0 \in \mathcal{U}$ in the direction $u - u_0$. This is given in the next theorem:

THEOREM 2. *Consider the system* (5) *for fixed additive disturbance* $v \in L_2(I,H)$, *fixed initial disturbance* $\rho \in V \times H$, *and the desired trajectory* $\varphi^d \in L_2(I,H) \times L_2(I,H)$. *Then the optimal control* $u_0 \in L_2(I,H)$ *that minimizes the cost* (6) *is characterized by the solution of the two-point-boundary-value problem:*

$$\frac{\partial \varphi}{\partial t} + \mathcal{A}\varphi + \mathcal{B}R_1^{-1}\mathcal{B}^*\psi = \mathcal{C}v, \quad \varphi(0) = \rho \tag{8}$$

$$-\frac{\partial \psi}{\partial t} + \mathcal{A}^*\psi = Q(\varphi - \varphi^d), \quad \psi(T) = 0 \tag{9}$$

The optimal control u_0 *is then given by*

$$u_0 = -R_1^{-1}\mathcal{B}^*\psi. \tag{10} \quad ∎$$

At this point we return to the disturbance rejecting control problem introduced earlier. Clearly $J(u_0)$ is a function of v and ρ which are yet to be determined. We substitute $J_1(u_0)$ into the denominator of the cost function (3) leading to

$$J(v, \rho) = \frac{\frac{1}{2}\langle \rho, S\rho \rangle_H + \frac{1}{2}\int_I \langle v, R_2 v \rangle_H \, dt}{\frac{1}{2}\int_I \langle \varphi - \varphi^d, Q(\varphi - \varphi^d) \rangle_{H \times H} \, dt + \frac{1}{2}\int_I \langle \mathcal{B}R_1^{-1}\mathcal{B}^*\psi, \psi \rangle \, dt} \tag{11}$$

Then the disturbance rejecting control problem is equivalent to finding a scalar λ^* so that

$$\lambda^* = \inf_{\substack{v \neq 0 \\ \rho \neq 0}} J(v, \rho) \tag{12}$$

subject to the dynamics (8) - (9). Note that since λ^* is the optimal solution, we have $0 < \lambda^* \leq \lambda = J(v, \rho)$. Hence clearly, the following function

$$J_2(v, \rho) = \frac{1}{2}\langle \rho, S\rho \rangle_H + \frac{1}{2}\int_I \langle v, R_2 v \rangle_H \, dt - \frac{\lambda^*}{2}\int_I \langle \varphi - \varphi^d, Q(\varphi - \varphi^d) \rangle_{H \times H} \, dt - \frac{\lambda^*}{2}\int_I \langle BR_1^{-1}B^*\psi, \psi \rangle \, dt \tag{13}$$

is convex and nonnegative, and has a minimum at $J_2 = 0$. Thus the problem of finding the infimum indicated in (12) is equivalent to minimizing (13) subject to the system dynamics (8) - (9).

By virtue of Theorem 1, it is clear that for any $v \in L_2(I, H)$, $\rho \in V \times H$, and $\varphi^d \in L_2(I, H) \times L_2(I, H)$, the equations (8) - (9) have a unique solution $\varphi \in L_2(I, V) \times L_2(I, H)$ and $\psi \in L_2(I, V) \times L_2(I, H)$. In addition, the solution has a unique Gateaux derivative satisfying the following theorem:

THEOREM 3. *The solution* (φ, ψ) *of the two-point-boundary-value problem* (8) - (9) *corresponding to* $v \in L_2(I, H)$ *and* $\rho \in V \times H$ *has a unique Gateaux derivative at every* $v_0 \in L_2(I, H)$ *and* $\rho_0 \in V \times H$ *satisfying*

$$\frac{\partial \widehat{\varphi}}{\partial t} + \mathcal{A}\widehat{\varphi} + \mathcal{B}R_1^{-1}\mathcal{B}^*\widehat{\psi} = \mathcal{C}(v - v_0), \quad \widehat{\varphi}(0) = \rho - \rho_0 \tag{14}$$

$$-\frac{\partial \widehat{\psi}}{\partial t} + \mathcal{A}^*\widehat{\psi} - Q\widehat{\varphi} = 0, \quad \widehat{\psi}(T) = 0 \tag{15}$$

with $\widehat{\varphi} \in L_2(I, V) \times L_2(I, H)$ *and* $\widehat{\psi} \in L_2(I, V) \times L_2(I, H)$ ∎

Necessary conditions of optimality for minimization of (13) are now derived with the help of the above results and the fact that the Gateaux derivative

$$J_2'(v_0, \rho_0; v - v_0, \rho - \rho_0) \geq 0 \tag{16}$$

for all $v \in L_2(I, H)$ and $\rho_0 \in V \times H$, where J_2' is the Gateaux derivative at v_0, ρ_0 in the direction $v - v_0$, $\rho - \rho_0$. We present the result in the following theorem:

THEOREM 4. *The worst additive disturbance* v_0 *and the worst initial disturbance* ρ_0 *that can be attenuated by the optimal control* u_0 *are characterized by simultaneous solution of the following equations:*

$$\frac{\partial \varphi}{\partial t} + \mathcal{A}\varphi + \mathcal{B}R_1^{-1}\mathcal{B}^*\psi = \mathcal{C}R_2^{-1}\mathcal{C}^*\xi, \tag{17}$$

$$-\frac{\partial \psi}{\partial t} + \mathcal{A}^*\psi = Q(\varphi - \varphi^d), \tag{18}$$

$$-\frac{\partial \xi}{\partial t} + \mathcal{A}^*\xi - Q\eta = \lambda^*Q(\varphi - \varphi^d) \tag{19}$$

$$\frac{\partial \eta}{\partial t} + \mathcal{A}\eta + \mathcal{B}R_1^{-1}\mathcal{B}^*\xi = \lambda^*\mathcal{B}R_1^{-1}\mathcal{B}^*\psi \tag{20}$$

with the boundary conditions

$$\begin{aligned} \varphi(0) &= \rho_0 & \psi(T) &= 0 \\ \xi(0) &= S\rho_0 & \xi(T) &= 0 \\ \eta(0) &= 0 \end{aligned} \tag{21}$$

The worst disturbances are given by

$$v_0 = R_2^{-1} C^* \xi$$

$$\rho_0 = S^{-1} \xi(0) \tag{22}$$

The optimal control that regulates the system in the presence of the worst disturbance is given by

$$u_0 = -R_1^{-1} B^* \psi \tag{23}$$

PROOF: Taking the Gateaux derivative of the J_2 at $v_0 \in L_2(I, H)$ and $\rho_0 \in V \times H$, we have

$$0 \leq J_2'(v_0, \rho_0; v-v_0, \rho-\rho_0) = \langle S\rho_0, \rho-\rho_0 \rangle_H + \int_I \langle R_2 v_0, v-v_0 \rangle \, dt - \lambda^* \int_I \langle \widehat{\varphi}, Q(\varphi-\varphi^d) \rangle \, dt - \lambda^* \int_I \langle \widehat{\psi}, BR_1^{-1} B\psi \rangle \, dt$$

The result follows from Theorem (3) and adjoint system (19) - (20). ∎

It is worthwhile to mention here that equations (17) - (21) represent a two-point-boundary-value problem with λ^* as a parameter which is unknown. The smallest value of λ for which this TPBVP, i.e., (17) - (21) has a solution is the optimal λ^* or the disturbance rejection capacity of the system. The corresponding control u_0 is then obtained using (23) and the worst disturbance v_0 and ρ_0 that can be attenuated is given by (22).

IV. EXAMPLE

We consider the cantilever beam equation (normalized)

$$\frac{\partial^2 y}{\partial t^2} + \frac{\partial^4 y}{\partial x^4} = g(x)u(t) + h(x)v(t), \qquad x \in \Omega \equiv (0,1), \quad t > 0 \tag{24}$$

subject to boundary conditions

$$y(0,t) = 0, \quad \frac{\partial y}{\partial x}(0,t) = 0, \quad \frac{\partial^2 y}{\partial x^2}(1,t) = 0, \quad \frac{\partial^3 y}{\partial x^3}(1,t) = 0 \tag{25}$$

Define the operator A in $H = L_2(\Omega)$ by

$$A\phi = \frac{\partial^4 \phi}{\partial x^4}, \qquad D(A) = \left\{ \phi : \phi \in H^4(\Omega), \phi(0) = 0, \frac{\partial \phi}{\partial x}(0) = 0, \frac{\partial^2 \phi}{\partial x^2}(1) = 0, \frac{\partial^3 \phi}{\partial x^3}(1) = 0 \right\}$$

where $H^4(\Omega)$ is the Sobolev space of order four on Ω. For V we take $V = \{\phi \in H^2(\Omega), \phi(0) = 0, \frac{\partial \phi}{\partial x}(0) = 0\}$.

We assume that the desired state of the controlled system is the zero state, and that there is no initial disturbance. We compute the disturbance rejection capacity of the system using Theorem 4. Table I shows that a tighter regulation (i.e., higher Q) is possible only if less disturbance is allowed to be attenuated. It is intuitively correct to say that a better regulation of the state trajectory can be achieved if the disturbance amplitude is small. Similarly a cheaper control allows more disturbance accommodation by the controller as shown in Table II. Stated in a different way, this means that attenuation of larger amplitude disturbances will require more control energy.

TABLE I

Q	r_1	r_2	S	λ^*
1	1	1	10	0.5522
10	1	1	10	0.2130
20	1	1	10	0.1521
50	1	1	10	0.0922
100	1	1	10	0.0618

TABLE II

Q	r_1	r_2	S	λ^*
20	1	1	10	0.1521
20	2	1	10	0.1065
20	5	1	10	0.0637
20	10	1	10	0.0420

V. CONCLUSION

We present an H_∞-like control method for hyperbolic systems. Necessary conditions in the form of a two-point-boundary-value problem for determining the optimum controller and the worst exogenous input that can be attenuated by the optimum controller have been derived. The results are related to the H_∞ control problem in the sense that the H_∞ norm is given by the inverse of square root of λ^* [14]. The disturbance rejection capacity has been computed for a cantilever beam. Further research needs to be done to develop state feedback and output feedback controllers, and to extend the method to the infinite horizon control problems.

VI. REFERENCES

[1] Ahmed N.U. and K.L. Teo, *Optimal Control of Distributed parameter Systems*, North Holland, New York, 1981.

[2] Biswas S.K. and N.U. Ahmed, "Optimal Control of Large Space Structures Governed by a Coupled System of Ordinary and Partial Differential Equations", *Mathematics of Control, Signals, and Systems*, Vol. 2, pp. 1 - 16, 1989.

[3] Curtain R., "H_∞ Control for Distributed Parameter Systems: A Survey", *Proc. IEEE CDC*, pp. 22 - 26, 1990.

[4] Doyle John, K. Glover, P. Khargonekar, and B. Francis, "State- Space Solutions to Standard H_2 and H_∞ Control Problems", *IEEE Trans. on Automatic Control*, Vol. AC 34, pp. 831 - 847, 1989.

[5] Francis Bruce, *A Course in H_∞ Control theory*, Springer Verlag, Berlin, 1987.

[6] Francis B. and John Doyle, "Linear Control Theory with an H_∞ Optimality Criterion", *SIAM Jour. on Control and Optimization*, Vol. 25, pp. 815 - 844, 1987.

[7] Khargonekar P., I. Petersen, and M. Rotea, "H_∞ Optimal Control with State Feedback", *IEEE Trans. on Automatic Control*, Vol. AC 33, pp. 786 - 788, 1988.

[8] Lions J.L., *Optimal Control of Systems Governed by Partial Differential Equations*, Springer Verlag, Berlin, 1971.

[9] Ozbay H., "H_∞ Control of Distributed Systems: A Skew Toeplitz Approach", *Thesis*, University of Minnesota, June, 1989.

[10] Petersen Ian, "Disturbance Attenuation and H_∞ Optimization: A Design Method Based on the Algebraic Riccati Equation", *IEEE Trans. on Automatic Control*, Vol. AC 32, pp. 427 - 429, 1987.

[11] Pritchard A.J. and D. Salamon, "The Linear Quadratic Optimal Control Problem for Infinite Dimensional Systems with Bounded and Unbounded Operators", *SIAM Journal on Control and Optimization*, Vol. 25, pp. 121 - 144, 1987.

[12] Pritchard A.J. and S. Townley, "Robustness of Linear Systems", *Journal of Differential Equations*, Vol. 77, pp. 254 - 286, 1989.

[13] Subrahmanyam M.B., "Worst-Case Design of Optimal Controllers over a Finite Horizon", *Technical report, Naval Air Development center, NADC 91005-60*, Warminster, PA, January, 1991.

[14] Subrahmanyam M.B., *Optimal Control with a Worst Case Performance Criterion and Applications*, Lecture Notes in Control and Information Sciences, No. 145, Springer Verlag, New York, 1990.

[15] Wexler D., "On Frequency Domain Stability for Evolution Equations in Hilbert Space via the Algebraic Riccati equation", *SIAM Journal on Mathematical Analysis*, Vol. 11, pp. 969 - 983, 1980.

[16] Zhou K. and P.P. Khargonekar, "An Algebraic Riccati Equation Approach to H_∞ Optimization", *System and Control Letters*, Vol. 11, pp. 85 - 91, 1988.

Effects of Noise Variance Model on Optimal Feedback Design and Actuator Placement

Mifang Ruan and Ajit K. Choudhury
Dept. of Electrical Engineering
Howard University
Washington, DC 20059

ABSTRACT

In optimal placement of actuators for stochastic systems, it is commonly assumed that the actuator noise variances are not related to the feedback matrix and the actuator locations. In this paper, we will discuss the limitation of that assumption and develop a more practical noise variance model. Various properties associated with optimal actuator placement under the assumption of this noise variance model are discovered through the analytical study of a second order system.

Introduction

Refs. [1-4] are typical works in the literature for actuator placement of stochastic systems. In all of these works, it is assumed that the noise strengths of the actuators are given and not related to the feedback and actuator locations — an assumption made in the LQG theory. However, as shown in Ref. [5], this noise variance model is not always true in practice. For example, the noise strength of an actuator may depend on its capacity (the largest signal it can produce) and the magnitude of its producing signal. Clearly, if a person (actuator) is required to push an object with 1 lbf (small signal), the error of the produced force will be probably several ounces (small variance). However, if he is required to push the object with 100 lbf (large signal), the error of the produced force will be several or ten pounds (large variance). Also, the noise of a reaction wheel (actuator) may be caused by the bearing and eccentricity of the wheel, etc. If a reaction wheel is required to produce a larger signal (larger capacity), it is

usually required to increase the inertial of the wheel and/or the maximum spinning speed, then the noise caused by the bearing and eccentricity will be greater. These facts show that the actuator noise strength usually depends on the capacity and the signal magnitude of the actuator. Since the signal magnitude and the required capacity of the actuator depend on the feedback matrix and the actuator location, the noise strength of the actuator implicitly depends on the feedback matrix and the actuator location. Clearly, when an actuator is placed at a carefully selected location, the control force and the required capacity of the actuator will be smaller. Also, the signal and capacity will depend on the feedback matrix because a smaller feedback (slower system) usually requires a smaller control force. Since the ordinary LQG theory neglects these facts, it cannot be used to reduce the noise variance of the actuator through the selection of a feedback matrix and actuator locations, and thus results in unnecessarily noisy systems.

A New Noise Variance Model

In most practical applications, the actuator noise variance increases with its capacity and signal magnitude. Since the required capacity in steady state is related to the signal variance of the actuator, we can reasonably use the signal variance to represent the actuator capacity in the new noise variance model. To take into account the effects of the signal magnitude on the noise variance, we may use the signal square in the noise variance model. However, this method will result in time-dependent noise variance and make analysis very complicated. In order to simplify the analysis, we can use the time average method, then signal square again becomes signal variance. According to the discussion above, we can develop a realistic noise variance model of an actuator as

$$W = \alpha' \sigma_u^2 + \alpha'' \sigma_u^2 + \beta \triangleq \alpha \sigma_u^2 + \beta \tag{1}$$

where σ_u^2 is the variance of the actuator signal in steady state. α', α'' and β are non-negative constants which depend on manufacturing processes. The term $\alpha' \sigma_u^2$ reflects the contribution

of the actuator signal magnitude, and the term $\alpha'' \sigma_u^2$ reflects the contribution of the actuator's capacity. An advantage of this noise variance model is that the noise is still white, Gaussian with constant variance, and thus analysis can be simplified. The only difference from the ordinary model is that the noise variance in the new model will depend on the capacity and signal magnitude of the actuator, and will thus implicitly depend on the feedback and actuator locations.
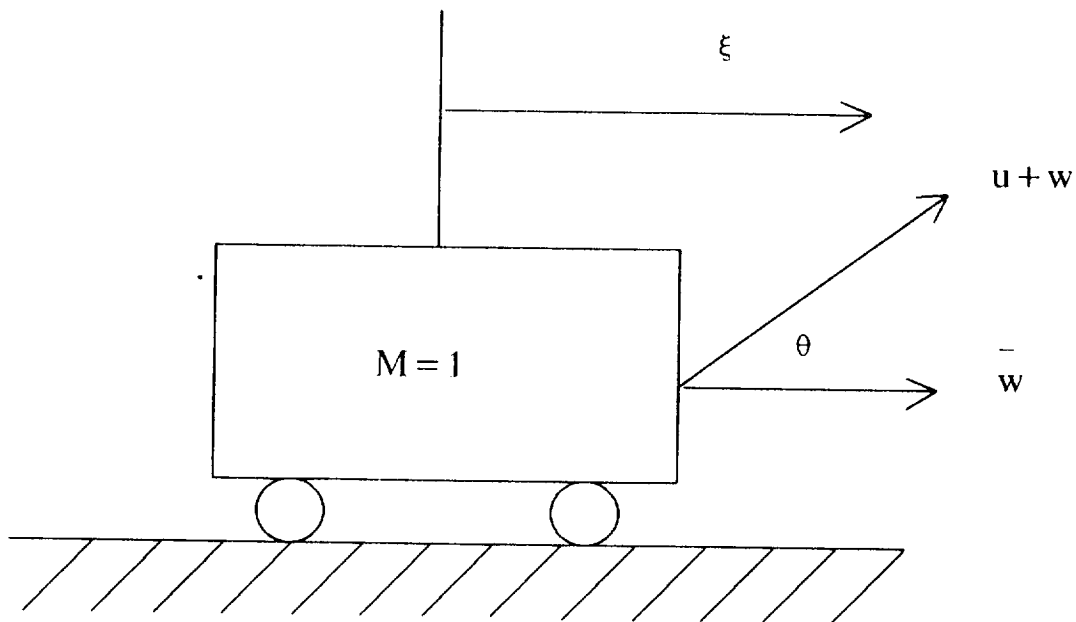

Figure 1. A second order system.

A Physical System

The new noise variance model, Eq. (1), will be applied to a second order system shown in figure 1. In the system, $\bar{w}$ is the plant disturbance with given strength $\bar{W}$, but w is actuator noise whose strength is governed by Eq. (1). The actuator orientation (location) is specified by angle, θ. Obviously, the actuator is most efficient when $\theta = 0$, and is most desirable for a deterministic system. However, as shown in Ref. [1], the selection of $\theta = 0$ may not give optimal performance for stochastic systems, especially when the ratio of plant disturbance to actuator noise is small.

The state equation is given by

$$\dot{x} = Ax + B(u+w) + G\,\bar{w} \tag{2}$$

with

$$x = \begin{bmatrix} \xi \\ \dot{\xi} \end{bmatrix} \;\; ; \;\; A = \begin{bmatrix} 0 & 1 \\ 0 & 0 \end{bmatrix} \;\; ; \;\; B = \begin{bmatrix} 0 \\ b \end{bmatrix} \;\; ; \;\; G = \begin{bmatrix} 0 \\ 1 \end{bmatrix} \tag{3}$$

where $b = \cos\theta$. Without losing generality, we assume $0 \le b \le 1$. Clearly, matrix G is fixed but matrix B changes with actuator location. The feedback control law is given by

$$u = -F\,x \tag{4}$$

The objective of the problem is to find the optimal feedback F, and the optimal actuator orientation b, so that the following cost function is minimized:

$$J = E_\infty \lfloor q\, x^T x + r\, u^2 \rfloor \tag{5}$$

where q and r are given weights, E_∞ is the mean operator when the time period approaches infinity.

Since the noise is still white and Gaussian with constant variance, we can use stochastic control theory to find the variance of the state, P_x:

$$P_x (A - BF)^T + (A - BF) P_x + BWB^T + G\bar{W}G^T = 0 \tag{6}$$

The solution of Eq. (6) is given by

$$P_x = \text{diag}\,[P_{x1}, P_{x2}] \tag{7}$$

with

$$P_{x1} = \frac{b^2 \beta + \bar{W}}{2b^2 f_1 f_2 - \alpha b^2 f_1^2 - \alpha b^3 f_1 f_2^2} \tag{8}$$

$$P_{x2} = bf_1 P_{x1} \tag{9}$$

The cost function (5) can be rewritten as

$$J = (q + rf_1^2) P_{x1} + (q + rf_2^2) P_{x2} \tag{10}$$

where f_1 and f_2 are elements of the feedback matrix. When the weights, noise parameters and the actuator orientation are all given, the cost will be a function of f_1 and f_2. The optimal feedback can be obtained by our equating the partial derivatives of the cost with respect to f_1 and f_2 to zero. After substantial mathematical manipulation, the equations for optimal feedback become

$$b\, f_1^2 - b\, f_2^2 + 2\, f_1 = 0 \tag{11}$$

$$f_1^2 = \frac{q}{r}(1 - \alpha b\, f_2) \tag{12}$$

These equations give optimal feedback when the actuator orientation is fixed. We can see that the feedback matrix does not depend on the plant disturbance and β since they correspond to the ordinary noise variance in LQG theory. Eqs. (11–12) are a parabolic equation and a hyperbolic equation. Those equations can be plotted in the $f_1 - f_2$ plane (Fig. 2), and may give up to 4 intersection points. By inspection, only one point out of the 4 corresponds to a stable system. It should be noted that for the new noise variance model the solution obtained from ordinary LQG method is no longer optimal. The solution of the feedback corresponding to ordinary noise variance model (LQG) can be obtained by our equating α to zero, and is also plotted in the figure. The trends of the new and ordinary solutions and their difference can be seen clearly from the figure when q/r, b, or α is changed. It shows that the optimal f_1 is between 0 and $1/(\alpha b)$, and the optimal f_2 is between 0 and $sqrt(q/r)$. When α becomes larger or q/r becomes larger, the difference between the optimal solution and the ordinary LQG solution becomes more significant. Both elements of the optimal feedback matrix are smaller than those obtained by LQG method. Clearly, smaller feedback elements help to reduce the actuator noise.

To find optimal actuator orientation, we differentiate the cost with respect to b by considering the feedback elements as functions of b. By equating the derivative to zero, we obtain a really complicated equation for optimal actuator location. After much mathematical manipulation the equation becomes:
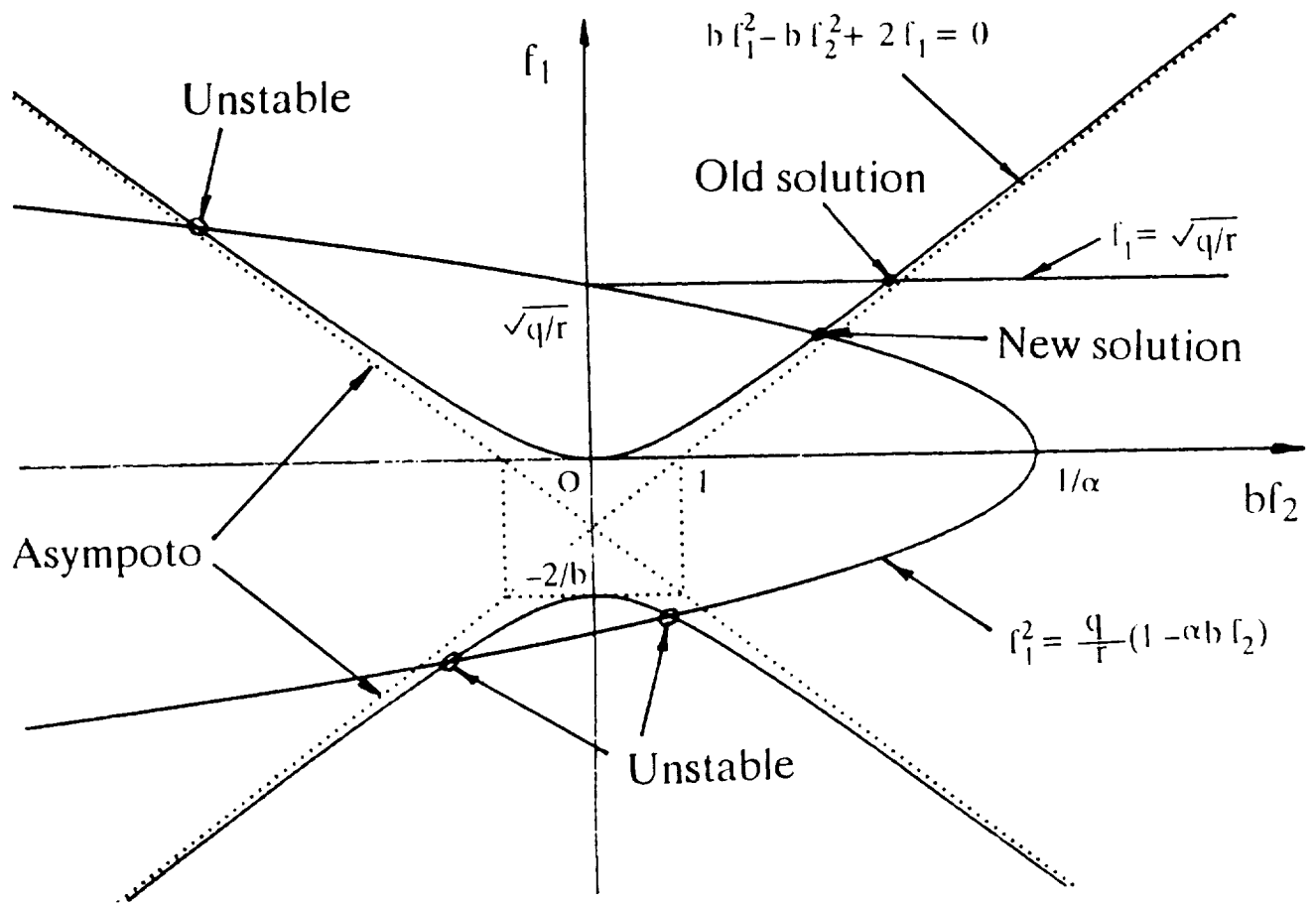
Figure 2. The plot of feedback for ordinary and new solutions.

$$b^2(1+bf_1) \mid \frac{q}{r} \alpha^2(1+bf_1)^2 + 4f_2^2 - 4\alpha f_1 f_2 \mid - (3+bf_1)[2f_2 - 3\alpha f_1 - b\alpha f_1^2]^2 \frac{\bar{W}}{\beta} = 0$$

$$(13)$$

It can be seen that $\bar{W}/\beta$ does not affect the feedback but it does affect the optimal actuator location. The optimal actuator location differs from that obtained by the ordinary noise variance model in Ref. [1], and the latter can also be obtained by our equating α to zero in Eq. (13).

Eqs. (11-13) can be solved simultaneously to obtain the optimal feedback and the optimal actuator location. Some properties of Eqs. (11-13) can simplify the computation of the optimal feedback and optimal actuator location. For example, there is one and only one solution of f_1 between 0 and sqrt(q/r) if α is not zero, and the left side of Eq. (13) is a monotonous function of b.

It is particularly interesting to investigate Eq. (13) when $b = 1$. In this case, for different values of α, we can plot $\bar{W}/\beta$ as a function of q/r, as shown in Fig. 3. In the $\bar{W}/\beta$-q/r plane, for a specific α, the optimal b in the area above the corresponding curve is larger than 1, and the optimal b in the area below the corresponding curve is smaller than 1. Since b (= cos θ) can not be greater than 1, we must use b = 1 in the area above the corresponding curve.

Fig. 4 shows the optimal b as a function of α and q/r when $\bar{W}/\beta = 1$. Clearly, optimal b decreases with α and q/r and could be significantly less than 1. Computation also shows that when $\bar{W}/\beta$ decreases the optimal b will also decrease; when $\bar{W}/\beta$ increases the optimal b will also increase.

Conclusion

In many applications, a more practical noise variance model of an actuator than the one in LQG theory is that its noise variance increases with its signal variance. In this paper, we investigated the optimal control and optimal actuator placement when the actuator noise variance increases linearly with its signal variance. In this case the feedback and actuator location obtained by ordinary LQG theory are no longer optimal.
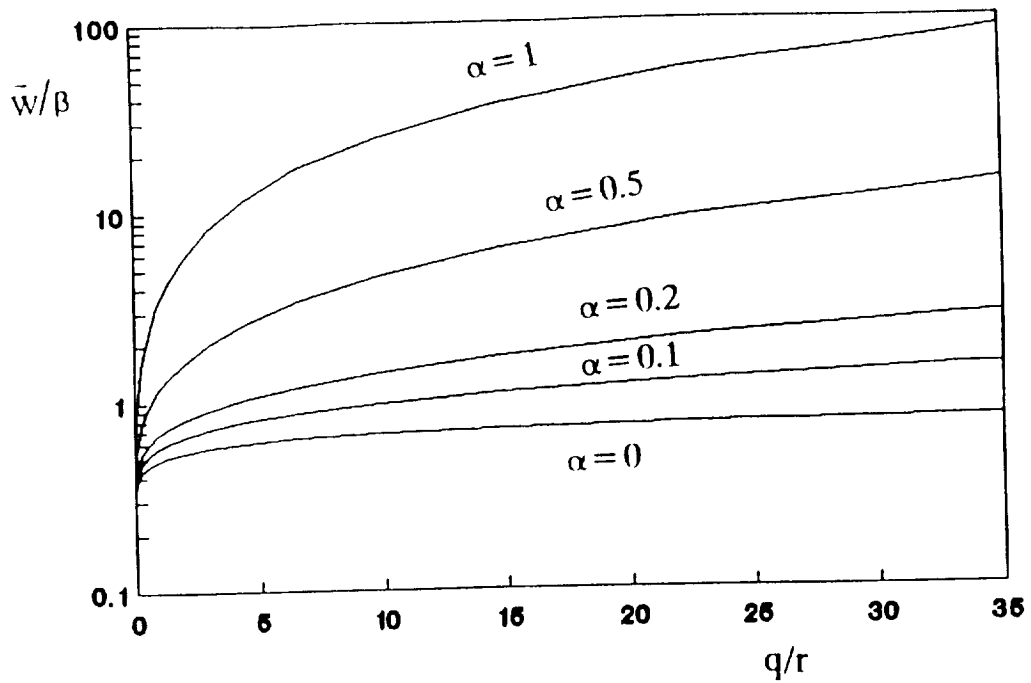
Figure 3. The areas of b < 0 and b = 1 for several values of α.
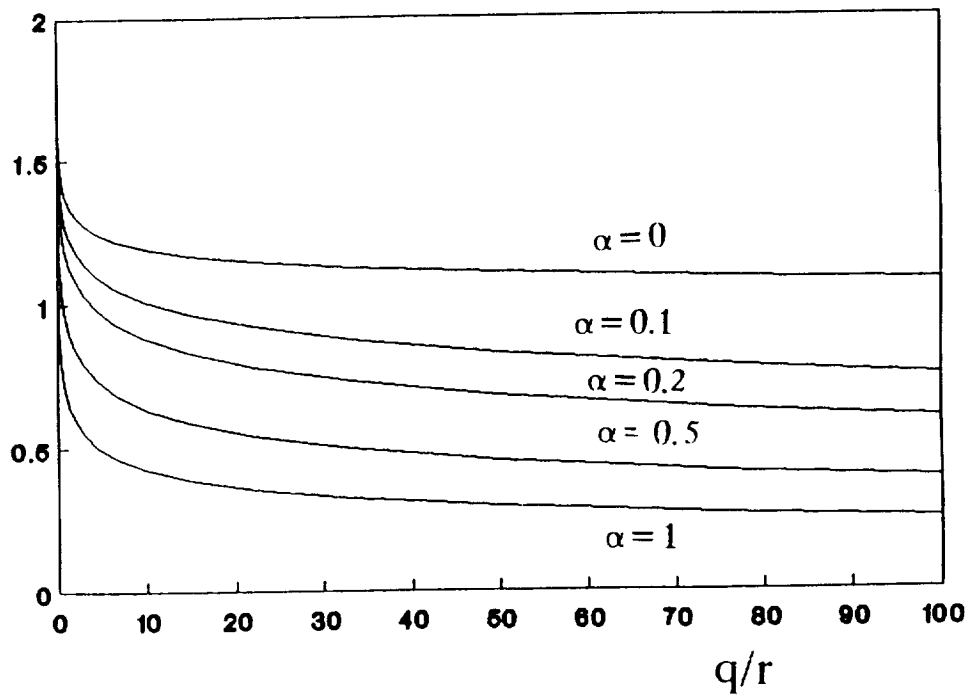
Optimal b

Figure 4. The optimal actuator location b as a function of q/r and α, when $\bar{W}/\beta = 1$.

References

1. Ruan, M., and Choudhury, A.K., "On Optimal Selection of Actuators and Sensors for Stochastic Systems," Proceedings of the Eighth VPI&SU Symposium on Dynamics and Control of Large Structures, Blacksburg, VA, May 6–8, 1991.

2. Skelton, R.E., and Delorenzo, M., "Selection of Noisy Actuators and Sensors in Linear Stochastic Systems," *Journal on Large Scale Systems, Theory and Applications,* Vol. 4, April 1983, pp. 108–136.

3. Skelton, R.E., and Delorenzo, M., "Space Structure Control Design by Variance Assignment," *J. Guidance,* Vol. 8, No. 4, 1985, pp. 454–462.

4. DeLorenzo, M.L., "Sensor and Actuator Selection for Large Space Structure Control," *J. Guidance,* V. 13, No. 2, 1990, pp. 249–257.

5. Ruan, M., and Choudhury, A.K., "Steady–State Optimal Controller with Actuator Noise Variance Linearly Related to Actuator Signal Variance," to appear on IEEE Trans. Auto. Contr.

p. 18

VIBRATION SUPPRESSION in FLEXIBLE STRUCTURES via the SLIDING-MODE CONTROL APPROACH

S. Drakunov and Ü. Özgüner

The Ohio State University
Department of Electrical Engineering
2015 Neil Avenue
Columbus, Ohio

33-2

Sliding-Mode Control of Differential-Difference Systems

Sliding modes in ordinary differential equations.

$$\dot{x}(t) = Ax(t) + Bu(t). \tag{1}$$

$$u(t,x) = \begin{cases} u^+(t,x), & \text{if } s(x) > 0 \\ u^-(t,x), & \text{if } s(x) < 0 \end{cases} \tag{2}$$

"Sliding modes" in continuous-time difference systems.

$$x(t + \tau) = Ax(t) + Bu(t). \tag{3}$$

$$S(x(t + \tau)) = 0 \Rightarrow u(t). \tag{4}$$

We consider two configurations:

Configuration A

$$\dot{x}(t) = A_{11}x(t) + A_{12}z(t)$$
$$z(t + \tau) = A_{21}x(t) + A_{22}z(t) + B_0u(t).$$

Configuration B

$$z(t + \tau) = A_{11}z(t) + A_{12}x(t)$$
$$\dot{x}(t) = A_{21}x(t) + A_{22}z(t) + B_0u(t).$$

It is assumed that $x \in R^{n_1}$, $z \in R^{n_2}$ and $u \in R^m$. A_{11}, A_{12}, A_{21}, A_{22}, B_0 are constant matrices of appropriate dimensions.

Sliding-Mode Control Design

$$A_{12} = B_1 C_2 \tag{5}$$

Quasicontrol:

$$v = C_2 z \tag{6}$$

Configuration A
1. Sliding mode in differential subsystem.

$$v = v^*(x) \Rightarrow S_0(x) = 0 \tag{7}$$

2. Sliding mode in difference subsystem.

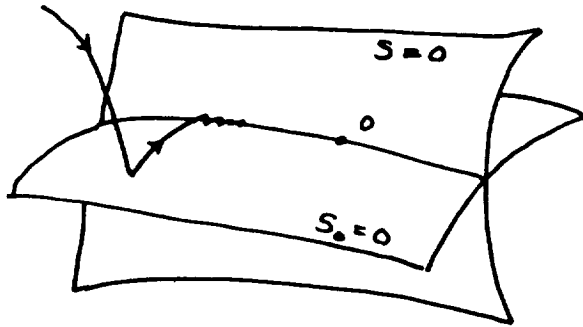$$u \Rightarrow S(x, z) = v^*(x) - C_2 z = 0 \tag{8}$$

Configuration B

1. "Sliding mode" in difference subsystem.

$$v = Dz(t) \Rightarrow S_0(z) = 0 \qquad (9)$$

2. Sliding mode in differential subsystem.

$$u \Rightarrow S = Dz(t) - C_2 x(t) = 0 \qquad (10)$$

Sliding Mode Control of Nondispersive Flexible Structures

Flexible rod in compression.

$$\frac{\partial^2 Q(t,x)}{\partial t^2} = \frac{\partial^2 Q(t,x)}{\partial x^2} \qquad (11)$$

$$\frac{\partial Q(t,0)}{\partial t} = -u(t)$$

$$\frac{\partial Q(t,1)}{\partial t} = 0.$$

Laplace transform approach.

$$p^2 \hat{Q}(p,x) = \hat{Q}''(p,x) \qquad (12)$$

$$\hat{Q}'(p,0) = -\hat{u}(p) \qquad (13)$$

$$\hat{Q}'(p,1) = 0, \qquad (14)$$

where $\hat{Q}(p,x) = \mathcal{L}Q(t,x)$, $\hat{u}(p) = \mathcal{L}u(t)$.

The solution of the boundary value problem

$$\hat{Q}(p,x) = \frac{e^{p(x-1)} + e^{-p(x-1)}}{e^p - e^{-p}} \cdot \frac{1}{p} \cdot \hat{u}(p). \quad (15)$$

If an output variable is

$$y(t) = Q(t,1) \quad (16)$$

then

$$\hat{y}(p) = \hat{Q}(p,1) = \frac{2}{e^p - e^{-p}} \frac{1}{p} \hat{u}(p). \quad (17)$$

In the time domain:

$$\dot{y}(t+1) - \dot{y}(t-1) = 2u(t) \quad (18)$$

or

$$\dot{y}(t) - \dot{y}(t-2) = 2u(t-1). \quad (19)$$

The equation can be written in the form of the difference-differential system as

Configuration A:

$$\dot{y}(t) = z_1(t)$$
$$z_1(t+1) = z_2(t) + 2u(t)$$
$$z_2(t+1) = z_1(t)$$

or

Configuration B:

$$y_1(t+1) = y_2(t) + 2v(t)$$
$$y_2(t+1) = y_1(t)$$
$$\dot{v}(t) = u(t),$$

where $y_1(t) = y(t)$.

Control Design
Configuration A

$$z_1(t) = -\lambda sgn(y(t)). \tag{20}$$

The equality is valid if

$$s(t) = z_1(t) + \lambda sgn(y(t)) = 0. \tag{21}$$

To achieve this the control should be

$$u(t) = -\frac{1}{2}z_2(t) - \frac{1}{2}\lambda sgn(y(t+1)). \tag{22}$$

$$y(t+1) = y(t) + \int_t^{t+1} z_1(\tau)d\tau. \tag{23}$$

As a result control is

$$u(t) = -\frac{1}{2}\dot{y}(t-1) - \frac{1}{2}\lambda sgn(y(t) +$$

$$y(t-1) - y(t-2) + 2\int_{t-1}^{t} u(\tau)d\tau).$$

With this control the system is stabilized in finite time.

Control Design
Configuration B

$$s(t) = (1 - \lambda)y_2(t) + 2v(t), \qquad (24)$$

where $|\lambda| < 1$. If the control is

$$u(t) = -\mu sgn(2v(t) + (1 - \lambda)y(t-1)) - (1 - \lambda)\dot{y}(t-1)$$

then

$$\dot{s} = -2\mu sgn(s). \qquad (25)$$

Rod with attached masses

$$\frac{\partial^2 Q(t,x)}{\partial t^2} = \frac{\partial^2 Q(t,x)}{\partial x^2} \qquad (26)$$

$$\frac{\partial Q(t,0)}{\partial t} = -u(t) \qquad (27)$$

$$\frac{\partial Q(t,1)}{\partial t} = -\frac{\partial^2 Q(t,1)}{\partial t^2}. \qquad (28)$$

Configuration A:

$$\dot{x}_1(t) = x_2(t)$$
$$\dot{x}_2(t) = -x_2(t) + z_1(t)$$
$$z_1(t) = z_2(t-1) + 2u(t-1)$$
$$z_2(t) = -z_1(t-1) + 2x_2(t-1),$$

where $y(t) = Q(t,1) = x_1(t)$.

$$u(t) = -\frac{1}{2}z_2(t) - \frac{1}{2}\mu sgn(\lambda x_1(t+1) + x_2(t+1)).$$

State Estimation and Prediction

Extrapolator

$$\begin{bmatrix} x_1(t+1) \\ x_2(t+1) \end{bmatrix} = \Phi(1) \begin{bmatrix} x_1(t) \\ x_2(t) \end{bmatrix} +$$

$$\int_t^{t+1} \Phi(t+1-\tau)h(\tau)d\tau,$$

where

$$h(\tau) = \begin{bmatrix} 0 \\ z_1(\tau-2) + 2u(\tau-1) - 2x_2(\tau-2) \end{bmatrix}.$$

Observer

$$\dot{\hat{x}}_1(t) = \hat{x}_2(t) + L_1(\hat{x}_1(t) - y(t))$$

$$\dot{\hat{x}}_2(t) = -\hat{x}_2(t) + \hat{z}_1(t) + L_2(\hat{x}_1(t) - y(t))$$

$$\hat{z}_1(t) = \hat{z}_2(t-1) + 2u(t-1) +$$
$$L_3(\hat{x}_1(t) - y(t))$$

$$\hat{z}_2(t) = -\hat{z}_1(t-1) + 2\hat{x}_2(t-1) +$$
$$L_4(\hat{x}_1(t) - y(t)).$$

The same approach can be used for systems of connected rods with many attached masses, multiple controls and also for the case of distributed actuators

$$\frac{\partial^2 Q(t,x)}{\partial t^2} = \frac{\partial^2 Q(t,x)}{\partial x^2} + \varphi(x)u(t) \qquad (29)$$

where $\varphi(x)$ is quasipolynomial. In all cases the solution of the boundary value problem for Laplace transformed variables leads to **Configuration A** or **Configuration B**.

Dispersive Structures

Euler-Bernoulli beam.

$$\frac{\partial^2 Q(t,x)}{\partial t^2} = -\frac{\partial^4 Q(t,x)}{\partial x^4} \qquad (30)$$

$$Q(t,0) = 0 \qquad (31)$$

$$Q'_x(t,0) = 0 \qquad (32)$$

$$Q''_{xx}(t,1) = 0 \qquad (33)$$

$$Q'''_{xxx}(t,1) = u(t). \qquad (34)$$

Second order dispersive structure.

$$\frac{\partial^2 Q(t,x)}{\partial t^2} = a(x)\frac{\partial^2 Q(t,x)}{\partial x^2} + b(x)\frac{\partial Q(t,x)}{\partial x}. \qquad (35)$$

General fourth order equation.

$$\frac{\partial^2 Q(t,x)}{\partial t^2} = -a(x)\frac{\partial^4 Q(t,x)}{\partial x^4} +$$
$$b(x)\frac{\partial^2 Q(t,x)}{\partial x^2} + c(x)\frac{\partial Q(t,x)}{\partial x}.$$

The boundary conditions

$$Q(t,0) = 0 \qquad\qquad\qquad (36)$$

$$\frac{\partial Q(t,0)}{\partial x} = 0. \qquad\qquad (37)$$

$$\frac{\partial^2 Q(t,1)}{\partial x^2} = u_1(t) \qquad\qquad (38)$$

$$\frac{\partial^3 Q(t,1)}{\partial x^3} = u_2(t). \qquad\qquad (39)$$

Integral Transform

$$P(t,\xi) = \int_0^1 \mathcal{D}(\xi,x)Q(t,x)dx \qquad (40)$$

If $\mathcal{D}$ satisfies an adjoint homogeneous boundary value problem then $P(\xi,x)$ satisfies equation

$$\frac{\partial^2 P(t,\xi)}{\partial t^2} = \frac{\partial^2 P(t,\xi)}{\partial \xi^2} + \varphi(\xi)u(t) \qquad (41)$$

$$\varphi(\xi) = -a(0)\mathcal{D}(\xi,0). \qquad\qquad (42)$$

Euler-Bernoulli beam

If $\mathcal{D}$ is a solution of the boundary value problem:

$$\frac{\partial^2 \mathcal{D}(\xi, x)}{\partial \xi^2} = -\frac{\partial^4 \mathcal{D}(\xi, x)}{\partial x^4}. \tag{43}$$

$$\mathcal{D}(\xi, 0) = 0 \tag{44}$$

$$\mathcal{D}'(\xi, 0) = 0 \tag{45}$$

$$\mathcal{D}''(\xi, 1) = 0 \tag{46}$$

$$\mathcal{D}'''(\xi, 1) = 0. \tag{47}$$

then $P(t, \xi)$ satisfies an equation:

$$\frac{\partial^2 P(t, \xi)}{\partial t^2} = \frac{\partial^2 P(t, \xi)}{\partial \xi^2} + \varphi(\xi) u(t), \tag{48}$$

where

$$\varphi(\xi) = -\mathcal{D}(\xi, 1). \tag{49}$$

Initial values: $\mathcal{D}(0,x)$ and $\mathcal{D}'_\xi(0,x)$.
If $\mathcal{D}'_\xi(0,x) = 0$ then

$$P'_\xi(t,0) = 0. \tag{50}$$

The possibility to choose $\mathcal{D}(0,x)$ is an additional degree of freedom that can be used to assign the desired value of $\varphi(\xi)$.
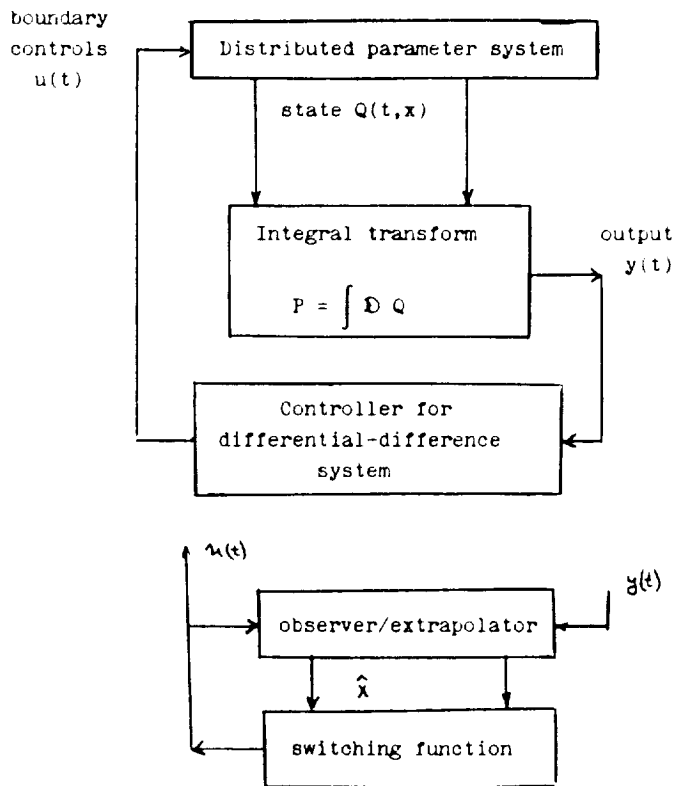
Nonsingularity condition

$$P \equiv 0 \Rightarrow Q \equiv 0. \tag{51}$$

Output

$$y(t) = P(t,0) = \int_0^1 \mathcal{D}(0,x)Q(t,x)dx. \tag{52}$$

Conclusions

Sliding mode control became very popular recently because it makes the closed loop system highly insensitive to external disturbances and parameter variations. Sliding algorithms for flexible structures have been used previously, but these were based on finite-dimensional models. An extension of this approach for differential-difference systems is obtained. That makes it possible to apply sliding-mode control algorithms to the variety of nondispersive flexible structures which can be described as differential-difference systems.

The main idea of using this technique for dispersive structures is to reduce the order of the controlled part of the system by applying an integral transformation. We can say that transformation "absorbs" the dispersive properties of the flexible structure as the controlled part becomes dispersive.

References

1. Bellman, R., Cooke K.L., *Differential-difference equations*, N.Y., Academic Press, 1963.

2. Drakunov, S.V., Izosimov D.B., Luk'yanov A.G., Utkin V.A. and Utkin V.I., *The Block Control Principle, Part II*, Automation and Remote Control, V. 51, no. 6,1990,pp. 737-746.

3. J. Martin, Ü. Özgüner, S. Yurkovich, *An Active Vibration Damper for Flexible Structures*, Proc. of 17th Pitts. Conf. on Modeling and Sim, April,1986.

4. Meirovitch L., *Elements of vibrational analysis*, McGraw-Hill Book Company, 1986.

5. Utkin V.I., *Sliding Modes and Their Application In Variable Structure Systems*. Moscow: MIR, 1978.

6. Drakunov S.V. and Utkin V.I., Sliding Mode Control in Dynamic Systems, *International Journal of Control*, v. 55, N. 4, pp.1029-1037, 1992.

I^2 $/3$

CONTROL OF THE SCOLE CONFIGURATION

USING DISTRIBUTED PARAMETER MODELS

Min-Hung Hsiao and Jen-Kuang Huang

Department of Mechanical Engineering and Mechanics
Old Dominion University, Norfolk, VA 23529-0247

OUTLINE

- INTRODUCTION

- DERIVATION OF THE CONTINUUM MODEL

- SYSTEM PARAMETERS

- CONTROL DESIGN USING CONTINUUM MODELS
  - -- POLE-ASSIGNMENT TECHNIQUE
  - -- LINEAR DYNAMIC CONTROLLER
  - -- LQG CONTROLLER

- NUMERICAL EXAMPLE

- CONCLUSION

- THE SCOLE CONFIGURATION
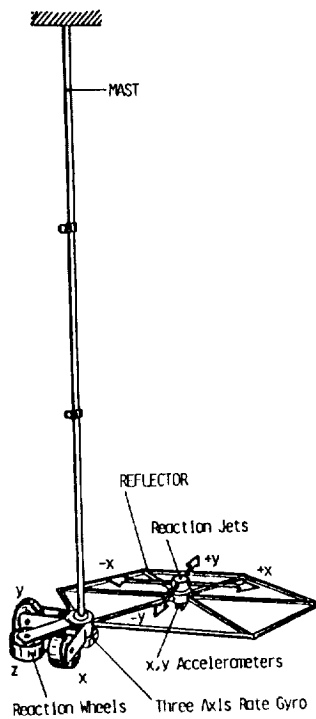
1. INTRODUCTION

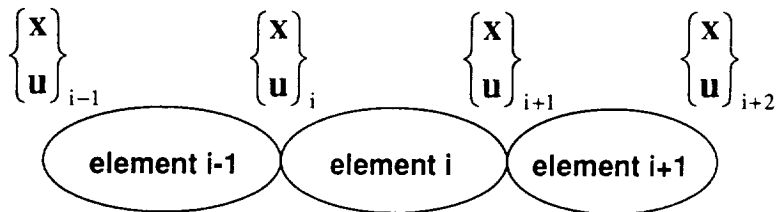(1) Assumptions

    -- The reflector of SCOLE is a rigid body

    -- The mast of SCOLE is an Euler beam

    -- Actuators and sensors are collocated

(2) Objectives

    -- Vibration suppression

    -- Controller designs using continuum models
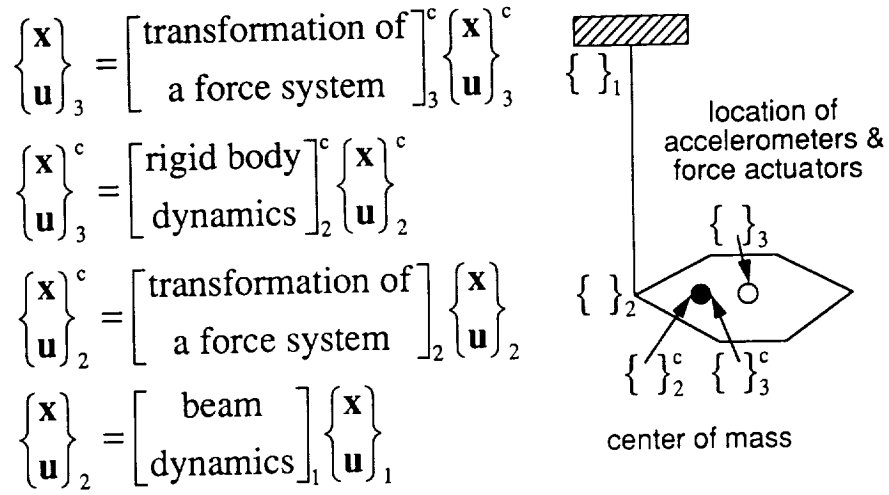
2. DERIVATION OF THE CONTINUUM MODEL

• Holzer's Transfer Matrix Method

$$\left\{ \begin{matrix} \mathbf{x} \\ \mathbf{u} \end{matrix} \right\}_{i-1} \qquad \left\{ \begin{matrix} \mathbf{x} \\ \mathbf{u} \end{matrix} \right\}_{i} \qquad \left\{ \begin{matrix} \mathbf{x} \\ \mathbf{u} \end{matrix} \right\}_{i+1} \qquad \left\{ \begin{matrix} \mathbf{x} \\ \mathbf{u} \end{matrix} \right\}_{i+2}$$

element i-1   element i   element i+1

$$\left\{ \begin{matrix} \mathbf{x} \\ \mathbf{u} \end{matrix} \right\}_{i+2} = \left[\quad \right]_{i+1} \left\{ \begin{matrix} \mathbf{x} \\ \mathbf{u} \end{matrix} \right\}_{i+1}, \quad \left\{ \begin{matrix} \mathbf{x} \\ \mathbf{u} \end{matrix} \right\}_{i+1} = \left[\quad \right]_{i} \left\{ \begin{matrix} \mathbf{x} \\ \mathbf{u} \end{matrix} \right\}_{i}, \quad \left\{ \begin{matrix} \mathbf{x} \\ \mathbf{u} \end{matrix} \right\}_{i} = \left[\quad \right]_{i-1} \left\{ \begin{matrix} \mathbf{x} \\ \mathbf{u} \end{matrix} \right\}_{i-1}$$

$$\left\{ \begin{matrix} \mathbf{x} \\ \mathbf{u} \end{matrix} \right\}_{i+2} = \left[\quad \right]_{i+1} \left[\quad \right]_{i} \left[\quad \right]_{i-1} \left\{ \begin{matrix} \mathbf{x} \\ \mathbf{u} \end{matrix} \right\}_{i-1}$$

• Application to the SCOLE configuration

$$\begin{Bmatrix} \mathbf{x} \\ \mathbf{u} \end{Bmatrix}_3 = \begin{bmatrix} \text{transformation of} \\ \text{a force system} \end{bmatrix}_3^c \begin{Bmatrix} \mathbf{x} \\ \mathbf{u} \end{Bmatrix}_3^c$$

$$\begin{Bmatrix} \mathbf{x} \\ \mathbf{u} \end{Bmatrix}_3^c = \begin{bmatrix} \text{rigid body} \\ \text{dynamics} \end{bmatrix}_2^c \begin{Bmatrix} \mathbf{x} \\ \mathbf{u} \end{Bmatrix}_2^c$$

$$\begin{Bmatrix} \mathbf{x} \\ \mathbf{u} \end{Bmatrix}_2^c = \begin{bmatrix} \text{transformation of} \\ \text{a force system} \end{bmatrix}_2 \begin{Bmatrix} \mathbf{x} \\ \mathbf{u} \end{Bmatrix}_2$$

$$\begin{Bmatrix} \mathbf{x} \\ \mathbf{u} \end{Bmatrix}_2 = \begin{bmatrix} \text{beam} \\ \text{dynamics} \end{bmatrix}_1 \begin{Bmatrix} \mathbf{x} \\ \mathbf{u} \end{Bmatrix}_1$$

$\{ \ \}_1$

location of
accelerometers &
force actuators

$\{ \ \}_3$

$\{ \ \}_2$

$\{ \ \}_2^c \ \{ \ \}_3^c$

center of mass

(1) Rigid Body--inertia and gravitational effects

$$m_i \ddot{w}_i = f_{i+1} - f_i - G_{1i}\theta_i - f_g$$

$$J_i \ddot{\theta}_i = \tau_{i+1} - \tau_i, \qquad w_{i+1} = w_i, \qquad \theta_{i+1} = \theta_i$$

where $G_1 = \begin{bmatrix} 0 & -mg & 0 \\ mg & 0 & 0 \\ 0 & 0 & 0 \end{bmatrix}$, $f_g = \begin{Bmatrix} 0 \\ 0 \\ m_i g \end{Bmatrix}$

$$\begin{Bmatrix} \mathbf{x} \\ \mathbf{u} \end{Bmatrix}_{i+1} = \begin{bmatrix} \mathbf{I} & \mathbf{0} \\ s^2\overline{\mathbf{M}} + \mathbf{G} & \mathbf{I} \end{bmatrix}_i \begin{Bmatrix} \mathbf{x} \\ \mathbf{u} \end{Bmatrix}_i + \begin{Bmatrix} \mathbf{0} \\ \mathbf{u}_g \end{Bmatrix}$$

where $x = \begin{Bmatrix} w \\ \theta \end{Bmatrix}$, $u = \begin{Bmatrix} f \\ \tau \end{Bmatrix}$, $\overline{M} = \begin{bmatrix} mI & 0 \\ 0 & J \end{bmatrix}$, $G = \begin{bmatrix} 0 & G_1 \\ 0 & 0 \end{bmatrix}$, $u_g = \begin{Bmatrix} f_g \\ 0 \end{Bmatrix}$

(2) Rigid Body--transformation of a force system

$$\mathbf{w}_{i+1} = \mathbf{w}_i + \boldsymbol{\theta}_i \times \mathbf{r}_i = \mathbf{w}_i - \mathbf{r}_i \times \boldsymbol{\theta}_i = \mathbf{w}_i - \mathbf{R}_i \boldsymbol{\theta}_i$$

$$\boldsymbol{\theta}_{i+1} = \boldsymbol{\theta}_i, \qquad \mathbf{f}_{i+1} = \mathbf{f}_i$$

$$\boldsymbol{\tau}_{i+1} = \boldsymbol{\tau}_i - \mathbf{r}_i \times \mathbf{f}_i = \boldsymbol{\tau}_i - \mathbf{R}_i \mathbf{f}_i$$

$$\text{where } \mathbf{R}_i = \begin{bmatrix} 0 & -r_z & r_y \\ r_z & 0 & -r_x \\ -r_y & r_x & 0 \end{bmatrix}_i$$

$$\begin{Bmatrix} \mathbf{x} \\ \mathbf{u} \end{Bmatrix}_{i+1} = \begin{bmatrix} \mathbf{T}_1 & 0 \\ 0 & \mathbf{T}_2 \end{bmatrix}_i \begin{Bmatrix} \mathbf{x} \\ \mathbf{u} \end{Bmatrix}_i$$

$$\text{where } \mathbf{x} = \begin{Bmatrix} \mathbf{w} \\ \boldsymbol{\theta} \end{Bmatrix}, \; \mathbf{u} = \begin{Bmatrix} \mathbf{f} \\ \boldsymbol{\tau} \end{Bmatrix}, \; \mathbf{T}_1 = \begin{bmatrix} \mathbf{I} & -\mathbf{R} \\ 0 & \mathbf{I} \end{bmatrix}, \; \mathbf{T}_2 = \begin{bmatrix} \mathbf{I} & 0 \\ -\mathbf{R} & \mathbf{I} \end{bmatrix}$$

(3) Beam-- elongation

$$E_i A_i w'' = \rho_i A_i s^2 w$$

$$\begin{Bmatrix} w \\ f \end{Bmatrix}_{i+1} = \begin{bmatrix} \cos\alpha^e L & -\dfrac{\sin\alpha^e L}{EA\alpha^e} \\ -EA\sin\alpha^e L & -\cos\alpha^e L \end{bmatrix}_i \begin{Bmatrix} w \\ f \end{Bmatrix}_i$$

$$= \begin{bmatrix} e_{11} & e_{12} \\ e_{21} & e_{22} \end{bmatrix}_i \begin{Bmatrix} w \\ f \end{Bmatrix}_i$$

$$\text{where, } \alpha_i^e = i\sqrt{\frac{\rho_i}{E_i}} s$$

(4) Beam-- torsion

$$G_i J_i \theta'' = \rho_i J_i s^2 \theta$$

$$\left\{ \begin{array}{c} \theta \\ \tau \end{array} \right\}_{i+1} = \left[\begin{array}{cc} \cos \alpha^t L & -\dfrac{\sin \alpha^t L}{GJ\alpha^t} \\ -GJ\sin \alpha^t L & -\cos \alpha^t L \end{array} \right]_i \left\{ \begin{array}{c} \theta \\ \tau \end{array} \right\}_i$$

$$= \left[\begin{array}{cc} t_{11} & t_{12} \\ t_{21} & t_{22} \end{array} \right]_i \left\{ \begin{array}{c} \theta \\ \tau \end{array} \right\}_i$$

where, $\alpha_i^t = i\sqrt{\dfrac{\rho_i}{G_i}}s$

(5) Beam-- bending

$$E_i I_i w'''' - \rho_i I_i s^2 + \rho_i A_i s^2 w = 0$$

$$\left\{ \begin{array}{c} w \\ \theta \\ f \\ \tau \end{array} \right\}_{i+1} = \frac{1}{2} \left[\begin{array}{cccc} cn+ch & \dfrac{sn}{\beta_1}+\dfrac{sh}{\beta_2} & -\dfrac{sn}{h_1}+\dfrac{sh}{h_2} & -\dfrac{cn}{h_3}+\dfrac{ch}{h_4} \\ -\beta_1 sn+\beta_2 sh & cn+ch & -\dfrac{\beta_1}{h_1}cn+\dfrac{\beta_2}{h_2}ch & \dfrac{\beta_1}{h_3}sn+\dfrac{\beta_2}{h_4}sh \\ -(h_1 sn+h_2 sh) & \dfrac{h_1}{\beta_1}cn-\dfrac{h_2}{\beta_2}ch & -(cn+ch) & \dfrac{h_1}{h_3}sn-\dfrac{h_2}{h_4}sh \\ h_3 cn-h_4 ch & \dfrac{h_3}{\beta_1}sn-\dfrac{h_4}{\beta_2}sh & -\dfrac{h_3}{h_1}sn-\dfrac{h_4}{h_2}sh & -(cn+ch) \end{array} \right]_i \left\{ \begin{array}{c} w \\ \theta \\ f \\ \tau \end{array} \right\}_i$$

where $\beta_1^2 = \dfrac{-\rho I s^2 + s\sqrt{(\rho I s)^2 - 4\rho AEI}}{2EI}$, $\beta_2^2 = \dfrac{\rho I s^2 + s\sqrt{(\rho I s)^2 - 4\rho AEI}}{2EI}$

$sn=\sin\beta_1 L$, $cn=\cos\beta_1 L$, $sh=\sinh\beta_2 L$, $ch=\cosh\beta_2 L$, $k_1=EI$, $k_2=\rho I$

$h_1=k_1\beta_1^3+k_2\beta_1 s^2$, $h_2=k_1\beta_2^3-k_2\beta_2 s^2$, $h_3=k_1\beta_1^2$, $h_4=k_1\beta_2^2$

(6) Beam-- overall transfer matrix

$$
\begin{Bmatrix} w_x \\ w_y \\ w_z \\ \theta_x \\ \theta_y \\ \theta_z \\ f_x \\ f_y \\ f_z \\ \tau_x \\ \tau_y \\ \tau_z \end{Bmatrix}_{i+1}
=
\begin{bmatrix}
b_{11} & 0 & 0 & 0 & -b_{12} & 0 & b_{13} & 0 & 0 & 0 & b_{14} & 0 \\
0 & b_{11} & 0 & b_{12} & 0 & 0 & 0 & b_{13} & 0 & -b_{14} & 0 & 0 \\
0 & 0 & e_{11} & 0 & 0 & 0 & 0 & 0 & e_{12} & 0 & 0 & 0 \\
0 & b_{21} & 0 & b_{22} & 0 & 0 & 0 & b_{23} & 0 & -b_{24} & 0 & 0 \\
-b_{21} & 0 & 0 & 0 & b_{22} & 0 & -b_{23} & 0 & 0 & 0 & -b_{24} & 0 \\
0 & 0 & 0 & 0 & 0 & t_{11} & 0 & 0 & 0 & 0 & 0 & t_{12} \\
b_{31} & 0 & 0 & 0 & -b_{32} & 0 & b_{33} & 0 & 0 & 0 & b_{34} & 0 \\
0 & b_{31} & 0 & b_{32} & 0 & 0 & 0 & b_{33} & 0 & -b_{34} & 0 & 0 \\
0 & 0 & e_{21} & 0 & 0 & 0 & 0 & 0 & e_{-2} & 0 & 0 & 0 \\
0 & -b_{41} & 0 & -b_{42} & 0 & 0 & 0 & -b_{43} & 0 & b_{44} & 0 & 0 \\
b_{41} & 0 & 0 & 0 & -b_{42} & 0 & b_{43} & 0 & 0 & 0 & b_{44} & 0 \\
0 & 0 & 0 & 0 & 0 & t_{21} & 0 & 0 & 0 & 0 & 0 & t_{22}
\end{bmatrix}_i
\begin{Bmatrix} w_x \\ w_y \\ w_z \\ \theta_x \\ \theta_y \\ \theta_z \\ f_x \\ f_y \\ f_z \\ \tau_x \\ \tau_y \\ \tau_z \end{Bmatrix}_i
$$

2. DERIVATION OF THE CONTINUUM MODEL

$$
\begin{Bmatrix} x \\ u \end{Bmatrix}_3
=
\begin{bmatrix} T_1 & 0 \\ 0 & T_2 \end{bmatrix}_3^c
\left(
\begin{bmatrix} I & 0 \\ s^2\overline{M}+G & I \end{bmatrix}_2^c
\begin{bmatrix} T_1 & 0 \\ 0 & T_2 \end{bmatrix}_2
\begin{bmatrix} F_1 & F_2 \\ F_3 & F_4 \end{bmatrix}_1
\begin{Bmatrix} x \\ u \end{Bmatrix}_1
+
\begin{Bmatrix} 0 \\ u_g \end{Bmatrix}
\right)
$$

$\Rightarrow \ Ms^2x + K(s)x = u - \overline{u}_g \quad$ for boundary condition $x_1 = 0$

where $M = [T_2]_3^c[\overline{M}]_2^c[T_1]_3^{c^{-1}}$, $K = [T_2]_3^c(G + [T_2]_2[F_4]_1[F_2]_1^{-1}[T_1]_2^{-1})[T_1]_3^{c^{-1}}$

$x = x_3, \ u = u_3, \ \overline{u}_g = [T_2]_3^c u_g$

- Feedforward control

$u = K_0 x_d + \overline{u}_g \quad$ where $K_0 = K|_{s=0}$ and x_d is the desired output

- Continuum Model

$\Rightarrow \ Ms^2x + K(s)x = u, \quad$ where u is the feedback control

3. SYSTEM PARAMETERS

(1) Rigid Body

element	$\bar{x}$	$\bar{y}$	$\bar{z}$ (in)	W(lb)	J_{xx}	J_{yy}	J_{zz} (slug$-$in^2)
rate gyro	0	0	-129.3	1.69	0	0	0
accelerometers	10	20.8	-129.3	0.17	0	0	0
	12	18.8	-129.3	0.17	0	0	0
thrusters	12	20.8	-124.3	1	0	0	0
reaction wheels	0	-6	-125.8	4.28	0	0	0
	6	0	-125.8	4.28	0	0	0
	-4.5	-4.5	-125.8	4.28	0	0	0
reflector	12	20.8	-125.8	4.76	24.8	24.6	49.67
solenoid	4	7	-123.8	5.5	0	0	0
manifold	0	0	-124.5	1.68	0	0	0

(2) Beam

$$E=30 \text{ Mpsi}, \quad I_{xx}=I_{yy}=6.66\times10^{-3} \text{ in}^4, \quad I_{zz}=2I_{xx}$$

$$G=15 \text{ Mpsi}, \quad L=125.5 \text{ in}, \quad m=4.48 \text{ lb}, \quad A=0.108 \text{ in}^2$$

- **Identified Modal Frequencies**

	measured(Hz)	identified(Hz)
1st out-of-plane bending	.4545	.4609
1st in-plane bending	.4764	.4707
1st torsion	1.98	1.9240
2nd in-plane bending	3.13	3.1455
2nd out-of plane bending	4.63	4.6839

4. CONTROL DESIGN USING CONTINUUM MODELS

(1) Pole-Assignment Technique

- Continuum Model $Ms^2x + K(s)x = u$

- Approximations $K(s) \approx K_0$ or $K(s) \approx K_0 + K_2s^2$

  where $K_0 = K|_{s=0}$ and $K_2 = \frac{1}{2}K''|_{s=0}$

- Pole - Assignment

  LTI system $M_t\ddot{x} + K_0x = u$ where $M_t = M$ or $M_t = M + K_2$

  Desired damping matrix ζ

  Rate feedback control $\boxed{u = -2M_t V\zeta\Omega V^{-1}\dot{x}}$

  where V satisfies $M_t^{-1}AV = V\Omega^2$, Ω^2 is diagonal

(1) Pole-Assignment Technique

- Advantages

  -- Easy to implement (use constant controller gains)

- Disadvantages

  -- Stability is not guaranteed (due to approximation
     of $K(s)$ at the beginning of the design process)

(2) Linear Dynamic Controller

- Continuum Model $(\mathbf{M}s^2 + \mathbf{D}s + \mathbf{K})\mathbf{x} = \mathbf{B}\mathbf{u}$

$$\mathbf{y} = (\mathbf{H}_a s^2 + \mathbf{H}_v s + \mathbf{H}_d)\mathbf{x}$$

- Controller Dynamics $(\mathbf{M}_c s^2 + \mathbf{D}_c s + \mathbf{K}_c)\mathbf{x}_c = \mathbf{B}_c \mathbf{u}_c$

$$\mathbf{y}_c = (\mathbf{H}_{ac} s^2 + \mathbf{H}_{vc} s + \mathbf{H}_{dc})\mathbf{x}_c$$

$$\mathbf{u} = \mathbf{y}_c, \quad \mathbf{u}_c = -\mathbf{y}$$

- Controller Transfer Function $\boldsymbol{\Psi}(s)$

$$\mathbf{u} = \mathbf{y}_c = -(\mathbf{H}_{ac} s^2 + \mathbf{H}_{vc} s + \mathbf{H}_{dc})(\mathbf{M}_c s^2 + \mathbf{D}_c s + \mathbf{K}_c)^{-1}\mathbf{B}_c \mathbf{y}$$

$$\boldsymbol{\Psi}(s) = -(\mathbf{H}_{ac} s^2 + \mathbf{H}_{vc} s + \mathbf{H}_{dc})(\mathbf{M}_c s^2 + \mathbf{D}_c s + \mathbf{K}_c)^{-1}\mathbf{B}_c$$

(2) Linear Dynamic Controller

- Overall System Dynamics

$$\begin{bmatrix} \mathbf{M}s^2 + \mathbf{D}s + \mathbf{K} & \mathbf{B}(\mathbf{H}_{ac} s^2 + \mathbf{H}_{vc} s + \mathbf{H}_{dc}) \\ -\mathbf{B}_c(\mathbf{H}_a s^2 + \mathbf{H}_v s + \mathbf{H}_d) & \mathbf{M}_c s^2 + \mathbf{D}_c s + \mathbf{K}_c \end{bmatrix} \begin{Bmatrix} \mathbf{x} \\ \mathbf{x}_c \end{Bmatrix} = 0$$

- Overall Characteristic Equation $\quad \det[\ ] = 0$
- Design Parameters $\mathbf{M}_c, \mathbf{D}_c, \mathbf{K}_c, \mathbf{B}_c, \mathbf{H}_{ac}, \mathbf{H}_{vc}$, and $\mathbf{H}_{dc}$
  by using knowledge of system parameters to
  achieve better performances

(2) Linear Dynamic Controller

- **Advantages**

  -- Explicit transfer function for continuum models
  -- Possible for guaranteed stability
  -- More design flexibilities

- **Disadvantages**

  -- Need approximations for $K(s)$ to realize controllers
  -- Hard to implement (need Runge-Kutta algorithm to solve for controller dynamics)

(3) LQG CONTROLLER

- **Continuum Model** $(\mathbf{M}s^2 + \mathbf{K})\mathbf{x} = \mathbf{B}(\mathbf{u} + \mathbf{n}_a)$

$$\mathbf{y} = \mathbf{B}^T\mathbf{x} + \mathbf{n}_r$$

  where $\mathbf{n}_a \rightarrow N(0, d_a\mathbf{I})$ and $\mathbf{n}_r \rightarrow N(0, d_r\mathbf{I})$

- **Performance Index** $\lim_{T \to \infty} \frac{1}{T} \left\{ \int_0^T (\|\mathbf{B}^T\mathbf{x}\|^2 + \lambda\|\mathbf{u}\|^2) dt \right\}$

- **Optimal Controller Transfer Function**

$$\Psi(s) = -h\mathbf{B}^T s(\mathbf{M}s^2 + \gamma\mathbf{B}\mathbf{B}^T s + \mathbf{K})^{-1}\mathbf{B}$$

  where $h = \dfrac{\sqrt{d_a/d_r}}{\sqrt{\lambda}}$, $\gamma = \sqrt{d_a/d_r} + \dfrac{1}{\sqrt{\lambda}}$

5. NUMERICAL EXAMPLE

(1) Pole-Assignment Technique

Open loop f(Hz)	ζ_d (%)	$K(s) \approx K_0$ f(Hz)	ζ(%)	$K(s) \approx K_0 + K_2 s^2$ f(Hz)	ζ(%)
.4609	10	.4586	9.790	.4586	10.000
.4707	10	.4684	9.790	.4683	10.000
1.9240	10	1.9145	9.960	1.9144	10.000
3.1455	10	3.1328	9.200	3.1310	9.840
4.6839	10	4.6741	7.800	4.6706	9.110
10.9675		10.9652	.370	10.9648	.390
12.0448		12.0325	1.340	12.0279	1.570
28.6392		28.6391	.023	28.6378	.025
29.0288		29.0278	.090	29.0275	.110
55.6990		55.6990	.006	55.6990	.007
55.8956		55.8957	.016	55.8957	.018
91.8160		91.8419	.036	91.8439	.037

(2) Linear Dynamic Controller

Design Parameters	f(Hz)	ζ(%)
$M_c = M + K_2$	.3757	4.88
	.5677	4.91
$K_c = K_0$	1.7300	4.95
	1.9144	10.00
D_c 10% damping for	2.1721	4.93
the first five modes	2.9420	4.92
	4.6928	2.79
$H_{ac} = H_{dc} = H_a = H_d = 0$	10.9420	.19
	12.0455	.38
$B_c = B = I$	28.6431	.013
	29.0289	.020
$H_{vc} = H_v = I$	55.6989	.006

6. CONCLUSION

(1) A continuum model for the SCOLE configuration has been derived using transfer matrices.

(2) Controller designs for distributed parameter systems have been analyzed.

(3) Pole-assignment controller design is easy to implement but stability is not guaranteed.

(4) Explicit transfer function of dynamic controllers has been obtained and no model reduction is required before the controller is realized.

(5) One specific LQG controller for continuum models had been derived, but other optimal controllers for more general performances need to be studied.

ACTIVE VIBRATION DAMPING USING SMART MATERIAL*

John S. Baras and Yan Zhuang
Electrical Engineering Department
and
Systems Research Center
The University of Maryland, College Park, MD 20742

SUMMARY

We consider the modeling and active damping of an elastic beam using distributed actuators and sensors. The piezoelectric ceramic material (PZT) is used to build the actuator. The sensor is made of the piezoelectric polymer polyvinylidene fluoride (PVDF). These materials are glued on both sides of the beam. For the simple clamped beam, the closed loop controller has been shown to be able to extract energy from the beam. The shape of the actuator and its influence on the closed loop system performance are discussed. It is shown that it is possible to suppress the selected mode by choosing the appropriate actuator layout. It is also shown that by properly installing the sensor and determining the sensor shape we can further extract and manipulate the sensor signal for our control need.

1 INTRODUCTION

There has been an increasing interest in the control of large space structures and flexible structures in recent years. These structural systems are usually large in size,light in mass and hence weakly damped. In order to achieve vibration suppression and precision pointing, it is necessary to introduce artificial damping to such systems. One approach is passive damping by adding the minimum weight of damping material to the effective locations on the structure. Another way is to use external mechanisms with feedback of the systems' state or output to counteract the undesired motion

modes. In modern structural engineering, active feedback controls to stabilize the structure are preferred.

Proper modeling is essential to control system design and to avoid spillover due to the infinite dimensional nature of these systems. Here we consider the beam model as part of the structure and study its modeling and active damping.

The actuator considered here is a distributed one made of piezoelectric ceramic material which is glued to the beam. Its constitutive property, i.e. its strain and stress relation, is influenced by the external voltage applied to it. Bonding or embedding segmented elements of this material in a structure would allow the application of the localized strain to be transferred to the structure whose deformation can be controlled. Under proper bonding conditions, the coupling between the actuator strain and the beam strain can be determined to implement the control mechanism. In [6] [2] [7] active vibration control is described using spatially distributed actuators. The PVDF sensor is bonded to the beam in a similar way. The output voltage is a functional of beam curvature. Unlike the conventional point sensor, this is a distributed one. Cudney [5] provides some detailed explanation of the nature of piezoelectric actuators.

We first discuss the modeling of the beam and the distributed actuator. A static model of the actuator coupled into the structure is developed. We have developed the beam model from the Euler-Bernoulli model with rotational inertia added. Next the sensor model is addressed. We then discuss the controller design using Lyapunov methods. We finally investigate the actuator and sensor shapes and their impact on the system elastic modes.

2   SYSTEM MODEL

One approach to build the desired actuator is to take advantage of the special constitutive properties of certain materials. The actuation is due to the property change under certain stimulation other than the external actuation force. Such materials are the so called smart materials. Once properly embedded into the structure the induced actuation will produce bending or stretching or both to control the structure deformation. One of the advantages of using smart materials as actuators and sensors is that the structure will not change much.

Piezoelectric actuators were used as elements of intelligent structures by Crawley and de Luis [4]. Bailey and Hubbard [1] have used PVDF actuators to control the vibration of a cantilever beam. The control voltage applied across the PVDF is the sign of the tip rotation velocity multiplied by a constant.

Figure 1 shows the structure of the beam with both the sensor and the actuator layers glued together. In this figure, h stands for the thickness of the different layers of the beam. The subscripts s, b and a denote sensor, beam and actuator respectively. The constitutive law for piezoelectric materials has several equivalent forms. The stress -strain relationship for the piezoelectric material is similar to that
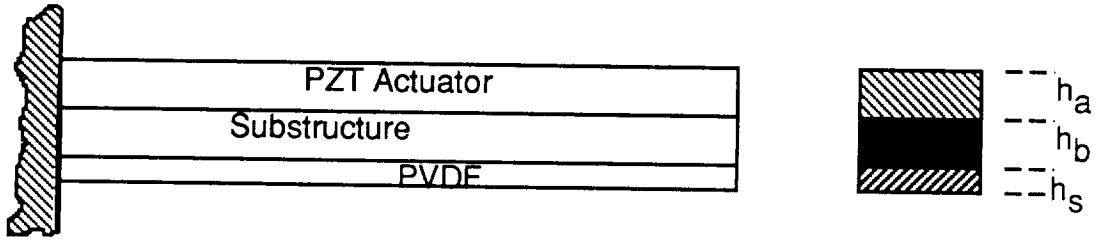
Figure 1: The composite beam

of thermoelastic materials, with the thermal strain term replaced by the piezoelectric strain Λ. The constitutive equation of the actuator is given by

$$\sigma = E_a(\epsilon - \Lambda) \tag{1}$$

where Λ is the actuation strain due to the external electric field, and ϵ is the strain without external electric field. E_a is the Young's modulus of the actuator, σ is the stress of the actuator. The actuation strain is given by

$$\Lambda(x,t) = \frac{d_{31}}{h_a} V(x,t) \tag{2}$$

where d_{31} is the piezoelectric field and strain field constant. $V(x,t)$ is the distributed voltage. The strain has two effects on the beam. One effect is that it induces a longitudinal strain ϵ_l to insure a force equilibrium along the axial direction. This steady state value of ϵ_l can be derived by solving a force equilibrium equation. The other effect is that the net force in each layer acts through the moment arm with the length from the midplane of the layer to the neutral plane of the beam. The resultant of the actions produces the bending moment. Taking a similar approach as in [1] the actuation moment can be expressed as

$$M_a = K_a \Lambda(x,t) \tag{3}$$

where K_a is a constant depending on the geometry and the materials of the beam.

We model the beam with linear bending, no shear but with the rotational inertia included. This is more accurate than the Euler-Bernoulli beam model. The Euler-Bernoulli beam model

$$EI\frac{\partial^4 w(x,t)}{\partial x^4} + \rho A\frac{\partial^2 w(x,t)}{\partial t^2} = 0 \tag{4}$$

is often used to describe the beam dynamics because of its simple form and ease for analysis. E stands for Young's modulus and I stands for moment of inertia. This equation can be rewritten as

$$\frac{\partial^2}{\partial x^2}[EI\frac{\partial^2 w(x,t)}{\partial x^2}] + \rho A\frac{\partial^2 w(x,t)}{\partial t^2} = 0 \tag{5}$$

where

$$EI = E_a I_a + E_b I_b + E_s I_s. \tag{6}$$

The bending moment of the composite beam without actuation is

$$M_b = EI\frac{\partial^2 w(x,t)}{\partial x^2}. \tag{7}$$

The Euler-Bernoulli model is a linear model without accounting the rotational inertia and the shear effect. It is easy to see that during vibration the beam elements perform not only a translational motion but also rotate. The variable angle of rotation which is equal to the slope of the deflection curve will be expressed by $\partial w/\partial x$ and the corresponding angular velocity and angular acceleration will be given by

$$\frac{\partial^2 w}{\partial x\partial t} \ and \ \frac{\partial^3 w}{\partial x\partial t^2}. \tag{8}$$

Therefore the moment of the inertia forces of the element about the longitudinal axis will be

$$- \rho I\frac{\partial^3 w}{\partial x\partial t^2}. \tag{9}$$

The equation with rotational inertia is [8]

$$EI\frac{\partial^4 w(x,t)}{\partial x^4} + \rho A\frac{\partial^2 w(x,t)}{\partial t^2} - \rho I\frac{\partial^4 w(x,t)}{\partial x^2\partial t^2} = 0. \tag{10}$$

where

$$\rho A = \rho_a A_a + \rho_b A_b + \rho_s A_s.. \tag{11}$$

We take this equation as our beam model under consideration. It falls in between the Euler-Bernoulli beam and the Timoshenko beam.

The total bending moment with actuation is

$$M = M_b + M_a. \tag{12}$$

Substituting Equation (12) into (10), we have

$$EI\frac{\partial^4 w(x,t)}{\partial x^4} - K_a\frac{\partial^2 \Lambda(x,t)}{\partial x^2} + \rho A\frac{\partial^2 w(x,t)}{\partial t^2} - \rho I\frac{\partial^4 w(x,t)}{\partial x^2 \partial t^2} = 0. \qquad (13)$$

Considering the actuation strain and the applied voltage, we get

$$EI\frac{\partial^4 w(x,t)}{\partial x^4} - c\frac{\partial^2 V(x,t)}{\partial x^2} + \rho A\frac{\partial^2 w(x,t)}{\partial t^2} - \rho I\frac{\partial^4 w(x,t)}{\partial x^2 \partial t^2} = 0 \qquad (14)$$

with boundary conditions

$$
\begin{aligned}
w(0,t) &= 0 \\
\frac{\partial w(0,t)}{\partial x} &= 0 \\
EI\frac{\partial^2 w(L,t)}{\partial x^2} &= c.V(L,t) \\
EI\frac{\partial^3 w(L,t)}{\partial x^3} &= c.\frac{\partial V(L,t)}{\partial x}
\end{aligned}
\qquad (15)
$$

where

$$c = \frac{d_{31}}{h_a}K_a.$$

The distributed voltage $V(x,t)$ is the control applied to the system. Equation (14) and the boundary conditions (15) form the control system model.

3 SENSOR MODEL

A distributed sensor is the one whose output is a function of structural responses at different locations. It can be a group of point sensors or a spatially continuous one. These responses are observed either discretely or continuously in space. Using the latter has the advantage that complicated computations based on point measurements can be reduced because the sensor geometry itself provides the processing. The spatial aliasing from an array of point sensors can be avoided. Typical noncausal sensor dynamics such as gain rolloff without phase shift is possible by using distributed sensors [3].

Figure 2 shows the sensor structure. PVDF is strain sensitive as it relies on the piezoelectric effect to produce the electric charge. The charge is proportional to the strain induced by the structure. This type of sensing is actually an inverse process of piezoelectric actuation. Based on the constitutive equation, the induced charge per unit length from the sensor strain is
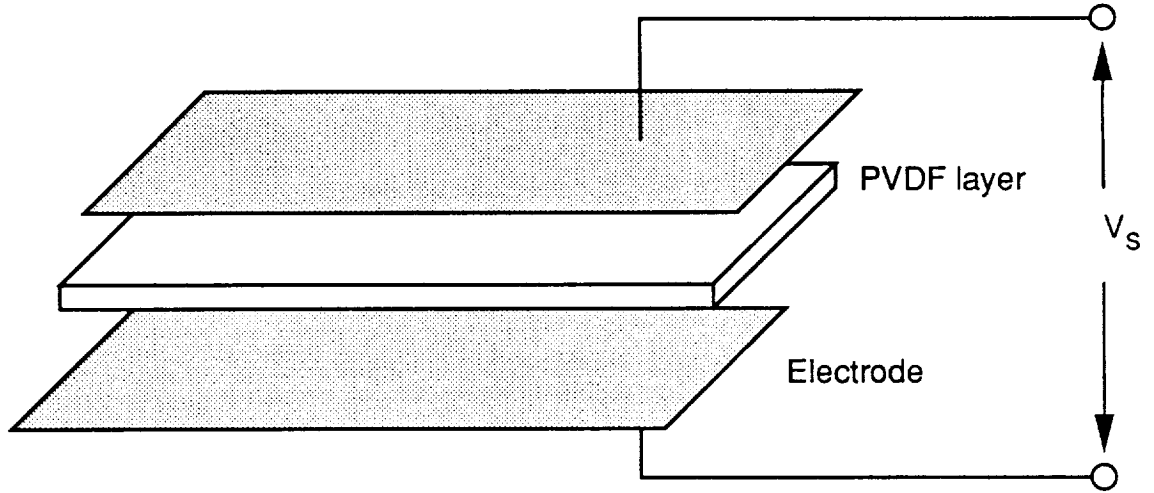
$$q(x,t) = -Esd_{31}\epsilon_s. \qquad (16)$$

Figure 2: The sensor model

The sensor strain is related to the beam curvature by

$$\epsilon_s = \frac{h_b + h_s}{2} \frac{\partial^2 w}{\partial x^2}. \tag{17}$$

The electrical charge along the beam is

$$
\begin{aligned}
Q(x,t) &= \int_0^x q(x,t)F(x)dx \\
&= -E_s d_{31} \frac{h_b + h_s}{2} \int_0^x F(x)\frac{\partial^2 w}{\partial x^2}dx
\end{aligned} \tag{18}
$$

where $F(x)$ is the weight function or shape function of the sensor. It is the local width of the electrodes covering both sides of the sensor layer. The function $F(x)$ can be designed according to the need for interpreting the sensor signal. The capacitance between the electrodes of the sensor layer is

$$C = \frac{\varepsilon_0 \varepsilon_r A_s}{h_s} \tag{19}$$

where ε_0 and ε_r are the vacuum permittivity and relative permittivity constants respectively. The output voltage from the sensor is

$$
\begin{aligned}
V_s(x,t) &= \frac{Q(x,t)}{C} \\
&= -K_s \int_0^x F(x)\frac{\partial^2 w}{\partial x^2}dx
\end{aligned} \tag{20}
$$

where

$$K_s = \frac{E_s d_{31}(h_b + h_s)}{2C} \tag{21}$$

is a constant. Suppose the sensor covers the whole beam, then

$$V_s(t) = -K_s \int_0^L F(x) \frac{\partial^2 w}{\partial x^2} dx. \tag{22}$$

Equation (22) is the sensor output equation. The output voltage is the weighted integration of the beam curvature. Integrating the output voltage by parts twice in spatial variable, we have another form of the sensor output,

$$V_s(t) = -K_s \frac{\partial w(L,t)}{\partial x} F(L) + w(L,t) \frac{\partial F(L)}{\partial x} - K_s \int_0^L w(x,t) \frac{\partial^2 F(x)}{\partial x^2} dx. \tag{23}$$

We shall see later from Equation (23) that different measurement outputs can be formulated to meet our control needs by choosing the appropriate sensor shape function $F(x)$.

4 DISTRIBUTED CONTROL ALGORITHM

We design the control algorithm by Lyapunov's direct method. The energy function is used to measure the amount of vibration of the system. We need to find a control algorithm such that the closed loop system is asymptotically stable. One advantage of this method is that there is no need for model truncation.

Given the system (14) with boundary conditions (15) and an energy functional $E(t)$, we need to find a control $V(x,t)$ such that

$$\lim_{t \to \infty} E(t) = 0. \tag{24}$$

It suffices to find a control $V(x,t)$, such that

$$\frac{dE(t)}{dt} < 0, \ t > 0. \tag{25}$$

We define the energy function as follows:

$$E(t) = \frac{1}{2} \int_0^L [a(\frac{\partial^2 w}{\partial x^2})^2 + (\frac{\partial w}{\partial t})^2 + b(\frac{\partial^2 w}{\partial x \partial t})^2] dx \tag{26}$$

The first term is the stored energy due to bending. The second term is the kinetic energy due to the translation motion. The last term of the integrand is the kinetic energy from rotation of the beam element corresponding to Equation (14). a and b are positive constants.

Taking derivative of $E(t)$ with respect to time and incorporating the system equation (14) into it, we have

$$
\frac{dE(t)}{dt} = \int_0^L [a\frac{\partial^2 w}{\partial x^2}\cdot\frac{\partial^3 w}{\partial x^2 \partial t} + b\frac{\partial^2 w}{\partial x \partial t}\cdot\frac{\partial^3 w}{\partial x \partial t^2} + \frac{I}{A}\frac{\partial w}{\partial t}\cdot\frac{\partial^4 w}{\partial x^2 \partial t^2}
$$
$$
+ \frac{c}{\rho A}\frac{\partial w}{\partial t}\cdot\frac{\partial^2 V}{\partial x^2} - \frac{EI}{\rho A}\frac{\partial w}{\partial t}\frac{\partial^4 w}{\partial x^4}]dx. \tag{27}
$$

Integrating by parts and setting

$$
a = \frac{EI}{\rho A}, \quad b = \frac{I}{A} \tag{28}
$$

We obtain

$$
\frac{dE(t)}{dt} = \frac{EI}{\rho A}\frac{\partial^2 w}{\partial x^2}\cdot\frac{\partial^2 w}{\partial x \partial t}\Big|_{x=0}^{x=L} - \frac{EI}{\rho A}\frac{\partial^3 w}{\partial x^3}\cdot\frac{\partial w}{\partial t}\Big|_{x=0}^{x=L}
$$
$$
+ \frac{I}{A}\cdot\frac{\partial w}{\partial t}\cdot\frac{\partial^3 w}{\partial x \partial t^2}\Big|_{x=0}^{x=L} + \frac{c}{\rho A}\int_0^L \frac{\partial w}{\partial t}\cdot\frac{\partial^2 V}{\partial x^2}dx. \tag{29}
$$

Introducing the boundary condition (15), we have

$$
\frac{dE(t)}{dt} = \frac{c}{\rho A}V(L,t)\frac{\partial^2 w}{\partial x \partial t}\Big|_{x=L} - \frac{c}{\rho A}\frac{\partial V(L,t)}{\partial x}\cdot\frac{\partial w}{\partial t}\Big|_{x=L}
$$
$$
+ \frac{I}{A}\cdot\frac{\partial w}{\partial t}\cdot\frac{\partial^3 w}{\partial x \partial t^2}\Big|_{x=L} + \frac{c}{\rho A}\int_0^L \frac{\partial w}{\partial t}\cdot\frac{\partial^2 V}{\partial x^2}dx. \tag{30}
$$

The first term in Equation (30) contains the rotational velocity of the beam at the end. The second term has the force applied by the actuator. The third term is the product of the velocity of the displacement and the angular acceleration at the end of the beam. There is a second partial derivative of $V(x,t)$ with respect to the spatial variable. We can design the appropriate modal controller by choosing the right $V(x,t)$. Our purpose here is to find the control such that the time derivative of the energy function is negative.

Let $V(x,t)$ be decomposed as the product of a spatial and a time function

$$
V(x,t) = v(x)q(t) \tag{31}
$$

where $v(x)$ is the actuator shape function, $q(t)$ is the coordinate function. We assume that the function $v(x)$ has continuous second derivative on the interval $(0,L)$ and has compact support over the interval; then the first two terms in Equation (30) vanish. Since the third term is negative from its physical meaning it will not cause energy

increase. We need to analyze the influence of the integration term in the equation. Substituting the voltage function into the last term in Equation (30)

$$\frac{c}{\rho A}\int_0^L \frac{\partial w}{\partial t}\cdot\frac{\partial^2 V}{\partial x^2}dx = \frac{c}{\rho A}q(t)\int_0^L \frac{\partial w}{\partial t}\cdot\frac{\partial^2 v(x)}{\partial x^2}dx \tag{32}$$

where $q(t)$ is the time coordinate of the controller.

We further introduce the feedback control by using the sensor output signal V_s,

$$\begin{aligned}
q(t) &= \frac{dV_s(t)}{dt} \\
&= -K_s\int_0^L \frac{\partial w(x,t)}{\partial t}\frac{\partial^2 F(x)}{\partial x^2}dx.
\end{aligned} \tag{33}$$

Then (32) becomes

$$\begin{aligned}
\frac{dE(t)}{dt} &\leq \frac{c}{\rho A}q(t)\int_0^L \frac{\partial w}{\partial t}\cdot\frac{\partial^2 v(x)}{\partial x^2}dx \\
&= -K_s\frac{c}{\rho A}\int_0^L \frac{\partial w}{\partial t}\cdot\frac{\partial^2 F(x)}{\partial x^2}dx\int_0^L \frac{\partial w}{\partial t}\cdot\frac{\partial^2 v(x)}{\partial x^2}dx \\
&< 0
\end{aligned} \tag{34}$$

Hence the system is asymptotically stable. The feedback control is given by

$$V(x,t) = -K_s v(x)\int_0^L \frac{\partial w(x,t)}{\partial t}\frac{\partial^2 F(x)}{\partial x^2}dx. \tag{35}$$

The introduced control is velocity feedback control. It takes into account the bending rate along the beam and introduces damping to the system. Here there is no need for the model modal truncation.

When the control $V(x,t)$ is uniformly distributed in space, $\frac{\partial V}{\partial x}=0$, if we further assume that there is no elastic bonding layer to be present between the piezoelectric and the substructure, that is, there is no shear lag between the two layers, the strain is transferred between the piezoelectric and the beam over an infinitesimal distance near the end of the actuator [4]. We then have the simplified equation,

$$EI\frac{\partial^4 w(x,t)}{\partial x^4} + \rho A\frac{\partial^2 w(x,t)}{\partial t^2} - \rho I\frac{\partial^4 w(x,t)}{\partial x^2\partial t^2} = 0 \tag{36}$$

with boundary conditions

$$\begin{aligned}
w(0,t) &= 0 \\
\frac{\partial w(0,t)}{\partial x} &= 0 \\
EI\frac{\partial^2 w(L,t)}{\partial x^2} &= c.V(t) \\
EI\frac{\partial^3 w(L,t)}{\partial x^3} &= 0.
\end{aligned} \tag{37}$$

V depends only on time in this case. This is a boundary control problem. We again use Equation (26) as the energy function. Repeating the procedure, we observe that only the first term in Equation (30) survives. This gives us

$$\frac{dE(t)}{dt} \leq \frac{c}{\rho A} V(L,t) \left. \frac{\partial^2 w}{\partial x \partial t} \right|_{x=L} \tag{38}$$

Notice that it is sufficient to choose

$$V(t) = -k \left. \frac{\partial^2 w}{\partial x \partial t} \right|_{x=L} \tag{39}$$

to make

$$\frac{dE(t)}{dt} < 0 \tag{40}$$

so as to asymptotically stable the system. The tip rotation speed is available from the sensor output Equation (23).

5   SENSOR AND ACTUATOR SHAPE CONSIDERATION

It is interesting to see that by introducing velocity feedback controller (35), the energy decay rate is given by (34) whose right hand side is a function of $F(x)$ and $v(x)$. Here $F(x)$ and $v(x)$ are the shape or weight functions of the actuator and the sensor. They add weight for the control and measurement at each cross section along the beam. If we consider the displacement of the beam as the sum of a series of products of modal function and its coordinate, we can further analyze the effect of sensor and actuator shapes to different vibration modes.

When the electric field is applied to the piezoelectric lamina, the actual piezoelectric actuation happens only in the region where both sides are covered by the electrodes. The same is true for collecting charge from the sensor layer. Hence, changing the width of the layout of the conductor is equivalent to varying the weighting functions. In this sense, it is possible to design the controller to suppress a particular mode or to design a distributed sensor to measure an interested mode.

Consider the sensor output (23). We can get different information from the system by tailoring the right weighting function $F(x)$. For example, we may select $F(x)$ in such a way that

$$
\begin{aligned}
\frac{\partial^2 F(x)}{\partial x^2} &= 0, \ 0 \leq x \leq L \\
\frac{\partial F(L)}{\partial x} &= 0, \ x = L \\
F(L) &= -\frac{1}{K_s}
\end{aligned}
\tag{41}
$$

the integral term vanishes, so does the second term, and then the sensor output

$$V_s(t) = \frac{\partial w(L, t)}{\partial x} \qquad (42)$$

represents the angular deflection at the tip of the beam. Similarly, we can measure the displacement of the tip. From (20), the sensor can be used to build strain gauge by setting $F(x)$ to be a spatial Dirac delta function $\delta(x)$.

We think that it is theoretically possible to use segmented sensors for the control of flexible structures. Digital control provides the ability to implement a sensing network with simple computation to rearrange the sensor layout and get different measurements with one sensor layer. Some measurements which are difficult to obtain in conventional way may be available by using distributed sensors. It may be feasible to implement full state feedback in relevant semigroup control formulations.

The effectiveness of the PZT controller in introducing structural damping and its influence to the system dynamics of realistic size is based on the control authority of the controller. Using velocity feedback shall increase the damping, but the control gain is limited to the electric field limit to avoid depolarization of the actuator. The actuator weighting function $v(x)$ also plays a role here. We know that the bending moment is concentrated mostly at the end of the actuator of the beam. Hence more weighting should be placed on the region with high average strain.

The feedback control (35) actually provides Voigt type damping since the rate of change of the bending curvature is used for feedback (22) and this rate is proportional to the rate of change of the structural strain. The augmented composite beam has an altered constitutive equation. The stress is no longer just proportional to the strain, but a linear combination of strain and the rate of strain change with respect to time.

We now analyze the effect of both sensor and actuator shape functions to the damping control of different vibration modes. We use a Ritz-Galerkin procedure to implement modal expansion. We write the beam displacement $w(x, t)$ as

$$w(x, t) = \sum_{k=1}^{n} \Phi_k(x)d_k(t) \qquad (43)$$

where $\Phi_k(x)$ is the modal function and d_k is the time coordinate. We can choose the orthogonal modal functions. We rewrite here the control form of the previous section

$$V(x, t) = v(x)q(t). \qquad (44)$$

Substituting the modal forms into Equation (14), multiplying each term with $\Phi_l(x)$ and then taking spatial integration along the beam, we get

$$\sum_{k=1}^{n} \left[\int \Phi_l(x)(\rho A\Phi_k(x) - \rho I\Phi_k^{(2)}(x))\ddot{d}_k + EI\Phi_l(x)\Phi_k^{(4)}(x)d_k dx \right] = cq(t) \int \Phi_l(x)v^{(2)}(x)dx \qquad (45)$$

where $\dot{d}$ and $\ddot{d}$ stand for the first and second time derivatives of the function $d(t)$; $v^{(i)}(x)$ stands for the ith spatial derivative of $v(x)$. We then have

$$\sum_{k=1}^{n} m_{lk}\ddot{d}_k + \sum_{k=1}^{n} k_{lk}d_k = Q_l \tag{46}$$

$$Q_l = -\sum_{k=1}^{n} c_{lk}\dot{d}_k(t) \tag{47}$$

where

$$m_{lk} = \sum_{k=1}^{n} \int \Phi_l(x)[\rho A\Phi_k(x) - \rho I\Phi_k^{(2)}(x)]dx \tag{48}$$

$$k_{lk} = \sum_{k=1}^{n} \int EI\Phi_l(x)\Phi_k^{(4)}(x)dx \tag{49}$$

$$c_{lk} = cq(t)\int \Phi_l(x)v^{(2)}(x)dx. \tag{50}$$

The compact modal form is

$$M\ddot{d}(t) + Kd(t) = Q(t) \tag{51}$$

where $d(t)$ and $Q(t)$ are nth order column vector functions. M is the inertial matrix, K is the stiffness matrix, $Q(t)$ is the modal control input. The damping of different elastic modes is influenced by

$$Q(t) = -C\dot{d}(t) \tag{52}$$

and

$$M\ddot{d}(t) + C\dot{d}(t) + Kd(t) = 0 \tag{53}$$

where C is a n by n damping coefficient matrix. Its elements are derived from the control law (35)

$$c_{lk} = cK_s \int_0^L \Phi_l \frac{d^2v(x)}{dx^2}dx \int_0^L \Phi_k \frac{d^2F(x)}{dx^2}dx. \tag{54}$$

Observing Equation (54), we notice that in addition to the control authority determined by the actuation and sensing constants c and K_a the added damping to a specific mode depends on the shape functions $F(x)$ and $v(x)$. The function $v(x)$ in the first integral decides the amount of control effort applied to the lth mode. Similarly, $F(x)$ provides the observation of the kth elastic mode. The coefficient c_{lk} can be viewed as a measure of the damping to the lth mode by control based on the information from the kth elastic mode. If we choose the sensor shape to be such a function that

$$\frac{d^2F(x)}{dx^2} = \Phi_k(x), \tag{55}$$

we can measure the kth mode completely. When the second spatial derivative contains several modes, we shall get the combined information from the sensor. The similarity holds for the actuator, too. Properly selecting $F(x)$ and $v(x)$, we can observe and suppress the vibration modes.

6 CONCLUSIONS

We have embedded a static PZT actuator model into the improved Euler-Bernoulli beam model to form a composite beam model with the rotational inertia effect considered. We further used a distributed PVDF sensor to measure the elastic bending modes. A closed loop controller has been designed by using Lyapunov's direct method. The closed loop system extracts energy from the system. The closed loop system is asymptotically stable. Finally, we have discussed the effects of different sensor and actuator shapes to the elastic modes. We point out that it is feasible to select suitable sensing and control weight to implement vibration control to some specified elastic modes.

Further research is needed regarding aspects of estimation of the energy decay rate and real time implementation of the control law. We also would like to consider modeling the substructure with the Timoshenko model or the geometric exact rod model. Also, the real impact of the modal controller needs to be verified and further explored by experiments.

References

[1] Thomas Bailey and James E. Hubbard Jr. Distributed piezoelectric-polymer active vibration control of a cantilever beam. *Journal of Guidance, Control and Dynamics*, 8(5):605–611, Sept.-Oct 1985.

[2] S.E. Burke and J.E. Hubbard,Jr. Active vibration control of a simply supported beam using a spatially distributed actuator. *IEEE Control Systems Magazine*, pages 25 – 30, August 1987.

[3] S.A. Collina, D.W.Miller, and A.H. von Flotow. Piezopolymer spatial filters for active structural control. In C.A. Rogers and C.R. Fuller, editors, *Recent Advances in Active Control of Sound and Vibration*, pages 64–77, VPI&SU, Blacksburg, Virginia, 15–17 1991. NASA Langley Research Center and others, Technomic Publishing Co. Inc.

[4] Edward F. Crawley and Javier de Luis. Use of piezoelectric actuators as elements of intelligent structures. *AIAA Journal*, 25(10):1373–1385, 1987.

[5] H.H. Cudney. *Distributed Structural Control Using Multilayered Piezoelectric Actuators*. PhD thesis, SUNY Buffalo, NY, 1989.

[6] C. K. Lee and F. C. Moon. Modal sensors/actuators. *Journal of Applied Mechanics*, 57:434–441, June 1990. Trans. of the ASME.

[7] M.J. Newman. Distributed active controllers. In C.A. Rogers and C.R. Fuller, editors, *Recent Advances in Active Control of Sound and Vibration*, pages 579–592, VPI&SU, Blacksburg, Virginia, 15–17 1991. NASA Langley Research Center and others, Technomic Publishing Co. Inc.

[8] S. Timoshenko and D.H. Young. *Vibration Problems In Engineering*. D.Van Nostrand Co.,Inc., Canada, third edition, 1955.

DYNAMIC ANALYSIS OF SPACE SHUTTLE/RMS CONFIGURATION USING CONTINUUM APPROACH

Jayant Ramakrishnan
Dynacs Engineering Company, Inc.
Palm Harbor, Florida

and

Lawrence W. Taylor, Jr.
NASA Langley Research Center
Hampton, Virginia

ABSTRACT

The initial assembly of Space Station Freedom involves the Space Shuttle, its Remote Manipulation System (RMS) and the evolving Space Station Freedom. The dynamics of this coupled system involves both the structural and the control system dynamics of each of these components. The modeling and analysis of such an assembly is made even more formidable by kinematic and joint nonlinearities.

The current practice of modeling such flexible structures is to use finite element modeling in which the mass and interior dynamics is ignored between thousands of nodes, for each major component. The model characteristics of only tens of modes are kept out of thousands which are calculated. The components are then connected by approximating the boundary conditions and inserting the control system dynamics.

In this paper continuum models are used instead of finite element models because of the improved accuracy, reduced number of model parameters, the avoidance of model order reduction, and the ability to represent the structural and control system dynamics in the same system of equations. Dynamic analysis of linear versions of the model is performed and compared with finite element model results. Additionally, the transfer matrix to continuum modeling is presented.

The continuum modeling approach is seen to offer a viable alternative to finite element modeling. The continuum approach enables increased insight for synthesis and integrated control/structures design.

NOMENCLATURE

<u>Symbols</u>

A, B, C, D	state vector elements, coefficients of the sinusoidal and hyperbolic functions
c	model parameter vector
EA	longitudinal stiffness
EI_x, EI_y	bending stiffness
Fo	constant axial force
GA	lateral shear
GIy	torsional stiffness
F	force distribution function
F_0	axial, steady force
I	inertia matrix
L	length of beam
Q_u	deflection coefficient matrix
Q_s	angular deflection matrix
s	real part of the roots
Q	state vector, coefficients of sinusoidal and hyperbolic mode shape basis functions
s	real part of root
w	modal frequency, imaginary part of the roots
Ω	angular velocity vector

Superscripts

T	transpose
-1	inverse
•	differention with respect to t
/	differention with respect to z

Subscripts

i	mode index
c.g.	center of gravity
n	general index
x	x axis
y	y axis
z	z axis
y	torsional axis, z

INTRODUCTION

The initial assembly of Space Station Freedom involves the Space Shuttle, its Remote Manipulation System (RMS) and the evolving Space Station Freedom. The assembly of the Space Station Freedom is performed by positioning and connecting 22 modules using a remote manipulation system (RMS). The dynamics of this coupled system involves both the structural and the control system dynamics of each of these components. The numerous configurations that result from this assembly process necessitate an efficient procedure for accurately modeling the structural and control dynamics. The modeling and analysis of such an assembly is made even more formidable by kinematic and joint nonlinearities.

Modeling of complex flexible spacecraft is an issue which has far reaching consequences in controller design and the subsequent spacecraft performance. Numerous difficulties in controlling flexible spacecraft have been attributed to inaccuracies in modeling [1]. With higher controller bandwidth, modeling issues assume greater significance. Increased size and more demanding control specifications promise to make high performance control more difficult [2]. Current modeling schemes for the design and analysis of structural and control systems have several limitations [3]. The conventional approach is to use elements which are void of dynamics on the interior of their boundaries. The computational cost and numerical inaccuracies involved in generating solutions to these equations impose a practical limit to the size (and consequently the accuracy) of these structural dynamics models. For problems with minimal control-structure interaction, the finite element models are adequate. High performance control systems will however require increased fidelity and accuracy in the models.

Distributed parameter modeling is proposed in this work to synthesize high fidelity spacecraft models. The distributed parameter models provide a single set of equations for control and structural dynamics. The conventional finite dimensional representation of complex spacecraft by the finite element method suffers from the following drawback. Finite element models are generally too large for control work. One performs model reduction to reduce the model order to controller synthesis amendable dimensions. Spillover of control energy into the unmodeled modes can result in instability. The proposed approach represents flexible structural members by partial differential equations offering significant advantages in modeling, parameter estimation and the integrated design of control/structural systems [4], [5], [6]. The present method differs from the finite element

method in that an individual element can represent all the modes of that "super" element and produce the force and moment vectors at its boundaries. These elements are then connected at their boundaries to form the model of the complete structure. Bishop [7] and Snowdon [8] have studied applications in which a limited number of such elements have been connected to form simple frames. The homogenization technique [9] and [10] for repetitive lattice trusses is particularly useful. For spacecraft control applications, it is necessary to connect many distributed parameter elements to represent the structural dynamics of complex flexible spacecraft. The software programs available for continuum modeling include: Poeleart's [11] DISTEL, Taylor's [12], PDEMOD and Anderson's [13] BUNVIS program. In this work, PDEMOD is used to generate some of the results.

This paper will discuss the generation of the system of partial differential equations for modeling complex, flexible spacecraft. A continuum model of the assembly configurations of the Space Shuttle RMS - Payload will be used to study the control problems involved. Continuum models are shown to have distinct advantages for control applications.

This paper is organized in the following manner. The formulation of the structural dynamics models, the transfer matrix approach to modeling and the control system embedding methods are presented in the next section. The numerical results for a simple model of the Shuttle/RMS Payload assembly are presented. The results compare the modal characteristics obtained using NASTRAN with the continuum results. The concluding remarks identify the salient features of the proposed approach and related modeling and analysis accomplishments to date.

Discussion

The formulation of the dynamics using a set of distributed parameter elements connected at their boundaries is key to obtaining the objectives of optimal parameter estimation. The types of elements to be considered are (1) rigid body with a full inertia matrix, and (2) dynamic, flexible beam element. The equations of motion for each of these elements will be considered in turn.

Equations of Motion

A Newtonian or inertial frame of reference is used for the motion of all beam elements and rigid bodies. For example, the point of attachment in the Newtonian axis of a reference, undeflected beam is:
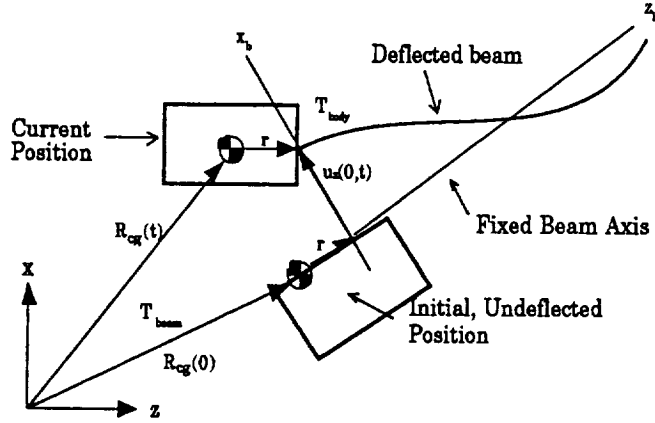

Figure 1: Diagram of a Rigid Body Attached to its Reference Flexible Beam

$$R_{\text{attach},0} = R_{\text{c.g.},o} + T_{\text{beam}}r \tag{1}$$

For the deflected beam:

$$
\begin{aligned}
R_{\text{attach},t} &= R_{\text{attach},0} + T_{\text{beam}}u \\
&= R_{\text{c.g.},0} + T_{\text{beam}}r + T_{\text{beam}}u
\end{aligned}
\tag{2}
$$

The position of the body center-of-gravity due to beam deflection is:

$$
\begin{aligned}
R_{\text{c.g.},t} &= R_{\text{attach},t} - T_{\text{body}}r \\
&= R_{\text{c.g.},0} + T_{\text{beam}}r + T_{\text{beam}}u - T_{\text{body}}r
\end{aligned}
\tag{3}
$$

For small angular deflections

$$T_{\text{body}} = T_{\text{beam}} + \text{Tilda}\left(T_{\text{beam}}u'\right) \tag{4}$$

Substituting, we get

$$R_{c.g.,t} = R_{c.g.,0} + T_{beam}u - \text{Tilda}\left(T_{beam}u'\right)r$$
$$= R_{c.g.,0} + T_{beam}u + R\left(T_{beam}u'\right) \tag{5}$$

Differentiating, we get the acceleration of the body center-of-gravity:

$$\ddot{R}_{c.g.,t} = T_{beam}\ddot{u} + \ddot{R}\left(T_{beam}\ddot{u}'\right) \tag{6}$$

Equations of motion are written for each rigid body and the forces and moments imparted by the beams are taken into account. In each case it is necessary to account for the different frames of reference and joints of attachment. Equations of motion for the linear and angular degrees of freedom for all of the bodies are assembled into a single matrix, A.

In the time domain the equations of motion are:

$$\ddot{R}_{c.g} = \sum\{\text{Forces}\} / m$$
$$\dot{\Omega} = I_{body}^{-1} \sum\{\text{Moments}\} \tag{7}$$

In the frequency domain, the linear and angular equations of motion are the basis for each block of elements:

$$A_{\text{Linear},j} = Q_{uj} + T_j^T R_j T_j Q_{uj} - \left(\frac{1}{m_j\omega^2}\right)\sum\left\{T_j^T T_i P_{Fi}\right\}$$

$$A_{\text{angular},j} = Q'_{uj} + T_j^T I_j^{-1}\left(\frac{1}{\omega^2}\right)\sum\left\{T_{beam-i}P_{Mi} + R_{beam-i}T_{beam-i}P_{Fi}\right\} \tag{8}$$

For each case in which a rigid body has more than one beam attached, a constraint equation is added to the system of equations. Assembly of the equations of motion and the constraint equations yields the system matrix from which we get the characteristic equation:

$$|A(\sigma + jw)| = 0 \tag{9}$$

Flexible Beam Equations

The flexible beam elements exhibit lateral bending in two axes, axial deformation, and torsion. The governing partial differential equations have a variety of terms so that parameter values can select, for example, a wave or string equation, Euler beam equation, or Timoshenko beam equation. A flexible beam element will be described by at least four partial differential equations.

Lateral Bending

The beam equations represent (1) Euler bending stiffness, (2) axial force stiffness, and (3) Torsion. For bending in the x-z plane:

$$Mu_{x,1,tt} + EI_{x,1}u_{x,1,zzzz} + GAu_{x,1,zztt} + F_o u_{x,1,zz} + K_x\left(u_{x,1} + u_{x,2}\right) = F_{x,1}(z,t)$$

$$F_{x,1}(z,t) \qquad (10)$$

Axial Deformation

Axial dynamics is represented by a wave equation with an additional term which represents a spring connected to a second distributed mass.

$$m\ddot{u}_{z,1} - EAu_{zz,1} + K_z\left(u_{z,2} + u_{z,1}\right) = F_{z,1}(z,t) \qquad (11)$$

Torsion

Torsional dynamics is represented by a wave equation

$$I_{\psi,1}\ddot{u}_{\psi,1} - GI_{\psi,1}u_{\psi zz,1} + K_\psi\left(u_{\psi,2} + u_{\psi,1}\right) = M_{z,1}(z,t) \qquad (12)$$

Solution of the Partial Differential Equations

The solutions of these partial differential equations for zero damping produce the sinusoidal and hyperbolic spatial equations which comprise the mode shape functions. For the case that $F_o = 0$, the bending mode shape in the x-z plane is:

$$u_x(z) = A_x \sin\beta_{1x}z + B_x \cos\beta_{1x}z + C_x \sinh\beta_{1x}z + D_x \cosh\beta_{1x}z \tag{13}$$

Similarly, for bending in the y-z plane:

$$u_y(z) = A_y \sin\beta_{1y}z + B_y \cos\beta_{1y}z + C_y \sinh\beta_{1y}z + D_y \cosh\beta_{1y}z \tag{14}$$

The undamped mode shape functions for torsion and elongation about the z axis are:

$$u_z(z) = A_z \sin\beta_z z + B_z \cos\beta_z z \tag{15}$$

$$u_\psi(z) = A_\psi \sin\beta_\psi z + B_\psi \cos\beta_\psi z \tag{16}$$

These undamped mode shapes are expected to be good approximations to the exact solutions for low level of damping. The mode shape of the entire configuration consists of these functions, repeated for each beam element. Because bending in two directions, torsion and elongation are considered, a total of 12 coefficients are needed. The vector of coefficients is the state vector of the structural dynamics. A vector of the coefficients of these sinusoidal and hyperbolic functions will serve as the state vector.

$$\Theta^T = \begin{bmatrix} A_x & B_x & C_x & D_x & A_y & B_y & C_y & D_y & A_z & B_z & A_\psi & B_\psi \end{bmatrix} \tag{17}$$

Under conditions of applied forces it is necessary to include rigid body modes. Their coefficients will expand the state vector accordingly. All deflections, forces, moments, and accelerations will be expressed in terms of such state vectors.

The motion of each rigid body is put in terms of the deflection at the point of attachment of a particular reference beam element. The linear and angular deflection vectors can be expressed as:

$$u = Q_u(z)\Theta \tag{18}$$

$$u = Q_s(z)\Theta \tag{19}$$

Next, it is necessary to express the forces and moments at either end of the beam elements. The force and moment vectors are:

$$F_{attach} = P_F(z)\Theta \tag{20}$$

$$F_{attach} = P_M(z)\Theta \tag{21}$$

It is also necessary to account for changes in axes from each beam to the body to which it is attached, and for points of attachment at some distance away from the center of gravity. The force and moment that a beam-i applies to a body-j are:

$$F_{body-j} = T_{body-j}{}^T T_{beam-i} P_{F,i}(z)\Theta \tag{22}$$

$$M_{body-j} = T_{body-j}{}^T \{T_{beam-i} P_{M,i}(z) + R_{beam-i}(z) T_{beam-i} P_F(z)\}\Theta \tag{23}$$

The partial differential equations provide the relationships between the modal frequency and the eigenvalues for the mode shape equations. The lateral beam, axial deformation and torsion equations can be solved for the zero damping cases to produce the following relationships between the modal frequency and the wave numbers in the mode shape function.

For bending in the x-z plane:

$$\beta_{1,x^2} = .5b + \sqrt{(.5b)^2 + m\omega^2 / EI_x} \tag{24}$$

$$\beta_{2,x^2} = -.5b + \sqrt{(.5b)^2 + m\omega^2 / EI_x} \tag{25}$$

where $b = m\omega^2 / GA + F_o / EI_x$.

The case for bending in the y-z plane is similar. For torsion and elongation:

$$\beta_\psi = \omega / \sqrt{GI_\psi / m} \tag{26}$$

$$\beta_z = \omega / \sqrt{EA / m} \tag{27}$$

388

Transfer Matrix Approach

The transfer matrix approach [14] is suitable for large systems made up of several subsystems. The typical subsystem may be simple elements like a scalar spring or a complex Bernoulli-Euler or Timoshenko beam element. The subsystems are cast in the form of a field and a point matrix. The formulation is in terms of the state vector which is a column matrix of displacements and internal forces. The treatment of the transfer matrix derivation for rigid bodies and flexible beams follows the work in [15].

Rigid Body

The translational and rotational equations of the jth body can be described by the following equations (figure 2).
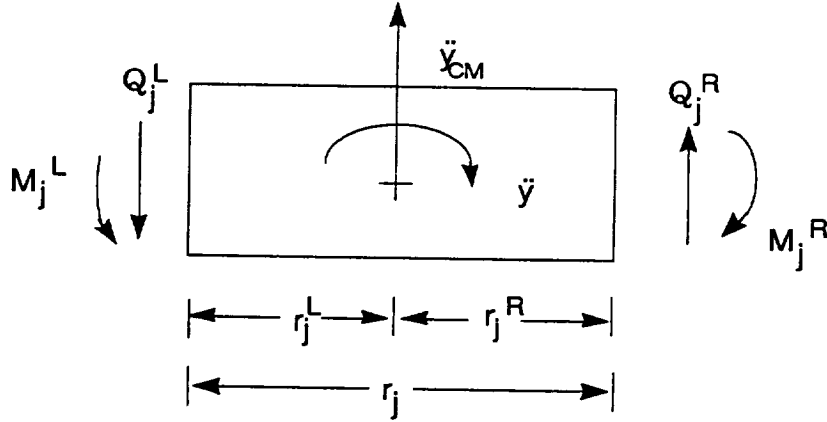
Figure 2: Free-Body Diagram of the rigid body

$$m_j \ddot{y}_{CM} = Q_j^R - Q_j^L \tag{28}$$

$$I_j \ddot{y}' = M_j^R - Q_j^R r_j^R - Q_j^L r_j^L \tag{29}$$

For harmonic motion, the equations are rewritten as

$$Q_j^R = Q_j^L - m_j \omega^2 Y_{CM} \tag{30}$$

$$M_j^R = M_j^L + Q_j^R r_j^R + Q_j^L r_j^L - I_j \omega^2 Y_j'^L \tag{31}$$

The displacement of the center of mass Y_{CM} is related to Y_j^R and Y_j^L by

$$Y_j^R = Y_{CM} - r_j^R Y_j'^R \qquad (32)$$

$$Y_j^L = Y_{CM} + r_j^R Y_j'^L \qquad (33)$$

Using the expression for Y_{CM} from equation (33) and by the property of slope continuity, equation (32) can be rewritten as

$$Y_j^R = Y_j^L - r_j Y_j'^L \qquad (34)$$

where $r_j = r_j^L + r_j^R$.

Substituting for Y_{CM} in equation (30), we get

$$Q_j^R = Q_j^L - m_j \omega^2 \left(Y_j^L - r_j Y_j'^L \right) \qquad (35)$$

Substituting the expression for Q_j^R in equation (31), we get

$$M_j^R = M_j^L + r_j Q_j^L - m_j \omega^2 r_j^R Y_j^L - \left(I_j - m_j r_j^L r_j^R \right) \omega^2 Y_j'^L \qquad (36)$$

Equations (34), (35), (36) and the slope continuity condition yield the point matrix $[PM]_j$ for the rigid body element

$$[PM]_j = \begin{bmatrix} 1 & -r_j & 0 & 0 \\ 0 & 1 & 0 & 0 \\ -m_j \omega^2 & m_j \omega^2 r_j^L & 1 & 0 \\ m_j \omega^2 r_j^R & -\left(I_j - m_j r_j^L r_j^R \right) & r_j & 1 \end{bmatrix} \qquad (37)$$

$$\begin{bmatrix} Y \\ Y' \\ Q \\ M \end{bmatrix}_j^R = [PM]_j \begin{bmatrix} Y \\ Y' \\ Q \\ M \end{bmatrix}_j^L \qquad (38)$$

390

Flexible Beam

The field matrix for Bernoulli-Euler beam is derived from the solution of the bending mode slope (Equation 13) as follows.

At the left end of the beam $(z = 0)$, the displacement $Y(0)$ slope $Y'(0)$, shear force $Q(0)$ and bending moment $M(0)$ will be

$$
\begin{bmatrix} Y \\ Y' \\ Q \\ M \end{bmatrix}_{j-1}^{R} = \begin{bmatrix} 0 & 1 & 0 & 1 \\ \beta & 0 & \beta & 0 \\ -k\beta^3 & 0 & +k\beta^3 & 0 \\ 0 & -k\beta^2 & 0 & -k\beta^2 \end{bmatrix} \begin{bmatrix} A_x \\ B_x \\ C_x \\ D_x \end{bmatrix}
\tag{39}
$$

where $Q = kY'''$ and $M = kY''$, $k = EI$. For notational simplicity, the subscript x on β is dropped. At the right end of the beam $(z = L)$

$$
\begin{bmatrix} Y \\ Y' \\ Q \\ M \end{bmatrix}_{j}^{L} = \begin{bmatrix} \sin \beta L & \cos \beta L & \sinh \beta L & \cosh \beta L \\ \beta \cos \beta L & -\beta \sin \beta L & \beta \cosh \beta L & \beta \sinh \beta L \\ k\beta^3 \cos \beta L & -k\beta^3 \sin \beta L & k\beta^3 \cosh \beta L & -k\beta^3 \sinh \beta L \\ k\beta^2 \sin \beta L & k\beta^2 \cos \beta L & -k\beta^2 \sinh \beta L & k\beta^2 \cosh \beta L \end{bmatrix} \begin{bmatrix} A_x \\ B_x \\ C_x \\ D_x \end{bmatrix}
\tag{40}
$$

Solving for the coefficients A_x, B_x, C_x, D_x from equation (39) and substituting in equation (40) we get the field matrix for the beam element as:

$$
[FM]_j = \begin{bmatrix} \frac{1}{2}(\cos \beta L + \cosh \beta L) & \frac{1}{2\beta}(\sin \beta L + \sinh \beta L) & \frac{1}{2k\beta^3}(\sin \beta L - \sinh \beta L) & \frac{1}{2k\beta^2}(\cos \beta L - \cosh \beta L) \\ \frac{-\beta}{2}(\sin \beta L + \sinh \beta L) & \frac{1}{2}(\cos \beta L + \cosh \beta L) & \frac{1}{2k\beta^3}(\cos \beta L - \cosh \beta L) & \frac{-1}{2k\beta}(\sin \beta L - \sinh \beta L) \\ \frac{-k\beta^3}{2}(\sin \beta L + \sinh \beta L) & \frac{1}{2}k\beta^2(\cos \beta L + \cosh \beta L) & \frac{1}{2}(\cos \beta L - \cosh \beta L) & \frac{-\beta}{2}(\sin \beta L - \sinh \beta L) \\ \frac{k\beta^2}{2}(\cos \beta L + \cosh \beta L) & \frac{1}{2}(\sin \beta L + \sinh \beta L) & \frac{1}{2\beta}(\sin \beta L - \sinh \beta L) & \frac{1}{2}(\cos \beta L - \cosh \beta L) \end{bmatrix}
$$

$$
\begin{bmatrix} Y \\ Y' \\ Q \\ M \end{bmatrix}_{j}^{L} = [FM]_j \begin{bmatrix} Y \\ Y' \\ Q \\ M \end{bmatrix}_{j-1}^{R}
\tag{41}
$$

The transfer matrix for a flexible beam with a mass at the right end is

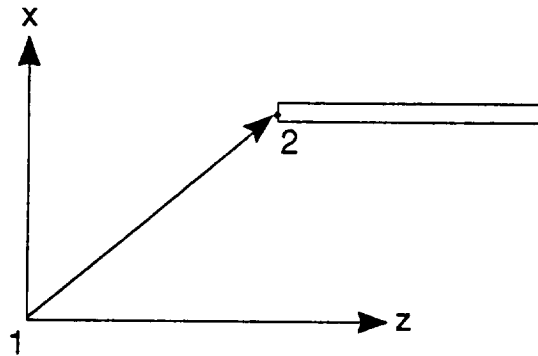$$[TF]_j = [PM]_j[FM]_j$$

(42)

Figure 3: Beam Offset

Offset Attachment

The planar offset attachment transfer matrix can derived from figure 3. The offset of point 2 from the origin (point 1) is given by r_x and r_z.

$$
\begin{bmatrix} u_x \\ u_z \\ \theta_y \\ F_x \\ F_z \\ M_y \end{bmatrix}_2 = \begin{bmatrix} 1 & 0 & -r_z & 0 & 0 & 0 \\ 0 & 1 & r_x & 0 & 0 & 0 \\ 0 & 0 & 1 & 0 & 0 & 0 \\ 0 & 0 & 0 & 1 & 0 & 0 \\ 0 & 0 & 0 & 0 & 1 & 0 \\ 0 & 0 & 0 & r_z & -r_x & 1 \end{bmatrix} \begin{bmatrix} u_x \\ u_z \\ \theta_y \\ F_x \\ F_z \\ M_y \end{bmatrix}_1
$$

(43)

Joint with Compliance

The joint compliance transfer matrix is derived for planar motion assuming a spring of stiffness k_θ . The joint equations for planar motion are

$$\left(M_y\right)_2 = \left(M_y\right)_1 \tag{44}$$

also

$$\left(M_y\right)_2 = k_\theta\left(\theta_1 - \theta_2\right) \tag{45}$$

The transfer matrix can be expressed as

$$
\begin{bmatrix} u_x \\ u_z \\ \theta_y \\ F_x \\ F_z \\ M_y \end{bmatrix}_2 =
\begin{bmatrix}
1 & 0 & 0 & 0 & 0 & 0 \\
0 & 1 & 0 & 0 & 0 & 0 \\
0 & 0 & 1 & 0 & 0 & -1/k_\theta \\
0 & 0 & 0 & 1 & 0 & 0 \\
0 & 0 & 0 & 0 & 1 & 0 \\
0 & 0 & 0 & 0 & 0 & 1
\end{bmatrix}
\begin{pmatrix} u_x \\ u_z \\ \theta_y \\ F_x \\ F_z \\ M_y \end{pmatrix}_1 \tag{46}
$$

Rigid Body Control

The rigid body point matrix for a body with mass and inertia but with r_j equal to zero is obtained from equation (37). Using the Laplace variable s^2 in the place of $-\omega^2$, we get

$$
\begin{pmatrix} u_x \\ u_z \\ \theta_y \\ F_x \\ F_z \\ M_y \end{pmatrix}_2 =
\begin{bmatrix}
1 & 0 & 0 & 0 & 0 \\
0 & 1 & 0 & 0 & 0 \\
0 & 0 & 1 & 0 & 0 \\
Ms^2 & 0 & 0 & 1 & 0 \\
0 & Ms^2 & 0 & 0 & 0 \\
0 & 0 & Is^2 & 0 & 1
\end{bmatrix}
\begin{pmatrix} u_x \\ u_z \\ \theta_y \\ F_x \\ F_z \\ M_y \end{pmatrix}_1 \tag{47}
$$

Rigid body controllers basically stabilize the system asymptotically and are of the proportional derivative type. The transfer matrix is modified in the following manner for control:

$$ms^2 \to ms^2 + c_x s + k_x$$
$$Is^2 \to Is^2 + c_\theta s + k_\theta$$

Joint Control

Analogous to the rigid body controller, it is also possible to embed local feedback control effects into the transfer matrix for a joint. Only one matrix element is affected. For proportional derivative control including sensor $f(s)$ and actuator $g(s)$ dynamics, the matrix in equation (46) is modified thus:

$$1/k_\theta \to 1/\left[f(s)g(s)(k_1 + k_2 s)\right] \tag{48}$$

Alignment Matrix

The alignment of each element with respect to global coordinates is accomplished by a simple matrix multiplication. The planar alignment transfer matrix is

$$
\begin{bmatrix} u_x \\ u_z \\ \theta_y \\ F_x \\ F_z \\ M_z \end{bmatrix}_2 =
\begin{bmatrix}
\cos\alpha & -\sin\alpha & 0 & 0 & 0 & 0 \\
\sin\alpha & \cos\alpha & 0 & 0 & 0 & 0 \\
0 & 0 & 1 & 0 & 0 & 0 \\
0 & 0 & 0 & \cos\alpha & -\sin\alpha & 0 \\
0 & 0 & 0 & \sin\alpha & \cos\alpha & 0 \\
0 & 0 & 0 & 0 & 0 & 1
\end{bmatrix}
\begin{bmatrix} u_x \\ u_z \\ \theta_y \\ F_x \\ F_z \\ M_z \end{bmatrix}_1 \tag{49}
$$

End-to-End Transfer Matrix

The transfer matrix which relates the deflections and loads at the space shuttle to those through the RMS to the Space Station consists of the product of all of the elements as shown in Figure 4.
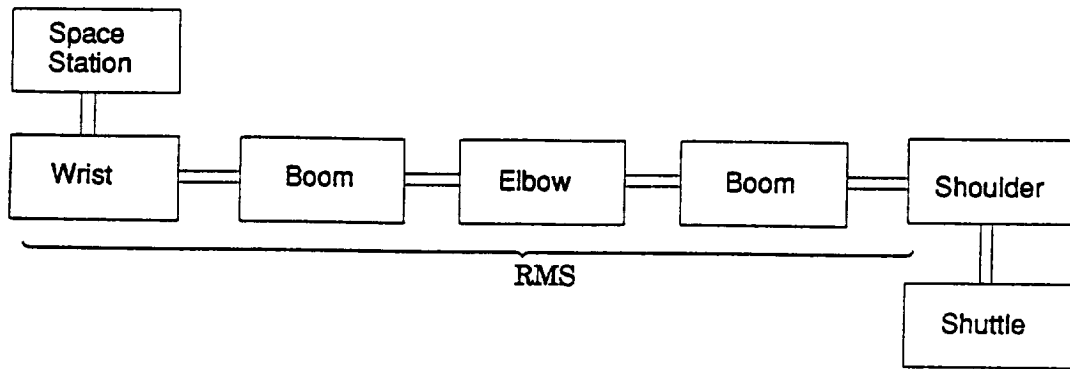
Figure 4: Shuttle/RMS/Station Configuration

$$\begin{bmatrix} Y \\ Y' \\ Q \\ M \end{bmatrix}_{station} = \begin{bmatrix} U_{station} & U_{wrist} & U_{boom\ 2} & U_{elbow} & U_{boom\ 1} & U_{shoulder} & U_{shuttle} \end{bmatrix} \begin{bmatrix} Y \\ Y' \\ Q \\ M \end{bmatrix}_{shuttle}$$

$$= U_{total} \begin{bmatrix} Y \\ Y' \\ Q \\ M \end{bmatrix}_{shuttle} \tag{50}$$

It is now possible to derive the characteristic equation for the total system. The effect of all the control systems will be reflected in the characteristic equation since they form a part of the rigid body and joint transfer matrices.

The transfer matrix forms an intermediate step in the computation of the characteristic equation. For beams and masses connected to one another, the transfer matrix between station 1 and station n is derived by multiplying the appropriate field and point matrices. The expression for a typical problem may be expressed as

$$\begin{bmatrix} Y \\ Y' \\ Q \\ M \end{bmatrix}_n = \begin{bmatrix} \phi_{11} & \phi_{12} & \phi_{13} & \phi_{14} \\ \phi_{21} & \phi_{22} & \phi_{23} & \phi_{24} \\ \phi_{31} & \phi_{32} & \phi_{33} & \phi_{34} \\ \phi_{41} & \phi_{42} & \phi_{43} & \phi_{44} \end{bmatrix} \begin{bmatrix} Y \\ Y' \\ Q \\ M \end{bmatrix}_1 \tag{51}$$

If the boundary is cantilevered, then

$$
\begin{bmatrix} Y \\ Y' \\ 0 \\ 0 \end{bmatrix}_n = \Phi \begin{bmatrix} 0 \\ 0 \\ Q \\ M \end{bmatrix}_1
\tag{52}
$$

Rearranging the state vector we have

$$
[A] \begin{bmatrix} Y_n \\ Y_n^1 \\ Q_1 \\ M_1 \end{bmatrix} = [0]
\tag{53}
$$

where

$$
[A] = \begin{bmatrix} -1 & 0 & \phi_{13} & \phi_{14} \\ 0 & -1 & \phi_{23} & \phi_{24} \\ 0 & 0 & \phi_{33} & \phi_{34} \\ 0 & 0 & \phi_{43} & \phi_{44} \end{bmatrix}
\tag{54}
$$

The characteristic equation is given by

$$
\det[A] = 0
\tag{55}
$$

or

$$
\det[\Phi_{22}] = 0
$$

or

$$
\phi_{33}\,\phi_{44} - \phi_{34}\,\phi_{43} = 0
\tag{56}
$$

For continuum models, equation (56) has infinite solutions and is solved by search techniques to determine the frequencies. Similar characteristic equations can be derived for other boundary conditions.

396

For free-free boundary conditions, the characteristic equation is given by

$$\det[\Phi_{21}] = 0$$

The transfer function relating the linear and angular deflection of the shuttle (for example) to applied forces and moments are:

$$\begin{bmatrix} Y \\ Y' \end{bmatrix}_{\text{shuttle}} = \Phi_{21}^{-1}\, \Phi_{22} \begin{bmatrix} F \\ M \end{bmatrix}_{\text{shuttle}}$$

The Shuttle/RMS/Payload configuration is now studied from the continuum viewpoint.

Study of Shuttle/RMS/Payload Assembly

The Space Shuttle/RMS/Payload assembly is modeled and analyzed using the continuum and the finite element approach. For the continuum analysis, the planar transfer matrix approach is used to generate the frequencies of the configuration and the transient response of the structure.

The data for the two link RMS configuration is extracted from the payload deployment and retrieval document [16]. Links 3 and 4 of the RMS arm are used in the simulation. In this work, each link was assumed to be made-up of one material with uniform section properties unlike reference [16] where the links were made-up of 3 segments each with different properties. The link properties are listed in Table 1.

The space shuttle and payload are modeled as rigid bodies with a mass of 6176 slugs and 124.22 slugs respectively. The inertia I_{yy} of the space shuttle is 6.99 E6 lbs-in^2.
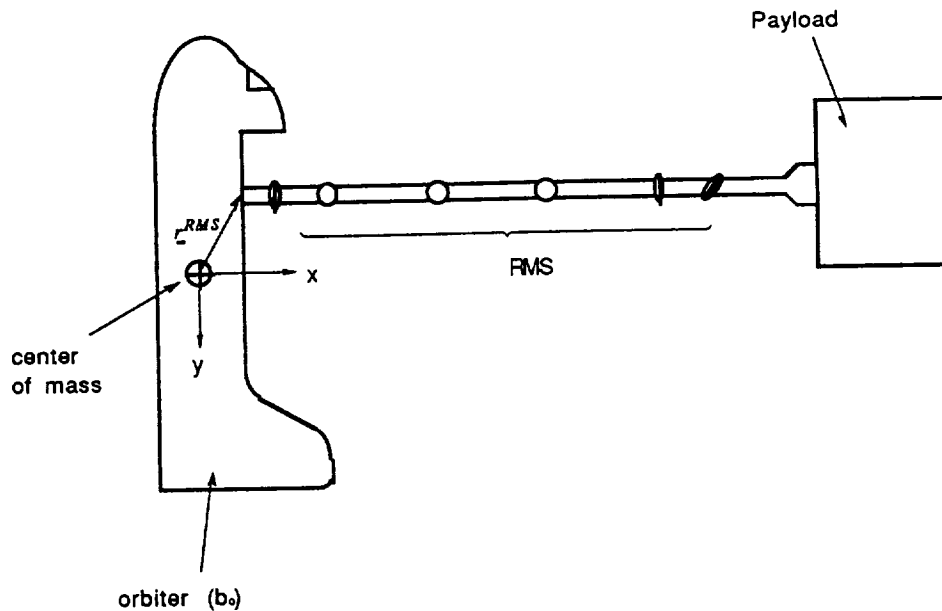
Figure 5: Shuttle/RMS/Payload Configuration

Figure 5 shows the Shuttle/RMS/Payload Configuration. The following three cases are considered in this work:

Case 1: Shuttle with zero inertia and offset

Case 2: Shuttle with inertia and zero offset

Case 3: Shuttle with inertia and offset

For the transfer matrix approach, the relationship between the shuttle and the payload is

$$[TM] = \left[U_{\text{payload}} \; U_{\text{link 2}} \; U_{\text{link 1}} \; U_{\text{shuttle}} \right]$$

The characteristic equation for the free-free configuration is derived and the frequencies are evaluated. In order to obtain the $y\text{-}z$ bending frequencies, the characteristic equation is again solved numerically using the appropriate flexural rigidity value. The results are compared with the frequencies from PDEMOD.

The NASTRAN model of the Shuttle/RMS/Payload assembly consisted of the RMS being modeled using 50 bar elements each. The shuttle and the payload were modeled

using two concentrated masses at either end of the RMS. For the shuttle with inertia and offset case, the concentrated mass card in NASTRAN was suitably modified.

Table 1: RMS Link Properties

Property	Link 1	Link 2
mass	9.5485 slugs	5.9901 slugs
length	21.0 ft	23.0 ft
EIyy	5.6458 E6 lbft^2	3.4166 E6 lbft^2
EIzz	5.2083 E6 lbft^2	2.4375 E6 lbft^2
G	3.846 E5 psf	3.846 E5 psf
J	6.7711 ft^4	5.0558 ft^4
m/l	0.4547 slug/ft	0.2604 slug/ft
A	0.9218 ft^2	0.9218 ft^2

The frequency spectrum in Hertz of the three configurations is shown in Tables 2-4.

Table 2: Frequencies for Case 1

Mode	NASTRAN	PDEMOD	Transfer
1	2.054	?	?
2	2.527	2.528	2.528
3	2.862	2.863	2.862
4	10.629	10.63	10.629
5	11.747	11.74	11.747
6	18.479	?	?
7	23.171	23.17	23.171
8	25.963	25.96	25.964

Table 3: Frequencies for Case 2

Mode	NASTRAN	PDEMOD	Transfer
1	0.1825	0.1961	0.1892
2	2.0548	2.0133	?
3	2.8627	?	?
4	4.2036	4.2065	4.2033
5	?	4.6983	4.6973
6		7.6745	?
7	11.7471	?	?
8	13.3324	13.3356	13.3337

Table 4: Frequencies for Case 3

Mode	NASTRAN	Transfer
1	?	0.3428
2	?	0.3685
3	4.2037	4.4246
4	4.7001	4.9433
5	?	9.8986
6	?	9.9017
7	13.3339	13.5996
8	14.7421	15.0281

Figure 6 shows a transient response obtained from PDEMOD for a similar configuration with and without joint control. The results show the promise of the continuum approach.
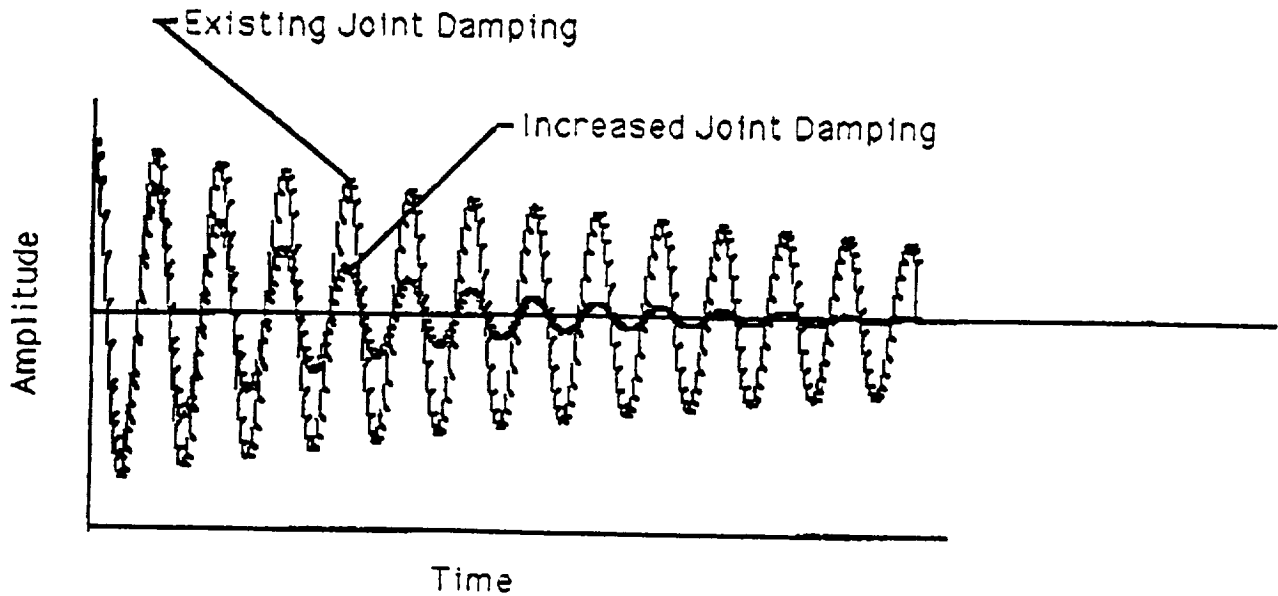
Figure 6: Transient response of MB-1 Configuration

CONCLUDING REMARKS

Partial differential equation models of flexible structures offer significant advantages over finite element models for parameter estimation and control studies because of the smaller number of model parameters. Until recently work was needed to generate distributed parameter models of complex configurations which were also flexible. The computer program, PDEMOD, enables the generation of distributed parameter models of flexible spacecraft. Any configuration which can be modeled by a network of flexible beam elements and rigid bodies can be modeled using PDEMOD. The modeling process is well suited for the evolving Space Station Freedom, for the cases in which (1) the Space Station assembly is attached to the Shuttle, (2) the assembly is linked to the Shuttle through the RMS arm, and (3) the Space Station assembly is free of the Shuttle.

Comparisons of the model accuracy of finite element and continuum models of flexible structures point out the limitations of finite element modeling. First, the level of complexity that is practical for finite element models is limited because of the computational burden. The result is a limit to the accuracy that can be obtained. Second, as high levels of accuracy are sought using finite element models, the difficulties in solving the eigenvalue problem become more significant. It is quite possible, then, that for certain applications continuum models can be more accurate.

A distributed parameter model of the Space Shuttle-RMS was generated using the transfer matrix method and the software PDEMOD. The results show a very good agreement with a detailed finite element model. Future directions include the frequency characterization of structures with embedded control.

Acknowledgements

REFERENCES

1. Likins, Peter W.; and Bouvier, H. Karl (1971), Attitude Control of Nonrigid Spacecraft. Astronautics and Aeronautics.

2. Tolivar, A. F. (1982). NASA LSS Missions and Control Requirements. NASA Workshop on Applications of Distributed System Theory to the Control of LSS, JPL, Pasadena, California, July.

3. Pappa, Richard; Miserentino, Bob; Bailey, Jim; Elliott, Ken; Perez, Cooper, Paul; and Williams, Boyd (1990), Mini-MAST Control Structure Interaction Testbed: A User's Guide, NASA TM - 102630, March.

4. Armstrong, Ernest S. Distributed System Research Motivated by Large Space Structures. IFIP-TC7 Conference on Control Problems for Systems Described by Partial Differential Equations and Applications. Gainesville, Florida, 1986.

5. Taylor, Lawrence W., Jr. and H. Rajiyah (1991), "Applications of Partial Differential Equation Modeling," Spaceflight Mechanics Meeting, Houston, Texas, February 1991.

6. Thomas, Segun (1989, "A Continuum Model for Dynamic Analysis of the Space Station," IAF, International Astronautical Congress, 40th, Malaga, Spain, October 7-13.

7. Bishop, R. E. D. and D. C Johnson, "The Mechanics of Vibration", Cambridge University Press, Cambridge.

8. Snowdon, "Vibration and Shock in Damped Mechanical Systems", John Wiley and Sons, New York.

9. Blankenship, Gilmer L (1988), "Applications of Homogenization Theory to the Control of Flexible Structures", IMA Volume 10, Stochastic Differential Systems, Stochastic Control Theory and Application, Springer-Verlag, New York.

10. Noor, Ahmed K.; Anderson, M. S.; and Greene, W. H. (1978), "Continuum Models for Beam- and Plate-Like Lattice Structures", AIAA Journal, 16, pp. 1219-1228.

11. Poelaert, D. (1983). DISTEL, "A Distributed Element Program for Dynamic Modelling and Response Analysis of Flexible Spacecraft", Dynamics and Control of Large Structures, Fourth VPI&SU/AIAA Symposium, Blacksburg, Virginia.

12. Taylor, Lawrence W., Jr. (1990), "PDEMOD - Computer Software for Partial Differential Equation Modeling of Flexible Spacecraft", 2nd USAF/NASA Workshop on System Identification and Health Monitoring of Precision Space Structures, Pasadena, California.

13. Anderson, Melvin S.; and Williams, F. W. (1987), "BUNVIS - RG: Exact Frame Buckling and Vibration Program, with Repetitive Geometry and Substructuring", Journal of Spacecraft and Rockets, Vol. 24, No. 4, July-August, page 353.

14. Pestel E.C. and Leckie, F.A., "Matrix Methods in Elastomechanics", McGraw Hill Book Company, Inc., New York, 1963.

15. Shen, J.Y. and Taylor, L.W., "Application of the Transfer Matrix Method to Estimate the modal Characteristics of the NASA Mini Mast Truss", NASA Technical Memorandum XXX 1990.

16. NASA Johnson Space Center, "Payload Deployment and Retrieval System Simulation Database, Version 1.0, Flight Support Equipment, RMS Operations", Document No: JSC-25134, July, 1991.

CONTROL OF FLEXIBLE SYSTEMS

PAGE 404 INTENTIONALLY BLANK

CSI, OPTIMAL CONTROL, & ACCELEROMETERS: TRIALS AND TRIBULATIONS*

JOHN R. SESAK

BRIAN J. BENJAMIN
Lockheed, Missiles & Space Company, Inc.
Sunnyvale, CA 94089

SUMMARY

New results concerning optimal design with accelerometers are presented. These results show that the designer must be concerned with the stability properties of two Linear Quadratic Gaussian (LQG) compensators, one of which does not explicitly appear in the closed-loop system dynamics. The new concepts of *virtual* and *implemented* compensators are introduced to cope with these subtleties: The virtual compensator appears in the closed-loop system dynamics and the implemented compensator appears in control electronics. The stability of one compensator does not guarantee the stability of the other. For strongly stable (robust) systems, both compensators should be stable. The presence of controlled and uncontrolled modes in the system results in two additional forms of the compensator with corresponding terms that are of like form, but opposite sign, making simultaneous stabilization of both the virtual and implemented compensator difficult. A new design algorithm termed *sensor augmentation* is developed that aids stabilization of these compensator forms by incorporating a static augmentation term associated with the uncontrolled modes in the design process.

1.0 INTRODUCTION

Dynamic systems that are not strictly proper complicate linear quadratic gaussian (LQG) control design. These dynamic systems are characterized by transfer functions where the order of the numerator equals the denominator. Sensors, such as accelerometers, whose transfer functions are not strictly proper can also generate such systems. Linear time invariant systems that employ these sensors may be represented in the time domain by state space equations characterized by the matrix quadruplet (A, B, C, D) where A is the plant matrix, B is the input (influence) matrix, C is the output (sensor) matrix, and D is a thru-put matrix representing the direct transmission properties associated with systems that are not strictly proper. The presence of the D matrix complicates LQG control design particularly in the area of compensator stability, and consequently closed-loop system robustness. The designer must consider two forms of the optimal compensator, one of which does not explicitly appear in the closed-loop system dynamics.

There is very little consideration of systems that are not strictly proper in the optimal control literature. Standard texts on optimal control (refs. 1-7) do not consider these systems in the context of LQG closed-loop control. A preliminary version of the material presented in this paper is contained in ref. (8).

This paper is organized as follows: Section 2 derives the two LQG compensator forms required for design and introduces the concepts of *implemented* and *virtual* compensators. Section 3 considers additional compensator forms caused by the presence of neglected known vibration modes (suppressed modes) which are not explicitly modeled in the control design process. Section 4 presents a design algorithm termed *sensor augmentation* that copes with the complexities introduced by the suppressed (neglected) vibration modes, and Section 5 presents our conclusions.

2.0 IMPLEMENTED AND VIRTUAL COMPENSATORS

The LQG compensator plays a significant role in the determination of closed-loop robustness properties. As shown in Figure 1, the compensator is that dynamic system that has the sensor vector as its input and the control vector as its output. Its dynamics are determined by the transfer function matrix between points "a" and "b" of Figure 1.
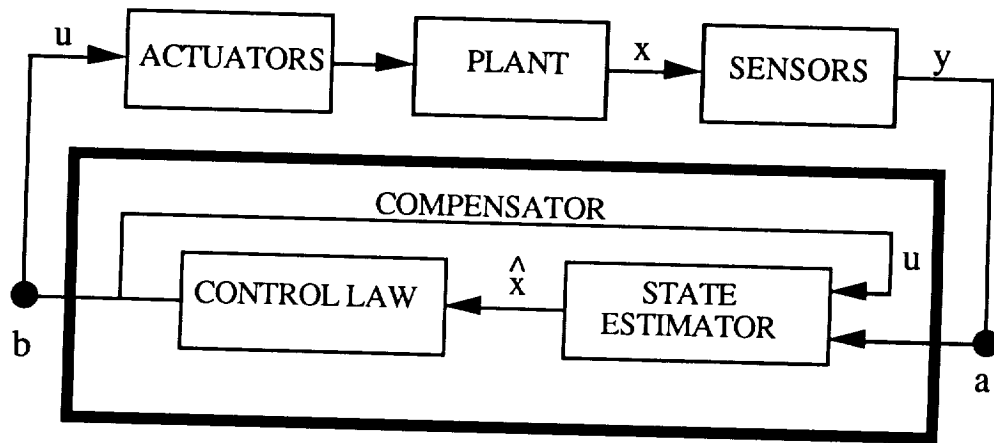
Figure 1. LQG compensator stability affects robustness.

In general, the stability properties of the compensator tend to influence the robustness properties of the closed-loop system. For strictly proper systems (no D matrix) the designer must consider only one compensator form; however, for systems incorporating a D matrix in their description, two compensator forms must be considered: an *implemented* and a *virtual* compensator. The implemented compensator has the sensor vector as its input, which drives the estimator-based dynamics. These dynamics, which are functions of the D matrix, do not explicitly appear in the matrix description of the closed-loop system. Conversely, the virtual compensator dynamics are not functions of the D matrix, but do appear in the closed-loop system matrix. For strictly proper systems (no D matrix) the implemented compensator dynamics and the virtual compensator dynamics are identical. The development of the two compensator forms is accomplished by direct substitution of the LQG control and estimation laws in the plant dynamics. The implemented compensator emerges by careful distinction between the sensed and computed variables of the closed-loop system.

Consider the following open-loop, dynamic system

$$\dot{x} = Ax + Bu \tag{1}$$
$$y = Cx + Du \tag{2}$$

where x(n x 1) is the state vector, u(r x 1) is the control vector, y(s x 1) is the output vector and (A, B, C, D) are matrices of appropriate dimension. For flexible structure control, the A matrix is composed of modal frequencies and damping factors, the B and C matrices are based on

eigenvector solutions of the finite element model characterizing the structure. For such systems employing accelerometers, the D matrix has the following form

$$D = CB \tag{3}$$

The control law is

$$u = -K\hat{x} \tag{4}$$

where $K(r \times n)$ is the optimal feedback control matrix and $\hat{x}(n \times 1)$ is the estimated state vector.

The state estimator has the following form

$$\dot{\hat{x}} = A\hat{x} + Bu + G(y - \hat{y}) \tag{5}$$

where $G(n \times s)$ is the estimator gain matrix and $\hat{y}(s \times 1)$ is the estimated output vector.

Implemented Compensator Derivation

The implemented compensator dynamics are now derived. Substituting $u = -K\hat{x}$ in the estimator dynamics for the control law, and $\hat{y} = C\hat{x} + Du$ for the estimated sensor vector yields

$$\dot{\hat{x}} = (A - BK)\hat{x} - G(C\hat{x} + Du) + Gy \tag{6}$$

Substituting $u = -K\hat{x}$ for the control vector in equation (6) and collecting terms yields

$$\dot{\hat{x}} = (A - BK - GC + GDK)\hat{x} + Gy \tag{7}$$

Equation (7) characterizes the implemented compensator dynamics for the closed-loop system. The sensor vector is an input that drives the estimation-based dynamic system for the compensator.

410

In sequel, we shall show that although the implemented compensator is necessary to generate the required closed-loop dynamics, it does not explicitly appear in the closed-loop system matrix.

Virtual Compensator Derivation

The virtual compensator dynamics are derived by continued expansion of the dynamic expression for the implemented compensator. Substituting $y = Cx + Du$ for the sensor vector in equation (7) yields

$$\dot{\hat{x}} = (A - BK - GC + GDK)\hat{x} + G(Cx + Du) \tag{8}$$

Substituting $u = -K\hat{x}$ in equation (8) yields

$$\dot{\hat{x}} = (A - BK - GC + GDK)\hat{x} + GCx - GDK\hat{x} \tag{9}$$

Collecting terms in $\hat{x}$ yields the virtual compensator dynamics

$$\dot{\hat{x}} = (A - BK - GC)\hat{x} + GCx \tag{10}$$

where we note that the D matrix has been eliminated from equation (10).

Inspection of the closed-loop dynamics matrix shows that the D matrix, which may influence robustness properties, has been eliminated from the closed-loop system description. Only the virtual compensator appears. Comparison of the implemented compensator dynamics (equation 7) and the virtual compensator dynamics (equation 10) shows that the two expressions are not identical and, in general, will not have the same eigenvalues. In fact, the stability of one of these compensator forms does not guarantee the stability of the other. Substituting $u = -K\hat{x}$ in equation (1) and assembling equations (1) and (10) in matrix form yields the closed-loop system matrix

$$
\begin{bmatrix} \dot{x} \\ \dot{\hat{x}} \end{bmatrix} = \begin{bmatrix} A & -BK \\ GC & A - BK - GC \end{bmatrix} \begin{bmatrix} x \\ \hat{x} \end{bmatrix}
\tag{11}
$$

As the expression containing the D matrix does not appear in equation (11), the implemented compensator could be unstable and this fact would not be detected by a closed-loop eigenvalue analysis. Thus, both compensator forms must be checked in order to ensure the design of a strongly stable system in the sense of reference 9.
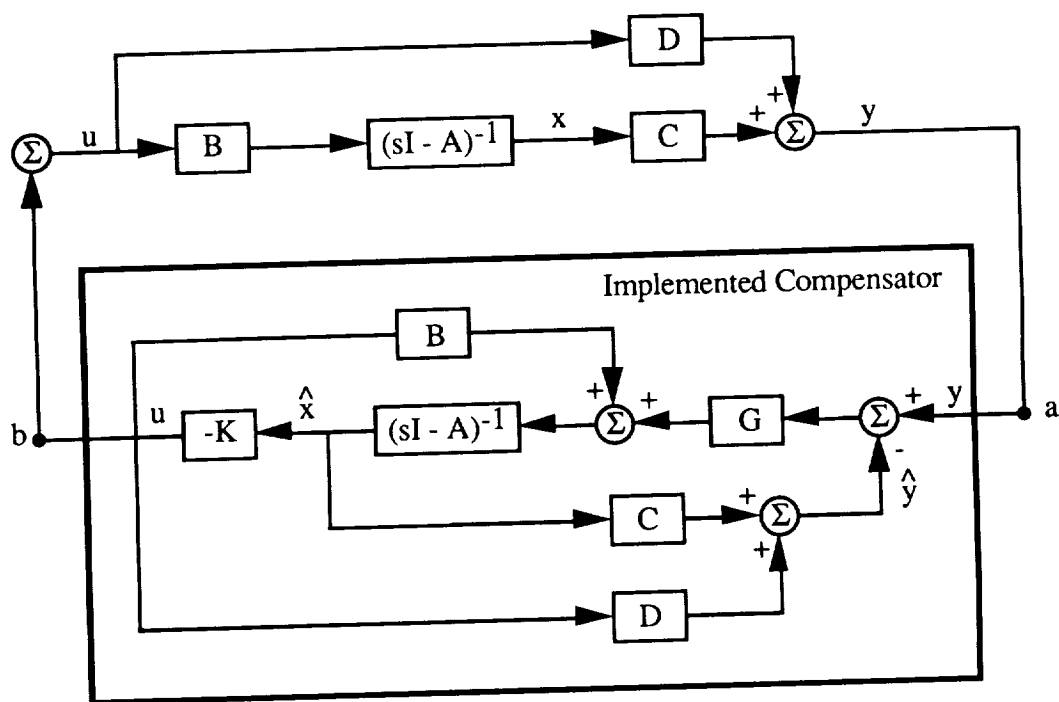
Figure 2. Implemented compensator detail shows the effect of the thru-put matrix

Figure 2 provides a detailed matrix block diagram of the implemented compensator for systems that are not strictly proper. Examination of this diagram provides insight to the compensator problem. The compensator dynamics are characterized by the transfer function matrix between points "a" and "b" of Figure 2. The control vector, u, is multiplied by the D matrix and summed with $C\hat{x}$ to form the estimated sensor vector, $\hat{y}$. However, the sensor vector, y, contains

an identical term, Du, involving the control vector. As the two sensor vectors, y and $\hat{y}$, are subtracted at the compensator summing junction, any terms involving the matrix D are eliminated from the closed-loop system matrix, i.e., the compensator is uncontrollable, in u, at the sensor summing junction. This condition is analogous to that which occurs during estimator design using the separation principle with strictly proper systems, i.e., the separation principle holds (ref. 10) and the estimator is uncontrollable via the control vector. The separation principle also holds for systems that are not strictly proper; however, one must consider both the error space and implementation space during the design process: the component of the control vector transmitted by the D matrix is eliminated from the closed-loop dynamics in the implementation space. In this context, a partial separation principle can be said to hold, and the compensator dynamics *appear* to be determined solely by the (A, B, C) matrices.

The presence of unmodeled dynamic (suppressed) modes further complicates the design process. In this case the D matrix cancellation is incomplete in the implementation space, and the implemented and virtual compensators have differing dynamics that *are* functions of different modal thru-put matrices. This phenomenon is discussed in the following section.

3.0 LQG COMPENSATOR DYNAMICS AND SUPPRESSED MODES

The presence of uncontrolled vibration dynamics significantly complicates the compensator design process. The implemented and virtual compensator dynamic matrices contain corresponding terms of similar form, but opposite sign, that can severely constrain the compensator stabilization process. Consider the following open-loop dynamic system representing a flexible structure

$$
\begin{bmatrix} \dot{x}_c \\ \dot{x}_s \end{bmatrix} = \begin{bmatrix} A_c & 0 \\ 0 & A_s \end{bmatrix} \begin{bmatrix} x_c \\ x_s \end{bmatrix} + \begin{bmatrix} B_c \\ B_s \end{bmatrix} u
$$ (12)

$$y = \begin{bmatrix} C_c & C_s \end{bmatrix} \begin{bmatrix} x_c \\ x_s \end{bmatrix} + \begin{bmatrix} D_c & + & D_s \end{bmatrix} u \tag{13}$$

where $x_c(n_c \times 1)$ is the controlled state vector, $x_s(n_s \times 1)$ is the suppressed state vector characterizing the uncontrolled but modeled modes (refs. 11, 12), $u(r \times 1)$ is the control vector, and $y(s \times 1)$ is the output vector. The plant submatrices, $A_c(n_c \times n_c)$ and $A_s(n_s \times n_s)$, are composed of modal frequencies and damping factors. The input matrices, $B_c(n_c \times r)$ and $B_s(n_s \times r)$, the output matrices, $C_c(s \times n_c)$ and $C_s(s \times n_s)$, and the thru-put matrices, $D_c(s \times r)$ and $D_s(s \times r)$, are based on eigenvector solutions of the finite element model characterizing the structure. For such systems employing accelerometers the submatrices comprising the D matrix are given by

$$D_t = D_c + D_s \tag{14}$$

$$D_c = C_c B_c \tag{15}$$

$$D_s = C_s B_s \tag{16}$$

The control law is

$$u = - K \hat{x}_c \tag{17}$$

where $K(r \times n_c)$ is the optimal feedback matrix and $\hat{x}_c(n_c \times 1)$ is the estimated state vector.

The state estimator has the following form

$$\dot{\hat{x}}_c = A_c \hat{x}_c + B_c u + G(y - \hat{y}_c) \tag{18}$$

414

where $G(n_c \times s)$ is the estimator gain matrix and $\hat{y}_c(s \times 1)$ is the estimated output vector for the controlled states.

Implemented Compensator With Suppressed Modes

The implemented compensator dynamics are now derived. Substituting $u = -K\hat{x}_c$ in the estimator dynamics for the control law, and $\hat{y}_c = C_c\hat{x}_c + D_c u$ for the estimated sensor vector yields

$$\dot{\hat{x}}_c = (A_c - B_c K)\hat{x}_c - G(C\hat{x}_c + D_c u) + Gy \tag{19}$$

Substituting $u = -K\hat{x}_c$ for the control law in equation (19) and collecting terms yields

$$\dot{\hat{x}}_c = (A_c - B_c K - GC_c + GD_c K)\hat{x}_c + Gy \tag{20}$$

Equation (20) characterizes the implemented compensator dynamics for the closed-loop system. We note that the implemented compensator is a function of D_c, the thru-put matrix for the controlled modes.

Virtual Compensator With Suppressed Modes

The virtual compensator dynamics are now derived. Substituting equation (13) for the sensor vector in equation (20) yields

$$\dot{\hat{x}}_c = (A_c - B_c K - G C_c + G D_c K)\hat{x}_c + G(C_c x_c + C_s x_s + D_c u + D_s u) \tag{21}$$

Substituting $u = -K\hat{x}_c$ in equation (21) yields

$$\dot{\hat{x}}_c = (A_c - B_c K - G C_c + G D_c K)\hat{x}_c + G(C_c x_c + C_s x_s) - G(D_c K + D_s K)\hat{x}_c \tag{22}$$

Collecting terms in $\hat{x}_c$ yields the virtual compensator dynamics

$$\dot{\hat{x}}_c = (A_c - B_c K - G C_c - G D_s K)\hat{x}_c + G C_c x_c + G C_s x_s \tag{23}$$

where the virtual compensator dynamics are a function of D_s, the thru-put matrix for the suppressed modes. A term by term examination of the submatrices comprising the dynamic matrix for the implemented compensator, equation (20), and the virtual compensator, equation (23), yields the interesting result: The dynamic matrices of the two compensators are composed of identical submatrices except for those terms arising from the modal thru-put matrices. These submatrices, $G D_c K$ and $-G D_s K$, are similar in form, but opposite in sign. Thus, in general, it will be difficult to simultaneously stabilize the implemented and virtual compensators. Conflicting constraints will tend to be placed on the gain matrices G and K.

The closed-loop dynamics in matrix form may be written as

$$
\begin{bmatrix} \dot{x}_c \\ \dot{x}_s \\ \dot{\hat{x}}_c \end{bmatrix} = \begin{bmatrix} A_c & 0 & -B_c K \\ 0 & A_s & -B_s K \\ GC_c & GC_s & A_c - B_c K - GC_c - GD_s K \end{bmatrix} \begin{bmatrix} x_c \\ x_s \\ \hat{x}_c \end{bmatrix} \tag{24}
$$

Examination of equation (24) shows that the implemented compensator dynamics do not appear in the closed-loop system matrix. Thus, an eigenvalue analysis of this closed-loop matrix would not reveal the stability properties of the implemented compensator. Both compensator forms must be checked for stability to design a strongly stable system.

Table 1 shows the dynamic matrices that occur during LQG control design of flexible structures that employ accelerometers. Included are matrices for the estimator, controller and various compensator forms. The number of matrix forms requiring stabilization or conditioning is five, and the number of gain matrices is two. This situation leads to difficulty in design, especially when one desires stable compensation matrices. A design algorithm is presented in Section 4 to cope with difficulties introduced by the suppressed modes.

Table 1. LQG Dynamic Matrices For Accelerometer Systems

Controller	$A_c - B_c K$
Estimator	$A_c - GC_c$
Virtual Compensator	$A_c - B_c K - GC_c$
Implemented Compensator	$A_c - B_c K - GC_c + GD_c K$
Virtual Compensator (Suppressed Modes)	$A_c - B_c K - GC_c - GD_s K$
Thru-put Term (Controlled Modes)	$D_c = C_c B_c$
Thru-put Term (Suppressed Modes)	$D_s = C_s B_s$

4.0 SENSOR AUGMENTATION

We now develop an algorithm that addresses the problem caused by the suppressed mode contamination of the virtual compensator dynamics. As shown in the previous section, the dynamic matrices of the implemented compensator and the virtual compensator differ only in terms arising from the modal dynamics (compare equations 20 and 23). These modal terms, GD_cK and $-GD_sK$, which are similar in form but opposite in sign, create difficulties for stable compensator design. The difficulty arises because we are requiring two similar matrix forms of opposite sign to stabilize identical matrices, i.e., if we define A_{comp} as the standard LQG dynamic compensator matrix

$$A_{comp} = A - BK - GC \qquad (25)$$

the dynamic matrix for the implemented compensator is

$$A_{comp} + GD_cK \qquad (26)$$

and that for the virtual compensator is

$$A_{comp} - GD_sK \qquad (27)$$

As D_c and D_s are of similar structure, the gain matrices G and K will tend to have opposing effects on the stability properties of the two compensator forms.

We can cope with this problem by developing an algorithm that eliminates the offending terms caused by the suppressed modes from one of the compensator forms. This is accomplished by augmenting the estimated sensor output vector with suppressed mode data, i.e., with reference to equation (14), D_c is replaced by D_t in the design process, where

$$D_t = D_c + D_s \qquad (28)$$

It should be noted that the number of controlled modes remains constant, and that this procedure is analogous to incorporating a "d.c. gain," or static portion of the suppressed mode transfer function, into the design process. The design algorithm may also be interpreted as using a hybrid dynamic model, augmented with the static gains of the uncontrolled, but modeled modes. The effect of this procedure on the implemented and virtual compensators is easily derived. Consider the following open-loop dynamic system representing a flexible structure

$$\begin{bmatrix} \dot{x}_c \\ \dot{x}_s \end{bmatrix} = \begin{bmatrix} A_c & 0 \\ 0 & A_s \end{bmatrix} \begin{bmatrix} x_c \\ x_s \end{bmatrix} + \begin{bmatrix} B_c \\ B_s \end{bmatrix} u \qquad (29).$$

$$y = \begin{bmatrix} C_c & C_s \end{bmatrix} \begin{bmatrix} x_c \\ x_s \end{bmatrix} + \begin{bmatrix} D_c + D_s \end{bmatrix} u \qquad (30)$$

where $x_c (n_c \times 1)$ is the controlled state vector, $x_s (n_s \times 1)$ is the suppressed state vector

characterizing the uncontrolled but modeled modes (refs. 11, 12), $u(r \times 1)$ is the control vector, and $y(s \times 1)$ is the output vector. The plant submatrices, $A_c(n_c \times n_c)$ and $A_s(n_s \times n_s)$, are composed

of modal frequencies and damping factors. The input matrices, $B_c(n_c \times r)$ and $B_s(n_s \times r)$, the

output matrices, $C_c(s \times n_c)$ and $C_s(s \times n_s)$, and the thru-put matrices, $D_c(s \times r)$ and $D_s(s \times r)$, are

based on eigenvector solutions of the finite element model characterizing the structure. For such systems employing accelerometers the submatrices comprising the D matrix are given by

$$D_t = D_c + D_s \qquad (31)$$

$$D_c = C_c B_c \qquad (32)$$

$$D_S = C_S B_S \tag{33}$$

The control law is

$$u = - K \hat{x}_c \tag{34}$$

where $K(r \times n_c)$ is the optimal feedback matrix and $\hat{x}_c(n_c \times 1)$ is the estimated state vector.

The state estimator has the following form

$$\dot{\hat{x}}_c = A_c \hat{x}_c + B_c u + G(y - \hat{y}_c) \tag{35}$$

where $G(n_c \times s)$ is the estimator gain matrix and $\hat{y}_c(s \times 1)$ is the estimated output vector for the controlled states. The estimated sensor vector is now given by

$$\hat{y}_c = C_c \hat{x}_c + (D_c + D_s)u \tag{36}$$

where D_s has now been included in the design process, i.e., the sensor has been augmented.

Implemented Compensator Using Sensor Augmentation

The implemented compensator dynamics are now derived. Substituting $u = -K\hat{x}_c$ in the estimator dynamics (equation 35) for the control law, and $\hat{y}_c = C_c \hat{x}_c + (D_c + D_s)u$ for the estimated sensor vector yields

420

$$\dot{\hat{x}}_c = (A_c - B_cK)\hat{x}_c - G(C_c\hat{x}_c + D_cu + D_su) + Gy \tag{37}$$

Substituting $u = -K\hat{x}_c$ in equation (37) yields

$$\dot{\hat{x}}_c = (A_c - B_cK - GC_c + GD_cK + GD_sK)\hat{x}_c + Gy \tag{38}$$

Substituting the relationship $D_t = D_c + D_s$ in equation (38) yields

$$\dot{\hat{x}}_c = (A_c - B_cK - GC_c + GD_tK)\hat{x}_c + Gy \tag{39}$$

which is the desired expression for the implemented compensator dynamics. Examination of the dynamics for this compensator, which uses augmented sensor data, and those of the unaugmented compensator of equation (20) shows that they differ by the term GD_sK which appears in equation (38).

Virtual Compensator With Sensor Augmentation

The expression for the augmented virtual compensator dynamics may now be derived. Substituting equation (13) for the sensor vector in equation (39), and noting that $D_t = D_c + D_s$, yields

$$\dot{\hat{x}}_c = (A_c - B_cK - GC_c + GD_tK)\hat{x}_c + G(C_cx_c + C_sx_s + D_tu) \tag{40}$$

Substituting $u = -K\hat{x}_c$ in equation (40) yields

$$\dot{\hat{x}}_c = (A_c - B_c K - GC_c + GD_t K)\hat{x}_c + G(C_c x_c + C_s x_s) - GD_t K\hat{x}_c \tag{41}$$

Collecting terms in $\hat{x}_c$ yields the virtual compensator dynamics

$$\dot{\hat{x}}_c = (A_c - B_c K - GC_c)\hat{x}_c + G(C_c x_c + C_s x_s) \tag{42}$$

The closed-loop dynamics may be written in matrix form as

$$\begin{bmatrix} \dot{x}_c \\ \dot{x}_s \\ \dot{\hat{x}}_c \end{bmatrix} = \begin{bmatrix} A_c & 0 & -B_c K \\ 0 & A_s & -B_s K \\ GC_c & GC_s & A_c - B_c K - GC_c \end{bmatrix} \begin{bmatrix} x_c \\ x_s \\ \hat{x}_c \end{bmatrix} \tag{43}$$

Examination of the virtual compensator dynamics, equation (42), or the closed-loop dynamics, equation (43), shows that optimal design using augmented sensor data allows the virtual LQG compensator dynamics to revert to the simpler form of the standard optimal compensator. However, the implemented compensator, equation (39), *does* contain the augmented thru-put matrix, D_t, and must be checked for stability independently of the closed-loop system matrix.

Thus, the use of sensor augmentation has eliminated the conflicting sign conditions present in the implemented and virtual compensator dynamics, equations (20) and (23) respectively, that can cause stabilization difficulties.

The system matrices requiring stabilization, or stability verification, using augmented sensor design for accelerometers on flexible structures are shown in Table 2.

Table 2. LQG Dynamic Matrices For Sensor Augmentation

- Controller

$$A_c - B_c K$$

- Estimator

$$A_c - G C_c$$

- Virtual Compensator

$$A_c - B_c K - G C_c$$

- Implemented Compensator

$$A_c - B_c K - G C_c + G D_t K$$

- Total Thru-Put Term

$$D_t = C_c^T B_c + C_s^T B_s$$

$$D_t = D_c + D_s$$

In summary, system matrices must be checked for stability, namely, those of the controller, the estimator, the virtual compensator, and the implemented compensator. The poles of the controller, estimator, and virtual compensator appear in the closed-loop system dynamics and may be checked for stability in the usual closed-loop stability analyses. The implemented compensator does not explicitly appear in the closed-loop dynamics and must be checked for stability independently of the closed-loop analysis.

5.0 CONCLUSION

Our analysis of LQG optimal control design involving systems that are not strictly proper has shown that such systems generate control complexities: Two different LQG compensator forms must be considered, namely, an *implemented* compensator and a *virtual* compensator. The implemented compensator resides in the control electronics and generates the estimator-based control signals. The virtual compensator appears in the closed-loop dynamics. The dynamic properties of both forms strongly affect the robustness of the closed-loop system.

With regard to flexible structure control, the direct feedback of accelerometer signals results in systems that are not strictly proper. The additional problems generated by uncontrolled modes

cause conflicting stability constraints in the implemented and virtual compensators that makes simultaneous stabilization of both forms difficult to achieve. A new algorithm, *Sensor Augmentation*, has been developed that copes with this situation by incorporating a static augmentation term in the design process that eliminates conflicting the stability constraints.

REFERENCES

1. Anderson, Brian D. O.; and Moore, John B.: *Optimal Control: Linear Quadratic Methods*, Prentice-Hall, 1990.

2. Athans, Michael; and Falb, Peter L.: *Optimal Control*, McGraw-Hill Book, Co., 1966.

3. Boyd, Stephen P.; and Barrat, Craig H.: *Linear Controller Design: Limits of Performance*, Prentice-Hall, 1991, Chapter 12, pp. 275-292.

4. Bryson, Arthur E.; and Ho, Yu-Chi: *Applied Optimal Control: Optimization Estimation and Control*, Revised printing, Hemisphere Publishing Corporation, 1975.

5. Kwakernaak, Huibert; and Sivan, Raphael: *Linear Optimal Control Systems*, Wiley-Interscience, 1972.

6. Lewis, Frank L.: *Optimal Control*, Wiley-Interscience, 1986.

7. Sage, Andrew P.; and White, Chelsea C., 3rd: *Optimum Systems Control*, Prentice-Hall, 1977.

8. Sesak, John R.; and Benjamin, Brian J.: Development of Integrated Design Methods for Flexible Space Structures; NASA Contract, NAS1-19241, Task 2 Report, Rev. 2, NASA-Langley Research Center (Dr. Suresh M. Joshi, Technical Monitor) April 1992.

9. Vidyasagar, M.: *Control System Synthesis: A Factorization Approach*, MIT Press, 1985.

10. Sesak, John R.; and Strong, Kristin M.: Reduced Bandwidth Compensator Design via Control and Observation Normalization. *Journal of Guidance, Control, and Dynamics*, vol. 15, no. 2, Mar.-Apr. 1992, pp. 457-460.

11. Sesak, John R.; Likins, Peter W.; and Coradetti, Thomas: Flexible Spacecraft Control by Model Error Sensitivity Suppression. *Journal of Astronautical Sciences*, vol 27, no. 2, 1979, pp. 131-156.

12. Sesak, John R.; and Likins, Peter W.: Model Error Sensitivity Suppression: Quasistatic Optimal Control for Flexible Space Structures. *Proceedings of the 18th IEEE Conference on Decision and Control*, Institute of Electrical and Electronics Engineers, New York, 1979, pp. 207-215.

AN OPTIMIZATION-BASED APPROACH FOR INTEGRATED CONTROLS-STRUCTURES DESIGN OF FLEXIBLE SPACECRAFT

P. G. Maghami, S. M. Joshi, and E. S. Armstrong

NASA Langley Research Center
Hampton, VA

$P - /7$

MOTIVATION

- Control of flexible spacecraft is a difficult problem

  - Large number of elastic modes
  - Low value, closely-spaced frequencies
  - Very small damping
  - Uncertainties in math models
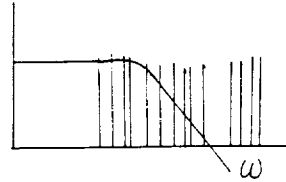
- Traditional design approach:

  - Design structure first
  - Design control system next

- Best achievable performance with traditional approach is limited

- **New Approach:** Design structure and control system *simultaneously*

OBJECTIVE

Conceive and develop methodology for spacecraft design which

- addresses control/structure interaction issues

- produces technology for simultaneous control/structure design

- translates into algorithms and computational tools for practical integrated computer-aided design

PROBLEM CLASSIFICATION

Class 1: Pointing, vib. sup., no articulation

Class 2: Pointing, vib. sup., with articulation

Class 3: Nonlinear version of class 1

Class 4: General nonlinear with robotics
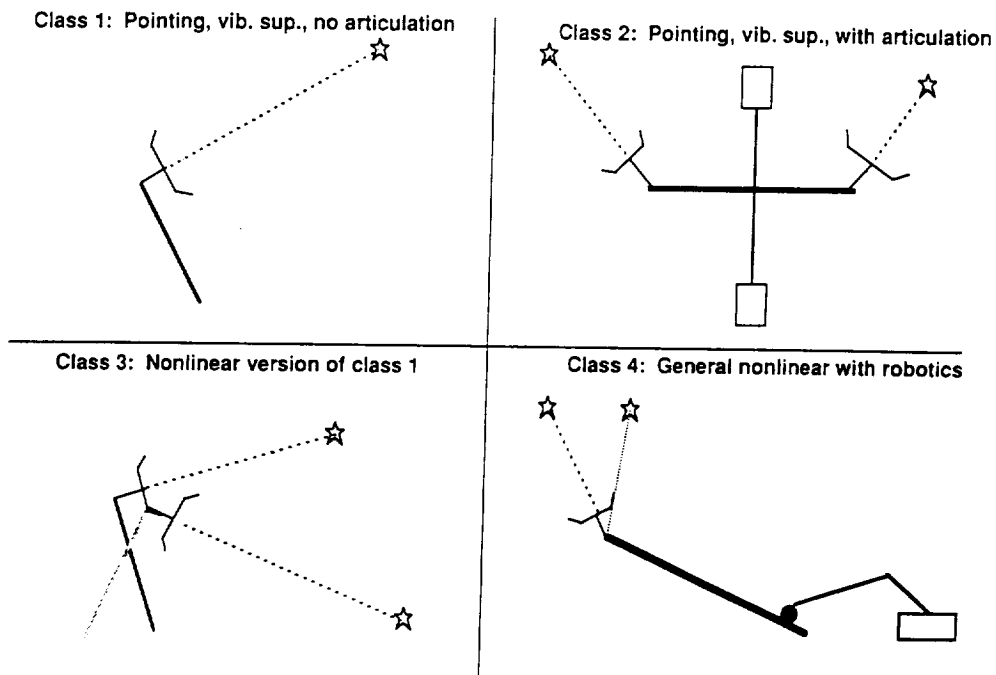
APPROACH

- Formulate integrated design problem as an optimization problem

    - Define objective function

    - Define design variables

        . Structural parameters
        . Control system parameters

    - Define constraints

    - Perform numerical optimization

- Validate the methodology through an integrated design of the CSI Evolutionary Model

INTEGRATED DESIGN METHODOLOGY VALIDATION

- Design and test optimal controllers for Phase Zero CEM

- Synthesize an optimal integrated design (Phase One CEM)

- Fabricate the closest structure to Phase One design

- Validate integrated design methodology by comparing Phase Zero and Phase One test performances

CONTROLLER ALTERNATIVES
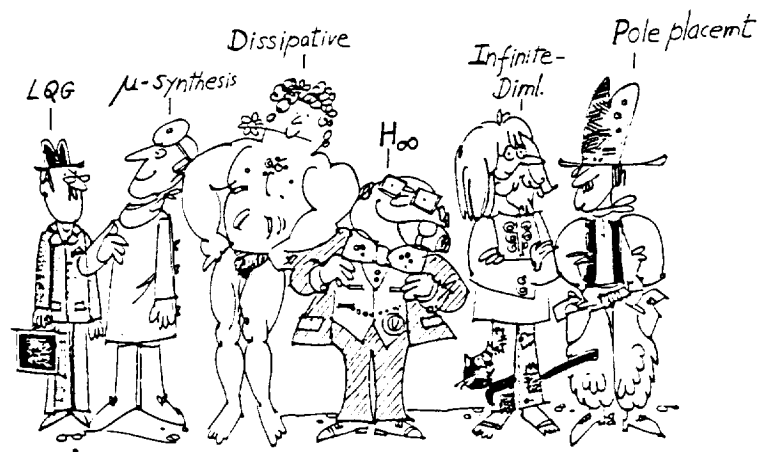
APPROACHES TO LSS CONTROL

o   **MODEL-BASED CONTROLLERS (MBC):**

>   State estimator/observer "tuned" to a low-order design model

>   Control gains via LQ regulator or eigensystem   assignment, etc.

o   **DISSIPATIVE CONTROLLERS:**

>   Utilize collocated/compatible actuators and sensors (e.g., attitude
>   and rate sensors and torque actuators)

>   -CONSTANT-GAIN dissipative controllers

>   -DYNAMIC dissipative controllers

MODEL-BASED DESIGN

A Loop-Shaping Procedure loosely based on LQG/LTR:
Iterate on KBF and LQR to satisfy performance specs and robustness cond.
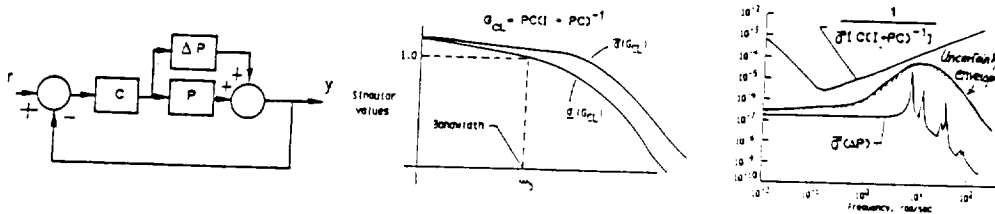
PROBLEM: Design robust to unmodeled dynamics, but NOT to parametric uncertainty

Small error in the design model frequency
can destabilize the system!
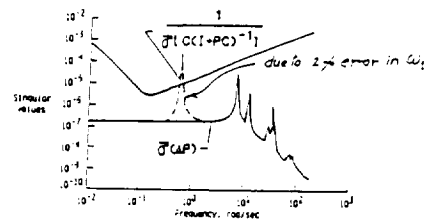
Robustness of MBC's to real parametric uncertainties is an unsolved problem

CONTROLLER REQUIREMENTS FOR INTEGRATED DESIGN

- Must be **robust** to:

    - Unmodeled dynamics

    - Parameter uncertainties

    - Nonlinearities and failures

- Must be **implementable**

- Must be amenable to inclusion
  in an optimization loop

♦ *Dissipative controllers (developed in-house) satisfy these requirements*

♦ *More research is needed to obtain even higher performance*

STATIC (CONST.-GAIN) DISSIPATIVE CONTROLLERS

o   Use collocated/compatible actuators and sensors

o   Control **attitude** and **vibration** (i.e., **rigid** and **flexible** modes)

o   Constant-gain dissipative controllers:

$$u = -G_p y_p - G_r y_r.$$

where G_p, G_r are symmetric and pos. def.

o   Robust stability is guaranteed in the presence of

a) Unmodeled elastic modes

b) Parameter uncertainties

c) Monotonically increasing
   actuator nonlinearities

c) $(0,\infty)$ sector sensor nonlinearities

d) First-order actuator dynamics

DYNAMIC DISSIPATIVE COMPENSATORS

o   Constant-gain dissipative controllers give limited performance

o   Next logical step is to use *dynamic* dissipative compensators

   Stability robustness is preserved in presence of

   - unmodeled elastic modes

   - parameter uncertainties

o   The transfer function from torque input to *attitude-rate* output is:

$$G(s) = \frac{J^{-1}}{s} + \sum_{1}^{n_q} \frac{\Phi_i \Phi_i^T s}{s^2 + 2\rho_i \omega_i s + \omega_i^2}$$

DYNAMIC DISSIPATIVE CONTROLLERS <u>WITH</u> DIRECT OUTPUT FEEDBACK INNER-LOOP

o $u = -Gz - G_p y_p - G_r y_r$

o $z = A_c z + B_c y_r$

o   Robustly stable if

   G_p, G_r are symmetric and posdef, and

   $C(s) = G(sI - A_c)^{-1}B_c$ is strictly positive real

   Easy to enforce via Kalman-Yakubovich lemma:

   C(s) is SPR if $\exists$ P, Q > 0 such that

   $A_c^T P + PA_c = -Q$ $G = B^T P$

o   When zero-freq. modes are absent (e.g., test article),
   G_p, G_r can be zero--degenerates to "positivity" controller

DYNAMIC DISSIPATIVE CONTROLLER
W/O DIRECT OUTPUT FEEDBACK
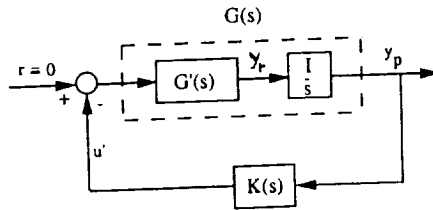
Theorem- Suppose K(s) is asymptotically stable (a.s.) and min. phase, and $[K(j\omega)/(j\omega)] > 0 \; \forall$ real ω. Then the closed-loop system is. a.s.

(Joshi, Maghami, Kelkar, GNC Conf, 1991)

K(s) not strictly proper, but can be implemented as strictly proper using feedback of y_p and y_r.

CONDITIONS FOR DIAGONAL [K(s)/s] TO BE STRONGLY PR

o   Suppose $K(s) = \text{diag}[K_1(s), K_2(s),...,K_m(s)]$

where
$$K_i(s) = k_i \frac{s^2 + \beta_{1i}s + \beta_{0i}}{s^2 + \alpha_{1i}s + \alpha_{0i}}$$

Then K(s)/s is strongly PR if

$$\alpha_{1i} \cdot \beta_{1i} > 0$$

$$\alpha_{1i}\beta_{0i} - \alpha_{0i}\beta_{1i} > 0$$

o   For higher order $K_i(s)$, Sturm's theorem can be applied to get such conditions

434

DESIGN PROBLEM

- Pose the integrated controls-structures design as a simultaneous optimization problem

- Minimize the average control power

$$J = \underset{t \to \infty}{E\{u^T u\}}$$

subject to:

$$\underset{t \to \infty}{E\{y_{los}^T \, y_{los}\}} \le \varepsilon$$

and

$$M \le M_{budget}$$

- Side constraints on structural design variables to accommodate safety, reliability, and fabrication issues

STRUCTURAL DESIGN VARIABLES

- Structure is divided into seven sections

- The effective cross-sectional areas of longerons, battens and diagonals are chosen as design variables

- Total of 21 structural design variables
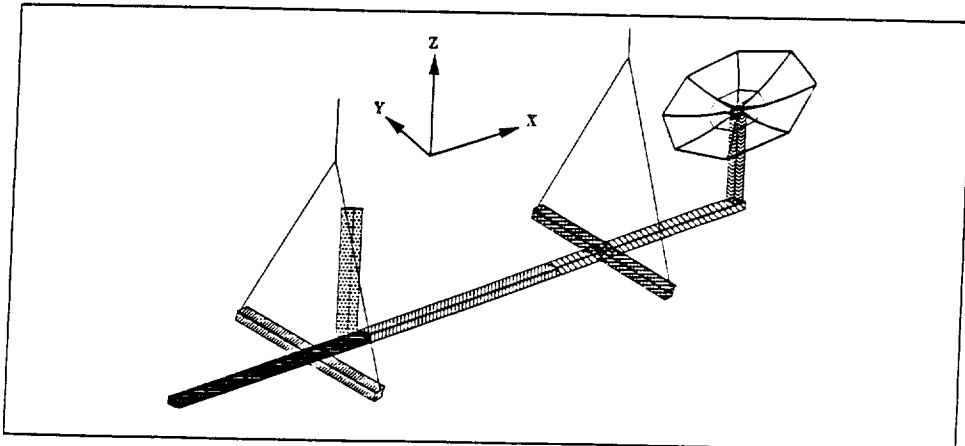
CONTROL DESIGN VARIABLES

- Static dissipative controller: elements of the Cholesky factor matrix of the rate gain matrix

$$G_r = L_r L_r^T$$

- Dynamic dissipative controller: elements of the compensator state and gain matrices (in a controllable canonical form)

$$A_c = \begin{bmatrix} 0 & 1 & 0 & \cdots & 0 \\ 0 & 0 & 1 & \cdots & 0 \\ 0 & 0 & 0 & \cdots & 0 \\ 0 & 0 & 0 & \cdots & 1 \\ \vdots & \vdots & \vdots & & \vdots \\ -\alpha_n & -\alpha_{n-1} & -\alpha_{n-2} & \cdots & -\alpha_1 \end{bmatrix} \quad ; \quad B_c = \begin{bmatrix} 0 \\ 0 \\ 0 \\ \vdots \\ 0 \\ 1 \end{bmatrix}$$

$$A_c^T P + P A_c = -Q \quad ; \quad G = B_c^T P$$

STRUT DESIGN
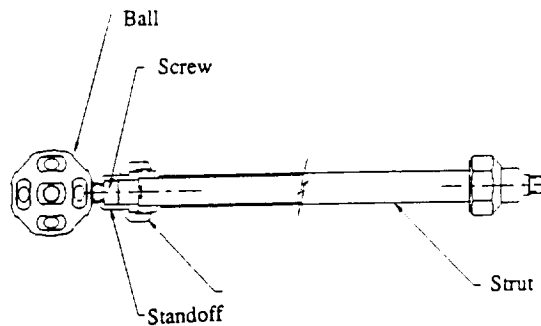
- Ideal Design: the effective density remains roughly constant

- Actual Design: the effective density varies considerably with the effective area

- The design is rather joint-dominated with respect to mass

STRUT DESIGN CURVES

Longeron/Batten — Effective Density (lb-sec²/in⁴) vs. Effective Area (in²)

Diagonal — Effective Density (lb-sec²/in⁴) vs. Effective Area (in²)
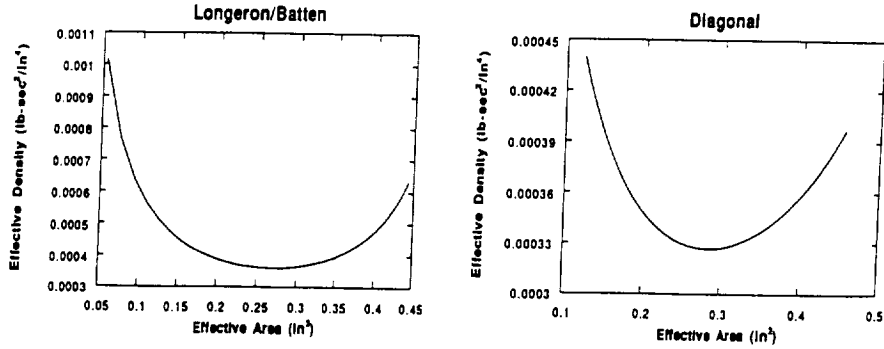
CONVENTIONAL VS. INTEGRATED

	RMS Displacement	Control Power
Open Loop (Phase-0)	22.54	0.00
Open Loop (Phase-1)	18.34	0.00
Control-Optimized (S) Design	2.4	7.11
Control-Optimized (D) Design	2.4	6.41
Integrated Design (S)	2.4	4.21
Integrated Design (D)	2.4	3.64

STRUCTURAL DESIGN VARIABLES

(Static Dissipative Controller)

	Design Var.	Phase-0 Areas	Phase-1 Areas
	1	0.134	0.330
	4	0.134	0.085
	7	0.134	0.173
Longerons	10	0.134	0.260
	13	0.134	0.257
	16	0.134	0.095
	19	0.134	0.096
	2	0.134	0.082
	5	0.134	0.083
	8	0.134	0.082
Battens	11	0.134	0.082
	14	0.134	0.081
	17	0.134	0.081
	20	0.134	0.081
	3	0.124	0.082
	6	0.124	0.085
	9	0.124	0.082
Diagonals	12	0.124	0.081
	15	0.124	0.079
	18	0.124	0.079
	21	0.124	0.082

STRUCTURAL DESIGN VARIABLES

(Dynamic Dissipative Controller)

	Design Var.	Phase-0 Areas	Phase-1 Areas
Longerons	1	0.134	0.330
	4	0.134	0.080
	7	0.134	0.142
	10	0.134	0.295
	13	0.134	0.258
	16	0.134	0.100
	19	0.134	0.117
Battens	2	0.134	0.077
	5	0.134	0.087
	8	0.134	0.086
	11	0.134	0.080
	14	0.134	0.078
	17	0.134	0.077
	20	0.134	0.083
Diagonals	3	0.124	0.098
	6	0.124	0.087
	9	0.124	0.082
	12	0.124	0.066
	15	0.124	0.066
	18	0.124	0.066
	21	0.124	0.083

PERTURBATION ANALYSIS

- The integrated phase-1 design can not be fabricated to exact specifications due to manufacturing and cost limitations

- Any viable integrated design should allow for possible perturbations in the structural design variables

- Carry out a post-design sensitivity analysis:

$$LOS(d + \delta) = LOS(d) + [\partial LOS/\partial \rho]^T \delta + \ldots$$

$$POW(d + \delta) = POW(d) + [\partial POW/\partial \rho]^T \delta + \ldots$$

- Upper bound values for the rms pointing error and control power

$$LOS_U = LOS(d) + |[\partial LOS/\partial \rho]^T|\delta_{max}$$

$$POW_U = POW(d) + |[\partial POW/\partial \rho]^T|\delta_{max}$$

PERTURBATION ANALYSIS (CONT'D)

	Control Power	RMS Pointing Error
Nominal Design	4.21	2.40
Perturbed Design	4.42 (5%)	2.56 (7%)
Fabricated Design	4.34 (3%)	2.38 (1%)

STRUCTURAL DESIGN VARIABLES

(Fabricated Structure)

	Design Var.	Phase-0 Areas	Phase-1 Areas
Longerons	1	0.134	0.347
	4	0.134	0.106
	7	0.134	0.182
	10	0.134	0.274
	13	0.134	0.274
	16	0.134	0.106
	19	0.134	0.106
Battens	2	0.134	0.094
	5	0.134	0.094
	8	0.134	0.094
	11	0.134	0.094
	14	0.134	0.094
	17	0.134	0.094
	20	0.134	0.094
Diagonals	3	0.124	0.087
	6	0.124	0.087
	9	0.124	0.087
	12	0.124	0.087
	15	0.124	0.087
	18	0.124	0.087
	21	0.124	0.087
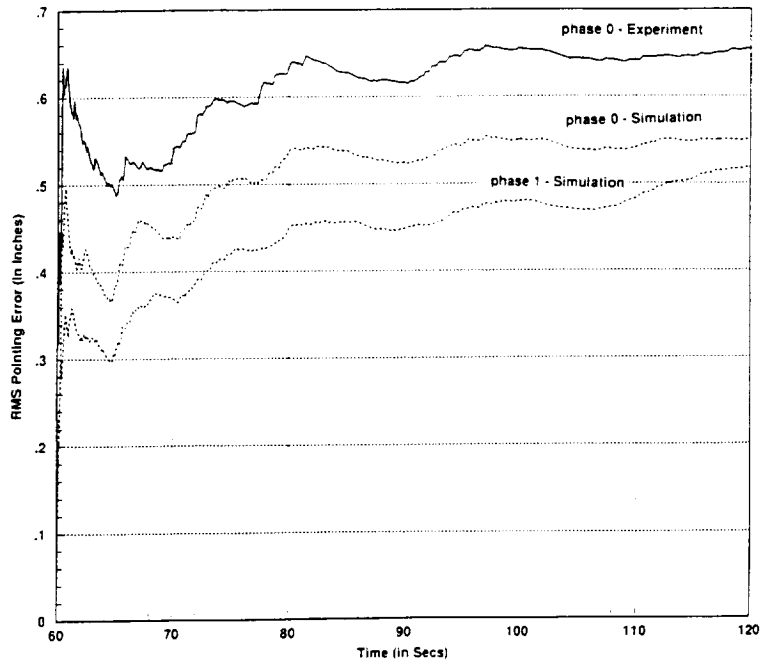
440

SIMULATION AND EXPERIMENTAL RESULTS
Static Dissipative Controller

SIMULATION AND EXPERIMENTAL RESULTS
Static Dissipative Controller
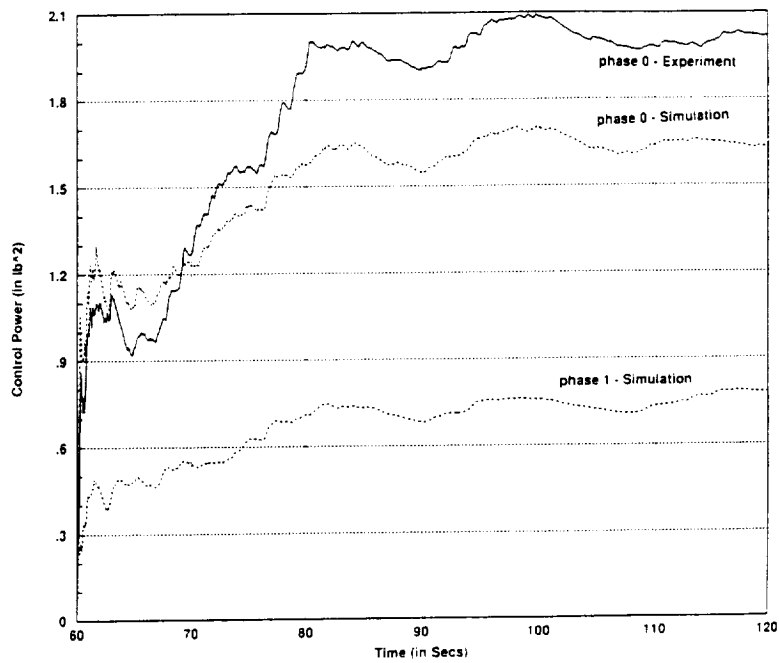
SIMULATION AND EXPERIMENTAL RESULTS
Dynamic Dissipative Controller
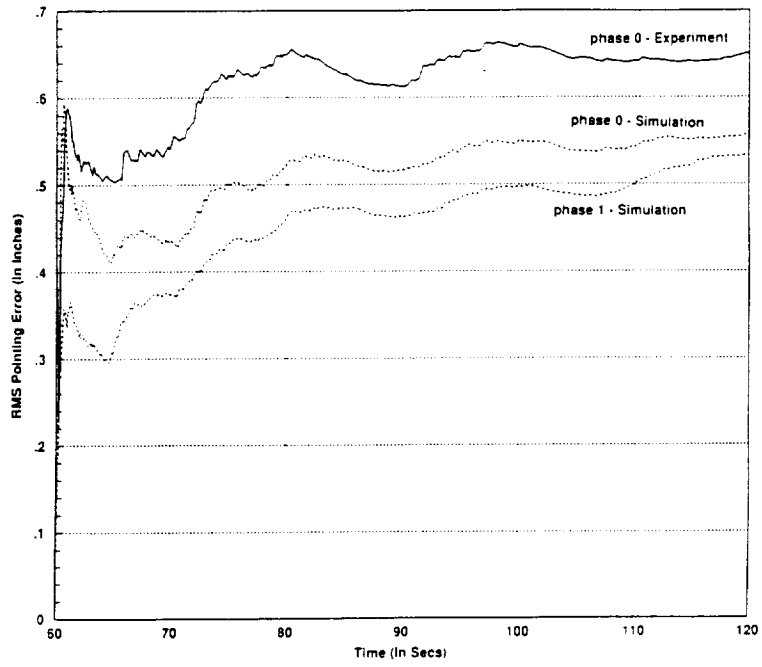
SIMULATION AND EXPERIMENTAL RESULTS
Dynamic Dissipative Controller
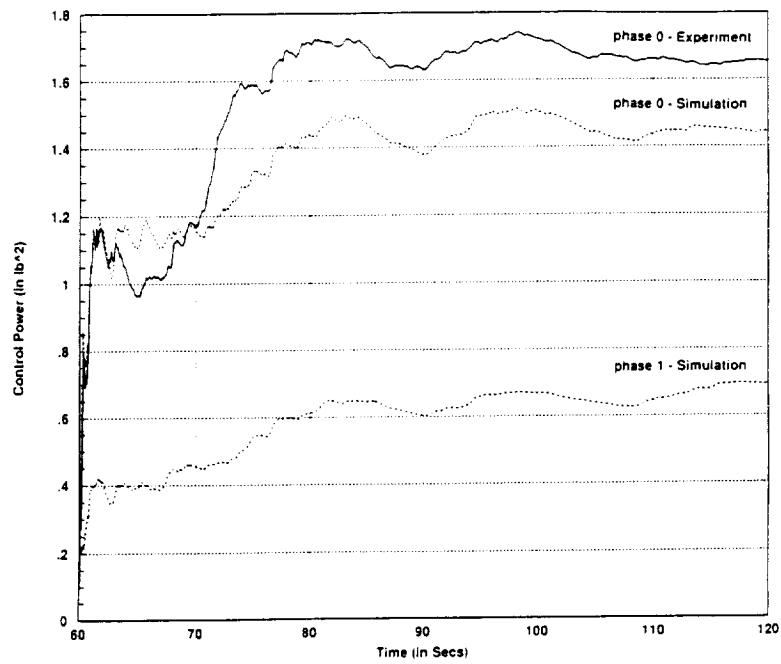
CONCLUDING REMARKS

- Basic integrated design methodology and software tool developed for Class I CSI problems

- Integrated redesign of evolutionary structure completed:
  Provides same LOS performance with 40% less control power

- Integrated controls-structures design is a feasible and practical design tool for modern spacecraft

- Additional studies (theory and experiment) are in progress to improve and extend the methodology

ROBUSTNESS PROPERTIES OF LQG OPTIMIZED COMPENSATORS

FOR COLLOCATED RATE SENSORS

A. V. Balakrishnan[†]

Flight Systems Research Center

University of California at Los Angeles

p 19

Abstract

In this paper we study the robustness with respect to stability of the closed-loop system with collocated rate sensors using LQG (mean square rate) optimized compensators. Our main result is that the transmission zeros of the compensator are precisely the structure modes when the actuator/sensor locations are "pinned" and/or "clamped": i.e., motion in the direction sensed is not allowed. We have stability even under parameter mismatch, except in the unlikely situation where such a mode frequency of the assumed system coincides with an undamped mode frequency of the real system and the corresponding mode shape is an eigenvector of the compensator transfer function matrix at that frequency. For a truncated modal model — such as that of the NASA LaRC Phase Zero Evolutionary model — the transmission zeros of the corresponding compensator transfer function can be interpreted as the structure modes when motion in the directions sensed is prohibited.

1. Introduction

The robustness of control laws to parameter uncertainty is of particular importance to Space applications because testing large structures under the micro-g conditions in Space is not possible on the ground. This paper explores the robustness issue for LQG optimized compensators using the explicit form discovered by the author for their time and/or frequency domain representation, whatever the structure model used — whether it is FEM, Truncated Modal, or Continuum.

The basic properties affecting robustness of the LQG optimized compensator are developed in Section 2 and how they relate to robustness is examined in Section 3. Section 4 deals with continuum models where in particular we show that the transmission zeros are the modes of the structure when the actuator/sensor locations are "pinned" and/or "clamped," i.e., motion in the directions sensed is restricted, generalizing the usual notions for simple beams.

When a truncated modal model is available, the compensator can be expressed explicitly also in terms of the given modes and mode shape vectors. The transmission zeros of these approximate compensators are studied in Section 5 and in particular some numerical results are presented for the NASA LaRC Phase Zero Evolutionary Model. Conclusions are in Section 6.

2. The LQG Optimized Compensator

To state the LQG problem, we begin with the canonical time-domain dynamics of a flexible structure with collocated rate sensors which, whether it is a Finite Element Model or Truncated Modal model (and hence finite dimensional) or a Continuum Model (and hence infinite-dimensional), can be expressed in the form:

$$M\ddot{x}(t) + A\dot{x}(t) + Bu(t) + BN_a(t) = 0 \quad \left.\begin{array}{c}\\ \\ \end{array}\right\}$$
$$v(t) = B^*\dot{x}(t) + N_r(t) \qquad (2.1)$$

where in the case of FEM,

M	is the mass matrix (nonsingular, nonnegative definite)
A	is the stiffness matrix (nonsingular, nonnegative definite)
B	is the control matrix (rectangular matrix)
$u(\cdot)$	is the control vector $(n\times1$, assuming n actuators)
$x(\cdot)$	is the "displacement" vector
$N_a(\cdot)$	is the actuator noise assumed white Gaussian with spectral density $d_a I$, I being the $n\times n$ Identity matrix
$v(\cdot)$	is the sensor output
B^*	represents the transpose of B
$N_r(\cdot)$	is the sensor noise assumed white Gaussian with spectral density $d_r I$.

446

For the Continuum Model such a representation continues to hold, however complicated the structure, with $x(\cdot)$ now allowed to range in a Hilbert space $\mathcal{H}$, with A, M, B being linear operators:

M bounded linear, self-adjoint, nonnegative definite with M^{-1} bounded;

A closed linear, self-adjoint, nonnegative definite with compact resolvent, the resolvent set including zero

B maps E^n Euclidean n-space into $\mathcal{H}$, and

B^* represents the adjoint of B.

See [1, 2].

The LQG problem we shall consider is that of finding the control $u(\cdot)$ (or equivalently the optimal compensator) that minimizes the mean square time average of the rate:

$$\lim_{T \to \infty} \left\{ \frac{1}{T} \int_0^T \|B^*\dot{x}(t)\|^2 \, dt \;+\; \frac{\lambda}{T} \int_0^T \|u(t)\|^2 \, dt \right\} \tag{2.2}$$

where $\lambda > 0$.

It is shown in [1, 3] that under the "controllability" assumption that

$$B^*\phi_k \;\neq\; 0$$

for any k, where ϕ_k are the modes orthonormalized with respect to the mass matrix:

$$A\phi_k \;=\; \omega_k^2 M\phi_k \;; \qquad [M\phi_k, \phi_k] \;=\; 1 \;, \tag{2.3}$$

the optimal compensator transfer function ($n \times n$ matrix function) can be expressed in the explicit analytical form:

$$\psi(p) \;=\; gpB^*(p^2M + A + \gamma pBB^*)^{-1}B \;, \qquad \text{Re. } p \geq 0 \tag{2.4}$$

where

$$g \;=\; \frac{\sqrt{d_a/d_r}}{\sqrt{\lambda}} \;; \qquad \gamma \;=\; \sqrt{d_a/d_r} + \frac{1}{\sqrt{\lambda}} \;. \tag{2.5}$$

Moreover, the corresponding mean square control power is given by

$$\lim_{T \to \infty} \frac{1}{T} \int_0^T \|u(t)\|^2 \, dt \;=\; \frac{d_a}{2\sqrt{\lambda}} \, \text{Tr.} \, (B^*MB)^{-1} \tag{2.6}$$

and the corresponding mean square displacement is:

$$\lim_{T \to \infty} \frac{1}{T} \int_0^T \|B^*x(t)\|^2 \, dt \;=\; \left[\sqrt{d_a/d_r} + \frac{\sqrt{\lambda}\, d_a}{2} \right] \text{Tr.} \, B^*A^{-1}B \;. \tag{2.7}$$

See [4] for the corresponding time-domain version of (2.4). From (2.3) we can deduce readily that

(i) As $\lambda \to 0$, $g \to \infty$ and $\gamma \to \infty$ we note that $\frac{g}{\gamma} \to \sqrt{d_a/d_r}$ and hence

$$\psi(p) \to I\sqrt{d_a/d_r}$$

where the right side is recognized as is the optimal "static" or "direct connection" or "PID" controller. Note that as $\lambda \to 0$, the control power given by (2.6) becomes infinite, as we expect.

(ii) $\psi(p)$ is "positive real" — that is to say:

$$\psi(p) \text{ holomorphic in } \mathrm{Re}.p > 0$$

$$\psi(p) + \psi(p)^* \text{ nonsingular, and positive definite, for } \mathrm{Re}.p > 0$$

where $*$ denotes conjugate transpose. We shall prove this directly, here, even though it may be deduced from the results in [1]. In fact

$$(p^2M + A + \gamma pBB^*)x = 0$$

implies that

$$p^2[Mx, x] + [Ax, x] + \gamma p\|B^*x\|^2 = 0$$

and normalizing so that

$$[Mx, x] = 1$$

we obtain

$$p^2 + \gamma p\|B^*x\|^2 + [Ax, x] = 0 .$$

Because of our assumption that $B^*\phi_k$ is not zero for any k, we see that

$$\|B^*x\| > 0$$

and hence

$$\mathrm{Re}.\, p < 0 .$$

This is enough to imply that in the finite-dimensional case:

$$(p^2M + A + \gamma pBB^*)^{-1}$$

is holomorphic in $\mathrm{Re}.p > 0$. In the infinite dimensional case the fact that A has a compact resolvent implies that so does

$$p^2M + A + \gamma pBB^*$$

and hence it follows that

$$B^*(p^2M + A + \gamma pBB^*)^{-1}B$$

is holomorphic in $\mathrm{Re}.p > 0$, and in fact is an $\mathcal{H}_\infty$ function.

Next let us calculate

$$\psi(p) + \psi(p)^* , \qquad\qquad \mathrm{Re}.p \geq 0 .$$

448

We have

$$\frac{\psi(p) + \psi(p)^*}{2} = B^*(p^2M + A + \gamma pBB^*)^{-1}$$

$$\cdot [|p|^2(p + \bar{p})M + (p + \bar{p})A + 2\gamma|p|^2BB^*](\bar{p}^2M + A + \gamma\bar{p}BB^*)^{-1}B$$

which is ≥ 0, since

$$|p|^2(p + \bar{p})M + (p + \bar{p})A + 2\gamma|p|^2BB^*$$

is, for Re. $p \geq 0$.

In particular for

$$p = i\omega, \qquad\qquad -\infty < \omega < \infty$$

we have

$$\frac{\psi(i\omega) + \psi(i\omega)^*}{2} = \gamma\omega^2\psi(i\omega)\psi(i\omega)^* . \qquad (2.8)$$

This leads to an important result which we state as:

Lemma 2.1

Suppose for some ω, $-\infty < \omega < \infty$,

$$\text{Re. } [\psi(i\omega)v, v] = 0 \qquad\qquad \text{for some } v . \qquad (2.9)$$

Then

$$\psi(i\omega)v = 0 \qquad (2.10)$$

and if $\omega \neq 0$,

$$B^*(-\omega^2M + A)^{-1}Bv = 0 . \qquad (2.11)$$

Proof.

$$\text{Re. } [\psi(i\omega)v, v] = \left[\left(\frac{\psi(i\omega) + \psi(i\omega)^*}{2}\right)v, v\right]$$

which by (2.8) is

$$= \gamma\omega^2\|\psi(i\omega)^*v\|^2$$

and hence (2.9) is equivalent to:

$$\omega\|\psi(i\omega)^*v\| = 0 .$$

If $\omega = 0$, $\psi(i\omega) = 0$ and hence $\psi(i\omega)v = 0$.
    If ω is not zero,

$$\psi(i\omega)^*v = 0$$

or

$$B^*(-\omega^2M + A - i\gamma\omega BB^*)^{-1}Bv = 0 .$$

Let

$$(-\omega^2M + A - i\gamma\omega BB^*)^{-1}Bv = x$$

or

$$Bv = -\omega^2Mx + Ax - i\gamma\omega BB^*x .$$

Since
$$B^*x = 0,$$

we have
$$Bv = (-\omega^2 M + A)x$$

and ω is not an eigenvalue of A, since $B^*x = 0$. Hence
$$B^*(-\omega^2 M + A)^{-1}Bv = 0.$$

Corollary.
Except for $\omega = 0$, the zeros of
$$\text{Det } |\psi(i\omega) + \psi(i\omega)^*|$$

in $-\infty < \omega < \infty$ are the same as those of
$$\text{Det } |B^*(-\omega^2 M + A)^{-1}B| = 0$$

and in particular independent of g and γ, for $g + \gamma < \infty$.

Proof.
$$\text{Det } |\psi(i\omega) + \psi(i\omega)^*| = 0$$

implies that
$$[(\psi(i\omega) + \psi(i\omega)^*)v, \ v] = 0, \qquad v \neq 0$$

and hence by the lemma,
$$\psi(i\omega)^*v = 0$$

and since $\omega \neq 0$,
$$B^*(-\omega^2 M + A)^{-1}Bv = 0$$

or,
$$\text{Det } |B^*(-\omega^2 M + A)^{-1}B| = 0.$$

Conversely if
$$\text{Det } |B^*(-\omega^2 M + A)^{-1}B| = 0,$$

so that
$$(B^*(-\omega^2 M + A)^{-1}B)v = 0$$

let
$$(-\omega^2 M + A)^{-1}Bv = x.$$

Then
$$Bv = -\omega^2 Mx + Ax = -\omega^2 Mx + A\gamma \pm \gamma(i\omega)BB^*x$$

for arbitrary value of γ, since $B^*x = 0$. Hence
$$B^*(-\omega^2 M + A \pm \gamma(i\omega)BB^*)^{-1}Bv = 0$$

or

$$(\psi(i\omega) + \psi(i\omega)^*)v = 0$$

or

$$\text{Det } |\psi(i\omega) + \psi(i\omega)^*| = 0 .$$

3. Robustness

The robustness of concern is that with respect to parameter uncertainty, in particular in the mode frequencies ω_k. Thus we want to be able to assert that the closed-loop system is stable even if the parameters chosen for the compensator transfer function $\psi(\cdot)$ are incorrect. Now the closed-loop transfer function corresponding to the compensator transfer function $\psi(\cdot)$ is given by

$$(p^2M + A + \gamma pB\psi(p)B^*)^{-1} . \tag{3.1}$$

Let p be a pole of (3.1), so that for some $x \neq 0$,

$$p^2Mx + Ax + \gamma pB\psi(p)B^*x = 0 . \tag{3.2}$$

Then

$$p^2[Mx, x] + [Ax, x] + \gamma p[B\psi(p)B^*x, x] = 0$$

where $[Mx, x] > 0$.

If $p = 0$, then

$$Ax = 0$$

which is not possible since zero is not an eigenvalue of A — this property of the system is assumed to be known with certainty. If $p \neq 0$, we may divide through by p to get

$$p[Mx, x] + \frac{[Ax, x]}{p} + \gamma[B\psi(p)B^*x, x] = 0 .$$

Let

$$p = \alpha + i\omega , \qquad\qquad \alpha \geq 0 .$$

Then

$$\alpha[Mx, x] + \frac{\alpha[Ax, x]}{\alpha^2 + \omega^2} + \gamma[B(\psi(p) + \psi(p)^*)B^*x, x] = 0 . \tag{3.3}$$

Suppose $\alpha > 0$. Then by the positive real property, the third term in (3.3) is positive and the first two terms are of course positive, and hence the sum cannot be zero and hence α cannot be positive. Consider next the case $\alpha = 0$. This yields

$$(i\omega)[Mx, x] - \frac{i[Ax, x]}{\omega} + \gamma[B\psi(i\omega)B^*x, x] = 0 .$$

For this to hold, it is necessary that

$$\text{Re. } [B\psi(i\omega)B^*x, x] = 0$$

where B^*x cannot be zero. Hence, by the lemma

$$\psi(i\omega)B^*x = 0 , \qquad\qquad B^*x \neq 0 .$$

But this in turn by (3.2) would imply that

$$-\omega^2 Mx + Ax = 0 \; ; \qquad B^*x \neq 0 \qquad \Big\}$$
$$\psi(i\omega)B^*x = 0 \qquad\qquad\qquad \Big\} \qquad (3.4)$$

In other words an undamped mode-frequency of the system must coincide with a zero of $\psi(i\omega)$ corresponding to the same value of B^*x ("mode shape at the sensor location"). Thus we have robustness with respect to stability so long as this is insured against. Because of the coincidence requirement on the mode shape in addition to the frequency, this is highly unlikely if the controller dimension (number of actuators) is higher than one.

4. Continuum Models

For the case of the continuum model, whether explicit or conceptual, we can relate the zeros of the compensator transfer function to the model in a simple way — viz., we can show that they are the "pinned" and/or "clamped" mode frequencies of the structure or a slight generalization thereof.

We begin with the general case of a multi-beam model as the NASA LaRC Phase Zero Evolutionary Model [5]. Here the state variable $x(\cdot)$ has the form (see [2]):

$$x = \begin{vmatrix} f \\ b \end{vmatrix}$$

where $f(\cdot)$ represents the displacement (6×1) vector and b the corresponding "boundary" values at the nodes, and thus a finite dimensional vector. Also

$$Mx = \begin{vmatrix} M_0 f \\ M_b b \end{vmatrix}$$

$$Ax = \begin{vmatrix} A_0 f \\ A_b f \end{vmatrix} \qquad\qquad x \in \mathfrak{D}(A)$$

$$Bu = \begin{vmatrix} 0 \\ B_u u \end{vmatrix} \qquad\qquad \text{(where } B_u^* B_u \text{ is nonsingular)}$$

where the dimension of U (the control vector) can be smaller than that of b, and B_u maps U into the finite-dimensional space spanned by b. In this case

$$\text{Det } |B^*(-\omega^2 M + A)^{-1} B| = 0 \qquad (4.1)$$

and equivalently, for some v:

$$(-\omega^2 M + A)x = Bv \; ; \qquad B^*x = 0 \; ;$$

which under the notation:

$$x = \begin{vmatrix} f \\ b \end{vmatrix}$$

452

becomes:

$$-\omega^2 M_0 f + A_0 f = 0 \tag{4.2}$$

$$B_u^* b = 0 \tag{4.3}$$

$$-\omega^2 M_b b + A_b f = B_u v \tag{4.4}$$

The condition (4.4) is superfluous since v is not specified and all we require is that v and hence $B_u v$ be nonzero. Thus the transmission zeros are the eigenvalues of the differential operator A_0 with the "boundary condition" specified by

$$-\omega^2 M_0 f + A_0 f = 0 \ ; \qquad B_u^* b = 0 \ . \tag{4.5}$$

These are recognized as structure modes when the control/sensor locations are "pinned" and/or "clamped" — motion in the directions sensed is not allowed. The structure modes when all nodes are clamped are of course given by:

$$\left. \begin{array}{c} -\omega^2 M_0 f + A_0 f = 0 \ , \qquad f \neq 0 \\ b = 0 \ . \end{array} \right\} \tag{4.6}$$

If all nodes are control nodes so that B_u is the identity, these are also transmission zeros but not in general because of the additional condition (4.4).

As shown in [3], (4.1) can be further reduced to:

$$|B_u^*(-\omega^2 M_b + T(i\omega))^{-1} B_u| = 0 \tag{4.7}$$

where the "clamped" mode frequencies given by (4.6) are the "poles" of the matrix $T(i\omega)$.

A textbook example of (4.7) is provided by the torsion of a one-dimensional beam with one end clamped and the other end the control node. Here $T(i\omega)$ is given by (see [3] for details):

$$T(i\omega) = \sqrt{\rho G} \ I_\psi \, \omega \cot (2\ell\sqrt{\rho/G})\omega$$

and hence the compensator transmission zeros are given by

$$\sin (2\ell\sqrt{\rho/G})\omega = 0$$

or

$$\omega = \frac{n\pi}{2\ell\sqrt{\rho/G}}$$

whereas the structure undamped modes are given by

$$m\omega = (\sqrt{\rho G})I_\psi \cot (2\ell\sqrt{\rho/G})\omega \ .$$

Note that asymptotically these frequencies merge — a phenomenon which can be proved to hold generally. In this (one-dimensional) case the zeros and poles of

$$(-\omega^2 m + T(i\omega))$$

alternate (an instance of Foster's Theorem familiar in classical circuit analysis [6]) and hence also the compensator transmission zeros and undamped mode frequencies — but this is no longer true in general in the multidimensional case.

5. Truncated Modal Model

Truncated Modal models provide both the (undamped) mode frequencies ω_k and the corresponding mode shapes (column vectors of dimension equal to the control dimension) $B^*\phi_k$ at the sensor locations up to a maximum frequency allegedly adequate for faithful representation of the structure. Assume thus that ω_k, $B^*\phi_k$ are given for $k = 1, ..., N$. Then we may consider this the "truth model" and the corresponding optimal compensator transfer function takes the form (see [4]):

$$gpB_N^*(p^2 I + D_N + \gamma p B_N B_N^*)^{-1} B_N \qquad (5.1)$$

where

$$D_N = \text{Diag.} (\omega_1^2, ..., \omega_N^2)$$

$$B_N^* = \begin{vmatrix} B^*\phi_1 & B^*\phi_2 & \cdots & B^*\phi_N \end{vmatrix}_{n \times N}$$

$$B_N = \begin{vmatrix} (B^*\phi_1)^* \\ \vdots \\ (B^*\phi_N)^* \end{vmatrix}_{N \times n}$$

where n is the control dimension (equivalently, the number of actuators). It is assumed that N is large enough so that the $n \times n$ matrix:

$$B_N^* B_N$$

is nonsingular. Then omitting $\omega = 0$, the transmission zeros of the transfer function (5.1) are given by

$$\text{Det} \, |B_N^*(-\omega^2 I + D_N)^{-1} B_N| = 0 . \qquad (5.2)$$

For large enough N we should expect these frequencies to closely approximate the structure mode frequencies when motion is restricted along the directions sensed at the actuator/sensor locations. In particular if the theoretical values of the latter are known, we have a means of checking the faithfulness of the truncated model.

For the NASA LaRC Phase Zero Evolutionary Model [5], the truncated modal model has 86 modes. For the corresponding mode shapes as determined by the LaRC team, the frequencies for which (5.2) hold are shown in Figures 1 through 6, where the minimum absolute value of the eigenvalues of

$$B_N^*(-\omega^2 I + D_N)^{-1} B_N$$

is plotted as a function of omega for $N = 86$. Note that all the eigenvalues are positive for $\omega < \omega_1$ and negative for $\omega > \omega_N$. Figure 1 shows the entire range from 0-300 radians/second. Figures 2-6 show more detail of the behavior over narrower ranges.

The dependence of zeros on the depth of the modal approximation is illustrated in Figures 7, 8, 9, 1a, 2a, 3a, 4a, 6a and 10a for $N = 8$, 16, 30, corresponding to $\omega_8 = 10.921$, $\omega_{16} = 25.225$, $\omega_{30} = 53.132$, respectively. Note that for the 8-mode model there are no zeros at all, while the 16-mode model shows three zeros (in the range 0-25 rad/sec). The 30-mode model shows excellent agreement with the 86-mode model for ω up to $\omega_{30} = 53.132$, comparing Figures 1 and 1a, 2 and 2a, 3 and 3a, 4 and 4a, 6 and 6a, and finally Figures 10 and 10a show the expected divergence for $\omega > \omega_{30}$. For illustrative purposes we list the first few zeros for the full 86-mode model in rad/sec:

$$(5.4913)$$

$$6.575$$

$$8.75$$

$$(9.2580)$$

$$(14.46)$$

$$14.7$$

$$(15.26)$$

where the numbers in parentheses are the nearest undamped mode frequencies.

6. Conclusions

It is shown that the optimal compensator transfer function for LQG rate minimization for flexible structures with collocated rate sensors has transmission zeros at frequencies to the modes of the corresponding continuum structure when the control-sensor locations are "pinned" and/or "clamped" (motion in the directions sensed is curbed). In particular the compensator is robust with respect to stability so long as any such mode of the assumed system does *not* coincide with an undamped mode frequency of the real system and the corresponding mode shape at the sensor locations is an eigenvector of the compensator transfer function matrix at that frequency. For Continuum Models the transmission zeros are shown to be the poles of a matrix function related to the undamped modes. Calculations of the zeros are given for the truncated modal models of the NASA LaRC Phase Zero Evolutionary Model illustrating the dependence on the number of modes used.

References

[1] A. V. Balakrishnan. "Compensator Design for Stability Enhancement with Collocated Controllers," *IEEE Transactions on Automatic Control*, vol. 36, no. 9 (September 1991), pp. 994-1007.

[2] A. V. Balakrishnan. "Modes of Interconnected Lattice Trusses Using Continuum Models, Part 1." NASA CR 189568. December 1991.

[3] A. V. Balakrishnan. "Compensator Design for Stability Enhancement with Collocated Controllers: Explicit Solutions. *IEEE Transactions on Automatic Control*, vol. 37, no. 1 (January 1993).

[4] A. V. Balakrishnan. "An Explicit Solution to the Optimal LQG Problem for Flexible Structures with Collocated Rate Sensors." In: *Proceedings of the 5th NASA-DOD CSI Technology Conference, Lake Tahoe, Nevada, March 3-5, 1992.*

[5] "Langley's CSI Evolutionary Model: Phase Zero." NASA TN 104165. November 1991.

[6] R. W. Newcomb. *Linear Multipart Synthesis.* New York: McGraw-Hill, 1966.
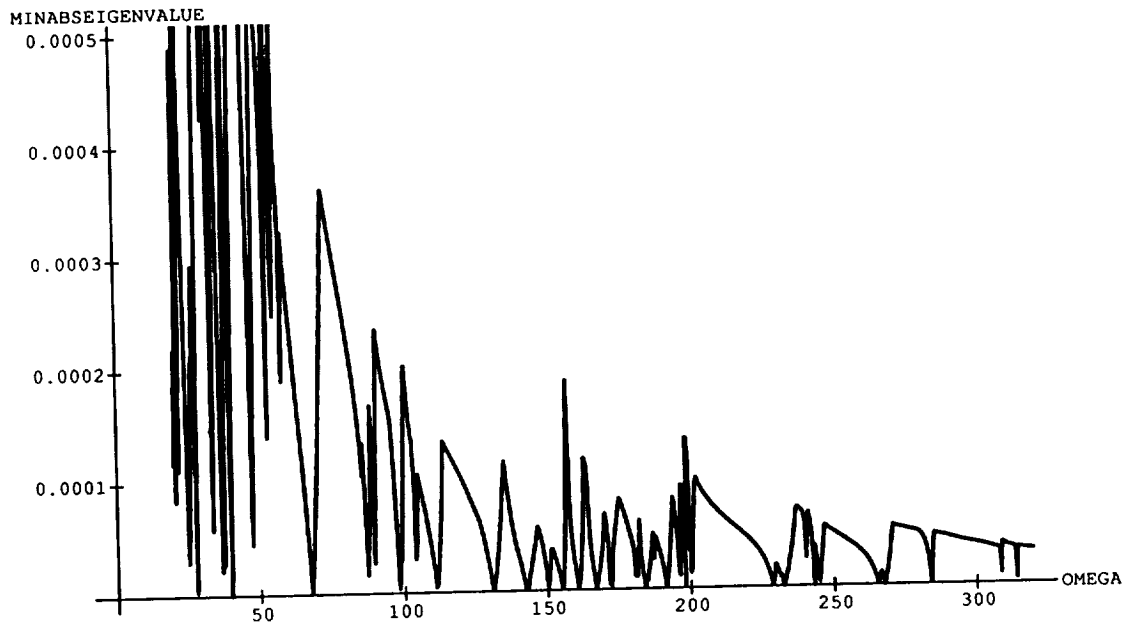
Figure 1

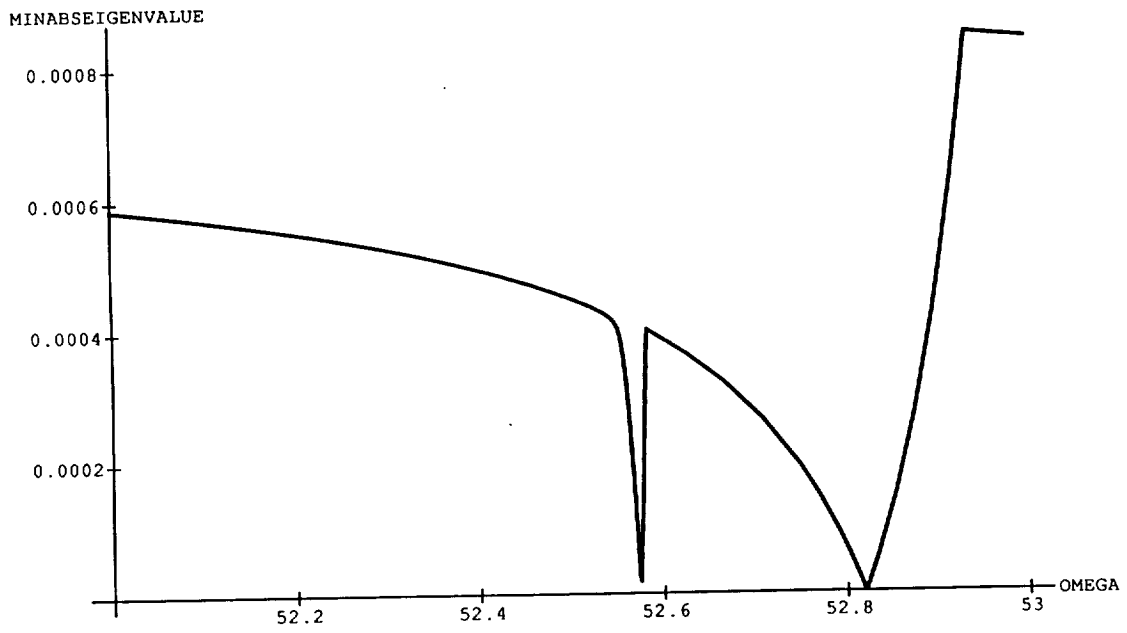Minimum Absolute Eigenvalue: 86-mode Truth Model
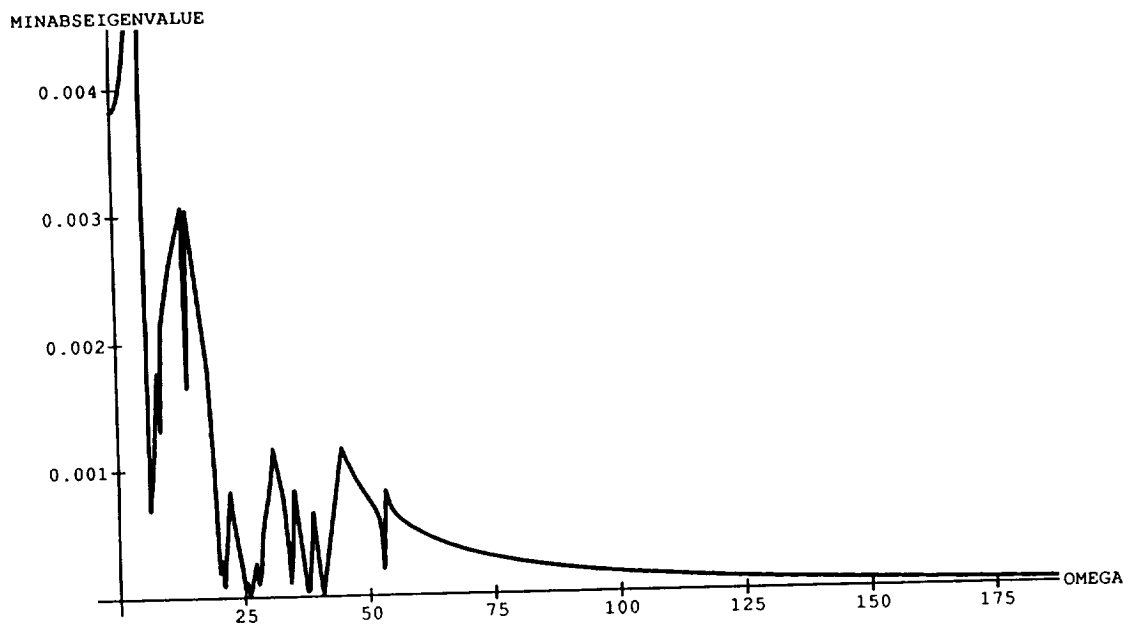
Figure 1a

Minimum Absolute Eigenvalue: 30-mode Truth Model
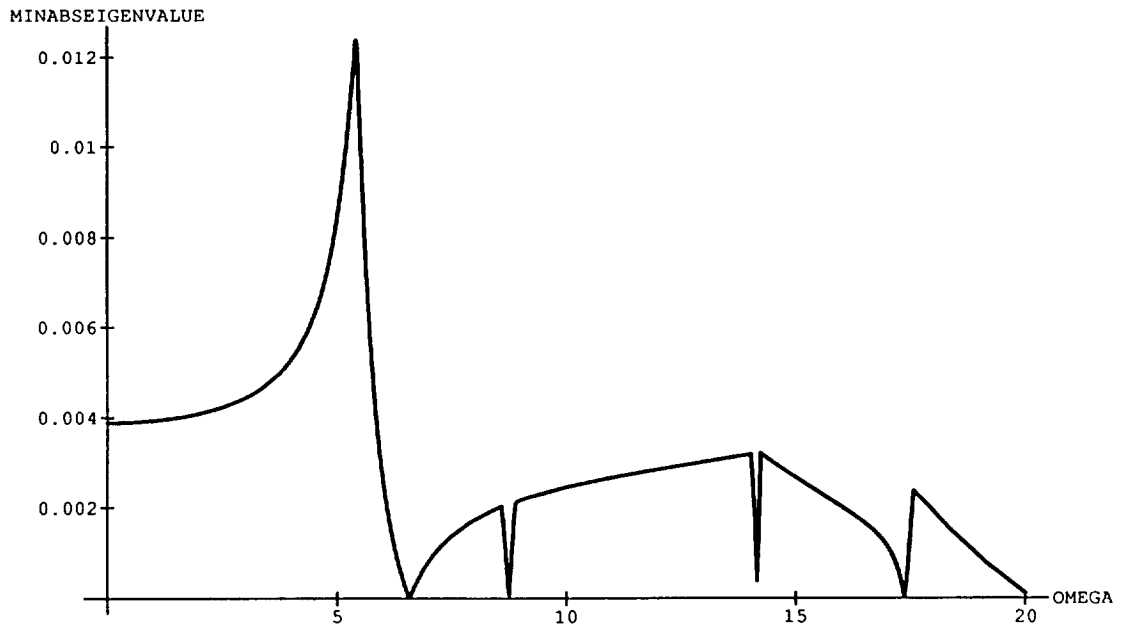
Figure 2

Minimum Absolute Eigenvalue: 86-mode Truth Model
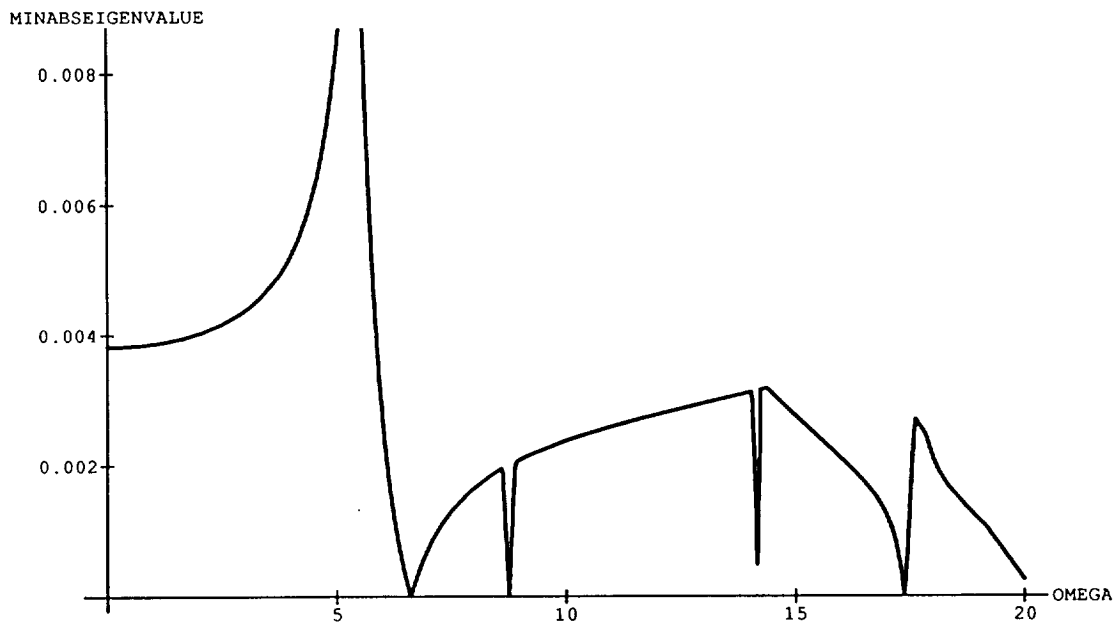
Figure 2a

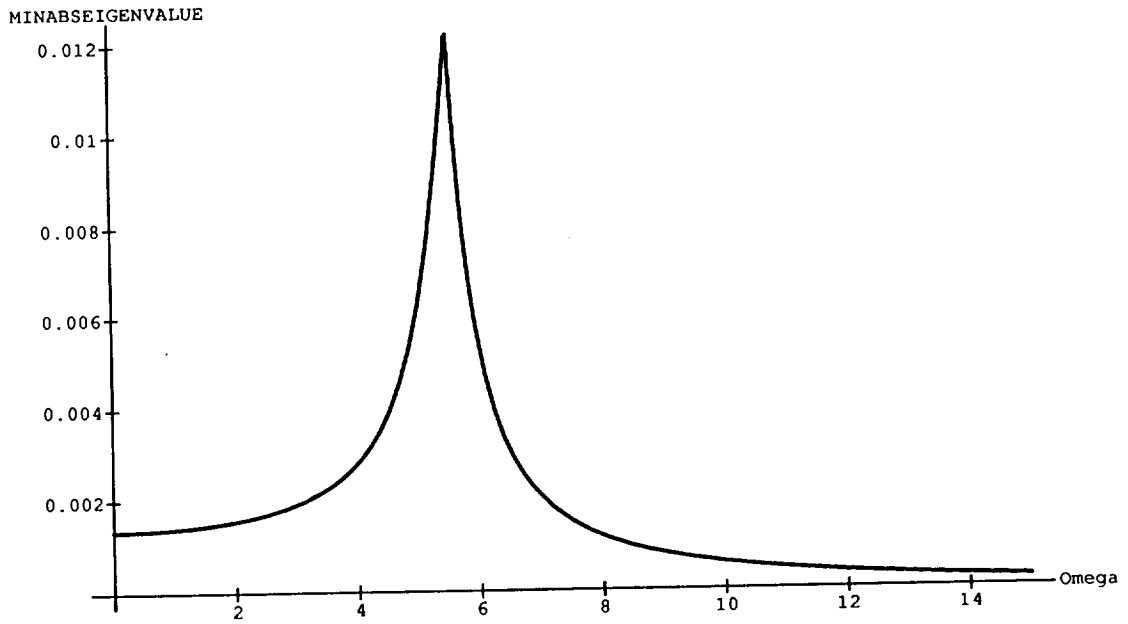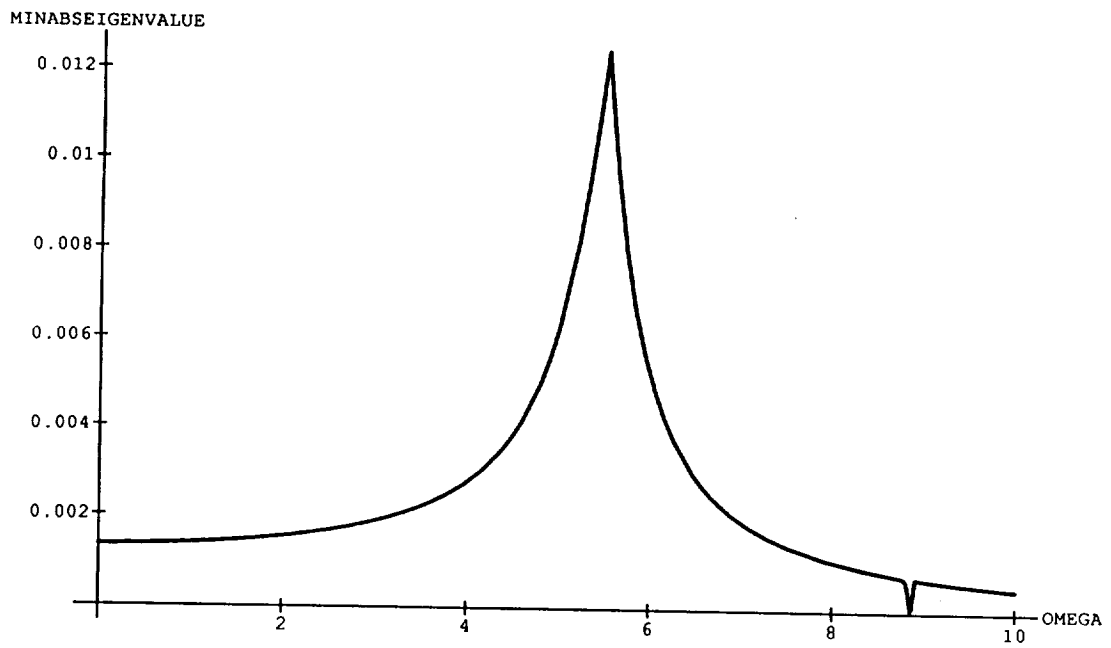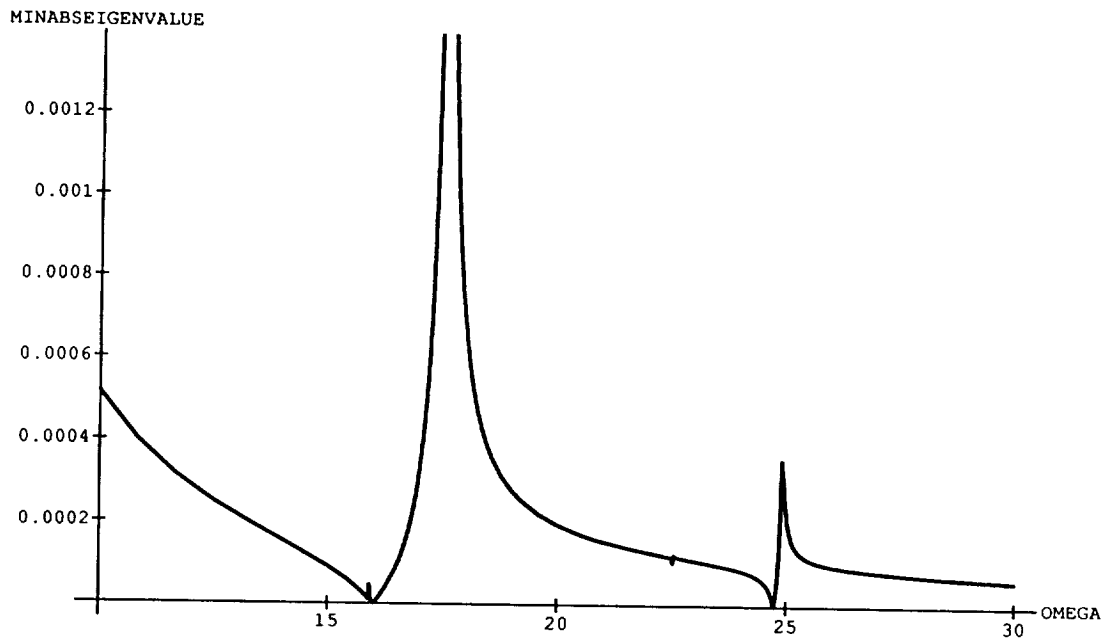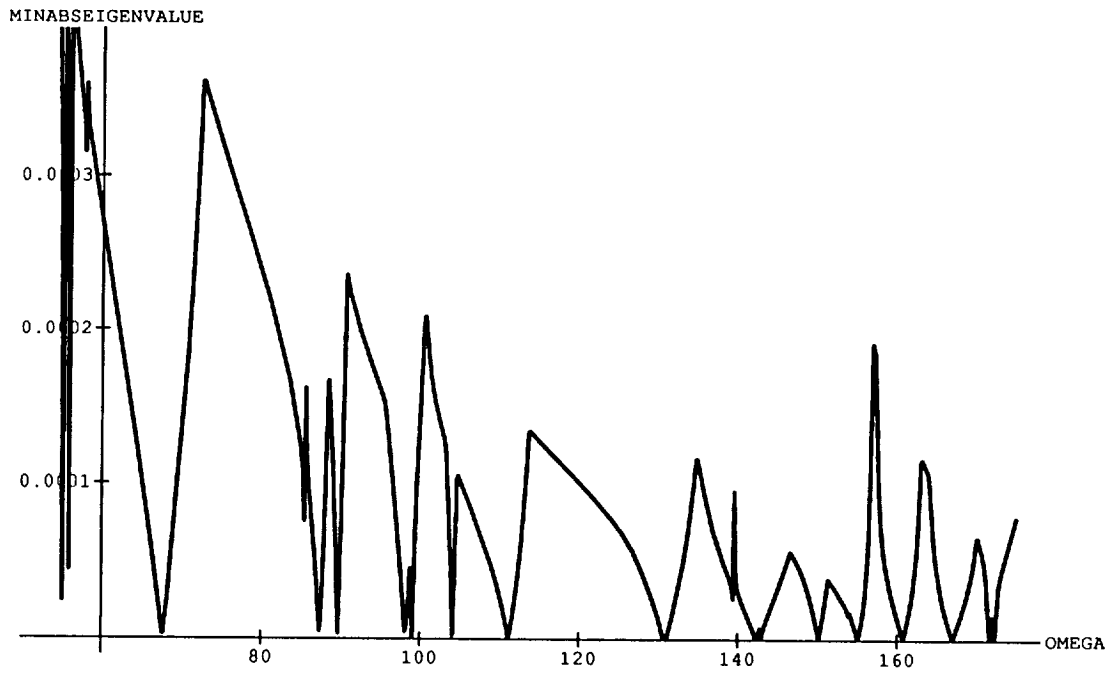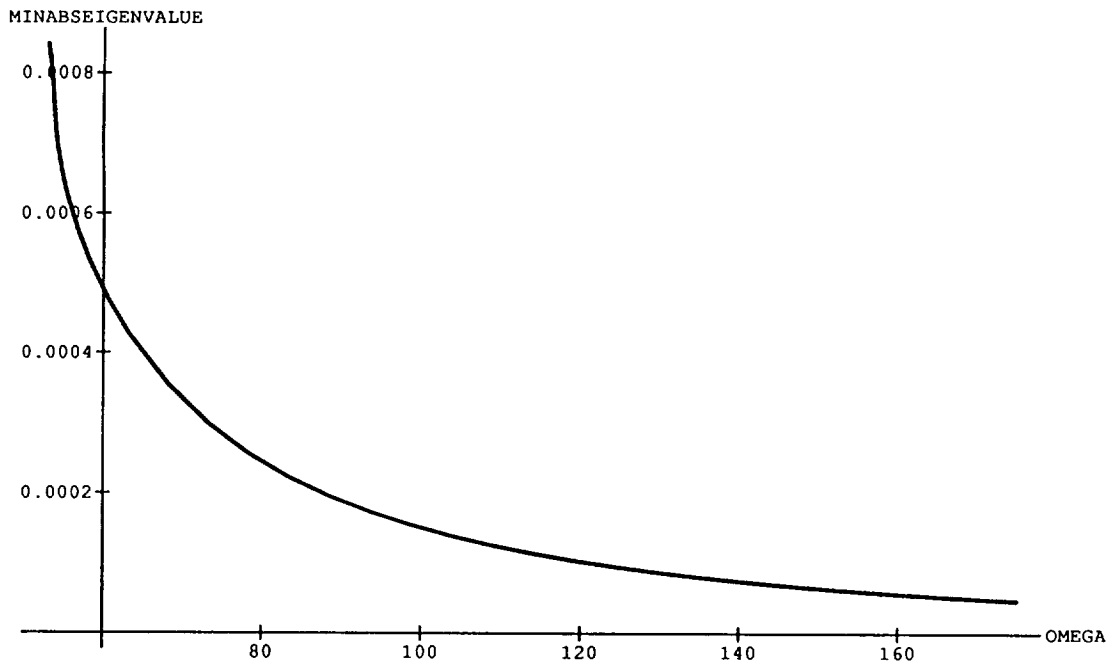Minimum Absolute Eigenvalue: 30-mode Truth Model
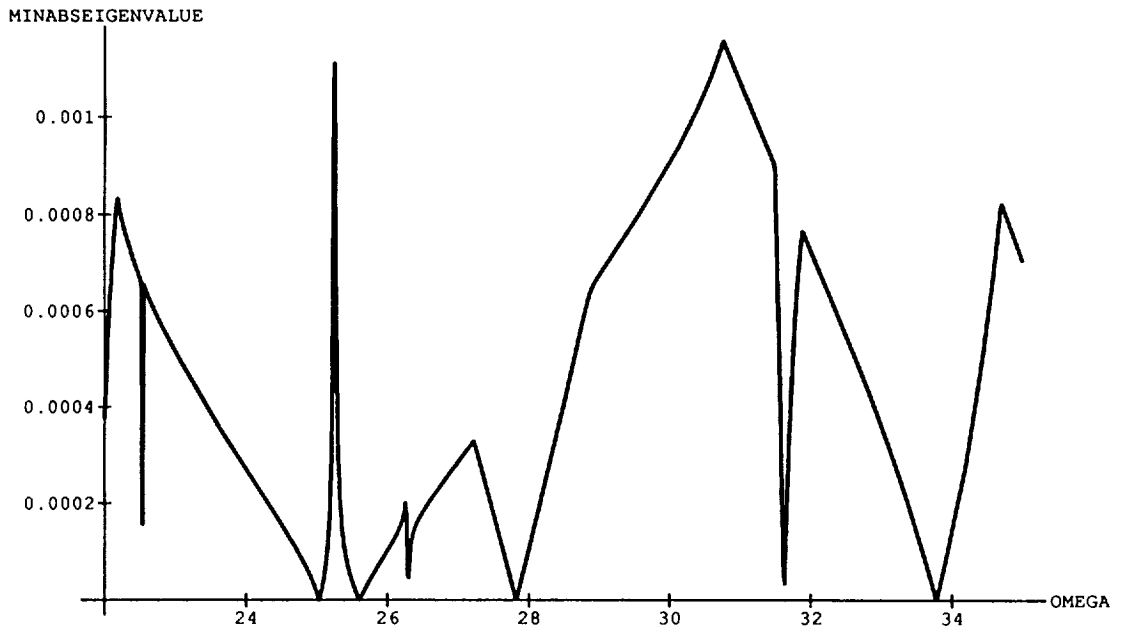
Figure 3

Minimum Absolute Eigenvalue: 86-mode Truth Model
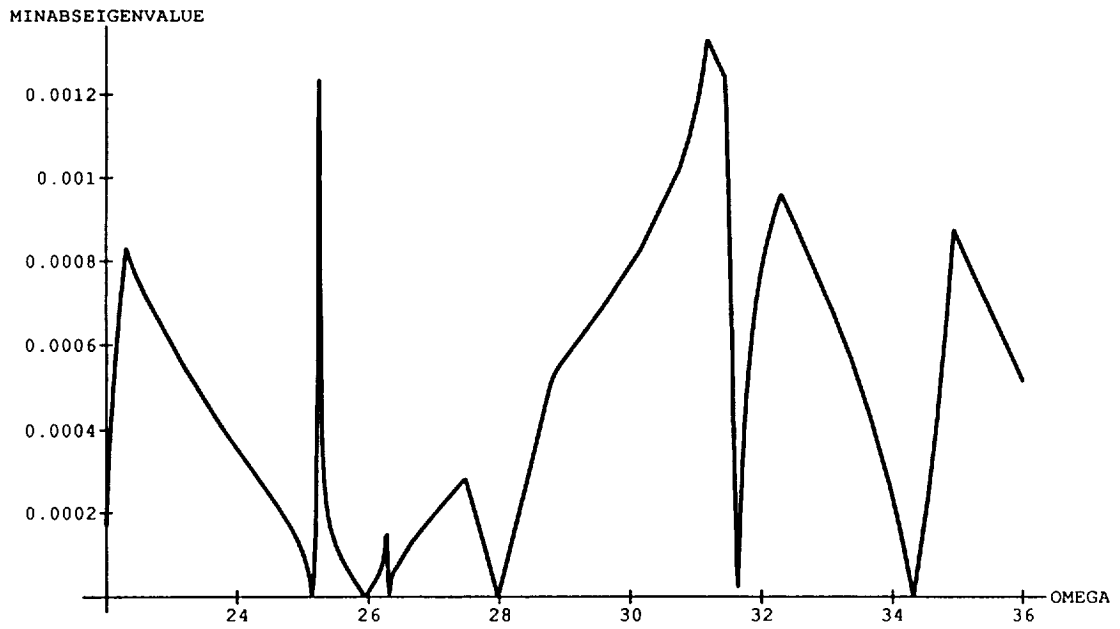
Figure 3a

Minimum Absolute Eigenvalue: 30-mode Truth Model

458
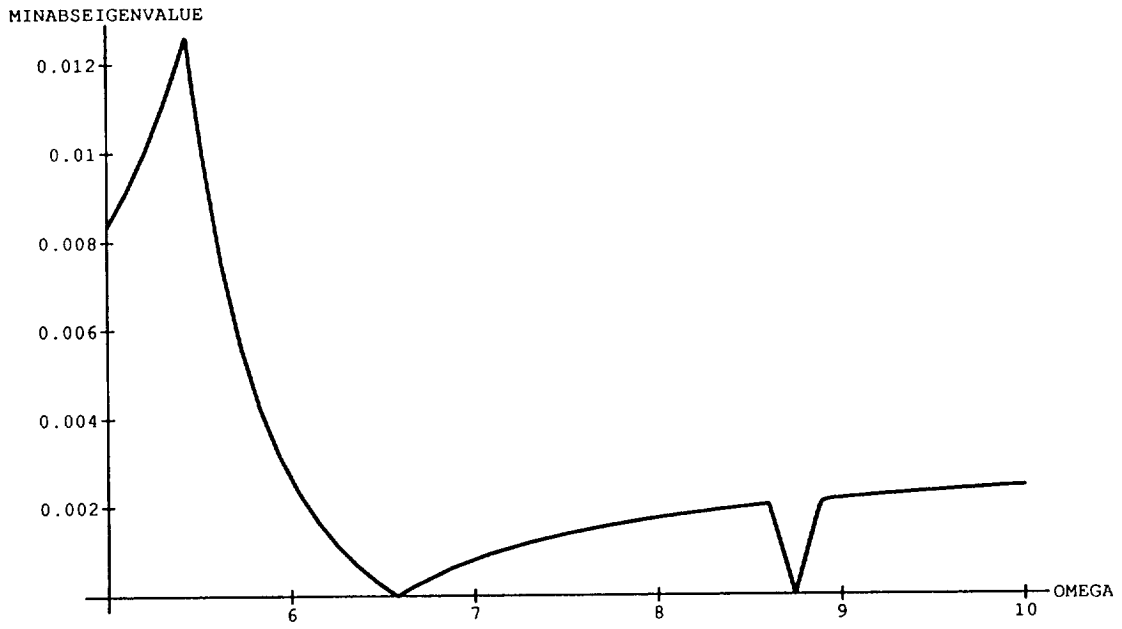
Figure 4

Minimum Absolute Eigenvalue: 86-mode Truth Model
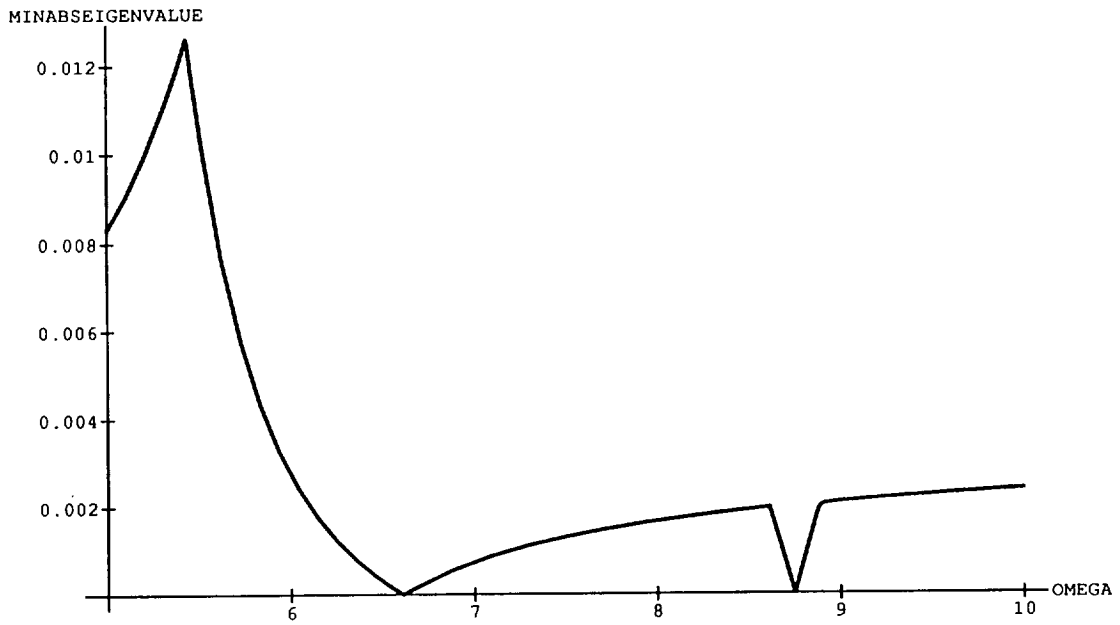
Figure 4a

Minimum Absolute Eigenvalue: 30-mode Truth Model
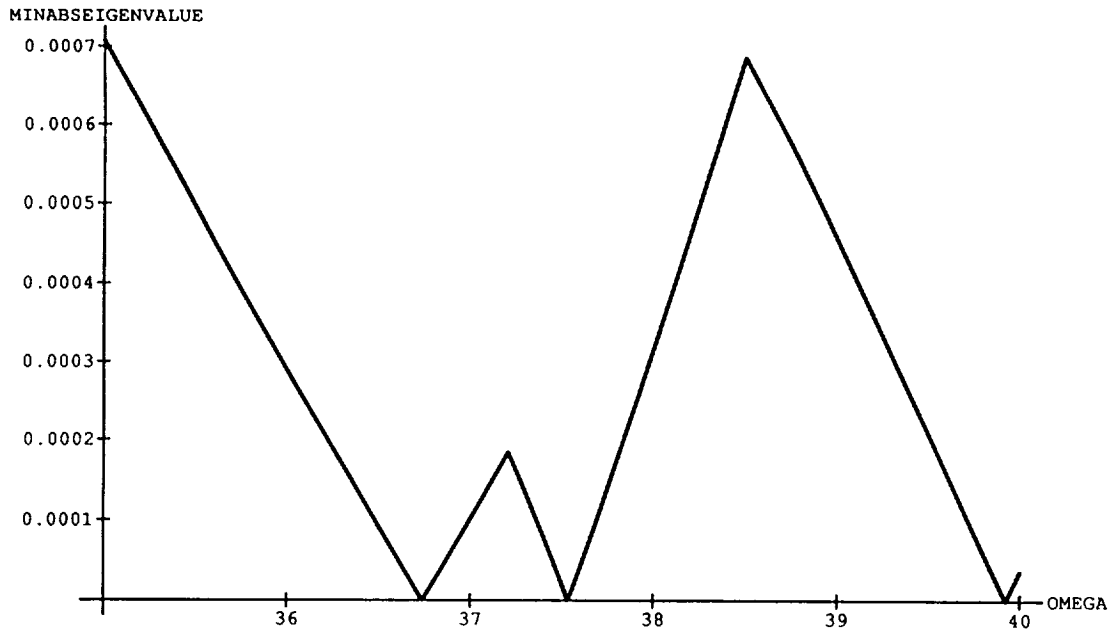
Figure 5

Minimum Absolute Eigenvalue: 86-mode Truth Model
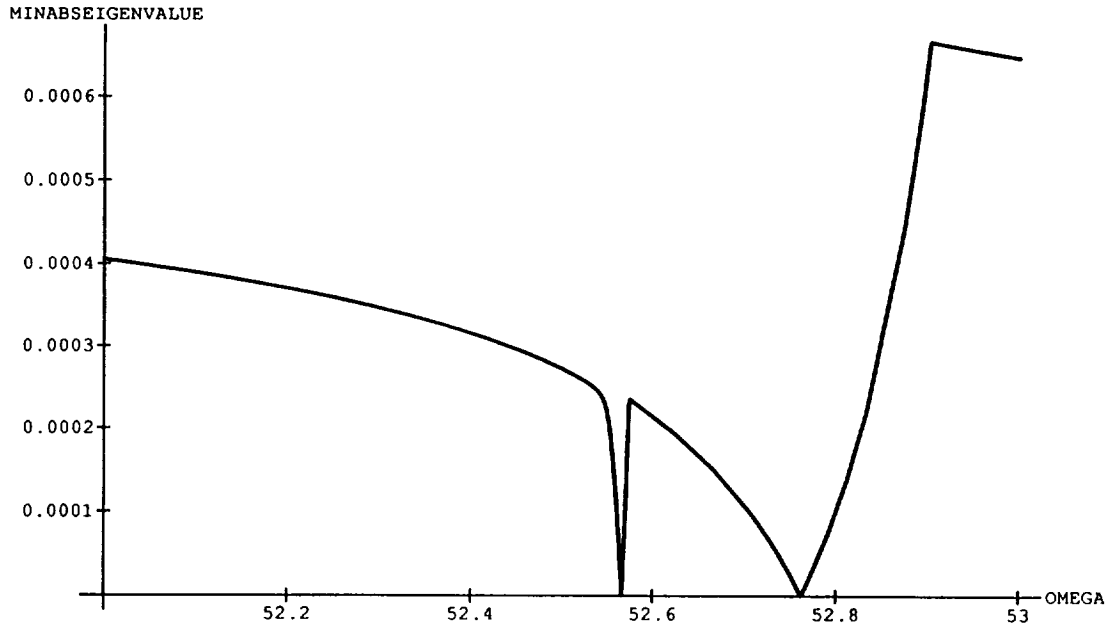
Figure 6

Minimum Absolute Eigenvalue: 86-mode Truth Model

Figure 6a

Minimum Absolute Eigenvalue: 30-mode Truth Model

Figure 7

Minimum Absolute Eigenvalue: 8-mode Truth Model

461

Figure 8

Minimum Absolute Eigenvalue: 16-mode Truth Model

Figure 9

Minimum Absolute Eigenvalue: 16-mode Truth Model

Figure 10

Minimum Absolute Eigenvalue: 86-mode Truth Model

Figure 10a

Minimum Absolute Eigenvalue: 30-mode Truth Model

LQG OPTIMAL COMPENSATOR TRANSFER FUNCTION
FOR THE NASA LaRC CSI EVOLUTIONARY MODEL

A. V. Balakrishnan[t]

Flight Systems Research Center

University of California at Los Angeles

Abstract

Following the general form for LQG optimal compensators for flexible structures with collocated rate sensors we develop an explicit compensator transfer function for the NASA LaRC CSI Evolutionary model in the form:

$$\psi(i\omega) = g\,i\omega B_u^*(-M_b\omega^2 + T(i\omega) + i\gamma\omega B_u B_u^*)^{-1} B_u$$

where $T(i\omega)$ is a 48×48 positive definite matrix whose derivation is the main result of this report. The undamped mode frequencies can be expressed in terms of $T(i\omega)$ as the zeros of

$$\text{Det }|-\omega^2 M_b + T(i\omega)|$$

while "clamped-clamped" modes of the structure (with all nodes clamped) are the poles.

1. Introduction

In this paper we present an explicit compensator transfer function for the NASA LaRC Evolutionary Model [1], using the Continuum Model developed in [2]. In particular the notation follows closely that in [2]. The compensator is obtained upon specialization of the general development in [3].

2. Compensator Transfer Function

The optimal compensator transfer function is given by (see [3]):

$$\frac{p}{\sqrt{\lambda}} \sqrt{d_a/d_r} \; B^*(p^2M + A + p\gamma BB^*)^{-1}B \; .$$

The main step is to calculate

$$\psi(p) \;=\; B^*(p^2M + A + p\gamma BB^*)^{-1}B \; .$$

We shall consider only the Continuum Model in [2] (case 3) in which the main bus, the tower and the appendages are flexible but the antenna is lumped.

Let

$$\psi(p)v \;=\; u$$

$$B^*(p^2M + A + p\gamma BB^*)^{-1}Bv \;=\; u \; .$$

Let

$$(p^2M + A + p\gamma BB^*)^{-1}Bv \;=\; \begin{vmatrix} f \\ b \end{vmatrix} \; .$$

Then

$$p^2M_0f \;+\; A_0f \;=\; 0 \tag{2.1}$$

where f is also subject to the "linkage conditions" (see [2]),

$$p^2M_bb \;+\; A_bf \;+\; p\gamma B_uB_u^*b \;=\; B_uv \tag{2.2}$$

and

$$u \;=\; B_u^*b \; .$$

We shall now specialize to $p = i\omega$, ω real.

To solve (2.1), we let

$$z \;=\; \begin{vmatrix} z_1 \\ \vdots \\ z_8 \end{vmatrix} \; ,$$

where

$$z_1 = f(0, 0, 0)$$

$$z_2 = f_x(0, 0, 0)$$

$$z_3 = f_y(s_2, 0-, 0)$$

$$z_4 = f_y(s_2, 0+, 0)$$

$$z_5 = f_z(s_T, 0, 0+)$$

$$z_6 = f_x(s_4+, 0, 0)$$

$$z_7 = f_y(s_5, 0-, 0)$$

$$z_8 = f_y(s_5, 0+, 0) \,.$$

Let

$$\mathcal{A}(-p^2) = \begin{vmatrix} 0 & I \\ A_2^{-1}(A_0 + p^2 M_0) & A_2^{-1} A_1 \end{vmatrix}$$

if $p = i\omega$,

$$\mathcal{A}(-p^2) = \mathcal{A}(\omega)$$

in the notation of [2]. From now on, let $p = i\omega$. Let

$$e^{\mathcal{A}(\omega)s} = \begin{vmatrix} P_{11}(s) & P_{12}(s) \\ P_{21}(s) & P_{22}(s) \end{vmatrix}$$

and

$$e^{\mathcal{A}_{S_2}(\omega)s} = \begin{vmatrix} P_{S_2,11}(s) & P_{S_2,12}(s) \\ P_{S_2,21}(s) & P_{S_2,22}(s) \end{vmatrix}$$

and $\mathcal{A}_{S_T}, \mathcal{A}_{S_5}$ as before in [2]. Then

$$\begin{vmatrix} f(s, 0, 0) \\ f_x(s, 0, 0) \end{vmatrix} = e^{\mathcal{A}(\omega)s} \begin{vmatrix} z_1 \\ z_2 \end{vmatrix}, \qquad 0 < s < s_2$$

and

$$\left|\begin{array}{c} f(s_2, 0, 0) \\ f_x(s_2-, 0, 0) \end{array}\right| = e^{A(\omega)s_2} \left|\begin{array}{c} z_1 \\ z_2 \end{array}\right|$$

$$\left|\begin{array}{c} f(s_2, s, 0) \\ f_y(s_2, s, 0) \end{array}\right| = e^{A S_2(\omega)s} \left|\begin{array}{c} f(s_2,0,0) \\ z_3 \end{array}\right| , \qquad -\ell_1, \leq s \leq 0$$

$$= e^{A S_2(\omega)s} \left|\begin{array}{c} f(s_2,0,0) \\ z_4 \end{array}\right| , \qquad 0 \leq s \leq \ell_1 .$$

Let us now display the values at the nodes only. Then going along the main bus: by Linkage Condition (2) (in [2]):

$$f_x(s_2+, 0, 0) = f_x(s_2-, 0, 0) + A_2^{-1} A_{2,S_2}(z_3 - z_4) .$$

Hence

$$\left|\begin{array}{c} f(s_T, 0, 0) \\ f_x(s_T-, 0, 0) \end{array}\right| = e^{A(\omega)(s_T-s_2)} \left|\begin{array}{c} f(s_2,0,0) \\ f_x(s_2+, 0, 0) \end{array}\right|$$

and

$$\left|\begin{array}{c} f(s_4, 0, 0) \\ f_x(s_4-, 0, 0) \end{array}\right| = e^{A(\omega)(s_4-s_T)} \left|\begin{array}{c} f(s_T,0,0) \\ f_x(s_T+, 0, 0) \end{array}\right| .$$

By Linkage Condition (1) (in [2]):

$$f_x(s_T+, 0, 0) = f_x(s_T-, 0, 0) - A_2^{-1}(L_{1,T}f(s_T,0,0) - A_{2,T}z_5)$$

$$\left|\begin{array}{c} f(s_5, 0, 0) \\ f_x(s_5-, 0, 0) \end{array}\right| = e^{A(\omega)(s_5-s_4)} \left|\begin{array}{c} f(s_4,0,0) \\ z_6 \end{array}\right|$$

and finally

$$\left|\begin{array}{c} f(L, 0, 0) \\ f_x(L, 0, 0) \end{array}\right| = e^{A(\omega)(L-s_5)} \left|\begin{array}{c} f(s_5, 0, 0) \\ f_x(s_5+, 0, 0) \end{array}\right|$$

where by Linkage Condition (3) (in [2]):

$$f_x(s_5+, 0, 0) = f_x(s_5-, 0, 0) + A_{2,S_3}(z_7 - z_8) .$$

Next:

$$\left| \begin{matrix} f(s_T, 0, L_T) \\ f_z(s_T, 0, L_T) \end{matrix} \right| = e^{A_{S_T}(\omega)L_T} \left| \begin{matrix} f(s_T,0,0) \\ z_5 \end{matrix} \right|$$

$$\left| \begin{matrix} f(s_5, -\ell_2, 0) \\ f_y(s_5, -\ell_2, 0) \end{matrix} \right| = e^{A_{S_5}(\omega)(-\ell_2)} \left| \begin{matrix} f(s_5,0,0) \\ z_7 \end{matrix} \right|$$

$$\left| \begin{matrix} f(s_5, +\ell_2, 0) \\ f_z(s_5, +\ell_2, 0) \end{matrix} \right| = e^{A_{S_5}(\omega)\ell_2} \left| \begin{matrix} f(s_5,0,0) \\ z_8 \end{matrix} \right| .$$

Hence we can calculate $f(\cdot, \cdot, \cdot)$ as

$$f = \mathcal{L}(\omega)z .$$

In particular we can calculate b in terms of z. Let

$$b = L_b(\omega)z$$

where $L_b(\omega)$ is a (matrix) function of ω. Let $b = \text{col. } (b_1, ..., b_8)$ and

$$L_b = \{L_{ij}\} , \qquad \text{each } L_{ij} \text{ being } 6 \times 6 .$$

Then

$$b_1 = z_1 ; \qquad L_{11} = I , \qquad L_{1i} = 0 , \qquad i \neq 1$$

$$b_2 = f(s_2, -\ell_1, 0)$$

$$= P_{S_2,11}(-\ell_1) f(s_2, 0, 0) + P_{S_2,12}(-\ell_1)z_3$$

$$= P_{S_2,11}(-\ell_1)[P_{11}(s_2)z_1 + P_{12}(s_2)z_2] + P_{S_2,12}(-\ell_1)z_3 .$$

Hence

$$L_{21} = P_{S_2,11}(-\ell_1)P_{11}(s_2)$$

$$L_{22} = P_{S_2,11}(-\ell_1)P_{12}(s_2)$$

$$L_{23} = P_{S_2,12}(-\ell_1)$$

$$b_3 = f(s_2, +\ell_1, 0) = P_{S_2,11}(+\ell_1)(P_{11}(s_2)z_1 + P_{12}(s_2)z_2) + P_{S_2,12}(\ell_1)z_4$$

$$L_{31} = P_{S_2,11}(\ell_1)P_{11}(s_2)$$

$$L_{32} = P_{S_2,11}P_{12}(s_2)$$

$$L_{33} = 0$$

$$L_{34} = P_{S_2,12}(\ell_1)$$

$$b_4 = f(s_T, 0, L_T)$$

$$= P_{S_T,11}(L_T)[P_{11}(s_T - s_2)(P_{11}(s_2)z_1 + P_{12}(s_2)z_2)$$
$$+ P_{12}(s_T - s_2)(P_{21}(s_2)z_1 + P_{22}(s_2)z_2 + A_2^{-1}A_{2,S_2}(z_3 - z_4))]$$
$$+ P_{S_T,12}(L_T)z_5$$

$$L_{41} = P_{S_T,11}(L_T)[P_{11}(s_T - s_2)P_{11}(s_2) + P_{12}(s_T - s_2)P_{12}(s_2)]$$

$$L_{42} = P_{S_T,11}(L_T)[P_{11}(s_T - s_2)P_{12}(s_2) + P_{12}(s_T - s_2)P_{22}(s_2)]$$

$$L_{43} = P_{S_T,11}(L_T)(P_{12}(s_T - s_2)A_2^{-1}A_{2,S_2})$$

$$L_{44} = -P_{S_T,11}(L_T)P_{12}(s_T - s_2)A_2^{-1}A_{2,S_2}$$

$$L_{45} = P_{S_T,12}(L_T)$$

470

$$b_5 = f(s_4, 0, 0)$$

$$L_{51} = P_{11}(s_4 - s_T)P_{11}(s_T - s_2)P_{11}(s_2) + P_{11}(s_4 - s_T)P_{12}(s_T - s_2)P_{21}(s_2)$$

$$+ P_{12}(s_4 - s_T)P_{21}(s_T - s_2)P_{11}(s_2) + P_{12}(s_4 - s_T)P_{22}(s_T - s_2)P_{21}(s_2)$$

$$- P_{12}(s_4 - s_T)P_{22}(s_T - s_2)A_2^{-1}L_{1,T}\{P_{11}(s_T - s_2)P_{11}(s_2) + P_{12}(s_T - s_2)P_{21}(s_2)\}$$

$$L_{52} = P_{11}(s_4 - s_T)P_{11}(s_T - s_2)P_{12}(s_2) + P_{12}(s_T - s_2)P_{22}(s_2)$$

$$+ P_{12}(s_4 - s_T)P_{21}(s_T - s_2)P_{12}(s_2) + P_{12}(s_4 - s_T)P_{22}(s_T - s_2)P_{22}(s_2)$$

$$- P_{12}(s_4 - s_T)P_{22}(s_T - s_2)A_2^{-1}L_{1,T}\{P_{11}(s_T - s_2)P_{12}(s_2) + P_{12}(s_T - s_2)P_{22}(s_2)\}$$

$$L_{53} = P_{11}(s_4 - s_T)P_{12}(s_T - s_2)A_2^{-1}A_{2,S_2} + P_{12}(s_4 - s_T)P_{22}(s_T - s_2)A_2^{-1}A_{2,S_2}$$

$$- P_{12}(s_4 - s_T)P_{22}(s_T - s_2)A_2^{-1}L_{1,T}\{P_{12}(s_T - s_2)A_2^{-1}A_{2,S_2}\}$$

$$L_{54} = -P_{11}(s_4 - s_T)P_{12}(s_T - s_2)A_2^{-1}A_{2,S_2}$$

$$+ P_{12}(s_4 - s_T)P_{22}(s_T - s_2)A_2^{-1}L_{1,T}\{P_{12}(s_T - s_2)A_2^{-1}A_{2,S_2}\}$$

$$L_{55} = P_{12}(s_4 - s_T)P_{22}(s_T - s_2)A_2^{-1}A_{2,T}$$

$$b_6 = f(s_5, -\ell_2, 0) = P_{S_5,11}(-\ell_2)(P_{11}(s_5 - s_4)b_5 + P_{12}(s_5 - s_4)z_6) + P_{S_5,11}(-\ell_2)z_7$$

$$L_{6i} = P_{S_5,11}(-\ell_2)P_{11}(s_4 - s_5)b_{5i}, \qquad i \leq 5$$

$$L_{66} = P_{S_5,11}(-\ell_2)P_{12}(s_4 - s_5)$$

$$L_{67} = P_{S_5,12}(-\ell_2)$$

$$b_7 = f(s_5, +\ell_2, 0)$$

$$L_{7i} = P_{S_5,11}(\ell_2)P_{11}(s_5 - s_4)L_{5i}, \qquad i \leq 5$$

$$L_{76} = P_{S_5,11}(\ell_2)P_{12}(s_5 - s_4)$$

$$L_{77} = 0$$

$$L_{78} = P_{S_5,12}(\ell_2)$$

$$b_8 = f(L, 0, 0)$$

$$L_{8i} = [P_{11}(L - s_5)P_{11}(s_5 - s_4) + P_{12}(L - s_5)P_{21}(s_5 - s_4)]L_{5i}, \qquad i \leq 5$$

$$L_{86} = P_{11}(L - s_5)P_{12}(s_5 - s_4) + P_{12}(L - s_5)P_{22}(s_5 - s_4)$$

$$L_{87} = P_{12}(L - s_5)A_2^{-1}A_{2,s_5}$$

$$L_{88} = -P_{12}(L - s_5)A_2^{-1}A_{2,s_5}$$

Hence

$$
L_b(\omega) = \begin{vmatrix}
I & 0 & 0 & 0 & 0 & 0 & 0 & 0 \\
L_{21} & L_{22} & L_{23} & 0 & 0 & 0 & 0 & 0 \\
L_{31} & L_{32} & L_{33} & L_{34} & 0 & 0 & 0 & 0 \\
L_{41} & L_{42} & L_{43} & L_{44} & L_{45} & 0 & 0 & 0 \\
L_{51} & L_{52} & L_{53} & L_{54} & L_{55} & 0 & 0 & 0 \\
L_{61} & L_{62} & L_{63} & L_{64} & L_{65} & L_{66} & L_{67} & 0 \\
L_{71} & L_{72} & L_{73} & L_{74} & L_{75} & L_{76} & 0 & L_{78} \\
L_{81} & L_{82} & L_{83} & L_{84} & L_{85} & L_{86} & L_{87} & L_{88}
\end{vmatrix}
$$

Suppose ω is a transmission zero of $\psi(i\omega)$:

$$\psi(i\omega)v = 0, \qquad\qquad v \neq 0,$$

then in the notation

$$x = \begin{vmatrix} f \\ b \end{vmatrix}$$

we have

$$A_0 f = \omega^2 M_0 f$$

$$A_b f = B_u v + \omega^2 M_b b; \qquad B_u^* b = 0$$

$$L_A(\omega)z - \omega^2 M_b L_b(\omega)z = B_u v.$$

Suppose for some z:

$$(L_A(\omega) - \omega^2 M_b L_b(\omega))z = 0.$$

Then

$$-\omega^2 M_b b + A_b f = 0$$

$$-\omega^2 M_0 f + A_0 f = 0$$

and hence

$$\omega \text{ is an undamped structure mode}$$

which would imply that

$$B_u^* b \neq 0$$

which is a contradiction. Hence

$$f = \mathcal{L}(\omega)z$$

where

$$B_u^* L_b(\omega)z = 0, \qquad\qquad z \neq 0$$

and conversely. Hence the transmission zeros of $\psi(i\omega)$ are precisely the zeros of

$$\text{Det } |B_u B_u^* L_b(\omega)| = 0 .$$

These values of ω are then the "clamped-clamped" modes of the articulated structure:

$$\left.\begin{array}{l} -\omega^2 M_0 f + A_0 f = 0, \qquad f \neq 0 \\ B_u^* b = 0 . \end{array}\right\}$$

and a subset of these corresponding to $b = 0$ or $L_b(\omega)z = 0$ are the clamped-clamped modes of the unloaded structure (every node is clamped). Let us consider first ω such that

$$\text{Det } |L_b(\omega)| \neq 0$$

so that we can invert $L_b(\omega)$. We have:

$$b_1 = z_1$$

$$b_2 - L_{21}b_1 = L_{22}z_2 + L_{23}z_3$$

$$b_3 - L_{31}b_1 = L_{32}z_2 + L_{34}z_4$$

$$b_4 - L_{41}b_1 = L_{42}z_2 + L_{43}(z_3 - z_4) + L_{45}z_5$$

where

$$z_5 = L_{55}^{-1}(b_5 - L_{51}z_1 - L_{52}z_2 - L_{53}z_3 - L_{54}z_4)$$

These four equations can be solved for z_1, z_2, z_3, z_4, in terms of b_1, ..., b_5, and then z_5 can be expressed in terms of b_5, b_4, b_3, b_2, b_1. Next

$$b_6 - P_{S_5,11}(-\ell_2)P_{11}(s_5 - s_4)b_5 = \tilde{b}_6 = L_{66}z_6 + L_{67}z_7$$

$$b_7 - P_{S_5,11}(\ell_2)P_{11}(s_5 - s_4)b_5 = \tilde{b}_7 = L_{76}z_6 + L_{78}z_8$$

$$b_8 - (P_{11}(L - s_5)P_{11}(s_5 - s_4) + P_{12}(L - s_5)P_{21}(s_5 - s_4))b_5$$
$$= \tilde{b}_8 = L_{86}z_6 + L_{87}z_7 - L_{87}z_8 .$$

These three equations can be solved for z_6, z_7, z_8:

$$L_{87}L_{67}^{-1}(\tilde{b}_6 - L_{66}z_6) - L_{87}L_{78}^{-1}(\tilde{b}_7 - L_{76}z_6) = \tilde{b}_8 - L_{86}z_6$$

$$L_{87}L_{67}^{-1}\tilde{b}_6 - L_{87}L_{78}^{-1}\tilde{b}_7 - \tilde{b}_8 = (L_{87}L_{67}^{-1}L_{66} - L_{87}L_{78}^{-1}L_{76} - L_{86})z_6 .$$

Hence

$$z_6 = (L_{87}L_{67}^{-1}L_{66} - L_{87}L_{78}^{-1}L_{76} - L_{86})^{-1}(L_{87}L_{67}^{-1}\tilde{b}_6 - L_{87}L_{78}^{-1}\tilde{b}_7 - \tilde{b}_8)$$

$$z_7 = L_{67}^{-1}(\tilde{b}_6 - L_{66}z_6)$$

$$z_8 = L_{78}^{-1}(\tilde{b}_7 - L_{76}z_6) .$$

Hence

$$z = L_b(\omega)^{-1}b , \qquad \text{Det } |L_b(\omega)| \neq 0 .$$

Next let

$$A_b f = L_A z .$$

Let us determine L_A. Now from the form of $A_b f$, it is convenient to break up L_A as

$$L_A = L_{A_1} + L_{A_2}$$

474

where

$$L_{A_1} z = \begin{vmatrix} -L_1 b_1 \\ -L_{1,S_2} b_2 \\ L_{1,S_2} b_3 \\ L_{1,T} b_4 \\ 0 \\ -L_{1,S_5} b_6 \\ L_{1,S_5} b_7 \\ L_1 b_8 \end{vmatrix}$$

and $\{b_i\}$ have been determined in terms of z_i. Next let

$$L_{A_2} z = h$$

so that

$$h_1 = -A_{21} z_2$$

$$h_2 = -A_{2,S_2} P_{S_2,21}(-\ell_1)[P_{12}(s_2)z_1 + P_{12}(s_2)z_2] - A_{2,S_2} P_{S_2,22}(-\ell_1)z_3$$

$$h_3 = A_{2,S_2} P_{S_2,21}(\ell_1)[P_{11}(s_2)z_1 + P_{12}(s_2)z_2] + A_{2,S_2} P_{S_2,22}(-\ell_1)z_3$$

$$h_4 = A_{2,S_T}\{P_{S_T,22}(L_T)z_5$$
$$+ P_{S_T,21}(L_T)[P_{11}(s_T - s_2)(P_{11}(s_2)z_1 + P_{12}(s_2)z_2)$$
$$+ P_{12}(s_T - s_2)(P_{21}(s_2)z_1 + P_{22}(s_2)z_2 + A_2^{-1}A_{2,S_2}(z_3-z_4))]\}$$

$$h_5 = A_2\Big[P_{21}(s_4 - s_T)[P_{11}(s_T - s_2)(P_{11}(s_2)z_1 + P_{12}(s_2)z_2)$$
$$+ P_{12}(s_T - s_2)(P_{21}(s_2)z_1 + P_{22}(s_2)z_2 + A_2^{-1}A_{2,S_2}(z_3 - z_4))]$$
$$+ P_{22}(s_4 - s_T)\{P_{21}(s_T - s_2)(P_{11}(s_2)z_1 + P_{12}(s_2)z_2)$$
$$+ P_{22}(s_T - s_2)(P_{21}(s_2)z_1 + P_{22}(s_2)z_2 + A_2^{-1}A_{2,S_2}(z_3 - z_4))$$
$$- A_2^{-1}L_{1,T}[P_{11}(s_T-s_2)(P_{11}(s_2)z_1 + P_{12}(s_2)z_2)$$
$$+ P_{12}(s_T-s_2)(P_{21}(s_2)z_1 + P_{22}(s_2)z_2 + A_2^{-1}A_{2,S_2}(z_3-z_4))]$$
$$+ A_2^{-1}A_{2,T}z_5\}\Big]$$

$$h_6 = -A_{2,s_5}\{P_{s_5,21}(-\ell_2)(P_{11}(s_5 - s_4)b_5 + P_{12}(s_5 - s_4)z_6) + P_{s_5,22}(-\ell_2)z_7\}$$

$$h_7 = A_{2,s_5}\{P_{s_5,21}(\ell_2)(P_{11}(s_5 - s_4)b_5 + P_{12}(s_5 - s_4)z_6 + P_{s_5,22}(\ell_2)z_8\}$$

$$h_8 = A_2\{P_{21}(L - s_5)[P_{11}(s_5 - s_4)b_5 + P_{12}(s_5 - s_4)z_6]$$
$$+ P_{22}(L - s_5)[P_{12}(s_5 - s_4)b_5 + P_{22}(s_5 - s_4)z_6 + A_2^{-1}A_{2,s_5}(z_7 - z_8)]\} .$$

Hence finally, in terms of L_A and L_b, (2.2) becomes

$$(-\omega^2 M_b L_b + L_A + \gamma i\omega B_u B_u^* L_b)z = B_u v .$$

For ω such that $L_b(\omega)$ is nonsingular we can write:

$$u = B_u^* b = B_u^* L_b(-\omega^2 M_b L_b + L_A + \gamma i\omega B_u B_u^* L_b)^{-1} B_u v$$

$$= B_u^*(-\omega^2 M_b + L_A L_b^{-1} + \gamma i\omega B_u B_u^*)^{-1} B_u v .$$

Here

$$B_u \text{ is } 48 \times 8$$

$$B_u^* \text{ is } 8 \times 48$$

and

$$(-\omega^2 M_b + L_A L_b^{-1} + \gamma i\omega B_u B_u^*)^{-1} \text{ is } 48 \times 48$$

and is conveniently broken up into 6×6 blocks, denoted

$$D = \{D_{ij}\} , \qquad i, j = 1,...,8 .$$

We can now calculate

$$B_u^* D B_u .$$

Now

$$B_u u = \begin{vmatrix} B_{u_1} u \\ \vdots \\ B_{u_8} u \end{vmatrix}$$

where each B_{u_i} is 6×8, and letting

$$u = \begin{vmatrix} u_1 \\ u_2 \\ \vdots \\ u_8 \end{vmatrix}$$

we have

$$B_{u_1} u = \text{col} [\ 0,\ u_1,\ u_2,\ 0,\ 0,\ 0\ ]$$

$$B_{u_2} = B_{u_3} = 0$$

$$B_{u_4} u = \text{col} [\ u_3,\ u_4,\ 0,\ 0,\ 0,\ 0\ ]$$

$$B_{u_5} u = \text{col} [\ 0,\ u_5,\ u_6,\ 0,\ 0,\ 0\ ]$$

$$B_{u_6} = B_{u_7} = 0$$

$$B_{u_8} u = \text{col} [\ u_7,\ u_8,\ 0,\ -40u_8,\ 40u_7,\ 0\ ].$$

Hence letting

$$b = \begin{vmatrix} b_1 \\ \vdots \\ b_8 \end{vmatrix}$$

$$B_u^* b = \sum_1^8 B_{u_i}^* b_i = B_{u_1}^* b_1 + B_{u_4}^* b_4 + B_{u_5}^* b_5 + B_{u_8}^* b_8$$

and writing

$$h = \begin{vmatrix} u \\ v \\ w \\ \phi_1 \\ \phi_2 \\ \phi_3 \end{vmatrix}$$

$$B_{u_1}^* h = \text{col} [\ v,\ w,\ 0,\ 0,\ 0,\ 0,\ 0,\ 0\ ]$$

$$B_{u_4}^* h = \text{col} [\ 0,\ 0,\ u,\ v,\ 0,\ 0,\ 0,\ 0\ ]$$

$$B_{u_5}^* h = \text{col} [\ 0,\ 0,\ 0,\ 0,\ v,\ w,\ 0,\ 0\ ]$$

$$B_{u_8}^* h = \text{col} [\ 0,\ 0,\ 0,\ 0,\ 0,\ 0,\ u+40\phi_2,\ v-40\phi_1\ ].$$

Hence

$$(B_u^* D B_u) v = B_{u_1}^* \sum_1^8 D_{1j} B_{u_j} v + B_{u_4}^* \sum_1^8 D_{4j} B_{u_j} v + B_{u_5}^* \sum_1^8 D_{5j} B_{u_j} v + B_{u_8}^* \sum_1^8 D_{8j} B_{u_j} v$$

$$= B_{u_1}^* (D_{11} B_{u_1} + D_{14} B_{u_4} + D_{15} B_{u_5} + D_{18} B_{u_8}) v$$

$$+ B_{u_4}^* (D_{41} B_{u_1} + D_{44} B_{u_4} + D_{45} B_{u_5} + D_{48} B_{u_8}) v$$

$$+ B_{u_5}^* (D_{51} B_{u_1} + D_{54} B_{u_4} + D_{55} B_{u_5} + D_{58} B_{u_8}) v$$

$$+ B_{u_8}^* (D_{81} B_{u_1} + D_{84} B_{u_4} + D_{85} B_{u_5} + D_{88} B_{u_8}) v .$$

This shows in particular that we do not need to calculate all the D_{ij}. Also the controls at location S_i, $i = 1, 4, 5, 8$ are given by

$$B_{u_i}^* (D_{i1} B_{u_1} + D_{i4} B_{u_4} + D_{i5} B_{u_5} + D_{i8} B_{u_8}) v = B_{u_i}^* D_{ii} B_{u_i} v + \sum_{j \neq i} B_{u_i}^* D_{ij} B_{u_j} v ,$$

where the first term involves only the sensors at locations S_i, and the summation represents the coupling to sensors at other locations. Also

$$B_{u_1}^* D_{11} B_{u_1} v = \begin{vmatrix} D_{11,22} v_1 + D_{11,23} v_2 \\ D_{11,32} v_1 + D_{11,33} v_2 \\ 0 \\ \vdots \\ 0 \end{vmatrix} \qquad v = \begin{vmatrix} v_1 \\ v_2 \\ \vdots \\ v_8 \end{vmatrix}$$

where

$$D_{11} = \{D_{11,ij}\} , \qquad i, j = 1, \ldots, 6 .$$

Similarly

$$B_{u_4}^* D_{44} B_{u_4} = \begin{vmatrix} 0 \\ 0 \\ D_{44,11} v_3 + D_{44,12} v_4 \\ D_{44,21} v_3 + D_{44,22} v_4 \\ 0 \\ 0 \\ 0 \\ 0 \end{vmatrix}$$

478

$$B_{u_5}^* D_{55} B_{u_5} = \begin{vmatrix} 0 \\ 0 \\ 0 \\ 0 \\ D_{55,22}v_5 + D_{55,23}v_6 \\ D_{55,32}v_5 + D_{55,33}v_6 \\ 0 \\ 0 \end{vmatrix}$$

$$B_{u_8}^* D_{88} B_{u_8} = \begin{vmatrix} 0 \\ 0 \\ 0 \\ 0 \\ 0 \\ 0 \\ (D_{88,11}+40D_{88,15})v_7 + (D_{88,12}-40D_{88,14})v_8 \\ \quad + 40\{(D_{88,51}+40D_{88,55})v_7 + (D_{88,52}-40D_{88,54})v_8\} \\ (D_{88,21}+40D_{88,25})v_7 + (D_{88,22}-40D_{88,24})v_8 \\ \quad + 40\{(D_{88,41}+40D_{88,45})v_7 + (D_{88,42}-40D_{88,44})v_8\} \end{vmatrix}$$

It must be noted that in terms of feedback

$$v_1 = \dot{v}(0)$$

$$v_2 = \dot{w}(0)$$

$$v_3 = \dot{u}(S_T) + 100\dot{\phi}_2(S_T)$$

$$v_4 = \dot{v}(S_T) - 100\dot{\phi}_1(S_T)$$

$$v_5 = \dot{v}(S_4)$$

$$v_6 = \dot{w}(S_4)$$

$$v_7 = \dot{u}(L) + 40\dot{\phi}_2(L)$$

$$v_8 = \dot{v}(L) - 40\dot{\phi}_1(L) ,$$

the dot denoting derviative.

Let

$$T(i\omega) = L_A(\omega)L_b(\omega)^{-1}$$

so that the poles of $T(i\omega)$ are the zeros of $L_b(\omega)$. We shall show that $T(i\omega)$ is self-adjoint but not nonnegative definite! Let b_1, b_2 be arbitrary real, and let

$$L_b(\omega)^{-1}b_1 = z_1$$

$$L_b(\omega)^{-1}b_2 = z_2$$

$$f_1 = \mathcal{L}(\omega)z_1$$

$$f_2 = \mathcal{L}(\omega)z_2$$

$$x_1 = \begin{vmatrix} f_1 \\ b_1 \end{vmatrix} ; \qquad x_2 = \begin{vmatrix} f_2 \\ b_2 \end{vmatrix} .$$

Then

$$[Ax_1, x_2] = [A_0 f_1, f_2] + [A_b f_1, b_2] = \omega^2 [M_0 f_1, f_2] + [A_b f_1, b_2] .$$

Similarly

$$[Ax_2, x_1] = [A_b f_2, b_1] + \omega^2 [M_0 f_2, f_1] .$$

Since

$$[Ax_1, x_2] = [Ax_2, x_1]$$

we have

$$[A_b f_2, b_1] = [A_b f_1, b_2]$$

or,

$$[A_b f_1, b_2] = [L_A(\omega)L_b(\omega)^{-1}b_1, b_2] = [A_b f_2, b_1] = [L_A(\omega)L_b(\omega)^{-1}b_2, b_1] .$$

Hence $T(i\omega)$ is self-adjoint. Next

$$[T(i\omega)b_1, b_1] = [A_b f_1, b_1] = [Ax_1, x_1] - \omega^2 [M_0 f_1, f_1] .$$

Hence $T(i\omega)$ is not nonnegative definite. Note finally that the structure modes frequencies can be expressed:

$$\text{Det } |-\omega^2 M_b + T(i\omega)| = 0 .$$

480

References

[1] "Langley's CSI Evolutionary Model: Phase Zero." NASA TN 104165. November 1991.

[2] A. V. Balakrishnan. "Modes of Interconnected Lattice Trusses Using Continuum Models, I." NASA CR 189568. December 1991.

[3] A. V. Balakrishnan. "An Explicit Solution to the Optimal LQG Problem for Flexible Structures with Collocated Rate Sensors." In: *Proceedings of the 5th NASA-DOD CSI Technology Conference, Lake Tahoe, Nevada, March 1992.*

RATIONAL POSITIVE REAL APPROXIMATIONS
FOR LQG OPTIMAL COMPENSATORS
ARISING IN ACTIVE STABILIZATION OF FLEXIBLE STRUCTURES

A. De Santis

IASI-CNR, v.le Manzoni 30, 00185 Rome, Italy.

p. 14

SUMMARY

In this paper the approximation problem for a class of optimal compensators for flexible structures is considered. The particular case of a simply supported truss with an offset antenna is dealt with. The nonrational positive real optimal compensator transfer function is determined, and it is proposed that an approximation scheme based on a continued fraction expansion method be used. Comparison with the more popular modal expansion technique is performed in terms of stability margin and parameters sensitivity of the relative approximated closed loop transfer functions.

INTRODUCTION

The problem of active stabilization of flexible structures with collocated sensors/actuators is addressed. In particular, the case of an offset antenna linked by a truss to the Shuttle body is considered. A general theory has been already established in [1] as optimal LQG problem for abstract wave equations. The results obtained were applied in [2] to design an optimal compensator for the antenna vibrations suppression after a slewing action, by modelling the truss as a uniform Bernouilli beam, simply supported at the Shuttle end, with rate-sensor/actuator collocated at the antenna end. The compensator transfer function was determined as nonrational, positive real function. This class of functions was shown to provide robust stabilizers for vibrating systems, even in the case of lumped parameter systems [3]. Nevertheless, rational approximation schemes are needed in order to instrument the compensator. A technique usually adopted is the modal expansion, and a typical controller realization can be found in [3] as a bank of filters, centered at the frequencies of the system undumped modes. Other methods can be borrowed from networks synthesis framework, where the rational approximation of positive real functions is a standard problem in telecommunications filters design. Standard references on these problems are [5], [6]. Despite a good approximation of some

characteristics of the frequency response (amplitude, real part, etc.) can be obtained, the positive real character of the approximating function is not guaranteed, as opposite the modal expansion does for the class of systems considered. This is crucial in our control problems since, as mentioned above, positive realness ensures the structure stabilization. Anyway, the main drawback is just the modal frequencies computation, obtained by solving a transcendental equation.

In this paper the compensator transfer function is explicitly computed in the vector case of yaw torsion plus roll bending deformation. It is shown to converge to a diagonal constant matrix as the control energy increases without bound. Rational positive real approximations are deviced via a continued fraction expansion technique [7]. Approximations of any order can be easily derived, with coefficients straightforwardly related to the system parameters. Moreover, the positive real character is guaranteed. The performances of the approximated closed loop transfer function are evaluated. Comparison with the modal approximation method is performed in terms of stability margins and sensitivity to parameters variations.

THE OPTIMAL COMPENSATOR DESIGN

We resume in this section the known results about the model and the LQG problem for the case of a simply supported uniform Bernouilli beam with an offset antenna, with rate-sensor/actuator collocated at the antenna end [2]. Actually, the particular case of roll bending deformation (x axis) plus yaw torsion (z axis) is considered. In the sequel $u_\phi(t,s)$ denotes the x axis displacement and $u_\psi(t,s)$ the angular displacement about the z axis; t and $s \in (0,l)$ indicate the time variable and the space displacement along the beam axis, respectively. The starting point is the following state space model

$$M\ddot{x}(t) + Ax(t) + Bu(t) + BN_s(t) = 0 \qquad (1.1)$$

$$v(t) = B^*\dot{x}(t) + N_o(t) \qquad (1.2)$$

where

$x(t) \in$ Hilbert Space $\mathcal{H}$

M : linear bounded, self-adjoint positive definite operator on $\mathcal{H}$ onto $\mathcal{H}$, with bounded inverse

A : closed linear operator with domain dense in $\mathcal{H}$ and range in $\mathcal{H}$

$u(\cdot)$: the control input $\in E^n$, Euclidean n-space

B : linear mapping $E^n \to \mathcal{H}$

$N_s(\cdot)$: white Gaussian noise with spectral density dsI, where I is the identity operator of suitable dimension

$N_o(\cdot)$: white Gaussian noise with spectral density d_oI, independent of $N_s(.)$

$v(.)$ sensor data.

The definiton of operators A, M and B, as well as the definition of the space $\mathcal{H}$, embody the beam plus antenna dynamical model and the boundary conditions stated in [2]. For convenience we report these definitions:

$$
x = \begin{bmatrix} u_\phi(\cdot) \\ u_\psi(\cdot) \\ u\phi(l) \\ u'_\phi(l) \\ u_\psi(l) \end{bmatrix} \; ; \quad
Ax = \begin{bmatrix} A_f f \\ A_b f \end{bmatrix} = \begin{bmatrix} EI_\phi u_\phi''''(\cdot) \\ -GI_\psi u_\psi''(\cdot) \\ -EI_\phi u_\phi'''(l) \\ EI_\phi u_\phi''(l) \\ GI_\psi u_\psi'(l) \end{bmatrix} \; ; \quad
Bu = \begin{bmatrix} 0 \\ u(\cdot) \end{bmatrix} \quad
Mx = \begin{bmatrix} M_f f \\ M_b b \end{bmatrix}
$$

$$
M_f f = \begin{bmatrix} \rho a\, u_\phi \\ \rho I_\psi\, u_\psi \end{bmatrix} \; ; \quad
M_b = \begin{bmatrix} m & 0 & mrx \\ & & \\ 0 & I_M & \\ m\,r_x & & \end{bmatrix} ,
$$

where ρ is the beam mass density, a the cross sectional area, l the beam length, EI_ϕ, GI_ψ are the beam flexural and torsional rigidity respectively, m is the antenna mass and r_x is the antenna c.o.g displacement, I_M is the 2×2 relevant moment of inertia matrix of the whole structure.

We consider the problem of stabilizing the antenna after a slewing action has occurred, by determining the control $u(.)$ that minimizes the time average

$$
\lim_{T \to \infty} \frac{1}{T} \left(\int_0^T \|B^* \dot{x}(t)\|^2 \, dt + \lambda \int_0^T \|u(t)\|^2 \, dt \right), \qquad \lambda > 0.
$$

If (A, B) is controllable in [2] it is shown that the optimal compensator transfer function is given by

$$
\Psi(\mu) = \alpha \mu B^* (\mu^2 M + A + \gamma \mu B B^*)^{-1} B \tag{1.3}
$$

where

$$\alpha = \sqrt{d_s/d_o}\,\lambda, \qquad \gamma = \sqrt{d_s/d_o} + \frac{1}{\lambda}.$$

$\Psi(\mu)$ is shown to be a positive real function, thus defining a robust controller [3].

THE APPROXIMATION SCHEME

The compensator transfer function explicit determination. In order to compute explicitly the compensator transfer function from eqn. (1.3) consider the following expression

$$(\mu^2 M + A + \mu\gamma BB^*)x = Bv \tag{2.1}$$

which, by taking into account the definitions given in the previous section, can be split in the following two relationships

$$\mu^2 M_f f + A_f f = 0 \tag{2.2}$$

$$\mu^2 M_b b + A_b f + \mu\gamma b = v. \tag{2.3}$$

By recalling that $f = [u_\phi(\cdot)\, u_\psi(\cdot)]^*$, (2.2) is solved with the clamped end conditions $u_\phi(0) = u'_\phi(0) = u_\psi(0) = 0$, obtaining

$$u_\phi(s) = c_1\,\phi_1(s) + c_2\,\phi_2(s)$$
$$u_\psi(s) = c_3 \sinh(k_\psi s) \qquad s \in [0, l),$$

where

$$\phi_1(s) = \sinh(k_\phi s) - \sin(k_\phi s) \qquad \phi_2(s) = \cosh(k_\phi s) - \cos(k_\phi s)$$

$$k_\phi = (\rho a/(EI_\phi))^{(1/4)} \sqrt{i\mu} \qquad k_\psi = \sqrt{\rho/G}\,\mu.$$

For the constants c_1, c_2 the following formulas hold

$$\begin{bmatrix} c_1 \\ c_2 \end{bmatrix} = \begin{bmatrix} \phi_1(l) & \phi(l) \\ \phi'_1(l) & \phi'_2(l) \end{bmatrix}^{-1} \begin{bmatrix} \phi_1(l) \\ \phi_2(l) \end{bmatrix}; \qquad c_3 = \frac{u_\psi(l)}{\sinh(k_\psi l)},$$

moreover

$$u_\phi^{(n)}(\cdot) = [\phi_1^{(n)}(\cdot) \quad \phi_2^{(n)}(\cdot)] \begin{bmatrix} \phi_1(l) & \phi_(l) \\ \phi_1'(l) & \phi_2'(l) \end{bmatrix}^{-1} \begin{bmatrix} \phi_1(l) \\ \phi_2(l) \end{bmatrix}, \qquad n = 0, 1, 2 \dots .$$

Now it can be shown that $A_b f$ can be actually expressed as $T(\mu)b$ [4] so that (2.1) becomes

$$(\mu M_b + T(\mu) + \mu\gamma I)b = v$$

and the compensator transfer function is defined as

$$\Psi(\mu) = \alpha\mu(\mu^2 M_b + T(\mu) + \mu\gamma I)^{-1}, \tag{2.4}$$

where I is the identity operator. Recalling the definition of α and γ, we see that

$$\lim_{\lambda \to 0} \Psi(\mu) = \sqrt{d_s/d_o}\, I$$

so that we have the "direct connection" if the control energy increases without bound.

We list below the non zero entries of the 3×3 matrix $T(\mu)$

$$T_{11}(\mu) = -EI_\phi k_\phi^3 \frac{\sinh(k_\phi l)\cos(k_\phi l) + \sin(k_\phi l)\cosh(k_\phi l)}{\Delta}$$

$$T_{12}(\mu) = T_{21}(\mu) = EI_\phi k_\phi^2 \frac{\sinh(k_\phi l)\sin(k_\phi l)}{\Delta}$$

$$T_{22}(\mu) = EI_\phi k_\phi \frac{\sinh(k_\phi l)\cos(k_\phi l) - \sin(k_\phi l)\cosh(k_\phi l)}{\Delta}$$

$$T_{33}(\mu) = GI_\psi k_\psi \coth(k_\psi l)$$

$$\Delta = -1 + \cosh(k_\phi l)\cos(k_\phi l).$$

$T(\mu)$ is a meromorphic function; i.e. it is analytic in all the plane but in a countable set of points, where it has polar singularities [8].

The continued fraction expansion approximation. In order to approximate (2.4) note that if a matrix is positive real so is its inverse; consequently it is of great simplification to work on

$$\frac{1}{\mu}(\mu^2 M_b + T(\mu) + \gamma \mu I). \tag{3.1}$$

Next, since for $\mu = i\omega$ the function $T(\mu)$ is real, we see that the real part of (2.5) does not depend on $T(\mu)$, so that whatever approximation we device, a positive real approximate function is obtained. Thus let us concentrate on $T(\mu)$.

The approximation scheme proposed consists of a continued fraction expansion of a meromorphic function $f(z)$, i.e.

$$f(z) = r_0(z) + \cfrac{1}{r_2(z) + \cfrac{1}{r_3(z) + \cfrac{1}{r_4(z) + \ldots}}} \tag{3.2}$$

where the $r_i(z), i = 0, 1, 2, \ldots$ are rational functions of finite degree suitably defined, and are called "convergents" of the continued fraction. The meaning of (3.1) is the following [7]: denoting $f_n(z)$ the function obtained by considering n convergents on the r.h.s we have

$$\lim_{n \to \infty} f_n(z) = f(z)$$

for every value of z in the complex plane.

The functions $r_i(z)$ can be determined according to the following algorithm.

step 1. Consider the Laurent expansion about the origin of $f(z)$ (see e.g. any standard book on complex analysis or passive networks synthesis)

$$f(z) = \sum_{k=0}^{n_0} a_{-k} z^{-k} + \sum_{k=1}^{\infty} a_k z^k.$$

The finite sum is called "singular part" of $f(z)$ at the origin, n_0 is the multiplicity of the pole at the origin and set $r_0(z) = \sum_{k=0}^{n_0} a_{-k} z^{-k}$; it can eventually be a constant ($n_0 = 0$); i.e. the function is regular at $z = 0$.

step 2. Compute

$$f_1(z) = f(z) - r_0(z),$$

then $f_1(z)$ has the same poles as $f(z)$ but the pole at $z = 0$. Moreover it holds

$$f(z) = r_0(z) + f_1(\cdot) \qquad (i)$$

$$\lim_{z \to 0} f_1(z) = 0. \qquad (ii)$$

Note that (i) is not a local expansion but an exact representation of $f(z)$ with its singular behaviour at $z = 0$ explicited.

step 3. Consider

$$f_2(z) = 1/f_1(z);$$

it has a pole in the origin according to (ii), then use the argument of steps 1 and 2 to determine $f_2(z) = r_1(z) + f_3(z)$ with $r_1(z) = \sum_{k=0}^{n_1} b_{-k} z^{-k}$ and n_1 is the multiplicity of the pole at $z = 0$ of $f_2(z)$. Since $f_1(z) = 1/f_2(z)$ we have

$$f(z) = r_0(z) + \frac{1}{r_1(z) + f_3(z)}.$$

It is clear at this point how to obtain expansion (3.1) by repeating step 3 and determining recursively all the convergents $r_k(z)$, $k = 0, 1, 2 \ldots$. For completeness let us see how to easily obtain the coefficients of the singular part of the Laurent expansion at the origin of a meromorphic function $f(z)$

$$a_{-n} = \lim_{z \to 0} z^n f(z)$$

$$a_{-k} = \lim_{z \to 0} z^k \left(f(z) - \sum_{i=1}^{n-k} a_{-n-1+i} z^{-n-1+i} \right).$$

The algorithm described can be applied to each entry of $T(\mu)$ obtaining an expansion of the following type

$$R^{i,j}(\mu) = k_0^{i,j} + \cfrac{1}{\dfrac{k_{11}^{i,j}}{\mu^4} + k_{10}^{i,j} + \cfrac{1}{\dfrac{k_{21}^{i,j}}{\mu^4} + k_{20}^{i,j} + \cfrac{1}{\dfrac{k_{31}^{i,j}}{\mu^4} + k_{30} + \cfrac{1}{\ldots}}}}, \qquad (3.3)$$

and consequently the n-th order approximation $T_n(\mu)$ of $T(\mu)$ is obtained as

$$T_n(\mu) = \begin{bmatrix} \dfrac{EI_\phi}{l^3} R_n^{1,1}(\mu) & \dfrac{EI_\phi}{l^2} R_n^{1,2}(\mu) & 0 \\[2mm] \dfrac{EI_\phi}{l^2} R_n^{2,1}(\mu) & \dfrac{EI_\phi}{l} R_n^{2,2}(\mu) & 0 \\[2mm] 0 & 0 & \dfrac{GI_\psi}{l} R_n^{3,3}(\mu) \end{bmatrix}$$

Here $R_n^{i,j}(\mu)$ is obtained by (3.3) including n convergents in the continued fraction. This number needs not be the same for all the entries, and in this case the order for $T_n(\mu)$ is determined by the highest value of n used.

In the following table are reported the coefficients of the continued fraction expansion up to the 4-th order of the entries of $T(\mu)$, for a particular choice of the system parameters (see [9]).

Table 1. Coefficients of the Continued Fraction Expansion of $T(\mu)$ entries.

	$R^{1,1}$	$R^{1,2}$	$R^{2,2}$	$R^{3,3}$
k_0	12	-6	4	1
k_{11}	-2.7	19.1	-105	3
k_{10}	.0026	$-.028$	.18	.2
k_{21}	411815.38	-74697.1	-10.2	-175
k_{20}	-451.03	50.57	21610.7	-7.7
k_{31}	94.35	714.4	-3434.97	35.64
k_{30}	.0185	$-.104$	.4	.61
k_{41}	5501900	-921286.76	244973.48	-782.41
k_{40}	321.53	44.58	-10.15	-7.08

We stress that the coefficients of the approximations are easily obtained just by computing limits in the origin of suitably defined functions, and are simple combinations of the system parameters which appear in the coefficients of the function to be approximated. As a result we have a procedure which is numerically robust

since no solution of transcendental equations are required, no derivatives determination, no inner products computations, no variable transformations as usually occurs in the most popular approximation methods. This straightforward relation to the system parameters determines also a low sensitivity to parameters variation of the approximated closed loop transfer functions, as we will show next.

For convenience, we report briefly the modal expansion technique (see [3]). Let ω_k, $k = 1, 2, \ldots$, the system undamped modes, and ψ_k, $k = 1, 2, \ldots$, the M-orthogonal eigenvectors, normalized as $[M\psi_k, \psi_k] = 1$. The following compensator transfer function modal approximation can be deviced

$$\sqrt{\frac{d_s}{\lambda d_0}} \sum_{k=1}^{\infty} \frac{\mu b_k b_k^*}{\mu^2 + \omega_k^2 + \mu \gamma b_{kk}}, \qquad \text{Re}\mu \geq 0,$$

where

$$b_k = B^* \psi_k, \qquad b_{kk} = [b_k, b_k].$$

Thus we have a bank of band pass filters centered at the undamped modes.

CLOSED LOOP TRANSFER FUNCTION PERFORMANCES EVALUATION

In this section we compare the performances of the approximation method proposed with respect to the modal expansion technique, widely used in this field. In particular the stability margins of the approximate closed loop transfer function are considered and the sensitivity of this performance index toward system parameter variation is evaluated.

As it is well known the stability properties mentioned can be derived by examining the frequency behaviour of the following function

$$S(\omega) = \det(I + P(\omega)\Psi(\omega)),$$

where $P(\omega)$ is the system transfer function, in our case defined as

$$P(\omega) = (T(\omega) - \omega^2 M_b)^{-1}.$$

Actually, we are more interested in the sensitivity of stability margins with respect to parameters variations. In Fig. 1 amplitude and phase plots of the diagonal

entries of $F(\omega) = P(\omega)\Psi(\omega)$ are reported for a second order continued fraction approximation of $\Psi(\omega)$. In Fig. 2 are reported the corresponding plots for a modal approximation based on two band pass filters centered on the first two modes. Particularly interesting are the phase plots showing that in the first case we obtain a higher phase margin, practically equal to $\pi/2$ for all frequencies. A similar result holds for the other entries of $F(\omega)$, thus giving a description of the stability features achieved in both approximation schemes, avoiding to get through the complexity of the function $S(\omega)$.

Moreover, in Fig. 3 are reported the plots of the sensitivity of the phase functions considered, with respect to the variation of the parameter $\theta = \frac{\rho a}{EI_\phi}$. Here we note that the continued fraction approximation shows a better performance in terms of robustness than the modal expansion.

CONCLUSIONS

The continued fraction method proposed allows to approximate any meromorphic function by operating simple computations on the coefficients, i.e. the determinations of the limit in the origin of suitable functions derived by the assigned one. This results in a good performance of the approximation in terms of stability margins and robustness of the approximate closed loop transfer function. This feature is highlighted by comparing the mentioned characteristics with the analogous one obtained by using the more popular modal approximation scheme.
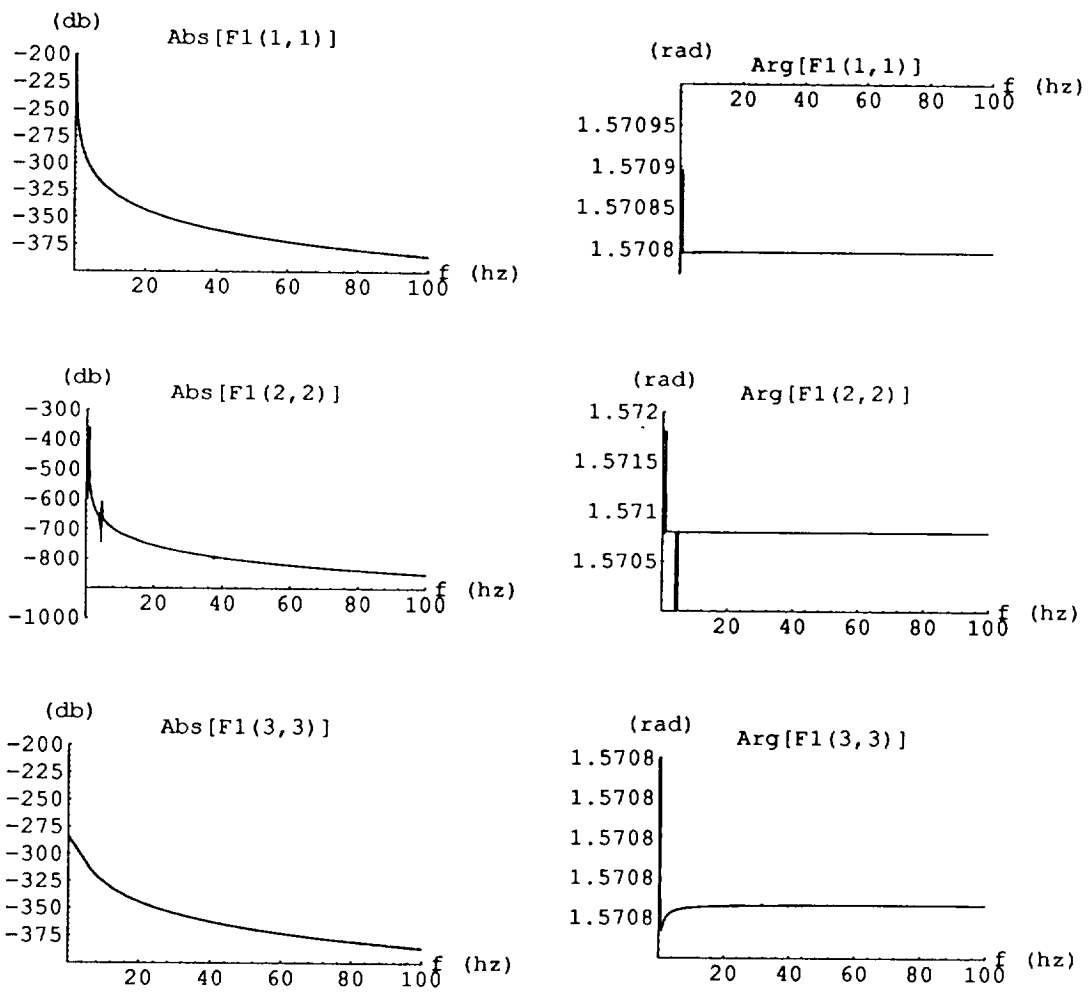
Fig. 1 Continued Fraction Approximation.
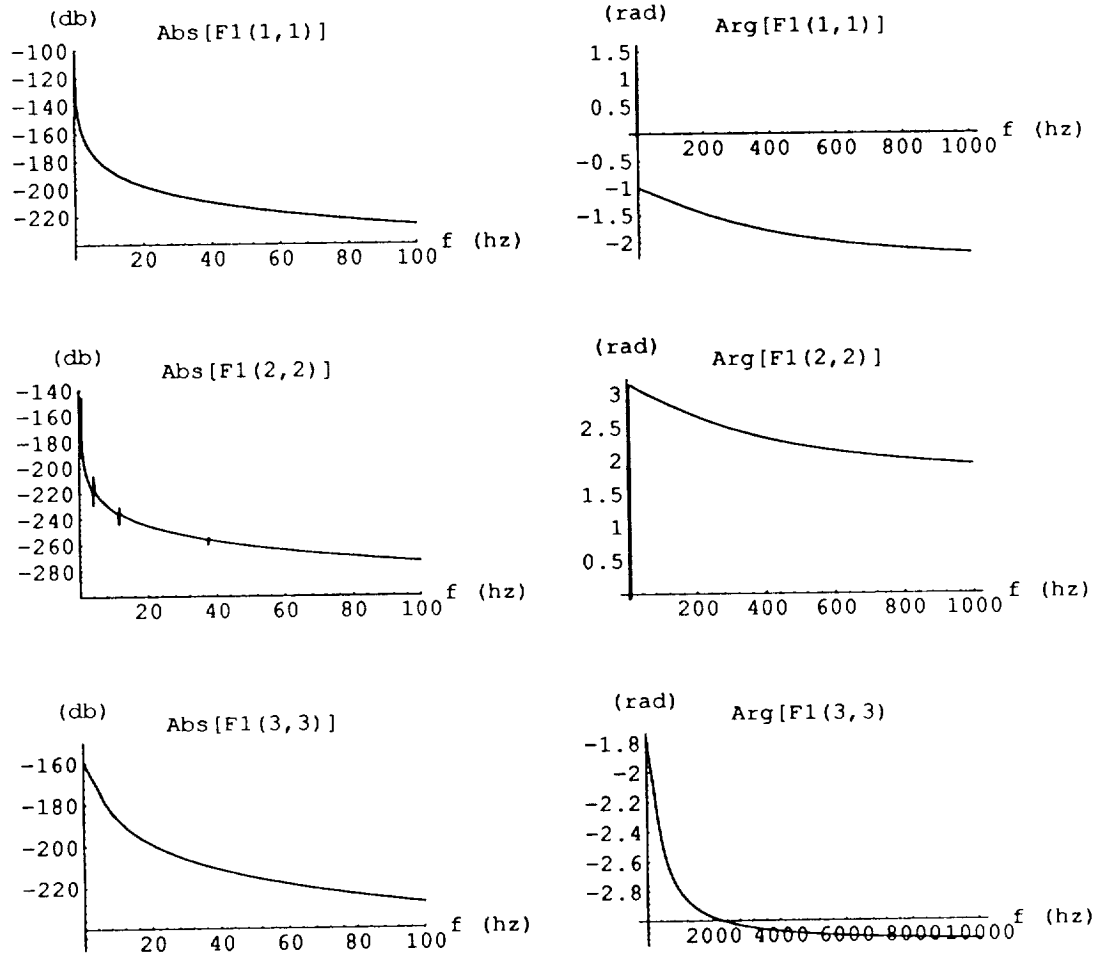
Fig. 2 Modal Expansion Approximation.

Fig. 3 Sensitivity to Parameter $\theta = \frac{\rho a}{EI_\phi}$

REFERENCES

1. A.V. Balakrishnan: Stochastic Regulator Theory for a Class of Abstract Wave Equations. *SIAM Jou. on Contr. Opt.*, vol. 29, no. 6, November 1991, pp. 1288-1299.

2. A.V. Balakrishnan: Compensator Design for Stability Enhancement with Collocated Controllers. *IEEE Trans. on A.C.*, vol. 36, no. 9, September 1991, pp. 994-1007.

3. A.V. Balakrishnan: Robust Stabilizing Compensator for Flexible Structures with Collocated Controls. Submitted to *IEEE Trans. on A.C.*, September 1991.

4. A.V. Balakrishnan:Compensator Design for Stability Enhancement with Collocated Controllers: Explicit Solutions. *IEEE Trans. on A.C.*, to appear in January 1993.

5. E.A. Guillemin:*Synthesis of Passive Networks*. Wiley, 1962.

6. D.F. Tuttle:*Network Synthesis*. Wiley, 1958.

7. E.W. Cheney:*Introduction to Approximation Theory*. McGraw-Hill, 1966.

8. E. Hille:*Analytic Function Theory*, vol 2. Ginn, 1962.

9. L.W. Taylor Jr; and A.V. Balakrishnan:*A Mathematical Problem and a Spacecraft Control Laboratory Experiment (SCOLE) Used to Evaluate Control Laws for Flexible Spacecraft*. NASA/IEEE Design Challenge, June, 1984.

DYNAMICAL OBSERVER FOR A FLEXIBLE BEAM VIA FINITE ELEMENT APPROXIMATIONS

Authors:

Andre Manitius

Hongxing Xia

Electrical & Computer Engineering

George Mason University

Fairfax, VA 22030

Motivation

1. The purpose of this work is a computational investigation of the closed-loop output feedback control of an Euler-Bernoulli beam based on finite element approximation.

2. The observer is part of the classical observer + state feedback control, but it is finite-dimensional.

3. In the theoretical work on the subject it is assumed (and sometimes proved) that increasing the number of finite elements will improve accuracy of the control. In applications,this may be difficult to achieve because of numerical problems.

4. The main difficulty in computing the observer and simulating its work is the presence of high frequency eigenvalues in the finite-element model and poor numerical conditioning of some of the system matrices (e.g. poor observability properties) when the dimension of the approximating system increases. This work dealt with some of these difficulties.

498

Euler-Bernoulli Beam
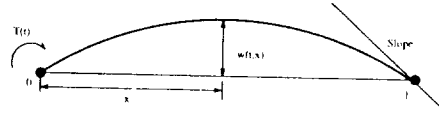
$$\rho w_{tt} + EI w_{xxxx} = 0 \qquad (1)$$
$$\text{on } [0 \ l]$$

where

$w(\bullet, \ 0) = w_0$

$w_t(\bullet, \ 0) = w_1$

$w_{xx}(t, \ 0) = u(t) \qquad \textbf{(Torque)}$

$w_{xx}(t, \ l) = 0$

$z(t) = w_x(t, \ l) \qquad \textbf{(Measurement)}$

Cubic FE Model

$$\phi_1 = 1 - 3(\frac{x - x_e}{h_e})^2 + 2(\frac{x - x_e}{h_e})^3 \qquad (2)$$

$$\phi_2 = -(x - x_e)(1 - \frac{x - x_e}{h_e})^2 \qquad (3)$$

$$\phi_3 = 3(\frac{x - x_e}{h_e})^2 - 2(\frac{x - x_e}{h_e})^3 \qquad (4)$$

$$\phi_4 = -(x - x_e)[(\frac{x - x_e}{h_e})^2 - \frac{x - x_e}{h_e}] \qquad (5)$$

Where

$\phi_1(x_e) = 1 \qquad \phi_i(x_e) = 0 \qquad i \neq 1$

$\phi_3(x_e + h_e) = 1$

$-\frac{d\phi_2}{dx}|_{x=x_e} = 1$

$-\frac{d\phi_4}{dx}|_{x=x_e + h_e} = 1$

Numerical Aspects

- System (8) is poorly conditioned numerically for large N.

- To improve numerical accuracy it is important to

a). solve directly (6) rather than (8).

b). use a Cholesky decomposition of M to avoid direct inversion of M in (6).

c). use a numerical integration method that is energy preserving on principal modes.

F-E Approximation to E-B beam

$$M\ddot{y} + Ly = Qu(t) \qquad (6)$$

$$z = C \begin{bmatrix} y \\ \dot{y} \end{bmatrix} \qquad (7)$$

First-order system

$$\dot{X}^N = \begin{bmatrix} 0 & I \\ -M^{-1}L & 0 \end{bmatrix} X^N + \begin{bmatrix} 0 \\ Q \end{bmatrix} u(t) \qquad (8)$$

$$z = C X^N \qquad (9)$$

Dimension of $\begin{bmatrix} 0 & I \\ -M^{-1}L & 0 \end{bmatrix}$:

$N \times$ position
$+ \; N \times$ slope
$+ \; N \times$ velocity
$+ \; N \times$ derivative of the slope
$= 4N + 1$ or 2, depending on Boundary Conditions

DIRK – Diagonally Implicit Runge-Kutta Method for Oscillatory Problems
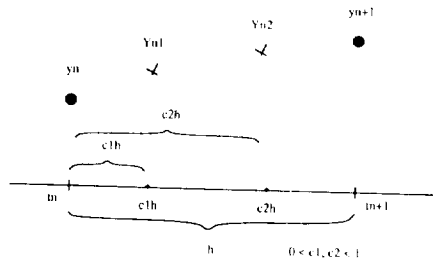
$$\ddot{y} = f(t, y) \tag{10}$$

$$Y_{nj} = y_n + c_j h\dot{y}_n + h^2 \sum_{i=1}^{l} a_{ji} f(Y_{ni}, \ t_n + c_i h)$$

$$y_{n+1} = y_n + h\dot{y}_n + h^2 \sum_{i=1}^{l} b_i f(Y_{ni}, \ t_n + c_i h)$$

$$\dot{y}_{n+1} = \dot{y}_n + h \sum_{i=1}^{l} f(Y_{ni}, \ t_n + c_i h)$$

Butcher Array for $l = 2$

$$
\begin{array}{cc|c}
a_{11} & a_{12} & c_1 \\
a_{21} & a_{22} & c_2 \\
b_1 & b_2 & \\
b_1' & b_2' &
\end{array}
$$

Explicit RK:

$$
\begin{array}{cc|}
0 & 0 \\
a_{21} & 0
\end{array}
$$

Diagonally Implicit RK:

$$
\begin{array}{cc|}
a_{11} & 0 \\
a_{21} & a_{22}
\end{array}
$$

Example of Butcher Array for DIRK:

$$
\begin{array}{cc|c}
1/2 & 0 & 1/2 \\
-5/12 & 1/2 & 1/2 \\
\hline
0 & 1/2 & \\
0 & 1 &
\end{array}
$$

Using DIRK on E-B beam (1)

E-B Beam via FE Method

$$M\ddot{y} + Ly = Qu(t) \qquad (11)$$

$u(t) = 0$ in the observer problem

$$\ddot{y} = -M^{-1}Ly = Fy \qquad (12)$$

(Actually $M^{-1}L$ is replaced by a Cholesky decomposition).

$$Y_{n1} = y_n + c_1 h\dot{y}_n + h^2[a_{11}FY_{n1} + a_{12}FY_{n2}]$$
$$Y_{n2} = y_n + c_2 h\dot{y}_n + h^2[a_{21}FY_{n1} + a_{22}FY_{n2}]$$

$$y_{n+1} = y_n + h\dot{y}_n + h^2[b_1 FY_{n1} + b_2 FY_{n2}]$$
$$\dot{y}_{n+1} = \dot{y}_n + h[b_1' FY_{n1} + b_2' FY_{n2}]$$

Where $a_{12} = 0$

Using DIRK on E-B beam (2)

Solve to get Y_{n1} and Y_{n2}

$$Y_{n1} = (I - h^2 a_{11}F)^{-1}(y_n + c_1 h\dot{y}_n)$$
$$Y_{n2} = (I - h^2 a_{22}F)^{-1}(y_n + c_2 h\dot{y}_n + h^2 a_{21}FY_{n1})$$

Discrete-Time Model:

$$\begin{bmatrix} y_{n+1} \\ \dot{y}_{n+1} \end{bmatrix} = AV \begin{bmatrix} y_n \\ \dot{y}_n \end{bmatrix}$$

Where matrix AV is

$$\begin{bmatrix} I + h^2 F(b_1 A_1 + b_2 A_3) & hI + h^2 F(b_1 A_2 + b_2 A_4) \\ hF(b_1' A_1 + b_2' A_3) & I + hF(b_1' A_2 + b_2' A_4) \end{bmatrix}$$

And

$$A_1 = (I - h^2 a_{11}F)^{-1} \qquad A_2 = c_1 h A_1$$
$$A_3 = (I - h^2 a_{22}F)^{-1}(I + h^2 a_{21}F A_1)$$
$$A_4 = (I - h^2 a_{22}F)^{-1}(c_2 hI + h^2 F a_{21} A_2)$$

502

Digital Observer Design

Define

$$X_n = \begin{bmatrix} y_n \\ \dot{y}_n \end{bmatrix}$$

Time-discretized FE System:

$$X_{n+1} = AV_{N_1} X_n \qquad (13)$$

$$Z_n = C_{N_1} X_n \qquad (14)$$

Observer:

$$\hat{X}_{N+1} = AV_{N_2} \hat{X}_n + G(Z_n - \hat{Z}_n) \qquad (15)$$

$$\hat{Z}_n = C_{N_2} \hat{X}_n \qquad (16)$$

Where N_1 and N_2 can be different, for example $N_1 = 64$ and $N_2 = 4, 8$ or 16.

Two Ways for Observer Design

A). Observer Design in continuous time → Conversion to discrete time →

B). Conversion to discrete time → Observer design in discrete time →
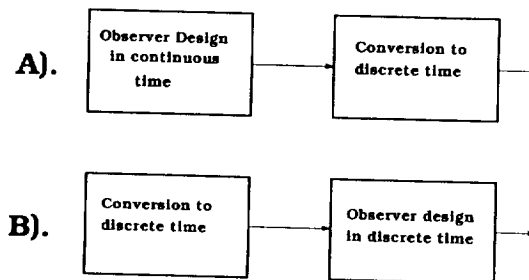
The above operations are not equivalent ("do not commute"). The discrete-time observer designed by variant B provides a more accurate tracking of beam's motion.

Eigenvalues of E-B Beam Using Finite Element Model

(Imaginary Part)

N	Max	Min	Ratio
4	135.9341	2.1817	6.2306e+01
8	541.9612	2.1805	2.4854e+02
16	2.1678e+03	2.1805	9.9419e+02
32	8.6712e+03	2.1805	3.9768e+03
64	3.4685e+04	2.1805	1.5907e+04
128	1.3874e+05	2.1805	6.3628e+04

Eigenvalues (NN=32) of RE (*), FD (o) and FE (+)
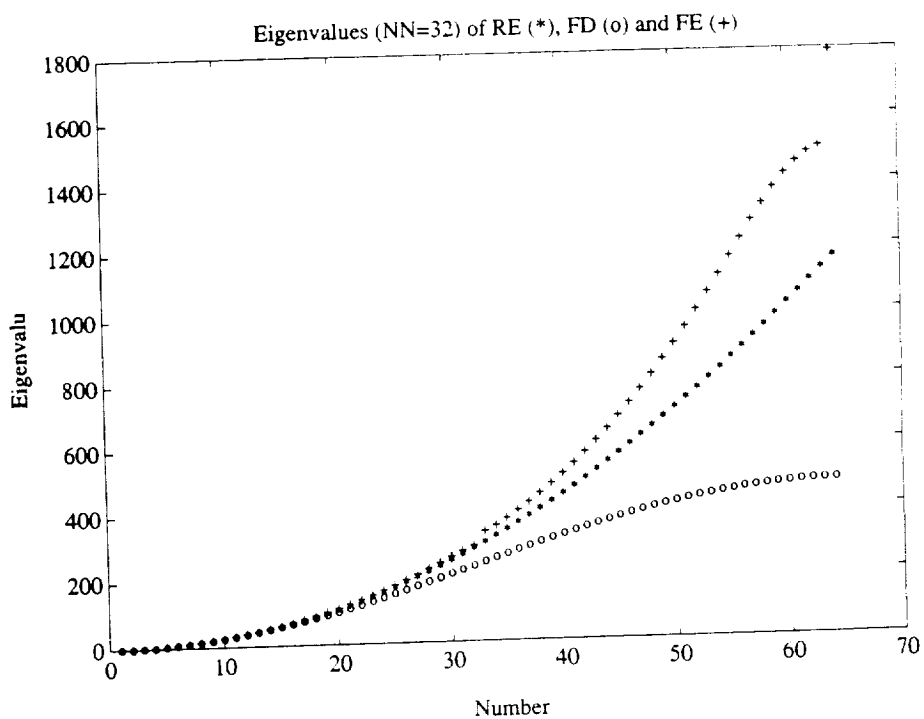
ideal beam: NN=64, Wst=4.3371, Wmax=1.8885
L=1, EI=0.02, K=0, m=1, A=1
Initial condition: sin(pi*x)

FE model: T= 10 s h= 0.01 hx=0.05

NN	E1 (FE Model)	E2(Max) (FE Model)
2	3.015 e-03	8.662 e-02
4	1.298 e-04	2.231 e-02
8	6.107 e-06	5.787 e-03
16	2.414 e-07	1.337 e-03
32	4.591 e-09	2.138 e-04

Ae --eigenvalues of AV, NN=64

E=X-Xv, (64,8), 2nd DIRK, h=.01, T=1:10s, Ns=1 (S L), S L

E=X-Xv,(64,16),2nd DIRK,h=.01,T=1:10s,Ns=1(S L),S L, m=2

E=X-Xv,(64,16),h=.01,T=1:10s,Ns=1(S L),S L,m=3

E=X-Xv,(64,16),h=.01,T=1:10s,Ns=1(S L),S L,m=4

E=X-Xv,(64,16),h=.01,T=1:10s,Ns=1(S L),S L,m=5

log(E), (64,8),h=.01,T=1:10s,Ns=1(S L),S L,m=1

508

log(E), (64,16),h=.01,T=1:10s,Ns=1(S L),S L,m=2

log(E), (64,16),h=.001,T=1:10s,Ns=1(S L),S L,m=2

log(E),(64,16),h=.01,Ns=1(S L),S L,m=4

log(E), (64,16),h=.01,T=1:10s,Ns=1(S L),S L,m=5

510
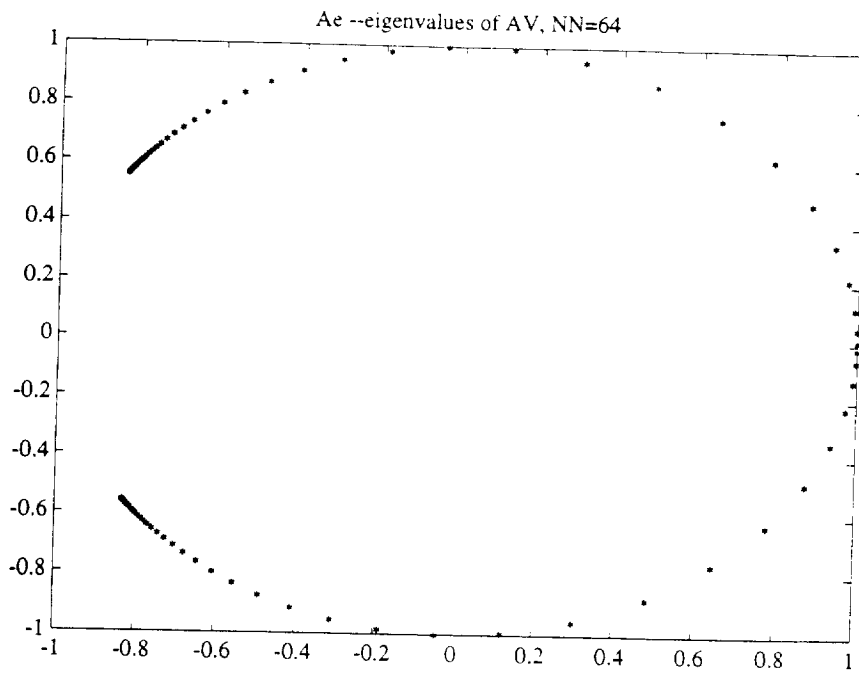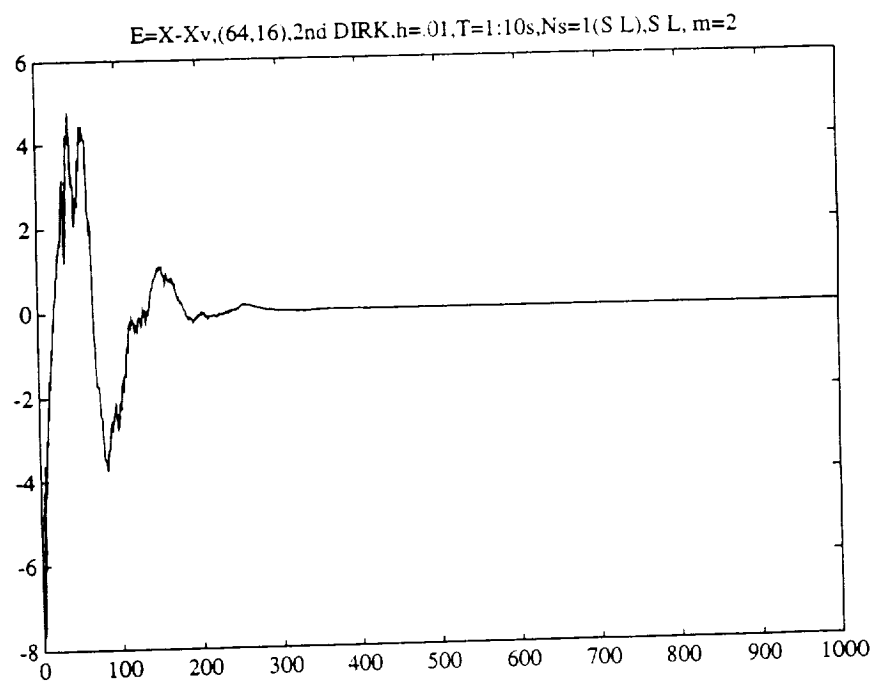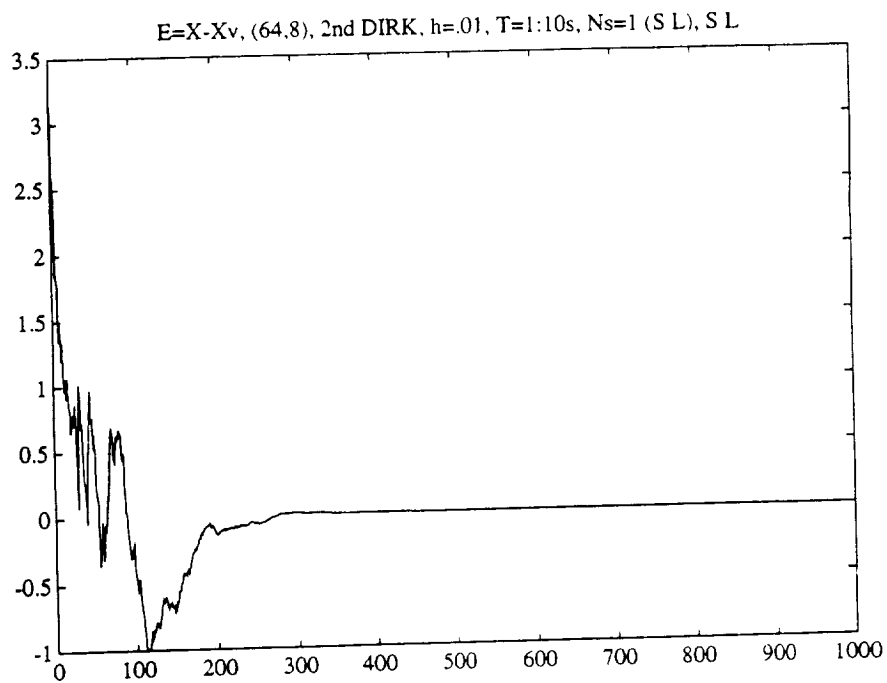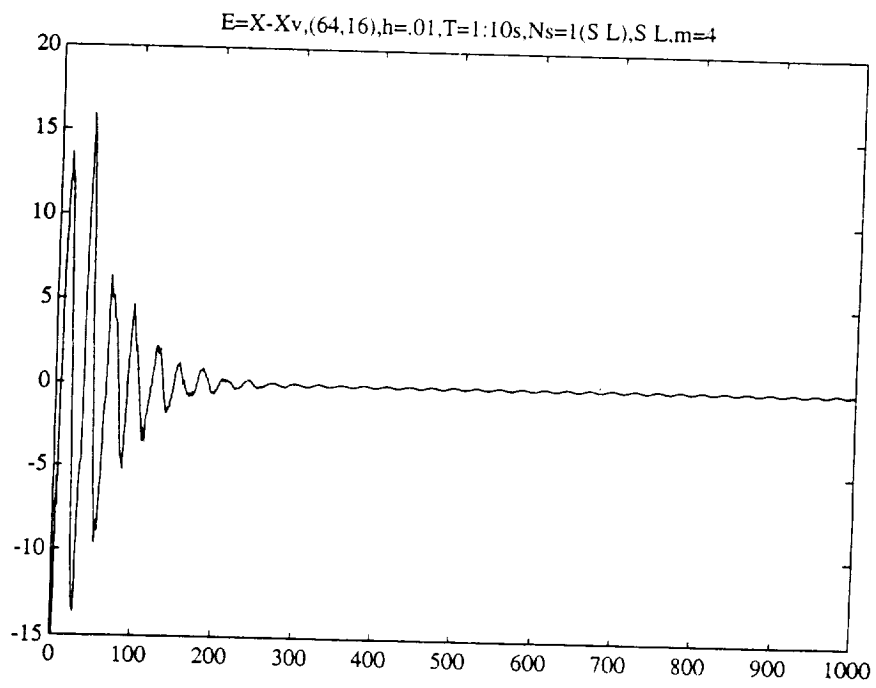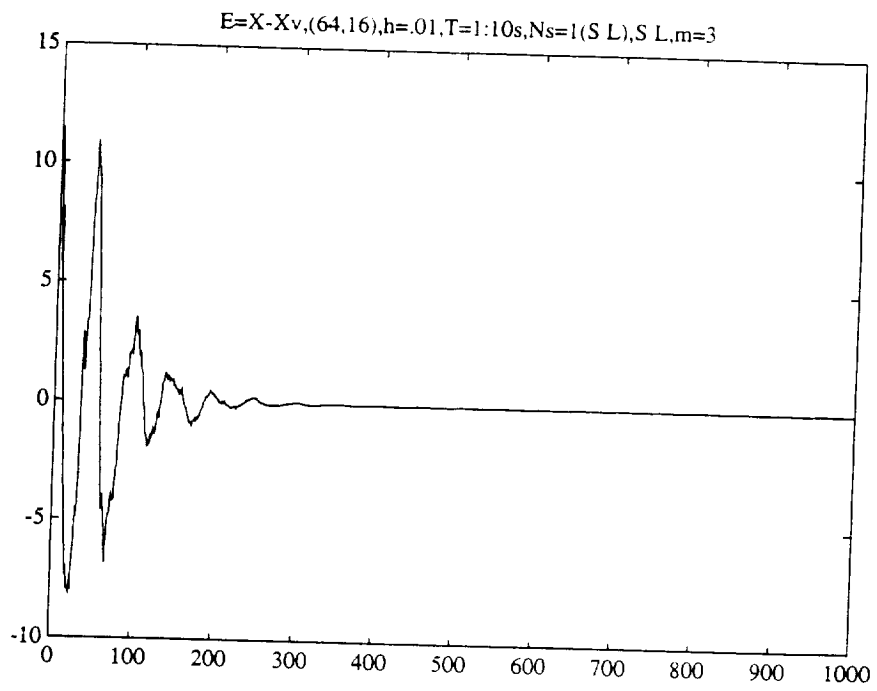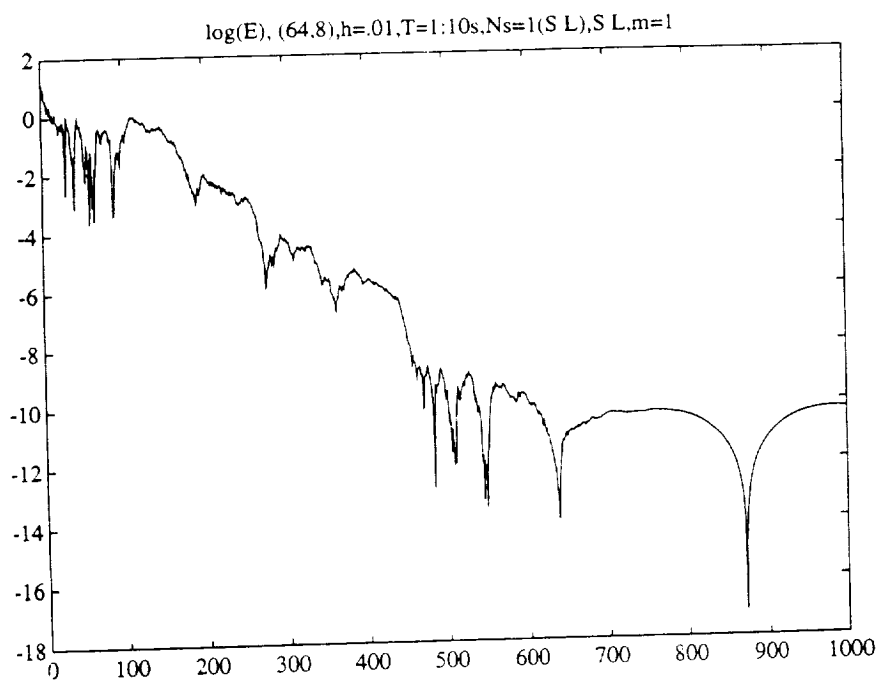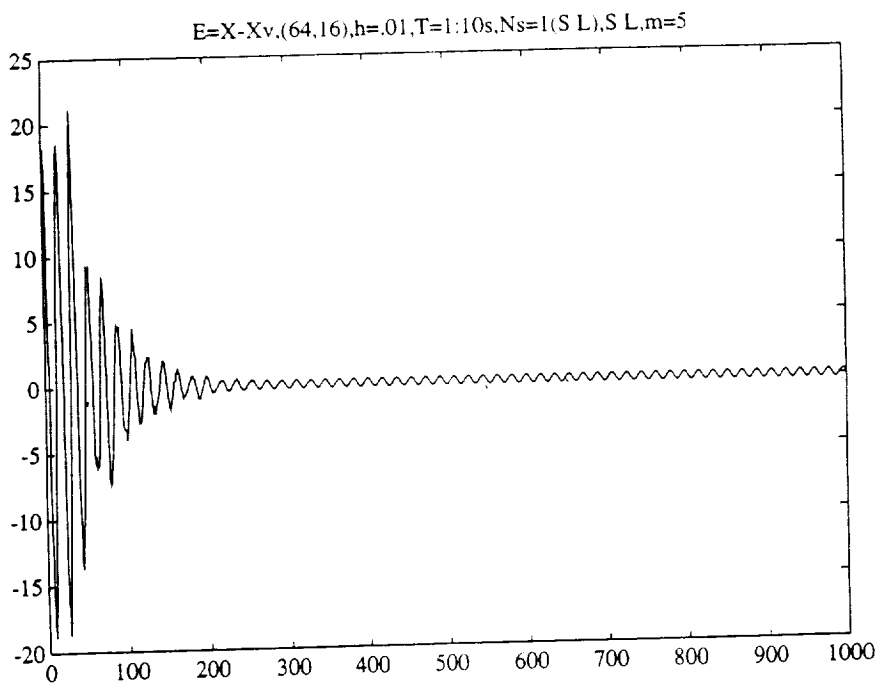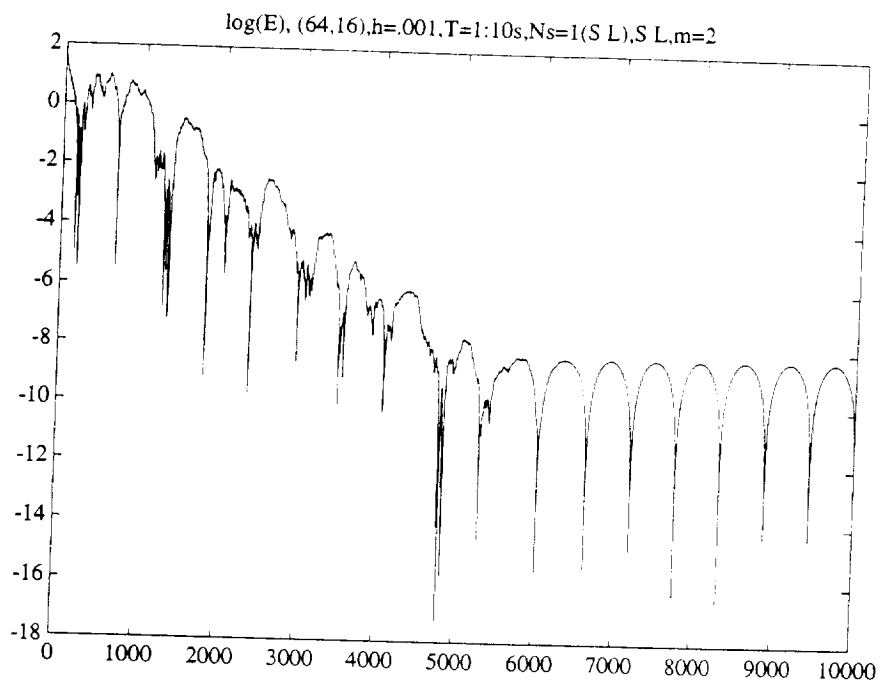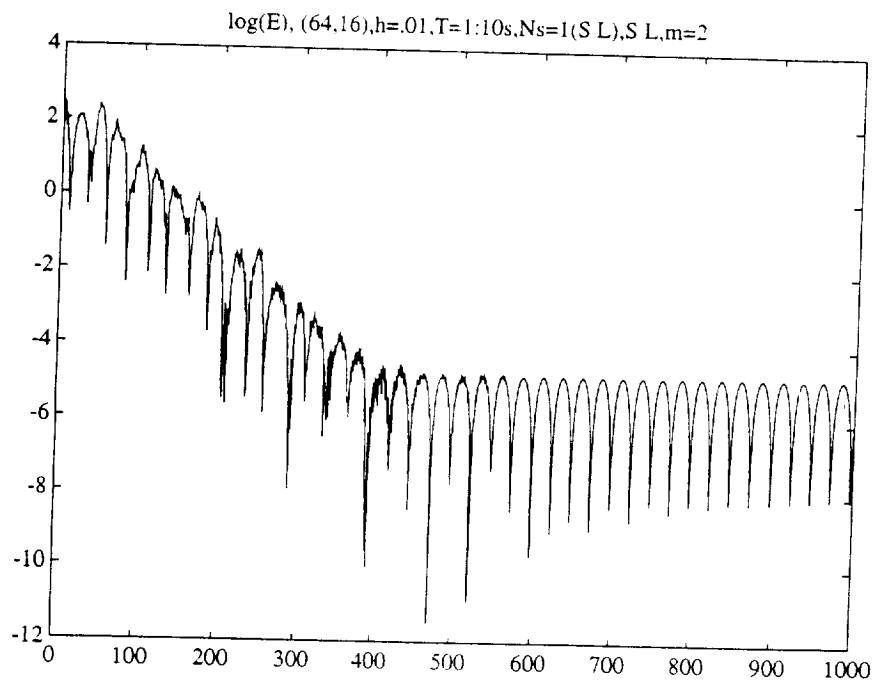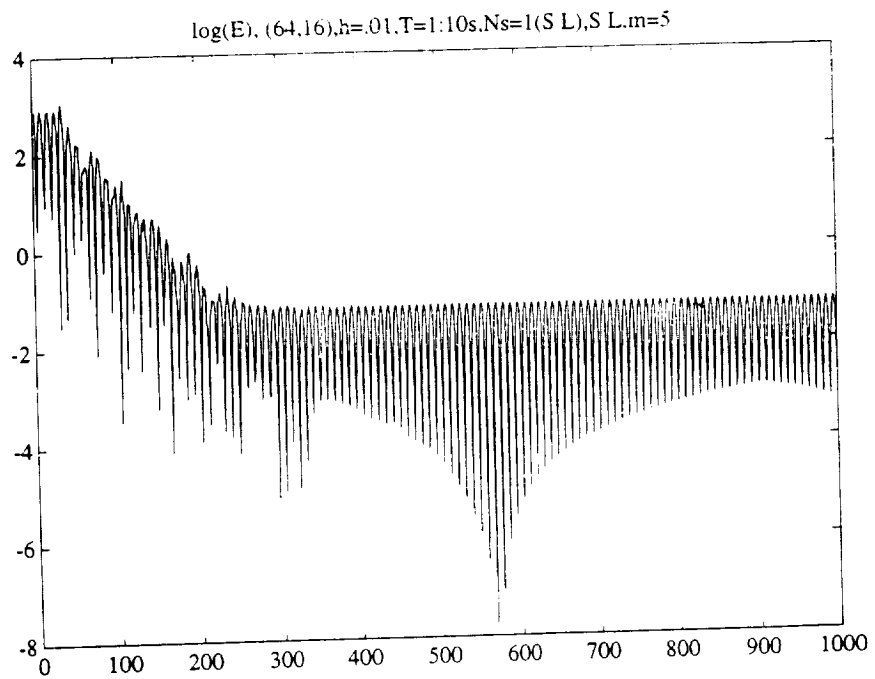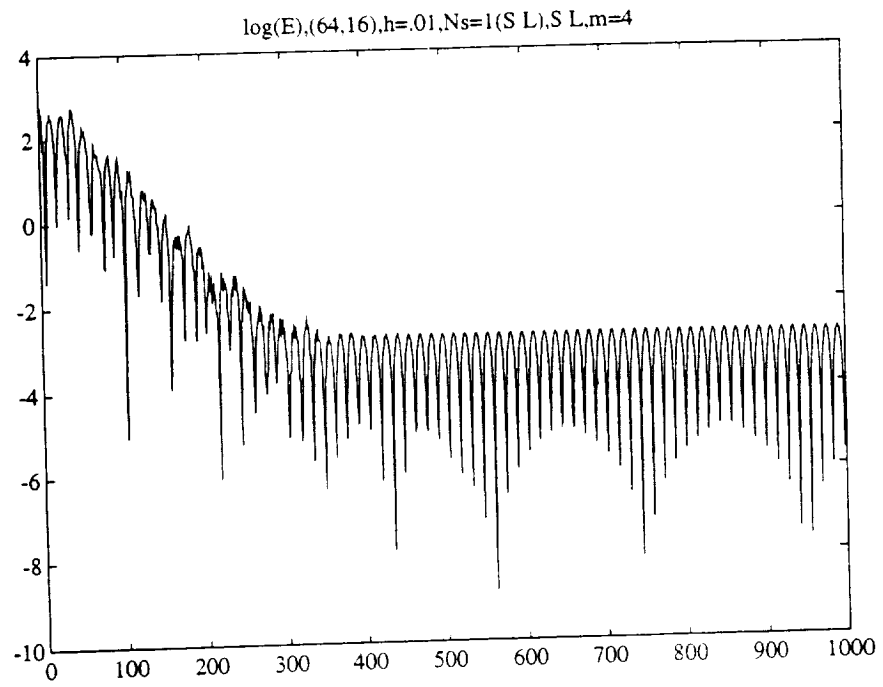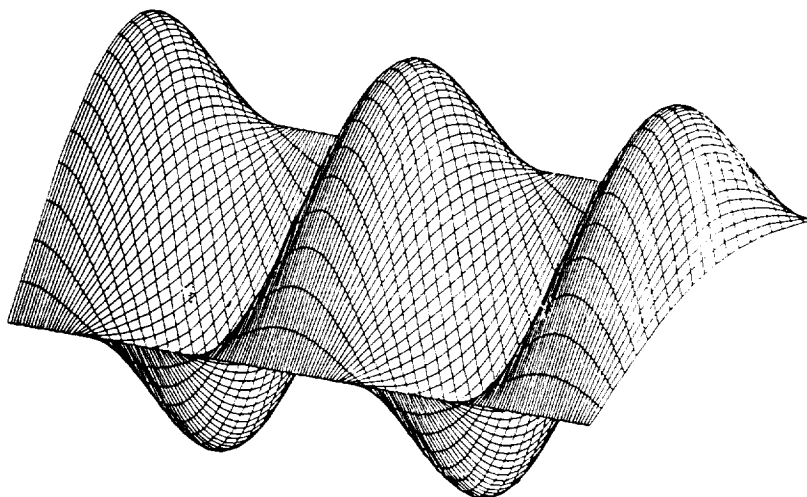
Spatial displacement of observer. NN=4. mode 1
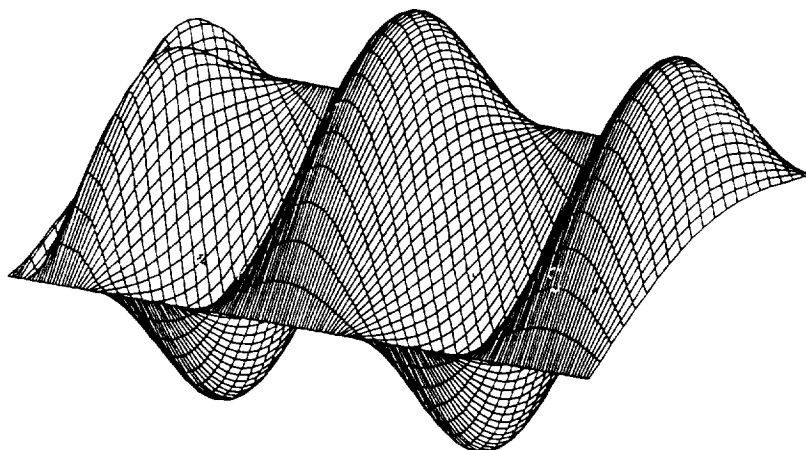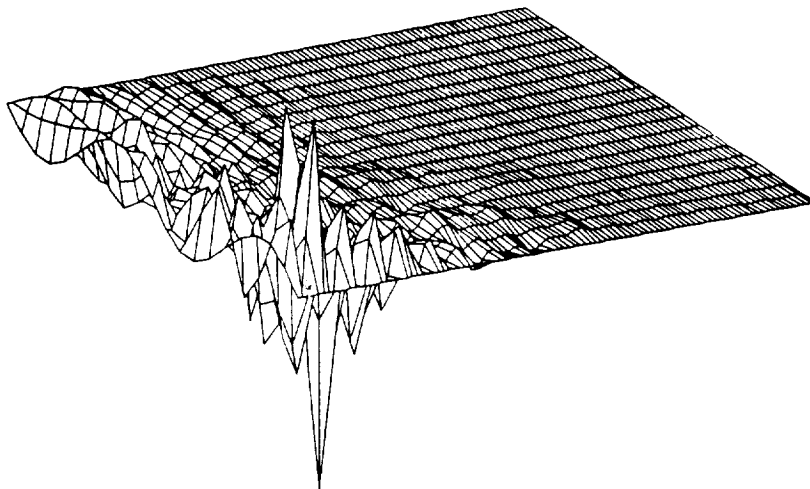
Spatial distribution of observer error, NN=4, e=-2, mode 1
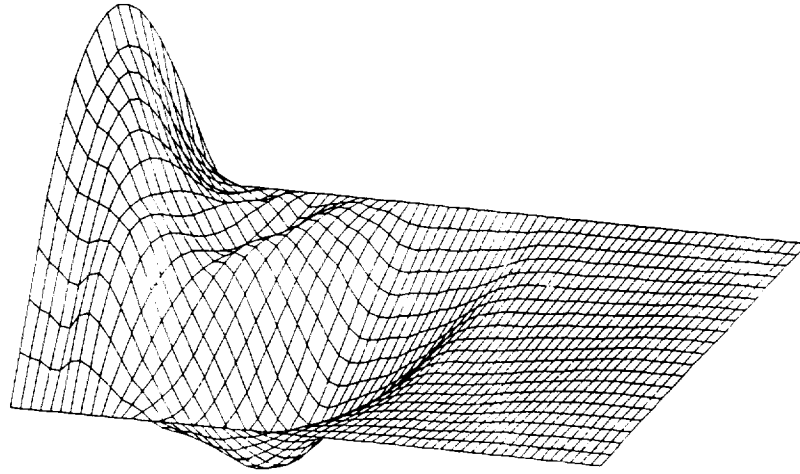
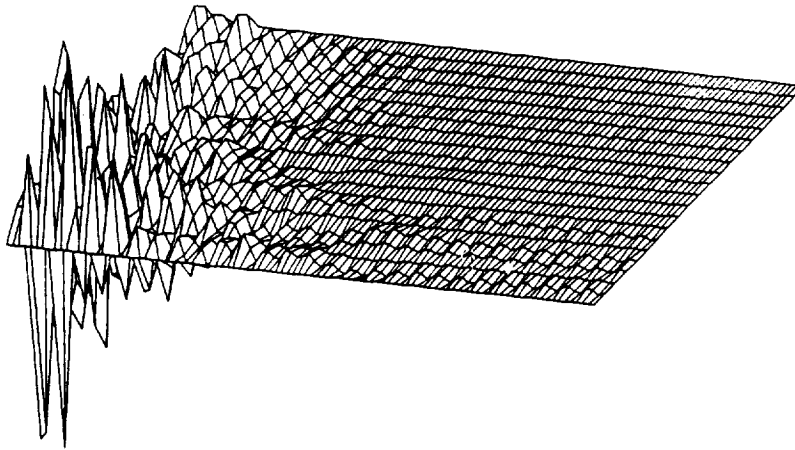Spatial distribution of observer error, NN=8, e=-2, mode 2, T=5s
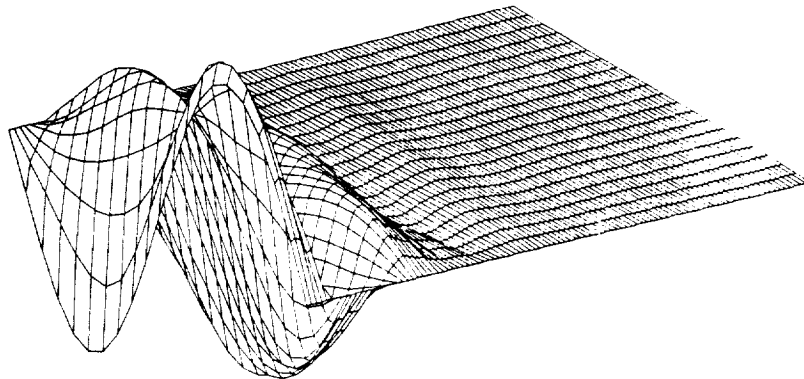
Spatial distribution of observer error, NN=8,e=-2,T=5s,mode 3
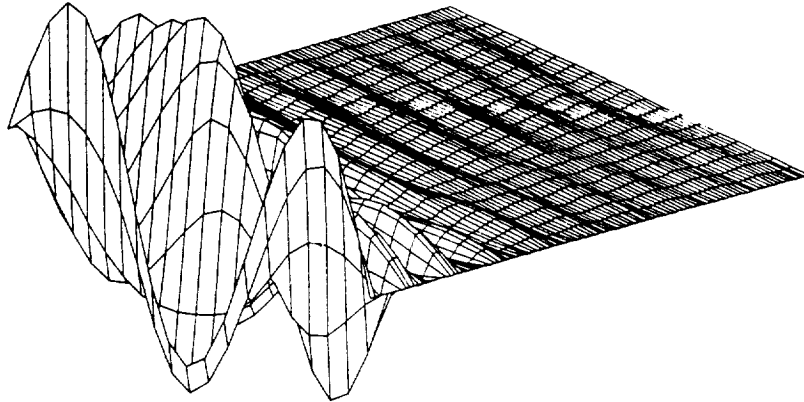
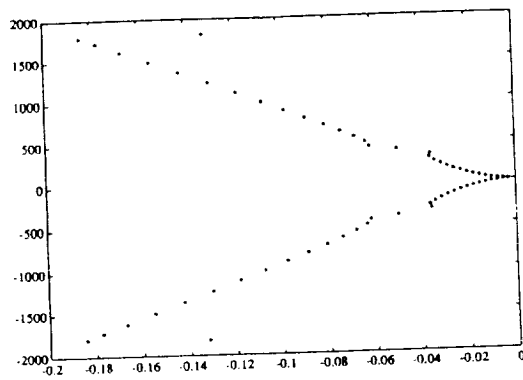Spatial distribution of observer error, NN=16,e=-2,T=5s,mode 4

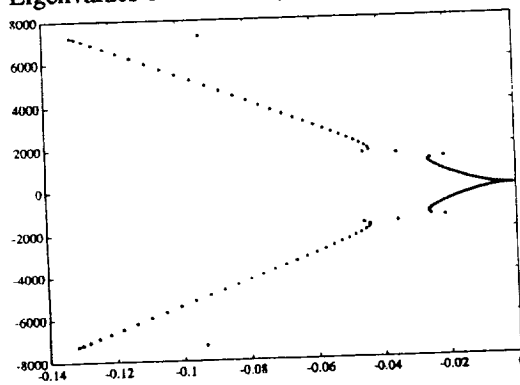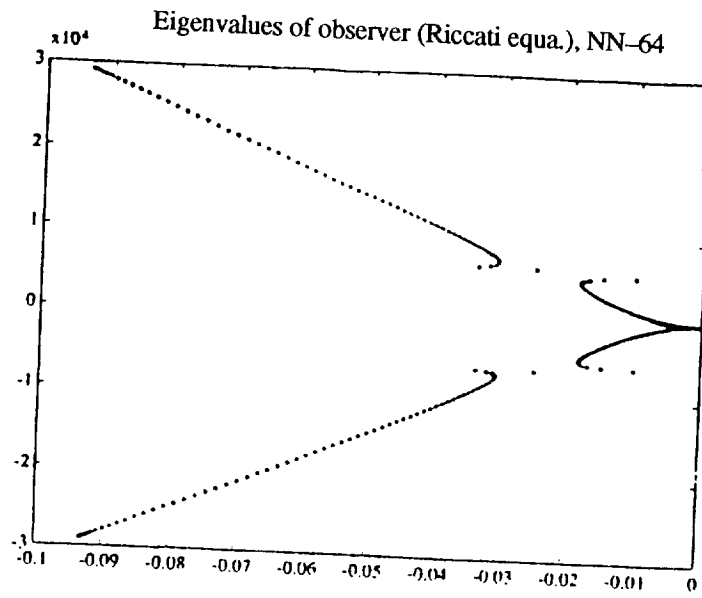## Eigenvalues of observer (Riccati equa.), NN=16

Eigenvalues of observer (Riccati equa.), NN=32
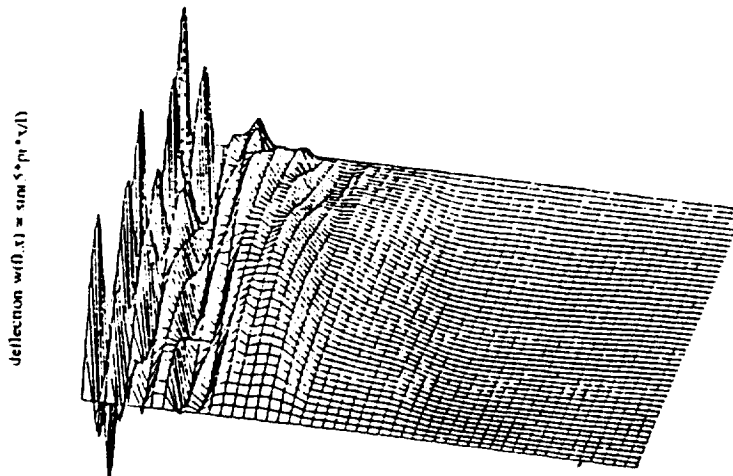

514

Eigenvalues of observer (Riccati equa.), NN–64

Stabilization of the beam via state feedback. NN=8, m=5, T=5s

Time 0 to 5 sec

Conclusions

1. The computations showed that the dynamically changing shape of the beam can be reconstructed by a finite-element based observer using just one point measurement of the slope at the end. This conclusion is limited to shapes involving only a few first modes. Additional measurements do not improve the process much.

2 In the process of designing the observer, one can <u>either</u> design gain G for a continuous-time model and then discretize in time $\dot{X} = (A - GC)X$ <u>or first discretize</u> in time $\dot{X} = AX$ and then design an observer. The second approach is more accurate.

3. For each mode of the E-B beam there is a steady state periodic error, whose amplitude depends on the mismatch of eigenvalues between the E-B beam and FE model.
The error can be decreased by further shifting eigenvalues of the observer, or by increasing the number of finite elements.

4. The Riccati equation approach yields a conical pattern of eigenvalues. The transients are different, but the steady state periodic error is nearly the same.

References

[1] M. A. Horn, "Uniform Decay Rates for the Solutions to the Euler Bernoulli Plate Equation With Boundary Feedback Acting via Bending Moments," Report, University of Virginia, 1991.

[2] M.A. Horn, "Exact Controllability of the Euler Bernoulli Plate via Bending Moments Only on The Space of Optimal Regularity," Report, University of Virginia, J. Math. Anal. Appl., to appear.

[3] I. Lasiecka, "Exponential Decay Rates for the Solutions of the Euler Bernoulli Equations With Boundary Dissipation Occurring in The Moments Only," Journal Differential Equations, to appear.

[4] D.J. Van der Houwen and B.P. Sommeijer, "Diagonally Implicit Runge-Kutta Nystrom Methods for Oscillatory Problems," SIAM J. Numerical Analysis, vol 26, 1989, 414-429.

[5] R. Alexander, "Diagonally Implicit Runge-Kutta Methods for Stiff 'ODEs," SIAM J. Numerical Analysis, vol 14, 1977, 1006-1021.

[6] J. C. Butcher, "The Numerical Analysis of Ordinary Differential Equations, Runge-Kutta and General Linear Methods," J. Wiley and Sons 1987.

[7] T.J.R. Hughes, "The Finite Element Method," Prentice Hall Inc., Englewood Cliffs, N.J. 07632.

Semigroup Approximation and Robust Stabilization of Distributed Parameter Systems

A.J. Kurdila[*], R. Fabiano[**], T. Strganac[*], S. Hsu
Texas A&M University
College Station, Texas 77843

ABSTRACT

Theoretical results that enable rigorous statements of convergence and exponential stability of Galerkin approximations of LQR controls for infinite dimensional, or distributed parameter, systems have proliferated over the past ten years. In addition, extensive progress has been made over the same time period in the derivation of robust control design strategies for *finite dimensional systems*. However, the study of the convergence of robust finite dimensional controllers to robust controllers for infinite dimensional systems remains an active area of research. In this paper we consider a class of soft-constrained differential games evolving in a Hilbert space. Under certain conditions, a saddle point control can be given in feedback form in terms of a solution to a Riccati equation. By considering a related LQR problem, we can show a convergence result for finite dimensional approximations of this differential game. This yields a computational algorithm for the feedback gain that can be derived from similar strategies employed in infinite dimensional LQR control design problems. The approach described in this paper also inherits the additional properties of stability robustness common to game theoretic methods in finite dimensional analysis. These theoretical convergence and stability results are verified in several numerical experiments.

(1) INTRODUCTION

During the past ten years, significant progress has been made in the derivation of convergence criteria for Galerkin approximations of linear quadratic regulator control problems in Hilbert spaces [Banks, Gibson79,Gibson91,Ito90...]. Usually, these methods synthesize classical results on the convergence of Galerkin approximations for elliptic, hyperbolic and parabolic partial differential equations with minimization strategies for convex cost functionals. During the past few years, however, researchers studying control theory have been increasingly interested in the derivation of control schemes that are *robust* with respect to uncertainty, either structured or unstructured, in the underlying model [McFarlane,Maciejowski].

One approach that has been employed with success in the development of *finite dimensional* controllers is the min-max, or soft-constrained differential game, formulation [Basar]. In this class of techniques the "best" controller is sought subject to a "worst case" disturbance. Extension of this approach to infinite dimensions has also been made recently *in principle* [Curtain]. However, the arguments regarding the convergence of the associated finite dimensional Riccati approximations can be more delicate than in the similar LQR minimization case [Attouch,Cavazzuti].

In this paper we show that, in certain cases, the solution to the min-max problem is equivalent to the solution of a related LQR minimization problem. In these cases the approximation theory for the LQR minimization problem [Gibson79,Gibson91,Ito90...] can be brought to bear, and the solution of the min-max problem can be approximated by a sequence of solutions to finite dimensional Riccati equations. Thus, this gives a computational method for obtaining a feedback control for a class of infinite dimensional problems which is both optimal and robust with respect to uncertainty.

(2) PROBLEM STATEMENT

Let H, U and W be real, separable Hilbert spaces and suppose that $B \in L(U, H)$ and $\Phi \in L(W, H)$ are bounded operators.

Consider the evolution equation on H

$$\dot{x}(t) = Ax(t) + Bu(t) + \Phi w(t)$$

$$x(0) = x_0 \in H \quad is \ given$$

(2.1)

where A is the infinitesimal generator of a strongly continuous exponentially stable semigroup S(t) on H. In the following discussion, it is assumed that the initial point x(0) is fixed. Furthermore, it is assumed that one can define the observation from the state via the relationship

$$y(t) = Cx(t)$$

$$C \in L(H, H)$$

(2.2)

The optimal control problem to be considered is the infinite dimensional version of the so-called "soft-constrained differential game" as described, for example, in [Basar]. This problem can be stated by first defining the "disturbance-augmented" cost functional

$$J(u, w) = \frac{1}{2}\int_0^\infty \{\|y(t)\|_H^2 + (Nu(t), u(t))_U - \frac{1}{\gamma^2}(Mw(t), w(t))_W\} dt \quad (2.3)$$

where $\gamma \in \Re$ is a fixed positive constant, and $N \in L(U, U), M \in L(W, W)$.

Define the spaces $\overline{U} = L^2(O, \infty; U)$ and $\overline{W} = L^2(O, \infty; W)$. The differential game to be solved is to find

$$J_0 = \inf_{u \in \overline{U}} \sup_{w \in \overline{W}} J(u, w) \quad (2.4)$$

subject to dynamics governed by (2.1) - (2.2).

A solution (u^0, w^0) is called a saddle point of $J(u,w)$ if and only if

$$J(u^0, w) \le J(u^0, w^0) \le J(u, w^0)$$
$$\forall (u, w) \in \overline{U} \times \overline{W} \quad (2.5)$$

Roughly speaking, the problem to be solved consists of two parts:

(P1) Find conditions that are applicable to a reasonably large class of problems for which there exists a unique saddle point solution
$$(u^0, w^0) \in \overline{U} \times \overline{W},$$

and such that the solution is given in feedback form.

(P2) Find a method for constructing a sequence of finite dimensional approximations whose feedback solutions converge to the solution of (2.4).

Next, we discuss conditions under which P1 and P2 can be solved.

(3.) CHARACTERIZATION OF A SOLUTION

We make the following assumptions (which we will show guarantee that there exists a unique saddle point value to the differential game outlined above):

(H1)   There exists $d_1 > 0$ such that $(Nu,u)_U \geq d_1 \|u\|_U^2$ for all $u \in U$

(H2)   There exists $d_2 > 0$ such that $(Mw,w)_W \geq d_2 \|w\|_W^2$ for all $w \in W$

(H3) $BN^{-1}B^* - \gamma^2 \Phi M^{-1} \Phi^* \geq 0$

Conditions H1 and H2 are necessary to ensure invertibility of N and M. Condition H3 is necessary for the characterization of the saddle point in feedback form, and for the arguments for convergence of finite dimensional approximations. *While condition H3 is somewhat strong, the assumptions above are applicable to a wide variety of distributed parameter control problems and are extremely convenient for consideration of the convergence of finite dimensional Galerkin approximations.* (In a future manuscript we will report on structures application for which H3 is not satisfied, and on our efforts to relax this assumption).

Before stating the main existence and uniqueness result, we consider a reformulation of the state equation. Define the space $\bar{H} = L^2(0, \infty; H)$ and observe that a homogeneous (zero initial data) version of (2.1) is given by

$$\Lambda x = \bar{B}u + \bar{\Phi}w.$$

Here the operator Λ is defined on the domain

$$dom\ \Lambda = \{x \in \bar{H}\ \frac{dx}{dt} - Ax \in \bar{H}, x(0) = 0\}$$

by

$$\Lambda x(t) = \frac{dx}{dt} - Ax(t),$$

and $\bar{B} \in L(\bar{U}, \bar{H})$, and $\bar{\Phi} \in L(\bar{W}, \bar{H})$ are multiplication operators given by

$$(\bar{B}u)(t) = Bu(t)$$
$$(\bar{\Phi}w)(t) = \Phi w(t).$$

We also define the multiplication operators $\bar{C} \in L(\bar{H}, \bar{H})$, $\bar{N} \in L(\bar{U}, \bar{U})$ and $\bar{M} \in L(\bar{W}, \bar{W})$ in the obvious way. In this paper we frequently will not distinguish between an operator (such as C) and the corresponding multiplication operator ($\bar{C}$) when it is clear from the context which operator is used.

   With these definitions, the variation of constants form of the solution to (2.1) can be

given by

$$x = \Lambda^{-1}\overline{B}u + \Lambda^{-1}\overline{\Phi}w + f \qquad (3.1)$$

where $f = S(t)x_0$. Here, $\Lambda^{-1} \in L(\overline{H}, \overline{H})$ is defined by $\Lambda^{-1}x(t) = \int_o^t S(t-s)x(s)ds$. Hence, the differential game is to find

$$J_0 = \begin{array}{c} inf \\ u \in \overline{U} \end{array} \begin{array}{c} sup \\ w \in \overline{W} \end{array} J(u,w)$$

subject to (3.1).

Theorem (3.1) : Suppose that conditions (H1), (H2) and (H3) hold. Then there exists a unique

$$(u^0, w^0) \in \overline{U} \times \overline{W}$$

such that

$$J_0 = \begin{array}{c} inf \\ u \in \overline{U} \end{array} \begin{array}{c} sup \\ w \in \overline{W} \end{array} J(u,w) = J(u^0, w^0)$$

Moreover, (u^0, w^0) is given by

$$w^0(t) = \gamma^2 M^{-1}\Phi^* \Pi x^0(t) \qquad (3.2)$$
$$u^0(t) = -N^{-1}B^* \Pi x^0(t) \qquad (3.3)$$

where

$$x^0 = \Lambda^{-1}Bu^0 + \Lambda^{-1}\Phi w^0 + f .$$

Here Π is a positive definite solution of the algebraic Riccati equation

$$(\Pi x, Ay)_H + (Ax, \Pi y)_H + (C^*Cx, y)_H - (\Pi \Omega \Omega \Pi x, y)_H = 0 \qquad (3.4)$$

for any $x, y \in D(A) \subset H$ where

$$\Omega \equiv [BN^{-1}B^* - \gamma^2 \Phi M^{-1}\Phi^*]^{1/2} \geq 0$$

Observe that (H3) guarantees that

$$\Omega = [BN^{-1}B^* - \gamma^2 \Phi M^{-1}\Phi^*]^{1/2}$$

is well defined. Since Equations (3.2), (3.3), and (3.4) relate the saddle point to the algebraic Ric-

cati equation, we can apply known methods and techniques for approximation of Riccati equations to this problem.

The proof of Theorem (3.1) is developed through a sequence of lemmas. (We are using notation and definitions from [Zeidler]).

First, recall that for each fixed (u,w), the G-derivative of J(u,w) with respect to u, denoted by J_u (u,w), is defined by

$$(J_u(u, w), x)_{\overline{U}} = \lim_{t \to 0} \frac{J(u + tx, w) - J(u, w)}{t} \tag{3.5}$$

Similarly, the G-derivative J_w(u,w) of J(u,w) with respect to w is given by

$$(J_w(u, w), y)_{\overline{W}} = \lim_{t \to 0} \frac{J(u, w + ty) - J(u, w)}{t} \tag{3.6}$$

for any $y \in W$. Also,

$$(J_u(u, w), -J_w(u, w)) \in \overline{U} \times \overline{W}$$

and for any $(x, y) \in U \times W$, we have

$$((J_u(u, w), -J_w(u, w)), (x, y))_{\overline{U} \times \overline{W}} = (J_u(u, w), x)_{\overline{U}} + (-J_w(u, w), y)_{\overline{W}} \quad .$$

Recall also that if X is a Hilbert space, then an operator Γ (which may not be linear) from X to X is called strongly monotone if there is a fixed positive number d such that

$$(\Gamma x_1 - \Gamma x_2, x_1 - x_2)_X \geq d \| x_1 - x_2 \|_X^2$$

for any $x_1, x_2 \in X$. The following lemma gives some nice properties about G-derivatives of J(u,w).

Lemma 3.1: If (H$_1$) and (H$_2$) hold, then the following are true:

i) for fixed $w \in \overline{W}, J_u$ (u, w) is strongly monotone on J.

ii) for fixed $u \in \overline{U}$, and sufficiently small $\gamma^2, -J_w$ is strongly monotone on $\overline{W}$.

iii) for sufficiently small $\gamma^2, (J_u, -J_w)$ is strongly monotone on $\overline{U} \times \overline{W}$.

Proof: By direct computation using (2.3) we have

$$J(u, w) = \frac{1}{2}(Du, u)_{\overline{U}} + (u, Gw + Ff)_{\overline{U}} + Q(w, f) \tag{3.7}$$

where

$$D = N + B^*(\Lambda^{-1})^* C^* C\Lambda^{-1}B$$

$$G = B^*(\Lambda^{-1})^* C^* C\Lambda^{-1}\Phi$$

$$F = B^*(\Lambda^{-1})^* C^* C$$

$$Q(w, f) = (C\Lambda^{-1}\Phi w, f)_{\overline{H}} - \frac{1}{2\gamma^2}(Mw, w)_{\overline{W}} + \frac{1}{2}(C\Lambda^{-1}\Phi w, C\Lambda^{-1}\Phi w)_{\overline{H}} + \frac{1}{2}(Cf, Cf)_{\overline{H}}$$

According to (3.5), we obtain

$$J_u(u, w) = Du + Gw + Ff \tag{3.8}$$

Therefore, for any $u_1, u_2 \in \overline{U}$, and fixed $w \in \overline{W}$, it follows from (H1) that

$$(J_u(u_1, w) - J_u(u_2, w), u_1 - u_2)_{\overline{U}} = (D(u_1 - u_2), u_1 - u_2)_{\overline{U}}$$

$$\geq (N(u_1 - u_2), u_1 - u_2)_{\overline{U}} \geq d_1\|u_1 - u_2\|_{\overline{U}}^2$$

Hence, i) is true. Similarly, we can write

$$J(u, w) = -\frac{1}{2}(D'w, w)_{\overline{W}} + (w, G^*u + F'f)_{\overline{W}} + Q'(u, f) \tag{3.9}$$

where

$$D' = \frac{1}{\gamma^2}M - \Phi^*(\Lambda^{-1})^* C^* C\Lambda^{-1}\Phi$$

$$G^* = \text{the adjoint of } G = \Phi^*(\Lambda^{-1})^* C^* C\Lambda^{-1}B$$

$$F' = \Phi^*(\Lambda^{-1})^* C^* C$$

$$Q'(u, f) = \frac{1}{2}((N + B^*(\Lambda^{-1})^* C^* C\Lambda^{-1}B)u, u)_{\overline{U}} + \frac{1}{2}(Cf, Cf)_{\overline{H}} + (C\Lambda^{-1}Bu, Cf)_{\overline{H}}$$

Hence, from (3.6), we have

$$J_w(u, w) = -D'w + G^* u + F'f \tag{3.10}$$

For any $w_1, w_2 \in \overline{W}$ and fixed $u \in \overline{U}$, it follows from (H2) that

$$(-J_w(u, w_1) + J_w(u, w_2), w_1 - w_2)_{\overline{W}} = (D'(w_1 - w_2), w_1 - w_2)_{\overline{W}}$$

$$= \frac{1}{\gamma^2} (M(w_1 - w_2), w_1 - w_2)_{\overline{W}} - (C\Lambda^{-1}\Phi(w_1 - w_2), C\Lambda^{-1}\Phi(w_1 - w_2))_{\overline{H}}$$

$$\geq \left(\frac{d_2}{\gamma^2} - \|C\Lambda^{-1}\Phi\|^2 \right) \|w_1 - w_2\|_{\overline{W}}^2$$

Therefore, for sufficiently small γ^2, there is a positive constant d so that

$$(-J_w(u, w_1) + J_w(u, w_2), w_1 - w_2)_{\overline{W}} \geq d \|w_1 - w_2\|_{\overline{W}}^2$$

Thus, ii) is verified. Finally, for any $(u_1, w_1), (u_2, w_2) \in \overline{U} \times \overline{W}$ and sufficiently small γ^2, it follows that,

$$((J_u(u_1, w_1) - J_w(u_1, w_1)) - (J_u(u_2, w_2) - J_w(u_2, w_2)), (u_1, w_1) - (u_2, w_2))_{\overline{U} \times \overline{W}}$$

$$= (J_u(u_1, w_1) - J_u(u_2, w_2), u_1 - u_2)_{\overline{U}} + (-J_w(u_1, w_1) + J_w(u_2, w_2), w_1 - w_2)_{\overline{W}}$$

$$= (D(u_1 - u_2) + G(w_1 - w_2), u_1 - u_2)_{\overline{U}} + (D'(w_1 - w_2) - G^*(u_1 - u_2), w_1 - w_2)_{\overline{W}}$$

$$= (D(u_1 - u_2), u_1 - u_2)_{\overline{U}} + (D'(u_1 - u_2), w_1 - w_2)_{\overline{W}}$$

$$+ (G(w_1 - w_2), u_1 - u_2)_{\overline{U}} - (G^*(u_1 - u_2), w_1 - w_2)_{\overline{W}}$$

$$= (D(u_1 - u_2), u_1 - u_2)_{\overline{U}} + (D'(w_1 - w_2), w_1 - w_2)_{\overline{W}}$$

$$\geq d_1 \|u_1 - u_2\|_{\overline{U}}^2 + d \|w_1 - w_2\|_{\overline{W}}^2$$

Hence, this lemma is completed.

The existence and uniqueness of a saddle point of J(u,w) are illustrated in the following lemma.

526

Lemma 3.2: Assume that (H1) and (H2) hold. There exists $\theta_0 > 0$ such that if $0 < \gamma^2 \leq \theta_0$, then $J(u,w)$ has a unique saddle point.

Proof: Clearly J(u,w) is continuous with respect to u and w. Further, it follows directly from (3.7) and (3.9) that for sufficiently small γ^2,

i) $u \rightarrow J(u, w)$ is convex for each fixed $w \in \overline{W}$,

ii) $w \rightarrow -J(u, w)$ is convex for each fixed $u \in \overline{U}$,

iii) $J(u, w) \rightarrow \infty$ as $\|u\| \rightarrow \infty$ for each fixed $w \in \overline{W}$,

iv) $-J(u, w) \rightarrow \infty$ as $\|w\| \rightarrow \infty$ for each fixed $u \in \overline{U}$.

The result follows from Theorem I.1 in [Bensoussan].

The following result characterizes the saddle point.

Corollary 3.1: (u^0,w^0) is the saddle point of J(u,w) if and only if $J_u(u^0,w^0)=J_w(u^0,w^0)=0$.

Proof: See [Zeidler], p. 467.

The next result gives a further characterization of the saddle point.

Lemma 3.3: Let

$$u^0(t) = -N^{-1}B^* (\Lambda^{-1})^* C^* Cx^0(t) \tag{3.11}$$

$$w^0(t) = \gamma^2 M^{-1} \Phi^* (\Lambda^{-1})^* C^* Cx^0(t) \tag{3.12}$$

where $x^0(t) = \Lambda^{-1}Bu^0(t) + \Lambda^{-1}\Phi w^0(t) + f$. Then (u^0, w^0) is the unique saddle point of J(u,w).

Proof: From corollary 3.1, we only need to check that

$$J_u(u^0, w^0) = J_w(u^0, w^0) = 0$$

where u^0, w^0 are given by (3.11) and (3.12). In fact, applying (3.8), we have

$$J_u(u^0, w^0) = (N + B^* (\Lambda^{-1})^* C^* C\Lambda B) (-N^{-1}B^* (\Lambda^{-1})^* C^* Cx^0)$$

$$+ (B^* (\Lambda^{-1})^* C^* C\Lambda^{-1}\Phi) (\gamma^2 M^{-1}\Phi^* (\Lambda^{-1})^* C^* Cx^0) + B^* (\Lambda^{-1})^* C^* Cf$$

$$= B^* (\Lambda^{-1})^* C^* C(-x^0 + \Lambda^{-1}Bu^0 + \Lambda^{-1}\Phi w^0 + f) = 0$$

Similarly, from (3.10) we have

$$J_w(u^0, w^0) = -(\frac{1}{\gamma^2}M + (-\Phi^* (\Lambda^{-1})^* C^* C\Lambda^{-1}\Phi))(\gamma^2 M^{-1}\Phi^* (\Lambda^{-1})^* C^* Cx^0)$$

$$+ (\Phi^* (\Lambda^{-1})^* C^* C\Lambda^{-1}B)(-N^{-1}B^* (\Lambda^{-1})^* C^* Cx^0) + \Phi^* (\Lambda^{-1})^* C^* Cf$$

$$= \Phi^* (\Lambda^{-1})^* C^* C(-x^0 + \Lambda^{-1}\Phi w^0 + \Lambda^{-1}Bu^0 + f) = 0 .$$

Hence, (u^0, w^0) is the unique saddle point of $J(u,w)$.

The following lemma characterizes the saddle point in terms of the solution to an algebraic Riccati equation. We note that H3 has not been used until now.

Lemma 3.4: Assume that (H1)-(H3) hold. Then the unique saddle point (u^0, w^0) of J can be expressed as

$$u^0(t) = -N^{-1}B^* \Pi x^0(t)$$

$$w^0(t) = \gamma^2 M^{-1}\Phi^* \Pi x^0(t)$$

where $\quad x^0(t) = (\Lambda^{-1}Bu^0)(t) + (\Lambda^{-1}\Phi w^0)(t) + f(t) \quad$ *, and Π is the unique solution of the Riccati equation*

$$(\Pi x, Ay)_{\bar{H}} + (Ax, \Pi y)_{\bar{H}} + (C^* Cx, y)_{\bar{H}} - (\Pi \Omega^2 \Pi x, y)_{\bar{H}} = 0$$

for any $\quad x, y \in D(A) \subseteq H \quad and \quad \Omega = (BN^{-1}B^* - \gamma^2 \Phi M^{-1}\Phi^*)^{1/2} .$

Proof: This result follows from [Bensoussan].

Therefore, the proof of Theorem 3.1 is completed.

(4.) CONVERGENCE OF GALERKIN APPROXIMATIONS

Perhaps one of the most attractive features of the method described in this paper is that the convergence of the Galerkin approximations of the saddle point solution to the differential game is guaranteed by the rich collection of Galerkin approximation results available from infinite dimensional LQR minimization formulations. This is because the solution of the infinite dimensional LQR minimization problem

528

$$\underset{v \in H}{\inf} \int_0^\infty \{|Cz(t)|_H^2 + |v(t)|_H^2\} \, dt \qquad (4.1)$$

subject to the evolution equation in H

$$\dot{z}(t) = Az(t) + \Omega v(t)$$
$$z(0) = z_0 \in H \qquad (4.2)$$

is characterized by the same algebraic Riccati equation that solves the differential game of the preceding section, namely

$$(\Pi x, Ay)_H + (Ax, \Pi y)_H + (C^* Cx, y)_H - (\Pi \Omega \Omega \Pi x, y)_H = 0 \qquad (4.3)$$

With this observation, the idea is to construct finite dimensional versions of (4.1) - (4.3) and then to apply known convergence results such as those found in [Ito] and [Kappel, Salamon]. To proceed, let $\{H_n\}_{n=1}^\infty$ be a family of finite dimensional subspaces of H satisfying

$$H = \overline{\bigcup_{n=1}^\infty H_n}$$

We assume that there are operators $A_n \in L(H_n, H_n)$, $\Omega_n \in L(H_n, H_n)$, $C_n \in L(H_n, H_n)$ and that P_n is the orthogonal projection from H to H_n.

With these finite dimensional operators and spaces, one can consider the following LQR minimization problem:

$$\underset{v \in H_n}{\inf} \int_0^\infty \{|C_n z_n(t)|_{H_n}^2 + |v(t)|_{H_n}^2\} \, dt \qquad (4.1)_n$$

subject to the evolution equation in H_n

$$\dot{Z}_n(t) = A_n Z_n t + \Omega_n v(t)$$
$$Z_n(0) = P_n Z_0 \qquad (4.2)_n$$

The optimal feedback gain for this problem is characterized by a solution to the following algebraic Riccati equation:

$$A_n^* \Pi + \Pi A_n + C_n^* C_n - \Pi \Omega_n \Omega_n \Pi = 0 \qquad (4.3)_n$$

If Π_n and Π are the minimal nonnegative solutions of (4.3)$_n$ and (4.3) respectively, then we may appeal to results in the distributed parameter control literature ([Banks & Kunisch], [Gibson91], [Ito87,Ito89], [Kappel, Salamon]) for conditions under which $\Pi_n P_n \to \Pi$. The following conditions can be found in [Ito87].

(H4)   For each $x \in H$, $S_n(t) P_n x \to S(t) x$ and $S_n^*(t) P_n x \to S^*(t) x$, and the convergence is uniform in t on bounded subintervals of $[0,t]$.

Here, $S_n(t) = exp(tA_n)$ is the semigroup generated by A_n. Note that at $t=0$, this condition implies that $P_n x \to x$ for all $x \in H$.

(H5)   For each $x \in H$, $\Omega_n P_n x \to \Omega x$, $C_n P_n x \to Cx$ and $C_n^* P_n x \to C^* x$.

(H6)   **The family of pairs** (A_n, Ω_n) **and** (A_n, C_n) are uniformly stabilizable and uniformly detectable, respectively. In other words,

(i) there exists a sequence of operators $K_n \in L(H_n, H)$ such that

$$sup\|K_n\| \leq \infty$$

$$\left\| e^{(A_n - \Omega_n K_n) t} P_n \right\| \leq M_1 e^{-\omega_1 t} \qquad t \geq 0$$

for some positive constants M_1 and ω_1, and

(ii) there exists a sequence of operators $G_n \in L(H_n, H)$ such that

$$sup\|G_n\| \leq \infty$$

$$\left\| e^{(A_n - G_n C_n) t} P_n \right\| \leq M_2 e^{-\omega_2 t} \qquad t \geq 0$$

for some positive constants $M_2 > 1$ and ω_2.

The following result is found in [Ito].

Theorem 2 : Under the assumptions (H4)-(H6), the unique nonnegative solution Π_n of (4.3)$_n$ converges strongly to the nonnegative solution Π of (4.3); that is,

$$\lim_{n \to \infty} \|\Pi x - \Pi_n P_n x\| \to 0$$

The point of all this, of course, is that (4.3)$_n$ is finite dimensional, and so we can solve for Π_n numerically. This is done in the next section for specific examples.

530

5. NUMERICAL EXAMPLES

In this section we report on some numerical results for a simple example involving the heat equation in a rod. Consider the equation

$$y_t(t, x) = a y_{xx}(t, x) + b(x) u(t) + \phi(x) w(t) \qquad 0 \le x \le 1$$

$$y(0, x) = y_0(x) \tag{5.1}$$

with Neumann boundary conditions

$$y_x(t, 0) = 0 = y_x(t, 1) \tag{5.2}$$

In addition, consider the LQR cost functional

$$J_0(u) = \frac{1}{2} \int_0^\infty \{ \int_0^1 q y(t, x)^2 dx + N |u(t)|^2 \} dt \tag{5.3}$$

and the disturbance augmented cost functional

$$J_1(u) = \frac{1}{2} \int_0^\infty \{ \int_0^1 q y(t, x)^2 dx + N |u(t)|^2 - \frac{1}{\gamma^2} M |w(t)|^2 \} dt \tag{5.4}$$

We set $U = \Re$, $W = \Re$, and consider the following two problems:

$$\inf_{u \in \overline{U}} J_0(u) \tag{5.5}$$

subject to dynamics governed by (5.1) with $\phi \equiv 0$, and

$$\inf_{u \in \overline{U}} \sup_{w \in \overline{W}} J_1(u, w) \tag{5.6}$$

subject to the dynamics governed by (5.1).

In our basic numerical experiment, we implement the LQR feed back controller (from (5.5)) in the presence of a disturbance, and then do the same for the game theoretic controller (from (5.6)). We then compare the performance of the two controllers in the presence of disturbance. Before giving some numerical results, we briefly discuss how this problem is reformulated within the framework developed earlier.

First, set $H = L^2(0, 1)$ and define the operators $B \in L(U, H)$, $\Phi \in L(W, H)$ by $Bu = b(x) u$, and $\Phi w = \phi(x) w$. In addition, define the operator A on the domain

$$dom\ A = \{ y \in H^2(0, 1); \quad y'(0) = y'(1) = 0 \} \tag{5.7}$$

by $Ay = ay''$.

Next we introduce Galerkin approximations based on finite dimensional spaces H^n with linear spline ("hat" functions) shape functions. This leads to the following finite dimensional version of (5.1):

$$\dot{\alpha}(t) = A^n \alpha(t) + B^n u(t) + \Phi^n w(t) \qquad (5.8)$$

$$\alpha(0) = \alpha_0$$

where $\alpha(t) \in \Re^n$, and A^n, B^n, Φ^n are $n \times n, n \times 1$ and $n \times 1$ dimensional matrices, respectively. We use Π_0 to represent the solution of the finite-dimensional algebraic Riccati equation associated with the LQR cost functional

$$J_0^n(u) = \int_0^\infty \{ q\alpha(t)^T \alpha(t) + N|u(t)|^2 \} dt$$

and Π_1 to represent the solution of the Riccati equation associated with the game theory cost functional

$$J_1^n(u, w) = \int_0^\infty \{ q\alpha(t)^T \alpha(t) + N|u(t)|^2 - \frac{1}{\gamma^2} M|w(t)^2| \} dt \qquad .$$

In the figures below we plot the approximation to $y\,(t,x)$ for several different problems.

As data for these examples, we used $a=1, N=1, M=1, q=10, \gamma = 0.5, b(x) \equiv 0.25, \phi(x) \equiv -0.35$ and $y_0(x)=10x$.

In Figure 1 we plot the open loop solution for the problem

$$\dot{\alpha}(t) = A^n \alpha(t) \qquad .$$

In Figure 2 we plot the LQR closed loop solution (no disturbance) for the problem

$$\dot{\alpha}(t) = (A^n - B^n N^{-1} B^{nT} \Pi_0) \alpha(t) \qquad .$$

In Figure 3 we plot the LQR closed loop solution (with disturbance term) for the problem

$$\dot{\alpha}(t) = (A^n - B^n N^{-1} B^{nT} \Pi_0) \alpha(t) + \Phi^n w(t) \qquad .$$

In Figure 4 we plot the game theory closed loop solution (with disturbance term) for the problem

$$\dot{\alpha}(t) = (A^n - B^n N^{-1} B^{nT} \Pi_1) \alpha(t) + \Phi^n w(t) \qquad .$$

While figures (1) - (4) describe the qualitative nature of the transient response in each of the four cases, figures (5)-(8) illustrate an important difference in the examples by taking a cross-section in space at x=2/3. The basic observation to be made is that the game theory controller improves performance (in the sense of driving the state to the zero equilibrium position) in the presence of disturbances. We have performed several such experiments with various parameters (including Dirichlet boundary data) and observed qualitatively the same behavior. We are currently applying this method to systems involving elastic structures. Preliminary results indicate that an LQR controlled system may, even worse than performing poorly, become destabilized in the presence of disturbance. These results will be reported in a future manuscript.
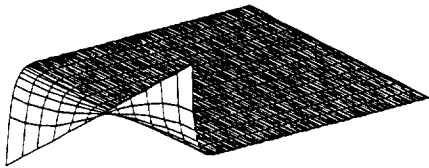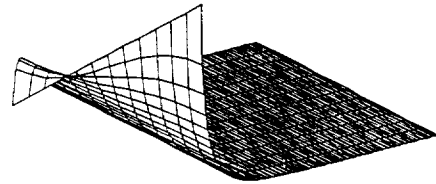
Figure (1) Open Loop Response
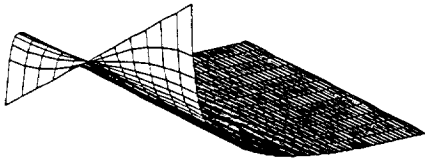

Figure (2) LQR Closed Loop Response
No Disturbance

Figure (3) LQR Closed Loop Response
With Disturbance

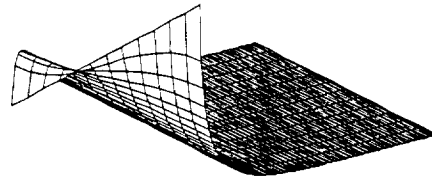

Figure (4) Game Theoretic Closed Loop
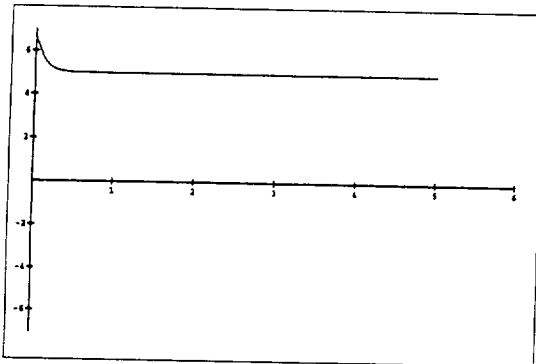Response with Disturbance
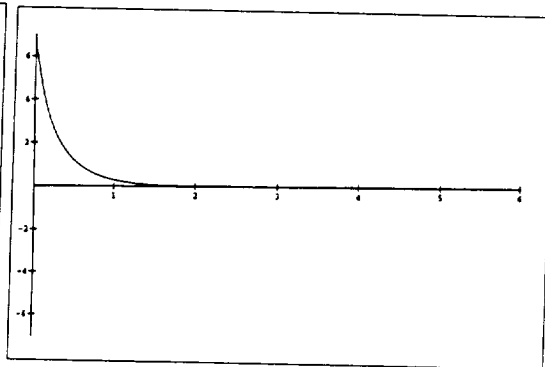

Figure (5) Open Loop Response, x=.75

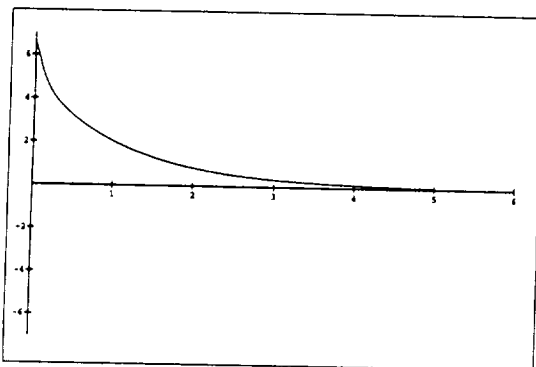

Figure (6) LQR Closed Loop Response, x=.75
Nó Disturbance

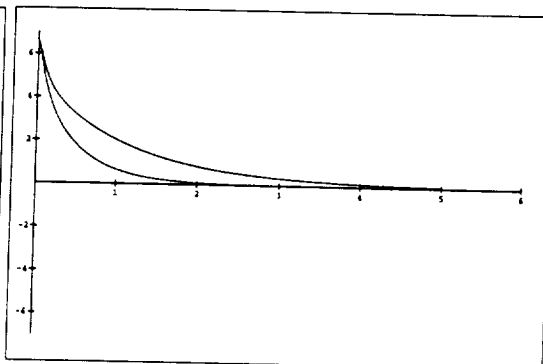Figure (7) LQR Closed Loop Response, x=.75
With Disturbance

Figure (8) Game / LQR Closed Loop Response, x=.75
With Disturbance

533

One of the key motivations for the work in this paper is the applicability of the approach to uncertain distributed parameter systems. A second numerical example outlined in this section has been based on examples in [Rosen], but with the introduction of a region of the structure in which the control influence is uncertain. Again, the problem is to find

$$\inf_{u \in \bar{U}} \ \sup_{w \in \bar{W}} \int_0^\infty \{ (Qy(t),y(t))_H + N(u(t),u(t))_U - \frac{1}{\gamma^2}(w(t),w(t))_W \} \, dt$$

where

$$H = L^2(0,1) \qquad \bar{H} = L^2(0,\infty;H)$$
$$U = L^2(0,1) \qquad \bar{U} = L^2(0,\infty;H)$$
$$W = \Re \qquad \bar{W} = L^2(0,\infty;\Re)$$

The min-max problem stated above is subject to the evolution equation

$$\frac{\partial}{\partial t}y(t,x) = a\frac{\partial^2}{\partial x^2}y(t,x) + bu(t,x) + \phi(x)w(t)$$

$$y(t,0) = y(t,1) = 0 \qquad for \qquad t \geq 0$$
$$y(0,\eta) = y^0(\eta) \qquad for \qquad 0 \leq \eta \leq 1$$

where the operator ϕ is defined by

$$\phi(x)w(t) = \begin{cases} \dfrac{w(t)}{\beta_2 - \beta_1} & \beta_1 < x < \beta_2 \\ 0 & otherwise \end{cases}$$

and where a=.25, b=1.0, N=.01, β_1=.49, and β_2=.51. Motivated by [Rosen], the operator Q is defined to be simply the projection onto the first three open loop modes

$$(Qf)(x) = \sum_{i=1}^{3} (f,e_i)e_i(x)$$

where $e_i(x) = \sqrt{2}\sin(i\pi x)$.

The operator ϕ represents the "spatially structured" disturbance. In actual applications, the disturbance could be due to sensor dynamics or structured parametric uncertainty. In either case, the

534

task is to design a finite dimensional controller that is robust with respect to the class of disturbances that can be input by φ. Figures (9) through (12) depict the transient response of the heat equation in the rod where

$$\theta = \frac{1}{\gamma^2}$$

is defined to be $\theta = 0.5$ in this example. The system is clearly exponentially stable, as predicted by the theory, despite the introduction of disturbance. From [Curtain] and the discussion earlier in this paper, one can conclude that the disturbance attenuation of the closed loop transfer function from disturbance to input and output is bounded by

$$\| T_{cl} \|_\infty < \gamma$$

where

$$\theta = \frac{1}{\gamma^2}$$

Even stronger conclusions can be obtained for this particular problem by noting that the entire heat equation, including disturbance, can be cast in terms of Hilbert-Schmidt operators as described in [Rosen]. The Hilbert-Schmidt norm of the difference between the approximating Riccati equation solutions and the actual Riccati equation solution converges to zero. This is demonstrated graphically in figures (13) through (15) which show the kernels used to represent the Riccati operators. The kernels clearly converge as the level of discretization increases. Furthermore, for the small value of θ=.0001 selected, the Riccati operators should be quite close to the LQR approximations. This is, in fact, the case, as can be concluded by comparing figures (13) - (15) with figures (4.1b), (4.1c) and (4.1d) of [Rosen]. The Riccati kernels for θ=.5 are depicted in figures (16)-(19).

Figure (9) Heat Equation Transient Response, $N_c = 8$
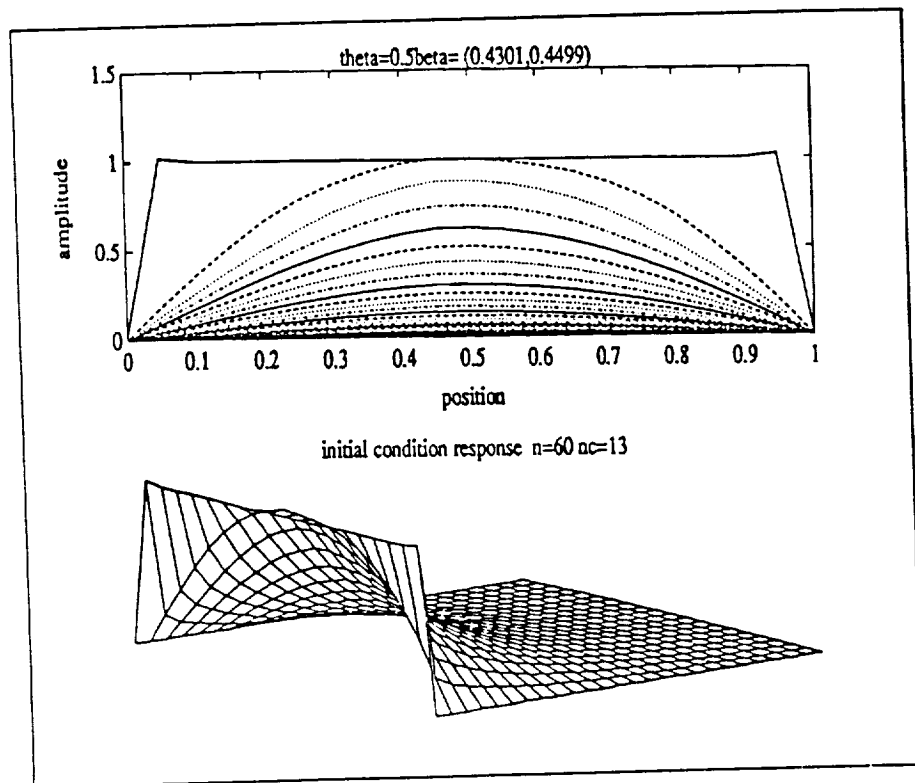
Figure (10) Heat Equation Transient Response, $N_c = 13$

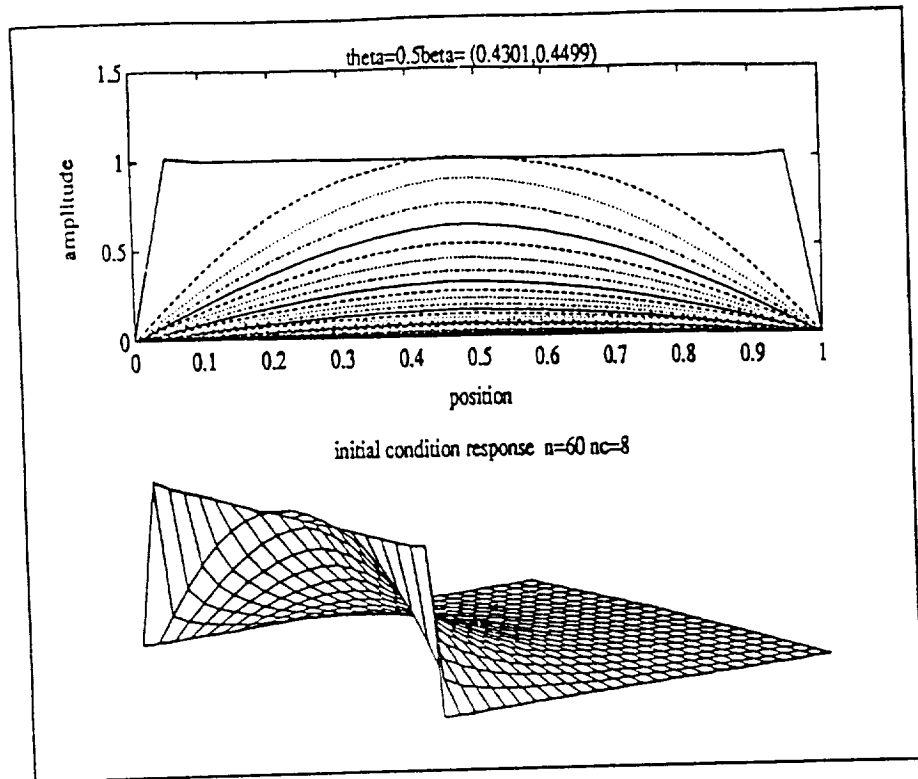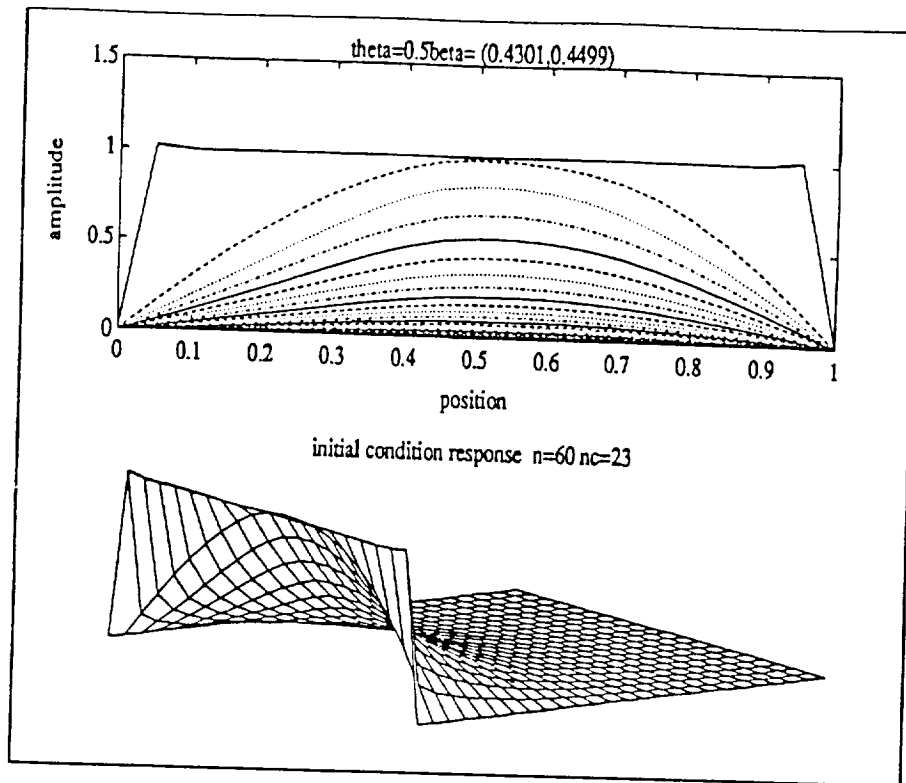Figure (11) Heat Equation Transient Response, N_c=23
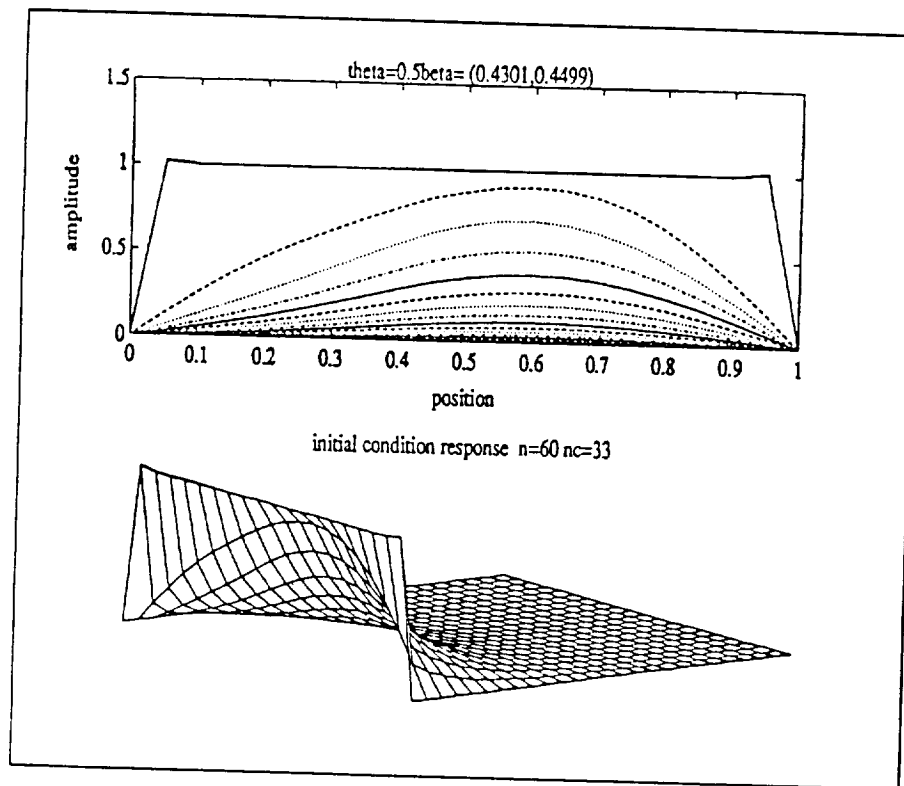
Figure (12) Heat Equation Transient Response, N_c=33

537

Figure (13) Heat Equation Riccati Kernel, N=8, θ=.0001

Figure (14) Heat Equation Riccati Kernel, N=8, θ=.0001

538

Figure (15) Heat Equation Riccati Kernel, N=8, θ=.0001

Figure (16) Heat Equation Riccati Kernel, N=8, θ=.5
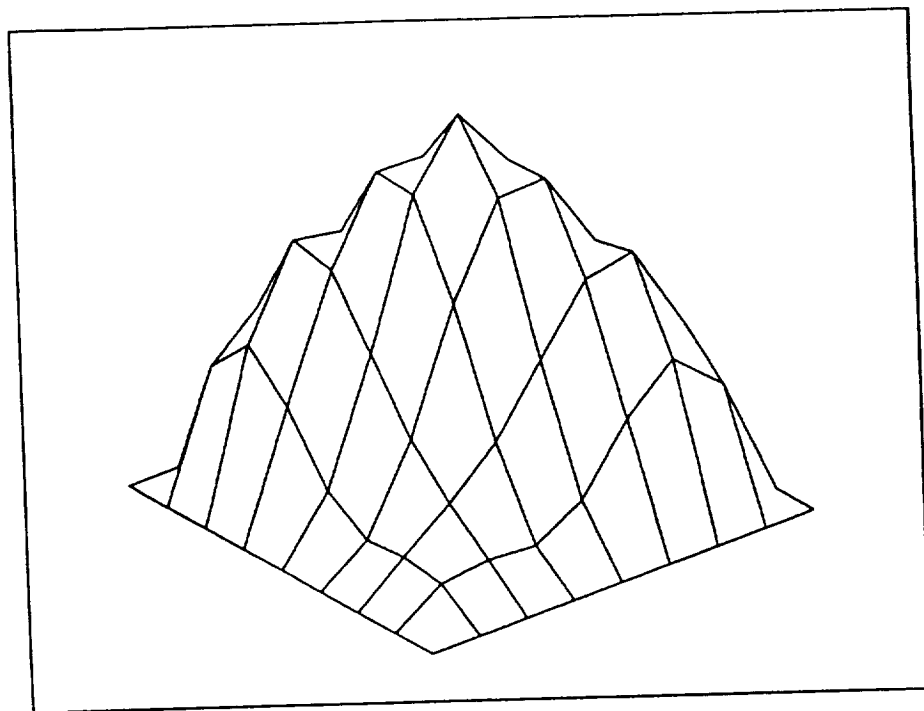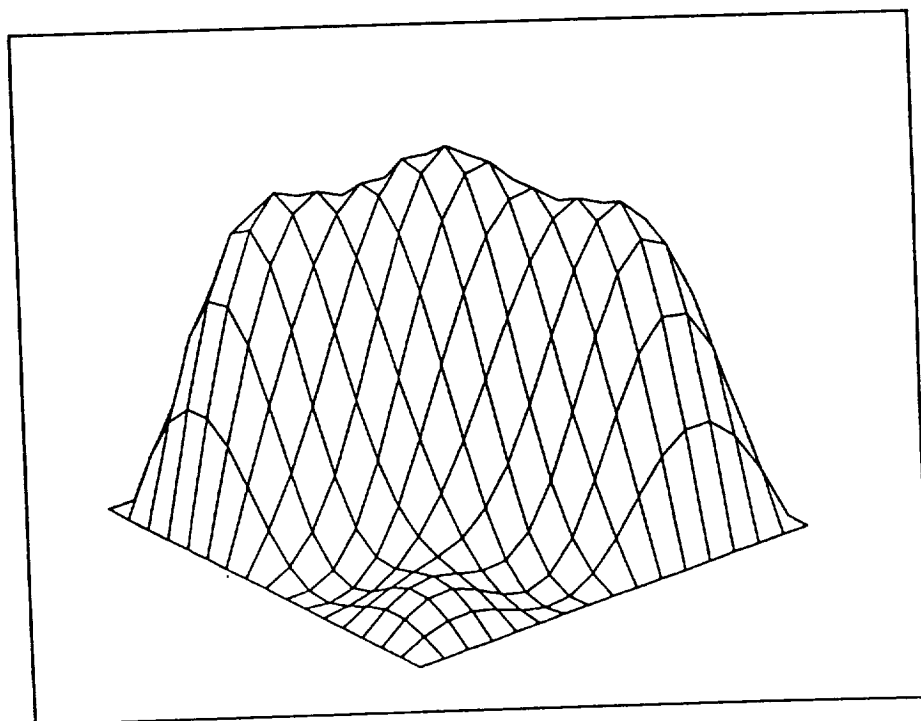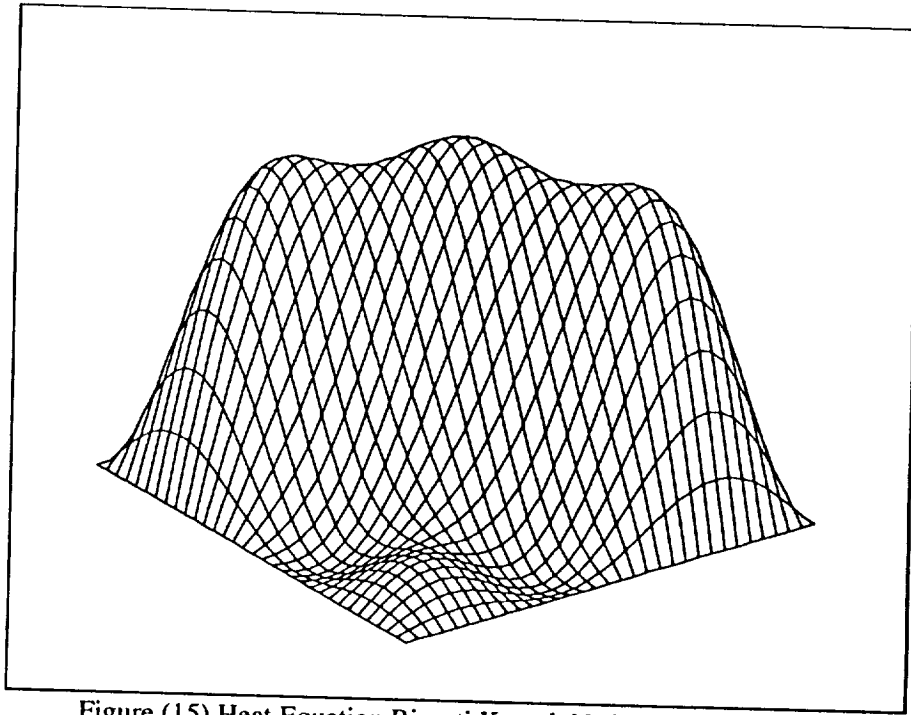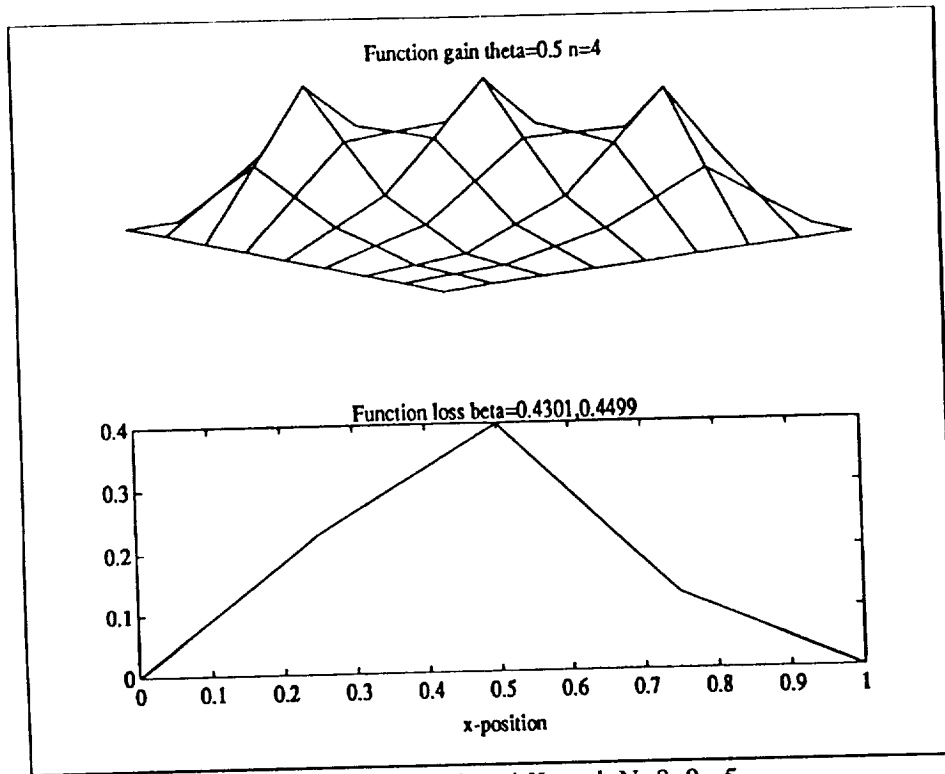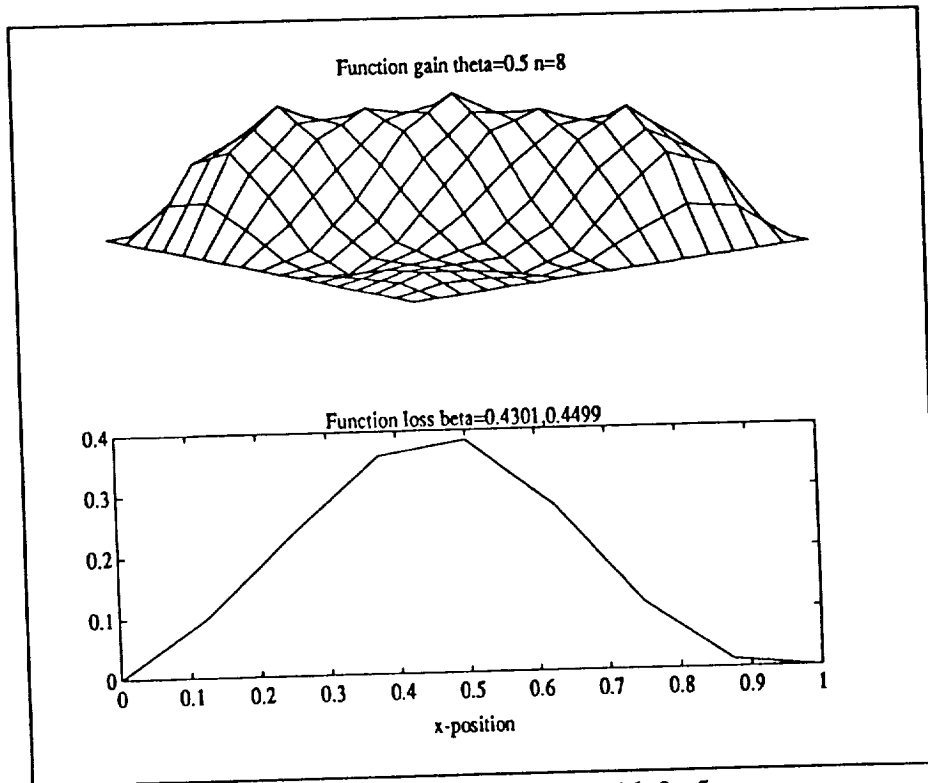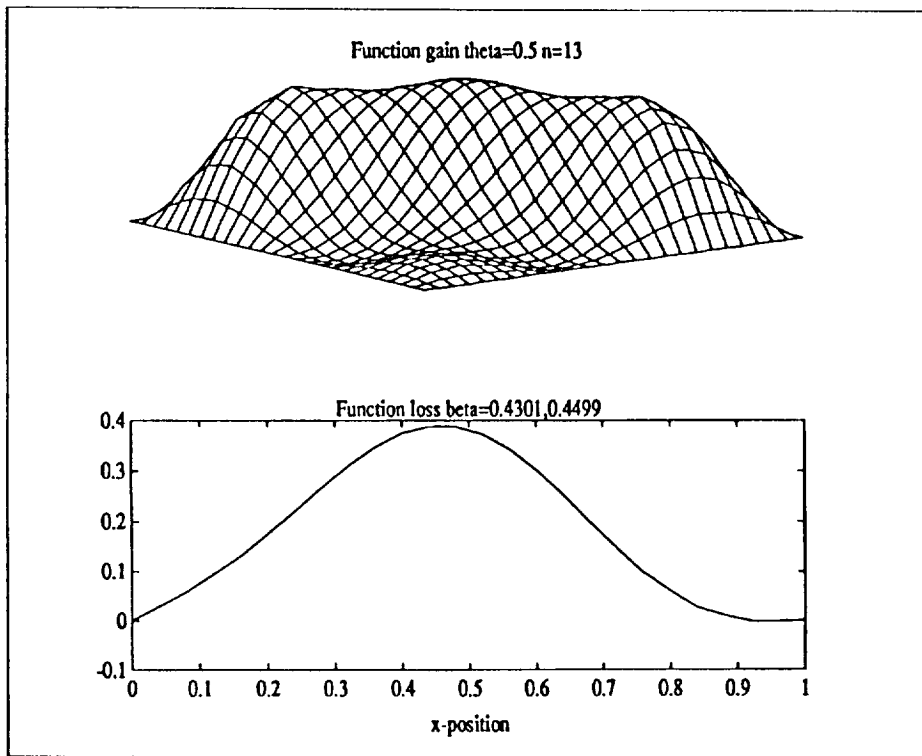

Figure (17) Heat Equation Riccati Kernel, N=16, θ=.5

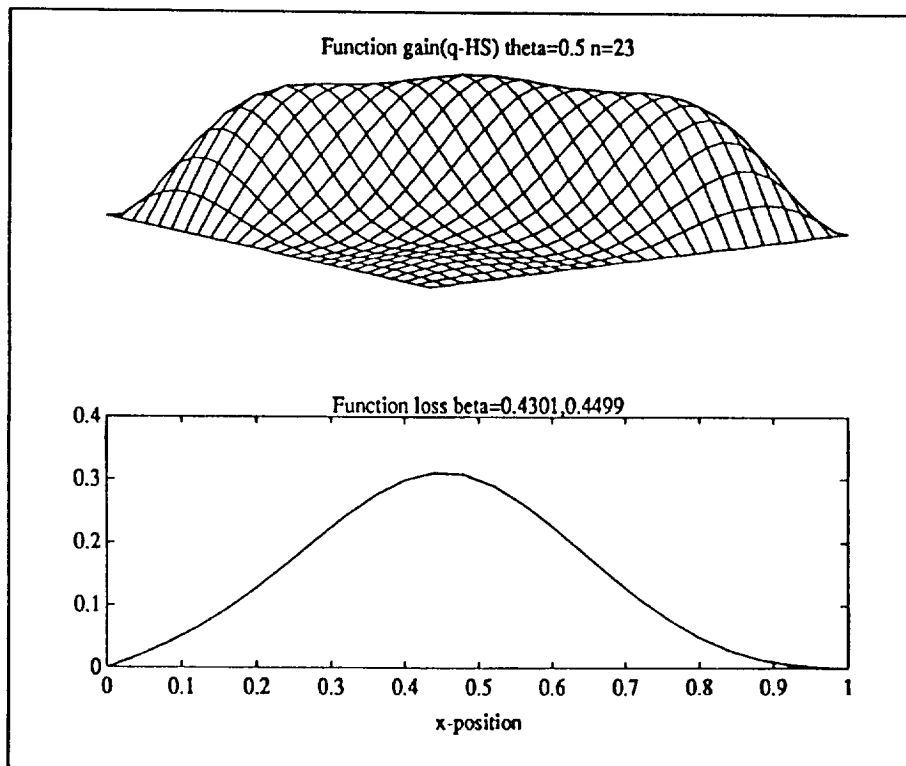540

Figure (18) Heat Equation Riccati Kernel, N=16, θ=.5

Figure (19) Heat Equation Riccati Kernel, N=32, θ=.5

541

REFERENCES

[1] Attouch, H., *Variational Convergence for Functions and Operators*, Pitman Advanced Publishing Program, Boston, 1984.

[2] Balakrishnan, A.V., *Applied Functional Analysis*, Springer-Verlag, New York, 1976.

[3] Banks, H.T. and Kunisch, K., "The Linear Regulator Problem for Parabolic Systems," *SIAM J. Control and Optimization*, vol. 22, no. 5, September, 1984, pp. 684-698.

[4] Basar, Tamer and Bernhard, Pierre, *H-inf Optimal Control and Related Minimax Design Problems*, Birkhauser, Boston, 1991.

[5] Bensoussan, A., "Saddle Points of Convex Concave Functionals," *Differential Games and Related Topics*, H.W. Kuhn and G.P. Szego, eds., North-Holland Publishing Company, Amsterdam, 1971.

[6] Cavazzuti, E., "Convergence of Equilibria in the Theory of Games," *Optimization and Related Fields*, Springer-Verlag Lecture Notes, pp. 95-130.

[7] Curtain, R.F., "H-inf Control for Distributed Parameter Systems: A Survey," *Proceedings of the 29th Conference on Decision and Control*, Honolulu, Hawaii, December, 1990, pp. 22-26.

[8] Gibson, J.S., "The Riccati Integral Equations For Optimal Control Problems On Hilbert Spaces," *SIAM J. Control and Optimization*, vol. 17, no. 4, July, 1979, pp. 537-559.

[9] Gibson, J.S., "An Analysis of Optimal Modal Regulation: Convergence and Stability," *SIAM J. Control and Optimization*, vol. 19, no. 5, September, 1981, pp. 686-707.

[10] Gibson, J.S. and Adamian, A., "Approximation Theory for Linear-Quadratic-Gaussian Optimal Control of Flexible Structures," *SIAM J. Control and Optimization*, vol. 29, no. 1, January, 1991, pp. 1-37.

[11] De Giorgi, "Γ-convergenza e G-convergenza," *Bull. Un. Mat. Ital.*, no. 5, 14-A, 1977, pp. 213-220.

[12] Girko, V.L., Lyashko, S.I., and Nakonechnyi, A.G., "Minimax Regulators for Evolution Equations in Hilbert Spaces, Under Indeterminacy Conditions," *Kibernetika*, No. 1, January-February, 1987, pp. 67-68.

[13] Ito, Kazufumi, "Strong Convergence and Convergence Rates of Approximating Solutions for Algebraic Riccati Equations in Hilbert Spaces," *Lecture Notes in Control and Information Sciences*, vol. 102, Springer-Verlag, New York, 1987.

[14] Ito, K., and Tran, H.T., "Linear Quadratic Optimal Control Problem for Linear Systems with Unbounded Input and Output Operators: Numerical Approximations," *International Series of Numerical Mathematics*, Vol. 91, Birkhauser Verlag Basel, 1989, pp. 171-195.

[15] Kappel, F. and Salamon, D., "An Approximation Theorem for the Algebraic Riccati Equation," *SIAM J. Control and Optimization*, vol. 28, no. 5., 1136-1147, September, 1990, pp. 1136-1147.

[16] McFarlane, D.C., and Glover, K., *Robust Controller Design Using Normalized Coprime Factor Plant Descriptions*, Springer-Verlag, New York, 1989.

[17] Maciejowski, J.M., *Multivariable Feedback Design*, Addison-Wesley Publishing Company, Cornwall, Great Britain, 1989.

542

[18] Rosen, I.G., , "On Hilbert-Schmidt Norm Convergence of Galerkin Approximations for Operator Riccati Equations," *International Series of Numerical Mathematics*, Vol. 91, Birkhauser Verlag Basel, 1989, pp. 335-349.

[19] Zeidler, E., "Nonlinear Functional Analysis and its Applications II/B : Nonlinear Monotone Operators," Springer Verlag, New York, 1990.

543

SIMULATION AND MODELING SOFTWARE

TRANSFER FUNCTION MODELING OF DAMPING MECHANISMS IN DISTRIBUTED PARAMETER MODELS

J.C. Slater* and D.J. Inman†
Mechanical Systems Lab, Department of Mechanical and Aerospace Engineering
State University of New York at Buffalo, Buffalo, NY 14260
(716) 636-2733

INTRODUCTION

This work formulates a method for the modeling of material damping characteristics in distributed parameter models which may be easily applied to models such as rod, plate and beam equations. The general linear boundary value vibration equation is modified to incorporate hysteresis effects represented by complex stiffness using the transfer function approach proposed by Golla and Hughes. The governing characteristic equations are decoupled through separation of variables yielding solutions similar to those of undamped classical theory, allowing solution of the steady state as well as transient response. Example problems and solutions are provided demonstrating the similarity of the solutions to those of the classical theories and transient responses of non-viscous systems.

BACKGROUND

Classical damping models assume a simple damping term proportional to velocity and/or strain rate such that the equations of motion decouple readily.(See for instance Reismann[1] and Soedel[2]). This modeling technique is more often an equivalent viscous damping representation of non-viscous damping than a representation of the real structural damping[3]. Banks et.al.[4] have shown experimentally that hysteretic effects dominate the damping mechanisms in a cantilevered composite beam. However, analysis of hysteretic models is quite difficult. Inman[5] proposed using the Golla and Hughes viscoelastic model for modeling damping in composite beams, and Slater[6] extended this theory to plates. A simple method of representing damping mechanisms over a wide frequency range which can be included in the general linear boundary value vibration equation to arrive at a closed form solution for the damped response is presented in the following.

The time hysteretic stress-strain relation is given by

$$\sigma(x, t) = \varepsilon(x, t)E - \int_0^t g(t - s)\varepsilon(x, s)ds \qquad (1)$$

where $\sigma(x, t)$ is the stress, x is the vector of spacial coordinates, $\varepsilon(x,t)$ is the strain, and the kernel $g(t - s)$ describes the hysteresis as developed by Christensen[7] or Banks[8], for example. The general linear boundary value vibration equation incorporating viscous and hysteretic damping may then be written as

$$\ddot{w}(x, t) + d\dot{w}(x, t) + L_2\big[L_3(x)w(x, t) + L_1 w(x, t)\big] = f(x, t) \qquad (2)$$

*Graduate Research Assistant, Mechanical Systems Lab, Department of Mechanical and Aerospace Engineering

†Professor and Department Chair, Mechanical Systems Lab, Department of Mechanical and Aerospace Engineering

where $w(x,t)$ is the displacement, d is the viscous damping coefficient, and $f(x,t)$ is the forcing function. The operators L_2 and L_3 are stiffness operators; L_1 represents the integral part of (1) and (˙) denotes partial differentiation with respect to time.

In modeling damping using finite element models, Golla and Hughes[9] have shown that the variation of material damping and stiffness properties as a function of frequency (i.e. time hysteresis) can be represented by

$$E^*(s) = E\left[1 + \sum_{i=1}^{k} \alpha_i \frac{\beta_i s^2 + \gamma_i s}{\beta_i s^2 + \gamma_i s + \eta_i}\right] \tag{3}$$

where $E^*(s)$ is the complex modulus of elasticity, E is the static modulus of elasticity, and s is the Laplace domain operator. The symbols α_n, β_n, γ_n, and η_n represent constants for curve fitting to match complex modulus data. Ideally, k would be infinite in order to perfectly match the material properties over all frequencies. However, it is up to the analyst to determine the value of k in order to obtain sufficient accuracy. Although this transfer function has been developed for finite element models, it is easily extendable to distributed parameter theory.

Using (3) to model the time hysteretic stress-strain effects of (1) gives

$$\sigma(x,s) = E^*(s)\varepsilon(x,s) = E\left[1 + \sum_{i=1}^{k} \alpha_i \frac{\beta_i s^2 + \gamma_i s}{\beta_i s^2 + \gamma_i s + \eta_i}\right]\varepsilon(s) \tag{4}$$

Incorporating the GHM model into the Laplace domain representation of (2) results in

$$s^2 W(x,s) - s w(x,0) - w_t(x,0) + s d W(x,s)$$
$$- d w(x,0) + L_2\left[E^*(s)N(x)W(x,s)\right] = F(x,s) \tag{5}$$

where the operator L_1 has been replaced by

$$L_1 = E\sum_{i=1}^{k} \alpha_i \frac{\beta_i s^2 + \gamma_i s}{\beta_i s^2 + \gamma_i s + \eta_i} \tag{6}$$

and the operator L_3 has been factored into

$$L_3 = E N(x) \tag{7}$$

to yield a linear partial differential equation. The purpose of the factorization of (7) is for the case of the beam or rod of varying cross section. For example, for a beam with varying cross section,

$$N(x) = \frac{I(x)}{\rho A} \frac{\partial^2}{\partial^2 x} \tag{8}$$

where x is the distance along the beam, $I(x)$ is the moment of area, ρ is the material density, and A it the cross sectional area. Note that when the force or displacement is represented by capital letters it denotes the Laplace transformed variable.

ANALYSIS

Consider the solution of (5) by separation of variables/modal expansion with associated permissible boundary conditions. The solutions are then in the form

$$w(\mathbf{x},s) = \sum_{n=1}^{\infty} w_n(\mathbf{x},s) = \sum_{n=1}^{\infty} a_n(s)\Phi_n(\mathbf{x}) \tag{9}$$

Substituting (9) into (5) yields

$$\sum_{n=1}^{\infty}\left[\left(s^2 + sd + E^*(s)L_2 N(\mathbf{x})\right)A_n(s)\right]\Phi_n(\mathbf{x}) - (s+d)w(\mathbf{x},0) - \dot{w}(\mathbf{x},0) = F(\mathbf{x},s) \tag{10}$$

If $\Phi_n(\mathbf{x})$ are chosen to be the eigenfunctions of the operator $L_2 N(\mathbf{x})$ such that the boundary conditions are satisfied and

$$L_2 N(\mathbf{x})\Phi_n = \lambda_n \Phi_n \tag{11}$$

then (10) becomes

$$\sum_{n=1}^{\infty}\left[\left(s^2 + sd + E^*(s)\lambda_n\right)A_n(s)\right]\Phi_n(\mathbf{x}) - (s+d)w(\mathbf{x},0) - \dot{w}(\mathbf{x},0) = F(\mathbf{x},s) \tag{12}$$

where λ_n are the eigenvalues of the associated with the eigenfunctions $\Phi_n(\mathbf{x})$. Note that (11) is the usual modal assumption for the undamped equations of motion.

The functions are assumed to be orthonormal such that

$$\int_{\Omega} \Phi_n(\mathbf{x})\Phi_m(\mathbf{x})d\Omega = \delta_{nm} \tag{13}$$

where Ω is the spacial domain of the equation, i.e. length for a beam and area for a plate.

Multiplying (12) by $\Phi_m(\mathbf{x})$, integrating over the region Ω and applying (13) yields the n temporal equations

$$\left[\left(s^2 + sd + E^*(s)\lambda_n\right)A_n(s) - (s+d)a_n(0) - \dot{a}_n(0)\right] = f_n(s) \tag{14}$$

where

$$f_n(s) = \int_{\Omega} F(\mathbf{x},s)\Phi_n(\mathbf{x})d\Omega \tag{15}$$

and

$$a_n(0) = \int_{\Omega} w(\mathbf{x},0)\Phi_n(\mathbf{x})d\Omega \quad , \quad \dot{a}_n(0) = \int_{\Omega} \dot{w}(\mathbf{x},0)\Phi_n(\mathbf{x})d\Omega \tag{16}$$

The solution of the temporal equation is then

$$A_n(s) = \frac{\left[f_n + (s+d)a_n(0) + \dot{a}_n(0)\right]\prod_{j=1}^{k} d_j}{\prod_{j=1}^{k} d_j \left(s^2 + sd + E\lambda_n\right) + E\lambda_n \sum_{i=1}^{k}\left[\alpha_i(d_i - \eta_i)\prod_{\substack{j=1 \\ j\neq i}}^{k} d_j\right]} \qquad (17)$$

where (3) has been substituted into the solution and $d_i = \beta_i s^2 + \gamma_i s + \eta_i$.

EXAMPLE

Consider a problem involving decay from initial conditions of a simply supported 1 cm thick 1.5m x 2m plate given an assumed complex modulus. A complex modulus represented by a single expansion term has been arbitrarily chosen in order to obtain a simple solution. The parameters are as labeled.
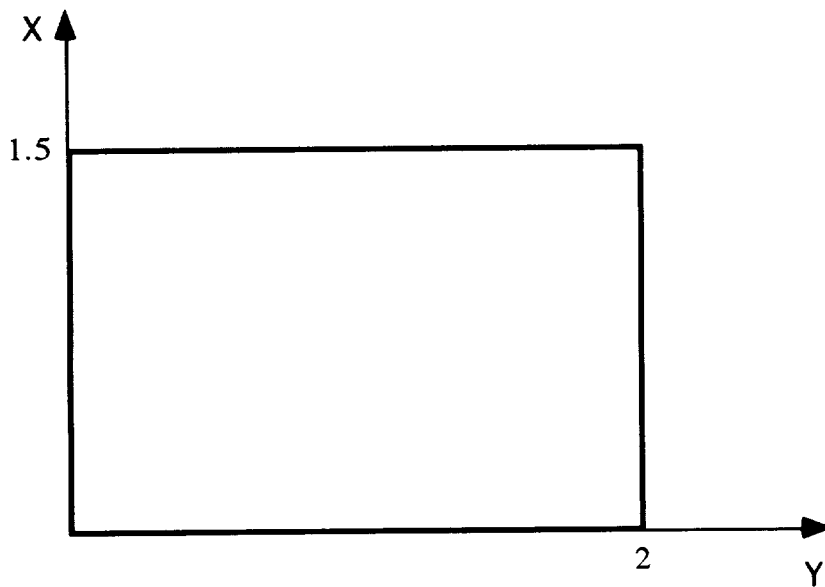
Figure 1

$$\rho = 2700\frac{kg}{m^3}, E = 6.89 \times 10^{10}\,Pa, v = .34, h = .01m$$

The viscoelastic properties are $\alpha = .6, \beta = 1, \gamma = 1.5 \times 10^4, \mu = 1.5 \times 10^6$.

The initial conditions are given as $w(x, y, 0) = .01\sin(\frac{x\pi}{1.5})\sin(\frac{y\pi}{2})$, which is the first mode shape, with an amplitude of .01. The following time derivatives are also set: $\dot{w}(x, y, 0) = \ddot{w}(x, y, 0) = \dddot{w}(x, y, 0) = 0$. The need for this will become apparent. The equation of motion for a plate is

550

$$s^2 W(x, y, s) + \frac{D^*(s)}{\rho h} \nabla^4 W(x, y, s) = \frac{F(x,y,s)}{\rho h} \tag{E1}$$

From eqns. (3) and (5),

$$\frac{D(s)}{\rho h} = \frac{1}{\rho h} \frac{E^*(s) h^3}{12(1 - v^2)} = 240.5\left(1 + .6 \frac{s^2 + 1.5 \times 10^4 s}{s^2 + 1.5 \times 10^4 s + 1.5 \times 10^6}\right) \tag{E2}$$

where m and n are integers from 1 to ∞. The natural frequencies of an undamped simply supported plate are given by (See Reismann [1] for instance)

$$\Omega_{mn} = \sqrt{Re(D(s)/\rho h)} \left[\left(\frac{m\pi}{1.5}\right)^2 + \left(\frac{n\pi}{2}\right)^2\right] \tag{E3}$$

Using eqns. (E2) and (E3), $\Omega_{11} = 124.14$ rad/sec, and $K(124.14\ i) = 328.3\ (1 + .217\ i)$. From eqn. (17)

$$A(s) = \frac{s^2 + 1.5 \times 10^4 s + 1.5 \times 10^6}{s^4 + 1.5 \times 10^4 s^3 + 1.5247 \times 10^6 s^2 + 3.6986 \times 10^8 s + 2.3116 \times 10^{10}} \tag{E4}$$

which can be represented in state space form as

$$\begin{bmatrix} \dot{z}_1 \\ \dot{z}_2 \\ \dot{z}_3 \\ \dot{z}_4 \end{bmatrix} = \begin{bmatrix} 0 & 1 & 0 & 0 \\ 0 & 0 & 1 & 0 \\ 0 & 0 & 0 & 1 \\ -1.69 \times 10^{10} & -2.71 \times 10^8 & -1.52 \times 10^6 & -1.5 \times 10^4 \end{bmatrix} \begin{bmatrix} z_1 \\ z_2 \\ z_3 \\ z_4 \end{bmatrix} \tag{E5}$$

and

$$a(t) = \begin{bmatrix} 5.6 \times 10^4 & 5.6 \times 10^4 & 3.7 \times 10 - 2 & 0 \end{bmatrix} \begin{bmatrix} z_1 \\ z_2 \\ z_3 \\ z_4 \end{bmatrix} \tag{E6}$$

where the states z are related to the displacement by equation (E6) and the initial conditions are $a(0) = .01$ and $\dot{a}(0) = \ddot{a}(0) = \dddot{a}(0) = 0$.

From eqn. (E6), its time derivatives, and the initial conditions,

$$\begin{bmatrix} a \\ \dot{a} \\ \ddot{a} \\ \dddot{a} \end{bmatrix}_{t=0} = \begin{bmatrix} 5.6 \times 10^4 & 5.6 \times 10^2 & 3.7 \times 10^{-2} & 0 \\ 0 & 5.6 \times 10^4 & 5.6 \times 10^2 & 3.7 \times 10^{-2} \\ -6.3 \times 10^8 & -1.0 \times 10^7 & -6.7 \times 10^2 & 0 \\ 0 & -6.3 \times 10^8 & -1.0 \times 10^7 & -6.7 \times 10^2 \end{bmatrix} \begin{bmatrix} z_1 \\ z_2 \\ z_3 \\ z_4 \end{bmatrix}_{t=0} = \begin{bmatrix} .01 \\ 0 \\ 0 \\ 0 \end{bmatrix}, \tag{E7}$$

the solution of which is

$$\begin{bmatrix} z_1 \\ z_2 \\ z_3 \\ z_4 \end{bmatrix}\Bigg|_{t=0} = \begin{bmatrix} 4.8 \times 10^{-7} \\ -1.6 \times 10^{-6} \\ -4.3 \times 10^{-1} \\ 6.4 \times 10^3 \end{bmatrix} \qquad (E8)$$

The results of a digital simulation of the plate response are shown in figure 2. The decay envelope for an equivalent viscous damped plate ($\xi = \eta/2$ where η is the loss factor of the material at 124.14 rad/sec) is shown for comparison.
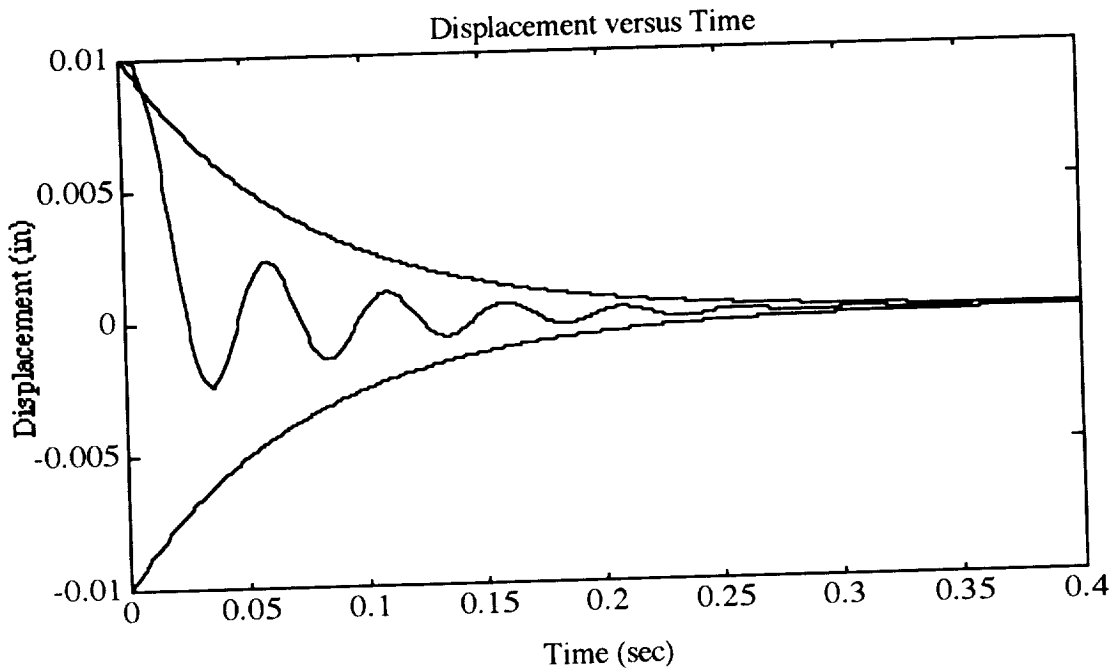
Figure 2

DISCUSSION

A method has been presented solving viscoelastic plate problems which accounts for frequency dependent modulus of elasticity. The solution yields the same orthogonal eigenfunctions/modes as classical plate theory while producing decaying temporal functions representing viscoelastic effects. This method provides a simple approximation for modelling viscoelastic plates. The solution reduces to the classical Sophie Germain solution when the hysteresis terms are dropped, as can be seen in equation (17) when α_n is set equal to zero.

552

ACKNOWLEDGEMENTS

REFERENCES

1) Reismann, H., *Elastic Plates, Theory and Application*, John Wiley & Sons, New York, 1988.

2) Soedel, W., *Vibration of Shells and Plates*, Marcel Dekker, Inc., New York, 1981.

3) Cudney, H.H. and Inman, D.J., "Determining Damping Mechanisms in a Composite Beam by Experimental Modal Analysis," *International Journal of Analytical and Experimental Modal Analysis*, Vol. 4, No. 4, Oct. 1989, pp. 138-143.

4) Banks, H.T., Fabiano, R.H., Wang, Y., Inman, D.J., and Cudney, H.H., "Spatial Versus Time Hysteresis in Damping Mechanisms," *Proceedings of the 27th IEEE CDC*, 1988, pp. 1674-1677.

5) Inman, D.J., "Vibration Analysis of Viscoelastic Beams by Separation of Variables and Model Analysis," *Mechanics Research Communications*, Vol. 16, Apr. 1989, pp. 213-218.

6) Slater, J.C. and Inman, D.J., "Transfer Function Modeling of Damping Mechanisms in Viscoelastic Plates," *32nd Structures, Structural Dynamics, and Materials Conference*, Apr. 1991, pp. 2381-2383.

7) Christensen, R.M., *Theory of Viscoelasticity: An Introduction*, Academic Press, New York, 1982.

8) Banks, H.T. and Inman, D.J., "On Damping Mechanisms in Beams," No. #89-3, University of Southern California, Sep. 1989.

9) Golla, D.F. and Hughes, P.C., "Dynamics of Viscoelastic Structures—a Time Domain Finite Element Formulation," *ASME Journal of Applied Mechanics*, Vol. 52, Dec. 1985, pp. 897-906.
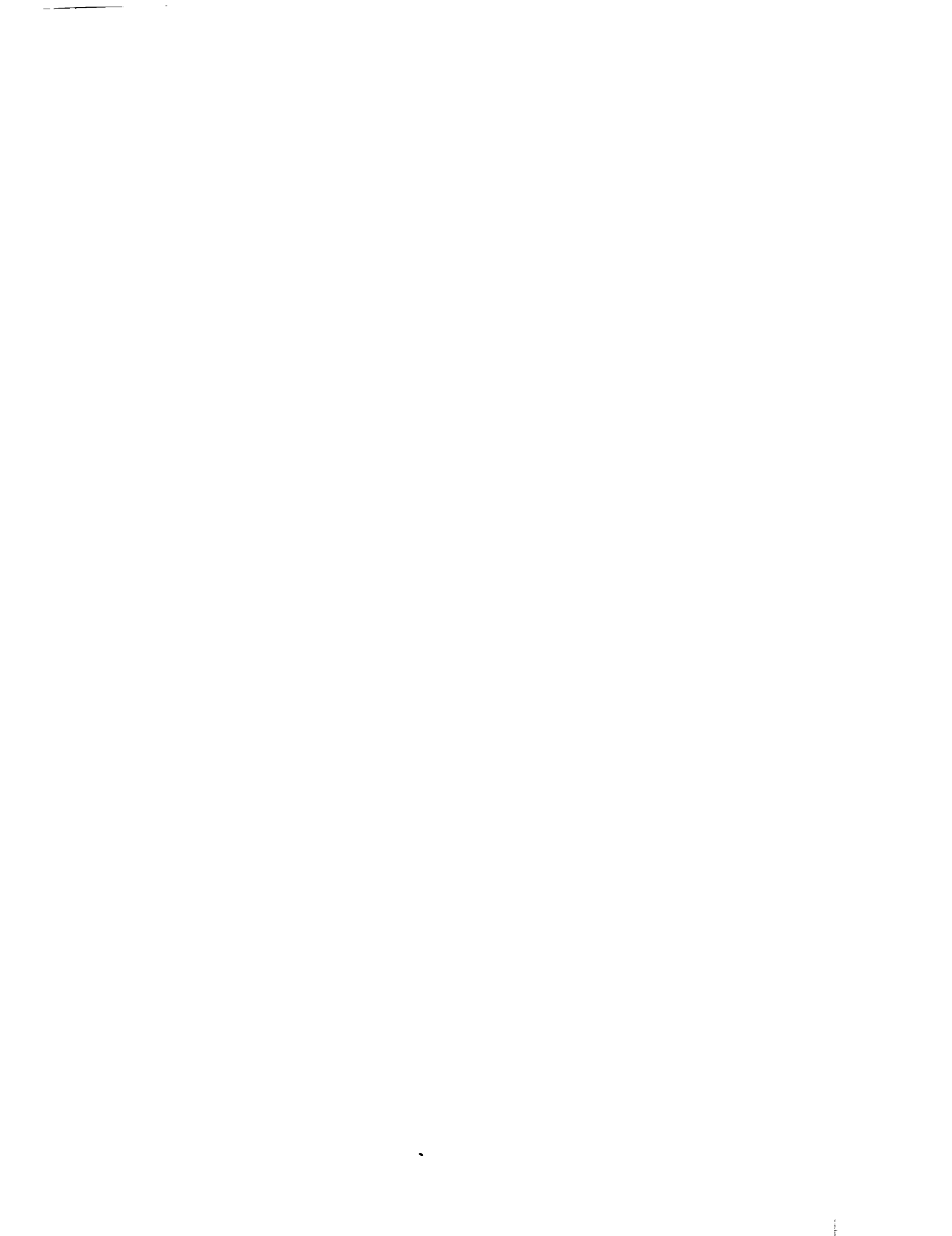
Computationally Efficient Multibody Simulations

Jayant Ramakrishnan
and
Manoj Kumar

Dynacs Engineering Company, Inc.
34650 US Hwy 19 North
Suite 301
Palm Harbor, FL 34684

Abstract

Computationally efficient approaches to the solution of the dynamics of multibody systems are presented in this work. The computational efficiency is derived from both the algorithmic and implementation standpoint. Order(n) approaches provide a new formulation of the equations of motion eliminating the assembly and numerical inversion of a system mass matrix as required by conventional algorithms. Computational efficiency is also gained in the implementation phase by the symbolic processing and parallel implementation of these equations. Comparison of this algorithm with existing multibody simulation programs illustrates the increased computational efficiency.

1 Introduction

Current multi-link mechanism control systems are based on inverse kinematic approaches. These approaches are used primarily because of the complexity and computational cost associated with the solution of the dynamics of such systems. Typical systems include robotic manipulators and mobile station servicing modules. In real-time control applications, a need exists for highly efficient dynamics solution algorithms (as opposed to kinematic) that will make the dynamic control of these mechanisms possible. The evolution of the formulation algorithm and the numerical solution methodology over the past decade to accomplish real-time control objectives is now presented.

TREETOPS developed in the mid-eighties was based on the minimum dimension formulation of the multibody equations of motion. Originally developed for bodies in a tree topology, kinematic relations were written for the sequence of joints in terms of relative coordinates. The dynamics of the multibody configuration were derived by projecting the translation and rotation equations along the generalized speeds. The generalized speeds were defined as the partial derivative of the expressions for body j translation and rotational velocities with respect to the degrees of freedom [1]. The algorithm resulted in a mass matrix of order(n) where (n) is the number of degrees of freedom. As the complexity of the multibody systems increased, the computational cost associated with this approach became prohibitively large (order of n^3).

The numerical order(n) approach was proposed in 1988 as a solution to the prohibitively high computational cost associated with the n^3 algorithms. Developed initially for chains of rigid bodies, the method was later extended to flexible bodies. The equations of motion are again formulated in minimum dimension (by the elimination of the non-working constraint forces) but now a frontal and back substitution approach is used. The inertia and active forces are shifted inboard to the core body for the solution of the equations and then the procedure is reversed to obtain outboard body variables. This frontal part and backsubstitution part result in the computational savings through inversions of mass matrices of much smaller dimension than n, the order of the system.

Symbolic processing of equations was the next step towards higher efficiency. A generic equation file was used to provide the inputs to a symbolic processor which eliminated unnecessary computations and generated a *configuration specific* simulation code. By parsing, layering and simplifying equations, an order of magnitude improvement over numerical implementation was achieved.

In 1990 , parallel implementation of the multibody dynamics algorithm was attempted on four Intel 860 chips connected to a host IRIS workstation. In the verification runs, for the class of problems tested (Large Space Structures, Space Station), a speed-up of more than two orders of magnitude was obtained.

The current efforts in this area are focusing on bringing this technology to fruition by refining and automating the implementation procedure.

556

Additionally, graphical user interfaces based on X-windows are being developed for pre and post processing. A symbolic programming language that supports a whole family of entities (partioned matrix operations, vector operations, etc.) is being developed to support the quick and painless generation of symbolic code for a variety of engineering applications. The concept behind these technology thrust areas is presented in this paper.

The paper is organized as follows. A flavor of the Order(n) approach is first presented. This is followed by a section on symbolic code generation. Issues and our past experience with the implementation of equations on a parallel hardware platform are then presented. Some of the practical problems solved using these simulations and performance comparisons are then presented followed by conclusions.

2 Algorithm Formulation

A multibody dynamic system is characterized by several bodies interconnected by joints that permit relative motion across them. Robots and space-craft with articulated appendages such as solar arrays are typical examples for such systems. The first step in the study of such systems is the derivation of the equations of motion.

Early approaches to the dynamics formulation for multibody systems required the inversion of the system mass matrix for every integration step. Since the inversion of an $n \times n$ matrix involves operations of the Order(n^3), these are called Order(n^3) approaches. As the number of degrees of freedom (DOF) increases, this matrix inversion, for every integration step, becomes computationally expensive.

An Order (n) algorithm - so called because the computational burden increases only linearly with the number of bodies - presented earlier in [2] for systems containing rigid bodies demonstrated the achievable computational efficiency. Such an algorithm is attractive especially in on-line control schemes that consider system dynamics. The algorithm was extended in [3] systems containing flexible bodies.

2.1 System Description

A multibody system in a topological tree is shown in Figure 1. Body 1 is an arbitrarily selected reference body assumed to be connected to an imaginary
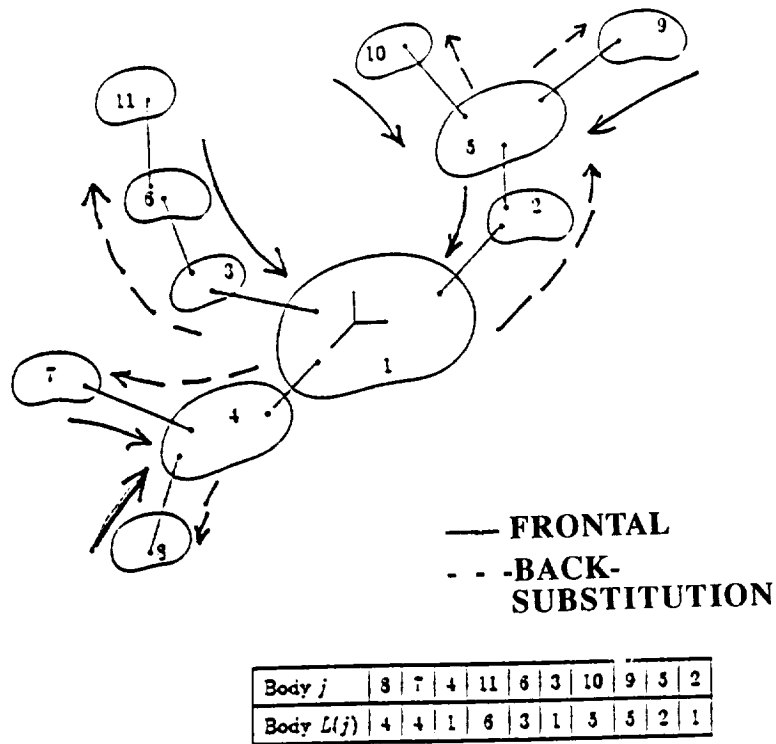
Figure 1: General Tree Configuration and Body Pair Definition

Body j	8	7	4	11	6	3	10	9	5	2
Body $L(j)$	4	4	1	6	3	1	5	5	2	1

inertially fixed body, numbered 0. For any other Body j, Body $L(j)$ is the adjacent body leading inward to Body 0 (or to the core body, Body 1). Body $L(j)$ is then defined as the body directly inboard of Body j. A kinematic joint between the body pair j and $L(j)$ allows relative motion between these bodies. Let NT_j and NR_j denote the number of translational and rotational DOF at j^{th} hinge, respectively.

2.2 Mathematical Formulation

The equations of motion are derived via Kane's method. The formulation and the corresponding solution algorithm are based on the kinematic relationships between body pairs j and $L(j)$. A joint between these bodies is defined between the q node on body j and the p node on body $L(j)$. Referring to Figure 2, we proceed as follows. The vector locating an elemental mass dm on Body j, in the inertial frame, is given by

$$\underline{R}_j = \underline{R}_f^{L(j)} + \underline{r}_p^{L(j)} + \underline{u}_p^{L(j)} + {}^{L(j)}\underline{y}^j - \left(\underline{r}_q^j + \underline{u}_q^j\right) + \underline{r}^j + \underline{u}^j \qquad (1)$$

where, $\underline{R}_f^j$ locates the body frame $\mathbb{b}_j$, $\underline{r}^j$ is a vector that defines the undeformed configuration of the elemental mass dm in $\mathbb{b}_j$, and $\underline{u}^j$ represents

558
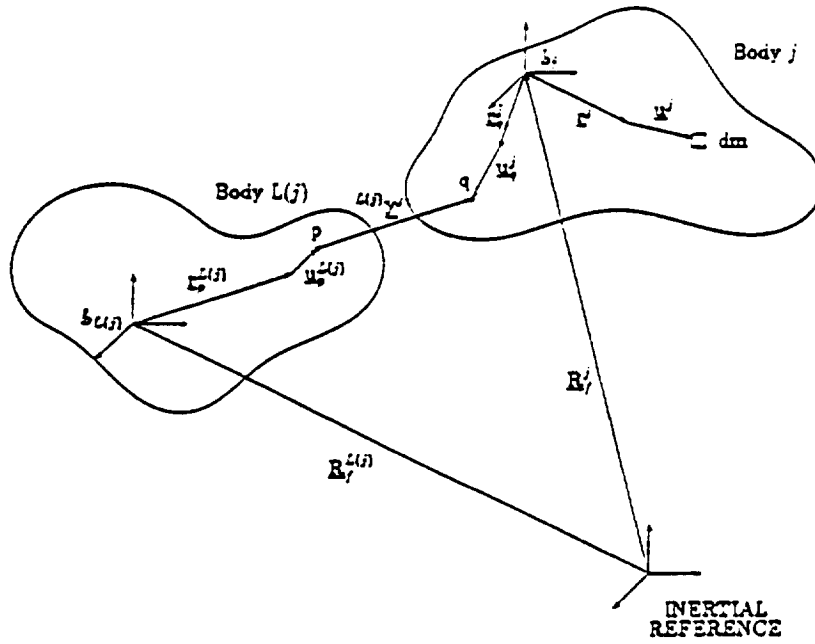
Figure 2: A Generic Hinge Between a Pair of Deformable Bodies

the elastic deformation (vector) experienced by dm. Using the method of assumed modes, the elastic deformation of body j can be expressed as the sum of the product of a set of assumed mode shape vectors $\underline{\phi}_\ell^j(\underline{r}^j)$ and their time-varying amplitudes $\eta_\ell^j(t)$ as:

$$\underline{u}^j = \sum_{\ell=1}^{NM_j} \underline{\phi}_\ell^j\left(\underline{r}^j\right) \eta_\ell^j(t) \tag{2}$$

where, NM_j denotes the number of retained modes for Body j.

The acceleration of the elemental mass dm is obtained by differentiating Eq.(1) twice with respect to time, as:

$$\underline{\ddot{R}}_j = \underline{\ddot{R}}_{L(j)}^j + \underline{\dot{\omega}}_{L(j)}^j \times \left(\underline{r}^j + \underline{u}^j\right) + {}^{L(j)}\underline{\overset{oo}{y}}{}^j + \underline{\overset{oo}{u}}{}^j - \underline{\overset{oo}{u}}{}_q^j$$
$$+ \left({}^{L(j)}\underline{\overset{o}{\omega}}{}_m^j - \underline{\overset{oo'}{u}}{}_q^j\right) \times \left(\underline{r}^j + \underline{u}^j - \underline{r}_q^j - \underline{u}_q^j\right) + \underline{\ddot{R}}_j^{rem} \tag{3}$$

$$\underline{\ddot{R}}_{L(j)}^j \triangleq \underline{\ddot{R}}_f^{L(j)} + \underline{\omega}^{L(j)} \times \left(\underline{r}_p^{L(j)} + \underline{u}_p^{L(j)} + {}^{L(j)}\underline{y}^j - \underline{r}_q^j - \underline{u}_q^j\right)$$
$$+ \underline{\overset{oo}{u}}{}_p^{L(j)} + \underline{\overset{oo'}{u}}{}_p^{L(j)} \times \left({}^{L(j)}\underline{y}^j - \underline{r}_q^j - \underline{u}_q^j\right), \tag{4}$$

$$\underline{\dot{\omega}}_{L(j)}^j \triangleq \underline{\dot{\omega}}^{L(j)} + \underline{\overset{oo'}{u}}{}_p^{L(j)} \tag{5}$$

559

and $\ddot{\underline{R}}_j^{rem}$ in Eq.(3) represents the remainder term that contains only centrifugal and coriolis accelerations. Solid and open dots represent differentiation in the inertial and local frames, respectively. Eqs.(4) and (5) provide the recursive expressions needed for the Order(n) algorithm.

Now consider a leaf body, Body j in the tree topology. The total relative degrees of freedom associated with this body are: $NT_j + NR_j + NM_j$. For the modal degrees of freedom associated with this body one can obtain the equations of motion as:

$$\left[\mathcal{M}_\eta^j\right]\left\{\ddot{\eta}^j\right\} + \left[M_\eta^{jL(j)}\right]\left\{\begin{array}{c} \mathbb{b}_j \\ \mathbb{b}_j \end{array}\right\} \cdot \left\{\begin{array}{c} \ddot{\underline{R}}_{L(j)}^j \\ \underline{\dot{\omega}}_{L(j)}^j \end{array}\right\} + \left[M_\eta^{jj}\right]\left\{\begin{array}{c} \{\ddot{y}^j\} \\ \{\ddot{\theta}^j\} \end{array}\right\} = \left\{f_{\eta^j}\right\} - \left\{f_{\eta^j}^*\right\}_R \tag{6}$$

The variables $\{\ddot{y}^j\}$ and $\left\{\ddot{\theta}^j\right\}$ denote the translational and rotational accelerations across joint j, and are of dimension NT_j and NR_j, respectively. The modal accelerations are denoted by $\{\ddot{\eta}^j\}$ which is of dimension NM_j. Similarly, the equations of motion associated with joint j^{th} DOF can be obtained, as:

$$\left[M_{y\theta}^{jL(j)}\right]\left\{\begin{array}{c} \mathbb{b}_j \\ \mathbb{b}_j \end{array}\right\} \cdot \left\{\begin{array}{c} \ddot{\underline{R}}_{L(j)}^j \\ \underline{\dot{\omega}}_{L(j)}^j \end{array}\right\} + \left[\mathcal{M}_{y\theta}^{jj}\right]\left\{\begin{array}{c} \{\ddot{y}^j\} \\ \{\ddot{\theta}^j\} \end{array}\right\} + \left[\mathcal{M}_\eta^j\right]\left\{\ddot{\eta}^j\right\}$$

$$= \left\{\begin{array}{c} \{f_y^j\} \\ \{f_\theta^j\} \end{array}\right\} - \left\{\begin{array}{c} \{f_{jy}^*\}_R \\ \{f_{j\theta}^*\}_R \end{array}\right\} \tag{7}$$

The right hand side terms $\left\{f_{\eta^j}\right\}$, $\{f_y^j\}$ and $\{f_\theta^j\}$ represent the active force contributions and terms with $*$ contain the remainder terms in Eqs. (6) and (7). The Order (n) solution algorithm, consisting of a Frontal part and a Backsubstitution part, is as follows:

2.3 Order (N) Algorithm

2.3.1 Frontal Part

Starting with the leaf bodies in the tree topology, first the modal accelerations $\{\ddot{\eta}^j\}$ are solved for, in terms of the body j joint accelerations, and inboard body accelerations $\ddot{\underline{R}}_{L(j)}^j$ and $\underline{\dot{\omega}}_{L(j)}^j$, using Eq.(6). The result is then substituted in Eq.(7), and then the joint accelerations are solved for, solely

in terms of $\underline{\ddot{R}}^j_{L(j)}$ and $\underline{\dot{\omega}}^j_{L(j)}$. The recursive relations in Eq.(4) are then utilized to shift the inertia and active forces of Body j in terms of its inboard body DOF and the procedure is carried out for all the bodies in the tree topology, until the core body is reached. The core body accelerations are then obtained in terms of external forces. This completes the Frontal part.

2.3.2 Backsubstitution

The steps involved in this part are the reverse of the steps outlined above. Once the corebody accelerations are obtained, Eq.(4) is utilized to obtain the outboard body accelerations and, using a modified form of Eq.(4), in which the modal accelerations $\{\ddot{\eta}^j\}$ are eliminated, we obtain the joint accelerations $\{\ddot{y}^j\}$ and $\{\ddot{\theta}^j\}$. The body modal accelerations $\{\ddot{\eta}^j\}$ are then obtained using Eq.(6). This procedure is continued for all the bodies in the topology, starting with the bodies directly outboard of the core body.

The Frontal and Backsubstitution steps outlined above are also shown in Figure 1. Note that the matrix inversions required in setting up the functional evaluations needed for integration in the simulation correspond to individual joint DOF and the modal DOF, and thus much smaller than the system mass matrix. This is because, the matrix $\left[m^j_\eta\right]$ is of order $NM_j \times NM_j$ and the mass matrix $\left[\mathcal{M}^{jj}_{y\theta}\right]$ associated with the joint DOF is at the most a 6×6 matrix. Thus, it can be seen that substantial computational savings can be achieved using this algorithm, because the system mass matrix is never explicitly inverted.

3 Symbolic Processing

Symbolic processing of the equations of motion of a multi-body structure can result in a substantially more efficient simulation [4]. The increase in efficiency is achieved through simplifications that are possible because of special configuration characteristics as well as arithmetic and algebraic simplifications. The symbolic processing module described here receives its input from three sources:

(a) A configuration data file which describes the multi-body system being simulated, its topology and properties.

(b) A flexible body data file which contains data relating to the flexibility properties of each flexible body in the system.
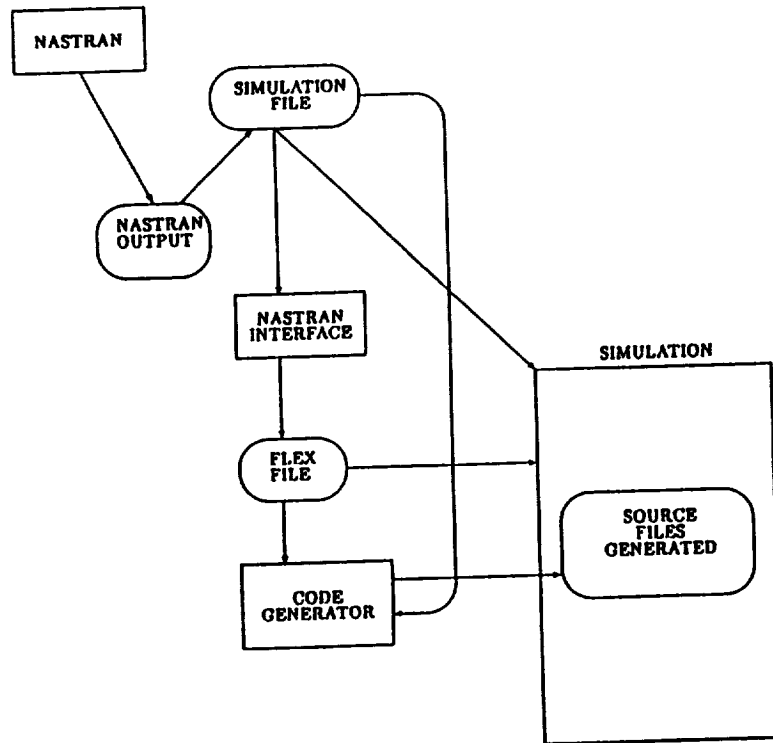
Figure 3: Context Diagram

(c) An equation file containing the equations of motion of a generic multi-flexible body system.

The output from the processor is a set of FORTRAN files containing an implementation of the specific set of equations of motion that are applicable to this multibody configuration. A context diagram is shown in Figure 3. The process involved in symbolically manipulating the equations of motion consists of the following sequence: parsing, layering, simplification, scalarization and code generation. These processes are described below.

3.1 Background

An equation consists of a left-hand-side and a right-hand-side. Equations can be represented in several forms. A convenient method of representation uses factors, terms and expressions. A factor is the smallest building block of an equation. The second building block of an equation is a term. A term may have a single factor as its element or a combination of factors separated by some operation between them. One or more of the terms when summed or multiplied together result in an expression. The left-hand-side of the equation consists of a single factor. The right-side of the equation is usually in the form of expression. If the factors are multiplied together to

make up a term, and the terms are summed together to form an expression, the equation is said to be in Sum of Products (SOP) form. If the factors are summed together to make up a term, and the terms are multiplied together to form an expression, the equation is said to be in Product of Sums (POS) form. The equations input to the symbolic manipulator are usually in matrix-vector form. The equations produced as a result of processing are in a scalar form. The different processing steps for each of the equations are parsing, reducing, layering, simplification and scalarization.

3.2   Parsing

Parsing is the translation of an algebraic expression from a form readable by humans to an internal form which can be easily manipulated by a computer. Once a set of equations representing a specific multibody model has been selected, they are "parsed" to generate the desired form of the equation so that they can be further processed.

The primary stage of the parsing process involves scanning each of the equation strings. The parser scans each of the equation strings and produces a stream of token representations. A brief description of the process of scanning and tokenization is contained below.

3.2.1   Scanning

The primary function of the scanning process is to read each input equation string and group the input characters into tokens. A token is basically an identifier. The approach used to scan the equation string could be either Top-Down, i.e., starting with the largest building block, or Bottom-Up, i.e., starting with the smallest building block. The method used here is the Top-Down method. The scanner first finds the first token (the LHS of the equation string). It inspects it to check for validity. An error message is sent if the token is not valid. Next the scanner looks for the separators of the LHS and the RHS.

Scanning of the RHS involving an expression is a slightly more complicated process. The scanner first starts out with the first expression. It then searches for the tokens that make up the expression, as well as the operators between the tokens. Once all the tokens have been parsed the scanner searches for the next expression in the list and carries out the same process until all of the expressions have been parsed. The next step is tokenizing.

3.2.2 Tokenizing

As the equation string is scanned, the tokens are inserted into their respective data structures. The information that needs to be stored for each of the tokens includes the names, their types (matrix, vector, scalar), dimensions, the pointer to the next token in the expression, and the operation between the two tokens. Once all the tokens defining the LHS and the RHS of an equation string have been created, they are linked together with the help of pointers to form the internal representation of the equation string.

3.3 Layering

This is a method by which a complex equation is split into a set of simpler equations. The method of splitting is selected in such a way that it results in the least number of operations (multiplies and adds) to be performed. An example given below demonstrates this process:

$$Z = A * B * C$$

where A is a matrix of size (1×2), B is a matrix of size (2×2) and C is a matrix of size (2×3).

The process of layering results in two equations

$$
\begin{aligned}
X_1 &= A * B \\
Z &= X_1 * C
\end{aligned}
$$

For the matrix sizes shown, if Z is computed explicitly without the use of intermediate variables, it would require 24 multiplies and 9 adds. Using the layering technique shown above, it would require only 10 multiplies and 5 adds.

3.4 Simplification

Once an equation is parsed and layered, it undergoes simplification to produce a minimal form of the equation. Simplification occurs at two stages. First the matrix-vector equation itself is simplified. Second the scalar equations describing the elements of the factor are simplified. The two stages are discussed in more detail below.

3.4.1 Matrix-Vector

The parser converts the matrix-vector algebraic equations to matrix-vector data structures. Simplifications of the equations involve operations such as the elimination of factors which are zero or have zero coefficients, identifying factors which are diagonal, etc. Basic rules of matrix-vector arithmetic follow.

3.4.2 Scalar

The scalar elements of each equation may allow simplification using the basic rules of scalar arithmetic. For space considerations, these rules are not presented here.

3.5 Scalarization

The process of generating the scalar elements of a matrix-vector equation is called scalarization. Scalarization of the factor that forms the left-hand-side of the equation results in multiple scalar equations, one for each element of that factor.

3.6 Code Generation

Finally, the parsed, layered, simplified and scalarized equation has to be converted into FORTRAN source code. This involves the conversion of the internal data structure into a string format, taking into account the various syntax rules of the FORTRAN language. This process is referred to as code generation.

4 Parallel Processing

The recursive nature of the Frontal solution algorithm makes it amenable to parallelization for a wide class of space structures. The availability of relatively inexpensive high-speed processors makes it possible to design and build parallel architectures at relatively low cost. A dedicated system with four Intel 860 processors was built to demonstrate the suitability of parallel architectures to the dynamics of multibody systems.
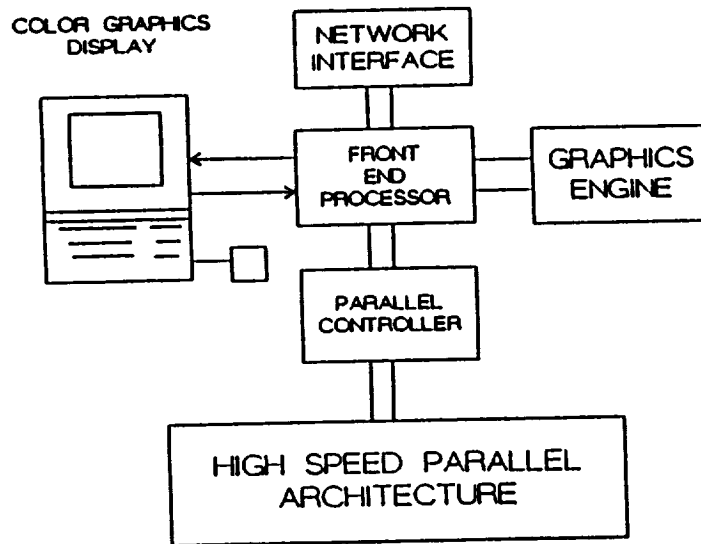
Figure 4: Hardware architecture

4.1 Architecture

The system consisted of a host machine on which all the graphical modeling, animation and all user interaction were performed and a dedicated parallel architecture on which the dynamics computations were performed. The host machine which acted as the front-end was a standalone SGI Personal Iris whereas the numeric intensive back-end consisted of a Sun SparcEngine hosting four Inter 860 processors on the VME bus (an individual 860 processor running at a 40 MHz rate is capable of a peak floating point performance of 80 MFLOPS). Details of the architecture are shown in Figure 4.

Communication between the processors was implemented using message passing. Message passing routines (send and receive) were implemented using memory shared over the VME bus.

4.2 Parallelization

The symbolic code generator discussed in the previous section was used to generate the parallelized software. The code generator read in the topology information and identified the segments of the topology which could be processed concurrently. The generated code reflected distribution of the

a-7.
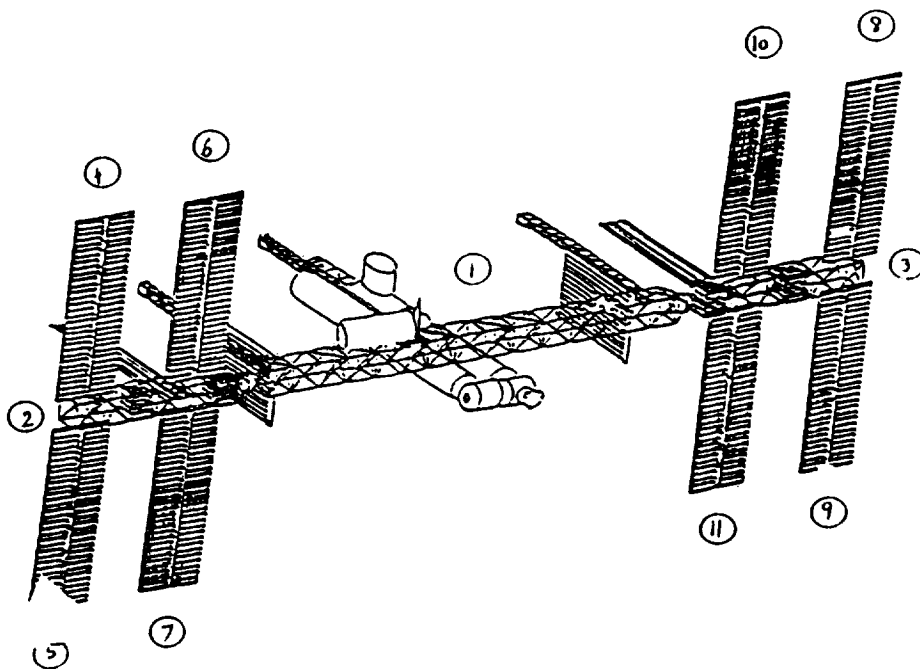
Figure 5: Assembly complete Space Station

code on the different processors and also included the messages to be passed between processors.

An 11 body (140 DOF) model of the Space Station has been chosen to demonstrate the parallelization process. Figure 5 shows the Assembly complete model of the Space Station as per the November 1989 model. This model of the Space Station has 8 photo-voltaic arrays, two power booms and the main truss (core body) making up the 11 body configuration. The 8 PV arrays are treated as leaf bodies and the frontal and kinematic computations (up to Eq. 7) for these bodies are computed simultaneously. This process is repeated recursively with the two power booms being processed simultaneously on two processors. Finally the core body accelerations are solved on a single processor and the backsubstitution is performed concurrently in the reverse sequence. The division of the frontal computations on to the four processors is shown in Figure 6.

5 Results

There are two sets of comparison results that are presented in this section. The first set is for rigid 7 body models of the Space Station and the second

Figure 6: Division of computational load

set is for flexible 11 body models of the Station.
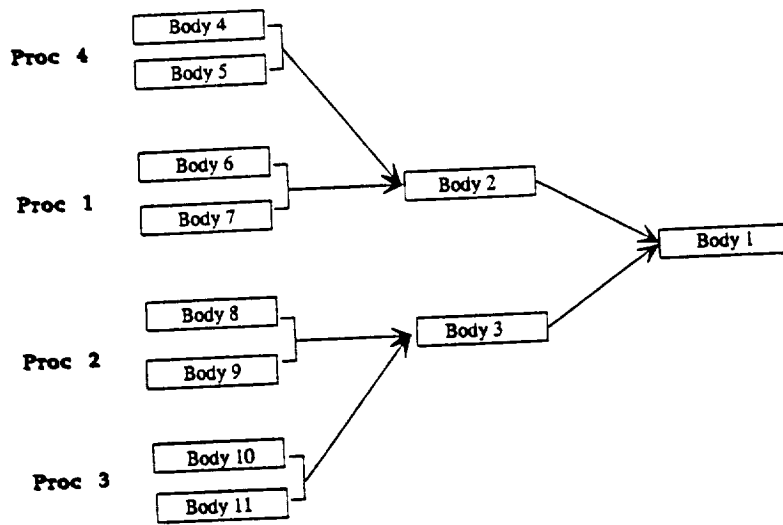
The 7 body model of the Space Station was integrated with the integrated Space Station Attitude Control System (SS-ACS) and several simulations were performed with varying degrees of freedom. This comparison primarily highlights the performance of the frontal solution algorithm discussed in this paper with Kane's approach as used in TREETOPS. The comparison results are presented in Figure 7.

The 11 flexible body (140 DOF) model of the Assembly complete Space Station has been used here to demonstrate the performance gain by the use of computationally efficient algorithms in combination with dedicated high speed parallel hardware. The dynamic model of the Space Station was combined with the baseline integrated SS-ACS. All the component modes in the bandwidth of the controller were retained. (The controller was running at 5 Hz whereas the highest component mode used was at 10 Hz). For this case, a total of approximately 40000 lines of FORTRAN code were generated. The complete non-linear multibody simulation for the 140 DOF system was performed for a complete orbit (90 minutes) of simulation time.

The performance comparison of the dedicated parallel processing system for the flexible body case with other commercially available hardware
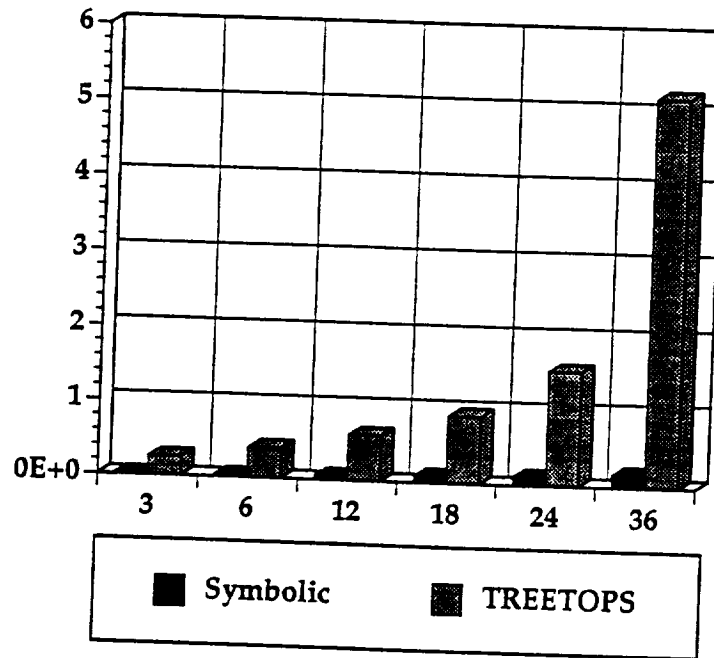
Figure 7: Rigid body comparisons

is shown below in Figure 8. Also shown are the comparisons to conventional approaches such as TREETOPS. These comparisons show that a simulation run that took over 315 hours using TREETOPS was completed in approximately 85 minutes, showing over two orders of magnitude improvement. This comparison is for the same problem with TREETOPS running on a single Intel 860 processor.

6 SUMMARY

The application of efficient algorithms to solve multibody dynamics problems has been presented in this work. While algorithms contribute to better solution strategies, efficient software implementation enhances the speed-up using these strategies further. In this work, the application of Order (n), symbolic processing approach on a parallel platform has been demonstrated. For the space station application considered in this work, a substantial performance improvement was obtained.

	Symbolic/O(n)	TREETOPS
System(4proc)	85	
System(1proc)	225	18900
SGI	675	
Sun-4	2025	
Vax-8850	2355	

Figure 8: Flexible body comparisons

References

[1] R. Singh, R. VanderVoort and P. Likins, *Dynamics of Flexible Bodies in a Tree Topology - A Computer Oriented Approach*, Journal of Guidance, Control and Dynamics, Vol. 8, No. 5, Sept-Oct 1985, pp. 584-590.

[2] R.P. Singh and B. Schubele, *Computationally Efficient Algorithm for Dynamics of Multi-Link Mechanisms*, AIAA GN&C Conference, Boston, MA, Aug. 1989.

[3] R.P. Singh, B. Schubele and S.S.K Tadikonda, *Efficient Dynamics Models for Flexible Multibody Systems Continuing Open Loop Topologies*, Accepted for presentation at the PACAM III Conference, Brazil, Jan 5-8, 1993.

[4] P.E. Nielan, *Efficient Computer Simulation of Motions of Multi-body Systems*, Dissertation, Stanford University, September 1986.

NUMERICAL METHODS FOR MULTIBODY SYSTEMS

Roland Glowinski
University of Houston
Houston, TX

Mahmoud G. Nasser
Lockheed Engineering & Sciences Company
Houston, TX

INTRODUCTION

This article gives a brief summary of some results obtained by Nasser (ref. 1) on modeling and simulation of inequality problems in multibody dynamics. In particular, the augmented Lagrangian method discussed here is applied to a constrained motion problem with impulsive inequality constraints. A fundamental characteristic of the multibody dynamics problem is the lack of global convexity of its Lagrangian. The problem is transformed into a convex analysis problem by localization (piecewise linearization), where the augmented Lagrangian has been successfully used [see Glowinski and Le Tallec (ref. 2); Glowinski, Lions, and Tremolières (ref. 3); and Fortin and Glowinski (ref. 4)]. A model test problem is considered, and a set of numerical experiments is presented (Figures 1 through 9).

MATHEMATICAL MODEL

Functional Context

$$X = H^m\left(0, T; \mathbf{R}^N\right),$$
(1)

$$H^m\left(0, T; \mathbf{R}^N\right) = \left\{v: v \in C^{m-1}\left([0, T]; \mathbf{R}^N\right), \frac{d^m v}{dt^m} \in L^2\left(0, T; \mathbf{R}^N\right)\right\},$$
(2)

$£$ is a Lagrangian function, J is a nonlinear functional, and K is a closed subset of X.

Find $\theta \in K$, for which J is stationary

$$K = K_1 \cap K_2,$$
(3)

$$K_1 = \left\{ v \in X : g_j(v(t)) = 0 \quad , \quad j = 1, 2, \ldots, k \quad \text{a.e. on } (0, T) \right\},$$
(4)

$$K_2 = \left\{ v \in X : g_j(v(t)) \leq 0 \quad , \quad j = k + 1, \ldots, k + l \quad \text{a.e. on } (0, T) \right\}.$$
(5)

The functions $g_i(v(t))$ are real valued; finally, J is defined by

$$J(v) = \int_0^T \pounds(v, \dot{v}, t) \, dt.$$
(6)

The stationarity of J at θ can be formulated as shown in the following section.

AUGMENTED LAGRANGIAN FORMULATION

Following a well-known technique [Glowinski and Le Tallec (ref. 2); Glowinski, Lions, and Tremolières (ref. 3); and Fortin and Glowinski (ref. 4)], we associate to (1)-(6) the following problem:

Find θ and λ, with $\theta \in K$ and $\lambda \in \Lambda$, for which the following augmented functional J_r is stationary:

$$J_r(v, \mu) = \int_0^T \pounds_r(v, \dot{v}, \mu) \, dt,$$
(7)

where

$$\pounds_r(v, \mu) = \pounds(v, v) + <\mu_1, G_1(v)> + <\mu_2, G_2(v)> + \frac{r}{2} \left[<G_1, G_1> + <G_2^+, G_2^+> \right],$$
(8)

$$G(v) = \left[g_1(v), g_2(v), \ldots, g_{k+l}(v) \right]^T,$$
(9)

572

$$G_1 = \left[g_1, g_2, \ldots, g_k \right]^T, \tag{10}$$

$$G_2^+ = \left[g_{k+1}^+, g_{k+2}^+, \ldots, g_{k+l}^+ \right]^T, \tag{11}$$

$$g_j^+ = \frac{1}{2} \left(g_j + \left| g_j \right| \right), \tag{12}$$

$$\Lambda = \left\{ \mu : \left\{ \mu_i \right\}_{i=1}^{k+l} \in L^2\left(0, T; \mathbf{R}^{k+l}\right) , \; \mu_i \in \mathbf{R} \; \text{if} \; i = 1, 2, \ldots, k \; , \; \mu_i \geq 0 \; \text{if} \; i = k+1, \ldots, k+l \right\}. \tag{13}$$

There exists a large amount of literature dealing with the case $K_2 = \varnothing$, which leads to index 3 differential algebraic equations. The case when K_2 is nonempty is considerably more difficult from a mathematical point of view, and hence fewer technical papers have been devoted to it. The methodology we shall present includes treatment of both cases.

SOLUTION ALGORITHMS

Given $\theta_k(t_n)$, $\dot\theta_k(t_n)$, and $\lambda_k(t_n)$, compute $\theta_{k+1}(t_n)$, $\dot\theta_{k+1}(t_n)$, and $\lambda_{k+1}(t_n)$ via the following:

$$\nabla_\theta J_r\left(\theta_{k+1}, \dot\theta_{k+1}, \lambda_k\right) = 0, \tag{14}$$

$$\lambda_{k+1} = P_\Lambda\left[\lambda_k + \rho\, G\left(\theta_{k+1}\left(t_n\right)\right)\right]; \tag{15}$$

P_Λ is the projection operator associated with the set Λ. For the choice of r and ρ, see Nasser (ref. 1) and Glowinski, Lions, and Tremolières (ref. 3).

LINEARIZATION AND TIME DISCRETIZATION

Following Nasser (ref. 1), we introduce the perturbation $\delta\theta$, $\delta\dot\theta$, $\delta\ddot\theta$ of θ, $\dot\theta$, $\ddot\theta$ to obtain the following system:

$$M(\theta)\,\delta\ddot\theta + C(\theta, \dot\theta)\,\delta\dot\theta + K(\theta, \dot\theta)\,\delta\theta + R(\theta)\,\delta\theta + S(\theta)\,\delta\theta = r.h.s.\,(\theta). \tag{16}$$

$$S = \sum_{i=1}^{k+l} \lambda_i \nabla_\theta^2 g_i(\theta) , \tag{17}$$

$$R = r \left\{ \sum_{i=1}^{k} \left(\nabla_\theta^2 g_i(\theta) \cdot g_i(\theta) + \left[\nabla_\theta g_i(\theta) \right]^2 \right) + \sum_{i=k+1}^{k+l} \left(\nabla_\theta^2 g_i(\theta) \cdot g_i(\theta) + \left[\nabla_\theta g_i^+(\theta) \right]^2 \right) \right\} , \tag{18}$$

$$r.h.s.\,(\theta) = - \left\{ \sum_{i=1}^{k} \lambda_i \nabla_\theta g_i(\theta) + \sum_{i=k+1}^{k+l} \lambda_i \nabla_\theta g_i^+(\theta) + r \left[\sum_{i=1}^{k} g_i(\theta) \cdot \nabla_\theta g_i(\theta) \right. \right.$$
$$\left. \left. + \sum_{i=k+1}^{k+l} g_i^+(\theta) \cdot \nabla_\theta g_i^+(\theta) \right] \right\} . \tag{19}$$

Taylor Series Expansion of θ and $\dot\theta$

Using Taylor series expansion for θ and $\dot\theta$, we get

$$\theta(t + \Delta t) = \theta(t) + \theta^{(1)}(t)\Delta t + \theta^{(2)}(t)\frac{\Delta t^2}{2} + \theta^{(3)}(t)\frac{\Delta t^3}{6} + \theta^{(4)}(t)\frac{\Delta t^4}{24} + O\left(\Delta t^5\right) , \tag{20}$$

$$\dot\theta(t + \Delta t) = \theta^{(1)}(t + \Delta t) = \theta^{(1)}(t) + \theta^{(2)}(t)\Delta t + \theta^{(3)}(t)\frac{\Delta t^2}{2} + \theta^{(4)}(t)\frac{\Delta t^3}{6} + O\left(\Delta t^4\right) , \tag{21}$$

where dots or superscripts denote the order of the derivatives.

Let

$$\delta\theta(t) = \theta(t + \Delta t) - \theta(t) , \tag{22}$$

$$\delta\dot\theta(t) = \dot\theta(t + \Delta t) - \dot\theta(t) , \tag{23}$$

$$\theta^{(3)}(t) \approx \frac{\theta^{(2)}(t + \Delta t) - \theta^{(2)}(t)}{\Delta t} , \tag{24}$$

574

$$\delta\ddot{\theta}(t) = \ddot{\theta}(t + \Delta t) - \ddot{\theta}(t), \tag{25}$$

$$\delta\theta^{(2)} = \theta^{(3)}(t)\Delta t. \tag{26}$$

Time Discretization of the Differential Equation (16)

Linear Acceleration Method

This is a widely used scheme in structural dynamics. It consists of assuming that terms involving $\theta^{(4)}(t)$ in equations (20) and (21) are negligible and that the acceleration between t and $t + \Delta t$ varies linearly [i.e., according to equation (26)]. Substituting equation (26) into equation (20), we get

$$\delta\ddot{\theta} = \frac{6}{\Delta t^2}\delta\theta(t) - \frac{6}{\Delta t}\dot{\theta}(t) - 3\ddot{\theta}(t). \tag{27}$$

Taking equations (26) and (27) into account in equation (21), we obtain

$$\delta\dot{\theta} = \frac{3}{\Delta t}\delta\theta(t) - 3\dot{\theta}(t) - \frac{\Delta t}{2}\ddot{\theta}(t). \tag{28}$$

Substituting equations (27) and (28) into equation (16), we get the following linear system (in $\delta\theta$):

$$A\delta\theta = b, \tag{29}$$

where

$$A = \frac{6}{\Delta t^2}M + \frac{3}{\Delta t}C + K + R + S, \tag{30}$$

$$b = \frac{6}{\Delta t}\dot{\theta}(t)M + 3M\ddot{\theta}(t) + 3C\dot{\theta}(t) + \frac{\Delta t}{2}\ddot{\theta}(t)C. \tag{31}$$

575

Higher Order Time Discretization Schemes

We assume that terms involving derivatives of order 5 and higher are negligible and that

$$\theta^{(3)}(t) = \frac{\theta^{(2)}(t + \Delta t) - \theta^{(2)}(t - \Delta t)}{2\Delta t}, \tag{32}$$

$$\theta^{(4)}(t) = \frac{\theta^{(2)}(t + \Delta t) - 2\theta^{(2)}(t) + \theta^{(2)}(t - \Delta t)}{\Delta t^2}, \tag{33}$$

and

$$\delta\ddot{\theta}(t) = \ddot{\theta}(t + \Delta t) - \ddot{\theta}(t). \tag{34}$$

Substituting equations (32), (33), and (34) into (20)-(21) and rearranging terms, we get (analogous to the linear acceleration method):

$$A^* \delta\theta = b^*, \tag{35}$$

where

$$A^* = \frac{8}{\Delta t^2} M + \frac{10}{3\Delta t} C + K + R + S, \tag{36}$$

$$b^* = -Md_1 - Cd_2, \tag{37}$$

$$d_1 = \frac{8}{\Delta t^2} \left[\frac{\Delta t^2}{24} \ddot{\theta}(t - \Delta t) - \dot{\theta}(t)\Delta t - \frac{13\Delta t^2}{24} \ddot{\theta}(t) \right], \tag{38}$$

$$d_2 = \frac{13\Delta t}{12} \left[\ddot{\theta}(t) - \frac{\Delta t}{12} \ddot{\theta}(t - \Delta t) + \frac{5\Delta t}{12} d_1 \right]. \tag{39}$$

A second algorithm is as follows: Given $\theta(t_n)$, $\dot{\theta}(t_n)$, $\ddot{\theta}(t_n)$, $\ddot{\theta}(t_{n-1})$, and $\lambda(t_n)$, update $\delta\theta(t_n)$, $\theta_{k+1}(t_n)$, and $\lambda_{k+1}(t_n)$ via

576

$$\delta\theta_k = A^{-1}b, \tag{40}$$

$$\lambda_{k+1} = P_{\Lambda^*}\left[\lambda_k + \rho G\left(\theta_{k+1}\right)\right], \tag{41}$$

where

$$\Lambda^* = \left\{\mu : \mu \in R^{k+l} \quad, \quad \mu_i \in R \quad, \quad i = 1,2,\ldots,k \quad, \quad \mu \geq 0 \quad, \quad i = k+1,\ldots,k+l\right\}. \tag{42}$$

In fact,

$$\Lambda = L^2\left(0,T;\Lambda^*\right). \tag{43}$$

Algorithm (40)-(41) can be used if A and b are replaced by A^* and b^*.

Other integration schemes, such as the ones in Dean, Glowinski, Kuo, and Nasser (ref. 5), may be used, also.

The acceleration $\ddot{\theta}(t)$ may be updated from the solution of equation (14) after convergence on $(\delta\theta(t),\lambda(t))$ has been achieved.

Choice of r and ρ

The parameters r, ρ, and Δt are the variables controlling the stability. For optimal choice of these parameters, refer to Glowinski and Le Tallec (ref. 2) and Glowinski, Lions, and Tremolières (ref. 3).

Using the projection method substantiated and systematically developed in Nasser (ref. 1), the equations of motion of the unconstrained system can be obtained in the following form:

$$M\,\delta\ddot{\theta} + C\,\delta\dot{\theta} + K\,\delta\theta = 0. \tag{44}$$

The projection method without piecewise linearization has been used by Keat (ref. 6) and is equivalent to the well-known Kane's method (ref. 7).

Consider a planar two-body system with a rigid obstacle, as shown in Figure 1. The Cartesian coordinates are related to the Lagrangian coordinates by

$$x_1 = a_1 \sin \theta_1, \tag{44}$$

$$x_2 = l \sin \theta_1 + a_2 \sin \theta_2, \tag{45}$$

$$y_1 = a_1 \cos \theta_1, \tag{46}$$

$$y_2 = l \cos \theta_1 + a_2 \cos \theta_2, \tag{47}$$

$$2\,KE = \left[m_1\left(\dot{x}_1 + \dot{y}_1 \right) + I_1 \dot{\theta}_1^2 \right] + \left[m_2\left(\dot{x}_2 + \dot{y}_2 \right) + I_2 \dot{\theta}_2^2 \right], \tag{48}$$

$$PE = m_1 g a_1 \left(1 - \cos \theta_1 \right) + m_2 g \left[l\left(1 - \cos \theta_1 \right) + a_2\left(1 - \cos \theta_2 \right) \right]. \tag{49}$$

The stationarity of the Lagrangian £ is given by

$$\left(I_1 + m_1 a_1 + m_2 l \right)\ddot{\theta}_1 + m_2 l a_2 \cos \left(\theta_2 - \theta_1 \right)\ddot{\theta}_2 - m_2 l a_2 \dot{\theta}_2^2 \sin \left(\theta_2 - \theta_1 \right) + m_1 g l \sin \theta_1$$
$$+ m_2 g l \sin \theta_1 = 0, \tag{50}$$

$$\left(I_2 + m_2 a_2 \right)\ddot{\theta}_2 + m_2 l a_2 \cos \left(\theta_2 - \theta_1 \right)\ddot{\theta}_1 - m_2 l a_2 \dot{\theta}_1^2 \sin \left(\theta_2 - \theta_1 \right) + m_2 g a_2 \sin \theta_2 = 0. \tag{51}$$

Data:
m_1 = mass of body 1
m_2 = mass of body 2
l = length
I_1 = moment inertia of body 1
I_2 = moment inertia of body 2
g = acceleration of gravity

Constraints:

$$g_1 = l_1 \sin \theta_1 + d \geq 0$$
$$g_2 = g_1 + l_2 \sin \theta_2 \geq 0$$

For the case $r = 0$, the augmented Lagrangian method reduces to the multiplier method used for the treatment of Coulomb or dry friction problems in Dean, Glowinski, Kuo, and Nasser (ref. 8). For the case $r \neq 0$, $\lambda = 0$, the scheme reduces to the well-known penalty method. The parameter r is the spring stiffness coefficient used in classical contact problems.

CONCLUSION

The augmented Lagrangian method successfully applies to contact/constrained motion problems of multibody dynamics. For constraints involving θ, the technique still applies; however, the details are rather lengthy and were omitted. The case of elastic bodies offers no mathematical difficulty except in the details, and the convergence is influenced by the spatial discretization largest mesh size. For further details, refer to Kikuchi and Oden (ref. 9) and Nasser (ref. 1).

ACKNOWLEDGMENTS

REFERENCES

1. Nasser, M. G.: Numerical Methods for Multibody Elastic Systems and Contact Problems. Ph.D. diss., University of Houston, Aug. 1992.

2. Glowinski, R.; and Le Tallec, P: *Augmented Lagrangian and Operator-Splitting Methods in Nonlinear Mechanics*. SIAM Studies in Applied Mathematics, vol. 9. Society for Industrial and Applied Mathematics, 1989.

3. Glowinski, R.; Lions, J. L.; and Tremolières, R: *Numerical Analysis of Variational Inequalities*. North-Holland, 1981.

4. Fortin, M.; and Glowinski, R., eds.: *Augmented Lagrangian Methods*. North-Holland, 1983.

5. Dean, E.; Glowinski, R.; Kuo, Y.; and Nasser, M. G.: On the Discretization of Some Second Order in Time Differential Equations: Applications to Nonlinear Wave Problems. *Proceedings of the NASA-UCLA Workshop on Computational Techniques in Identification and Control of Flexible Flight Structures*, Dec. 2-4, 1989.

6. Keat, J.: A Formulation for Simulating Deployment Dynamics of Large Space Structures. *Proceedings of the Workshop on Multibody Simulation*, Jet Propulsion Laboratory, JPLD-5190, vol. I, Apr. 15, 1988.

7. Kane, T. R.; and Levinson, D. A.: *Dynamics: Theory and Applications*. McGraw-Hill, 1985.

8. Dean, E.; Glowinski, R.; Kuo, Y.; and Nasser, M. G.: Multiplier Techniques for Some Dynamical Systems with Dry Friction. *C. R. Acad. Sci. Paris*, t. 314, série I, pp. 153-159, 1992.

9. Kikuchi, N.; and Oden, J. T.: *Contact Problems in Elasticity: A Study of Variational Inequalities and Finite Element Methods*. SIAM Studies in Applied Mathematics, vol. 8. Society for Industrial and Applied Mathematics, 1989.
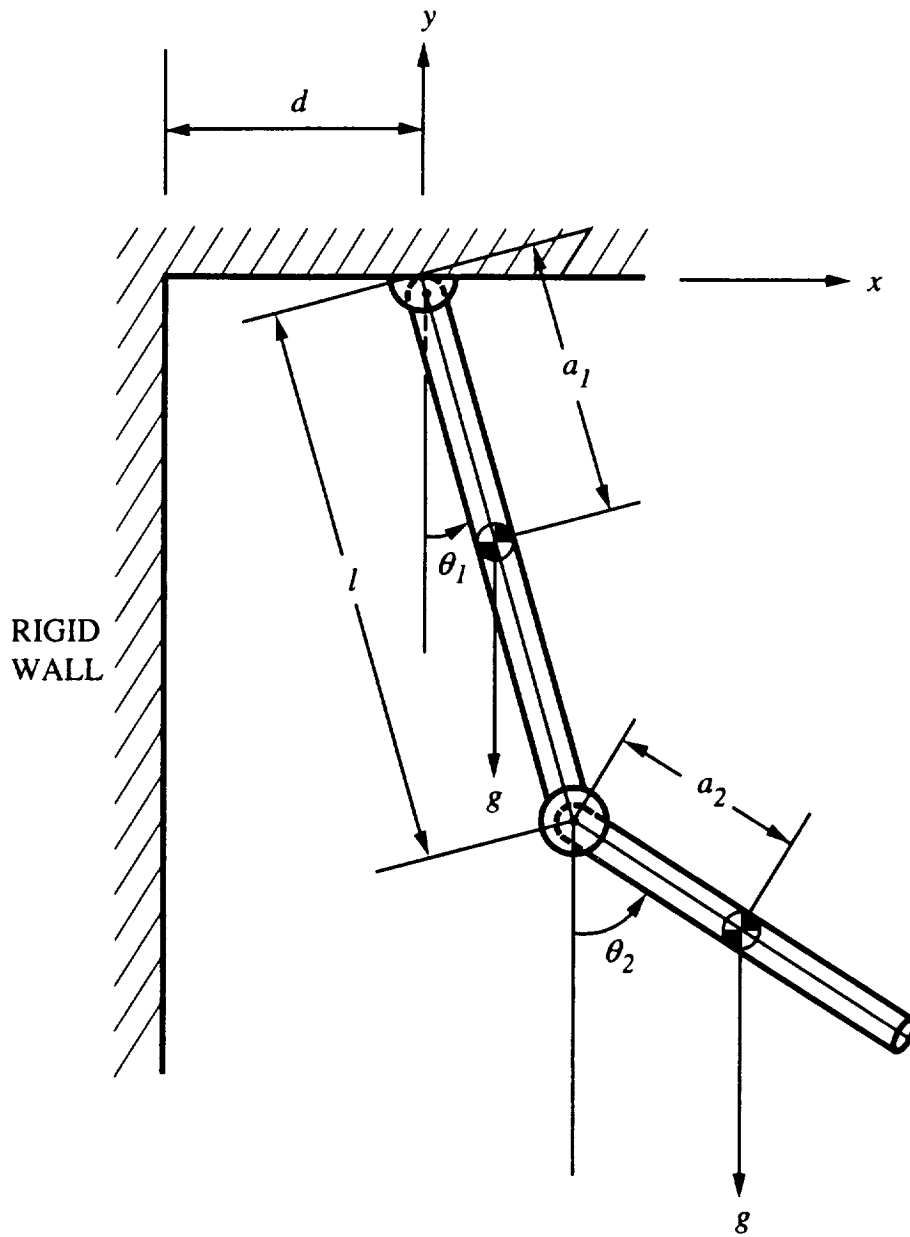
Figure 1. Planar two-body system.
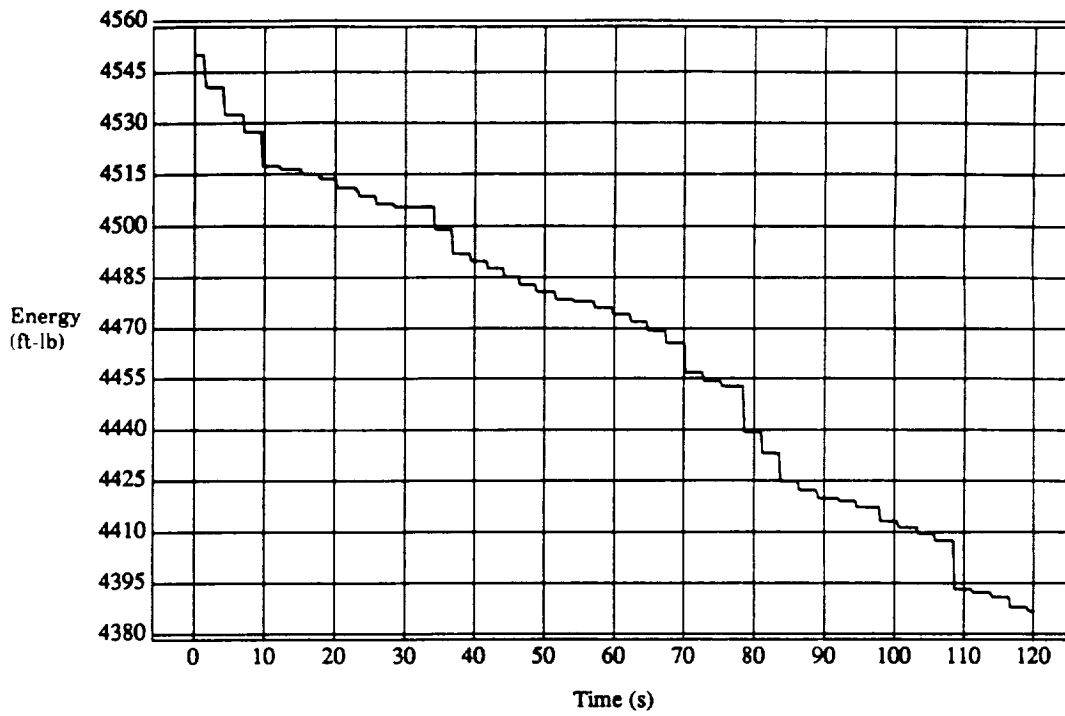
$$\theta_1(0) = \pi/3, \theta_2(0) = \pi/2$$

Figure 2. Multiplier method/high-order scheme – energy.
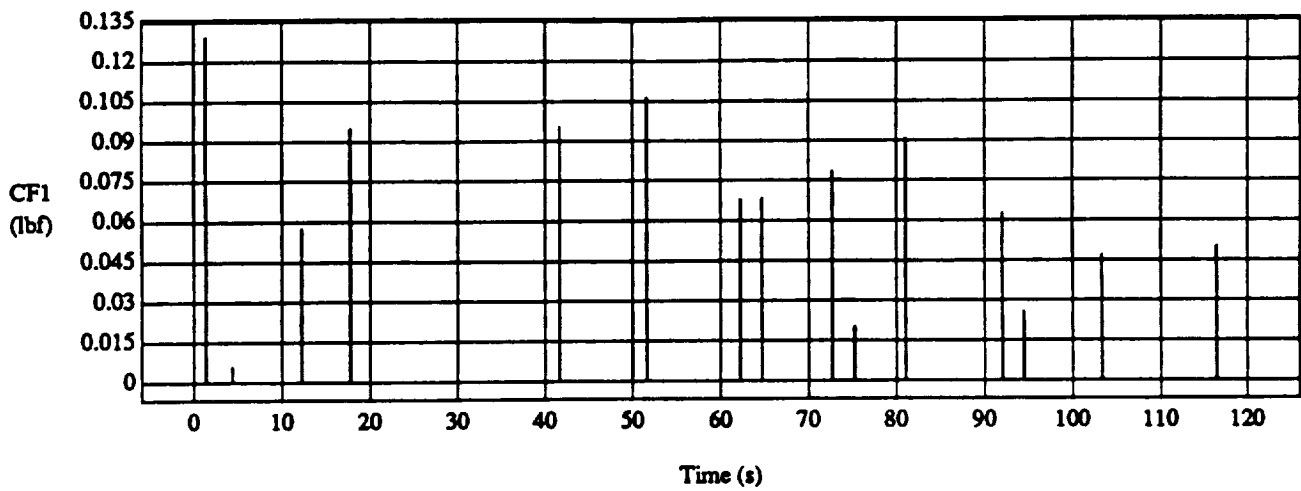
$$\theta_1(0) = \pi/3, \theta_2(0) = \pi/2$$

Figure 3. Multiplier method/high-order scheme – constraint force.

582
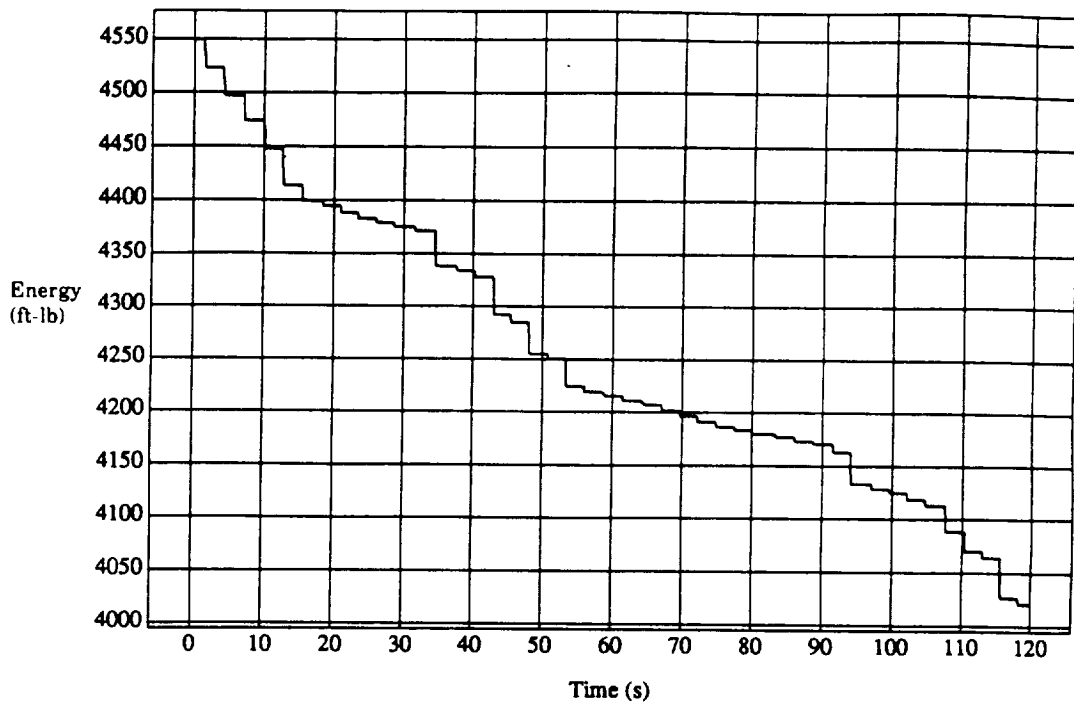
$\theta_1(0) = \pi/3, \theta_2(0) = \pi/2$

Figure 4. Augmented Lagrangian/high-order scheme – energy.

$\theta_1(0) = \pi/3, \theta_2(0) = \pi/2$

Figure 5. Augmented Lagrangian/high-order scheme – constraint force.

$\theta_1(0) = \pi/3, \theta_2(0) = \pi/2$

Figure 6. Penalty method/high-order scheme – energy.
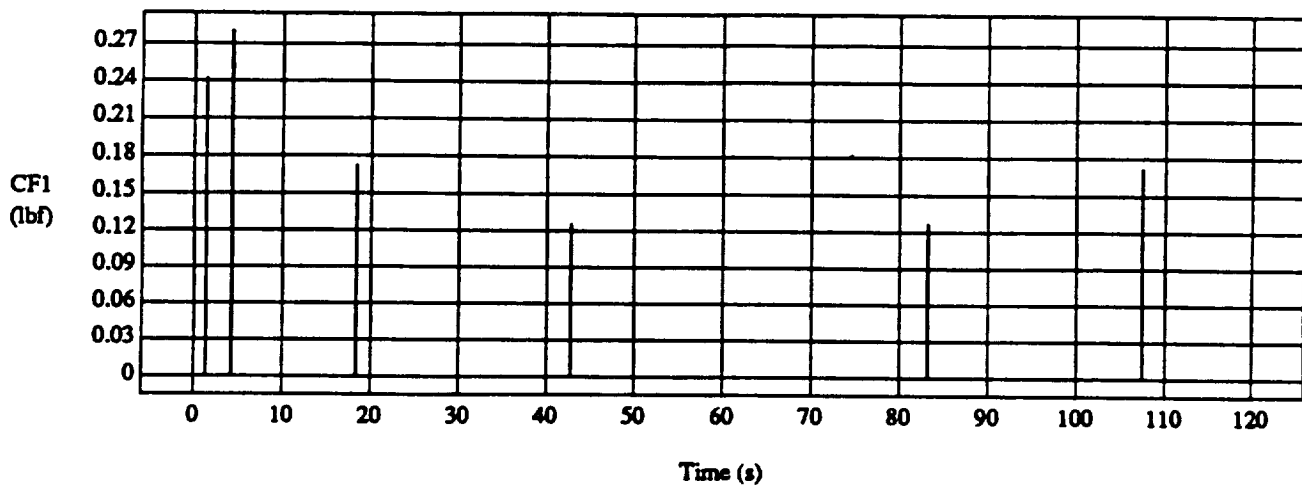

$\theta_1(0) = \pi/3, \theta_2(0) = \pi/2$

Figure 7. Penalty method/high-order scheme – constraint force.

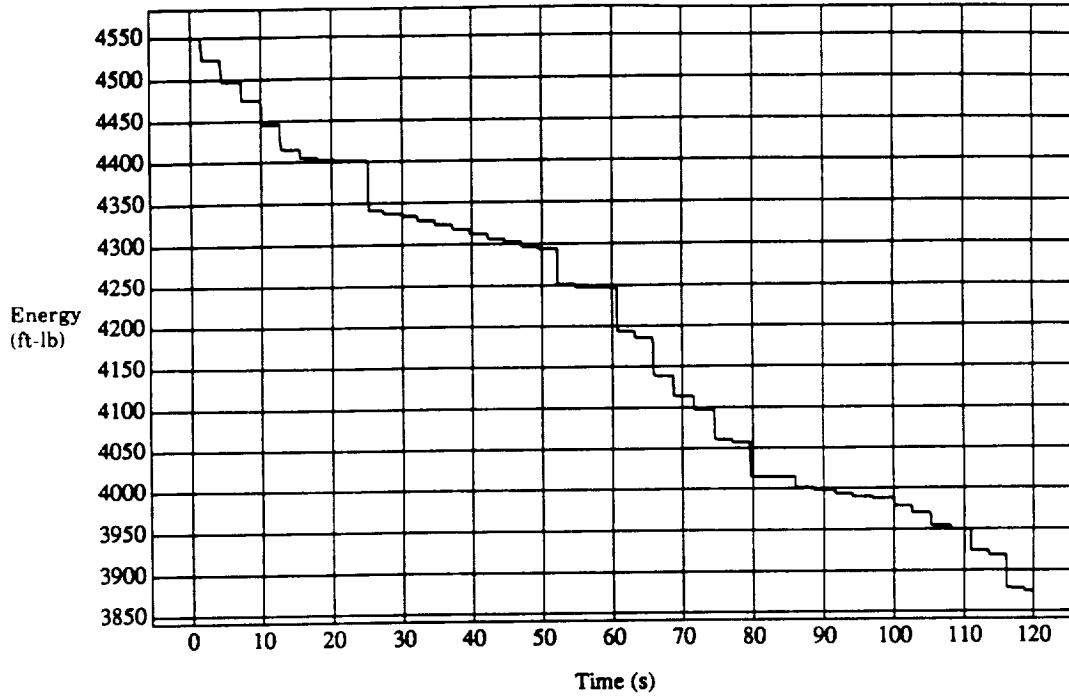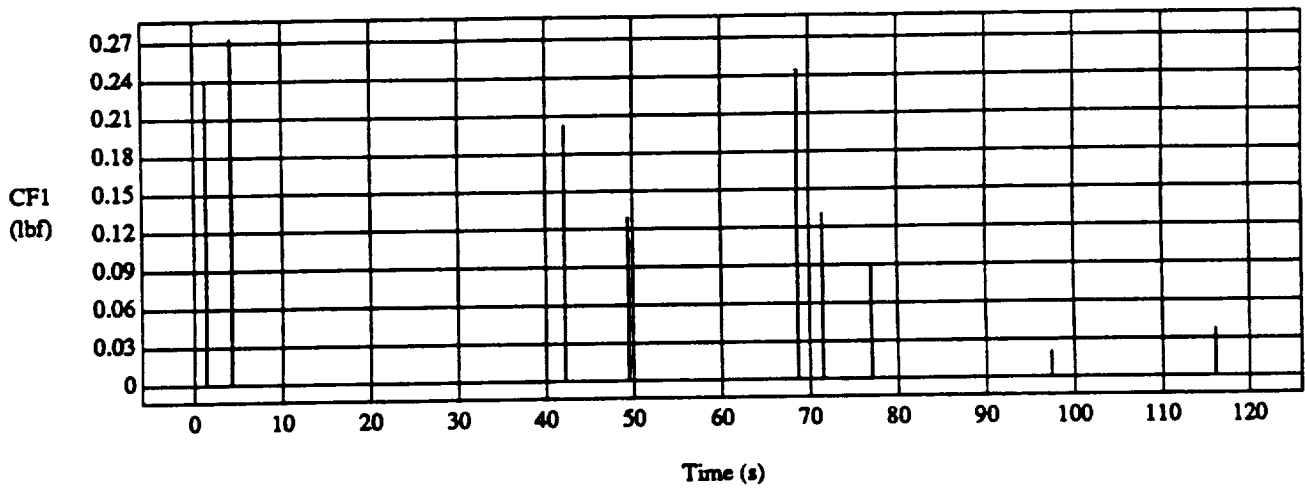584

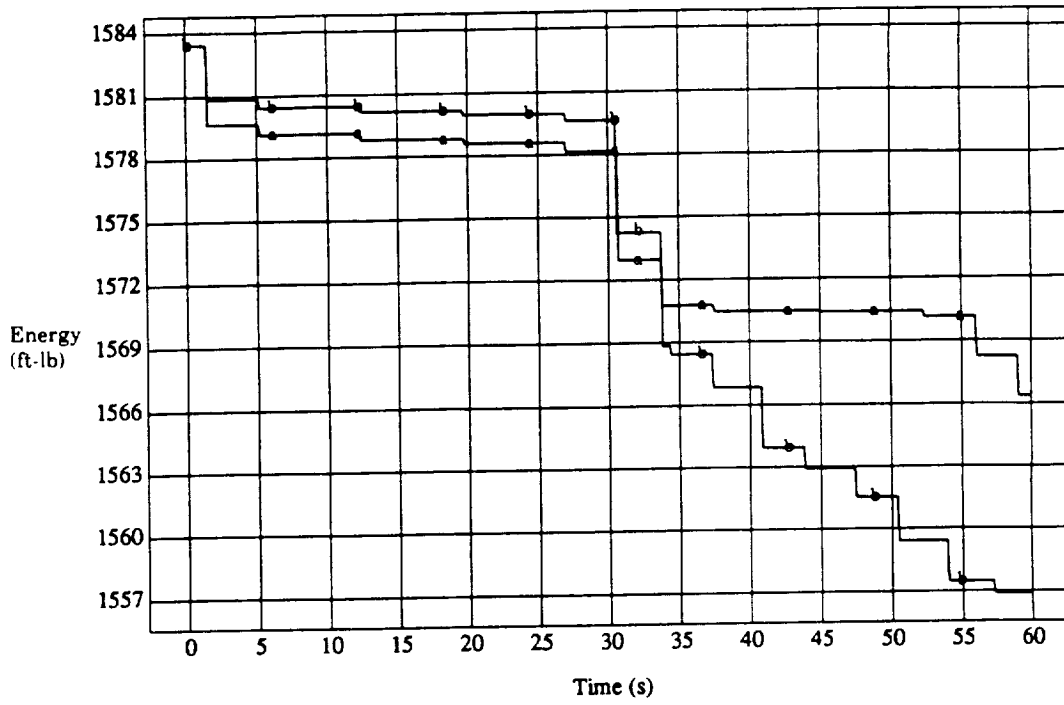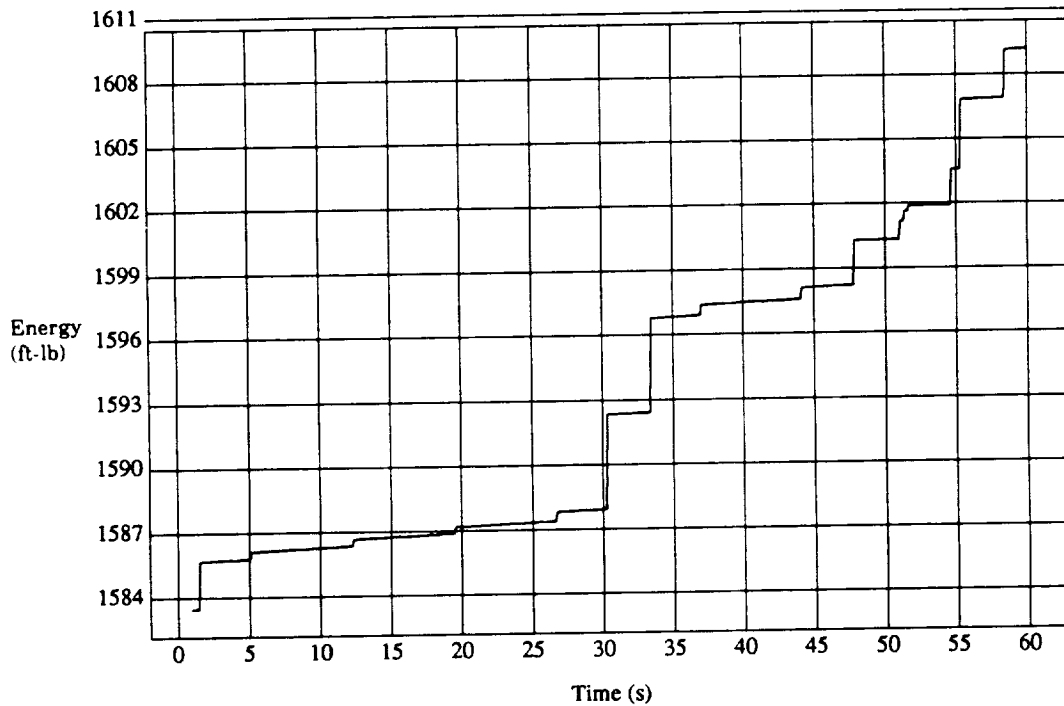$\theta_1(0) = \pi/3, \theta_2(0) = 0$

Figure 8. Augmented Lagrangian energy comparison for high-order scheme versus the linear acceleration method.

$\theta_1(0) = \pi/3, \theta_2(0) = 0$

Figure 9. Penalty/explicit Euler scheme – energy.

Software for Continuum Modeling of Controls-Structures Interactions

Larry Taylor
NASA Langley Research Center
Hampton, Virginia 23665

ABSTRACT

It is clear that computer software is needed to assist in the generation of the equations of motion for complex, flexible spacecraft. Daniel Poelaert of ESTEC has developed the software DISTEL with which he has modeled the structural dynamics for different satellites. He is interested in expanding the capabilities of DISTEL to include structural damping and control systems. Unfortunately, the software has not been released. The author has developed similar software, PDEMOD, which has been used to model the Spacecraft control Laboratory Experiment (SCOLE), the Solar Array Flight Experiment (SAFE), the Mini-MAST truss, and the LACE satellite. PDEMOD has been used also for optimal parameter estimation and integrated control-structures design. PDEMOD is also being extended to include structural damping and control systems which are imbedded into the same equations for the structural dynamics.

This paper will address the formulation of the equations for the structural dynamics of spacecraft structures which are constructed of a 3-dimensional arrangement of rigid bodies and flexible beam elements. Control system dynamics are imbedded into the same equations so that model order reduction approximations are not necessary. The input data consists of the physical data of the elements and the topological information describing how the elements are connected. PDEMOD (1) automatically assembles the equations of motion for the entire structural model, (2) calculates the modal frequencies, (3) calculates the mode shapes, (4) generates perspective views of the mode shapes, and (5) forms selected transfer functions.

The software PDEMOD continues to be developed to provide additional features to assist in analyzing and synthesizing control and structural systems for flexible spacecraft.

Issues in Modeling Composite Structure

Finite Element Modeling

- Excessive Complexity

- Parameter Estimation is Difficult

- Model Order Reduction Required for Control Analysis

Distributed Parameter Modeling

- Fewer Model Parameters

- Parameter Estimation Straightforward

- Closed-Loop Stability Analysis does not Require Order Reduction

The current practice of modeling flexible structures is to use finite element modeling. It is then necessary to dispose of most of the modal characteristics because of their inaccuracy. Damping is also defined in an ad hoc manner. When designing a control law for such a model it is necessary to iterate because of the order reduction process. Also the number of model parameters is too great to allow optimal parameter estimation.

The recommended alternative is to use distributed parameter modeling. It is not necessary to reduce the order of the model since the control system dynamics can be imbedded into the same equation which represent the structural dynamics. Damping can be included more accurately into the structural equations. The reduced number of model parameters enables optimum parameter estimation.

Current Practice

Input
Data

Test
Data

```
Finite
Element  ──────►──○──────── OK ────────┐
Modeling          │                    │
     ▲            │ ReDo               ▼
     │            ▼                
     │        ┌────────┐        ┌────────────┐
     └────────│ Manual │        │   Order    │
              │ Adjust │        │ Reduction  │
              └────────┘        └────────────┘
                                  ▲       │
                                  │       ▼
                      ┌──────────────┐
         Control  ◄───│   Control    │
         Design       │  Synthesis   │
                      └──────────────┘
```

P.D.E. Modeling

Input
Data

Test
Data

```
Partial Diff.
Equation  ──────►──○──────── OK ────────┐
Modeling          │                     │
     ▲            │ ReDo                ▼
     │            ▼                
     │        ┌─────────┐        ┌────────────┐
     └────────│ Optimal │        │   Imbed    │
              │ Adjust  │        │  Control   │
              └─────────┘        │  System    │
                                 └────────────┘
                                   ▲       │
                                   │       ▼
                      ┌──────────────┐
    Control/      ◄───│  Control/    │
    Structure         │  Structure   │
    Design            │  Optimize    │
                      └──────────────┘
```

589
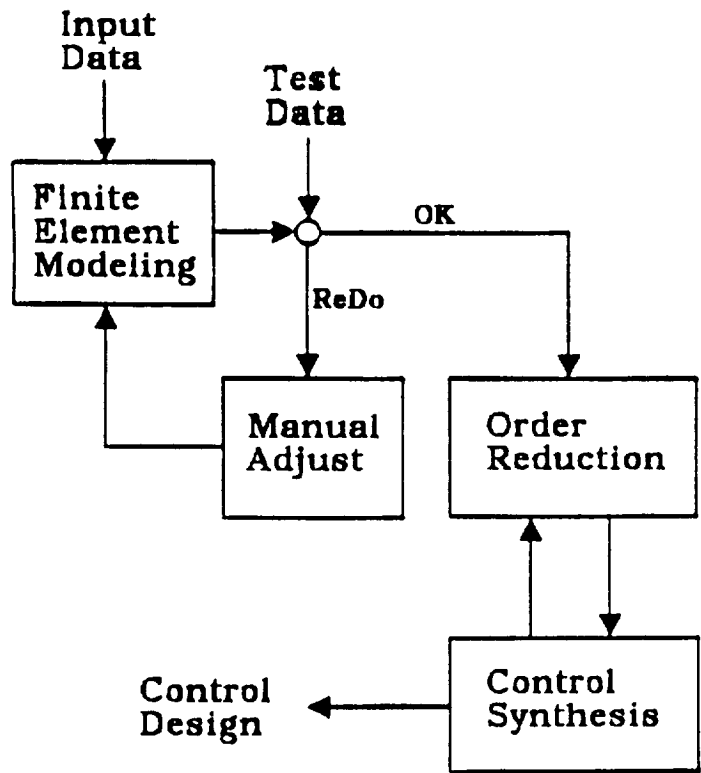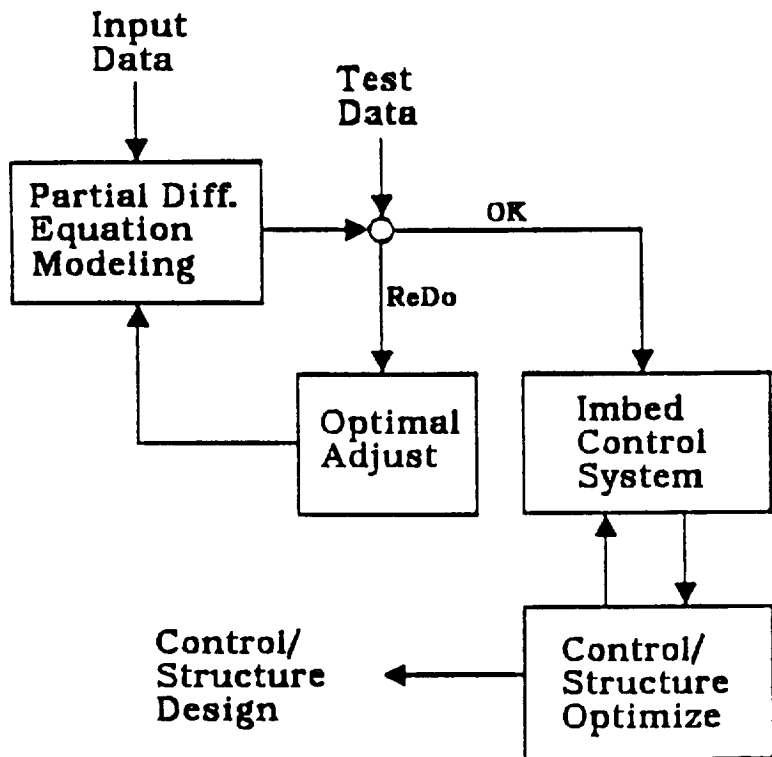
Hurdles for P.D.E. Modeling

- ## Ability to Generate P.D.E. Models
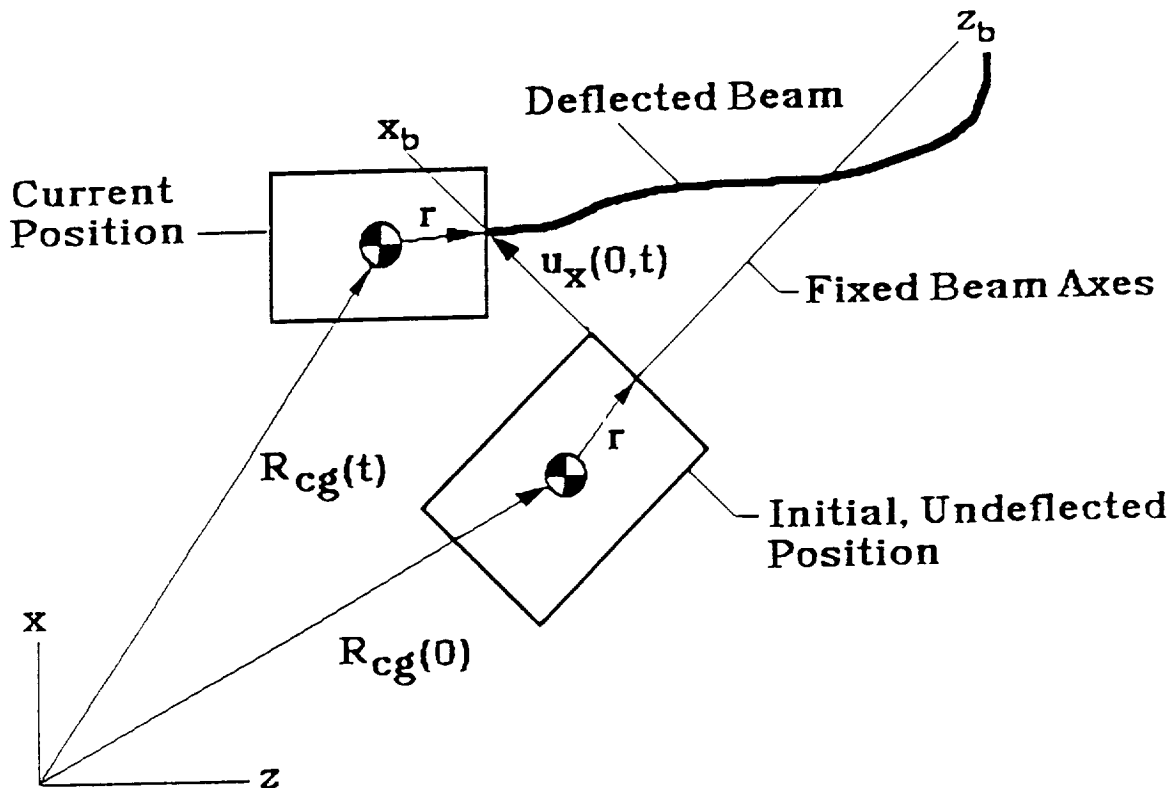 ### of Complex Structures

- ## Accuracy of P.D.E. Models for
  ### Different Types of Structure

- ## Ability to Imbed Control/Structural
  ### Dynamics

Before continuum or distributed parameter modeling can become a viable alternative to finite element modeling, it is necessary to develop software which will enable the modeling of complex structures. The software, PDEMOD, can provide that capability. The software continues to be developed to provide additional features.

It is also necessary to examine the accuracy of continuum models. The number of example configurations continues to grow. The accuracy can be equal to or better than that of finite element models. Eventually, it will be possible to use both approaches in the same software, thereby taking advantage of the features of both approaches.

It is valuable to control applications to imbed the control system dynamics into the same equations for the structural dynamics. The inaccuracies due to order reduction can then be avoided.

Current Position

x_b

Deflected Beam

z_b

r

$u_x(0,t)$

Fixed Beam Axes

$R_{cg}(t)$

r

Initial, Undeflected Position

x

$R_{cg}(0)$

z

The equations of motion are formulated in terms of the motion of bodies attached to the ends of flexible beam elements. The coordinates of a body are chosen to be those of one of the beams to which it is attached. The reference beam axes remain fixed. When the beam element deflects the body moves accordingly. Account must be taken of both linear and angular deflection, however.

The acceleration of the body is then related to the sum of the forces and moments that result from the attached beam elements.

SCHEMATIC

BODY #1

BEAM #3

BEAM #1

BODY #2

BEAM #2

BODY #3
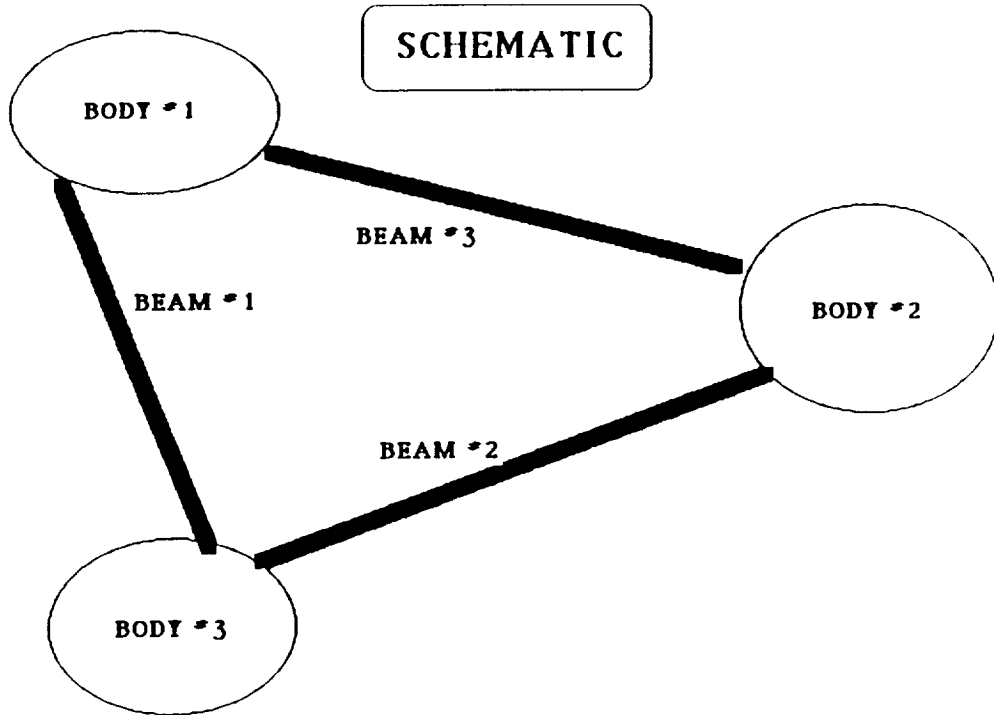
Three-dimensional configurations can
be modeled which are comprised of
rigid bodies and beams which deflect
laterally (two directions), longitudinally,
and twist.

Beam Model
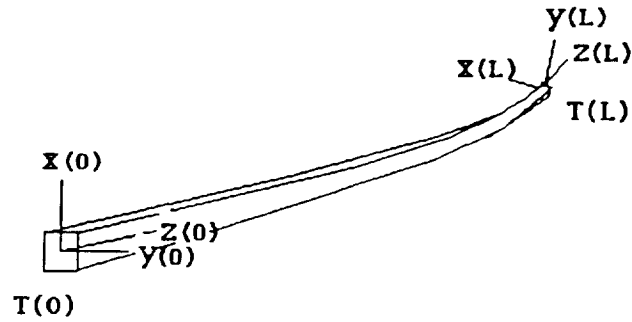
The Moments and Forces at (0) in Beam Axes are:

$$M_x = EI_y u_y''(0) \qquad\qquad F_x = EI_y u_y'''(0)$$

$$M_y = -EI_x u_x''(0) \qquad\qquad F_y = -EI_x u_x'''(0)$$

$$M_z = EI_\psi u_\psi'(0) \qquad\qquad F_z = EA_z u_z'(0)$$

The force and moment vectors are first expressed in terms of spatial derivatives of the deflection of the beam element. After noting that the beam deflections are functions of sinusoidal and hyperbolic functions and their coefficients, the linear deflection, angular deflection, and force and moment vectors are expressed in terms of a vector of the beam deflection coefficients.

593

Beam Deflection Function

$$u_x(z) = a_x + b_x z + A_x \sin(b_x z) + B_x \cos(b_x z)$$

$$+ C_x \sinh(b_x z) + D_x \cosh(b_x z)$$

$$u_y(z) = a_y + b_y z + A_y \sin(b_y z) + B_y \cos(b_y z)$$

$$+ C_y \sinh(b_y z) + D_y \cosh(b_y z)$$

$$u_\psi(z) = a_\psi + A_\psi \sin(b_\psi z) + B_\psi \cos(b_\psi z)$$

$$u_z(z) = a_z + A_z \sin(b_z z) + B_z \cos(b_z z)$$

The shape of the beam super element can be expressed in terms of sinusoidal and hyperbolic functions for lateral bending. The axial elongation and torsion deformations require only sinusoidal terms. This is true for general configurations which are comprised of such super elements and rigid bodies as well. The introduction of slight damping and dissipative control effects causes only slight errors, so that sinusoidal and hyperbolic functions remain useful approximations to the actual deformations.

594

$$u(z) = \begin{bmatrix} u_x(z) \\ u_y(z) \\ u_z(z) \end{bmatrix} \qquad u'(z) = \begin{bmatrix} -u_y'(z) \\ u_x'(z) \\ u_\psi(z) \end{bmatrix}$$

$$= Q_u(z) \begin{bmatrix} A_x \\ B_x \\ C_x \\ D_x \\ A_y \\ B_y \\ C_y \\ D_y \\ A_z \\ B_z \\ A_\psi \\ B_\psi \end{bmatrix} = Q_u(z)\theta \qquad = Q_{u'}(z) \begin{bmatrix} A_x \\ B_x \\ C_x \\ D_x \\ A_y \\ B_y \\ C_y \\ D_y \\ A_z \\ B_z \\ A_\psi \\ B_\psi \end{bmatrix}$$

The forces and moments in body axes are:

$$F_{beam} = P_F \begin{bmatrix} A_x \\ B_x \\ C_x \\ D_x \\ A_y \\ B_y \\ C_y \\ D_y \\ A_z \\ B_z \\ A_\psi \\ B_\psi \end{bmatrix} \qquad M_{beam} = P_M \begin{bmatrix} A_x \\ B_x \\ C_x \\ D_x \\ A_y \\ B_y \\ C_y \\ D_y \\ A_z \\ B_z \\ A_\psi \\ B_\psi \end{bmatrix}$$

It is useful to express the linear and angular deflections, force and moment as matrices multiplying a vector of the coeffecients of the sinusoidal and hyperbolic finctions. The equations of motion, transfer matrix, or the dynamic stiffness matrix can then be expressed in terms of these matrices.

A similar result is obtained for the other bending equation.

$$m\ddot{u}_y + EI_y u_y'''' = 0$$

$$(\beta_y L)^2 = \frac{\omega}{\sqrt{\dfrac{EI_y}{mL^4}}}$$

For the elongation equation:

$$m\ddot{u}_z + EA_z u_z'' = 0$$

$$\beta_z L = \frac{\omega}{\sqrt{\dfrac{EA_z}{mL^2}}}$$

Similarly for the torsion equation:

$$\rho I_\psi \ddot{u}_\psi + EI_\psi u_\psi'' = 0$$

$$\beta_\psi L = \frac{\omega}{\sqrt{\dfrac{EI_\psi}{\rho I_\psi L^2}}}$$

All of the "b" parameters have been related to the frequency, ω.

The beam equation relates the frequency to the β coefficients that appear in the sinusoidal and hyperbolic beam deflection functions. There are different relationships for bending in the x-z plane, bending in the y-z plane, elongation along the z axis, and twisting about the z axis.

The relationships are more complicated for the Timoshenko beam equation, for a constant axial force, and for attached, smeared appendages.

596

Structural Damping

Small levels of structural damping would not affect the mode shapes for zero damping. It should be possible to handle small levels of damping. The mode shapes would become complex and the eigen values would have both real and complex parts.

The beam equation might be:

$$m\ddot{u} - C\dot{u}'' + EIu'''' = 0$$

The string equation might be:

$$m\ddot{u} + C\dot{u}' - EAu'' = 0$$

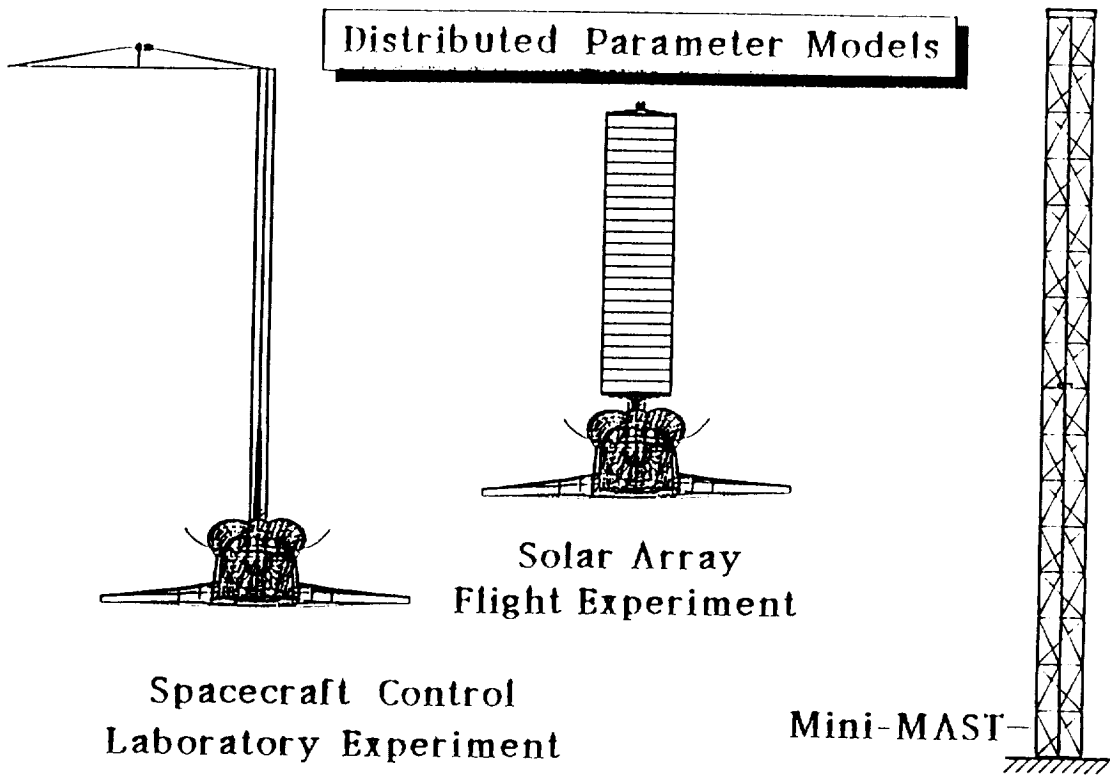The undamped mode shapes will be used as Galerkin approximate damped mode shapes.

PDEMOD

The continuum modeling software PDEMOD forms the total system equations from the input data of the mass, stiffness, damping, control and geometrical information. The dynamics of the total system is analyzed and particular responses and functional relationships can then be generated.
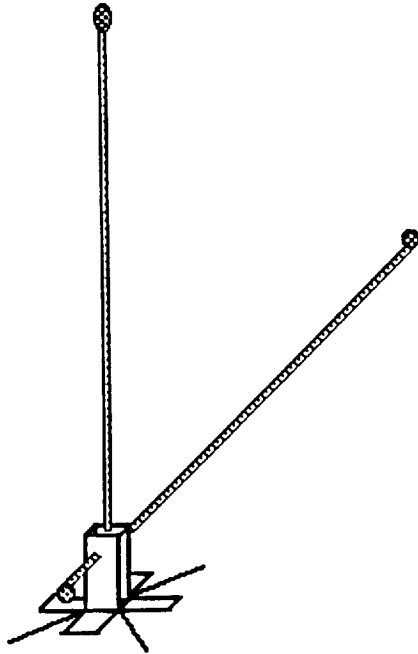
Distributed Parameter Models

Spacecraft Control
Laboratory Experiment

Solar Array
Flight Experiment

Mini-MAST

Model Accuracy

R.M.S. Error
in Frequency

Finite Element Model — 6.4%

Distributed Parameter Model —

4%

3.2%

1.7

1.6%

1.4%

.7%

0%

6
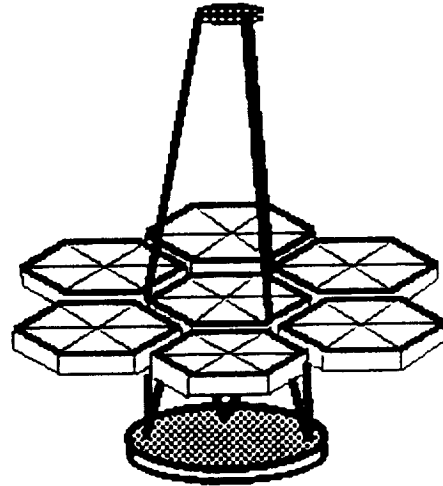
Frame #1   Frame #2   SCOLE   Solar Array   Mini-MAST Truss
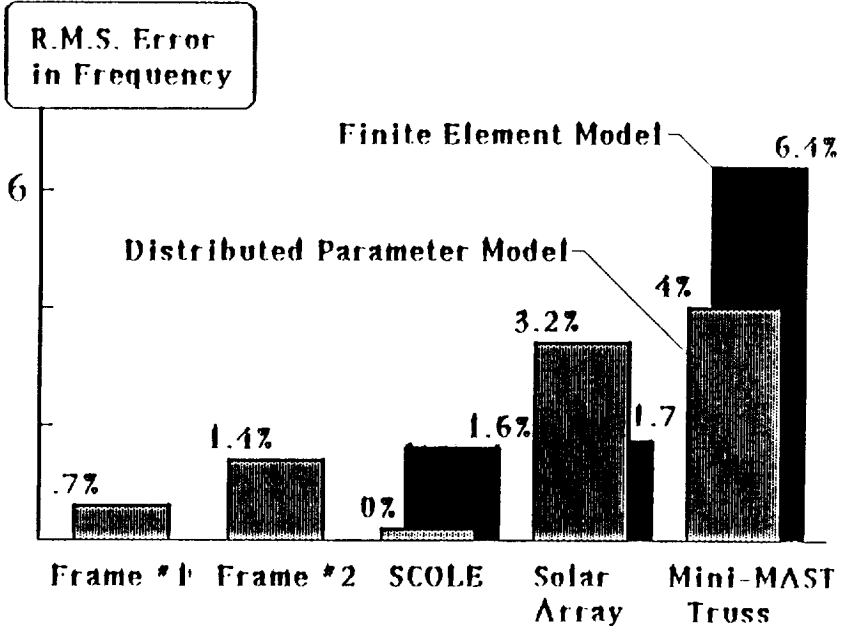
Distributed Parameter Models

LACE Satellite

**Multi-Hex
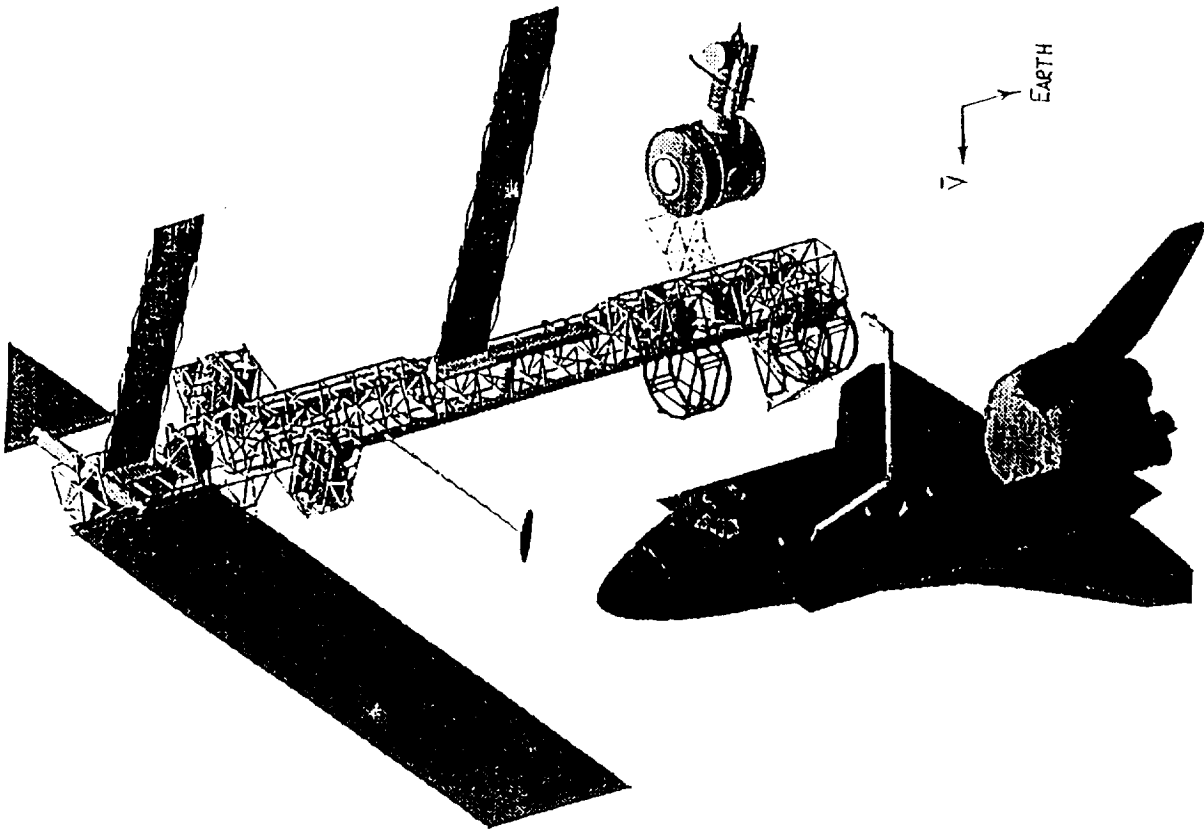Prototype Experiment**

Although a number of flexible spacecraft configurations have been successfully modeled, additional models of the LACE Satellite, the Multiple Hex Prototype Experiment and the Shuttle Remote Manipulating System are being generated. By modeling more complex configurations, the experience of continuum modeling and the capabilities of the PDEMOD software will continue to grow.

EARTH
↓V

Distributed Parameter Model

R. M. S. Control System
Flexible Joints

Flexible Booms

Flexible Station
Station Control Sys.

Rigid Shuttle
Shuttle Control System

601

Station Control

Space Station — Attach Point

R. M. S. Control

Wrist Gimbal — Outer Boom — Elbow Gimbal — Inner Boom — Shoulder Gimbal

Attach Point — Space Shuttle

Shuttle Control

$$\begin{pmatrix} u \\ u' \\ F \\ M \end{pmatrix}_{i+1} = \begin{pmatrix} \text{Transfer} \\ \text{Matrix, } U_i \end{pmatrix} \begin{pmatrix} u \\ u' \\ F \\ M \end{pmatrix}_i$$

$$\begin{pmatrix} u \\ u' \\ F \\ M \end{pmatrix}_{10} = U_9 U_8 U_7 U_6 U_5 U_4 U_3 U_2 U_1 \begin{pmatrix} u \\ u' \\ F \\ M \end{pmatrix}_1$$

The task of developing a continuum model of the Space Shuttle-RMS-Space Station Freedom assembly configurations brings together all of the modeling experience to date. Previous models of the Mini-MAST truss, the Spacecraft Control Laboratory Experiment, and the Solar Array Flight Experiment models will contribute to the complete model of Station assembly. Similarly, the tasks of estimating the model parameters are steps toward estimating the total model parameters of the Station assembly model. The success of this task should serve as an example of the power and usefulness of the distributed parameter modeling approach.

Concluding Remarks

- The use of Finite Element Modeling presents Obstacles to Parameter Estimation and Optimization

- Partial Differential Equation Modeling Facilitates Control/Structure Optimization

- P.D.E. Models have been Successfully Generated for
    1. Spacecraft Control Laboratory Experiment
    2. Solar Array Flight Experiment
    3. Mini-MAST Truss

- P.D.E. Model Accuracy is Competitive with Finite Element Models

- The Software PDEMOD Enables Modeling Complex, Flexible Spacecraft. PDEMOD Continues to be Developed, is being Applied to:
    1. Evolutionary Model Experiment
    2. Space Station Scaled Model
    3. LACE Satellite

REPORT DOCUMENTATION PAGE

Public reporting burden for this collection of information is estimated to average 1 hour per response, including the time for reviewing instructions, searching existing data sources, gathering and maintaining the data needed, and completing and reviewing the collection of information. Send comments regarding this burden estimate or any other aspect of this collection of information, including suggestions for reducing this burden, to Washington Headquarters Services, Directorate for Information Operations and Reports, 1215 Jefferson Davis Highway, Suite 1204, Arlington, VA 22202-4302, and to the Office of Management and Budget, Paperwork Reduction Project (0704-0188), Washington, DC 20503.

1. AGENCY USE ONLY *(Leave blank)*	2. REPORT DATE June 1994	3. REPORT TYPE AND DATES COVERED Conference Publication

4. TITLE AND SUBTITLE

NASA Workshop on Distributed Parameter Modeling and Control of Flexible Aerospace Systems

5. FUNDING NUMBERS

233-01-01-05

6. AUTHOR(S)

Virginia B. Marks and Claude R. Keckler, Compilers

7. PERFORMING ORGANIZATION NAME(S) AND ADDRESS(ES)

NASA Langley Research Center
Hampton, VA 23681-0001

8. PERFORMING ORGANIZATION REPORT NUMBER

L-17362

9. SPONSORING/MONITORING AGENCY NAME(S) AND ADDRESS(ES)

National Aeronautics and Space Administration
Washington, DC 20546-0001

10. SPONSORING/MONITORING AGENCY REPORT NUMBER

NASA CP-3242

11. SUPPLEMENTARY NOTES

12a. DISTRIBUTION/AVAILABILITY STATEMENT

Unclassified - Unlimited

Subject Categories 18, 31, and 66

12b. DISTRIBUTION CODE

13. ABSTRACT *(Maximum 200 words)*

Although significant advances have been made in modeling and controlling flexible systems, there remains a need for improvements in model accuracy and in control performance. The finite element models of flexible systems are unduly complex and are almost intractable to optimum parameter estimation for refinement using experimental data.

Distributed parameter or continuum modeling offers some advantages and some challenges in both modeling and control. Continuum models often result in a significantly reduced number of model parameters, thereby enabling optimum parameter estimation. The dynamic equations of motion of continuum models provide the advantage of allowing the embedding of the control system dynamics, thus forming a complete set of system dynamics. There is also increased insight provided by the continuum model approach.

The challenges of distributed parameter modeling include (1) overcoming the burden of the complexity of partial derivative equations, (2) developing software for model making and analysis, and (3) overcoming complacency.

14. SUBJECT TERMS

Modeling; Controlling flexible systems; Model accuracy; Control performance; Continuum modeling; Partial derivative equations

15. NUMBER OF PAGES

617

16. PRICE CODE

A99

17. SECURITY CLASSIFICATION OF REPORT Unclassified	18. SECURITY CLASSIFICATION OF THIS PAGE Unclassified	19. SECURITY CLASSIFICATION OF ABSTRACT Unclassified	20. LIMITATION OF ABSTRACT